Fall 12-15-2015

# Mineralogy and geochemistry of Late Archean and Paleoproterozoic granites and pegmatites in the Northern Penokean terrane of Marquette and Dickinson Counties, Michigan

Christopher M. Johnson
cmjohns6@uno.edu

Christopher M. Van Daalen
cmjohns6@uno.edu

# Mineralogy and geochemistry of Late Archean and Paleoproterozoic granites and pegmatites in the Northern Penokean terrane of Marquette and Dickinson Counties, Michigan

A Thesis

Submitted to the Graduate Faculty of the
University of New Orleans
in partial fulfillment of the
requirements for the degree of

Master of Science
In
Earth and Environmental Science

By
C. Mark "Leopold" Van Daalen
B.Sc. (Hons.), University of New Orleans, 2013
December, 2015

# ACKNOWLEDGEMENTS

I would like to express my profound gratitude to Dr. William Simmons, Mr. Alexander Falster, and Dr. Karen Webber for providing an unbelievable amount of opportunities to see many, many rocks! Thank you for pushing me to push myself. Thank you for your patience, guidance, and faith throughout this entire process. I will be forever grateful.

Thanks to the University of New Orleans Earth and Environmental Sciences department for funding and scholarships. Each and every professor had a hand in making this thesis possible.

Thanks very much to the $MP^2$ Research Lab and the Maine Gem and Mineral Museum for their quality analytical work and guidance with the data.

Thanks to Tom Buchholz, Dan Fountain, and the Yelsky Sisters. Without their help and permission, I would not have been able to have had access to many of the locations from which I gathered samples.

A heartfelt thanks to my office mates: Drew Boudreaux, Karen Marshal, Kimberly Simon, Kristen Camp, Leah Grassi, Myles Felch, Jon Guidry, and Sasha Kreinik. You guys are the best! Also, to the Unna Ibbers: Joe P. Frank, Elijah Adedeji, Trey Kramer, and Josh Flathers. Ikpikpuk! Thanks to Ms. Linda and Norman for their support over the years.

I would also like to thank my parents and family for their support and understanding. And to my Aunt who bought me my first book about rocks.

A very special thanks to Mr. Alexander Falster. Of all the names you have ever called me… Bruder is the one I cherish the most.

And last, but certainly not least, I would like to thank my husband, Nicholas Van Daalen. Every day I ask myself how I ever got so lucky as to have you in my life.

# Table of Contents

# LIST OF FIGURES

LIST OF TABLES

# ABSTRACT

This thesis focuses on mineralogy, geochemistry, and origin of eight pegmatites and two spatially associated granites of Late Archean and Paleoproterozoic ages located in Marquette and Dickinson Counties, Michigan. Biotite geochemistry reveals that both granites and all pegmatites are peraluminous and have an orogenic signature. However, bulk composition reveals the Humboldt granite is a peraluminous A-type granite and the Bell Creek granite is a peraluminous mix between I-, S-, and A-type granites. The Republic Mine pegmatite appears to be geochemically similar to the Bell Creek granite and Grizzly pegmatite. The Crockley pegmatite is genetically related to the Humboldt granite. The Groveland Mine, Sturgeon River, and Hwy69 pegmatites appear to be a product of the Peavy Pond Complex being contaminated with the Marquette Range Super Group. Contamination and anatexis have made classification of the granites and pegmatites problematic. The Grizzly should be classified as a primitive LCT-type even though this pegmatite lacks characteristic enrichment associated with LCT pegmatites. Mineralogical geochemistry reveals that the Republic Mine is relatively more primitive than other pegmatites and should be classified as a primitive Mixed-type pegmatite. Groveland Mine has mineralogy and geochemistry not normally associated with NYF-type pegmatites and should be classified as Mixed. The Crockley pegmatite should be classified as NYF-type with a primitive LCT overprint. Dolfin, Hwy69, Sturgeon River, and Black River pegmatites should be classified as Rare Element, REE, NYF-type, although the Black River has slight tantalum enrichment expressed in columbite group minerals.

*pegmatite; Groveland Mine; Republic Mine; gneiss domes; Penokean Orogeny; Humboldt; Bell Creek*

# INTRODUCTION

The geology of upper Michigan records a complex tectonic history of rifting, deposition, deformation, and metamorphism that extends across 3.5 billion years. Upper Michigan is unique in that five major stratigraphic units comprising this geologic history are exposed: 1) a 2.7 – 3.4 Ga Mesoarchean gneiss-amphibolite terrane (Southern Terrane), 2) a 2.7 – 2.9 Ga Neoarchean granite-greenstone belt (Northern Terrane), 3) 2.3 – 1.8 Ga Paleoproterozoic metasedimentary layers that include banded iron formations, 4) 1.8 Ga granites, interpreted to be intruded during the Penokean orogeny, and 5) the 1.85 Ga volcano-plutonic Wisconsin Magmatic Terrane (Tohver *et al*., 2007). This thesis focuses specifically on two granitic bodies and eight pegmatites of Late Archean and Paleoproterozoic ages in the Marquette and Dickinson counties, Michigan located in the Northern Penokean terrane between the Great Lakes Tectonic Zone to the north and the Niagara Fault to the south. Figure 1 shows the locations of the pegmatites within the migmatites of the Southern Terrane. They are clustered into a northern and a southern group. The northern group is spatially associated with two potentially genetically related plutons: the Humboldt granite and the Bell Creek granite. The southern group consists of the Sturgeon River, Groveland Mine, and Hwy69. These three pegmatites are spatially associated with the Peavy Pond Complex and may potentially be genetically related to this igneous intrusive complex.

The 2.6 Ga Bell Creek granite is the older of the two granites (Hoffman, 1987). It is genetically associated with the Bell Creek Gneiss (Tinkham & Marshak, 2004) and hosts the Grizzly pegmatite. The younger 1.8 Ga Humboldt granite is associated with the Penokean Orogeny (Holm, *et al*., 2001). The Crockley pegmatite, Republic Mine, Black River, and Dolfin

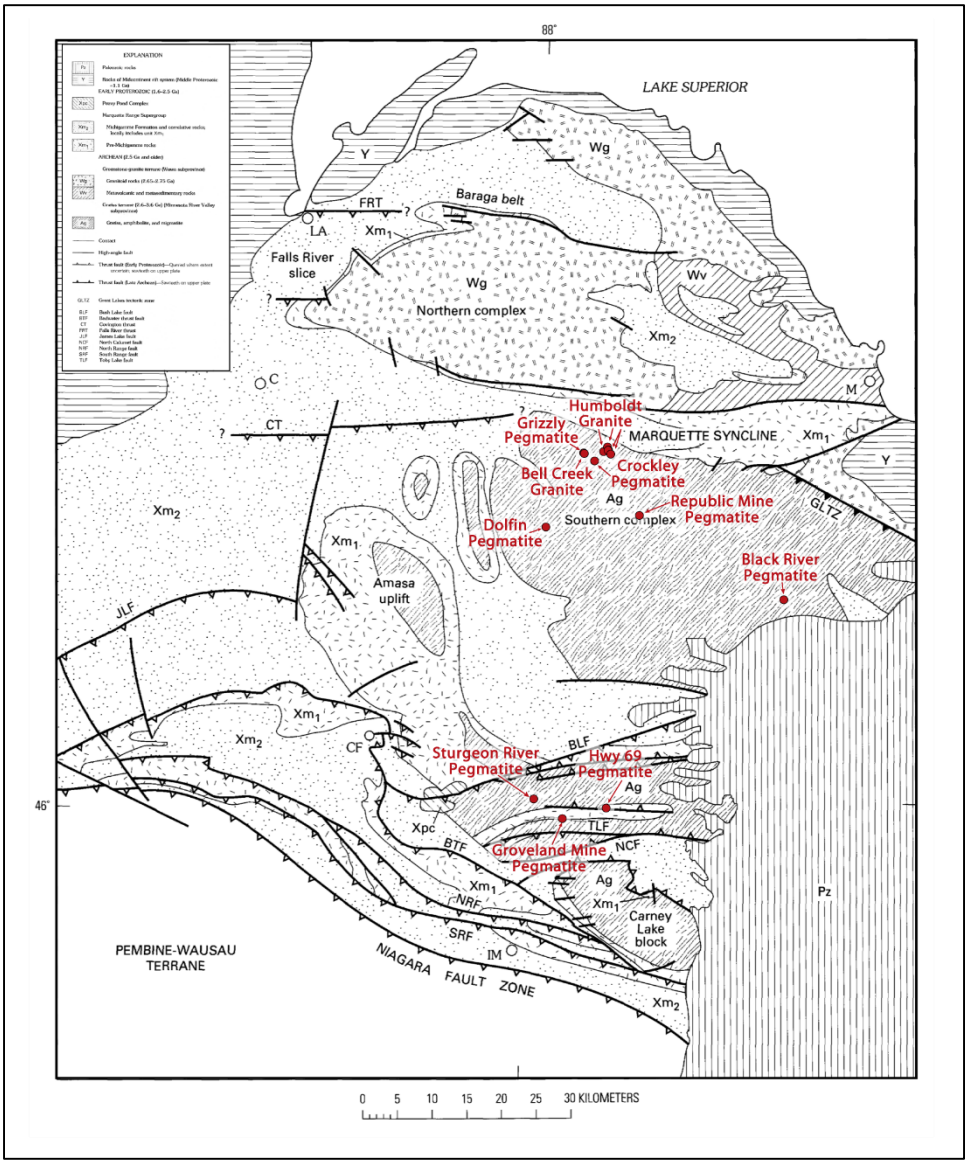


Figure 1 Generalized structure map compiled by P.K. Sims, 1991.

pegmatites are all spatially related to the Humboldt granite. All of the pegmatites and granites are within a migmatitic gneiss-amphibolite domain of Late to Early Archean age with the exception of the Sturgeon River, Groveland Mine, and Hwy 69 pegmatites. These three pegmatites are geographically south of the other sampled locations either very near or in the Felch Trough and spatially associated with the Peavy Pond Complex. The Sturgeon River

pegmatite is hosted by biotite schist of the Late Archean Dickinson Group metasediments. The Groveland and Hwy 69 pegmatites are both located in metavolcanic and metasedimentary rocks of the Menominee and Chocolay Groups.

All of the sampled locations are located within either the Republic or Peavy nodes of metamorphism. These zones are annular or concentric in shape and represent amphibolite facies metamorphism. The Sturgeon River, Groveland Mine, and Hwy 69 pegmatites are within the Peavy metamorphic node; the other sampled locations are within the Republic node. The Black River pegmatite appears to be the exception, as it is located outside the biotite isograd of the Republic node, but assumed to be within the chlorite isograd. The Dolfin pegmatite is within the sillimanite isograd of the Republic node; all other granites and pegmatites are within their respective staurolite isograds. Both metamorphic nodes are associated with the remobilization of hot Archean gneissic domes during the Penokean orogeny.

The purpose of this research is to determine the mineralogy, geochemistry, and origin of the pegmatites and the spatially associated granites. Furthermore, the geochemistry of pegmatites hosted by either migmatite, schist, or metavolcanic rock and those with granitic plutons will determine whether the pegmatitic body fractionated from the host granitic melt or whether the pegmatitic melt was derived from partial melting of a felsic protolith and subsequently intruded into the existing country rock. In addition, a mineralogical description of each of the eight pegmatites will be provided. In conjunction with results from bulk composition analyses of whole rock chemistry of the granites, geochemistry of specific mineral groups will be examined to determine tectonic origin. The overall mineralogical content and geochemical character of the pegmatites will be used to determine whether to classify each as NYF-, LCT-, or

mixed-type (Černý & Ercit, 2005). Monazite crystals will be used for age dating in order to correlate the pegmatites to tectonic events.

## GEOLOGIC HISTORY

The Great Lakes Tectonic Zone (GLTZ) is a ~1400 km long paleosuture associated with formation of the Superia/Kenorland supercontinent around 2.6 Ga (Tohver *et al*., 2007). The GLTZ separates the Southern Complex, a 2.7 – 3.4 Mesoarchean gneiss-amphibolite terrane, from the Northern Complex, a 2.7 – 2.9 Ga Neoarchean granite-greenstone terrane (Sims, 1996; Schneider *et al*., 2004; Tohver *et al*., 2007). Rifting along the GLTZ began around 2.5 Ga in the Lake Huron region to the east and migrated westward in time, possibly beginning around 2.1 Ga in the Lake Superior region (Sims & Peterman, 1983). The Marquette Range Supergroup (MRSG) is an epicratonic sequence of interbedded sedimentary and volcanic rocks (Figure 2) overlying the Archean Southern Complex basement south of the GLTZ (Sims & Peterman, 1984) and is associated with rifting. Greenberg and Brown (1983) refer to this area as the Northern Penokean terrane and it is in fault contact with the Wisconsin Magmatic terrane to the south. The Niagara fault zone is recognized as the main suture dividing the Northern Penokean terrane from the Wisconsin Magmatic terrane that lies south of the fault (Schneider *et al*., 2004).

The epicratonic MRSG (Figure 2) is composed of three primary depositional cycles (Sims & Peterman, 1984): the Baraga, Menominee, and Chocolay Groups. Deposition of MRSG ceased either before or during the main pulse of deformation accompanying the Penokean Orogeny (Sims & Peterman, 1984). Volcanic rocks of the MRSG are largely bimodal with minor $K_2O$-rich rhyolite and abundant tholeiitic basalt; rhyolites have been dated at around 1.9 Ga old (Sims & Peterman, 1984).

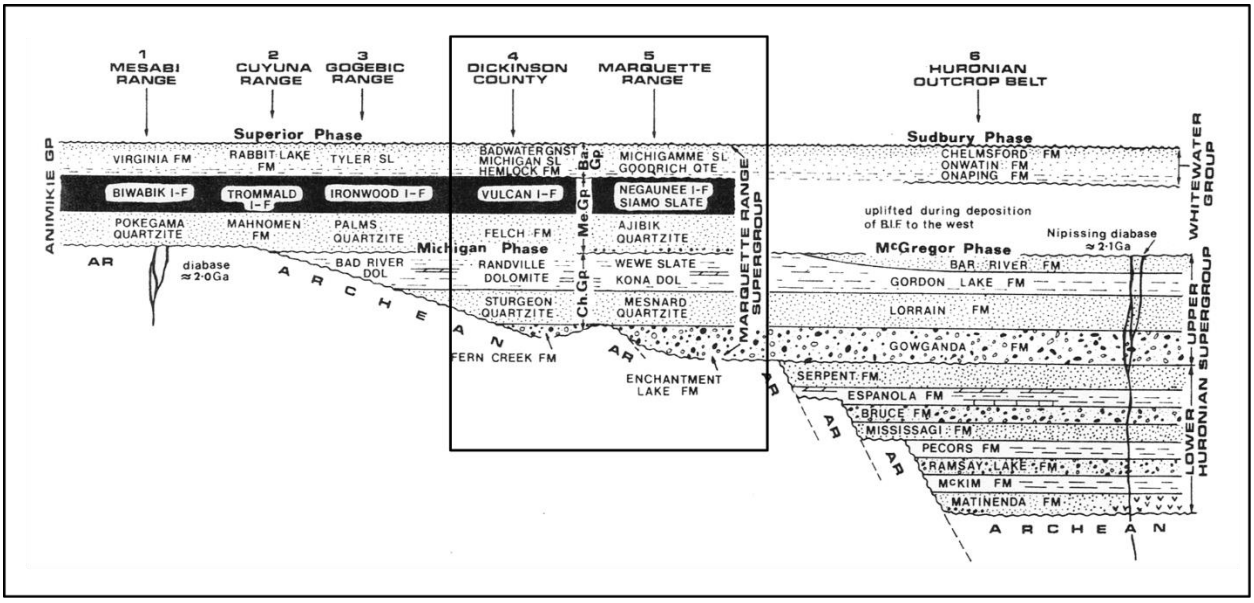


Figure 2 Stratigraphy of the Great Lakes region (Young, 1983).

Young (1983) uses the term Penokean orogeny to include the main phases of deformation and associated thermal and igneous events that affected the Great Lakes region between an approximate age range of 2.1 to 1.8 Ga. The Penokean orogeny is a Paleoproterozoic event (Van Schmus, 1976; 1980) and one of several southward accretionary events (Figure 4), including Yavapai and Mazatzal orogenies, associated with agglomeration of Laurentia (Tohver *et al*., 2007). Early Proterozoic Penokean igneous rocks suggest a plate-tectonic process that began with crustal rifting, followed relatively quickly by subduction and formation of a complex volcanic arc system in northern Wisconsin, and finally collision of that arc with Archean crust and continental-margin sequences present in northern Michigan (Figure 3) (Schulz, 1984). Penokean deformation resulted from collision of the southern margin of the Northern Penokean terrane with 1.85 Ga volcano-plutonic Wisconsin Magmatic terranes to the south (Holm *et al*., 1998; Riller *et al*., 1999; Schneider *et al*., 2002).

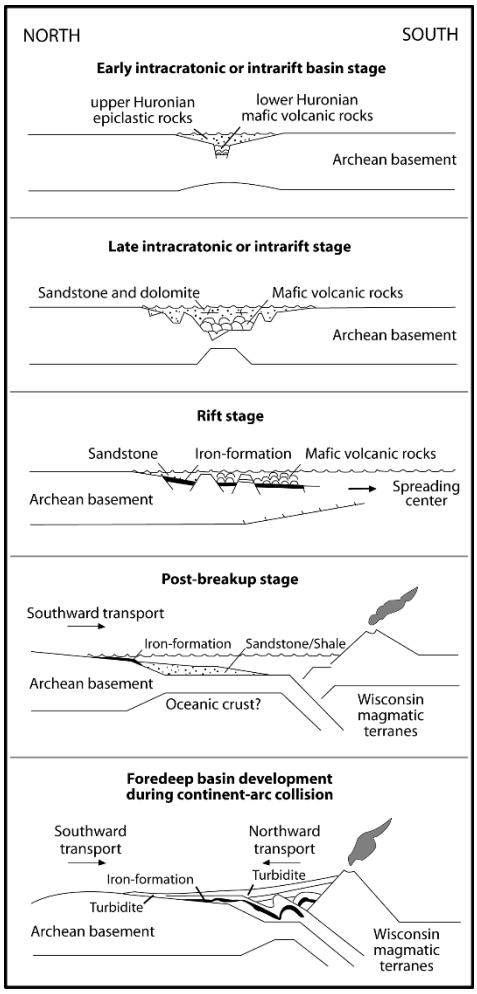


Figure 3 Penokean Orogenic cross section modified from Morey, 1983.

Initial deformation involved subhorizontal compression (Cannon, 1973) followed by a more dominant vertical style of tectonism due to reactivation of Archean basement gneiss (Sims & Peterman, 1984). Archean gneisses and granites were reworked into domes along with the overlying MRSG (Sims, 1980). Archean basement of the Northern Penokean terrane underwent little deformation north, near the southern shore of Lake Superior in Upper Michigan, but farther south near the Niagara Fault, folding and faulting appears to be much more widespread (Figure 1) (Maass *et al*., 1980; Young, 1983). Metamorphism and deformation typically intensify on either side of the Niagara fault, but these effects are not always restricted to the fault zone

(Greenberg & Brown, 1983). The main phase of Penokean deformation in the Lake Superior region specifically, is considered to have ceased about 1.82 -1.9 Ga ago (Young, 1983). Thermochronologic data indicating widespread cooling very shortly after post-tectonic plutons were emplaced, suggests that the Penokean orogen was exhumed differentially, by 1.7 Ga (Holm *et al*., 2005). Slab rollback after Penokean orogeny (Figure 4) would have not supported over-thickened crust and would have facilitated collapse of the Northern Penokean terrane (Holm & Lux, 1996; Schneider *et al*., 1996; Marshak *et al*., 1997; Holm *et al*., 1998b).

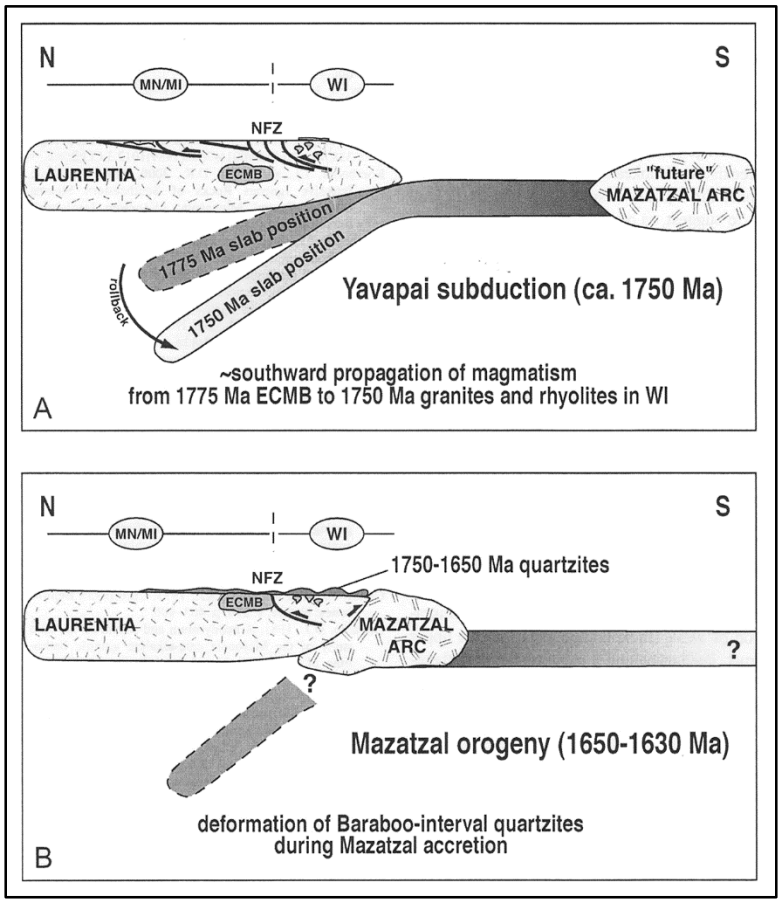


Figure 4 Slab roll back after main phase of Penokean Orogeny (Holm *et al*., 2005).

## GNEISS DOME FORMATION

A cluster of gneiss domes occur in the southern Lake Superior region of the Northern Penokean terrane. Most domes are elongated east-west, except within the Republic area where the domes trend northwest-southeast to north-south (Schneider *et al*., 2004). Whitney *et al*. (2004) highlight fundamental contributions gneiss domes provide during orogeny as being mechanisms for the transfer of heat and mass, their influence on an orogen's P-T-t (pressure, temperature, and time) evolution, as well as long-term processes of felsic differentiation of continental crust. The gneiss dome corridor is more variably metamorphosed and more strongly deformed than the Northern Complex and Wisconsin Magmatic terranes that lie north of the GLTZ and south of the Niagara Fault respectively, and generally the grade of metamorphism decreases to the north (Schneider *et al*., 2004; Attoh & Klasner, 1989). Whitney *et al*. (2004) believe that anatexis of crustal material is intimately involved with the production of most gneissic domes and suggest that most are migmatitic domes formed by anatectic processes. Domes are flanked by metamorphic supracrustal sequences that represent the overlying Paleoproterozoic sedimentation and are cored by older Archean gneiss (Schneider *et al*., 2004).

Domes typically consist of a core: composed of metamorphic, migmatitic, and granitic rocks, which are then buried by metavolcanic and/or metasedimentary strata (Eskola, 1949). Eskola (1949) suggests that gneiss dome formation results from superposition of two orogenic events: (1) the production of a granitic basement and (2) the partial melting and remobilization of basement material. The second event leads to a density inversion of crustal material that then generates an upward flow of a metamorphic core (Eskola, 1949). Yin (2004) suggests that granitic plutons dominate cores of some gneiss domes, particularly in domes of Precambrian age (Whitney *et al*., 2004).

According to Tinkham & Marshak (2004), dome and keel (troughs) structures occur due to orogenic processes involving gneiss domes. This dome-and-keel architecture can involve Paleoproterozoic strata (Marshak, 1999; Marshak *et al*., 1992; Holm & Lux, 1996), but is quite typical of Archean terranes (Tinkham & Marshak, 2004). Evidence for both, an Archean phase and a Paleoproterozoic dome-and-keel phase (Figure 5), appear to be preserved in the Penokean Dome-and-Keel belt (Figure 6) (Tinkham & Marshak, 2004). The Archean phase involved plastic flow and diapiric ascent of intrusive and intermediate and silicic metamorphic rocks of the Southern Complex into the supracrustal assemblage of the Archean age greenstone and associated sedimentary rocks (Tinkham & Marshak, 2004). The Paleoproterozoic phase formed by displacement along shear zones and resulted in deposition of Paleoproterozoic MRSG into grabens or keels (Tinkham & Marshak, 2004).

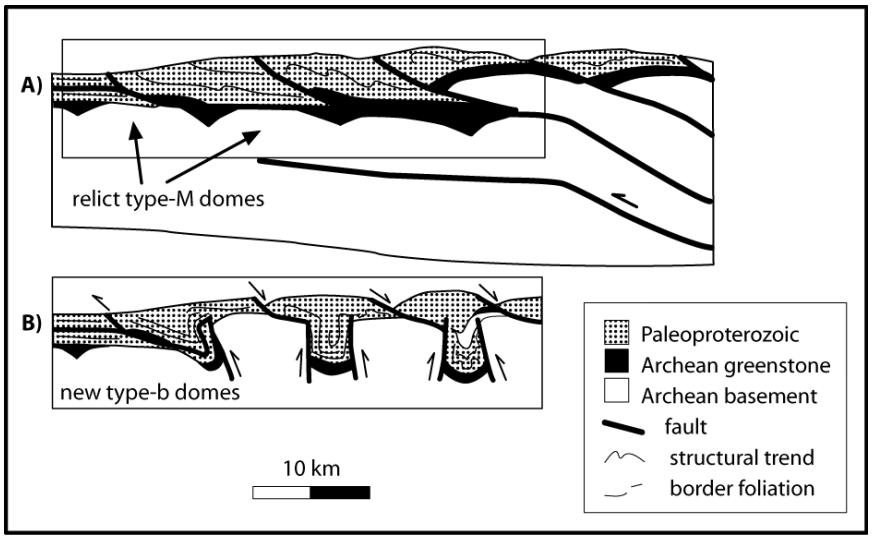


Figure 5 Archean A) and Proterozoic B) gneiss dome formation. Modified from Tinkham & Marshak, 2004.

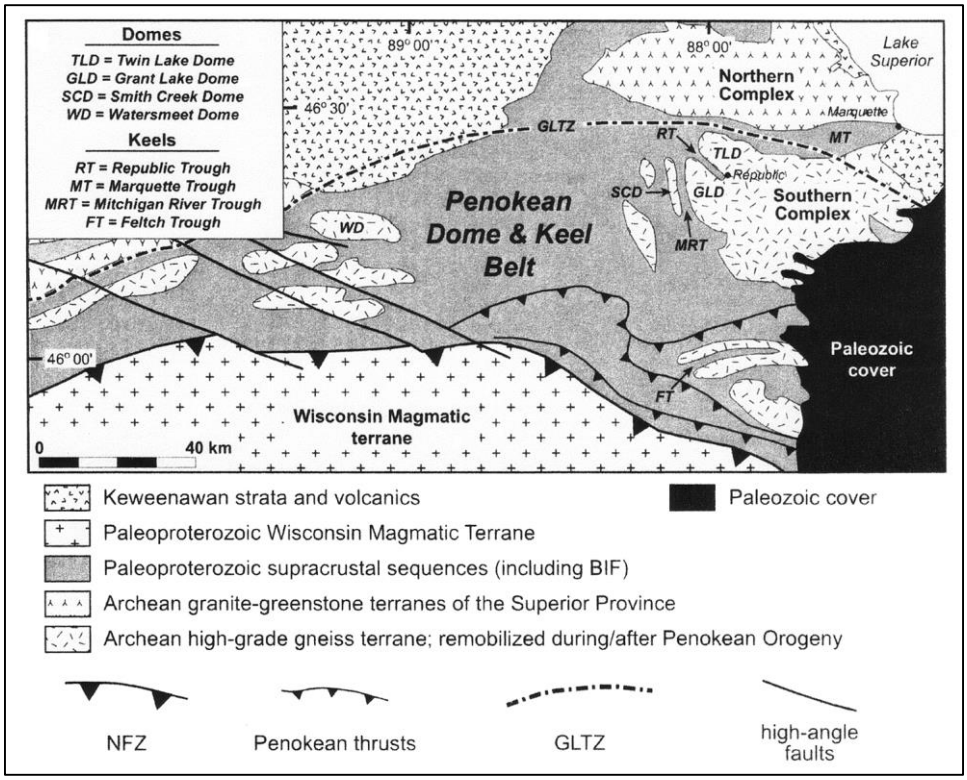


Figure 6 Penokean Dome & Keel Belt (Tinkham & Marshak, 2004).

Hoffman (1987) interprets the Bell Creek Gneiss as syntectonic and is associated with collision of the Southern and Northern Complexes at ca. 2.69 Ga along the GLTZ. When the Bell Creek gneiss/granite intruded into the Twin Lake Assemblage at ~2614 Ma, the Assemblage was penetratively deformed, intensely metamorphosed, and arched into a dome shape (Tinkham & Marshak, 2004). The domal geometry has lead Tinkham & Marshak (2004) to suggest that this represents the Archean phase of gneiss dome formation driven by density inversion and related to diapiric processes (Tinkham & Marshak, 2004). The second, Paleoproterozoic domal event was initiated by the Penokean Orogeny (Tinkham & Marshak, 2004). Original domal architecture established during the Archean phase was subjected to compressional forces during this orogenic event (Marshak *et al*., 1997). Pre-existing dome-and-keel structure likely led to the reactivation of the Southern Complex and subsequent development of solid-state domes during

post-orogenic collapse (Marshak, 1997). Gregg & Saja (1998) report finding post-collisional extensional structures within the MSRG of the Penokean orogenic belt that support this conclusion.

## METAMORPHISM IN THE NORTHERN PENOKEAN TERRANE

It was James (1955) that first described that in the eastern portion of the Northern Penokean terrane, there were concentric zones of amphibolite facies metamorphism associated with gneiss domes. Amphibolite facies metamorphism around some of the domes was superimposed on regional greenschist metamorphism (Sims & Peterman, 1984). Tinkham & Marshak (2004) suggest that development of dome-and-keel structures corresponds to peak metamorphism in the Paleoproterozoic and thermal modeling by Attoh (2000) attributes heating by radiogenic elements in Archean gneiss to the formation of metamorphic zones in the Northern Penokean terrane. There are four main zones, hereafter referred to as either nodes or zones: Watersmeet, Felch, Peavy, and Republic. Sampled locations are located in either the Republic or Peavy nodes (Figure 7). The Peavy and Republic nodes have been interpreted to lack overlap, so the assumption is that sampled locations have only been influenced by either one or the other, in addition to any pre- or post-Penokean metamorphic events.

In the Peavy node, Paleoproterozoic strata (MSRG) include Hemlock, Baraga, and Michigamme Formations (Attoh & Klasner, 1989). The Peavy Pond Complex (PPC) is located in the southwest metamorphic high of the Peavy node (Bayley, 1959). The PPC is a suite of mafic to intermediate to felsic intrusive rocks (Attoh & Klasner, 1989), which later intruded and assimilated parts of the MRSG during the Penokean Orogeny (Bayley, 1959). Cooling of the PPC was slow due to being intruded into an area undergoing regional metamorphism and as a

result, high temperatures were sustained longer than normal (Bayley, 1959). The Felch Trough, (site of the Groveland Mine, Sturgeon River, and Hwy 69 pegmatites) is located east of the Peavy Pond Complex, which contain MSRG metasedimentary and metavolcanic units of Late Archean age (Sims, 1992).

The Felch Trough is located south of the Bush Lake Fault and indications are that the metamorphic conditions reached the staurolite zone. The sillimanite zone of the Peavy node has reached peak temperatures and pressures of about 600º C and about 4.0 kbar (Attoh & Klasner, 1989). North of Bush Lake fault record different peak pressures and temperatures. James (1955) has determined that in the Felch district, where the Felch Trough is located, that peak metamorphism occurred after the peak of deformation. Monazite age dating has yielded two different metamorphic events in the Peavy node (Rose *et al*., 2003). The first of which occurring at approximately 1828-1832 Ma as well as a younger event occurring at approximately 1795 Ma (Rose *et al*., 2003).

Paleoproterozoic metasedimentary strata in the Republic node area include Michigamme Formation, Siamo Slate, and Neguanee Iron Formations (Attoh and Klasner, 1989). Upper pressure limits of metamorphism in the Republic node is set by the 500-600º C andalucite-sillimanite field of Holdaway (1971), due to the rare occurrence of sillimanite as compared to relatively widespread occurrences of andalucite (Attoh & Klasner, 1989). Pressures of 3 kbar at 550º C and 2 kbar at 600º C are considered the high and low metamorphic conditions present in the Republic node (Attoh and Klasner, 1989). Due to high temperatures that the Republic node was exposed to at relatively shallow crustal levels, there is a distinct possibility of anatexis of crustal rocks with granitic and/or pelitic composition (Attoh and Klasner, 1989). In fact, modeling by Attoh and Klasner (1989) of negative gravity anomalies present near the surface of

both Peavy and Republic nodes are interpreted as being the product of partial melting. They believe that the presence of remobilized gneiss domes offer strong support for the hypothesis originally introduced by Hoffman (1987) and that gravity anomalies provide further support for partial melting at Peavy and Republic nodes.

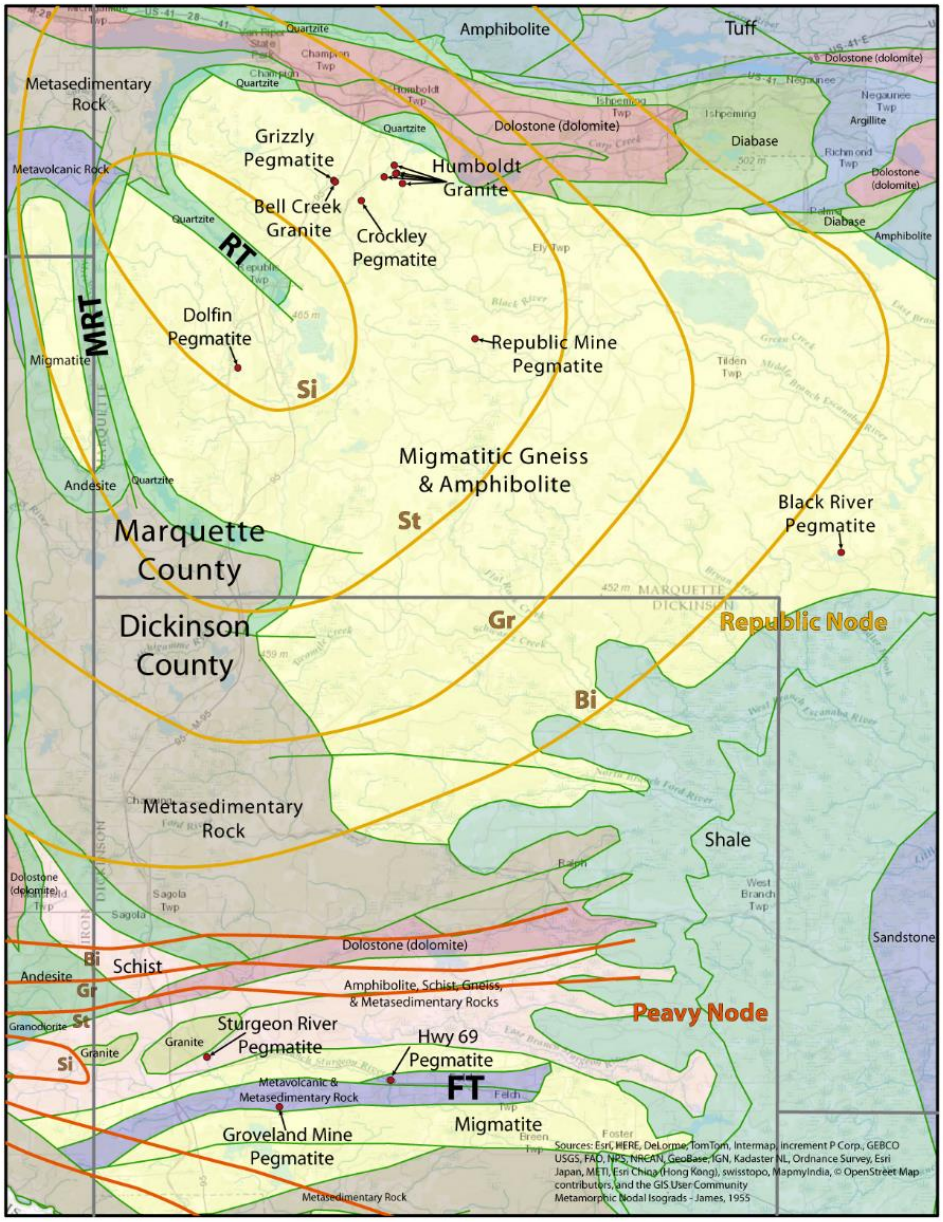


Figure 7 Metamorphic isograds. Republic isograds in orange. Peavy isograds in red. FT-Felch Trough, MRT-Mitchigamme Trough, RT-Republic Trough. Locations of pegmatites and granites locations are as indicated. Sources listed on image.

## LOCAL GEOLOGY

The Grant Lake and Twin Lake domes are separated from one another by the northwest-trending Republic Trough which contains MRSG (Tinkham & Marshak, 2004) and are very near the GLTZ (Figure 6). The Felch Trough (Figure 6) is south of both the Grant Lake and Twin Lake Domes and is close to the Niagara Fault. Archean Southern Complex lithologies consist of two main units, the Twin Lake Assemblage and the Bell Creek Assemblage (Figure 8).

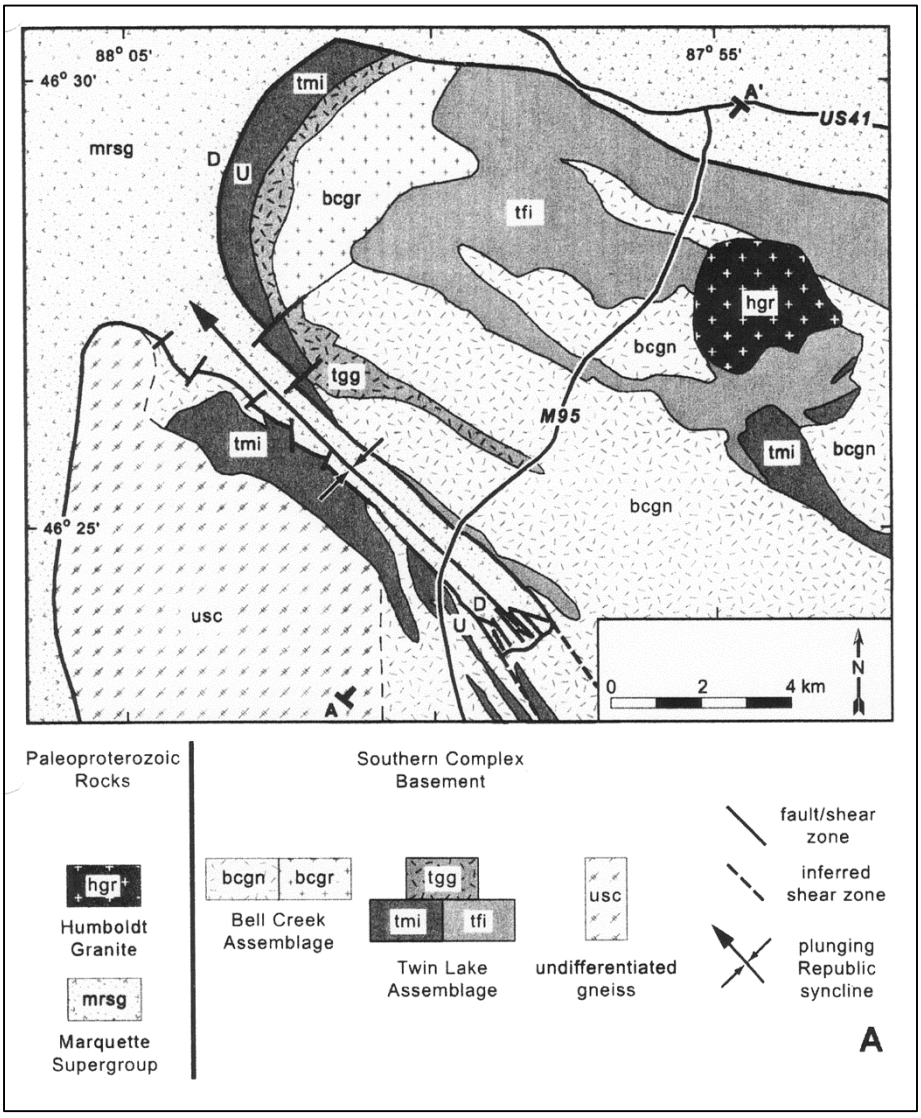


Figure 8 Geologic map of Southern Complex supracrustals (Tinkham & Marshak, 2004).

The Archean Southern Complex also includes the Palmer Gneiss, mafic dikes, and exposures of the 1.8 Ga Humboldt granite (Holm *et al*., 2001; Tinkham & Marshak, 2004). The Twin Lake assemblage is only of any importance due to its lithology (felsic to mafic gneisses) and its proximity to the Bell Creek Assemblage (Tinkham & Marshak, 2004). The mafic dikes and Palmer gneiss are also considered of little import. The Bell Creek Assemblage, which consists primarily of Bell Creek gneiss, contains the Bell Creek granite (Tinkham & Marshak, 2004) and the Grizzly pegmatite. The Bell Creek Gneiss is described as a medium to mostly coarse-grained, and megacrystic gneissic granite- to granodiorite- to quartz monzonite and being light pink to gray in color (Tinkham & Marshak, 2004). Hoffman (1987) interpreted the Bell Creek gneiss as representing a syntectonic granite that is associated with collision of the Southern and Northern Complexes at ca. 2.69 Ga along the GLTZ. The Humboldt granite, located within the Twin Lake Dome, is a medium grained albite granite that is light red in color (Tinkham & Marshak, 2004). Recent zircon U-Pb dating yielded an age of 1806 ± 21 Ma (Holm *et al*., 2001) for the Humboldt indicating that it is younger than the Southern Complex lithologies (Tinkham and Marshak, 2004) and is associated with post-Penokean collapse. The Grant Lake Dome lacks sufficient exposure, however Tinkham and Marshak (2004) proposed that it too, is also composed of Bell Creek and Twin Lake Assemblages.

The Dolfin pegmatite is located in the Grant Lake Dome area, south of the Republic Trough. It is located within the sillimanite isograd of the Republic node (Figure *7*). The Bell Creek and Humboldt Granites, Crockley and Grizzly pegmatites are located in the Twin Lake Dome area, north of the Republic Trough. These are within the staurolite isograd of the Republic node. The Republic Mine pegmatite is within the staurolite isograd as well, but it is outside the region considered to be either the Grant Lake or Twin Lake Domes. The Black River

is the eastern most pegmatite in the study area as well as being in the lowest metamorphic isograd. It is located outside the biotite isograd in what is considered to be the Republic chlorite zone. The other three pegmatites are located near or within the Felch Trough. This area is believed to have undergone deformation and/or metamorphism after emplacement of the pegmatites. The Peavy Pond Complex (PPC) is west of the Felch trough. It is a syntectonic igneous gabbroic body intruded into the Michigamme and Hemlock Formations during the Penokean orogeny (Bayley, 1959). The PPC is situated in the Peavy Pond area and is located at the metamorphic high (sillimanite zone) of the Peavy node (Bayley, 1959). The Sturgeon River, Groveland Mine, and Hwy 69 pegmatites are in the staurolite isograd of the Peavy node.

# METHODOLOGY

## TITRATION

$Fe^{2+}$ determinations were conducted using ammonium meta-vanadate method of titration using ferrous ammonium sulfate solution and diphenylamine solution (Von Arnd Peters, 1968). Solid ammonium meta-vanadate weighing 0.10 g was added to 0.20 g of ground sample in 100 ml dry polyethylene bottles with secure, air-tight, water-proof lids. A mixture of 8 ml of 51% hydrofluoric acid and 2 ml of 38% hydrochloric acid was added to each bottle and allowed to stand until all sample powder was completely dissolved (approximately 4 days). To each mixture, 10 ml 50% sulfuric acid and 10 ml of diphenylamine solution were added and transferred to 600 ml a beaker containing 400 ml of distilled water and 10 g of boric acid. The solution was placed on a magnetic stirrer and titrated with ferrous ammonium sulfate until the solution turned from purple to bright green. A blank (no sample powder) was measured as a control. $Fe^{3+}$ was calculated as the difference between microprobe (total Fe) and wet-chemical ($Fe^{2+}$) results from the equation (Von Arnd Peters 1968):

$$\textbf{\% FeO} = [100\,(x' - y')\,z] / w$$

Where x = ml of ferrous ammonium sulfate required to titrate blank, normalized to 100 mg. x' = x [(sample) mg / 100 mg]

y' = ml of ferrous ammonium sulfate required for titration of sample

z = mg of FeO per ml ferrous ammonium sulfate

w = weight of sample in mg

## FUSION ICP

Fusion Inductively-Coupled Plasma (ICP) Optical Emission Spectrometry (OES) is a bulk chemical analysis technique used for the identification and quantification of trace elements in whole rock samples. Granitic samples and one sample from the Crockley was analyzed by this method. Samples were crushed and powdered in a ceramic wall-lined container containing a ceramic puck and covered with a ceramic lid. The container was secured in an 8510 Shatter Box and milled for a minimum of 40 minutes or longer until the sample was pulverized to at least 95% minus 150 mesh (106 microns) powder consistency. Contamination was prevented by milling and disposing of an aliquot of sample prior to actual sample preparation. The milled samples were stored in 50 ml polyethylene bottles with secure air-tight, water-proof lids. The powdered rock samples were sent for Fusion ICP analysis to Activation Laboratories Ltd. in Ancaster, Ontario using the Lithium Metaborate/tetraborate Fusion method on a combination simultaneous/sequential Thermo Jarrell-Ash ENVIRO II ICP or a Varian Vista 735 ICP. Calibration was performed using 7 prepared USGS and CANMET certified reference materials.

DCP

A Beckman Spectraspan V, Direct-Coupled Plasma Spectrophotometer (DCP) was used for trace element and whole rock analyses to verify EMP results, including Li content in muscovite, biotite, and beryl based on calculations. Each sample was prepared for analysis by crushing samples with a SPEX 4200 Jaw Crusher into < 6 mm – sized pieces. Approximately 0.2 g of clean biotite, muscovite, and beryl were separated from samples containing the minerals using tweezers and stereomicroscope. The micas and beryl were digested in 5-10 ml of a mixture of 51% hydrofluoric acid and 38% hydrochloric acid at room temperature for approximately 4 days or until completely dissolved. The samples were then diluted to a volume of 35 ml and analyzed using standard DCP methods. DCP analyses were graciously conducted at the Maine Mineral & Gem Museum.

SEM

An AMRAY 1820 Digital Scanning Electron Microscope (SEM) was used for spot chemical analysis, acquisition of elemental maps, and mineral identification using the EDS 2009 system. Tourmalines, biotites, muscovites, apatites, garnets, zircons, monazites, xenotimes, magnetite, columbite-tantalites, feldspars, ilmenite-pyrophanite, and rutile were hand-picked from heavy mineral separations containing the minerals and individually placed on sticky pads on stubs and stored in a desiccator. Each stub was viewed under SEM for mineral identification. The minerals were then encased in epoxy on a microprobe mount and allowed to cure for a minimum of 24-hours. Each microprobe mount was ground flat using grinding powder on a grinding wheel, cleaned in an ultrasonic bath, polished using a polishing wheel and 1 micron, 0.3 micron, and 0.05 micron polishing compound, then cleaned in an ultrasonic bath. Samples were dried and carbon-coated with 250 Ångstroms of carbon under a vacuum of 1x10-5 torr prior to SEM analysis. Each sample was analyzed by SEM for the minerals. Samples were subsequently stored in a desiccator for further analysis by microprobe.

EMP

A fully-automated, nine-spectrometer ARL SEMQ Electron Microprobe (EMP) was used for major and minor element analysis of minerals on microprobe mounts. Minerals were handpicked from heavy mineral separates. The following minerals analyzed by EMP: tourmaline, garnet, muscovite, biotite, apatite, plagioclase, k-feldspar, zircon, monazite, ilmenite-pyrophanite, and xenotime. Sample preparation process that was conducted for microprobe analysis was the same as SEM sample preparation. Quantitative chemical analyses of these samples were obtained using an ARL-SEMQ electron microprobe in the wavelength dispersive mode with an accelerating potential of 15-20 kV, 15 nA beam current, and 2 μm beam diameter. The following standards were used: Adularia (Fibbia) (K, Si), albite (Tiburon) (Na, K, Al), $An_{50}$ (Ca, Al), Cpx-26 (Fe, Mg), rhodonite (Broken Hill) (Mn), $TiO_2$ synthetic (Ti), pollucite (Cs), Rb-leucite (Rb), fluorapatite (P), fluorphlogopite (F). Five spots per sample were analyzed with count times was of 30 seconds per spot. Backgrounds were determined using the MAN method (Donovan & Tingle, 1996), using applicable standards listed above and the following standards: hematite (Elba), $V_2O_5$, $ZrO_2$, MgO, PbO, ZnO, ZrO, and $Al_2O_3$. Matrix effects were corrected using Φ (ρZ) correction procedure (Pouchou & Pichoir 1991). Data were plotted in MS Excel or PSI-plot software.

## BELL CREEK GRANITE

Figure 9 Bell Creek granite road-cut exposure.

Samples from the Bell Creek granite were collected from a road cut along Hwy 95 in Marquette County, Michigan. It was found to be as Tinkham and Marshak (2004) previously described. Overall, the Bell Creek granite is light gray and in some instances light pink in hue. It is in sharp contact with country rock. Xenoliths of country rock were not seen in the exposure of the Bell Creek granite. Visual inspection revealed that the granite is composed of feldspar, quartz, and dark colored mica assumed to be biotite. Heavy mineral separations of Bell Creek granite were inspected by binocular microscope and further analyzed by SEM and/or electron microprobe. Apatite, biotite mica, feldspar (both potassium and plagioclase), fluorite, muscovite mica, monazite-(Ce), titanite, quartz, and zircon were found in samples. Biotite and muscovite micas, monazite-(Ce), and zircon were quantitatively confirmed by electron microprobe.

## APATITE

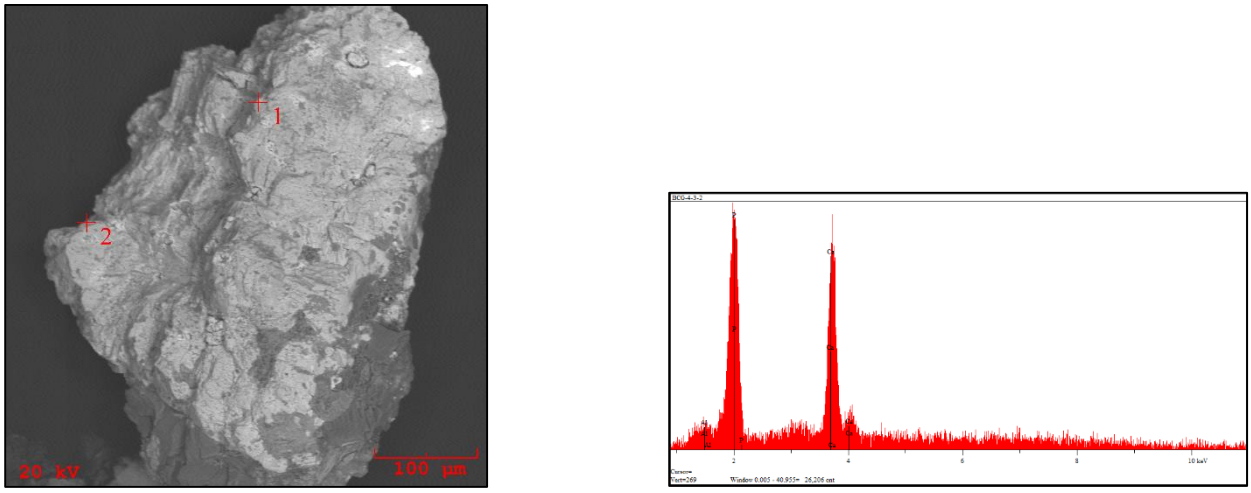


Figure 10 Apatite (crosshairs 1 & 2) with corresponding EDS spectrum. Darker region is feldspar.

Apatite is very rare in heavy mineral separations from the Bell Creek granite. Only two grains have been discovered. Both are anhedral. Both have been qualitatively investigated by SEM.

## BIOTITE

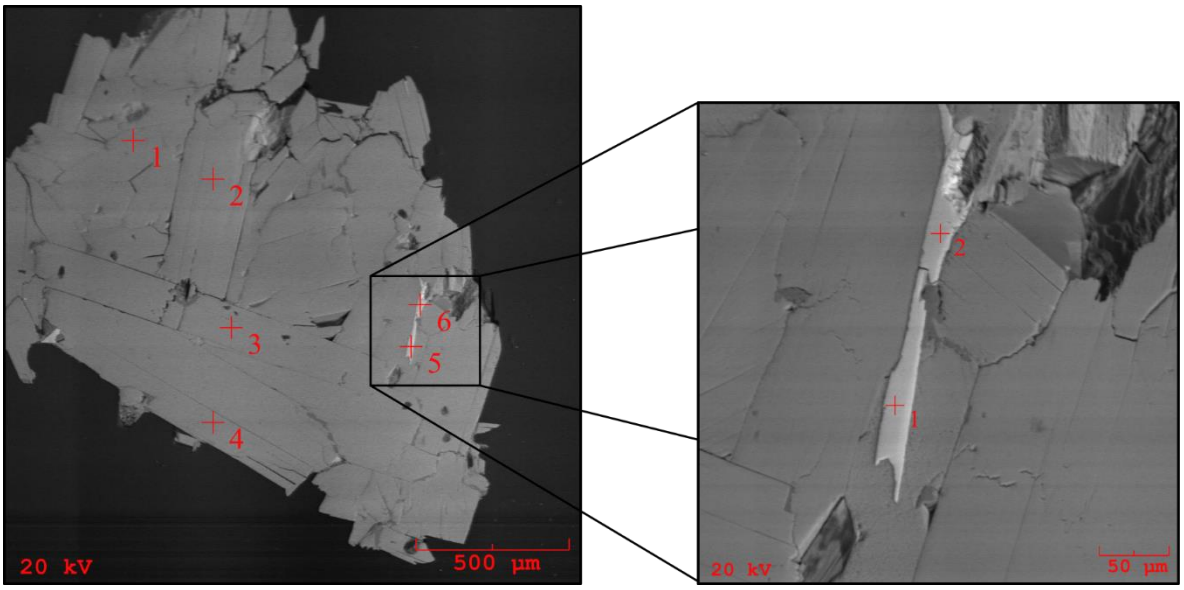


Figure 11 BSE image of biotite mica grain (left – crosshairs 1, 2, 3, & 4) with ilmenite inclusion (crosshairs 5 & 6). Close-up of ilmenite inclusion (right – crosshairs 1 & 2).

Biotite is very common in Bell Creek granite heavy mineral separations. Biotite has been investigated by SEM and confirmed as Fe-biotite mica using Tischendorf's (1997) classification scheme via microprobe analyses (Figure 186). Rubidium weight percent is just within detection limits and cesium is below detectable limits. Lithium and trivalent iron are unable to be determined by DCP and titration respectively due to lack of homogeneous grains. Figure 11 demonstrates homogeneity concerns as biotite frequently has inclusions (in this particular instance, crosshairs 1 & 2 indicate an ilmenite inclusion). Even though lithium content has not been determined by DCP analysis, lithium is stoichiometrically accounted for using the equation 155 * magnesium weight percent$^{-3.1}$ (Tischendorf, 1997). Table 1 lists the representative biotite mica analyses.

| **BIOTITE – BELL CREEK GRANITE** | | | | | |
|---|---|---|---|---|---|
| Wt % Ox. | BCG mica 1-1 | BCG mica 1-2 | BCG mica 2-1 | BCG mica 2-2 | BCG mica 3-1 |
| $SiO_2$ | 34.214 | 34.276 | 34.300 | 34.445 | 34.500 |
| $TiO_2$ | 3.543 | 3.720 | 3.654 | 3.334 | 3.228 |
| $Al_2O_3$ | 16.699 | 16.712 | 17.003 | 17.122 | 17.433 |
| $Fe_2O_3$ | 0.000 | 0.000 | 0.000 | 0.000 | 0.000 |
| FeO | 23.556 | 23.544 | 23.343 | 23.355 | 23.165 |
| MnO | 0.210 | 0.189 | 0.155 | 0.174 | 0.211 |
| MgO | 7.823 | 7.699 | 7.534 | 7.523 | 7.265 |
| CaO | 0.165 | 0.112 | 0.092 | 0.1 | 0.144 |
| $Li_2O$ (*calc.*) | 0.264 | 0.277 | 0.296 | 0.298 | 0.332 |
| $Na_2O$ | 0.112 | 0.165 | 0.133 | 0.165 | 0.2 |
| $K_2O$ | 9.236 | 9.045 | 8.940 | 8.700 | 8.233 |
| $Rb_2O$ | 0.017 | 0.02 | 0.02 | 0.022 | 0.016 |
| $Cs_2O$ | *bdl* | *bdl* | *bdl* | *bdl* | *bdl* |
| F | 1.222 | 1.312 | 1.227 | 1.224 | 1.154 |
| $H_2O$ | 3.278 | 3.238 | 3.277 | 3.276 | 3.305 |
| F=O | - 0.515 | - 0.552 | - 0.517 | - 0.515 | - 0.486 |
| Total | 99.824 | 99.757 | 99.458 | 99.222 | 98.700 |
| *apfu* | | | | | |
| Si | 5.318 | 5.324 | 5.330 | 5.356 | 5.370 |
| $^{IV}Al$ | 2.682 | 2.676 | 2.670 | 2.644 | 2.630 |
| **Σ T-site** | 8.000 | 8.000 | 8.000 | 8.000 | 8.000 |
| $^{VI}Al$ | 0.378 | 0.384 | 0.444 | 0.493 | 0.569 |
| Ti | 0.414 | 0.435 | 0.427 | 0.390 | 0.378 |
| $Fe_t$ | 3.062 | 3.058 | 3.034 | 3.037 | 3.016 |
| Mn | 0.028 | 0.025 | 0.020 | 0.023 | 0.028 |
| Mg | 1.813 | 1.783 | 1.746 | 1.744 | 1.686 |
| Li (*calc.*) | 0.165 | 0.173 | 0.185 | 0.186 | 0.208 |
| **Σ Y-site** | 5.860 | 5.858 | 5.856 | 5.873 | 5.885 |

Table 1 Biotite mica representative microprobe analyses. *Apfu* calculated based on 24 anions.
Continued on next page.

| | | | | | |
|---|---|---|---|---|---|
| K | 1.832 | 1.793 | 1.772 | 1.726 | 1.635 |
| Ca | 0.027 | 0.019 | 0.015 | 0.017 | 0.024 |
| Na | 0.034 | 0.050 | 0.040 | 0.050 | 0.060 |
| Rb | 0.002 | 0.002 | 0.002 | 0.002 | 0.002 |
| Cs | *bdl* | *bdl* | *bdl* | *bdl* | *bdl* |
| **Σ X-site** | 1.895 | 1.864 | 1.829 | 1.795 | 1.721 |
| F | 0.601 | 0.645 | 0.603 | 0.602 | 0.568 |
| OH* | 3.399 | 3.355 | 3.397 | 3.398 | 3.432 |
| **Σ W-site** | 4.000 | 4.000 | 4.000 | 4.000 | 4.000 |

## CHLORITE

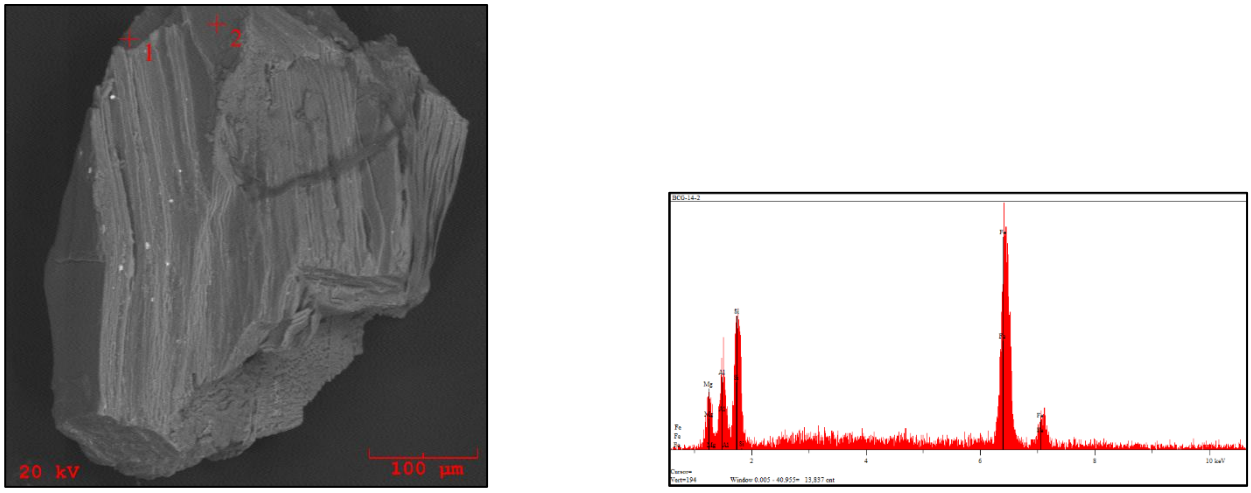


Figure 12 Unconfirmed chlorite grain with associated EDS spectrum (crosshairs 1 & 2).

Quantitatively unconfirmed chlorite has been found in heavy mineral separations from Bell Creek granite samples. Grains have a platy texture associated with mica and appear texturally homogeneous.

## FELDSPARS

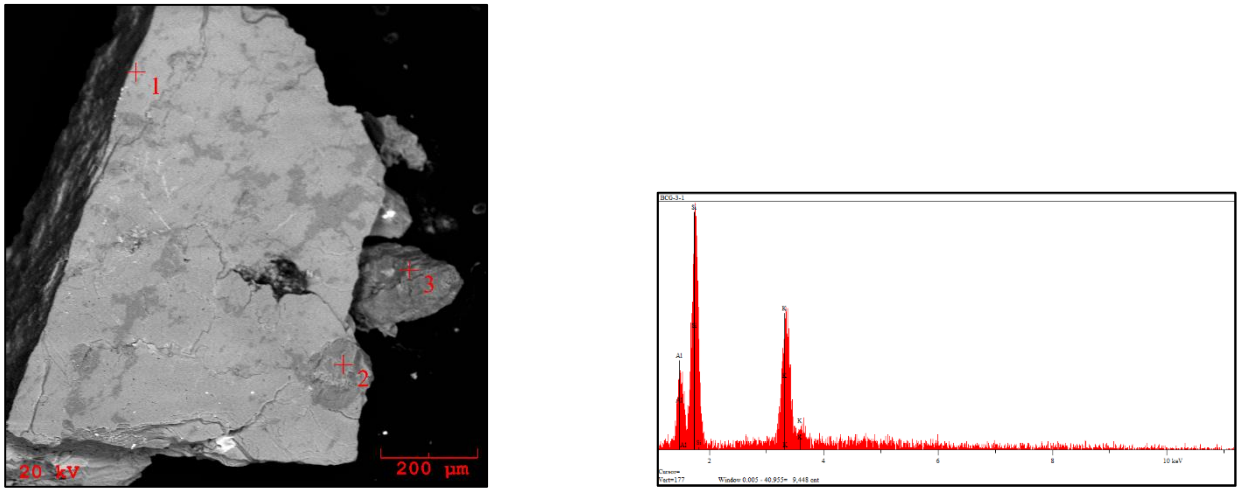


Figure 13 K-feldspar grain with EDS spectrum. Lighter areas are K-feldspar (crosshair 1). Darker areas are plagioclase feldspar (crosshairs 2 & 3).

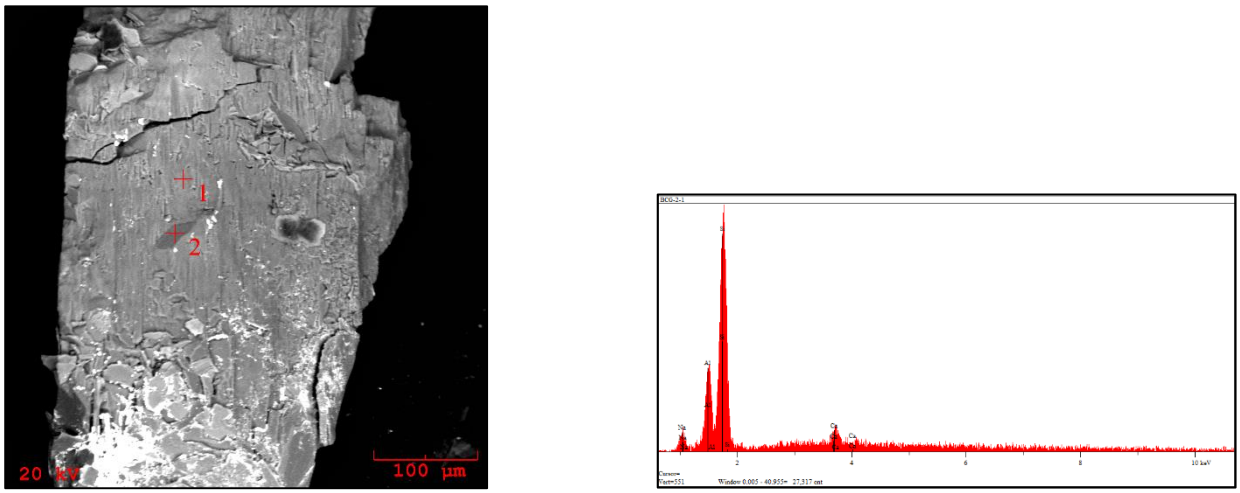


Figure 14 BSE image of plagioclase feldspar grain and EDS spectrum (crosshairs 1 & 2).

Both K-feldspar (Figure 13) and plagioclase feldspar (Figure 14) are found in heavy mineral separations from the Bell Creek granite and have been qualitatively investigated by SEM. Feldspar from Bell Creek has been further analyzed by XRD. Although there is some margin of error with XRD analyses, the analyses plotted very near max microcline field (Figure 173) (Wright & Stewart, 1968).

## FLUORITE

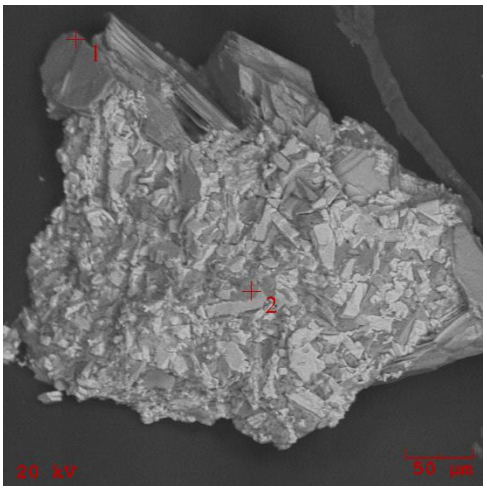


Figure 15 BSE image of fluorite grain. Crosshair 1 – mica species. Crosshair 2 and lighter areas are fluorite.

Fluorite has been discovered in heavy mineral separations from Bell Creek granite samples and has been qualitatively investigated by SEM.

## ILMENITE

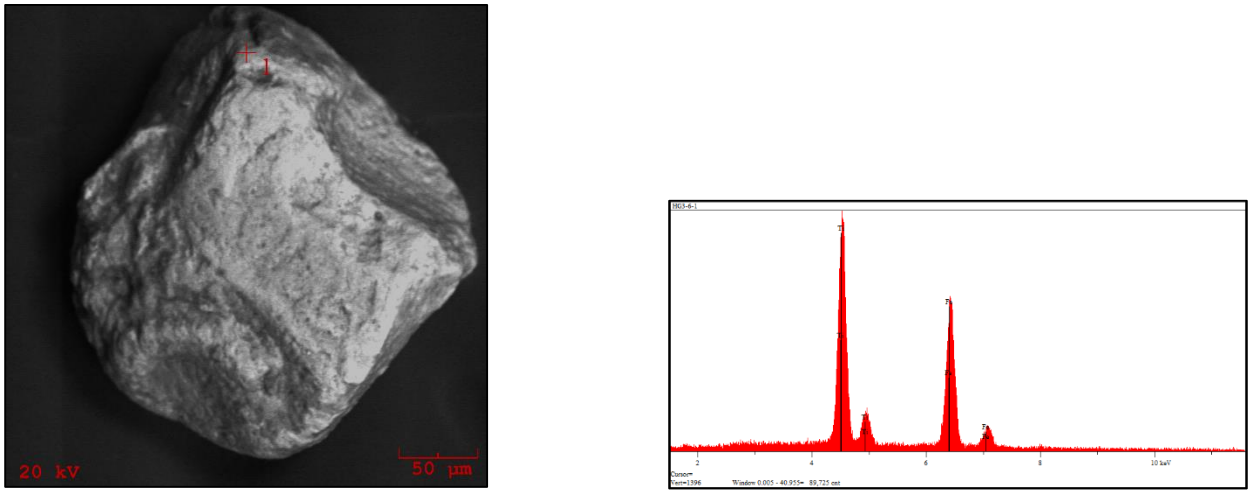


Figure 16 BSE image of ilmenite grain and associated EDS spectrum.

Ilmenite is extraordinarily rare in heavy mineral separations as only one grain has been found in all of the samples investigated. The grain is subhedral and only a few hundred microns in diameter.

## MONAZITE

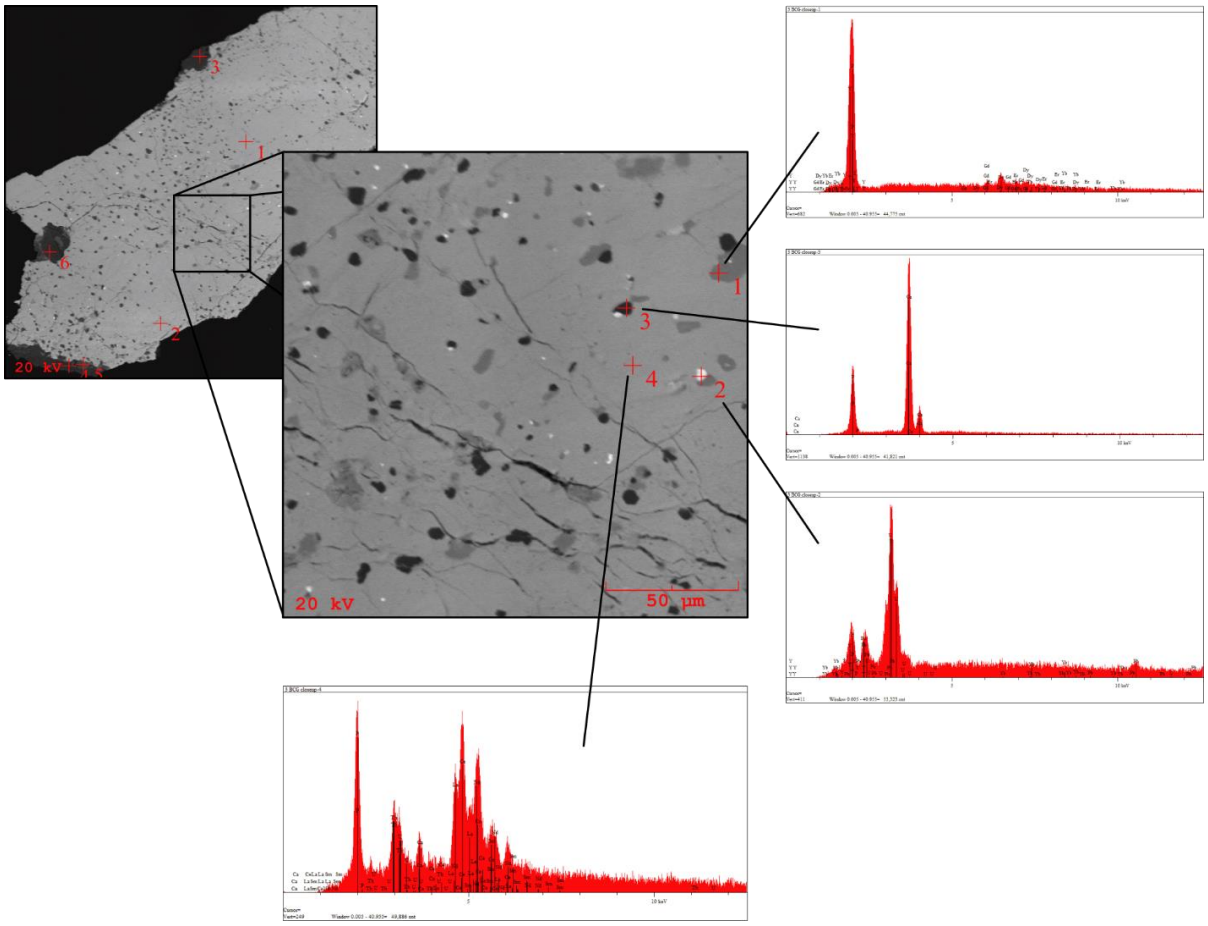


Figure 17 Bell Creek monazite-(Ce) grain with close-up of inclusions. Associated EDS spectra included.

"Monazite" is for the most part, uncommon in Bell Creek Granite samples except for one group of heavy mineral separations, which was found to contain eight grains. As Figure 17 illustrates, "monazite" grains are far from being texturally and mineralogically homogeneous as there are numerous fractures as well as inclusions of apatite, relatively phosphorus-poor /uranium-rich inclusions with possible radiogenic lead, as well as possible yttrium-rich "xenotimes" with depleted HREE's. The analyzed grains should be classified as monazite-(Ce) based on X-site cation dominance. Table 2 lists the representative microprobe analyses.

| MONAZITE-(CE) – BELL CREEK GRANITE | | | | | |
|---|---|---|---|---|---|
| Wt % Ox. | 3-BCG | 4-BCG | grain 20 BCG | grain 21 BCG | grain 22 BCG |
| $P_2O_5$ | 29.366 | 29.226 | 28.870 | 28.565 | 28.764 |
| $SiO_2$ | 0.133 | 0.176 | 0.093 | 0.100 | 0.067 |
| $TiO_2$ | 0.000 | 0.000 | 0.000 | 0.000 | 0.000 |
| $ThO_2$ | 5.430 | 6.740 | 6.332 | 6.877 | 6.445 |
| $UO_2$ | 0.892 | 0.893 | 0.689 | 0.787 | 0.567 |
| $Al_2O_3$ | 0.051 | 0.047 | 0.045 | 0.023 | 0.033 |
| $La_2O_3$ | 13.111 | 12.153 | 12.454 | 12.223 | 12.676 |
| $Ce_2O_3$ | 27.899 | 26.882 | 27.556 | 27.343 | 27.094 |
| $Pr_2O_3$ | 2.521 | 3.556 | 2.560 | 2.512 | 2.457 |
| $Nd_2O_3$ | 14.672 | 14.121 | 15.211 | 15.898 | 15.700 |
| $Sm_2O_3$ | 1.334 | 1.144 | 1.091 | 1.112 | 1.143 |
| $Eu_2O_3$ | 0.008 | 0.000 | 0.000 | 0.000 | 0.000 |
| $Gd_2O_3$ | 0.455 | 0.600 | 0.476 | 0.512 | 0.489 |
| $Dy_2O_3$ | 0.166 | 0.214 | 0.000 | 0.000 | 0.000 |
| $Yb_2O_3$ | 0.016 | 0.015 | 0.216 | 0.220 | 0.200 |
| $Y_2O_3$ | 0.678 | 0.655 | 0.000 | 0.000 | 0.000 |
| $Sc_2O_3$ | 0.034 | 0.023 | 0.000 | 0.000 | 0.000 |
| MgO | 0.000 | 0.030 | 0.000 | 0.000 | 0.000 |
| CaO | 2.334 | 1.998 | 0.067 | 0.154 | 0.112 |
| MnO | 0.050 | 0.020 | 0.000 | 0.000 | 0.000 |
| FeO | 0.262 | 0.267 | 0.455 | 0.567 | 0.600 |
| PbO | 0.188 | 0.198 | 0.043 | 0.032 | 0.065 |
| **Total** | 99.600 | 98.958 | 99.182 | 99.459 | 99.432 |
| *apfu* | | | | | |
| Th | 0.049 | 0.061 | 0.057 | 0.063 | 0.058 |
| U | 0.008 | 0.008 | 0.006 | 0.007 | 0.005 |
| Al | 0.002 | 0.002 | 0.002 | 0.001 | 0.002 |
| La | 0.190 | 0.178 | 0.183 | 0.181 | 0.186 |
| Ce | 0.402 | 0.391 | 0.401 | 0.401 | 0.395 |
| Pr | 0.036 | 0.051 | 0.037 | 0.037 | 0.036 |
| Nd | 0.206 | 0.200 | 0.216 | 0.228 | 0.223 |
| Sm | 0.018 | 0.016 | 0.015 | 0.015 | 0.016 |
| Gd | 0.006 | 0.008 | 0.006 | 0.006 | 0.008 |
| Dy | 0.002 | 0.003 | 0.003 | 0.003 | 0.003 |
| Yb | 0.000 | 0.000 | 0.001 | 0.002 | 0.001 |
| Y | 0.014 | 0.014 | 0.010 | 0.012 | 0.013 |
| Ca | 0.098 | 0.085 | 0.114 | 0.091 | 0.108 |
| **Σ X** | 1.046 | 1.031 | 1.060 | 1.055 | 1.063 |
| P | 0.979 | 0.982 | 0.973 | 0.969 | 0.971 |
| Si | 0.005 | 0.007 | 0.004 | 0.004 | 0.003 |
| **Σ Y** | 0.984 | 0.989 | 0.977 | 0.973 | 0.974 |

Table 2 Monazite-(Ce) representative EMP analyses. *Apfu* calculations based on 4 oxygens.

## MUSCOVITE

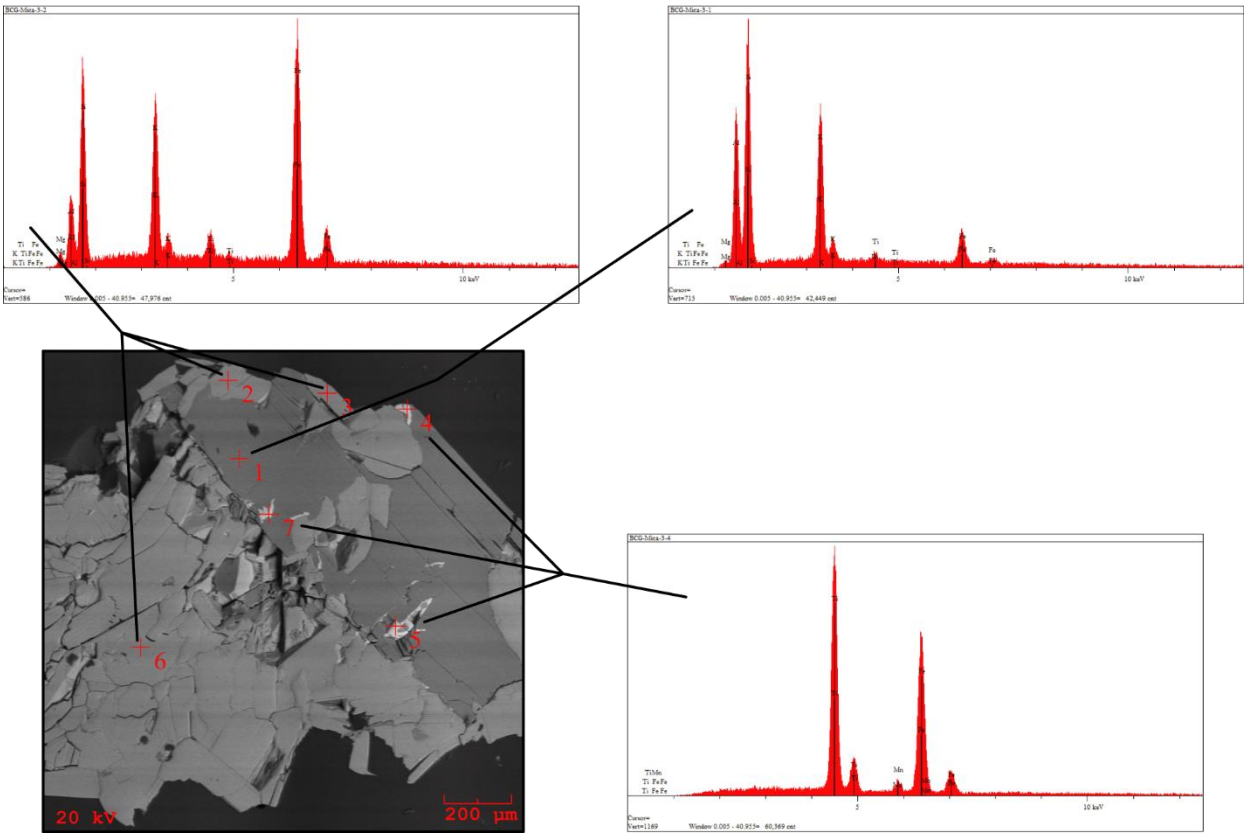


Figure 18 BSE image and associated EDS spectra. Lighter regions – biotite (crosshairs 2, 3, & 6); darker regions – muscovite (crosshair 1); lightest regions – ilmenite (crosshairs 4, 5, & 7).

Grains have been qualitatively investigated by SEM and quantitatively confirmed by microprobe as muscovite using Tischendorf's (1997) classification scheme (Figure 185). Muscovite is relatively uncommon in heavy mineral separations. Rubidium is just within detectable limits and cesium is below detection limits. As is the case with biotites from the Bell Creek granite, there is insufficient material to further investigate muscovite for lithium and trivalent iron via DCP and titration respectively. Lithium has been, however, accounted for stoichiometrically by using an equation based on fluorine weight percent: 0.3935 * fluorine weight percent$^{1.326}$ (Tischendorf, 1997). Table 3 lists the representative analysis.

| **MUSCOVITE – BELL CREEK PEGMATITE** | | |
|---|---|---|
| Wt % Ox. | BCG Mica 2-3 | BCG Mica 3-2 |
| $SiO_2$ | 46.487 | 46.511 |
| $TiO_2$ | 0.206 | 0.175 |
| $Al_2O_3$ | 34.776 | 34.812 |
| $Fe_2O_3$ | 0.000 | 0.000 |
| FeO | 2.455 | 2.143 |
| MnO | 0.033 | 0.065 |
| MgO | 0.544 | 0.344 |
| CaO | 0.054 | 0.067 |
| $Li_2O$ (*calc.*) | 0.442 | 0.570 |
| $Na_2O$ | 0.455 | 0.512 |
| $K_2O$ | 9.64 | 9.334 |
| $Rb_2O$ | 0.018 | 0.020 |
| $Cs_2O$ | *bdl* | *bdl* |
| F | 1.091 | 1.322 |
| $H_2O$ (*calc.*) | 3.986 | 3.867 |
| F=O | - 0.459 | - 0.557 |
| Total | 99.727 | 99.185 |
| *apfu* | | |
| Si | 6.191 | 6.206 |
| $^{IV}Al$ | 1.809 | 1.794 |
| **Σ T-site** | 8.000 | 8.000 |
| $^{VI}Al$ | 3.649 | 3.682 |
| Ti | 0.021 | 0.018 |
| $Fe_t$ | 0.273 | 0.239 |
| Mn | 0.004 | 0.007 |
| Mg | 0.108 | 0.068 |
| Li (*calc.*) | 0.237 | 0.306 |
| **Σ Y-site** | 4.292 | 4.320 |

Table 3 Representative EMP analysis of muscovite mica. *Apfu* based on 24 anions.
Table continued on next page.

| | | |
|---|---|---|
| K | 1.638 | 1.589 |
| Ca | 0.008 | 0.010 |
| Na | 0.117 | 0.132 |
| Rb | 0.002 | 0.002 |
| Cs | *bdl* | *bdl* |
| **Σ X-site** | 1.765 | 1.733 |
| F | 0.459 | 0.558 |
| OH (*calc.*) | 3.541 | 3.442 |
| **Σ W-site** | 4.000 | 4.000 |

## TITANITE

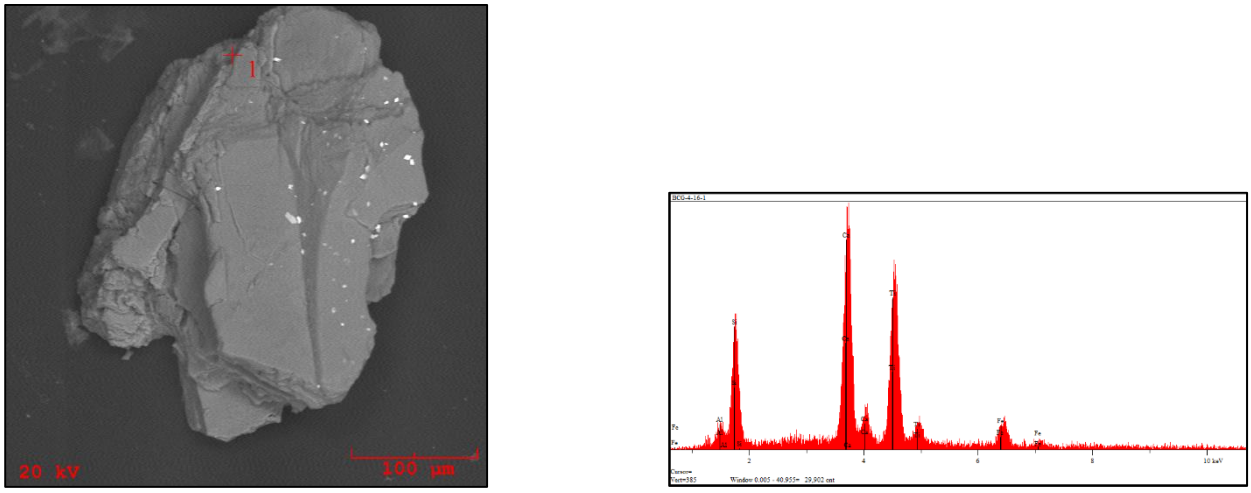


Figure 19 BSE image of unconfirmed titanite and EDS spectrum. Lighter specks are lithium metatungstate.

Possible titanite has been discovered in heavy mineral separations, although it is exceedingly rare. Only one grain has been analyzed by SEM.

## ZIRCON

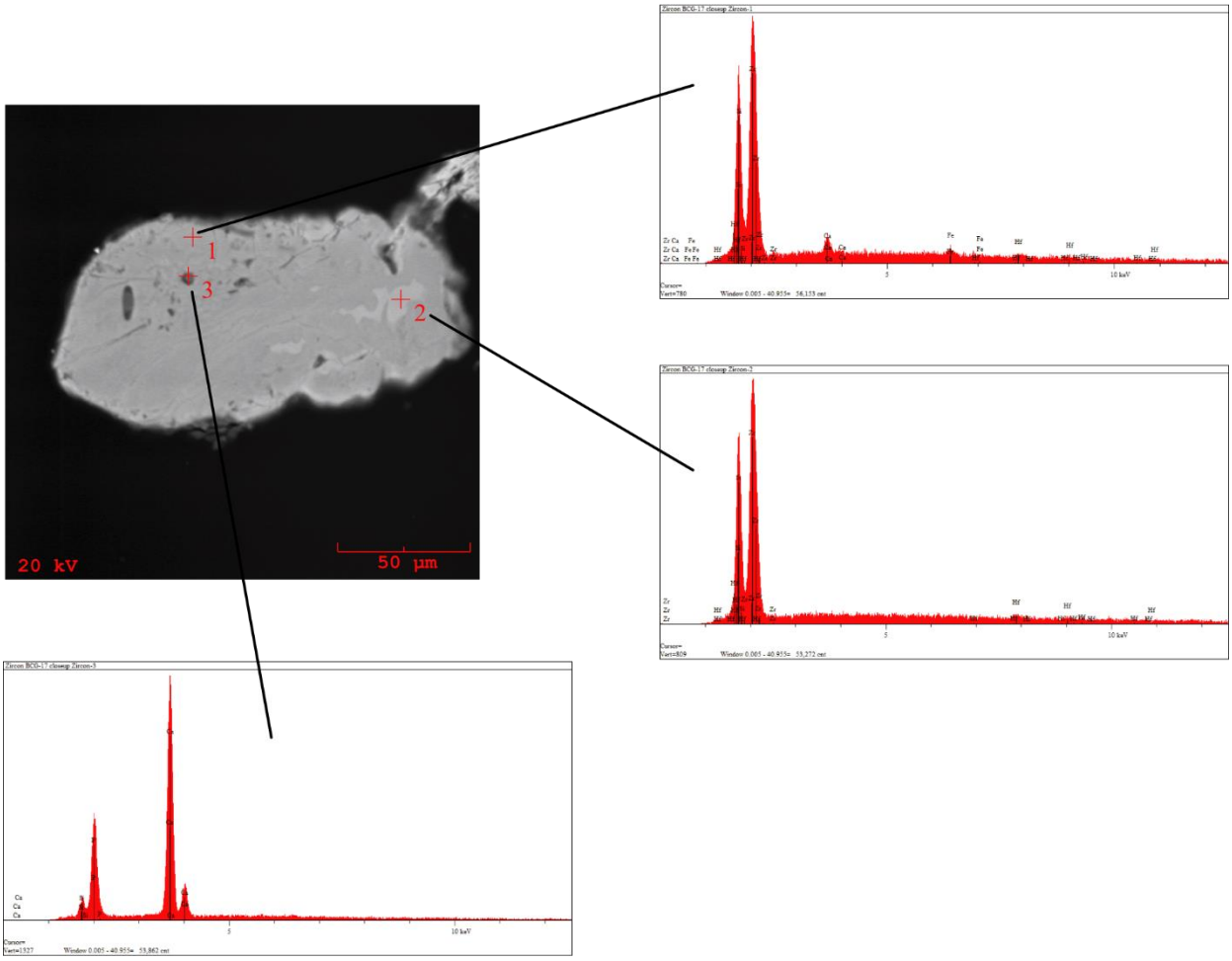


Figure 20 Zircon BSE image with associated spectra. Crosshair 1 – area of grain with relatively higher Ca & Fe content. Crosshair 2 – contains relatively less Ca & Fe. Crosshair 3 is a possible apatite inclusion.

Zircon is uncommon in heavy mineral separations from Bell Creek granite samples. Zircons have been qualitatively investigated by SEM and confirmed by microprobe analysis. The BSE image in Figure 20 shows a region of the grain that is relatively more enriched in calcium and iron (crosshair 1) as well as an area that is relatively depleted in iron and calcium (crosshair 2). There is an inclusion of apatite (crosshair 3) in the grain as well. Zr/Hf *apfu* ratios are approximately 30%. Table 4 lists the representative zircon analyses.

| ZIRCON – BELL CREEK GRANITE | | | |
|---|---|---|---|
| Wt % Oxide | BCG-1 | | BCG Goi-1 |
| $SiO_2$ | 32.155 | 32.13 | 32.566 |
| $TiO_2$ | 0.012 | 0.017 | 0.038 |
| $Al_2O_3$ | 0.055 | 0.074 | 0.054 |
| $ZrO_2$ | 64.945 | 64.799 | 63.156 |
| $HfO_2$ | 1.344 | 1.400 | 3.009 |
| FeOt | 0.212 | 0.188 | 0.100 |
| MnO | 0.000 | 0.008 | 0.054 |
| MgO | 0.000 | 0.000 | 0.000 |
| CaO | 0.345 | 0.412 | 0.055 |
| $UO_2$ | 0.012 | 0.014 | 0.020 |
| $ThO_2$ | 0.034 | 0.043 | 0.009 |
| Total | 99.114 | 99.085 | 99.061 |
| *apfu* | | | |
| Zr | 0.979 | 0.977 | 0.952 |
| Hf | 0.016 | 0.017 | 0.036 |
| U | 0.000 | 0.000 | 0.000 |
| Th | 0.000 | 0.000 | 0.000 |
| Fe | 0.005 | 0.005 | 0.003 |
| Mg | 0.000 | 0.000 | 0.001 |
| Mn | 0.000 | 0.000 | 0.000 |
| Ca | 0.011 | 0.014 | 0.002 |
| **Σ X** | 1.011 | 1.013 | 0.994 |
| Si | 0.994 | 0.994 | 1.007 |
| Ti | 0.000 | 0.000 | 0.001 |
| Al | 0.002 | 0.003 | 0.002 |
| **Σ Y** | 0.996 | 0.997 | 1.010 |
| **Zr/Hf Ratios** | 60.849 | 58.284 | 26.430 |

Table 4 Representative EMP zircon analyses.
*Apfu* calculations based on 4 oxygens.

## HUMBOLDT GRANITE

Figure 21  Field pictures of Humboldt granite samples.

Samples of Humboldt granite have been collected from exposures of granitic material that coincide with previously mapped locations (Hoffman, 1987).  Additional samples are provided by Tom Buchholz.  Specimens have been gathered using a sledge hammer to ensure freshness.  Visual inspection of Humboldt granite reveal a medium- to coarse-grained texture with abundant feldspar and quartz with moderate amounts of mica.  Humboldt granite has a range of reddish hues as can be seen from the photographs in Figure 21.  Weathered portions have a grayish color, however, once broken, pink to reddish hues are clearly present.

Five GPS locations are sampled from the Marquette County area in Michigan. These samples have been crushed then qualitatively and quantitatively analyzed by SEM and EMP respectively. Apatite, biotite mica, feldspar (potassium and plagioclase), flurorite, ilmenite, magnetite, “monazite”, muscovite mica, pyrite, a quantitatively unconfirmed tantalum/niobium mineral, a thorium/uranium-rich mineral species, vanadinite, quartz, and zircon have all been qualitatively investigated by SEM. Biotite and muscovite micas and zircon have been quantitatively confirmed by EMP.

## APATITE

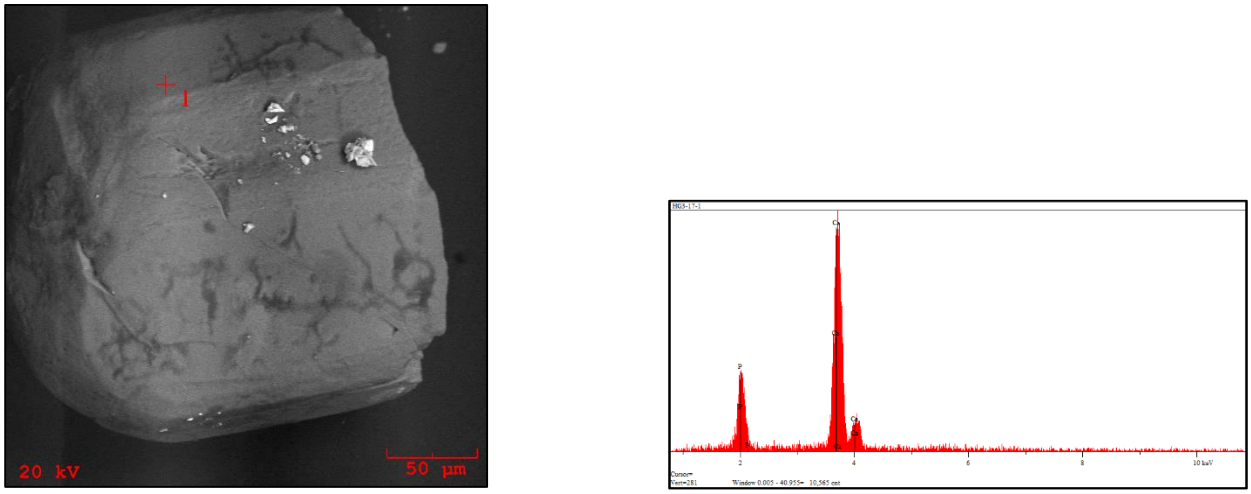


Figure 22 BSE image of apatite grain and associated EDS spectrum.

Apatite is very rare in Humboldt granite samples. Only four grains have been discovered and qualitatively investigated by SEM. The BSE image in Figure 22 shows the only grain to be relatively euhedral. The other three grains are anhedral. All grains are less than 300 microns in diameter. Further analyses by microprobe has been unsuccessful owing to the scarcity and size of apatite in heavy mineral separations

## BIOTITE

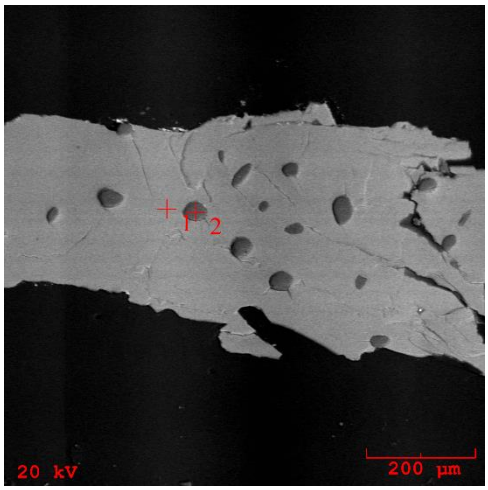


Figure 23 Biotite BSE image with quartz inclusions.

Biotite mica is common in all Humboldt granite samples. Biotite has been qualitatively explored via SEM and quantitatively confirmed as Fe-biotite (Figure 186) after investigation by microprobe (Tischendorf, 1997). Rubidium weight percent is just within detectable limits. Cesium is below detection limits. Biotite micas from the Humboldt granite are considered to be relatively primitive due to the low rubidium content. There is insufficient homogeneous grains of biotite to determine trivalent iron contents (the sample in Figure 23 has quite a few quartz inclusions) by titration analyses. Determination of lithium contents by DCP has likewise not been conducive owing to lack of sufficient quantities of homogeneous grains. Lithium is accounted for regardless by using Tischendorf's equations. Table 5 lists the representative analyses from each of the Humboldt granite locations.

| BIOTITE – HUMBOLDT GRANITE | | | | | | | | | | | |
|---|---|---|---|---|---|---|---|---|---|---|---|
| Wt % Ox. | GPS.1-1 | GPS.1-2 | GPS.1-3 | GPS.2-5 | GPS.3-7 | HG.2-18 | HG.4-19 | HG.4-20 | HG.5-22 | HG.5-23 | HG.5-24 |
| $SiO_2$ | 33.454 | 33.387 | 33.410 | 33.298 | 33.412 | 33.544 | 34.336 | 34.400 | 34.312 | 34.500 | 34.512 |
| $TiO_2$ | 0.450 | 0.483 | 0.367 | 0.856 | 0.565 | 0.423 | 3.433 | 3.298 | 1.565 | 0.891 | 0.900 |
| $Al_2O_3$ | 17.211 | 17.184 | 17.423 | 17.236 | 17.009 | 17.655 | 17.322 | 17.400 | 17.877 | 17.988 | 18.092 |
| $Fe_2O_3$ | 0.000 | 0.000 | 0.000 | 0.000 | 0.000 | 0.000 | 0.000 | 0.000 | 0.000 | 0.000 | 0.000 |
| FeO | 26.332 | 26.417 | 26.310 | 26.093 | 26.712 | 26.012 | 22.788 | 22.854 | 22.771 | 22.800 | 22.566 |
| MnO | 0.438 | 0.388 | 0.341 | 0.354 | 0.212 | 0.255 | 0.164 | 0.132 | 0.100 | 0.091 | 0.132 |
| MgO | 6.766 | 6.388 | 6.551 | 6.400 | 6.344 | 6.223 | 6.988 | 6.789 | 6.721 | 6.671 | 6.552 |
| CaO | 0.065 | 0.056 | 0.040 | 0.044 | 0.044 | 0.060 | 0.115 | 0.091 | 0.083 | 0.112 | 0.100 |
| $Li_2O$ (*calc.*) | 0.249 | 0.271 | 0.261 | 0.270 | 0.273 | 0.281 | 0.374 | 0.409 | 0.422 | 0.432 | 0.457 |
| $Na_2O$ | 0.076 | 0.066 | 0.111 | 0.121 | 0.093 | 0.143 | 0.132 | 0.099 | 0.115 | 0.165 | 0.099 |
| $K_2O$ | 8.654 | 8.723 | 8.556 | 8.712 | 8.566 | 8.788 | 8.556 | 8.700 | 8.679 | 8.888 | 8.780 |
| $Rb_2O$ | 0.013 | 0.014 | 0.014 | 0.016 | 0.016 | 0.017 | 0.020 | 0.016 | 0.017 | 0.021 | 0.019 |
| $Cs_2O$ | *bdl* | *bdl* | *bdl* | *bdl* | *bdl* | *bdl* | *bdl* | *bdl* | *bdl* | *bdl* | *bdl* |
| F | 1.187 | 1.224 | 1.312 | 1.223 | 1.191 | 1.100 | 1.091 | 1.115 | 1.150 | 1.215 | 1.211 |
| $H_2O$ | 3.162 | 3.128 | 3.095 | 3.135 | 3.139 | 3.201 | 3.313 | 3.299 | 3.225 | 3.187 | 3.183 |
| F=O | - 0.500 | - 0.515 | - 0.552 | - 0.515 | - 0.501 | - 0.463 | - 0.459 | - 0.469 | - 0.484 | - 0.512 | - 0.510 |
| Total | 97.558 | 97.214 | 97.239 | 97.243 | 97.075 | 97.238 | 98.173 | 98.133 | 96.553 | 96.449 | 96.093 |
| *apfu* | | | | | | | | | | | |
| Si | 5.385 | 5.398 | 5.390 | 5.375 | 5.410 | 5.404 | 5.375 | 5.389 | 5.457 | 5.498 | 5.508 |
| $^{IV}Al$ | 2.615 | 2.602 | 2.610 | 2.625 | 2.590 | 2.596 | 2.625 | 2.611 | 2.543 | 2.502 | 2.492 |
| **Σ T-site** | 8.000 | 8.000 | 8.000 | 8.000 | 8.000 | 8.000 | 8.000 | 8.000 | 8.000 | 8.000 | 8.000 |
| $^{VI}Al$ | 0.651 | 0.673 | 0.703 | 0.654 | 0.656 | 0.756 | 0.571 | 0.601 | 0.808 | 0.876 | 0.911 |
| Ti | 0.055 | 0.059 | 0.045 | 0.104 | 0.069 | 0.051 | 0.404 | 0.389 | 0.187 | 0.107 | 0.108 |
| $Fe_t$ | 3.545 | 3.572 | 3.550 | 3.523 | 3.617 | 3.505 | 2.983 | 2.994 | 3.029 | 3.039 | 3.012 |
| Mn | 0.060 | 0.053 | 0.047 | 0.048 | 0.029 | 0.035 | 0.022 | 0.018 | 0.013 | 0.012 | 0.018 |
| Mg | 1.624 | 1.540 | 1.575 | 1.540 | 1.531 | 1.494 | 1.631 | 1.585 | 1.594 | 1.585 | 1.559 |
| Li (*calc.*) | 0.161 | 0.176 | 0.170 | 0.175 | 0.178 | 0.182 | 0.235 | 0.258 | 0.270 | 0.277 | 0.293 |
| **Σ Y-site** | 6.096 | 6.073 | 6.089 | 6.044 | 6.080 | 6.023 | 5.846 | 5.845 | 5.902 | 5.896 | 5.901 |

Table 5 Representative EMP analyses of biotite mica. *Apfu* calculations based on 24 anions. Table continues on next page.

| | | | | | | | | | | | |
|---|---|---|---|---|---|---|---|---|---|---|---|
| K | 1.777 | 1.799 | 1.761 | 1.794 | 1.769 | 1.806 | 1.709 | 1.739 | 1.761 | 1.807 | 1.788 |
| Ca | 0.011 | 0.010 | 0.007 | 0.008 | 0.008 | 0.010 | 0.019 | 0.015 | 0.014 | 0.019 | 0.017 |
| Na | 0.024 | 0.021 | 0.035 | 0.038 | 0.029 | 0.045 | 0.040 | 0.030 | 0.035 | 0.051 | 0.031 |
| Rb | 0.001 | 0.001 | 0.001 | 0.002 | 0.002 | 0.002 | 0.002 | 0.002 | 0.002 | 0.002 | 0.002 |
| Cs | *bdl* | *bdl* | *bdl* | *bdl* | *bdl* | *bdl* | *bdl* | *bdl* | *bdl* | *bdl* | *bdl* |
| **Σ X-site** | 1.813 | 1.831 | 1.804 | 1.842 | 1.808 | 1.863 | 1.770 | 1.786 | 1.812 | 1.879 | 1.838 |
| F | 0.604 | 0.626 | 0.669 | 0.624 | 0.610 | 0.560 | 0.540 | 0.552 | 0.578 | 0.612 | 0.611 |
| OH* | 3.396 | 3.374 | 3.331 | 3.376 | 3.390 | 3.440 | 3.460 | 3.448 | 3.422 | 3.388 | 3.389 |
| **Σ W-site** | 4.000 | 4.000 | 4.000 | 4.000 | 4.000 | 4.000 | 4.000 | 4.000 | 4.000 | 4.000 | 4.000 |

## FELDSPARS

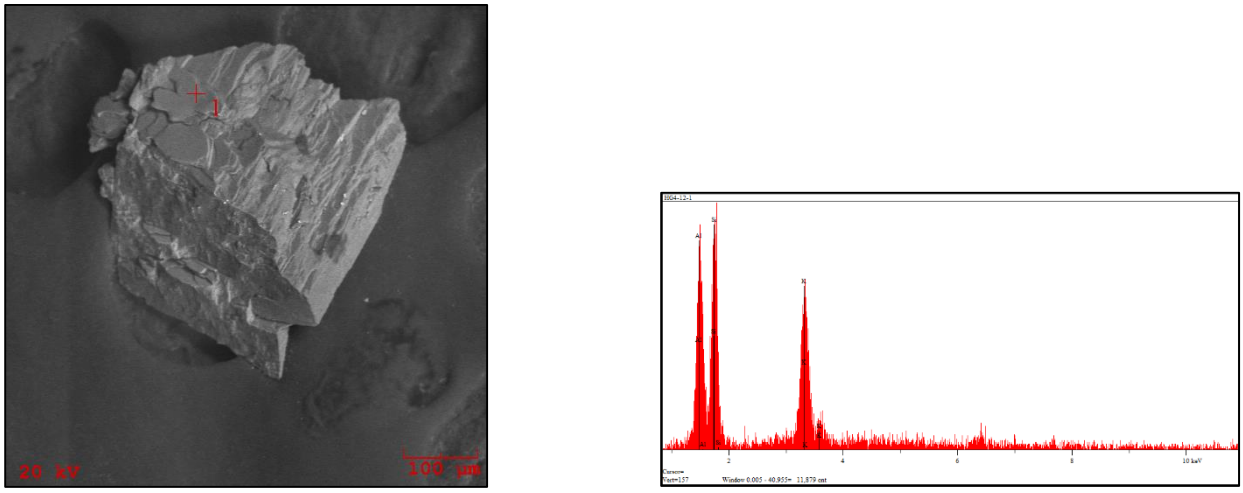


Figure 24 BSE image of K-feldspar grain and EDS spectrum.

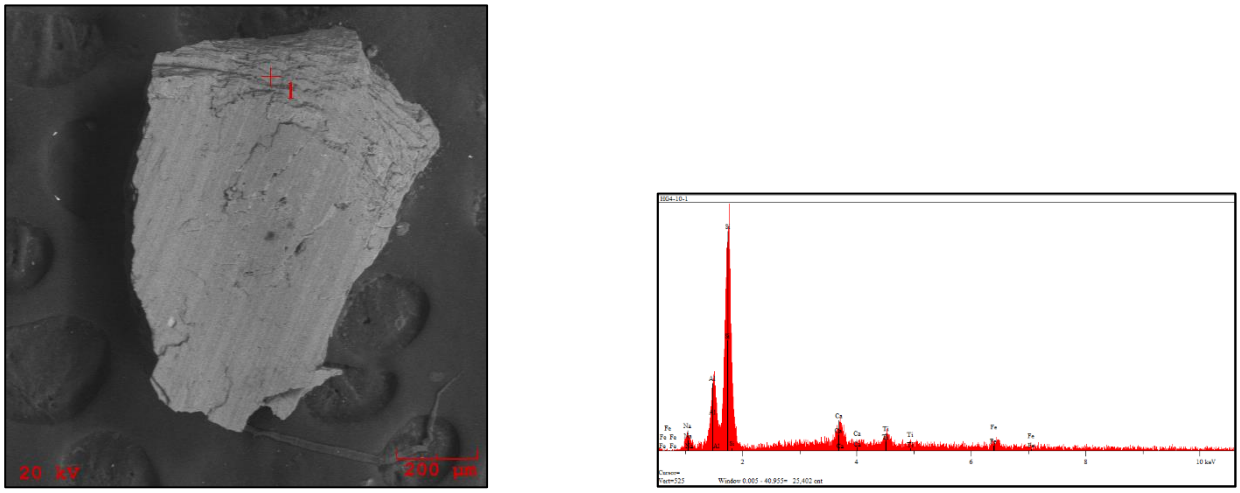


Figure 25 BSE image of plagioclase feldspar grain with associated EDS spectrum.

Both K-feldspar and plagioclase feldspar are present in Humboldt granite samples and have been qualitatively analyzed by SEM. A sample of feldspar from one of the GPS locations has been further analyzed by XRD. There is a margin of error in the analysis (Figure 173); however, the analysis plots very near the maximum microcline field (Wright & Stewart, 1968).

## FLUORITE

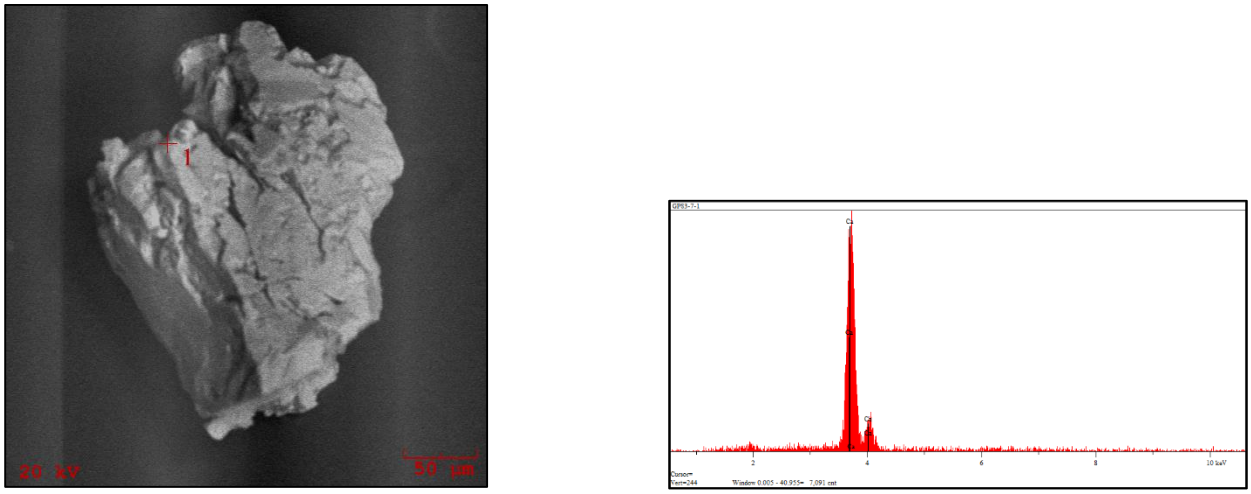


Figure 26 Fluorite BSE image with EDS spectrum.

Fluorite is present in heavy mineral separations, but not all Humboldt samples have fluorite. Grains are small and only few hundred microns in diameter.

## MAGNETITE

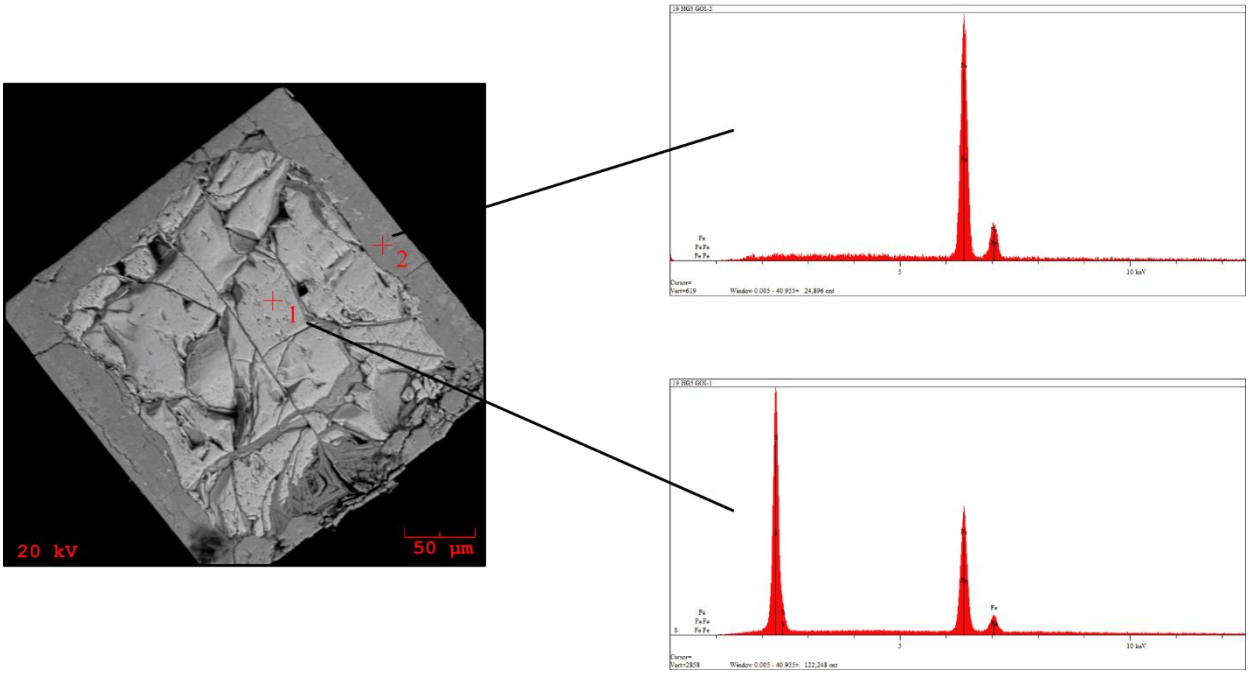


Figure 27 BSE image of grain with pyrite core (crosshair 1) and magnetite cube overgrowth (crosshair 2). Associated EDS spectra on right.

In addition to finding discrete grains of magnetite, there are a few instances where magnetite forms an overgrowth on pyrite. The BSE image in Figure 27 shows a magnetite cube with a pyrite core.

## MONAZITE

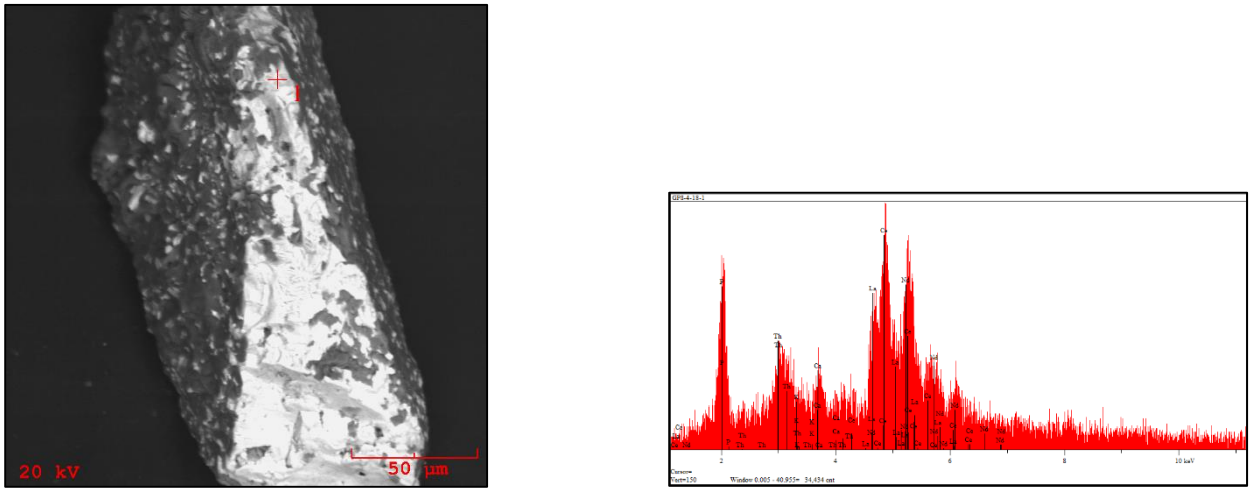


Figure 28 BSE image of "monazite" (lighter area – crosshair 1) and EDS spectrum. Darker region is feldspar.

"Monazite" is very rare to find in heavy mineral separations and has been qualitatively investigated by SEM. "Monazite" and apatite are the only two phosphate accessory minerals and other than a single "bastnäsite" grain, the only REE-bearing accessory mineral found in Humboldt granite samples.

## MUSCOVITE

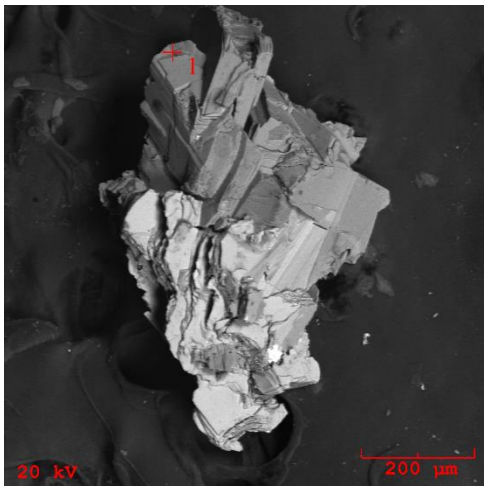


Figure 29 BSE image of muscovite mica (crosshair 1).

Muscovite mica is found in heavy mineral separations and has been qualitatively investigated by SEM, and confirmed by microprobe (Figure 185) (Tischendorf, 1997). Rubidium levels are just within detectable limits and cesium is below detection limits, therefore it is suggested that muscovites are poorly evolved. Sufficient quantities of homogeneous grains are not available to determine lithium and trivalent iron by DCP and titration respectively. Lithium is accounted for stoichiometrically using the equation 0.3935 * fluorine weight percent$^{1.326}$ (Tischendorf, 1997). Table 6 lists the representative analyses.

| **MUSCOVITE – HUMBOLDT GRANITE** | | | | |
|---|---|---|---|---|
| Wt % Ox. | HG6-1 | HG6-2 | HG12-1 | HG15-2 |
| $SiO_2$ | 46.344 | 46.351 | 46.433 | 46.337 |
| $TiO_2$ | 0.151 | 0.148 | 0.093 | 0.110 |
| $Al_2O_3$ | 34.232 | 34.187 | 34.054 | 34.211 |
| $Fe_2O_3$ | 0.000 | 0.000 | 0.000 | 0.000 |
| FeO | 2.987 | 3.112 | 3.566 | 3.143 |
| MnO | 0.050 | 0.049 | 0.052 | 0.110 |
| MgO | 0.211 | 0.115 | 0.114 | 0.091 |
| CaO | 0.121 | 0.131 | 0.094 | 0.054 |
| $Li_2O$ (*calc.*) | 0.706 | 0.659 | 0.566 | 0.547 |
| $Na_2O$ | 0.477 | 0.400 | 0.345 | 0.455 |
| $K_2O$ | 9.088 | 8.934 | 8.730 | 8.345 |
| $Rb_2O$ | 0.023 | 0.021 | 0.017 | 0.020 |
| $Cs_2O$ | *bdl* | *bdl* | *bdl* | *bdl* |
| F | 1.554 | 1.476 | 1.316 | 1.282 |
| $H_2O$ | 3.736 | 3.764 | 3.834 | 3.838 |
| F=O | - 0.654 | - 0.621 | - 0.554 | - 0.540 |
| Total | 99.026 | 98.726 | 98.660 | 98.003 |
| *apfu* | | | | |
| Si | 6.213 | 6.228 | 6.246 | 6.250 |
| $^{IV}Al$ | 1.787 | 1.772 | 1.754 | 1.750 |
| **Σ T-site** | 8.000 | 8.000 | 8.000 | 8.000 |
| $^{VI}Al$ | 3.622 | 3.641 | 3.645 | 3.689 |
| Ti | 0.015 | 0.015 | 0.009 | 0.011 |
| $Fe_t$ | 0.335 | 0.350 | 0.401 | 0.355 |
| Mn | 0.006 | 0.006 | 0.006 | 0.013 |
| Mg | 0.042 | 0.023 | 0.023 | 0.018 |
| Li (*calc.*) | 0.381 | 0.357 | 0.307 | 0.297 |
| **Σ Y-site** | 4.401 | 4.392 | 4.391 | 4.383 |

Table 6 Representative muscovite mica EMP analyses. *Apfu* calculations based on 24 anions.
Table continues on next page.

| | | | | |
|---|---|---|---|---|
| K | 1.554 | 1.531 | 1.498 | 1.436 |
| Ca | 0.017 | 0.019 | 0.014 | 0.008 |
| Na | 0.124 | 0.104 | 0.090 | 0.119 |
| Rb | 0.002 | 0.002 | 0.001 | 0.002 |
| Cs | *bdl* | *bdl* | *bdl* | *bdl* |
| **Σ X-site** | 1.697 | 1.656 | 1.603 | 1.565 |
| F | 0.659 | 0.626 | 0.560 | 0.547 |
| OH* | 3.341 | 3.374 | 3.440 | 3.453 |
| **Σ W-site** | 4.000 | 4.000 | 4.000 | 4.000 |

## PYRITE

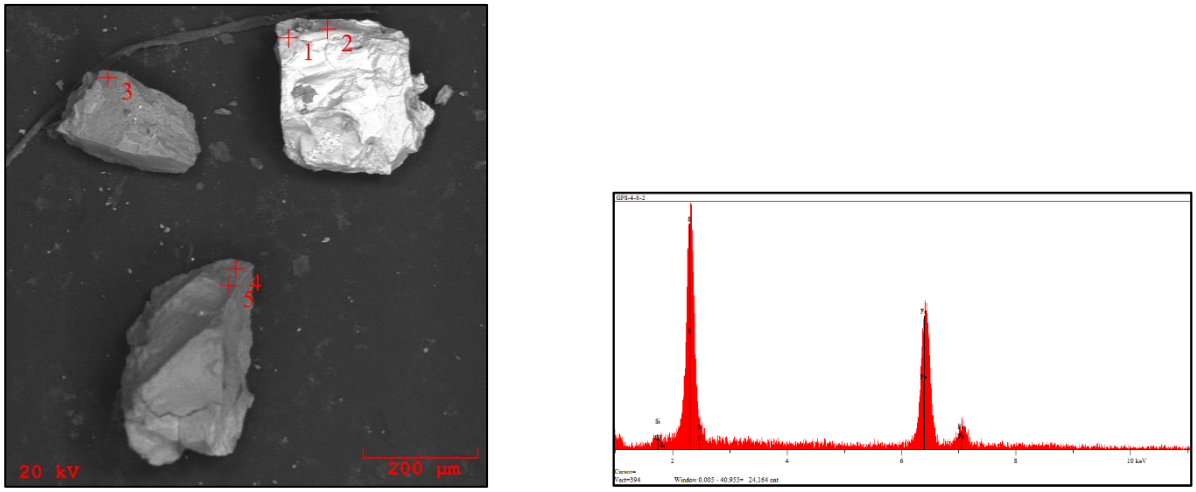


Figure 30 BSE image of pyrite grain (top right grain – crosshairs 1 & 2) and associated EDS spectrum. Crosshairs 3, 4, & 5 are feldspar.

Discrete pyrite grains are found in heavy mineral separations (crosshairs 1 & 2), although it is relatively uncommon.

## TA/NB SPECIES

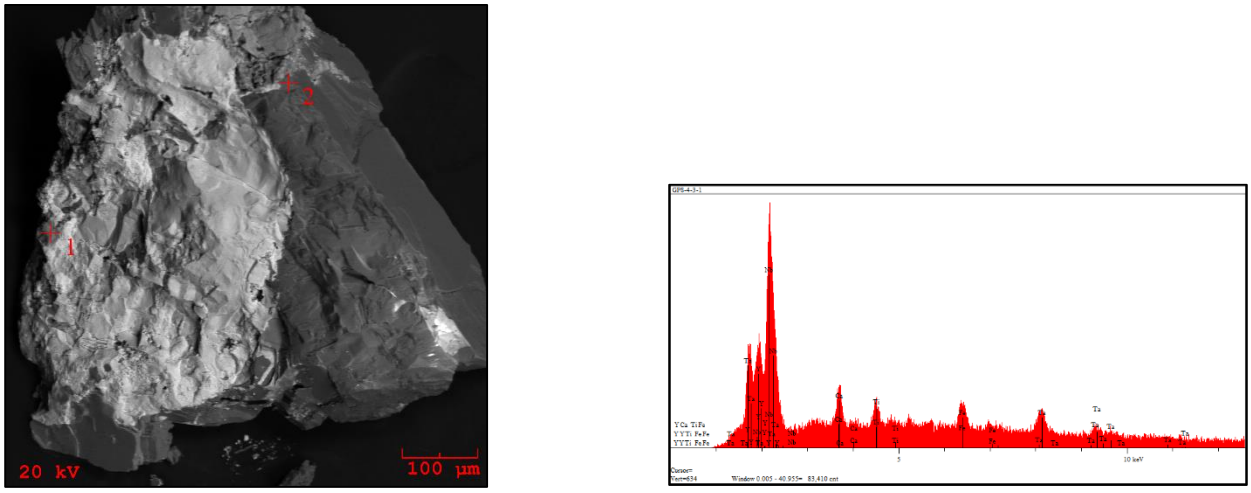


Figure 31 BSE image and associated spectrum of tantalum/niobium mineral (crosshair 1) on a feldspar grain (crosshair 2).

A tantalum/niobium mineral species is very rare as only a single grain has been found in heavy mineral separations. Unfortunately, the grain did not survive sample preparation in order to quantitatively assess the mineral chemistry. The lighter portion of the BSE image in Figure 31 corresponds to the associated spectrum on the right. Buchholz *et al*. (2014) did confirm the occurrence of ferrocolumbite from Humboldt granite samples; however, none have been found in samples collected for this study.

## TH/U SPECIES

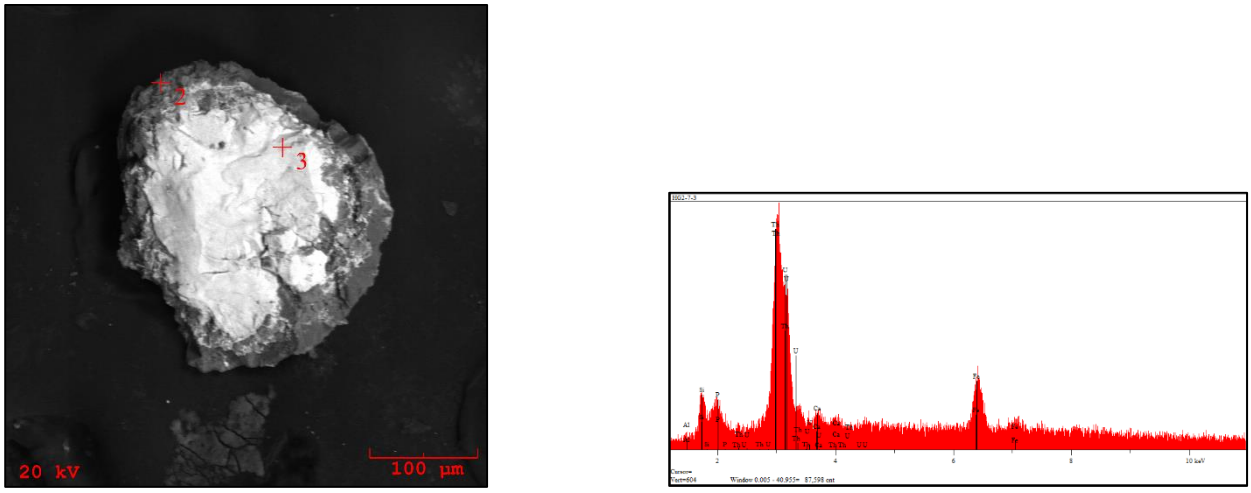


Figure 32 BSE image and spectrum of a thorium/uranium-rich mineral species (crosshair 3) on a feldspar grain (crosshair 2).

A thorium/uranium-rich overgrowth on a single grain of quantitatively unconfirmed mineral chemistry was discovered in heavy mineral separations by SEM. The bright area (crosshair 3) in Figure 32 corresponds to the EDS spectrum on the right.

## VANADINITE?

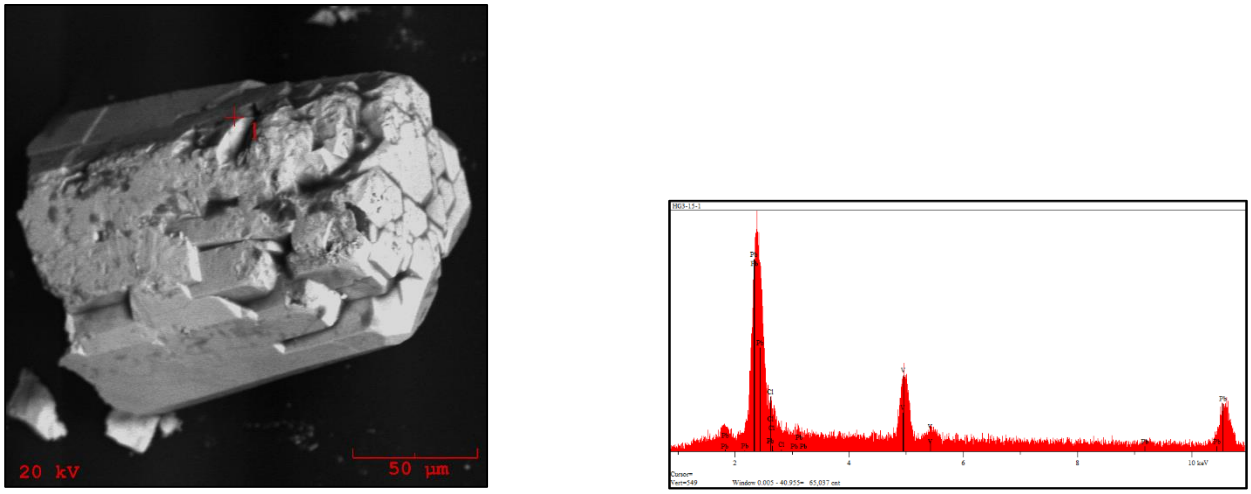


Figure 33 Vanadinite crystal BSE image and EDS spectrum.

An extraordinary (and small!) vanadinite crystal has been discovered in heavy mineral separations from HG3 location samples. If this is indeed from the Humboldt granite, it would indicate a new means of genesis for the mineral species. However, this has been the only grain found. Matrix is completely lacking, further complicating the assumption that vanadinite does indeed occur in Humboldt samples. The grain was very fragile and removal of the grain from the SEM mount resulted in its destruction.

# ZIRCON

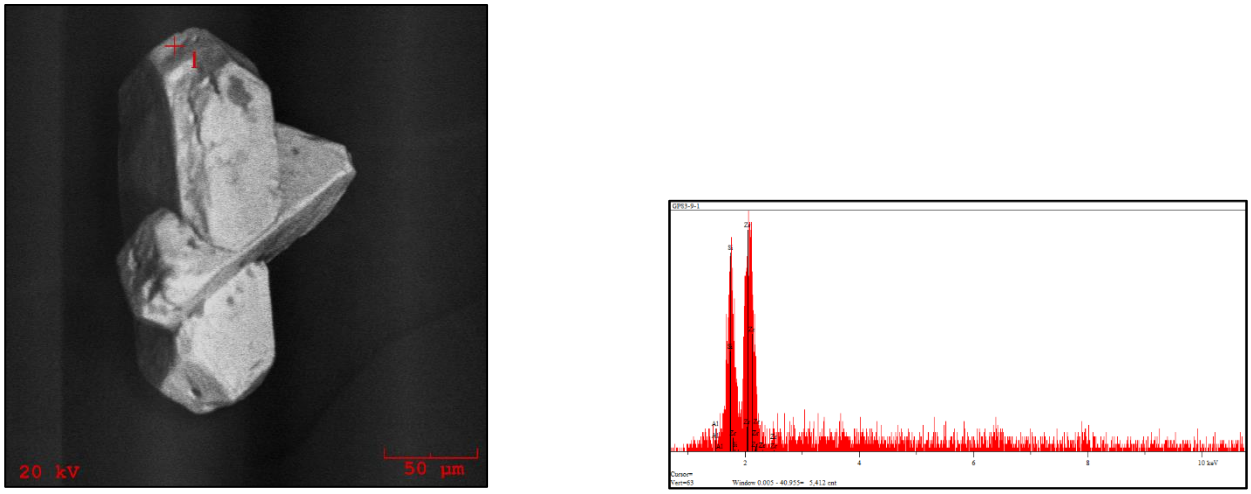


Figure 34 BSE image of twinned zircon with EDS spectrum.

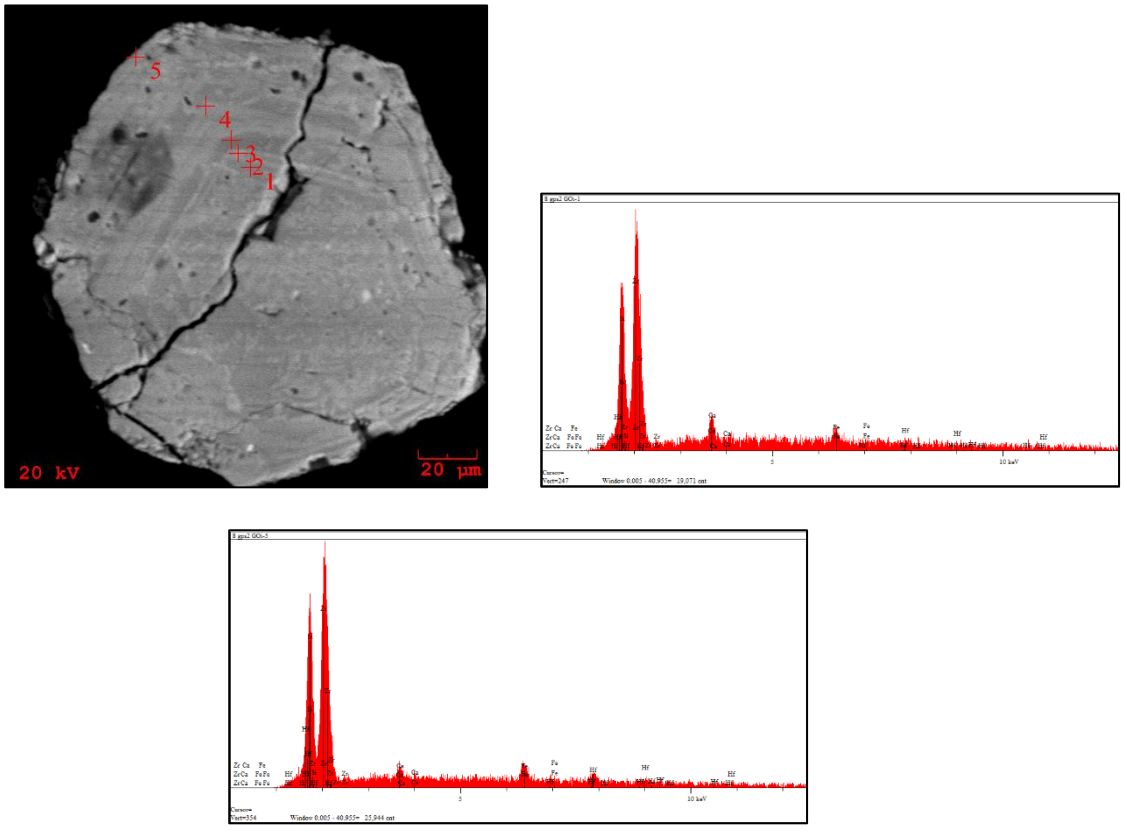


Figure 35 BSE image of polished zircon grain with internal zonation along with associated EDS spectra. Lighter areas (crosshairs 2, 4, & 5) have relatively lower Ca content. Darker areas (crosshairs 1 & 3) have relatively higher Ca content.

Zircon is present in all the samples from the Humboldt granite. Heavy mineral separations from GPS.3 are especially rich in zircon. Most zircons are small (only a few hundred microns at most) with Zr/Hf ratios between 50-60%. Table 7 lists the representative analyses.

| **ZIRCON - HUMBOLDT GRANITE** | | | | | | | | |
|---|---|---|---|---|---|---|---|---|
| Wt % Oxide | HG-2 | | HG5-1 | | HG-GPS.1 | | HG-2 Goi 8-1 | |
| $SiO_2$ | 32.001 | 31.899 | 31.822 | 31.911 | 31.771 | 31.67 | 33.800 | 33.650 |
| $TiO_2$ | 0.020 | 0.013 | 0.022 | 0.027 | 0.012 | 0.022 | 0.021 | 0.019 |
| $Al_2O_3$ | 0.101 | 0.121 | 0.032 | 0.040 | 0.020 | 0.043 | 0.056 | 0.070 |
| $ZrO_2$ | 63.677 | 64.122 | 63.544 | 63.6 | 62.788 | 62.678 | 63.500 | 63.676 |
| $HfO_2$ | 1.440 | 1.560 | 1.544 | 1.393 | 1.500 | 1.565 | 1.311 | 1.388 |
| FeOt | 0.545 | 0.123 | 0.433 | 0.388 | 0.452 | 0.500 | 0.222 | 0.211 |
| MnO | 0.011 | 0.013 | 0.030 | 0.022 | 0.455 | 0.532 | 0.056 | 0.023 |
| MgO | 0.000 | 0.000 | 0.000 | 0.000 | 0.000 | 0.000 | 0.013 | 0.011 |
| CaO | 0.833 | 0.104 | 0.774 | 0.749 | 0.655 | 0.722 | 0.766 | 0.211 |
| $UO_2$ | 0.033 | 0.0310 | 0.030 | 0.024 | 0.071 | 0.091 | 0.023 | 0.033 |
| $ThO_2$ | 0.122 | 0.109 | 0.092 | 0.111 | 0.200 | 0.232 | 0.081 | 0.089 |
| Total | 98.783 | 98.095 | 98.323 | 98.265 | 97.924 | 98.055 | 99.849 | 99.381 |
| *apfu* | | | | | | | | |
| Zr | 0.964 | 0.977 | 0.967 | 0.967 | 0.960 | 0.958 | 0.940 | 0.947 |
| Hf | 0.017 | 0.019 | 0.019 | 0.017 | 0.018 | 0.019 | 0.015 | 0.016 |
| U | 0.000 | 0.000 | 0.000 | 0.000 | 0.000 | 0.001 | 0.000 | 0.000 |
| Th | 0.001 | 0.001 | 0.001 | 0.001 | 0.001 | 0.002 | 0.001 | 0.001 |
| Fe | 0.014 | 0.003 | 0.011 | 0.010 | 0.012 | 0.013 | 0.006 | 0.005 |
| Mg | 0.000 | 0.000 | 0.001 | 0.001 | 0.012 | 0.014 | 0.001 | 0.001 |
| Mn | 0.000 | 0.000 | 0.000 | 0.000 | 0.000 | 0.000 | 0.001 | 0.001 |
| Ca | 0.028 | 0.003 | 0.026 | 0.025 | 0.022 | 0.024 | 0.025 | 0.007 |
| **Σ X-site** | 1.024 | 1.004 | 1.025 | 1.021 | 1.026 | 1.031 | 0.989 | 0.978 |
| Si | 0.993 | 0.996 | 0.993 | 0.995 | 0.996 | 0.993 | 1.026 | 1.026 |
| Ti | 0.000 | 0.000 | 0.001 | 0.001 | 0.000 | 0.001 | 0.000 | 0.000 |
| Al | 0.004 | 0.004 | 0.001 | 0.001 | 0.001 | 0.002 | 0.002 | 0.003 |
| **Σ Y-site** | 0.998 | 1.001 | 0.995 | 0.997 | 0.997 | 0.995 | 1.028 | 1.029 |
| **Zr/Hf ratios** | 55.683 | 51.759 | 51.824 | 57.493 | 52.710 | 50.432 | 60.993 | 57.769 |

Table 7 Humboldt granite zircon Microprobe analyses. *Apfu* calculations based on 4 oxygens.

## GRIZZLY PEGMATITE

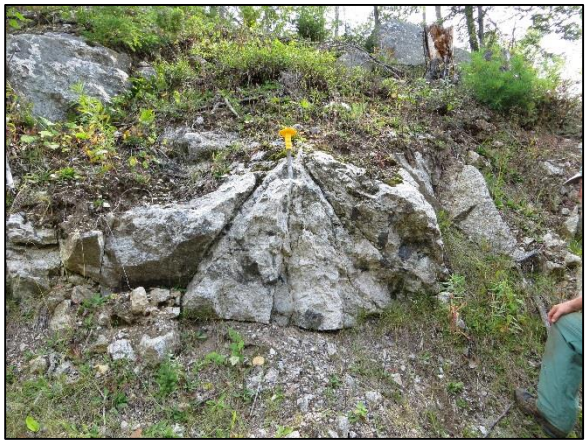


Figure 36 Field pictures of Grizzly pegmatite.

The Grizzly pegmatite is of a gray color with a slight pink hue. On a macroscopic scale, the Grizzly is composed primarily of feldspar and biotite mica. Quartz is also present, although moderately abundant. Samples from Grizzly pegmatite outcrops were collected along Hwy 95 in Marquette County, Michigan directly across from the Bell Creek granite. Samples were crushed and exposed to lithium metatungstate to float out lighter minerals. In addition, material from a boulder of muscovite schist similar to one previously described by Simmons (2009) was investigated. Samples from the boulder were provided by Tom Buchholz. The following minerals were identified by SEM and EMP from the Grizzly pegmatite: apatite, K-feldspar, zircon, “monazite”, “xenotime”, elemental bismuth, fluorite, quartz, mica, ilmenite, and possible “bastnäsite”. From the muscovite schist boulder, muscovite mica, fluorite, uraninite and quite possibly radiogenic lead, as well as pyrite were identified by the previously mentioned methods. Apatite, biotite and muscovite mica, K-feldspar, ilmenite, monazite-(Ce), elemental bismuth, and plagioclase were all quantitatively confirmed via electron microprobe.

## APATITE

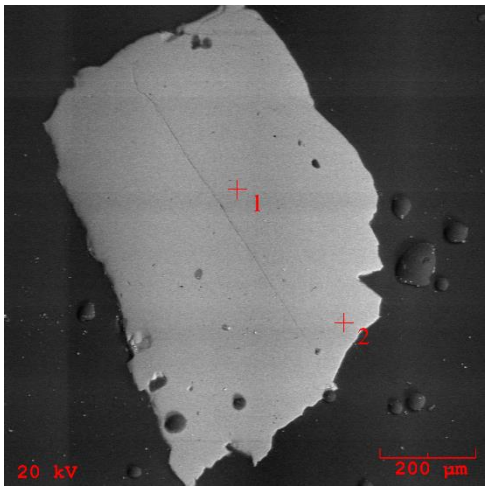


Figure 37 BSE image of polished apatite grain (crosshair 1 & 2).

Apatite has been identified from the Grizzly pegmatite by SEM and quantitatively analyzed by microprobe. Apatite, along with "monazite" and "xenotime"' are the only confirmed phosphorus-bearing minerals found within samples collected from the Grizzly pegmatite. Apatites are fluorine dominant and therefore should be classified as fluorapatite. Three EMP analyses are listed in Table 8. Grains are sub- to anhedral and approximately one millimeter in size. Grains are translucent, free of inclusions, and lack visible zonation. Grains were identified by using UV lighting as the lack of crystal faces and coloration made recognizing discrete grains with a binocular microscope difficult.

| **APATITE – GRIZZLY PEGMATITE** | | | |
|---|---|---|---|
| Wt % Oxide | 13 GrP | 14 GrP | 15 GrP |
| $P_2O_5$ | 43.199 | 42.245 | 42.244 |
| $SiO_2$ | 0.015 | 0.034 | 0.027 |
| $Al_2O_3$ | 0.022 | 0.000 | 0.000 |
| FeO | 0.000 | 0.011 | 0.014 |
| CaO | 55.575 | 55.700 | 55.677 |
| $H_20$ (*calc.*) | 0.491 | 0.491 | 0.491 |
| F | 3.021 | 3.034 | 2.822 |
| F=O | -1.272 | -1.277 | -1.188 |
| Total | 101.051 | 100.238 | 100.087 |
| *apfu* | | | |
| Ca | 4.916 | 4.986 | 4.996 |
| Fe | 0.000 | 0.001 | 0.001 |
| **Σ X** | 4.916 | 4.987 | 4.997 |
| P | 3.019 | 2.988 | 2.995 |
| Si | 0.001 | 0.003 | 0.002 |
| Al | 0.002 | 0.000 | 0.000 |
| **Σ Y** | 3.022 | 2.991 | 2.997 |
| F | 0.791 | 0.804 | 0.748 |
| H (*calc.*) | 0.209 | 0.196 | 0.252 |
| **Σ W** | 1.000 | 1.000 | 1.000 |

Table 8 Representative EMP analyses of apatite. *Apfu* calculations based on 13 anions.

## BIOTITE

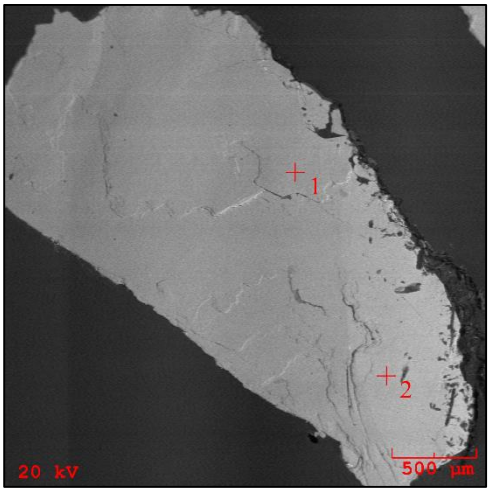


Figure 38 BSE image of polished biotite grain (crosshairs 1 & 2).

Biotite is relatively abundant at the Grizzly pegmatite. Lithium has been detected by Direct Coupled Plasma Spectroscopy and calculated based on recommended equations of Tischendorf (1997). Lithium weight percent is calculated by using $SiO_2$ and MgO weight percent totals ($0.289*SiO_2 – 9.658$) as recommended by Tischendorf (1997). DCP results of lithium weight percent content, 0.325, are slightly higher than calculated weight percent.

Based on mica classification (Tischendorf, 1997), samples are Fe-biotite (Figure 186). There is some amount of $Fe^{3+}$ that contributes to T-site, although the suggestion is that analyzed samples rarely contain more than one weight percent of trivalent iron. Rubidium is at or below detection limits and fluorine content rarely exceeds one weight percent. Cesium is below detection limits. Table 9 lists the representative analyses.

| **BIOTITE – GRIZZLY PEGMATITE** | | | | | | | | | |
|---|---|---|---|---|---|---|---|---|---|
| Wt % Ox. | 3-1 | 6-1 | 6-3 | 5a-1-2 | 5a-2-2 | 5a-3-2 | 5b-1-1 | 5b-2-1 | 5b-4-2 |
| $SiO_2$ | 34.217 | 34.166 | 34.234 | 34.355 | 34.300 | 34.400 | 34.233 | 34.233 | 34.154 |
| $TiO_2$ | 3.099 | 3.221 | 2.678 | 3.077 | 2.872 | 2.677 | 2.556 | 2.434 | 2.800 |
| $Al_2O_3$ | 16.233 | 16.444 | 16.512 | 16.522 | 16.332 | 16.676 | 17.123 | 16.988 | 16.700 |
| $Fe_2O_3$ | 1.279 | 0.918 | 0.984 | 0.872 | 1.422 | 0.809 | 0.683 | 0.921 | 1.055 |
| FeO | 24.615 | 24.615 | 24.615 | 24.615 | 24.615 | 24.615 | 24.615 | 24.615 | 24.615 |
| MnO | 0.098 | 0.132 | 0.093 | 0.092 | 0.091 | 0.088 | 0.100 | 0.232 | 0.056 |
| MgO | 5.766 | 5.743 | 4.990 | 5.334 | 5.665 | 5.334 | 4.766 | 4.445 | 4.800 |
| CaO | 0.126 | 0.089 | 0.083 | 0.188 | 0.109 | 0.114 | 0.100 | 0.109 | 0.095 |
| $Li_2O$ (*calc.*) | 0.231 | 0.126 | 0.236 | 0.271 | 0.255 | 0.284 | 0.235 | 0.235 | 0.213 |
| $Na_2O$ | 0.100 | 0.122 | 0.114 | 0.122 | 0.156 | 0.232 | 0.155 | 0.181 | 0.176 |
| $K_2O$ | 9.222 | 9.200 | 9.455 | 9.315 | 9.221 | 9.116 | 9.330 | 9.092 | 9.346 |
| $Rb_2O$ | 0.016 | 0.016 | 0.011 | 0.019 | 0.016 | 0.015 | 0.016 | 0.012 | 0.012 |
| $Cs_2O$ | *bdl* | *bdl* | *bdl* | *bdl* | *bdl* | *bdl* | *bdl* | *bdl* | *bdl* |
| F | 1.091 | 0.930 | 0.922 | 1.111 | 1.012 | 0.932 | 0.966 | 0.944 | 0.997 |
| $H_2O$ | 3.274 | 3.349 | 3.314 | 3.261 | 3.314 | 3.335 | 3.298 | 3.291 | 3.280 |
| F=O | - 0.459 | -0.392 | - 0.388 | - 0.468 | - 0.426 | -0.376 | -0.407 | -0.397 | -0.420 |
| Total | 98.907 | 98.748 | 97.852 | 98.686 | 98.954 | 98.234 | 97.771 | 97.336 | 97.879 |
| *apfu* | | | | | | | | | |
| Si | 5.412 | 5.406 | 5.473 | 5.439 | 5.422 | 5.461 | 5.465 | 5.490 | 5.457 |
| $^{IV}Al$ | 2.588 | 2.594 | 2.527 | 2.561 | 2.578 | 2.539 | 2.535 | 2.510 | 2.543 |
| **Σ T-site** | 8.000 | 8.000 | 8.000 | 8.000 | 8.000 | 8.000 | 8.000 | 8.000 | 8.000 |
| $^{VI}Al$ | 0.438 | 0.469 | 0.584 | 0.522 | 0.465 | 0.582 | 0.686 | 0.701 | 0.602 |
| Ti | 0.369 | 0.383 | 0.322 | 0.367 | 0.342 | 0.320 | 0.307 | 0.294 | 0.337 |
| $Fe_t$ | 3.408 | 3.367 | 3.409 | 3.363 | 3.423 | 3.365 | 3.368 | 3.413 | 3.416 |
| Mn | 0.013 | 0.018 | 0.013 | 0.012 | 0.012 | 0.012 | 0.014 | 0.032 | 0.008 |
| Mg | 1.360 | 1.355 | 1.189 | 1.259 | 1.335 | 1.263 | 1.135 | 1.063 | 1.144 |
| Li (*calc.*) | 0.147 | 0.137 | 0.151 | 0.172 | 0.162 | 0.181 | 0.151 | 0.152 | 0.137 |
| **Σ Y-site** | 5.735 | 5.689 | 5.668 | 5.695 | 5.739 | 5.723 | 5.661 | 5.655 | 5.644 |

Table 9 Grizzly pegmatite biotite Microprobe analyses (continued on next page).
*Apfu* calculations based on 24 anions.

| | | | | | | | | | |
|---|---|---|---|---|---|---|---|---|---|
| K | 1.861 | 1.857 | 1.928 | 1.881 | 1.860 | 1.846 | 1.900 | 1.860 | 1.905 |
| Ca | 0.021 | 0.015 | 0.014 | 0.032 | 0.018 | 0.019 | 0.017 | 0.019 | 0.016 |
| Na | 0.031 | 0.037 | 0.035 | 0.037 | 0.048 | 0.071 | 0.048 | 0.056 | 0.055 |
| Rb | 0.002 | 0.002 | 0.001 | 0.002 | 0.002 | 0.002 | 0.002 | 0.001 | 0.001 |
| Cs | *bdl* | *bdl* | *bdl* | *bdl* | *bdl* | *bdl* | *bdl* | *bdl* | *bdl* |
| **Σ X-site** | 1.915 | 1.911 | 1.979 | 1.952 | 1.928 | 1.938 | 1.967 | 1.936 | 1.977 |
| F | 0.546 | 0.465 | 0.466 | 0.556 | 0.506 | 0.468 | 0.488 | 0.479 | 0.504 |
| OH* | 3.454 | 3.535 | 3.534 | 3.444 | 3.494 | 3.532 | 3.512 | 3.521 | 3.496 |
| **Σ W-site** | 4.000 | 4.000 | 4.000 | 4.000 | 4.000 | 4.000 | 4.000 | 4.000 | 4.000 |

BISMUTH

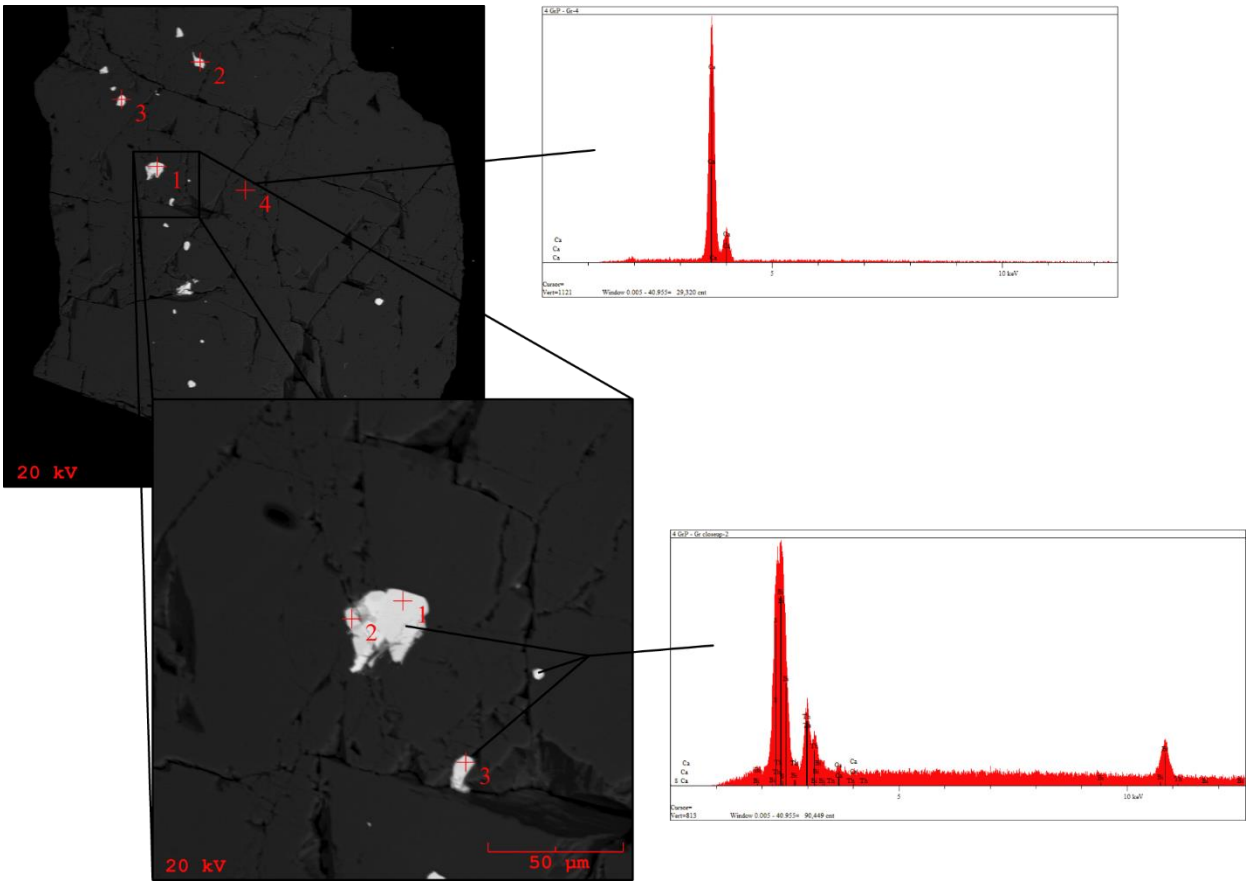


Figure 39 BSE image of elemental bismuth inclusions (crosshairs 1, 2, & 3 in both top and close-up) in fluorite grain (crosshair 4) with corresponding EDS spectra.

Elemental bismuth inclusions have been discovered in a polished fluorite mount. These inclusions are no bigger than 50 microns in diameter. Weight percent total for the single analysis are very close to 100% with trace amounts of both lead and iron.

This is the first reported and quantitatively confirmed occurrence of elemental bismuth having been found at the Grizzly pegmatite.

## FLUORITE

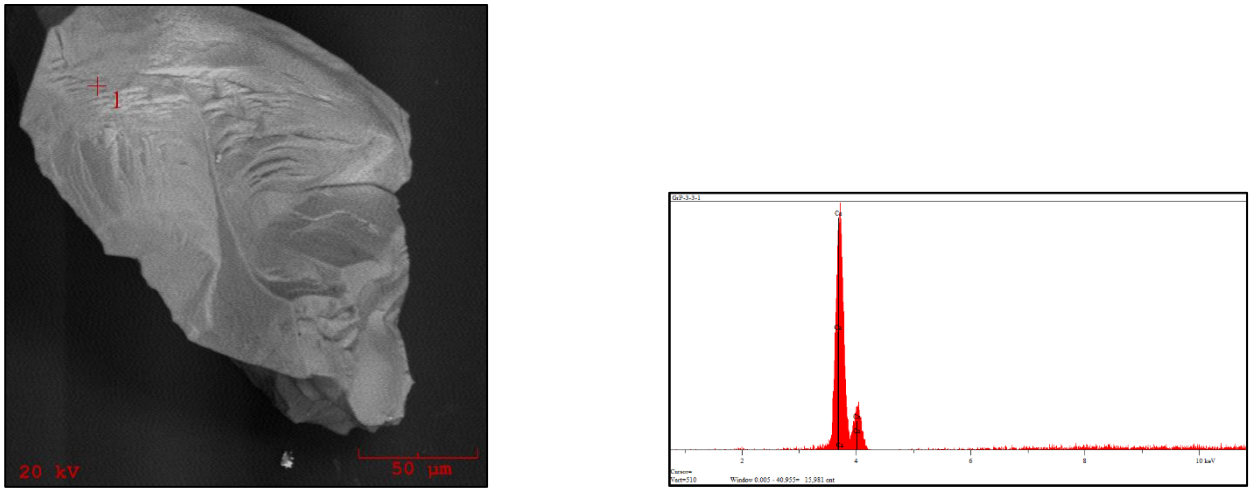


Figure 40 BSE image of fluorite grain along with corresponding EDS spectrum.

Fluorite has been identified under binocular microscope in both the Grizzly pegmatite and the muscovite schist boulder. There are no discrete fluorite grains larger than millimeter size in samples from the Grizzly. Analyzed grains from the Grizzly pegmatite are colorless with purple splotches. Fluorite from the muscovite schist boulder are dark purple to almost completely black. Fluorite from the schist are a few millimeters in size and when subjected to heat turn completely colorless with visible inclusions of quartz, "monazite", zircon, possible biotite mica, and feldspar. These inclusions are approximately 100 micrometers in size. Fluorite is relatively more abundant in the schist than the Grizzly pegmatite.

## FELDSPARS

### K-FELDSPAR

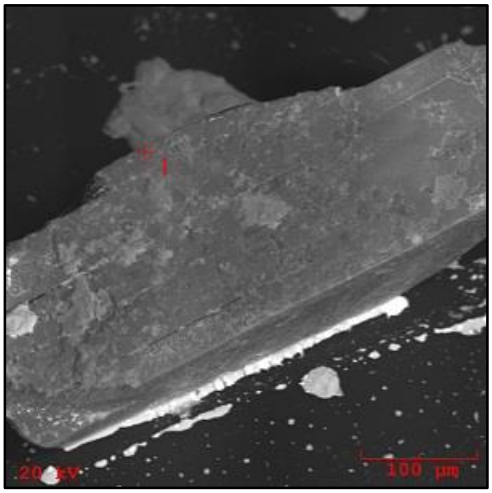


Figure 41 BSE image of K-feldspar grain.

Feldspar from the Grizzly pegmatite is mostly potassium-rich. Barium and rubidium are below and at detection limits respectively suggesting that analyzed feldspars are poorly evolved. Grains do contain exsolution lamellae of Na-rich plagioclase, but these are not uniform in appearance. Analyzed grains contain plagioclase inclusions similar in description to previously published data by Hoffman (1987). His samples are from the Bell Creek granite.

Plagioclase inclusions Hoffman has described have a more sodium-rich rim than core, as do samples from the Grizzly, but Grizzly plagioclase inclusions have submillimeter inclusions of muscovite mica, fluorite, and "monazite" not previously described in Bell Creek samples. Table 10 shows analyses of K-feldspar and sodium-rich "lamellae". Figure 42 shows BSE images and corresponding EDS spectra of the rim and core of plagioclase inclusions as well as inclusions of fluorite and muscovite mica.

Grizzly feldspars have been analyzed by X-ray diffraction (Figure 173). An accurate determination of structural ordering has not been possible, owing perhaps to the geochemical variability imparted by inclusions. However, analyses did plot over the maximum microcline field indicating there is some amount of structural ordering present (Wright & Stewart, 1968).

| **K-FELDSPAR - GRIZZLY PEGMATITE** | | | | | | | | |
|---|---|---|---|---|---|---|---|---|
| Wt% ox | 5a grain 2-1 | 5a grain 2-2 | 5a grain 3-1 | 5a grain 3-2 | 5b grain 1-1 | 5b grain 1-2 | 5b grain 2-1 | 5b grain 2-2 |
| $P_2O_5$ | 0.009 | 0.000 | 0.000 | 0.000 | 0.009 | 0.000 | 0.000 | 0.000 |
| $SiO_2$ | 64.722 | 68.633 | 64.722 | 67.276 | 64.762 | 67.345 | 64.743 | 67.377 |
| $TiO_2$ | 0.011 | 0.000 | 0.013 | 0.000 | 0.009 | 0.000 | 0.013 | 0.000 |
| $Al_2O_3$ | 18.302 | 19.677 | 18.383 | 20.222 | 18.344 | 20.322 | 18.344 | 20.304 |
| $FeO_t$ | 0.009 | 0.000 | 0.011 | 0.000 | 0.012 | 0.000 | 0.012 | 0.000 |
| CaO | 0.000 | 0.822 | 0.000 | 1.981 | 0.000 | 2.455 | 0.000 | 2.333 |
| $Na_2O$ | 0.422 | 10.566 | 0.411 | 10.211 | 0.500 | 9.776 | 0.383 | 9.812 |
| $K_2O$ | 16.500 | 0.066 | 16.432 | 0.156 | 16.223 | 0.054 | 16.612 | 0.034 |
| Rb2O | 0.000 | 0.000 | 0.000 | 0.000 | 0.000 | 0.000 | 0.000 | 0.000 |
| **Total** | 99.986 | 99.764 | 99.983 | 99.855 | 99.871 | 99.952 | 100.116 | 99.860 |
| *apfu* | | | | | | | | |
| K | 0.975 | 0.004 | 0.970 | 0.009 | 0.958 | 0.003 | 0.981 | 0.002 |
| Na | 0.038 | 0.895 | 0.037 | 0.868 | 0.045 | 0.830 | 0.034 | 0.833 |
| Ca | 0.000 | 0.038 | 0.000 | 0.093 | 0.000 | 0.115 | 0.000 | 0.109 |
| Rb | 0.000 | 0.000 | 0.000 | 0.000 | 0.000 | 0.000 | 0.000 | 0.000 |
| **Σ X-site** | 1.013 | 0.937 | 1.007 | 0.970 | 1.003 | 0.948 | 1.015 | 0.944 |
| Al | 0.999 | 1.000 | 1.003 | 1.000 | 1.001 | 1.000 | 1.000 | 1.000 |
| Fe | 0.000 | 0.000 | 0.000 | 0.000 | 0.000 | 0.000 | 0.000 | 0.000 |
| **Σ Y-site** | 0.999 | 1.000 | 1.003 | 1.000 | 1.001 | 1.000 | 1.000 | 1.000 |
| Si | 2.997 | 2.997 | 2.995 | 2.950 | 2.998 | 2.948 | 2.995 | 2.950 |
| Ti | 0.000 | 0.000 | 0.000 | 0.000 | 0.000 | 0.000 | 0.000 | 0.000 |
| P | 0.000 | 0.000 | 0.000 | 0.000 | 0.000 | 0.000 | 0.000 | 0.000 |
| Al | 0.000 | 0.013 | 0.000 | 0.045 | 0.000 | 0.049 | 0.000 | 0.048 |
| **Σ Z-site** | 2.997 | 3.010 | 2.995 | 2.995 | 2.998 | 2.997 | 2.995 | 2.998 |

Table 10 K-feldspar EMP analyses. *Apfu* calculations based on 8 oxygens.

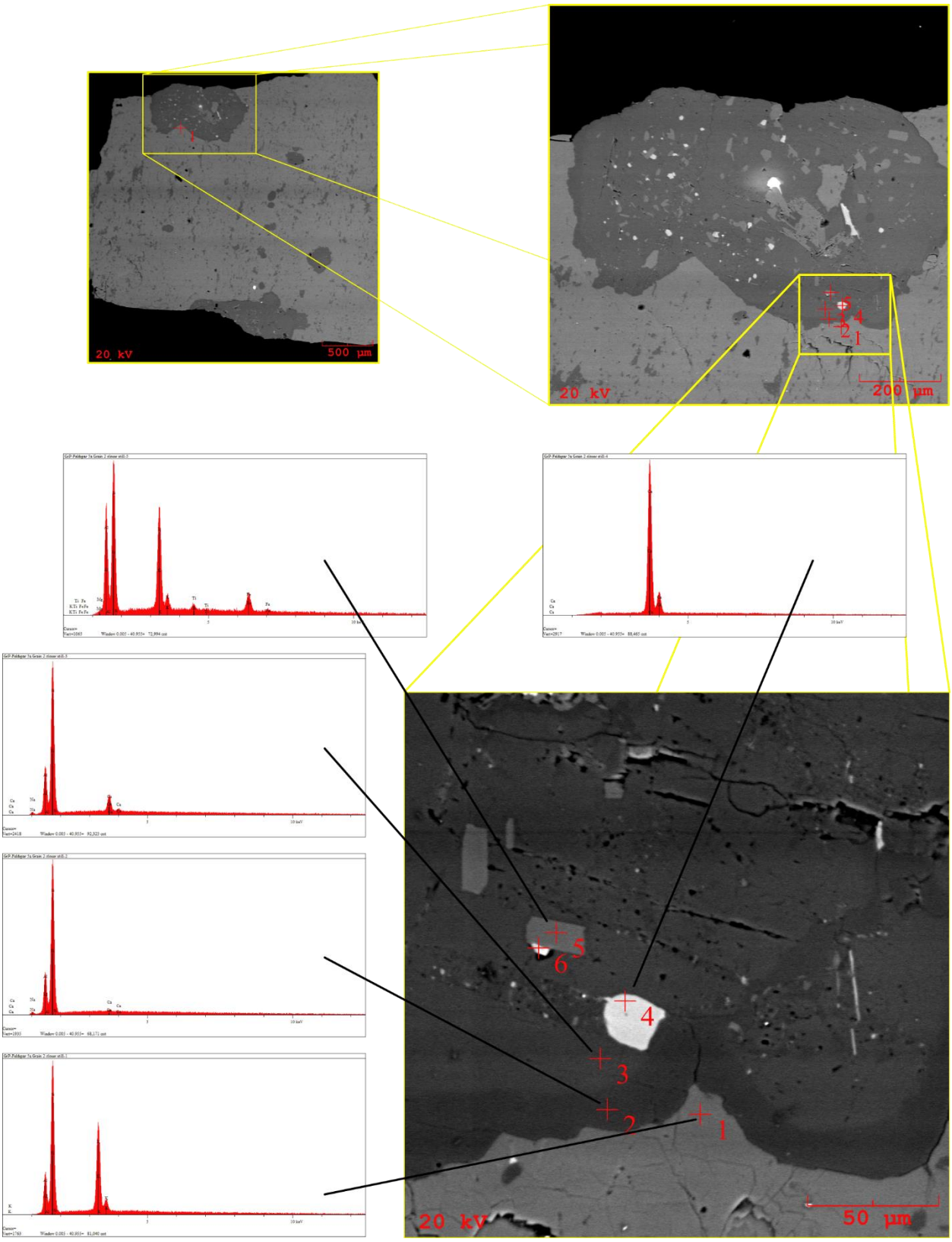


Figure 42 BSE image of K-feldspar grain with close-up of plagioclase inclusion. Associated EDS spectra of all inclusions as well as main K-feldspar grain.

## ILMENITE

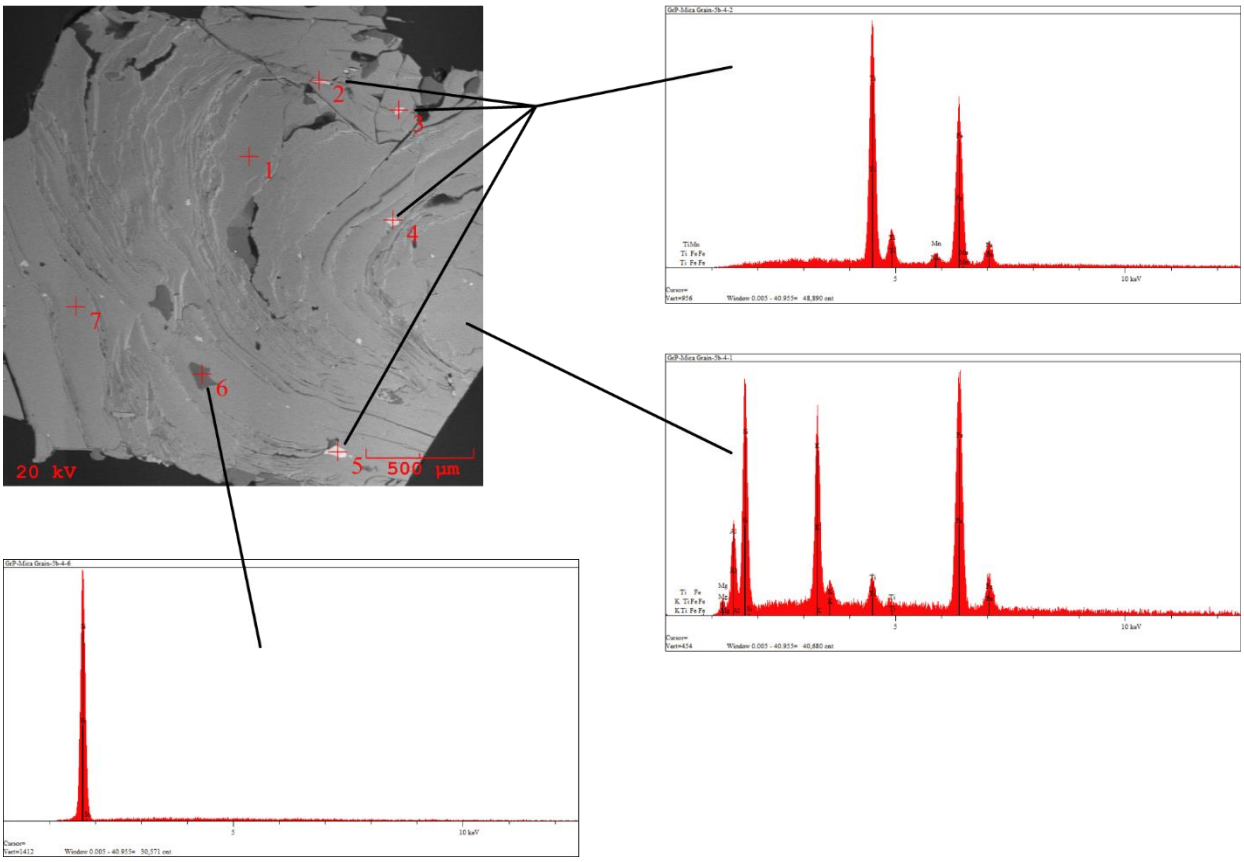


Figure 43 Ilmenite (crosshairs 2-5) and quartz (crosshair 6) inclusions in biotite grain (crosshairs 1 & 7) shown in above BSE image along with EDS spectra.

Ilmenite inclusions have been identified by SEM and analyzed by EMP. A detectable amount of niobium is present, as is approximately one weight percent of manganese. Of importance is that Fe-biotite micas from the Grizzly contain an appreciable amount of titanium, in excess of three weight percent in some cases. Table 11 shows EMP analyses. Tantalum and magnesium are both below detection limits. Weight percent totals are approximately 97% suggesting that these ilmenite inclusions may be altered in some way.

| **ILMENITE – GRIZZLY PEGMATITE** | | |
|---|---|---|
| Wt % Ox | Grain 6-2 | 5b-4-3 |
| $SiO_2$ | 0.122 | 0.088 |
| $TiO_2$ | 54.354 | 54.112 |
| $Al_2O_3$ | 0.143 | 0.211 |
| FeO | 41.899 | 41.781 |
| MnO | 1.121 | 0.981 |
| MgO | *bdl* | *bdl* |
| CaO | 0.089 | 0.143 |
| $Nb_2O_5$ | 0.022 | 0.025 |
| **Total** | 97.750 | 97.314 |
| *apfu* | | |
| Fe | 0.956 | 0.958 |
| Mn | 0.057 | 0.050 |
| Mg | *bdl* | *bdl* |
| Ca | 0.008 | 0.013 |
| Nb | 0.002 | 0.002 |
| **Σ X-site** | 1.032 | 1.031 |
| Ti | 2.479 | 2.479 |
| Al | 0.002 | 0.003 |
| Si | 0.007 | 0.005 |
| **Σ Y-site** | 2.479 | 2.479 |

Table 11 Representative EMP analyses of ilmenite.
*Apfu* calculations based on 3 oxygens.

## MONAZITE

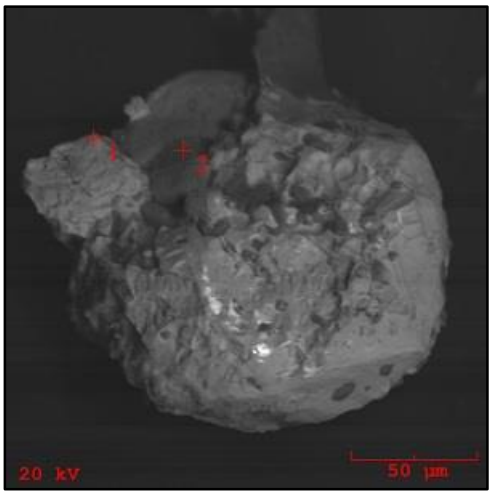


Figure 44 BSE image of monazite-(Ce) grain (crosshair 1) and feldspar (crosshair 2).

"Monazite" has been identified in Grizzly samples by SEM and further analyzed by EMP. Cerium is the dominant REE in the X-site. Monazite-(Ce) grains are far from homogeneous, having numerous inclusions of fluorite, a thorium-rich mineral species containing uranium and possible radiogenic lead, calcium and iron, as well as pyrite grains. Monazite-(Ce) grains appear to be altered in many areas within the grains as well. Table 12 shows representative EMP analyses. Figure 45 shows a BSE image of a polished grain with associated EDS spectra. Monazite-(Ce) is the most common REE-bearing accessory mineral at the Grizzly, ("bastnäsite" and "xenotime" are rarely found) and is only one of three identified phosphate-bearing accessory minerals.

| GRIZZLY – MONAZITE-(CE) | | |
|---|---|---|
| Wt % Ox. | 5-GrP-1 | 6-GrP-1 |
| $P_2O_5$ | 28.772 | 29.453 |
| $SiO_2$ | 0.210 | 0.093 |
| $TiO_2$ | 0.000 | 0.000 |
| $ThO_2$ | 8.340 | 4.998 |
| $UO_2$ | 0.933 | 0.457 |
| $Al_2O_3$ | 0.065 | 0.076 |
| $La_2O_3$ | 11.653 | 13.041 |
| $Ce_2O_3$ | 25.875 | 28.454 |
| $Pr_2O_3$ | 2.889 | 2.670 |
| $Nd_2O_3$ | 13.778 | 14.877 |
| $Sm_2O_3$ | 1.231 | 1.446 |
| $Eu_2O_3$ | 0.000 | 0.000 |
| $Gd_2O_3$ | 0.630 | 0.477 |
| $Dy_2O_3$ | 0.000 | 0.000 |
| $Yb_2O_3$ | 0.236 | 0.200 |
| $Y_2O_3$ | 0.000 | 0.000 |
| $Sc_2O_3$ | 0.000 | 0.000 |
| MgO | 0.000 | 0.000 |
| CaO | 0.000 | 0.022 |
| MnO | 0.000 | 0.000 |
| FeO | 0.562 | 0.773 |
| PbO | 0.019 | 0.023 |
| Total | 98.271 | 99.388 |
| *apfu* | | |
| Th | 0.076 | 0.045 |
| U | 0.008 | 0.004 |
| Al | 0.003 | 0.004 |
| La | 0.172 | 0.190 |
| Ce | 0.379 | 0.411 |
| Pr | 0.042 | 0.038 |
| Nd | 0.197 | 0.209 |
| Sm | 0.017 | 0.020 |
| Y | 0.012 | 0.016 |
| Ca | 0.110 | 0.084 |
| **Σ X** | 1.042 | 1.038 |
| P | 0.976 | 0.983 |
| Si | 0.008 | 0.004 |
| **Σ Y** | 0.984 | 0.987 |

Table 12 Grizzly "monazite" Microprobe analyses. *Apfu* calculations based on 4 oxygens.

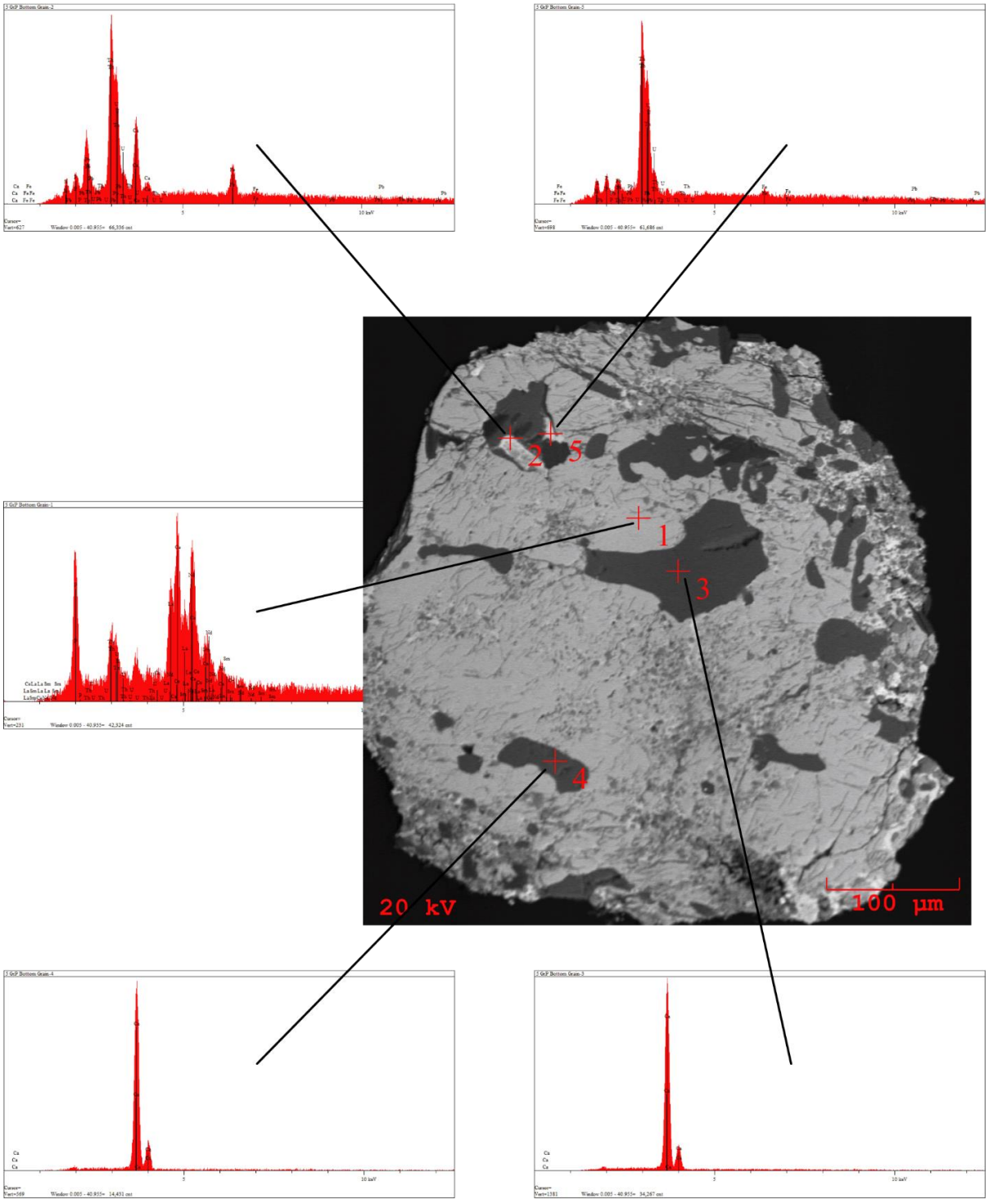


Figure 45 BSE image of polished monazite-(Ce) grain illustrating numerous inclusions and fractures within the grain.

## MUSCOVITE

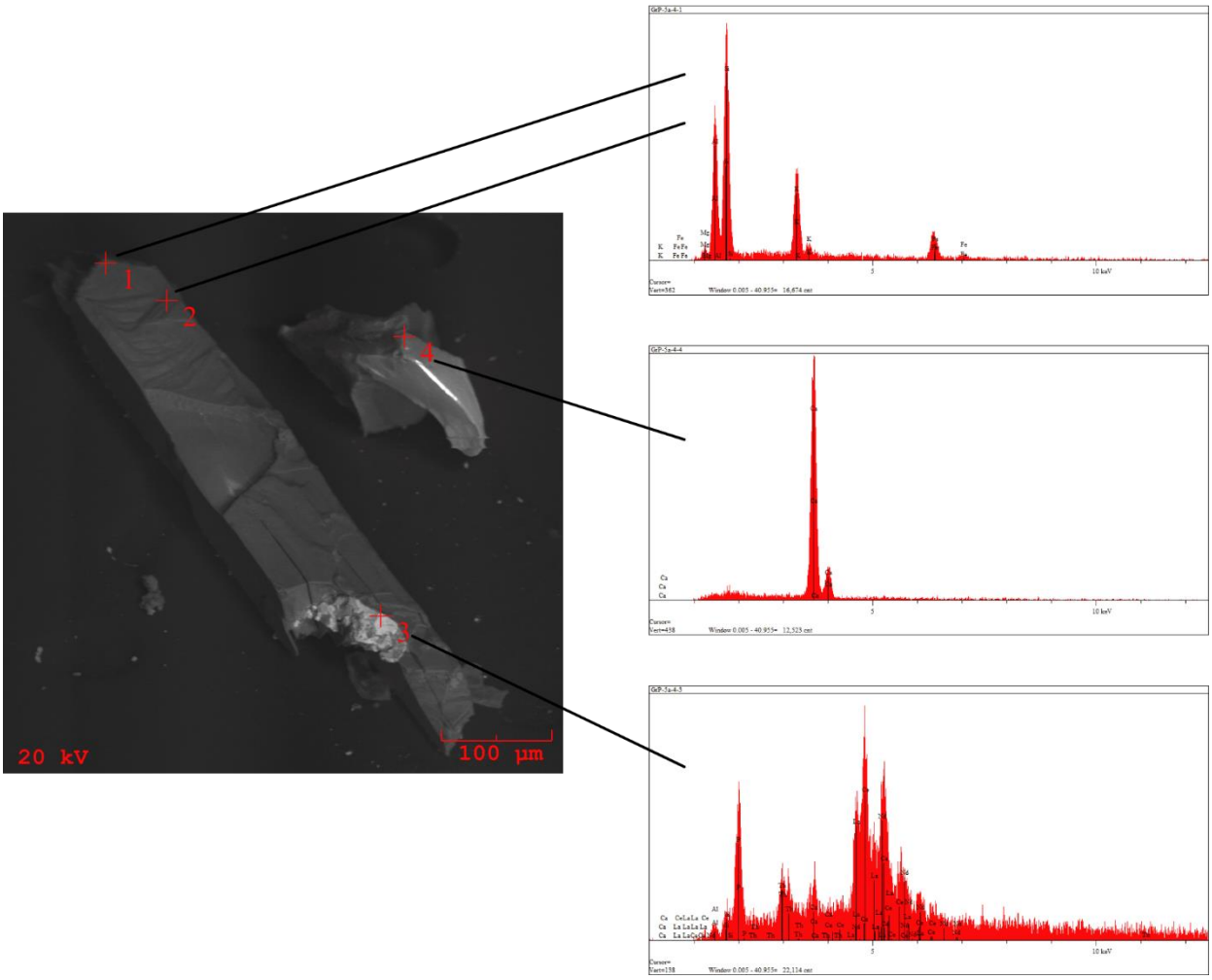


Figure 46 BSE image of muscovite mica grain. Associated spectra reveal what might have been a "monazite" grain.

Muscovite mica is rare in Grizzly samples; biotite is much more common. One analysis determines that the mica is indeed muscovite (Figure 185), based on the classification scheme of Tischendorf. The BSE image (Figure 46) of a muscovite grain with associated spectra is shown. Table 13 shows the EMP analysis. Lithium was calculated based on fluorine content using the equation 0.3935 * fluorine weight percent$^{1.326}$ (Tischendorf, 1997).

| **MUSCOVITE – GRIZZLY PEGMATITE** | |
|---|---|
| Wt % Ox. | 6-1 |
| $SiO_2$ | 45.210 |
| $TiO_2$ | 1.454 |
| $Al_2O_3$ | 30.874 |
| $Fe_2O_3$ | 0.000 |
| FeO | 1.322 |
| MnO | 0.080 |
| MgO | 2.422 |
| CaO | 0.066 |
| $Li_2O$ (*calc.*) | 0.387 |
| $Na_2O$ | 0.223 |
| $K_2O$ | 9.766 |
| $Rb_2O$ | 0.012 |
| $Cs_2O$ | *bdl* |
| F | 0.988 |
| $H_2O$ (*calc.*) | 3.873 |
| F=O | - 0.416 |
| Total | 96.261 |
| *apfu* | |
| Si | 6.245 |
| $^{IV}Al$ | 1.755 |
| **Σ T-site** | 8.000 |
| $^{VI}Al$ | 3.271 |
| Ti | 0.151 |
| $Fe_t$ | 0.153 |
| Mn | 0.009 |
| Mg | 0.499 |
| Li (*calc.*) | 0.215 |
| **Σ Y-site** | 4.298 |

Table 13 Representative EMP analysis of muscovite mica.
*Apfu* calculated based on 24 anions.
Table continues on next page.

| | |
|---|---|
| K | 1.721 |
| Ca | 0.010 |
| Na | 0.060 |
| Rb | 0.001 |
| Cs | *bdl* |
| **Σ X-site** | 1.792 |
| F | 0.432 |
| OH (*calc.*) | 3.568 |
| **Σ W-site** | 4.000 |

## RUTILE

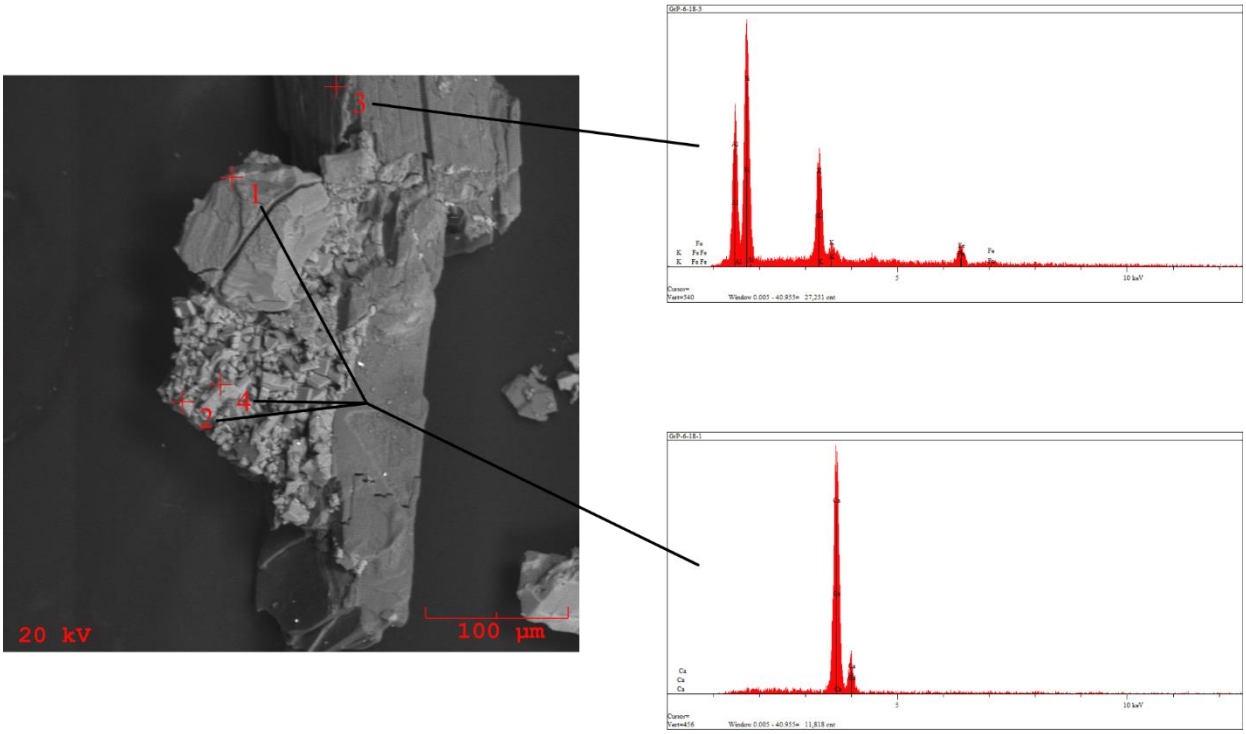


Figure 47  Muscovite mica and rutile grains in BSE image with associated EDS spectra.

Rutile has been identified by SEM from samples, and along with ilmenite, is an accessory titanium-bearing mineral at the Grizzly pegmatite.

## "XENOTIME", "BASTNÄSITE", ZIRCON

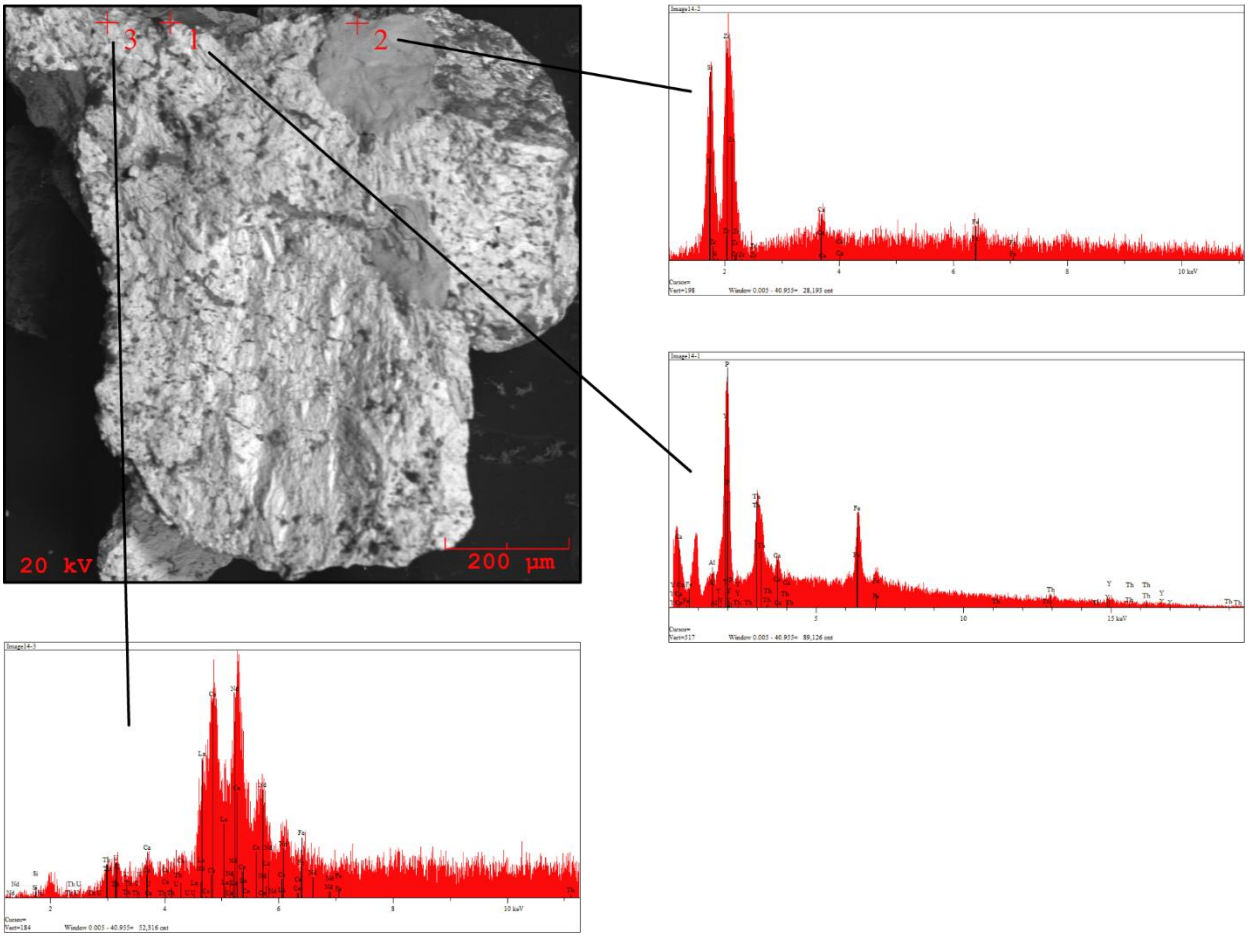


Figure 48 BSE image shows a grain with possible "bastnäsite", "xenotime", and zircon.

Quantitatively unconfirmed "bastnäsite" and "xenotime" have been found in heavy mineral separations. Both of these minerals are extremely uncommon.

## ZIRCON

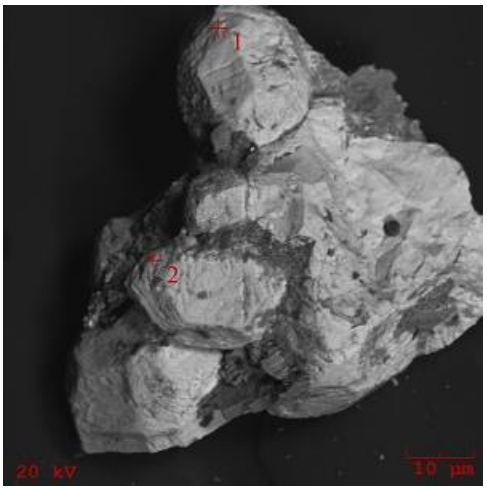


Figure 49 BSE image of zircon crystals.

Zircon is a somewhat common accessory mineral present at the Grizzly pegmatite. Zircon has been identified in heavy mineral separates by binocular microscope and qualitatively analyzed by SEM. Representative microprobe analyses are listed in Table 14. Figure 49 shows a BSE image of a zircon sample with very nice micron-sized crystal faces.

| ZIRCON – GRIZZLY PEGMATITE | | | | | | | | | | | | |
|---|---|---|---|---|---|---|---|---|---|---|---|---|
| Wt % Oxide | GRP-Goi-1-1 | GRP-Goi-1-2 | GRP-Goi-2-1 | GRP-Goi-2-2 | GRP-Goi-3-1 | GRP-Goi-4-1 | GRP-Goi-4-2 | GRP-Goi-4-3 | GRP-Goi-5-1 | GRP-Goi-5-2 | GRP-Goi-6-1 | GRP-Goi-6-2 |
| $SiO_2$ | 34.023 | 33.983 | 33.787 | 33.677 | 33.760 | 33.782 | 33.544 | 33.488 | 33.655 | 33.577 | 33.700 | 33.634 |
| $TiO_2$ | 0.023 | 0.019 | 0.011 | 0.018 | 0.010 | 0.022 | 0.018 | 0.011 | 0.011 | 0.012 | 0.009 | 0.021 |
| $Al_2O_3$ | 0.112 | 0.211 | 0.155 | 0.200 | 0.081 | 0.034 | 0.066 | 0.020 | 0.050 | 0.054 | 0.043 | 0.065 |
| $ZrO_2$ | 63.683 | 63.610 | 63.455 | 63.332 | 63.544 | 63.455 | 63.355 | 63.256 | 63.540 | 63.766 | 63.412 | 63.844 |
| $HfO_2$ | 1.312 | 1.377 | 1.345 | 1.400 | 1.544 | 1.277 | 1.456 | 1.811 | 1.311 | 1.433 | 1.366 | 1.477 |
| FeOt | 0.112 | 0.344 | 0.145 | 0.210 | 0.322 | 0.232 | 0.101 | 0.055 | 0.132 | 0.133 | 0.144 | 0.133 |
| MnO | 0.043 | 0.050 | 0.033 | 0.041 | 0.199 | 0.020 | 0.022 | 0.015 | 0.054 | 0.040 | 0.034 | 0.054 |
| MgO | 0.000 | 0.009 | 0.000 | 0.000 | 0.000 | 0.000 | 0.000 | 0.000 | 0.000 | 0.009 | 0.000 | 0.009 |
| CaO | 0.655 | 0.566 | 0.488 | 0.512 | 0.454 | 0.677 | 0.700 | 0.550 | 0.766 | 0.222 | 0.658 | 0.122 |
| $UO_2$ | 0.023 | 0.030 | 0.011 | 0.016 | 0.071 | 0.033 | 0.056 | 0.050 | 0.022 | 0.055 | 0.033 | 0.041 |
| $ThO_2$ | 0.092 | 0.084 | 0.066 | 0.060 | 0.112 | 0.100 | 0.880 | 0.112 | 0.132 | 0.233 | 0.155 | 0.100 |
| Total | 100.078 | 100.283 | 99.496 | 99.466 | 100.097 | 99.632 | 100.198 | 99.368 | 99.673 | 99.534 | 99.554 | 99.500 |
| *apfu* | | | | | | | | | | | | |
| Zr | 0.939 | 0.937 | 0.941 | 0.940 | 0.940 | 0.941 | 0.940 | 0.943 | 0.943 | 0.949 | 0.942 | 0.949 |
| Hf | 0.015 | 0.016 | 0.016 | 0.017 | 0.018 | 0.015 | 0.017 | 0.021 | 0.015 | 0.017 | 0.016 | 0.017 |
| U | 0.000 | 0.000 | 0.000 | 0.000 | 0.000 | 0.000 | 0.000 | 0.000 | 0.000 | 0.000 | 0.000 | 0.000 |
| Th | 0.001 | 0.001 | 0.000 | 0.000 | 0.001 | 0.001 | 0.006 | 0.001 | 0.001 | 0.002 | 0.001 | 0.001 |
| Fe | 0.003 | 0.009 | 0.004 | 0.005 | 0.008 | 0.006 | 0.003 | 0.001 | 0.003 | 0.003 | 0.004 | 0.003 |
| Mn | 0.001 | 0.001 | 0.001 | 0.001 | 0.005 | 0.001 | 0.001 | 0.000 | 0.001 | 0.001 | 0.001 | 0.001 |
| Mg | 0.000 | 0.000 | 0.000 | 0.000 | 0.000 | 0.000 | 0.000 | 0.000 | 0.000 | 0.000 | 0.000 | 0.000 |
| Ca | 0.021 | 0.018 | 0.016 | 0.017 | 0.015 | 0.022 | 0.023 | 0.018 | 0.025 | 0.007 | 0.021 | 0.004 |
| **Σ X-site** | 0.980 | 0.982 | 0.978 | 0.980 | 0.987 | 0.985 | 0.990 | 0.985 | 0.989 | 0.980 | 0.985 | 0.977 |
| Si | 1.029 | 1.026 | 1.028 | 1.025 | 1.024 | 1.027 | 1.021 | 1.024 | 1.024 | 1.024 | 1.026 | 1.025 |
| Ti | 0.001 | 0.000 | 0.000 | 0.000 | 0.000 | 0.001 | 0.000 | 0.000 | 0.000 | 0.000 | 0.000 | 0.000 |
| Al | 0.004 | 0.008 | 0.006 | 0.007 | 0.003 | 0.001 | 0.002 | 0.001 | 0.002 | 0.002 | 0.002 | 0.002 |
| **Σ Y-site** | 1.033 | 1.034 | 1.034 | 1.033 | 1.027 | 1.029 | 1.024 | 1.025 | 1.026 | 1.027 | 1.028 | 1.028 |
| **Zr/Hf Raios** | 61.122 | 58.170 | 59.409 | 56.964 | 51.824 | 62.572 | 54.793 | 43.983 | 61.031 | 56.034 | 58.456 | 54.431 |

Table 14 Representative EMP zircon analyses. *Apfu* calculations bases on 4 oxygens.

## GRIZZLY? URANINITE

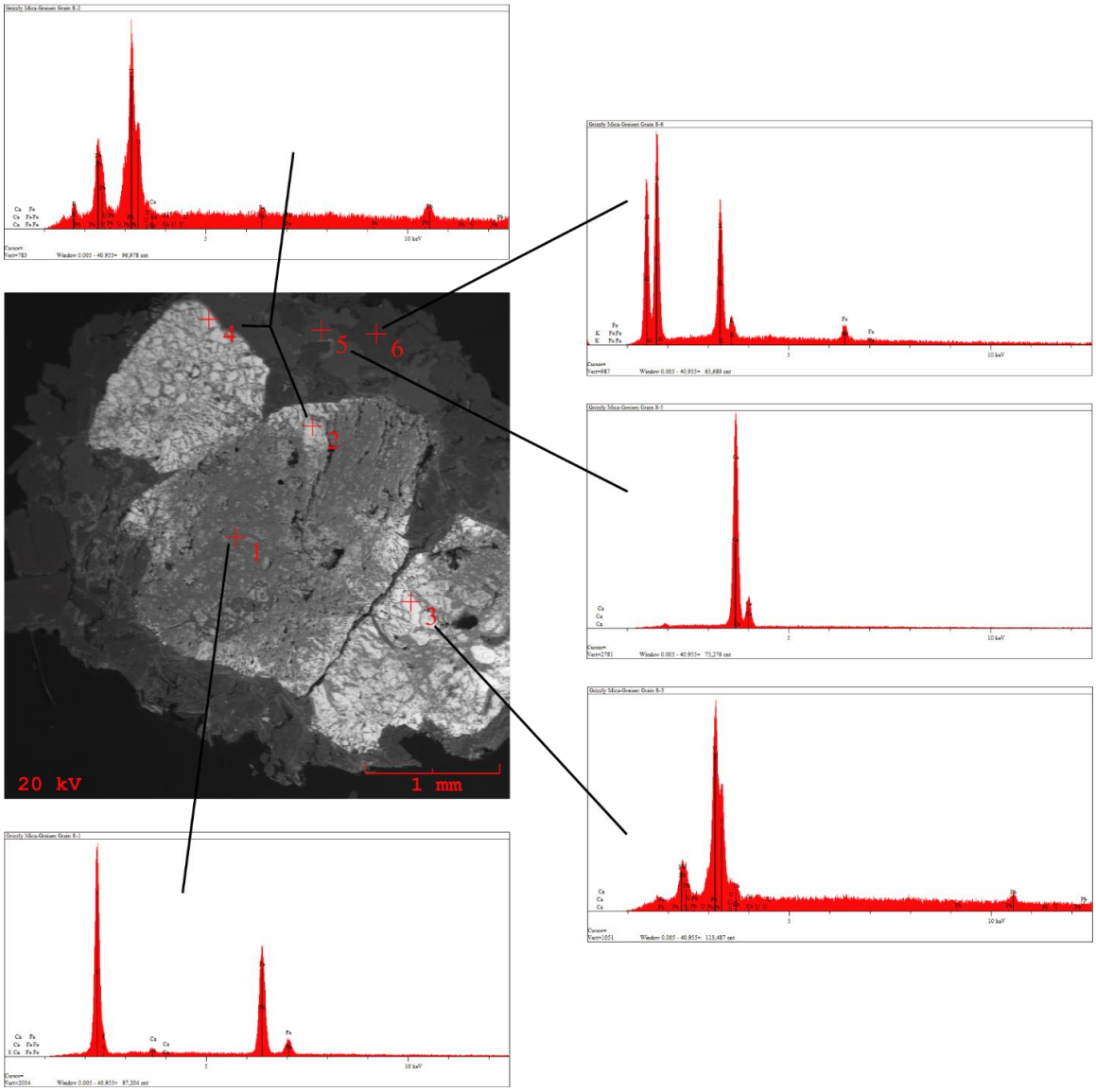


Figure 50 BSE image of uraninite, pyrite, and apatite grains embedded within muscovite mica and associated EDS spectra.

It is uncertain whether or not greisen material collected near Bell Creek granite and Grizzly pegmatite is associated with either of these two bodies. However, samples have been included in the Grizzly pegmatite section. The BSE image and EDS spectra show the close association between muscovite mica, fluorite, apatite, and uraninite. The color of fluorite can be greatly affected by radiation, perhaps explaining why fluorites are such a deep purple hue.

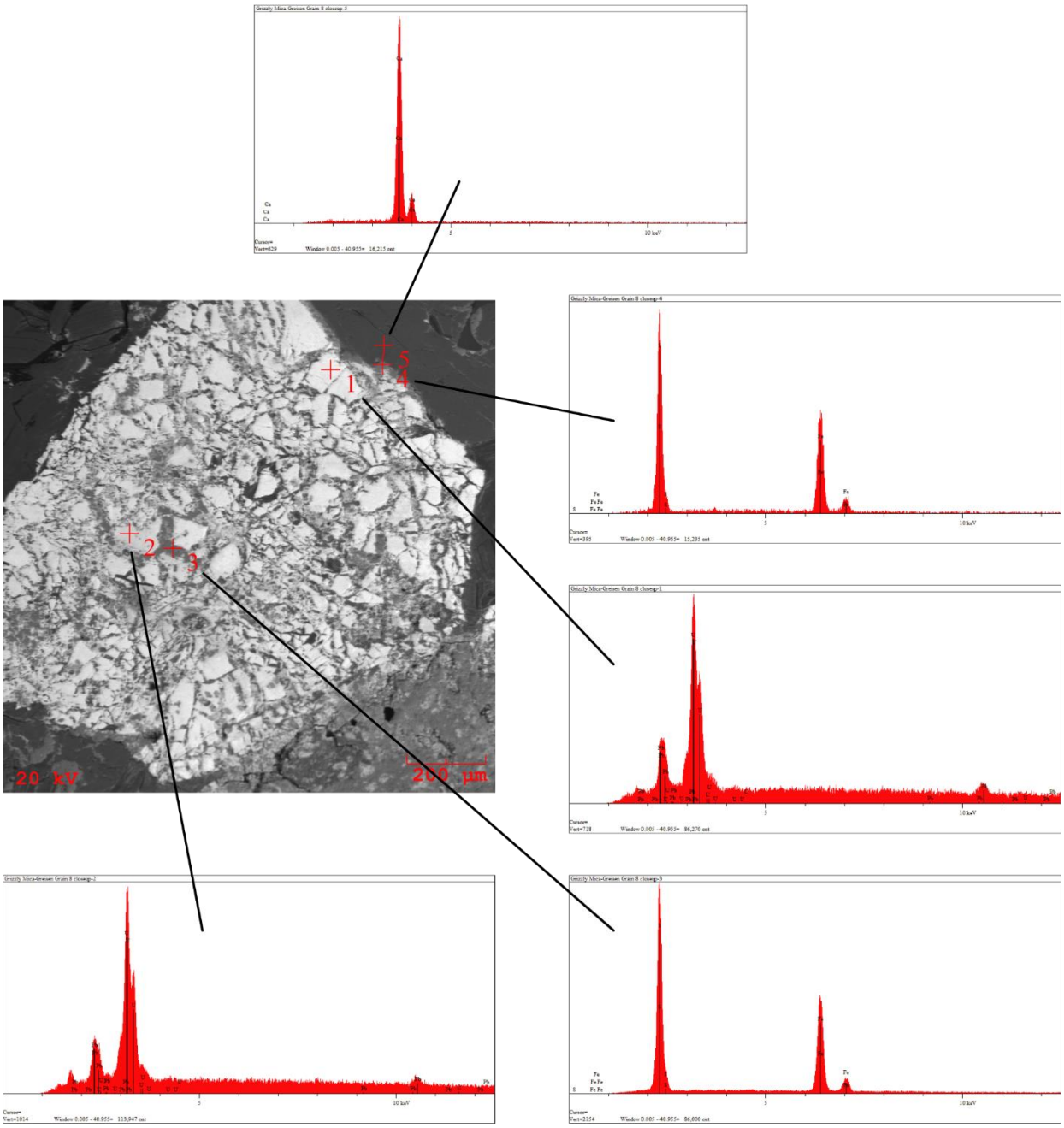


Figure 51 BSE image showing close-up of uraninite crystal in Figure 50 along with corresponding EDS spectra.

## DOLFIN PEGMATITE

Figure 52 Dolfin pegmatite image showing poor exposure of pegmatite

In the late 1800's the Dolfin pegmatite (named after the current property owner) was briefly mined for mica, but little more was heard about the pegmatite until after the turn of the century. During WWII it was part of the strategic minerals survey (Snelgrove *et al*., 1943), but owing to the paucity of important mineral deposits and relatively high iron content in feldspar, the Dolfin pegmatite was considered economically unviable.

The Dolfin pegmatite is the most poorly exposed of the locations sampled. It is located in Marquette County, Michigan. Of the minerals identified previously, only biotite, fluorite, microcline, molybdenite, quartz, and chlorophane (a variety of fluorite exhibiting green thermo-luminescence) are listed. The following are a list of minerals identified by qualitative and quantitative means: biotite, K-feldspar, fluorite, garnet, "monazite", muscovite mica, pyrite,

quartz, uraninite, “xenotime”, and zircon have been qualitatively analyzed by SEM; Fe-biotite, K-feldspar, garnet, monazite-(Ce), muscovite, uraninite, xenotime-(Y), and zircon are all quantitatively confirmed by electron microprobe analysis.

## BIOTITE

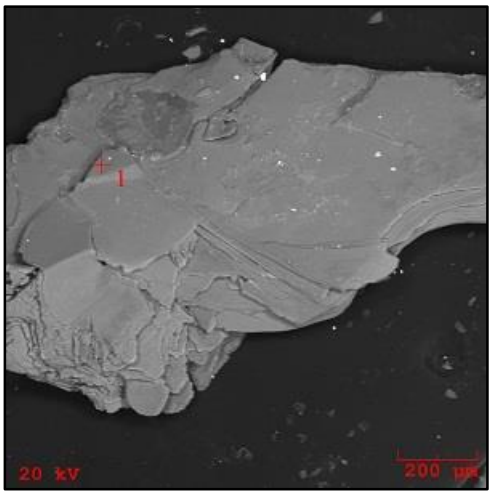


Figure 53 BSE image of biotite mica grain.

Biotite is present in heavy mineral separations and has been further analyzed by SEM and EMP. Titration of biotites from the Dolfin pegmatite reveal that there is a measureable amount of trivalent iron as FeO weight percent contents do not account for total iron. Titration reveals a weight percent FeO total of 24.560. Total Fe content from microprobe analyses are approximately 26 wt%. Lithium is calculated based on equations of Tischendorf (1997) despite lack of homogeneous grains of mica for DCP analysis. The equation (2.7/(0.35+MgO) – 0.13 has been used to calculate lithium content. Microprobe analyses determine that these biotites should be classified as Fe-biotite (Figure 186). Representative analyses are listed in Table 15.

| **BIOTITE – DOLFIN PEGMATITE** | | | | |
|---|---|---|---|---|
| Wt % Ox. | DP mica 3 top-1 | DP mica 3 top-2 | DP mica 3 bottom-2 | DP mica 8 top 1 |
| $SiO_2$ | 32.912 | 33.003 | 32.946 | 32.788 |
| $TiO_2$ | 2.113 | 2.225 | 2.332 | 2.400 |
| $Al_2O_3$ | 16.987 | 17.004 | 16.899 | 16.788 |
| $Fe_2O_3$ | 1.703 | 1.582 | 1.835 | 2.328 |
| FeO | 24.560 | 24.560 | 24.560 | 24.560 |
| MnO | 0.377 | 0.400 | 0.292 | 0.181 |
| MgO | 5.765 | 5.623 | 5.699 | 5.887 |
| CaO | 0.045 | 0.054 | 0.073 | 0.067 |
| $Li_2O$ (*calc.*) | 0.312 | 0.322 | 0.316 | 0.303 |
| $Na_2O$ | 0.212 | 0.232 | 0.311 | 0.083 |
| $K_2O$ | 9.655 | 9.599 | 9.723 | 9.444 |
| $Rb_2O$ | 0.011 | 0.013 | 0.012 | 0.014 |
| $Cs_2O$ | *bdl* | *bdl* | *bdl* | *bdl* |
| F | 1.054 | 1.100 | 1.091 | 0.972 |
| $H_2O$ | 3.247 | 3.227 | 3.240 | 3.294 |
| F=O | - 0.444 | - 0.463 | - 0.459 | - 0.409 |
| **Total** | 98.508 | 98.481 | 98.870 | 98.700 |
| *apfu* | | | | |
| Si | 5.268 | 5.280 | 5.258 | 5.236 |
| $^{IV}Al$ | 2.732 | 2.720 | 2.742 | 2.764 |
| **Σ T-site** | 8.000 | 8.000 | 8.000 | 8.000 |
| $^{VI}Al$ | 0.472 | 0.486 | 0.436 | 0.396 |
| Ti | 0.254 | 0.268 | 0.280 | 0.288 |
| $Fe_t$ | 3.493 | 3.476 | 3.498 | 3.560 |
| Mn | 0.051 | 0.054 | 0.039 | 0.024 |
| Mg | 1.376 | 1.341 | 1.356 | 1.402 |
| Li (*calc.*) | 0.201 | 0.207 | 0.203 | 0.195 |
| **Σ Y-site** | 5.847 | 5.832 | 5.812 | 5.865 |

Table 15 Representative biotite mica EMP analyses. *Apfu* calculations based on 24 anions.
Table continues on next page.

| | | | | |
|---|---|---|---|---|
| K | 1.972 | 1.959 | 1.980 | 1.924 |
| Ca | 0.008 | 0.009 | 0.012 | 0.011 |
| Na | 0.066 | 0.072 | 0.096 | 0.026 |
| Rb | 0.001 | 0.001 | 0.001 | 0.001 |
| Cs | *bdl* | *bdl* | *bdl* | *bdl* |
| **Σ X-site** | 2.047 | 2.041 | 2.089 | 1.962 |
| F | 0.534 | 0.557 | 0.551 | 0.491 |
| OH* | 3.466 | 3.443 | 3.449 | 3.509 |
| **Σ W-site** | 4.000 | 4.000 | 4.000 | 4.000 |

## K-FELDSPAR

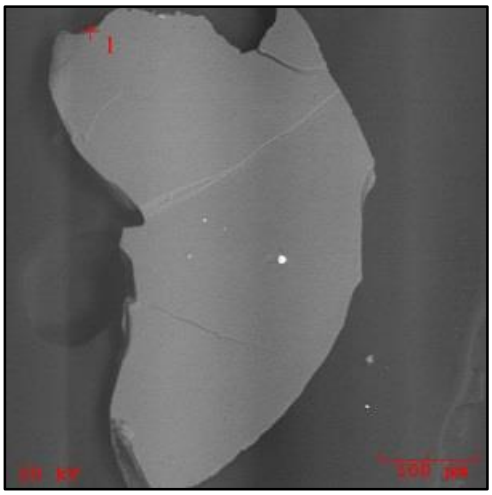

Figure 54 BSE image of K-feldspar grain.

Analysis of K-feldspar by SEM reveal 100 to 250 micron thick exsolution lamellae of plagioclase feldspar. Lamellae are irregular in appearance and roughly parallel. Lamellae contain little calcium ($An_{06} – An_{10}$). Barium is below detection limits and rubidium is at or below detection limits suggesting that K-feldspar samples are poorly evolved. In two samples, SEM analyses of fluorite inclusions reveal a detectable amount of yttrium. Analysis by XRD suggests that there is a high degree of structural ordering as the sample plots very near the maximum microcline field (Figure 173) (Wright & Stewart, 1968). Table 16 shows a representative list of feldspar analyses with corresponding analyses of lamellae. Additional feldspar analyses are listed in the appendices in Table 85.

| K-FELDSPAR - DOLFIN PEGMATITE | | | | | | | | |
|---|---|---|---|---|---|---|---|---|
| Wt% ox | DP3 grain 1-1 | DP3 grain 1-2 | DP3 grain 2-1 | DP3 grain 2-2 | DP 8 grain 3-1 | DP 8 grain 3-2 | DP 8 grain 2-1 | DP 8 grain 2-2 |
| $P_2O_5$ | 0.000 | 0.000 | 0.000 | 0.000 | 0.000 | 0.000 | 0.000 | 0.000 |
| $SiO_2$ | 64.776 | 69.111 | 68.687 | 64.799 | 64.766 | 68.576 | 68.688 | 64.699 |
| $TiO_2$ | 0.015 | 0.000 | 0.000 | 0.014 | 0.012 | 0.000 | 0.000 | 0.009 |
| $Al_2O_3$ | 18.405 | 19.433 | 19.432 | 18.399 | 18.388 | 19.755 | 19.444 | 18.414 |
| $FeO_t$ | 0.011 | 0.000 | 0.000 | 0.013 | 0.013 | 0.000 | 0.000 | 0.015 |
| CaO | 0.012 | 0.256 | 0.266 | 0.000 | 0.000 | 0.488 | 0.288 | 0.000 |
| $Na_2O$ | 0.494 | 10.987 | 11.091 | 0.293 | 0.455 | 10.566 | 10.877 | 0.455 |
| $K_2O$ | 16.005 | 0.310 | 0.181 | 16.100 | 15.889 | 0.255 | 0.211 | 15.877 |
| Rb2O | 0.013 | 0.000 | 0.000 | 0.009 | 0.016 | 0.000 | 0.000 | 0.013 |
| **Total** | 99.731 | 100.097 | 99.666 | 99.627 | 99.539 | 99.640 | 99.517 | 99.482 |
| *apfu* | | | | | | | | |
| K | 0.945 | 0.017 | 0.010 | 0.951 | 0.939 | 0.014 | 0.012 | 0.939 |
| Na | 0.044 | 0.928 | 0.941 | 0.026 | 0.041 | 0.896 | 0.923 | 0.041 |
| Ca | 0.001 | 0.012 | 0.012 | 0.000 | 0.000 | 0.023 | 0.014 | 0.000 |
| Rb | 0.000 | 0.000 | 0.000 | 0.000 | 0.000 | 0.000 | 0.000 | 0.000 |
| **Σ X-site** | 0.990 | 0.957 | 0.963 | 0.978 | 0.981 | 0.933 | 0.949 | 0.980 |
| Al | 1.004 | 0.998 | 1.002 | 1.005 | 1.004 | 1.018 | 1.003 | 1.006 |
| Fe | 0.000 | 0.000 | 0.000 | 0.000 | 0.000 | 0.000 | 0.000 | 0.000 |
| **Σ Y-site** | 1.004 | 0.998 | 1.002 | 1.005 | 1.004 | 1.018 | 1.003 | 1.006 |
| Si | 2.998 | 3.010 | 3.005 | 3.001 | 3.001 | 2.998 | 3.007 | 3.000 |
| Ti | 0.001 | 0.000 | 0.000 | 0.000 | 0.000 | 0.000 | 0.000 | 0.000 |
| P | 0.000 | 0.000 | 0.000 | 0.000 | 0.000 | 0.000 | 0.000 | 0.000 |
| Al | 0.000 | 0.000 | 0.000 | 0.000 | 0.000 | 0.000 | 0.000 | 0.000 |
| **Σ Z-site** | 2.999 | 3.010 | 3.005 | 3.002 | 3.001 | 2.998 | 3.007 | 3.000 |

Table 16 EMP representative analyses of K-feldspar. *Apfu* calculations based on 8 oxygens.

## FLUORITE

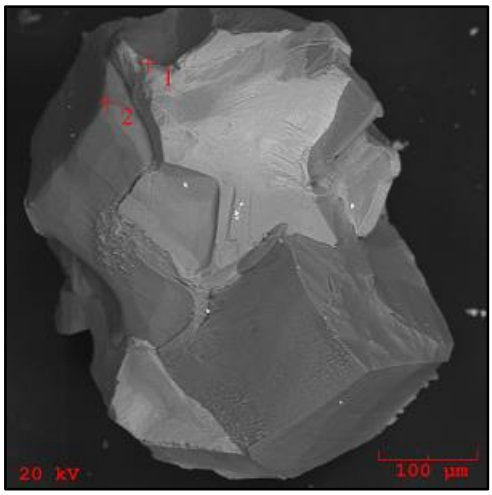


Figure 55 BSE image of fluorite grain (crosshair 1) on K-feldspar (crosshair 2).

Discrete grains of fluorite have been identified in hand sample with a binocular microscope and confirmed qualitatively by SEM. No discrete grains larger than a millimeter in size have been discovered.

## GARNET

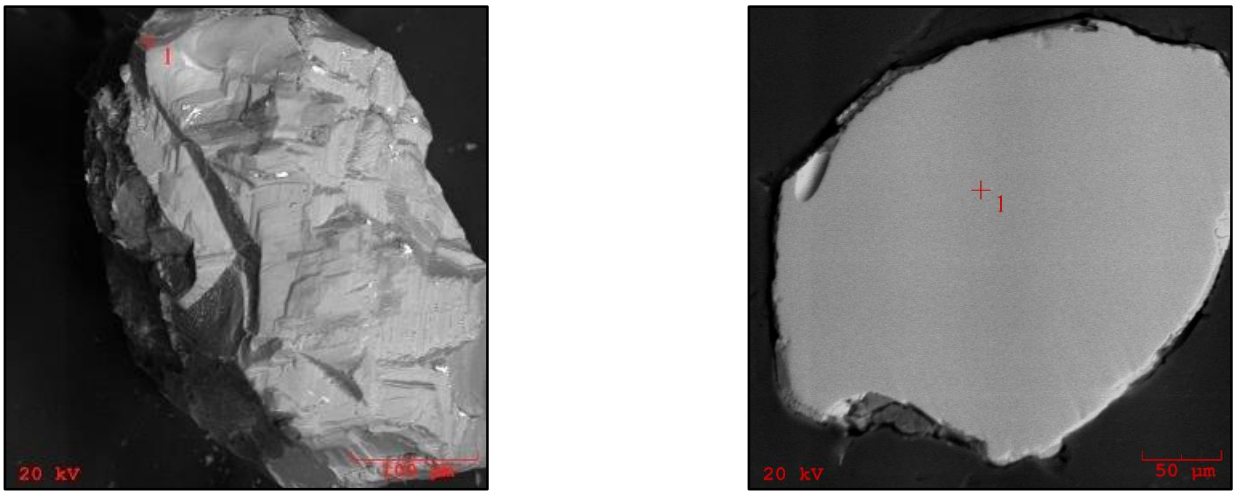


Figure 56 BSE image of garnet grain (left; crosshair 1) and polished garnet grain (right; crosshair 1).

Garnet grains identified in hand sample and heavy mineral separations rarely reach more than a millimeter in size. Garnets are sub- to euhedral and occasionally, anhedral. Of the grains analyzed by microprobe, none are zoned. A detectable amount of fluorine is present in some of the samples analyzed. Analyses also reveal that samples contain a significant almandine component (~$Al_{80}$), followed by a spessartine component ($Sp_{17}$ – $Sp_{20}$), and grossular ($Gr_{02}$ – $Gr_{04}$), with very minor pyrope and andradite components (>1%). Table 17 shows a list of representative garnet analyses. This is the first reported and confirmed occurrence of garnet at the Dolfin pegmatite. Additional analyses for Dolfin pegmatite garnets are listed in the appendices in Table 86.

| GARNETS – DOLFIN PEGMATITE | | | | | | | | | | | | |
|---|---|---|---|---|---|---|---|---|---|---|---|---|
| Wt % Ox | garnets 1-1 | garnets 1-2 | garnets 2-1 | garnets 2-2 | garnets 3-1 | garnets 3-2 | garnets 6-1 | garnets 6-2 | garnets-7-1 | garnets-7-2 | garnets-9-1 | garnets-9-2 |
| $SiO_2$ | 36.322 | 36.400 | 36.376 | 36.432 | 36.403 | 36.511 | 36.426 | 36.344 | 36.511 | 36.455 | 36.454 | 36.426 |
| $TiO_2$ | 0.011 | 0.010 | 0.009 | 0.011 | 0.021 | 0.009 | 0.012 | 0.011 | 0.014 | 0.013 | 0.009 | 0.013 |
| $Al_2O_3$ | 20.655 | 20.345 | 20.564 | 20.623 | 20.433 | 20.566 | 20.494 | 20.505 | 20.484 | 20.512 | 20.488 | 20.533 |
| FeO | 34.544 | 34.655 | 34.555 | 34.332 | 34.211 | 34.766 | 33.112 | 32.892 | 32.556 | 32.600 | 33.687 | 33.893 |
| MnO | 7.212 | 7.121 | 7.412 | 7.698 | 7.860 | 7.121 | 8.340 | 8.544 | 8.556 | 8.783 | 7.988 | 7.566 |
| MgO | 0.088 | 0.091 | 0.082 | 0.092 | 0.062 | 0.089 | 0.067 | 0.056 | 0.060 | 0.093 | 0.100 | 0.093 |
| CaO | 0.766 | 0.894 | 0.872 | 0.911 | 0.820 | 0.776 | 1.540 | 1.455 | 1.001 | 1.113 | 0.981 | 0.893 |
| **Total** | 99.598 | 99.516 | 99.870 | 100.099 | 99.810 | 99.838 | 100.002 | 99.812 | 99.182 | 99.569 | 99.707 | 99.417 |
| *apfu* | | | | | | | | | | | | |
| Ti | 0.001 | 0.001 | 0.001 | 0.001 | 0.001 | 0.001 | 0.001 | 0.001 | 0.001 | 0.001 | 0.001 | 0.001 |
| Fe | 2.402 | 2.401 | 2.389 | 2.368 | 2.365 | 2.408 | 2.275 | 2.268 | 2.275 | 2.261 | 2.332 | 2.359 |
| Mn | 0.504 | 0.500 | 0.518 | 0.537 | 0.550 | 0.497 | 0.582 | 0.597 | 0.599 | 0.614 | 0.559 | 0.530 |
| Mg | 0.011 | 0.011 | 0.010 | 0.011 | 0.008 | 0.011 | 0.008 | 0.007 | 0.007 | 0.011 | 0.012 | 0.011 |
| Ca | 0.068 | 0.079 | 0.077 | 0.080 | 0.073 | 0.069 | 0.136 | 0.129 | 0.089 | 0.099 | 0.087 | 0.079 |
| **Σ X-site** | 2.986 | 2.992 | 2.995 | 2.997 | 2.997 | 2.986 | 3.002 | 3.002 | 2.971 | 2.987 | 2.991 | 2.980 |
| Al | 2.010 | 1.986 | 2.000 | 2.002 | 1.990 | 1.998 | 1.990 | 1.995 | 2.000 | 1.998 | 1.995 | 2.003 |
| **Σ Y-site** | 2.010 | 1.986 | 2.000 | 2.002 | 1.990 | 1.998 | 1.990 | 1.995 | 2.000 | 1.998 | 1.995 | 2.003 |
| Si | 2.999 | 3.014 | 3.002 | 3.000 | 3.008 | 3.009 | 3.001 | 3.000 | 3.024 | 3.012 | 3.011 | 3.014 |
| **Σ Z-site** | 2.999 | 3.014 | 3.002 | 3.000 | 3.008 | 3.009 | 3.001 | 3.000 | 3.024 | 3.012 | 3.011 | 3.014 |
| **Component** | | | | | | | | | | | | |
| Spessartine | 17 | 17 | 17 | 18 | 18 | 17 | 20 | 20 | 20 | 21 | 19 | 18 |
| Grossular | 03 | 03 | 03 | 03 | 03 | 02 | 04 | 04 | 03 | 03 | 03 | 03 |
| Almandine | 80 | 80 | 80 | 79 | 79 | 81 | 76 | 76 | 77 | 76 | 78 | 79 |

Table 17 Representative EMP analyses of garnet. *Apfu* calculations based on 12 oxygens.

## MONAZITE

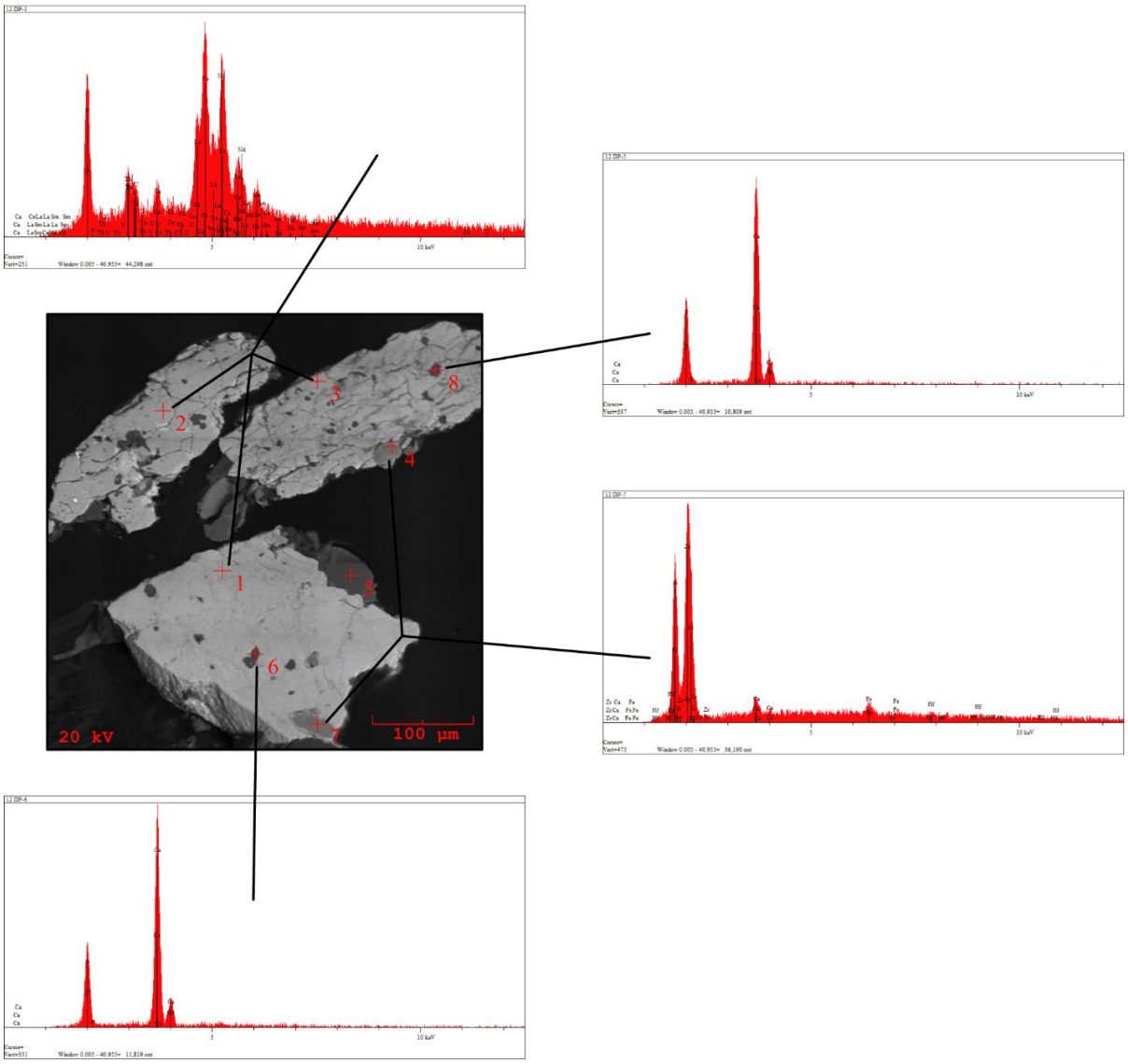


Figure 57 BSE image of polished monazite-(Ce) grain with inclusions of apatite and zircon. Associated spectra included.

"Monazite" has been identified by SEM and further analyzed by microprobe for dominant REE content. Quantitative results determine that grains be classified as monazite-(Ce) based on X-site cation dominance. Dolfin monazite-(Ce) samples lack homogeneity both texturally and mineralogically. Numerous inclusions are present within the three grains. Fluorite, zircon, apatite, and "xenotime" are among the more notable inclusions within grains.

"Xenotime" inclusions appear to have relatively low quantities of HREEs and are assumed to be xenotime-(Y) based on qualitative SEM data. Having been unable to identify discrete grains of "xenotime" or apatite, it is assumed that "monazite" is the most common phosphate and REE-bearing accessory mineral. Weight percent totals are approximately 95% suggesting that the grains are altered. Table 18 lists representative analyses and Figure 58 shows a BSE image with corresponding spectra. This represents the first reported and quantitatively confirmed occurrence of monazite-(Ce) at the Dolfin pegmatite.

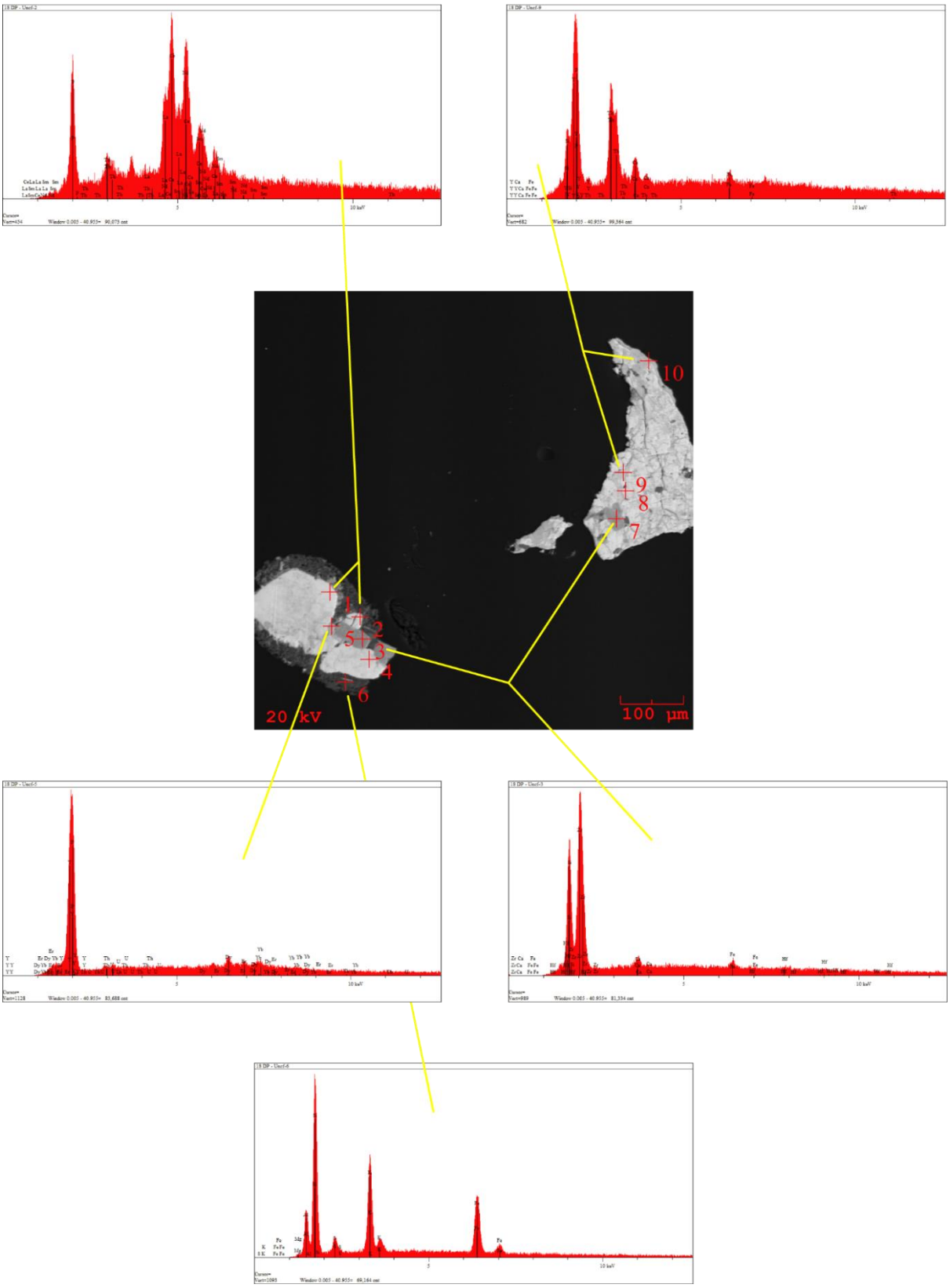


Figure 58 BSE image of monazite-(Ce) grains from the Dolfin pegmatite with corresponding spectra of grain and inclusions.

| **DOLFIN – MONAZITE-(CE)** | | |
|---|---|---|
| Wt % Ox. | DP-1 | 18 DP uncf-9 |
| $P_2O_5$ | 28.566 | 18.722 |
| $SiO_2$ | 0.344 | 3.411 |
| $TiO_2$ | 0.000 | 0.000 |
| $ThO_2$ | 4.984 | 53.223 |
| $UO_2$ | 0.334 | 0.455 |
| $Al_2O_3$ | 0.095 | 0.100 |
| $La_2O_3$ | 12.723 | 0.012 |
| $Ce_2O_3$ | 27.722 | 1.653 |
| $Pr_2O_3$ | 2.612 | 0.000 |
| $Nd_2O_3$ | 14.333 | 0.032 |
| $Sm_2O_3$ | 1.477 | 0.012 |
| $Eu_2O_3$ | 0.007 | 0.000 |
| $Gd_2O_3$ | 0.400 | 0.000 |
| $Dy_2O_3$ | 0.191 | 0.000 |
| $Yb_2O_3$ | 0.023 | 0.000 |
| $Y_2O_3$ | 0.420 | 0.000 |
| $Sc_2O_3$ | 0.000 | 0.000 |
| MgO | 0.000 | 0.000 |
| CaO | 1.823 | 0.000 |
| MnO | 0.033 | 0.000 |
| FeO | 0.254 | 0.000 |
| PbO | 0.322 | 0.022 |
| **Total** | 96.663 | 95.049 |
| *apfu* | | |
| Th | 0.046 | 0.619 |
| U | 0.003 | 0.005 |
| Al | 0.005 | 0.006 |
| La | 0.190 | 0.000 |
| Ce | 0.411 | 0.031 |
| Pr | 0.039 | 0.000 |
| Nd | 0.207 | 0.001 |
| Sm | 0.021 | 0.000 |
| Y | 0.009 | 0.00 |
| Ca | 0.079 | 0.098 |
| **Σ X** | 1.031 | 0.982 |
| P | 0.993 | 0.810 |
| Si | 0.014 | 0.174 |
| **Σ Y** | 1.007 | .984 |

Table 18 Dolfin monazite-(Ce) grain Microprobe analysis. *Apfu* calculations based on 4 oxygens.

## MUSCOVITE

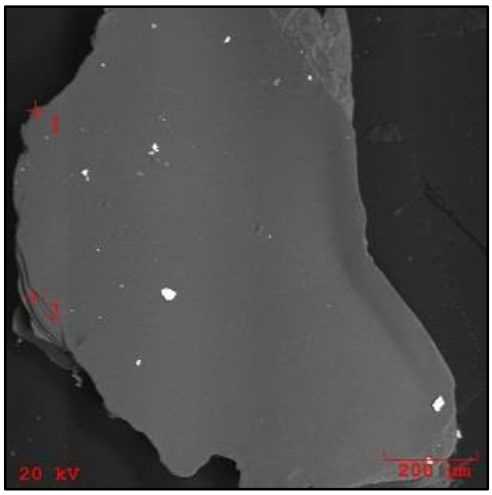


Figure 59 BSE image of muscovite mica grain (1 & 2).

Muscovite mica has been identified in hand samples and by SEM. Muscovite mica has been quantitatively confirmed by microprobe (Figure 185). Fluorine contents are approximately the same for muscovite mica as biotites in Dolfin samples. Homogeneous grains of mica are not present in sufficient quantities to perform DCP analyses in order to determine lithium content; however, stoichiometric lithium is calculated based on the dioctahedral equation $0.3935*F^{1.326}$ (Tischendorf, 1997). Table 19 shows two muscovite mica analyses.

This represents the first reported and quantitatively confirmed occurrence of muscovite mica at the Dolfin pegmatite.

| **MUSCOVITE – DOLFIN PEGMATITE** | | |
|---|---|---|
| Wt % Ox. | Mica 3 bottom 1 | Mica 8 bottom 1 |
| $SiO_2$ | 46.633 | 46.588 |
| $TiO_2$ | 0.211 | 0.276 |
| $Al_2O_3$ | 34.215 | 34.444 |
| $Fe_2O_3$ | 0.000 | 0.000 |
| FeO | 3.523 | 3.356 |
| MnO | 0.082 | 0.101 |
| MgO | 1.655 | 1.562 |
| CaO | 0.033 | 0.044 |
| $Li_2O$ (*calc.*) | 0.384 | 0.442 |
| $Na_2O$ | 0.312 | 0.282 |
| $K_2O$ | 9.677 | 9.700 |
| $Rb_2O$ | 0.010 | 0.013 |
| $Cs_2O$ | *bdl* | *bdl* |
| F | 0.981 | 1.091 |
| $H_2O$ (*calc.*) | 4.082 | 4.037 |
| F=O | -0.413 | -0.459 |
| Total | 101.385 | 101.477 |
| *apfu* | | |
| Si | 6.149 | 6.133 |
| $^{IV}Al$ | 1.851 | 1.867 |
| **Σ T-site** | 8.000 | 8.000 |
| $^{VI}Al$ | 3.467 | 3.478 |
| Ti | 0.021 | 0.027 |
| $Fe_t$ | 0.389 | 0.370 |
| Mn | 0.009 | 0.011 |
| Mg | 0.325 | 0.307 |
| Li (*calc.*) | 0.203 | 0.234 |
| **Σ Y-site** | 4.414 | 4.427 |

Table 19 Representative EMP analyses of muscovite mica.
*Apfu* calculations based on 24 anions.
Table continues on next page.

| | | |
|---|---|---|
| K | 1.628 | 1.629 |
| Ca | 0.005 | 0.006 |
| Na | 0.080 | 0.072 |
| Rb | 0.001 | 0.001 |
| Cs | *bdl* | *bdl* |
| **Σ X-site** | 1.714 | 1.708 |
| F | 0.409 | 0.454 |
| OH (*calc.*) | 3.591 | 3.546 |
| **Σ W-site** | 4.000 | 4.000 |

## PYRITE

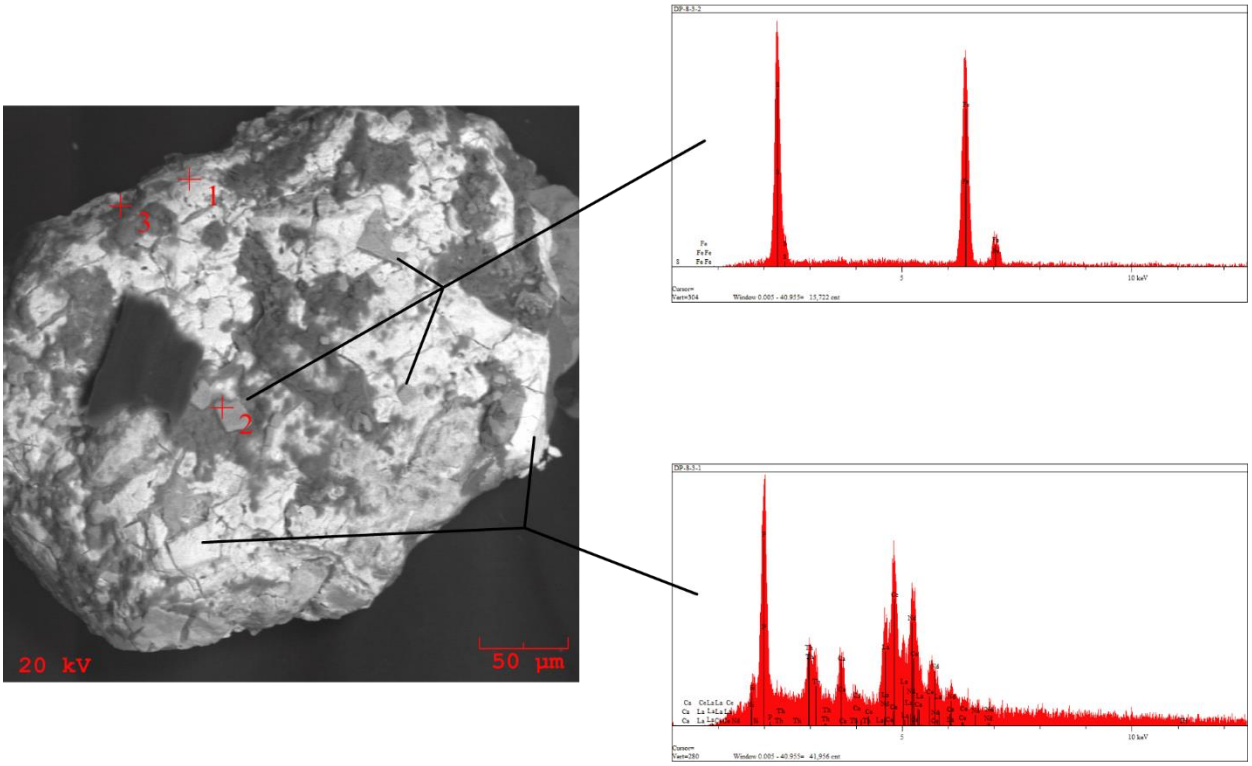


Figure 60 BSE image of pyrite grains embedded in a larger "monazite" grain.

Pyrite is an accessory mineral found at the Dolfin pegmatite and has been qualitatively confirmed by SEM. The BSE image in Figure 60 is a "monazite" crystal with numerous inclusions of pyrite cubes embedded in the grain. Pyrite has not been previously reported at the Dolfin pegmatite and this represents the first qualitatively confirmed occurrence.

## URANINITE

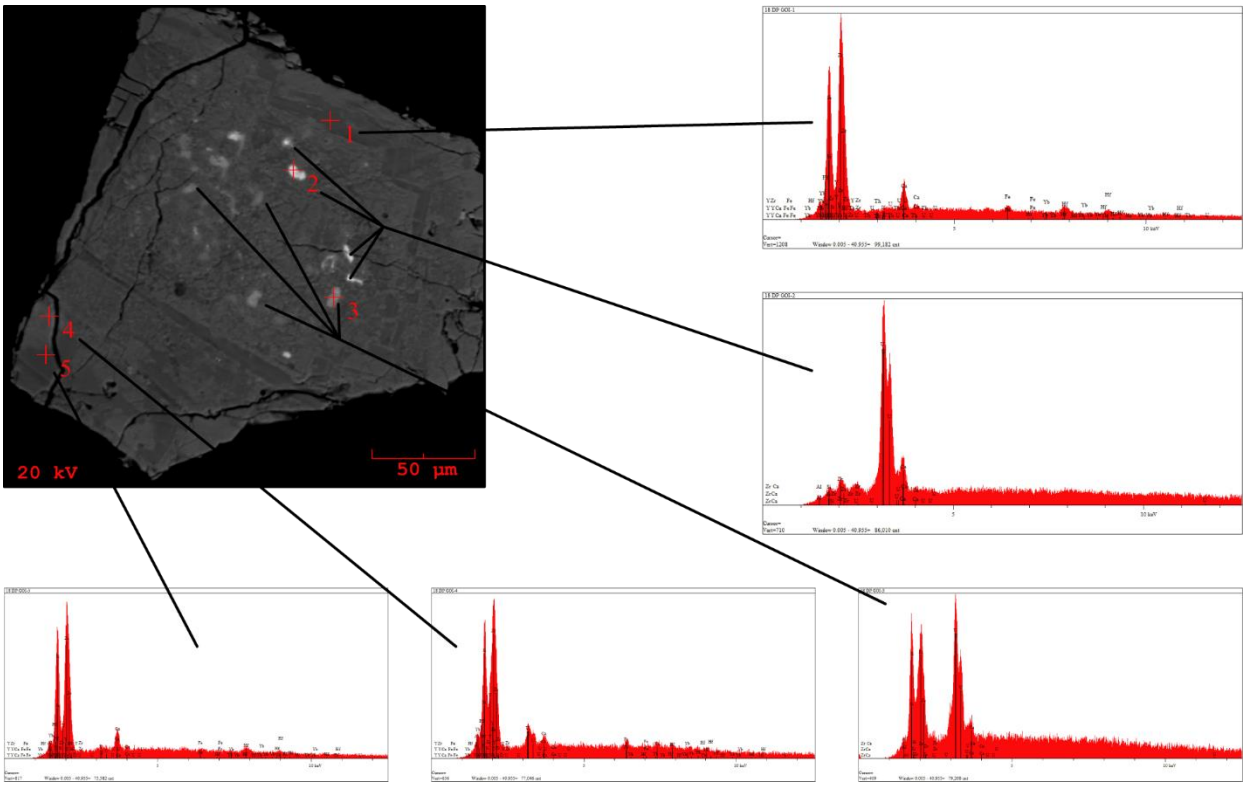


Figure 61 BSE image of zircon grain with uraninite inclusions.

Inclusions of uraninite have been found in a polished zircon mount. There is approximately 1.5 weight percent of lead (assumed to be radiogenic). Weight percent total of uraninite is very near 100%.

This represents the first confirmed reported occurrence of uraninite at the Dolfin pegmatite.

## XENOTIME

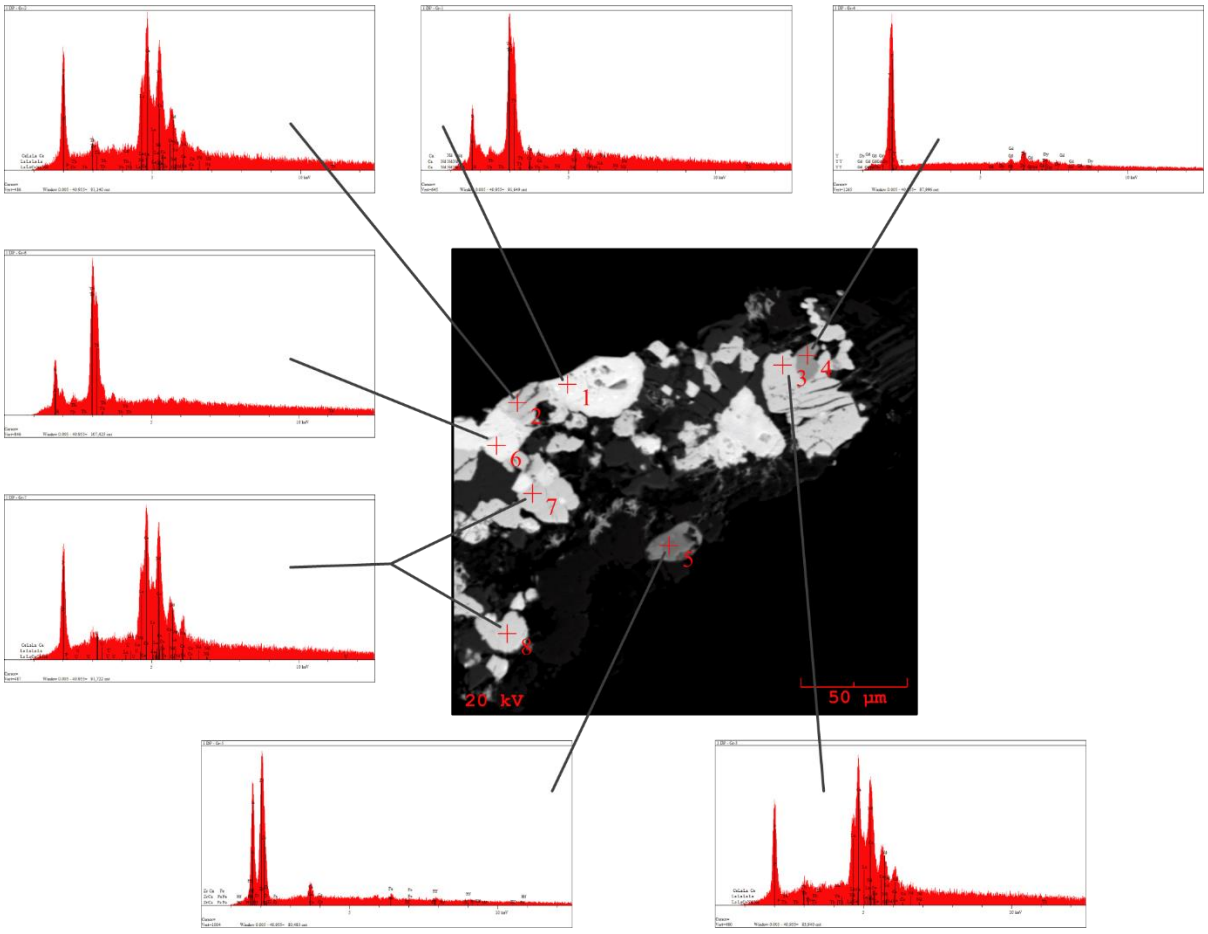


Figure 62 BSE image of "xenotime" (crosshair 4) and associated EDS spectra.

"Xenotime" has been discovered and quantitatively confirmed. Analysis reveal that yttrium is the dominant cation in the X-site therefore classification is xenotime-(Y). Table 20 lists the analysis.

This represents the first reported and confirmed occurrence of xenotime-(Y) at the Dolfin pegmatite.

| **XENOTIME-(Y) – DOLFIN PEGMATITE** | |
|---|---|
| Wt % Ox. | grain1 DP |
| $P_2O_5$ | 33.804 |
| $SiO_2$ | 0.31 |
| $TiO_2$ | 0.009 |
| $ThO_2$ | 2.334 |
| $UO_2$ | 0.112 |
| $Al_2O_3$ | 0.154 |
| $Nd_2O_3$ | 0.013 |
| $Sm_2O_3$ | 0.016 |
| $Gd_2O_3$ | 2.888 |
| $Tb_2O_3$ | 1.112 |
| $Dy_2O_3$ | 7.877 |
| $Ho_2O_3$ | 0.912 |
| $Er_2O_3$ | 4.223 |
| $Tm_2O_3$ | 0.696 |
| $Yb_2O_3$ | 5.877 |
| $Lu_2O_3$ | 0.166 |
| $Y_2O_3$ | 38.893 |
| $Sc_2O_3$ | 0.013 |
| MgO | 0.000 |
| CaO | 0.025 |
| MnO | 0.010 |
| FeO | 0.032 |
| PbO | 0.000 |
| **Total** | 99.476 |
| *apfu* | |
| Th | 0.018 |
| U | 0.001 |
| Al | 0.006 |
| Nd | 0.033 |
| Sm | 0.013 |
| Gd | 0.088 |
| Tb | 0.010 |
| Dy | 0.046 |
| Ho | 0.007 |
| Er | 0.062 |
| Tm | 0.002 |
| Yb | 0.714 |
| Lu | 0.000 |
| Y | 0.000 |
| Sc | 0.001 |
| Mg | 0.000 |
| Ca | 0.001 |
| Mn | 0.000 |
| Fe | 0.033 |
| Pb | 0.013 |
| **Σ X** | 1.002 |
| P | 0.987 |
| Si | 0.011 |
| **Σ Y** | 0.998 |

Table 20 Representative xenotime-(Y) EMP analyses.
*Apfu* calculations based on 4 oxygens.

## ZIRCON

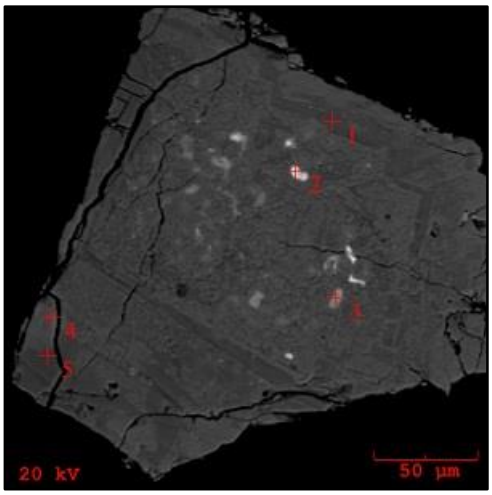


Figure 63 BSE image of zoned zircon (crosshairs 1, 4 & 5) with inclusions of uraninite (crosshairs 2 & 4).

Zircon has been identified from heavy mineral separations by SEM and later confirmed by microprobe. Hafnium content is relatively high, having weight percent totals ranging from approximately 4.1 to 4.6 percent. This indicates a relatively high degree of evolution. Most grains appear to have zonation and/or inclusions. One grain has a rim with elevated levels of thorium and uranium. Inclusions include a niobium-rich species and an inclusion that contains elevated ytterbium content. The grain in Figure 63 has zonation as well as uraninite inclusions. Representative microprobe analyses are presented in Table 21. Note that weight percent totals are very close to or at 100% indicating that these grains have not been altered.

This is the first reported and quantitatively confirmed occurrence of zircon at the Dolfin pegmatite.

| ZIRCON – DOLFIN PEGMATITE | | | | | |
|---|---|---|---|---|---|
| Wt % Oxide | grain 15 DP Goi-1 | | grain 16 DP Goi-1 | grain 17 DP Goi-1 | grain 18 DP Goi-1 |
| $SiO_2$ | 32.222 | 32.300 | 32.009 | 32.100 | 31.891 |
| $TiO_2$ | 0.009 | 0.022 | 0.034 | 0.040 | 0.033 |
| $Al_2O_3$ | 0.223 | 0.099 | 0.111 | 0.078 | 0.144 |
| $ZrO_2$ | 63.112 | 62.945 | 62.998 | 63.093 | 63.022 |
| $HfO_2$ | 4.600 | 4.554 | 4.330 | 4.112 | 4.220 |
| FeOt | 0.066 | 0.050 | 0.043 | 0.050 | 0.067 |
| MnO | 0.041 | 0.033 | 0.041 | 0.044 | 0.044 |
| MgO | 0.000 | 0.000 | 0.000 | 0.000 | 0.000 |
| CaO | 0.110 | 0.024 | 0.027 | 0.021 | 0.022 |
| $UO_2$ | 0.022 | 0.010 | 0.013 | 0.033 | 0.021 |
| $ThO_2$ | 0.011 | 0.014 | 0.009 | 0.012 | 0.023 |
| **Total** | 100.416 | 100.051 | 99.615 | 99.583 | 99.487 |
| *apfu* | | | | | |
| Zr | 0.946 | 0.946 | 0.951 | 0.952 | 0.953 |
| Hf | 0.055 | 0.054 | 0.052 | 0.049 | 0.051 |
| U | 0.000 | 0.000 | 0.000 | 0.000 | 0.000 |
| Th | 0.000 | 0.000 | 0.000 | 0.000 | 0.000 |
| Fe | 0.002 | 0.001 | 0.001 | 0.001 | 0.002 |
| Mg | 0.001 | 0.001 | 0.001 | 0.001 | 0.001 |
| Mn | 0.000 | 0.000 | 0.000 | 0.000 | 0.000 |
| Ca | 0.004 | 0.001 | 0.001 | 0.001 | 0.001 |
| **Σ X-site** | 1.008 | 1.003 | 1.006 | 1.004 | 1.008 |
| Si | 0.990 | 0.995 | 0.991 | 0.993 | 0.989 |
| Ti | 0.000 | 0.001 | 0.001 | 0.001 | 0.001 |
| Al | 0.008 | 0.004 | 0.004 | 0.003 | 0.005 |
| **Σ Y-site** | 0.998 | 1.000 | 0.996 | 0.997 | 0.995 |

Table 21 Representative EMP analyses of zircon. *Apfu* calculations based on 4 oxygens.

## CROCKLEY PEGMATITE

Figure 64 Field image of the Crockley pegmatite.

The Crockley pegmatite is located near the town of Republic in Marquette County just off of Hwy 601. According to Heinrich (1962), the quarry was open in 1902 and reopened for a short time in 1926. In Figure 64, large reddish blocks of feldspar lie higgledy-piggledy around the site. One sample from the south wall was collected for bulk compositional analysis. Minerals identified from previous studies include aeschynite-(Y), albite, allanite-(Ce), bastnäsite-(Y), biotite, bornite, calcite, ferrocolumbite, euxenite-(Y), fluorite, galena, microcline, molybdenite, muscovite, pyrrhotite, quartz, thorite, titianite, and zircon. The following is a list of both qualitative and quantitative analyzed samples: “Bastnäsite”, biotite mica, chalcopyrite, columbite, K-feldspar, plagioclase, fluorite, garnet, ilmenite, pyrite, “monazite”, muscovite, quartz, rutile, and zircon have qualitatively identified by SEM; Fe-biotite, ferrocolumbite, K-

feldspar, plagioclase (albite), garnet, ilmenite, monazite-(Ce), muscovite, rutile, and zircon have been quantitatively confirmed via microprobe analysis.

Figure 65 Field picture of Crockley pegmatite.

## BASTNÄSITE

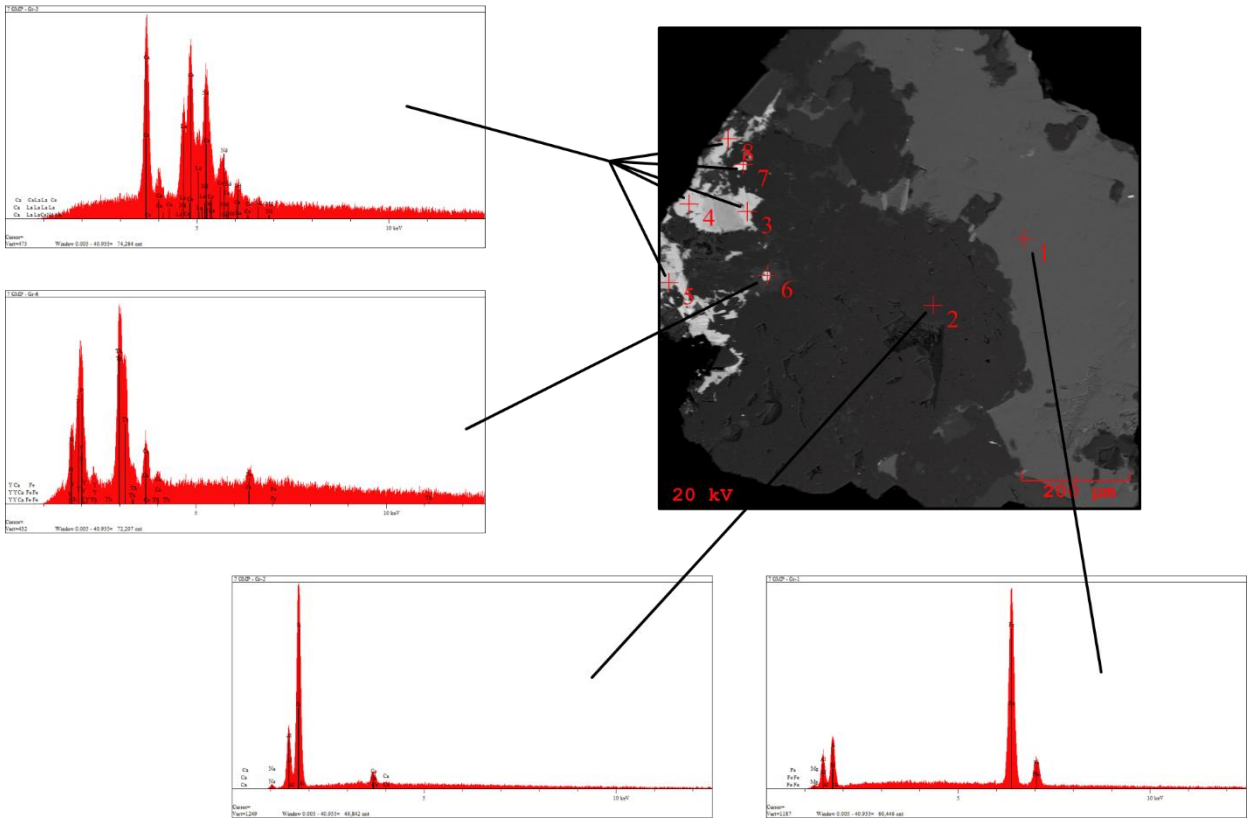


Figure 66 BSE image of "Bastnäsite" (crosshairs 3, 4, 5, 7, & 8), plagioclase (crosshair 2), and an iron aluminosilicates (crosshair 1).

"Bastnäsite" has been qualitatively investigated by SEM and confirmed via microprobe. "Bastnäsite" is a rare earth element fluorocarbonate classified on the basis of the dominance of yttrium, lanthanum, and cerium. Microprobe analyses reveal that cerium is the dominant cation in the A-site, thus classification is bastnäsite-(Ce). Discrete grains of bastnäsite-(Ce) are not found. Table 22 lists the representative EMP analyses.

| **BASTNÄSITE-(CE) – CROCKLEY PEGMATITE** | | |
|---|---|---|
| Wt.% oxide | CP-Grain 8-1 | CP-grain 8-2 |
| $P_2O_5$ | 0.232 | 0.093 |
| $SiO_2$ | 0.092 | 0.113 |
| $UO_2$ | 0.011 | 0.000 |
| $ThO_2$ | 0.332 | 0.210 |
| $Y_2O_3$ | 0.830 | 0.733 |
| $Al_2O_3$ | 0.000 | 0.088 |
| $La_2O_3$ | 14.221 | 15.443 |
| $Ce_2O_3$ | 29.234 | 29.454 |
| $Pr_2O_3$ | 2.443 | 2.600 |
| $Nd_2O_3$ | 15.034 | 14.398 |
| $Sc_2O_3$ | 0.032 | 0.033 |
| $Sm_2O_3$ | 0.890 | 1.082 |
| $Eu_2O_3$ | 0.000 | 0.000 |
| $Gd_2O_3$ | 0.422 | 0.465 |
| $Dy_2O_3$ | 0.198 | 0.211 |
| $Yb_2O_3$ | 0.043 | 0.034 |
| FeO | 0.276 | 0.188 |
| MnO | 0.038 | 0.055 |
| CaO | 8.655 | 2.334 |
| PbO | 0.000 | 0.000 |
| F | 7.650 | 7.544 |
| $CO_2$ | 20.082 | 20.082 |
| $H_2O$ | 2.504 | 8.015 |
| **Sub-Total** | 103.219 | 103.175 |
| Ox. cor. for F | - 3.219 | - 3.175 |
| **Total** | 100.000 | 100.000 |

Table 22 Representative EMP analyses of bastnäsite-(Ce).
*Apfu* calculations based on 4 anions. Table continues on next page.

| *apfu* | | |
|---|---|---|
| P | 0.007 | 0.003 |
| Si | 0.003 | 0.004 |
| U | 0.000 | 0.000 |
| Th | 0.003 | 0.002 |
| Y | 0.016 | 0.014 |
| Al | 0.000 | 0.004 |
| Fe | 0.000 | 0.000 |
| La | 0.191 | 0.208 |
| Ce | 0.390 | 0.393 |
| Pr | 0.032 | 0.035 |
| Nd | 0.196 | 0.188 |
| Sc | 0.001 | 0.001 |
| Sm | 0.011 | 0.014 |
| Eu | 0.000 | 0.000 |
| Gd | 0.005 | 0.006 |
| Dy | 0.002 | 0.002 |
| Yb | 0.000 | 0.000 |
| Fe | 0.008 | 0.006 |
| Mn | 0.001 | 0.002 |
| Ca | 0.338 | 0.091 |
| Pb | 0.000 | 0.000 |
| F | 0.882 | 0.870 |
| $CO_2$ | 1.000 | 1.000 |
| $H_2O$ | 0.609 | 1.949 |
| **Σ REE** | 0.830 | 0.846 |
| **REE + Ca** | 1.168 | 0.938 |
| **Σ A-Site** | 1.197 | 0.965 |

BIOTITE

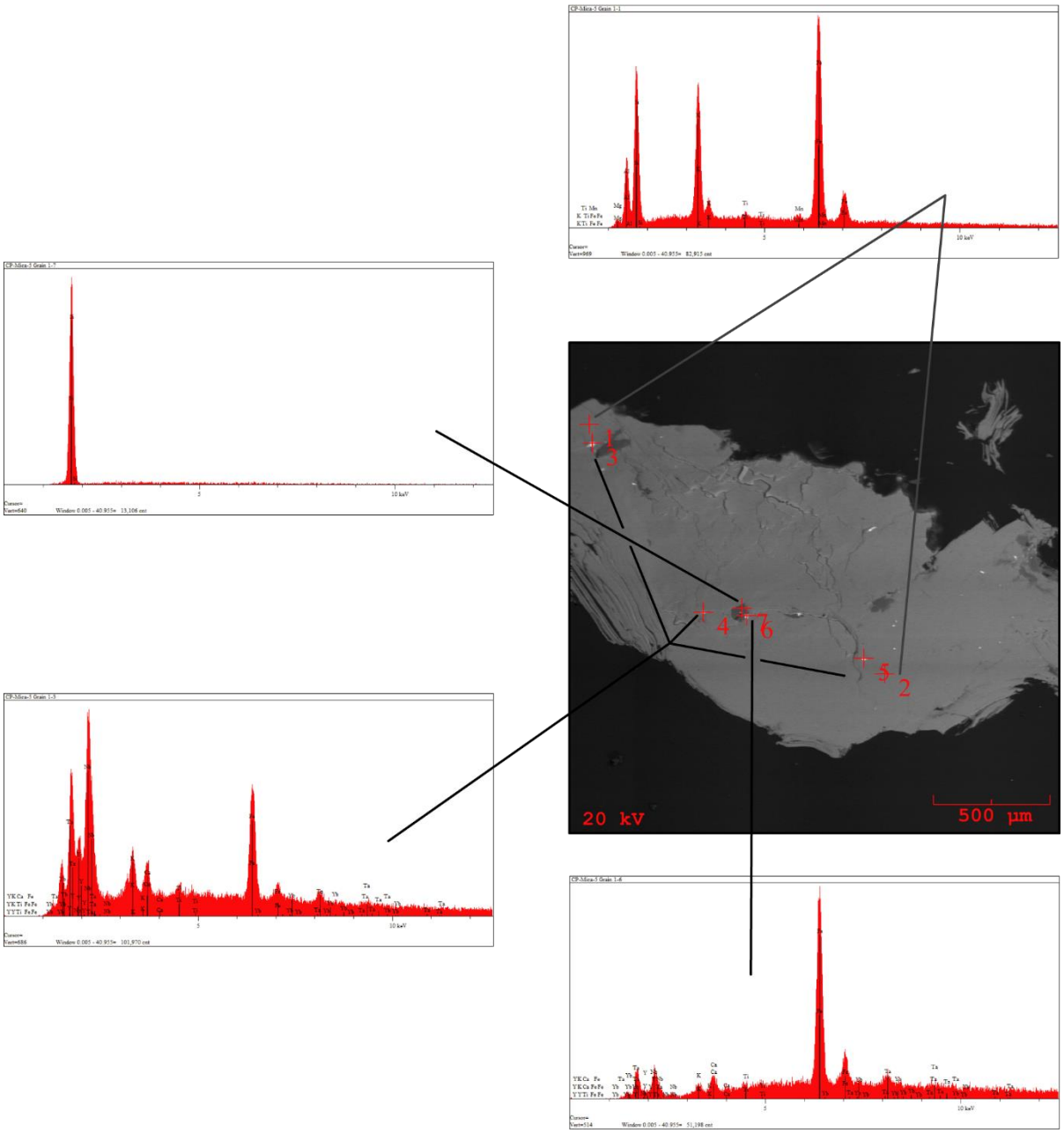


Figure 67 BSE image of biotite mica grain (crosshairs 1 & 2) and inclusions (crosshairs 3-7) along with EDS spectra.

Biotite mica has been identified in heavy mineral separations, qualitatively analyzed by SEM, and confirmed by microprobe as Fe-biotite (Figure 186). Lack of homogeneity has prevented accurate DCP and titration analyses to determine lithium and trivalent iron,

respectively. However, lithium is calculated based on the equation provided by Tischendorf (1997): (2.7/ (0.35 + MgO)) – 0.13 based on $SiO_2$ and MgO values. An alternate equation that is based on fluorine values yields slightly less lithium weight percent (>0.1 difference). Biotite is relatively more abundant at the Crockley than muscovite mica. Table 23 lists the representative analyses. Rubidium is at or below detection limits suggesting that biotites from the Crockley are poorly evolved.

| **BIOTITE – CROCKLEY PEGMATITE** | | | | | | |
|---|---|---|---|---|---|---|
| Wt % Ox. | mica 1b grain1-3 | mica 1b grain5-1 | mica 1b grain5-2 | mica 1b grain5-3 | mica 1b grain5-4 | Mica grain2-1 |
| $SiO_2$ | 32.655 | 32.877 | 32.766 | 32.655 | 32.560 | 32.523 |
| $TiO_2$ | 2.331 | 2.433 | 2.111 | 2.089 | 1.981 | 1.770 |
| $Al_2O_3$ | 16.800 | 16.622 | 16.700 | 16.877 | 17.044 | 17.091 |
| $Fe_2O_3$ | 0.000 | 0.000 | 0.000 | 0.000 | 0.000 | 0.000 |
| FeO | 26.344 | 26.455 | 26.554 | 26.456 | 26.234 | 25.985 |
| MnO | 0.433 | 0.344 | 0.299 | 0.213 | 0.191 | 0.172 |
| MgO | 6.116 | 6.005 | 5.956 | 6.099 | 5.855 | 5.776 |
| CaO | 0.067 | 0.099 | 0.087 | 0.077 | 0.100 | 0.100 |
| $Li_2O$ (*calc.*) | 0.288 | 0.295 | 0.298 | 0.289 | 0.305 | 0.311 |
| $Na_2O$ | 0.099 | 0.121 | 0.088 | 0.067 | 0.054 | 0.112 |
| $K_2O$ | 9.544 | 9.223 | 9.655 | 9.655 | 9.122 | 9.775 |
| $Rb_2O$ | 0.000 | 0.009 | 0.011 | 0.009 | 0.000 | 0.011 |
| $Cs_2O$ | *bdl* | *bdl* | *bdl* | *bdl* | *bdl* | *bdl* |
| F | 0.899 | 0.988 | 0.889 | 0.834 | 0.792 | 0.933 |
| $H_2O$ | 3.304 | 3.262 | 3.299 | 3.327 | 3.322 | 3.251 |
| F=O | - 0.379 | - 0.416 | - 0.374 | - 0.351 | - 0.333 | - 0.393 |
| **Total** | 98.501 | 98.317 | 98.339 | 98.296 | 97.227 | 97.417 |
| *apfu* | | | | | | |
| Si | 5.249 | 5.284 | 5.280 | 5.260 | 5.280 | 5.281 |
| $^{IV}Al$ | 2.751 | 2.716 | 2.720 | 2.740 | 2.720 | 2.719 |
| **Σ T-site** | 8.000 | 8.000 | 8.000 | 8.000 | 8.000 | 8.000 |
| $^{VI}Al$ | 0.432 | 0.433 | 0.452 | 0.464 | 0.538 | 0.552 |
| Ti | 0.282 | 0.294 | 0.256 | 0.253 | 0.242 | 0.216 |
| $Fe_t$ | 3.541 | 3.556 | 3.579 | 3.564 | 3.558 | 3.529 |
| Mn | 0.059 | 0.047 | 0.041 | 0.029 | 0.026 | 0.024 |
| Mg | 1.465 | 1.439 | 1.431 | 1.465 | 1.415 | 1.398 |
| Li (*calc.*) | 0.186 | 0.191 | 0.193 | 0.187 | 0.199 | 0.203 |
| **Σ Y-site** | 5.965 | 5.960 | 5.952 | 5.962 | 5.978 | 5.922 |

Table 23 Representative EMP analyses of biotite mica. *Apfu* calculations based on 24 anions. Table continues on next page.

| | | | | | | |
|---|---|---|---|---|---|---|
| K | 1.957 | 1.891 | 1.985 | 1.984 | 1.887 | 2.025 |
| Ca | 0.012 | 0.017 | 0.015 | 0.013 | 0.017 | 0.017 |
| Na | 0.031 | 0.038 | 0.028 | 0.021 | 0.017 | 0.035 |
| Rb | 0.000 | 0.001 | 0.001 | 0.001 | 0.000 | 0.001 |
| Cs | *bdl* | *bdl* | *bdl* | *bdl* | *bdl* | *bdl* |
| **Σ X-site** | 2.000 | 1.947 | 2.029 | 2.019 | 1.921 | 2.078 |
| F | 0.457 | 0.502 | 0.453 | 0.425 | 0.406 | 0.479 |
| OH* | 3.543 | 3.498 | 3.547 | 3.575 | 3.594 | 3.521 |
| **Σ W-site** | 4.000 | 4.000 | 4.000 | 4.000 | 4.000 | 4.000 |

## CHALCOPYRITE

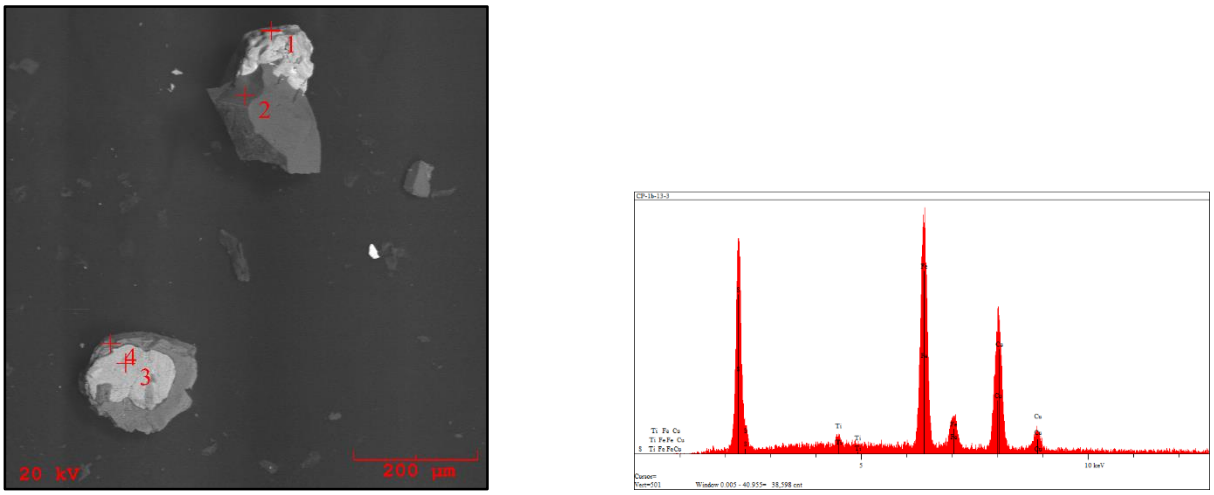


Figure 68 BSE image and corresponding EDS spectrum of chalcopyrite. Zircon (crosshair 1), quartz (crosshair 2), chalcopyrite (crosshair 3), & mica (crosshair 4).

Two grains of chalcopyrite have been qualitatively identified by SEM. Discrete grains have not been found. This represents the first reported occurrence of chalcopyrite having been identified at the Crockley pegmatite.

## COLUMBITE

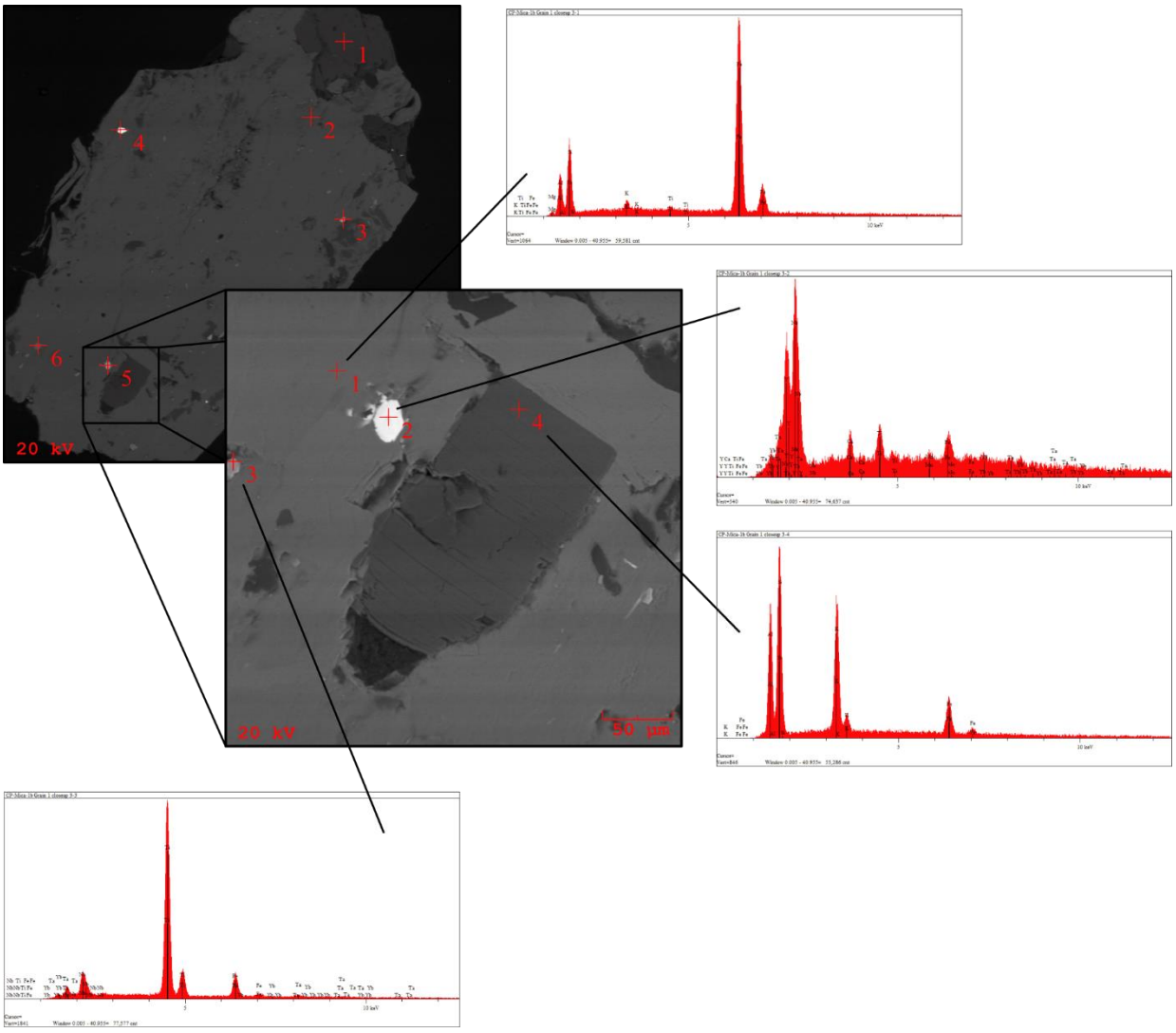


Figure 69 BSE image and associated spectra of biotite grain with columbite inclusion. Top left image: K-feldspar (crosshair 1); biotite mica (crosshair 2); quartz (crosshair 3); lead (crosshair 4); rutile (crosshair 6); crosshair 5 region is enlarged BSE image.

Columbite has been only found as inclusions in mica. No discrete grains have been identified. Based on stoichiometry from microprobe analyses, these inclusions should be classified as ferrocolumbite due to iron and niobium dominance. Other than pyrochlore no other tantalum or niobium mineralization has been found in Crockley pegmatite samples. Table 24 shows the analyses gleaned from EMP results.

| **FERROCOLUMBITE – CROCKLEY** | | | |
|---|---|---|---|
| Wt% Ox | Mica 1b grain 2-6 | Mica 1b grain 2-7 | Mica 1b grain 2-8 |
| $Nb_2O_5$ | 46.220 | 46.312 | 45.565 |
| $Ta_2O_5$ | 29.622 | 29.511 | 30.320 |
| $SiO_2$ | 0.044 | 0.037 | 0.027 |
| $TiO_2$ | 4.002 | 3.933 | 4.009 |
| $Al_2O_3$ | 0.023 | 0.031 | 0.023 |
| FeO | 17.740 | 17.544 | 17.655 |
| MnO | 1.980 | 2.112 | 2.012 |
| MgO | *bdl* | *bdl* | *bdl* |
| Total | 99.631 | 99.480 | 99.611 |
| *apfu* | | | |
| Fe | 0.937 | 0.928 | 0.935 |
| Mn | 0.106 | 0.113 | 0.108 |
| Si | 0.003 | 0.002 | 0.002 |
| Al | 0.002 | 0.002 | 0.002 |
| Mg | *bdl* | *bdl* | *bdl* |
| **Σ X-site** | 1.048 | 1.045 | 1.047 |
| Nb | 1.319 | 1.324 | 1.305 |
| Ta | 0.509 | 0.507 | 0.522 |
| Ti | 0.190 | 0.187 | 0.191 |
| **Σ Y-site** | 2.018 | 2.018 | 2.018 |

Table 24 Representative EMP analyses of ferrocolumbite. *Apfu* calculations based on 6 oxygens.

## FELDSPAR

### K-FELDSPAR

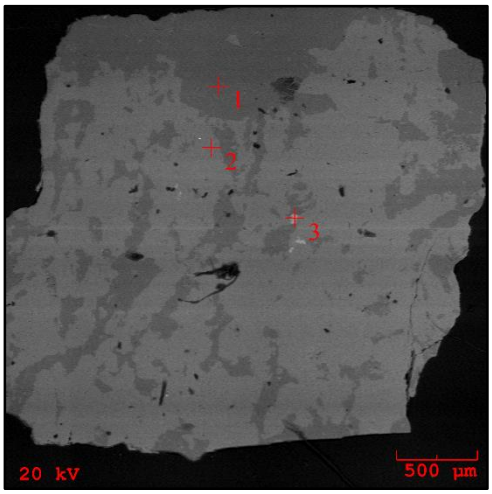


Figure 70 BSE image of K-feldspar.
Lighter region – K-feldspar (crosshair 1), darker region – plagioclase feldspar (crosshair 2), and fluorite inclusions (crosshair 3).

K-feldspar has been confirmed by microprobe. Exsolution of sodium-rich plagioclase is present, although these lamellae are irregular and rarely parallel. Strontium and rubidium are both at or within detection limits for some of the samples analyzed. Barium and cesium are below detection limits. Therefore, K-feldspar grains analyzed from the Crockley are thought to be poorly evolved. XRD analysis confirms that K-feldspar is maximum microcline (Figure 173) indicating a high degree of structural ordering (Wright & Stewart, 1968). Table 25 lists the representative microprobe analyses.

| K-FELDSPAR - CROCKLEY PEGMATITE | | | | | | | | |
|---|---|---|---|---|---|---|---|---|
| Wt% ox | CP 1b grain 1-1 | CP 1b grain 1-3 | CP 1b grain 3-2 | CP 1b grain 3-3 | CP 5 grain 2-1 | CP 5 grain 2-3 | CP 5 grain 3-1 | CP 5 grain 3-2 |
| $P_2O_5$ | *bdl* | *bdl* | *bdl* | *bdl* | *bdl* | *bdl* | *bdl* | *bdl* |
| $SiO_2$ | 64.894 | 68.822 | 64.801 | 68.799 | 68.811 | 64.783 | 64.755 | 64.788 |
| $TiO_2$ | 0.016 | 0.000 | 0.000 | 0.000 | 0.000 | 0.015 | 0.008 | 0.013 |
| $Al_2O_3$ | 18.222 | 19.734 | 18.344 | 19.811 | 19.487 | 18.422 | 18.367 | 18.399 |
| $FeO_t$ | 0.014 | 0.000 | 0.011 | 0.000 | 0.000 | 0.015 | 0.009 | 0.016 |
| CaO | 0.011 | 0.871 | 0.000 | 0.912 | 0.554 | 0.000 | 0.000 | 0.000 |
| $Na_2O$ | 0.712 | 10.112 | 0.581 | 10.012 | 10.433 | 0.611 | 0.565 | 0.610 |
| $K_2O$ | 15.895 | 0.134 | 16.009 | 0.211 | 0.211 | 16.278 | 16.300 | 16.166 |
| Rb2O | 0.009 | 0.000 | 0.015 | 0.000 | 0.000 | 0.009 | 0.012 | 0.013 |
| **Total** | 99.773 | 99.682 | 99.761 | 99.745 | 99.509 | 100.133 | 100.016 | 100.005 |
| *apfu* | | | | | | | | |
| K | 0.938 | 0.007 | 0.945 | 0.012 | 0.012 | 0.960 | 0.962 | 0.953 |
| Na | 0.064 | 0.855 | 0.052 | 0.847 | 0.885 | 0.055 | 0.051 | 0.055 |
| Ca | 0.001 | 0.041 | 0.000 | 0.043 | 0.026 | 0.000 | 0.000 | 0.000 |
| Rb | 0.000 | 0.000 | 0.000 | 0.000 | 0.000 | 0.000 | 0.000 | 0.000 |
| **Σ X-site** | 1.002 | 0.903 | 0.997 | 0.902 | 0.923 | 1.015 | 1.013 | 1.008 |
| Al | 0.994 | 1.015 | 1.001 | 1.018 | 1.005 | 1.003 | 1.001 | 1.003 |
| Fe | 0.000 | 0.000 | 0.000 | 0.000 | 0.000 | 0.000 | 0.000 | 0.000 |
| **Σ Y-site** | 0.994 | 1.015 | 1.001 | 1.018 | 1.005 | 1.003 | 1.001 | 1.003 |
| Si | 3.003 | 3.003 | 3.000 | 3.000 | 3.009 | 2.993 | 2.995 | 2.995 |
| Ti | 0.001 | 0.000 | 0.000 | 0.000 | 0.000 | 0.001 | 0.000 | 0.000 |
| P | 0.000 | 0.000 | 0.000 | 0.000 | 0.000 | 0.000 | 0.000 | 0.000 |
| Al | 0.000 | 0.000 | 0.000 | 0.000 | 0.000 | 0.000 | 0.000 | 0.000 |
| **Σ Z-site** | 3.003 | 3.003 | 3.000 | 3.000 | 3.009 | 2.994 | 2.995 | 2.995 |

Table 25 Representative K-feldspar analyses. *Apfu* calculations based on 8 oxygens.

PLAGIOCLASE FELDSPAR

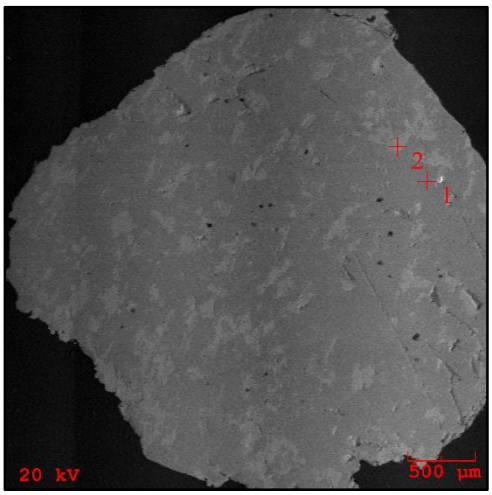


Figure 71 BSE image of plagioclase feldspar (crosshair 1) and K-feldspar exsolution (crosshair 2).

A few grains of plagioclase feldspar grains have been identified by SEM and confirmed by microprobe. Barium and cesium are below detection limits; a detectable amount of rubidium and strontium is present. These grains are considered to be poorly evolved. Table 26 shows a representative list of plagioclase grains with associated K-feldspar analyses.

| PLAGIOCLASE FELDSPAR - CROCKLEY PEGMATITE | | | | | | | | |
|---|---|---|---|---|---|---|---|---|
| Wt% ox | CP 1b grain 2-2 | CP 1b grain 2-3 | CP 5 grain 1-1 | CP 5 grain 1-2 | CP 6 grain 1-1 | CP 6 grain 1-2 | CP 6 grain 2-1 | CP 6 grain 2-2 |
| $P_2O_5$ | *bdl* | *bdl* | *bdl* | *bdl* | *bdl* | *bdl* | *bdl* | *bdl* |
| $SiO_2$ | 64.855 | 68.677 | 68.833 | 64.799 | 64.811 | 68.855 | 68.899 | 64.794 |
| $TiO_2$ | 0.009 | 0.000 | 0.000 | 0.012 | 0.011 | 0.000 | 0.000 | 0.008 |
| $Al_2O_3$ | 18.310 | 19.865 | 19.589 | 18.376 | 18.411 | 19.404 | 19.111 | 18.423 |
| $FeO_t$ | 0.008 | 0.000 | 0.000 | 0.014 | 0.011 | 0.000 | 0.000 | 0.011 |
| CaO | 0.000 | 1.112 | 0.768 | 0.000 | 0.000 | 0.452 | 0.223 | 0.000 |
| $Na_2O$ | 0.696 | 10.402 | 10.311 | 0.632 | 0.595 | 10.634 | 10.912 | 0.600 |
| $K_2O$ | 15.855 | 0.092 | 0.166 | 16.011 | 16.122 | 0.171 | 0.132 | 16.181 |
| Rb2O | 0.016 | 0.000 | 0.000 | 0.009 | 0.012 | 0.000 | 0.000 | 0.011 |
| **Total** | 99.749 | 100.170 | 99.678 | 99.853 | 99.973 | 99.525 | 99.291 | 100.028 |
| *apfu* | | | | | | | | |
| K | 0.936 | 0.005 | 0.009 | 0.945 | 0.951 | 0.010 | 0.007 | 0.954 |
| Na | 0.062 | 0.878 | 0.873 | 0.057 | 0.053 | 0.902 | 0.928 | 0.054 |
| Ca | 0.000 | 0.052 | 0.036 | 0.000 | 0.000 | 0.021 | 0.010 | 0.000 |
| Rb | 0.000 | 0.000 | 0.000 | 0.000 | 0.000 | 0.000 | 0.000 | 0.000 |
| **Σ X-site** | 0.999 | 0.935 | 0.918 | 1.002 | 1.004 | 0.932 | 0.945 | 1.008 |
| Al | 0.999 | 1.019 | 1.008 | 1.002 | 1.003 | 1.000 | 0.987 | 1.004 |
| Fe | 0.000 | 0.000 | 0.000 | 0.000 | 0.000 | 0.000 | 0.000 | 0.000 |
| **Σ Y-site** | 0.999 | 1.019 | 1.008 | 1.002 | 1.003 | 1.000 | 0.987 | 1.004 |
| Si | 3.001 | 2.989 | 3.005 | 2.997 | 2.996 | 3.011 | 3.020 | 2.995 |
| Ti | 0.000 | 0.000 | 0.000 | 0.000 | 0.000 | 0.000 | 0.000 | 0.000 |
| P | 0.000 | 0.000 | 0.000 | 0.000 | 0.000 | 0.000 | 0.000 | 0.000 |
| Al | 0.000 | 0.000 | 0.000 | 0.000 | 0.000 | 0.000 | 0.000 | 0.000 |
| **Σ Z-site** | 3.001 | 2.989 | 3.005 | 2.998 | 2.996 | 3.011 | 3.020 | 2.995 |

Table 26 Representative EMP analyses of plagioclase feldspar. *Apfu* calculations based on 8 oxygens.

## FLUORITE

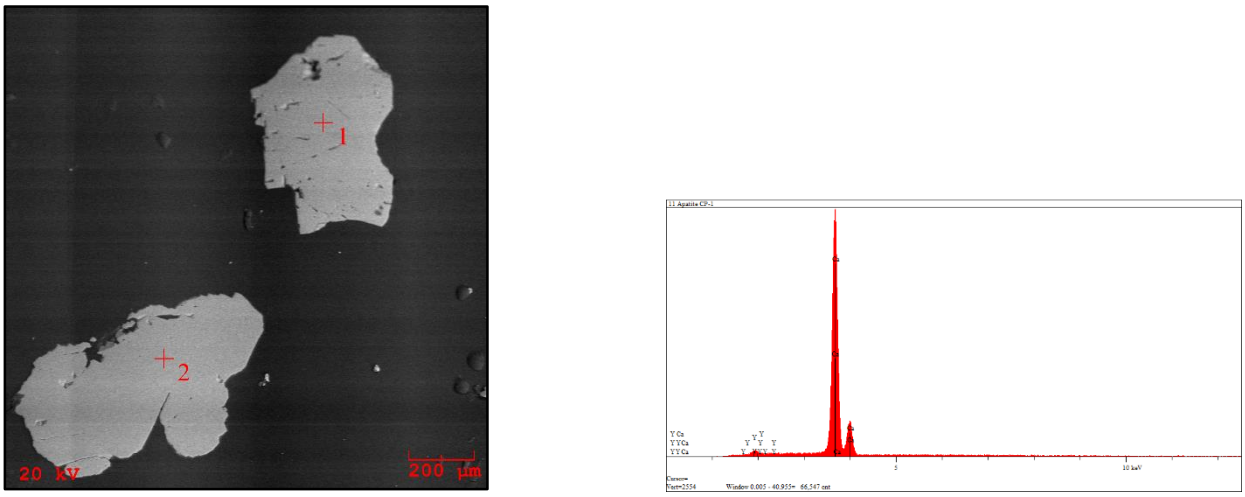


Figure 72 BSE image of fluorite (crosshairs 1 & 2) with corresponding spectrum.

Fluorite from the Crockley was accidently analyzed by microprobe. A few grains fluoresced under UV light and were assumed to be apatite. These grains gave off a yellowish-orange fluorescence and thus these "apatites" were mounted along with others. Once polished grains were investigated by SEM before microprobe analysis, it was discovered that these were, in fact, fluorite grains.

A detectable amount of yttrium is present in both SEM and microprobe analyses, although quantities are just within detectable limits for microprobe analyses.

## GARNET

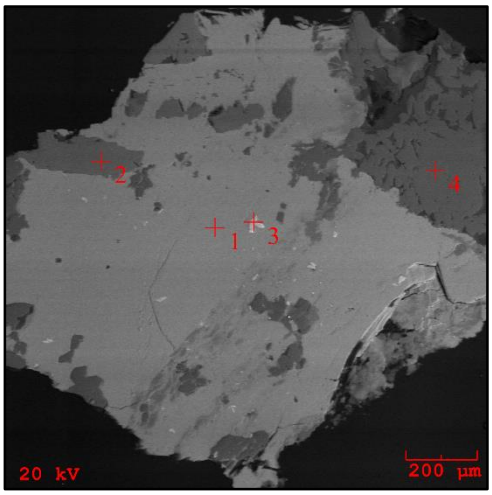


Figure 73 BSE image of garnet grain. Garnet (crosshair 1), K-feldspar (crosshair 2), rutile (crosshair 3), and quartz (crosshair 4).

A single grain of garnet has been identified by SEM and confirmed by microprobe. This is the first reported instance of garnet being found at the Crockley pegmatite. Weight percent total is approximately 98%, suggesting that there may have been possible alteration of the grain. The garnet grain is primarily almanditic with minor amounts of grossular, spessartine, and pyrope components. Table 27 lists the analysis. To convey the scarcity of garnet at the Crockley pegmatite, it is important to note that out of approximately 100 grains investigated by SEM and EMP, as well as a great amount of heavy mineral separations investigated by binocular microscope, that this is the only grain confirmed as garnet. .

| **GARNETS – CROCKLEY PEGMATITE** | |
|---|---|
| Wt % Ox | 1b grain 2-1 |
| $SiO_2$ | 36.658 |
| $TiO_2$ | 0.011 |
| $Al_2O_3$ | 20.922 |
| FeO | 38.544 |
| MnO | 0.877 |
| MgO | 0.898 |
| CaO | 0.998 |
| **Total** | 98.908 |
| *apfu* | |
| Ti | 0.001 |
| Fe | 2.655 |
| Mn | 0.061 |
| Mg | 0.110 |
| Ca | 0.088 |
| **Σ X-site** | 2.915 |
| Al | 2.022 |
| **Σ Y-site** | 2.022 |
| Si | 3.006 |
| **Σ Z-site** | 3.006 |
| **Component** | |
| Pyrope | 04 |
| Spessartine | 02 |
| Grossular | 03 |
| Almandine | 91 |

Table 27 Representative EMP analysis of garnet.
*Apfu* calculations based on 12 oxygens.
Components are normalized to 100.

ILMENITE

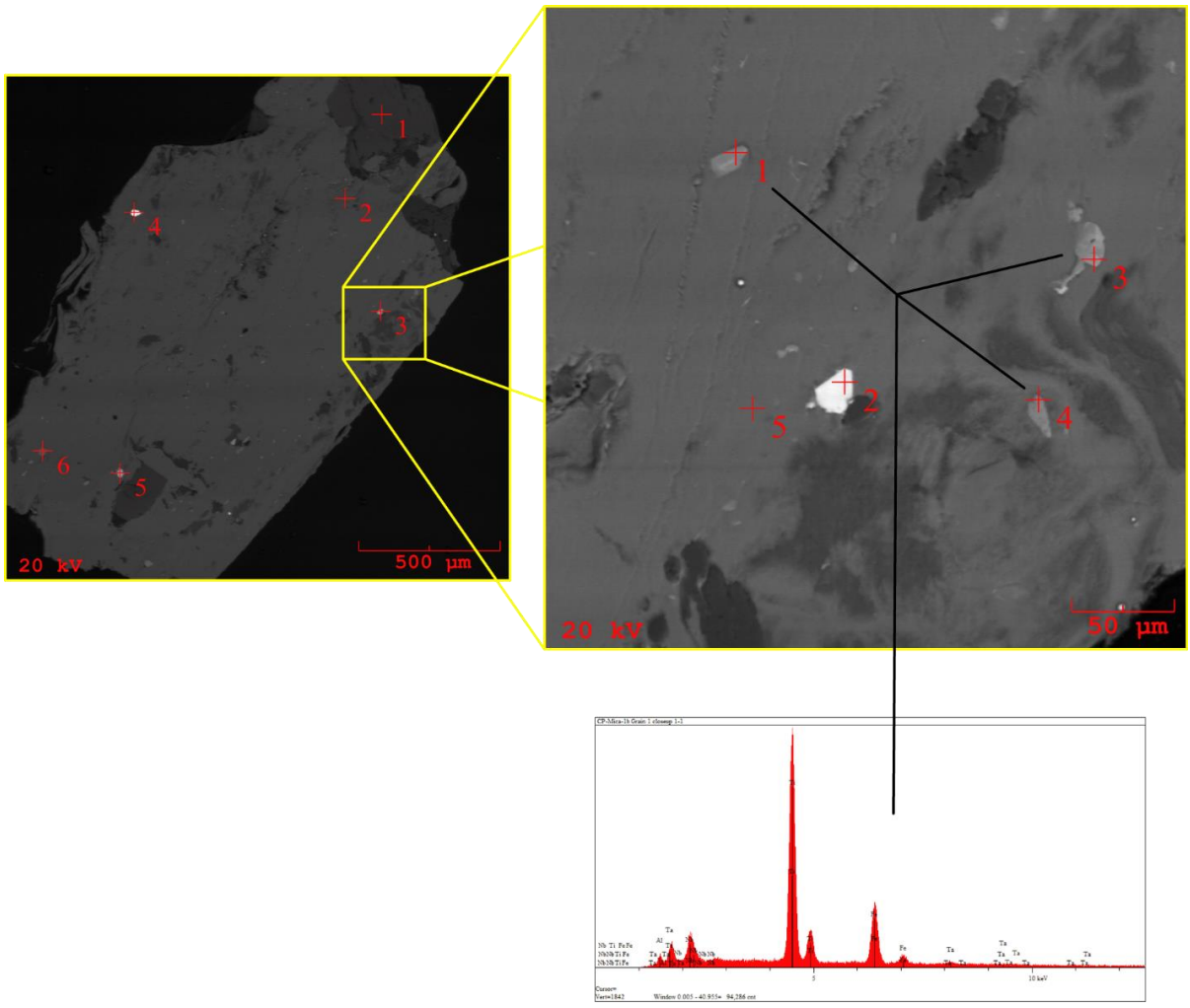


Figure 74 BSE image of ilmenite inclusions with corresponding spectrum. Refer to Figure 69 for additional EDS spectra of BSE image (left). Close-up BSE image: Biotite (crosshair 5) & possible pyrochlore (crosshair 2).

Ilmenite has only ever been identified as inclusions in biotite mica grains. No discrete grains have been found, either by visual inspection of heavy mineral separations or by SEM. Ilmenite is the iron dominant member of the mineral series that exists between pyrophanite (Mn-dominant) and geikielite (Mg-dominant). Manganese is below two weight percent in analyses and magnesium is below detection limits. There is less than a weight percent of niobium present and tantalum is below detection limits. This is first reported and quantitatively confirmed instance of ilmenite at the Crockley pegmatite. Table 28 lists the analyses.

| **ILMENITE – CROCKLEY PEGMATITE** | | |
|---|---|---|
| Wt% Oxide | 1b grain 1-6 | 1b grain 1-7 |
| $TiO_2$ | 54.660 | 56.220 |
| $SiO_2$ | 0.065 | 0.045 |
| FeO | 41.766 | 40.554 |
| MnO | 1.650 | 1.455 |
| MgO | *bdl* | *bdl* |
| CaO | 0.055 | 0.037 |
| $Nb_2O_5$ | 0.114 | 0.165 |
| $Ta_2O_5$ | *bdl* | *bdl* |
| **Total** | 98.420 | 98.568 |
| *apfu* | | |
| FeO | 1.765 | 1.697 |
| MnO | 0.055 | 0.048 |
| MgO | *bdl* | *Bdl* |
| CaO | 0.003 | 0.002 |
| Nb | 0.003 | 0.004 |
| Ta | *bdl* | *bdl* |
| **Σ X-site** | 1.826 | 1.751 |
| Ti | 2.077 | 2.116 |
| Al | 0.006 | 0.005 |
| Si | 0.003 | 0.002 |
| **Σ Y-site** | 2.086 | 2.123 |

Table 28 Representative EMP analyses of ilmenite. *Apfu* calculations based on 6 oxygens.

## PYRITE

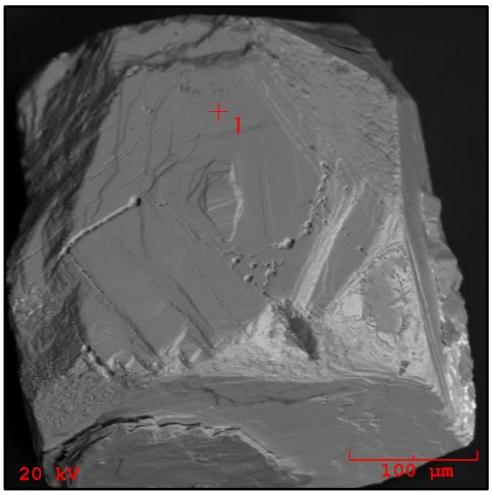


Figure 75 BSE image of pyrite grain.

Discrete pyrite grains have been identified in heavy mineral separations by binocular microscope and qualitatively confirmed by SEM. This is the first reported and qualitatively confirmed instance of pyrite found at the Crockley pegmatite.

## PYROCHLORE SUPERGROUP

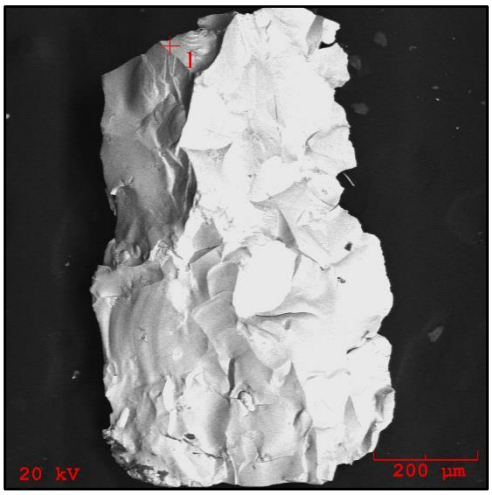


Figure 76 BSE image of pyrochlore supergroup grain.

A member of the pyrochlore supergroup has been identified qualitatively by SEM and confirmed by microprobe. Due to sodium and oxygen dominance, the mineral should be classified as oxynatropyrochlore (Atencio *et al*., 2010). The above BSE image shows that grains can be as large as a millimeter in size. This grain appears to be only a pyrochlore supergroup member, although most grains were associated with zircon.

| **OXYNATROPYROCHLORE – CROCKLEY PEGMATITE** | |
|---|---|
| Wt % Ox. | CP-M-1b |
| $Nb_2O_5$ | 49.988 |
| $Ta_2O_5$ | 15.988 |
| $SiO_2$ | 0.032 |
| $TiO_2$ | 6.878 |
| $UO_2$ | 0.223 |
| $Al_2O_3$ | 0.033 |
| CaO | 9.450 |
| MnO | 0.045 |
| FeO | 8.998 |
| PbO | 1.112 |
| $Na_2O$ | 5.988 |
| $H_2O$ | 1.800 |
| F | 0.998 |
| F=O | - 0.499 |
| **Total** | 101.032 |
| *apfu* | |
| U | 0.003 |
| Al | 0.003 |
| Ca | 0.668 |
| Mn | 0.003 |
| Fe | 0.496 |
| Pb | 0.020 |
| Na | 0.766 |
| **Σ A-site** | 1.959 |
| Nb | 1.490 |
| Ta | 0.287 |
| Si | 0.002 |
| Ti | 0.341 |
| **Σ B-site** | 2.120 |
| H (calc.) | 0.792 |
| F | 0.208 |
| **Σ C-site** | 1.000 |

Table 29 Representative EMP analysis of oxynatropyrochlore.
*Apfu* calculations based on 7 anions.

## "MONAZITE"

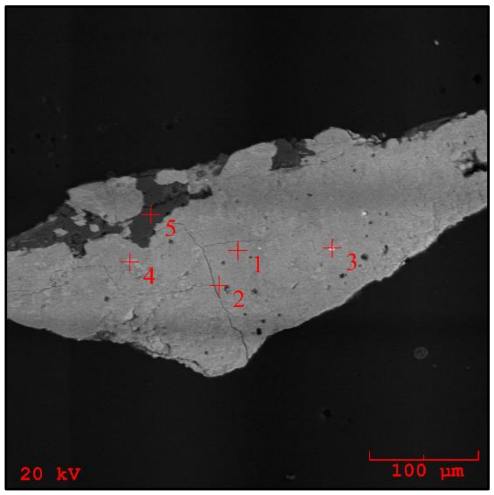


Figure 77 BSE image of polished "monazite" grain. "Monazite" (crosshairs 1 - 4) and fluorite (crosshair 5).

"Monazite" has been qualitatively analyzed and quantitatively confirmed from heavy mineral samples. This is the first reported and quantitatively analyzed instance of "monazite" at the Crockley pegmatite. Results show that "monazite" from the Crockley should be classified as monazite-(Ce) due to cerium dominance in the X-site cation site. It is important to note that the second most abundant cation in the X-site is thorium followed by neodymium. The grain is also relatively enriched with calcium due to the commonality of thorium ($^{+}4$) and calcium ($^{+}2$) forming a coupled substitution to satisfy the charge balance in the X-site. The analyzed grain has fluorite inclusions. Weight percent total is almost 98% suggesting possible alteration of the "monazite" grain. Table 30 lists the analysis.

| **MONAZITE-(CE) – CROCKLEY** | |
|---|---|
| Wt % Ox. | 16 CP-1 |
| $P_2O_5$ | 27.344 |
| $SiO_2$ | 0.211 |
| $ThO_2$ | 23.564 |
| $UO_2$ | 0.455 |
| $Al_2O_3$ | 0.077 |
| $La_2O_3$ | 6.091 |
| $Ce_2O_3$ | 17.887 |
| $Pr_2O_3$ | 1.933 |
| $Nd_2O_3$ | 11.655 |
| $Sm_2O_3$ | 2.112 |
| $Gd_2O_3$ | 0.834 |
| $Dy_2O_3$ | 0.278 |
| $Yb_2O_3$ | 0.055 |
| $Y_2O_3$ | 0.834 |
| MgO | 0.000 |
| CaO | 3.233 |
| MnO | 0.044 |
| FeO | 0.422 |
| PbO | 0.877 |
| **Total** | 97.896 |
| *apfu* | |
| Th | 0.223 |
| U | 0.004 |
| Al | 0.004 |
| La | 0.093 |
| Ce | 0.272 |
| Pr | 0.029 |
| Nd | 0.173 |
| Sm | 0.030 |
| Y | 0.018 |
| Mn | 0.000 |
| Fe | 0.015 |
| Ca | 0.143 |
| **Σ X** | 1.033 |
| P | 0.962 |
| Si | 0.009 |
| **Σ Y** | 0.971 |

Table 30 Representative EMP analysis of monazite-(Ce). *Apfu* calculations based on 4 oxygens.

MUSCOVITE

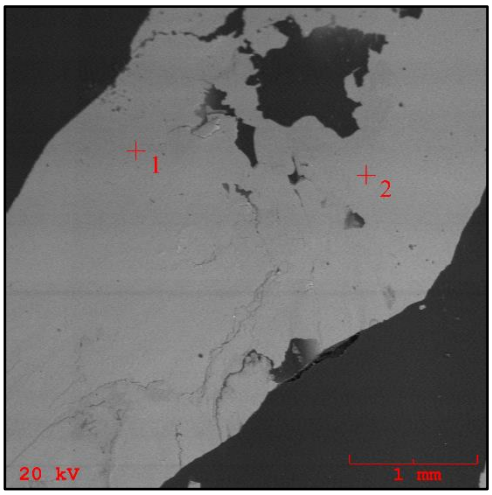


Figure 78 BSE image of muscovite mica (crosshairs 1 & 2).

Muscovite mica has been confirmed by microprobe after qualitatively analyzed by SEM (Figure 186). Lack of homogeneous grains has made further analyses of grains by titration and DCP impossible due to the expected lack of reliable results. Lithium is stoichiometrically accounted for by using equations provided by Tischendorf (1997). Since muscovite is a dioctahedral mica, the recommended equation: 0.3935 * wt% fluorine$^{1.326}$ has been used. Table 31 lists the analyses. Rubidium is just within detection limits and cesium is below detectable limits suggesting poor evolution.

| **MUSCOVITE – CROCKLEY PEGMATITE** | | | |
|---|---|---|---|
| Wt % Ox. | mica 1b grain 1-3 | mica 1b grain 5-1 | mica 1b grain 5-2 |
| $SiO_2$ | 46.334 | 46.766 | 46.612 |
| $TiO_2$ | 0.093 | 0.312 | 0.292 |
| $Al_2O_3$ | 33.766 | 34.676 | 34.588 |
| $Fe_2O_3$ | 0.000 | 0.000 | 0.000 |
| FeO | 3.870 | 2.433 | 2.377 |
| MnO | 0.024 | 0.132 | 0.127 |
| MgO | 0.143 | 1.778 | 1.723 |
| CaO | 0.015 | 0.033 | 0.028 |
| $Li_2O$ (*calc.*) | 0.526 | 0.446 | 0.447 |
| $Na_2O$ | 0.679 | 0.655 | 0.599 |
| $K_2O$ | 10.044 | 9.677 | 9.553 |
| $Rb_2O$ | 0.021 | 0.015 | 0.012 |
| $Cs_2O$ | *bdl* | *bdl* | *bdl* |
| F | 1.245 | 1.099 | 1.100 |
| $H_2O$ | 3.883 | 4.054 | 4.033 |
| F=O | 0.524 | 0.463 | 0.463 |
| **Total** | 100.119 | 101.613 | 101.027 |
| *apfu* | | | |
| Si | 6.211 | 6.130 | 6.137 |
| $^{IV}Al$ | 1.789 | 1.870 | 1.863 |
| **Σ T-site** | 8.000 | 8.000 | 8.000 |
| $^{VI}Al$ | 3.546 | 3.487 | 3.505 |
| Ti | 0.009 | 0.031 | 0.029 |
| $Fe_t$ | 0.434 | 0.267 | 0.262 |
| Mn | 0.003 | 0.015 | 0.014 |
| Mg | 0.029 | 0.348 | 0.338 |
| Li (*calc.*) | 0.284 | 0.235 | 0.237 |
| **Σ Y-site** | 4.305 | 4.383 | 4.385 |

Table 31 Representative EMP analyses of muscovite mica. *Apfu* calculations based on 24 anions.
Table continues on next page.

| | | | |
|---|---|---|---|
| K | 1.718 | 1.618 | 1.605 |
| Ca | 0.002 | 0.005 | 0.004 |
| Na | 0.176 | 0.166 | 0.153 |
| Rb | 0.002 | 0.001 | 0.001 |
| Cs | *bdl* | *bdl* | *bdl* |
| **Σ X-site** | 1.898 | 1.790 | 1.763 |
| F | 0.528 | 0.456 | 0.458 |
| OH* | 3.472 | 3.544 | 3.542 |
| **Σ W-site** | 4.000 | 4.000 | 4.000 |

## RUTILE

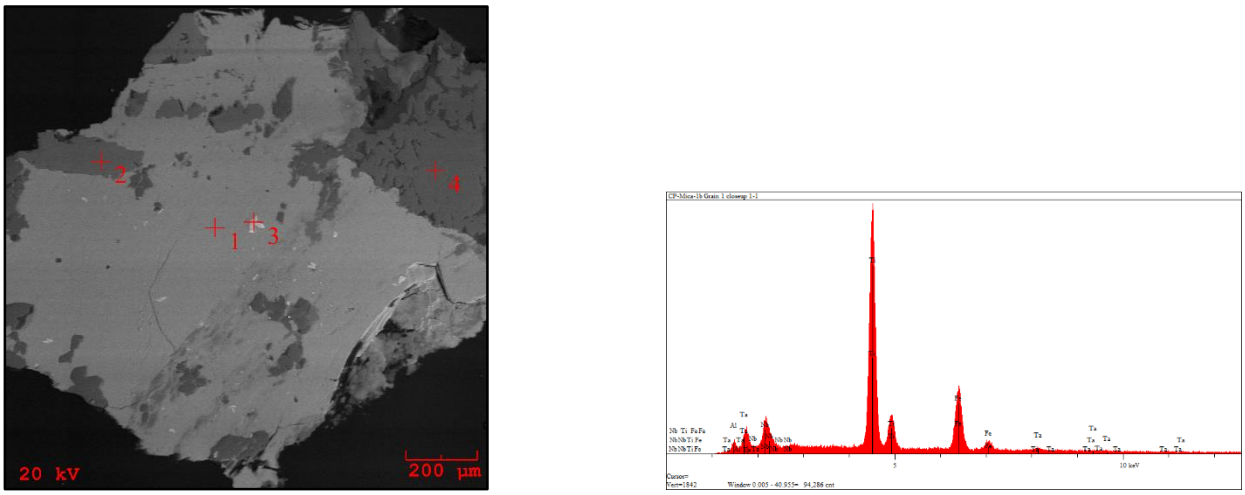


Figure 79 BSE image of rutile inclusion (crosshair 3) and associated EDS spectrum. Garnet (crosshair 1), K-feldspar (crosshair 2), & quartz (crosshair 4).

Rutile has been identified via SEM and confirmed via microprobe. There are inclusions of rutile in biotite mica grains and these are less than 100 microns in length. No discrete grains of rutile have been identified. This is first instance of rutile being quantitatively confirmed in samples from the Crockley pegmatite. Of the two analyses, one has over two, and not more than three, weight percent of both niobium and iron. Niobium and/or tantalum, along with divalent cations such as iron, calcium, and manganese can form coupled substitutions for titanium. Tantalum is present, but it is less than one half of a weight percent. Table 32 shows the two analyses.

| **RUTILE – CROCKLEY PEGMATITE** | | |
|---|---|---|
| Wt% Oxide | 1b grain 1-8 | 1b grain 2-5 |
| $TiO_2$ | 99.004 | 95.643 |
| $Al_2O3$ | 0.021 | 0.211 |
| $Nb_2O_5$ | 0.000 | 2.223 |
| $Ta_2O_5$ | 0.000 | 0.221 |
| FeO | 0.671 | 2.002 |
| MnO | 0.021 | 0.066 |
| MgO | 0.009 | 0.022 |
| CaO | 0.000 | 0.043 |
| $SiO_2$ | 0.033 | 0.022 |
| **Total** | 99.759 | 100.453 |
| *apfu* | | |
| Ti | 0.995 | 0.967 |
| Al | 0.000 | 0.003 |
| Nb | 0.000 | 0.014 |
| Ta | 0.000 | 0.001 |
| Fe | 0.008 | 0.023 |
| Mn | 0.000 | 0.001 |
| Mg | 0.000 | 0.000 |
| Ca | 0.000 | 0.001 |
| Si | 0.000 | 0.000 |
| **Σ X-site** | 1.004 | 1.009 |

Table 32 Representative EMP analyses of rutile. *Apfu* calculations are based on 2 oxygens.

## ZIRCON

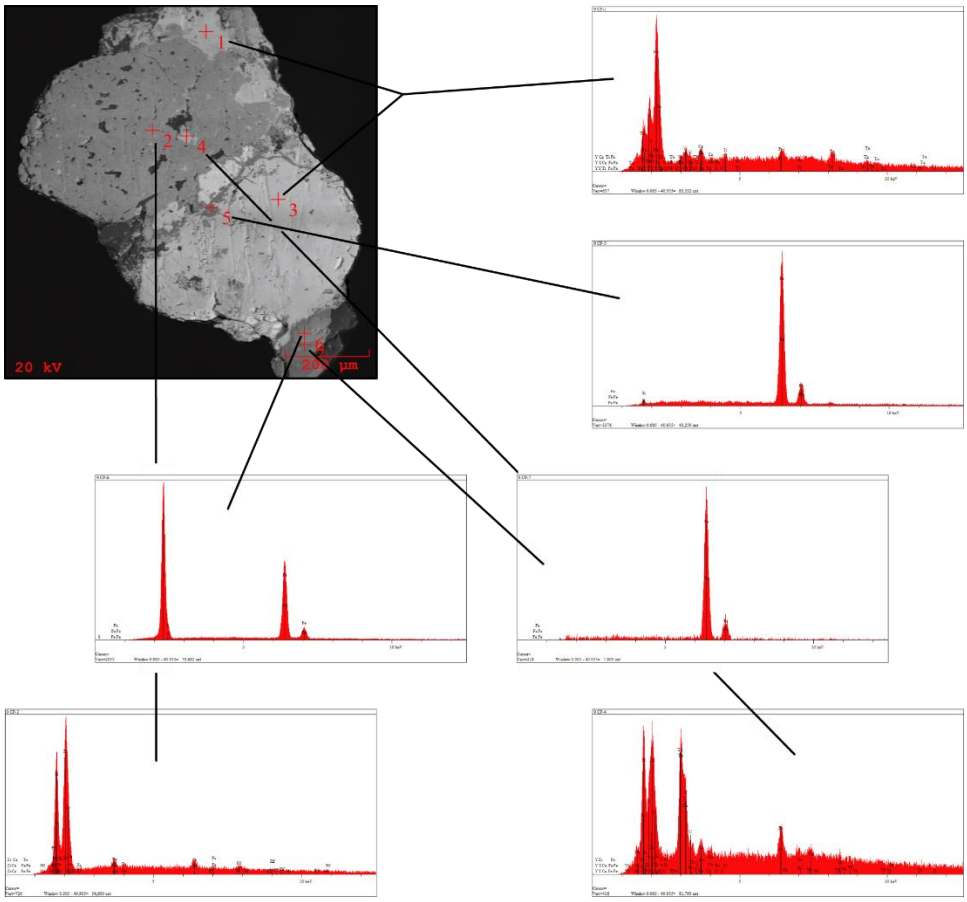


Figure 80 BSE image of zircon (crosshair 2) and associated EDS spectra of a niobium species (crosshairs 1 & 3), iron oxide (crosshairs 5 & 7), thorium-rich zircon (crosshair 4), and pyrite (crosshair 6).

Abundant zircon has been identified in heavy mineral separations by binocular microscope from the Crockley pegmatite. Zircon has been previously identified from this location. Hafnium contents never exceed two weight percent, yet are above one weight percent. Zircons from the Crockley are considered to be not very evolved. Some amount of thorium and uranium is found in zircons investigated by microprobe with one sample exceeding thirty-four weight percent. Table 33 shows a representative list of zircon analyses. Note grain 10, which has elevated thorium levels. Two grains have weight percent totals around 98% suggesting possible alteration.

| ZIRCON – CROCKLEY PEGMATITE | | | | | | |
|---|---|---|---|---|---|---|
| Wt % Oxide | grain 13-CP-1 | | grain 14-CP-1 | | grain 10-CP-1 | |
| $SiO_2$ | 32.22 | 32.191 | 32.012 | 32.072 | 31.77 | 30.123 |
| $TiO_2$ | 0.013 | 0.020 | 0.013 | 0.009 | 0.011 | 0.112 |
| $Al_2O_3$ | 0.021 | 0.024 | 0.030 | 0.037 | 0.052 | 0.097 |
| $ZrO_2$ | 64.220 | 64.651 | 64.874 | 64.894 | 61.89 | 29.120 |
| $HfO_2$ | 1.455 | 1.500 | 1.611 | 1.561 | 1.600 | 0.676 |
| FeOt | 0.166 | 0.200 | 0.312 | 0.262 | 0.877 | 1.212 |
| MnO | 0.009 | 0.012 | 0.009 | 0.000 | 0.012 | 0.115 |
| CaO | 0.211 | 0.181 | 0.200 | 0.211 | 0.377 | 0.445 |
| $UO_2$ | 0.011 | 0.013 | 0.010 | 0.009 | 0.143 | 0.988 |
| $ThO_2$ | 0.031 | 0.028 | 0.017 | 0.020 | 0.878 | **34.33** |
| **Total** | 98.357 | 98.820 | 99.088 | 99.075 | 97.610 | 97.218 |
| *apfu* | | | | | | |
| Zr | 0.974 | 0.977 | 0.980 | 0.980 | 0.952 | 0.530 |
| Hf | 0.018 | 0.018 | 0.019 | 0.019 | 0.020 | 0.010 |
| U | 0.000 | 0.000 | 0.000 | 0.000 | 0.001 | 0.008 |
| Th | 0.000 | 0.000 | 0.000 | 0.000 | 0.006 | 0.292 |
| Fe | 0.004 | 0.005 | 0.008 | 0.007 | 0.023 | 0.038 |
| Mg | 0.000 | 0.000 | 0.000 | 0.000 | 0.000 | 0.000 |
| Mn | 0.000 | 0.000 | 0.000 | 0.000 | 0.000 | 0.004 |
| Ca | 0.007 | 0.006 | 0.007 | 0.007 | 0.013 | 0.018 |
| **Σ X-site** | 1.003 | 1.006 | 1.015 | 1.013 | 1.015 | 0.900 |
| Si | 1.002 | 0.998 | 0.992 | 0.993 | 1.002 | 1.124 |
| Ti | 0.000 | 0.000 | 0.000 | 0.000 | 0.000 | 0.003 |
| Al | 0.001 | 0.001 | 0.001 | 0.001 | 0.002 | 0.004 |
| **Σ Y-site** | 1.003 | 0.999 | 0.993 | 0.994 | 1.004 | 1.131 |

Table 33 Representative EMP analyses of zircon. *Apfu* calculations based on 4 oxygens.

## REPUBLIC MINE PEGMATITE

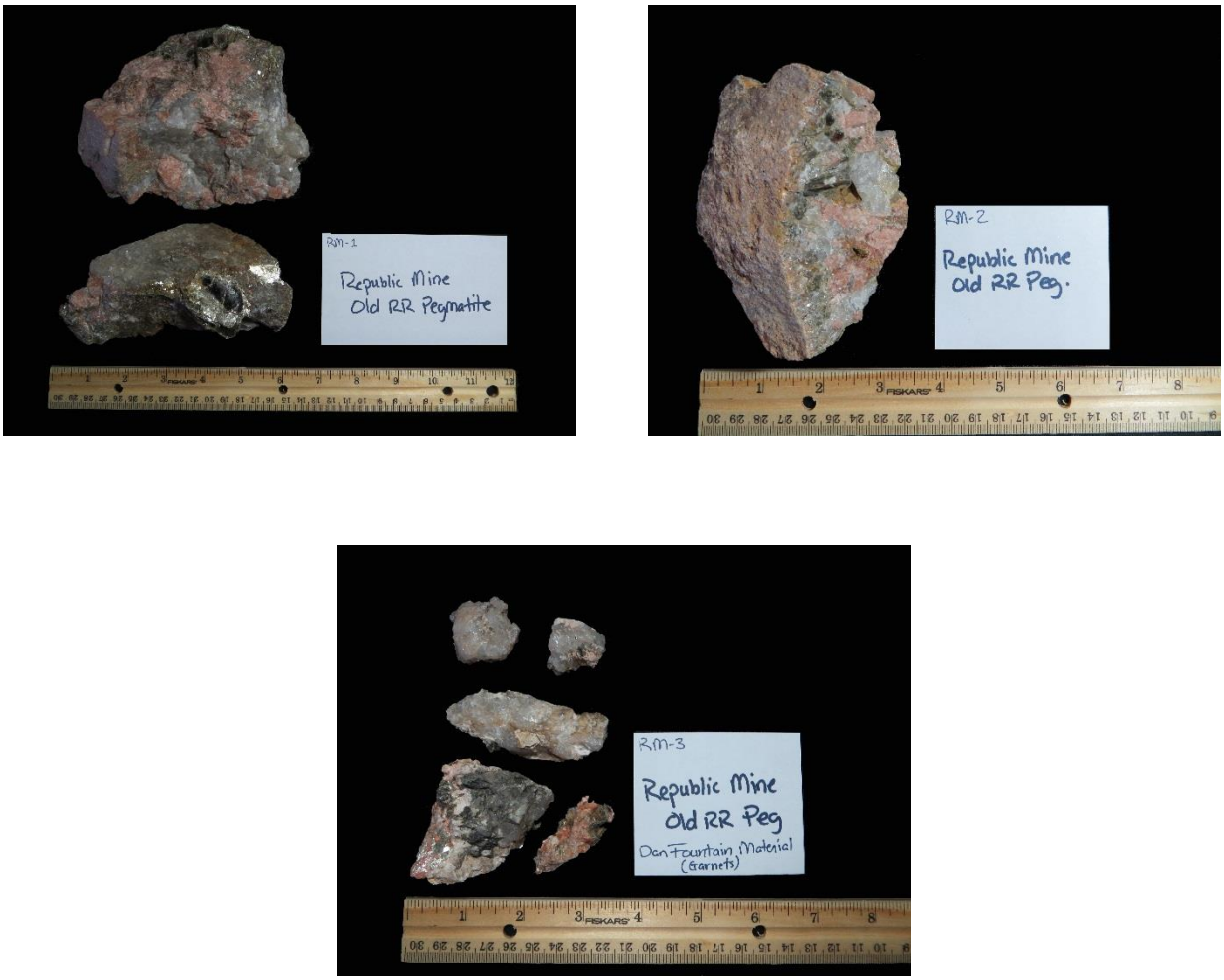


Figure 81 Representative pegmatite samples from the Republic Mine pegmatite.

Republic Mine samples have been provided by Dan Fountain. The Republic Mine pegmatite is the only pegmatite not personally visited. As can be seen in the above pictures, samples contain quartz, pink to orange hued feldspars, and mica. Very little to no literature exists for the Republic Mine pegmatite, but the Republic Mine itself is well known as it is the only open-pit mine in Michigan accessible to the public for free viewing. As such, the following minerals are the first qualitatively and quantitatively confirmed minerals identified from the Republic Mine pegmatite: Apatite, biotite, feldspar, garnet, ilmenite, "monazite", muscovite,

rutile, thalénite, tourmaline, and zircon have been qualitatively analyzed by SEM; Fe-biotite, K-feldspar and plagioclase feldspar, garnet, ilmenite, Ca-rich monazite, monazite-(Ce), muscovite mica, rutile, thalénite, fluorschorl, and zircon have all been quantitatively confirmed via microprobe analyses.

## APATITE

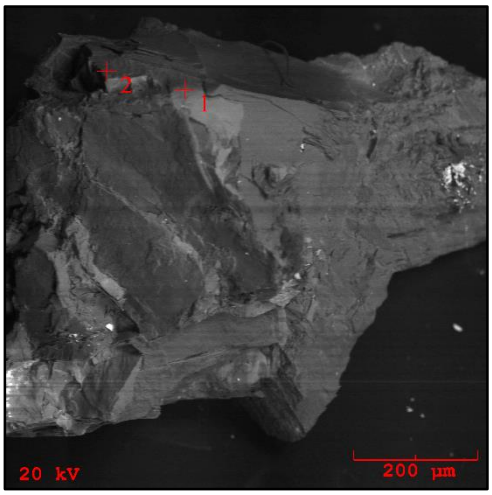


Figure 82 BSE image of apatite grain (1 & 2).

Only one grain of apatite has been identified from heavy mineral separations and qualitatively confirmed by SEM. Due to the apparent rarity of this mineral at the Republic Mine pegmatite, it is assumed that apatite is not an abundant accessory phosphate mineral. Unfortunately, the grain did not survive sample preparation. Efforts to identify additional grains for analysis have been unsuccessful.

## BIOTITE

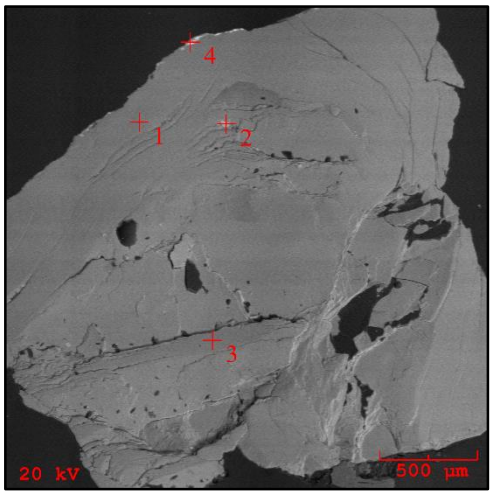


Figure 83 BSE image of polished muscovite grain (crosshairs 1 & 3) with biotite inclusions (crosshair 2) & rutile/ilmenite rim (crosshair 4).

Biotite mica is very rare in samples that have been collected from the Republic Mine pegmatite. No discrete grains have been identified. Only small inclusions of biotite mica are found in muscovite mica grains. Quantitative confirmation by microprobe dictates that biotite mica should be classified as Fe-biotite (Figure 186) (Tischendorf, 1997). Titration and DCP have not been performed due to lack of sufficient material with which to conduct these analyses on biotites. Lithium is calculated for Fe-biotite due to its presence in muscovite micas and has been accounted for stoichiometrically via the equation: 155 * wt% of $MgO^{-3.1}$ (Tischendorf, 1997). Rubidium is within detectable limits, but only just, suggesting that Fe-biotites are poorly evolved. It is important to note that the Republic Mine pegmatite biotite micas have high magnesium weight percent totals, suggestive of a more primitive character. Table 40 lists the representative analyses.

| **BIOTITE – REPUBLIC MINE PEGMATITE** | | |
|---|---|---|
| Wt % Ox. | RM-rr grain 2-2 | RM-rr grain 2-3 |
| $SiO_2$ | 34.322 | 34.412 |
| $TiO_2$ | 2.897 | 3.002 |
| $Al_2O_3$ | 17.009 | 16.985 |
| $Fe_2O_3$ | 0.000 | 0.000 |
| FeO | 23.443 | 23.488 |
| MnO | 0.254 | 0.237 |
| MgO | 7.978 | 8.004 |
| CaO | 0.276 | 0.241 |
| $Li_2O$ (*calc.*) | 0.248 | 0.246 |
| $Na_2O$ | 0.032 | 0.035 |
| $K_2O$ | 9.121 | 8.993 |
| $Rb_2O$ | 0.023 | 0.025 |
| $Cs_2O$ | *bdl* | *bdl* |
| F | 1.312 | 1.272 |
| $H_2O$ | 3.233 | 3.259 |
| F=O | - 0.552 | - 0.536 |
| **Total** | 99.596 | 99.662 |
| *apfu* | | |
| Si | 5.339 | 5.344 |
| $^{IV}Al$ | 2.661 | 2.656 |
| **Σ T-site** | 8.000 | 8.000 |
| $^{VI}Al$ | 0.457 | 0.452 |
| Ti | 0.339 | 0.351 |
| $Fe_t$ | 3.050 | 3.050 |
| Mn | 0.033 | 0.031 |
| Mg | 1.850 | 1.853 |
| Li (*calc.*) | 0.155 | 0.153 |
| **Σ Y-site** | 5.884 | 5.890 |

Table 34 Representative EMP biotite analyses. *Apfu* calculations based on 24 anions.
Table continues on next page.

| | | |
|---|---|---|
| K | 1.810 | 1.782 |
| Ca | 0.046 | 0.040 |
| Na | 0.010 | 0.011 |
| Rb | 0.002 | 0.002 |
| Cs | *bdl* | *bdl* |
| **Σ X-site** | 1.868 | 1.835 |
| F | 0.645 | 0.625 |
| OH* | 3.355 | 3.375 |
| **Σ W-site** | 4.000 | 4.000 |

## FELDSPARS

### K-FELDSPAR

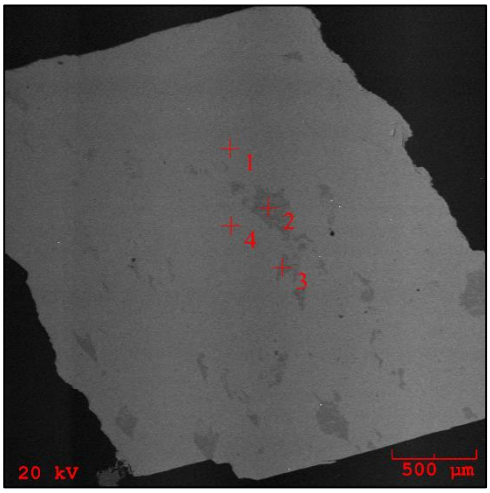


Figure 84 BSE image of polished K-feldspar grain (crosshairs 1 & 4). Darker areas of the grain are plagioclase feldspar (crosshairs 2 & 3).

K-feldspar has been identified in heavy mineral separations, qualitatively analyzed by SEM, and confirmed by microprobe. Feldspar grains are pink to dark red in hue. K-feldspar grains are almost entirely free of plagioclase. Blebs of a relatively sodium rich plagioclase are present, but these blebs are irregular both in shape and orientation. XRD analysis of K-feldspar reveal that a high degree of structural ordering (near maximum) exists suggesting that these grains should be classified as microcline (Figure 173) (Wright & Stewart, 1968). Rubidium, cesium, and barium are all below detection limits suggesting that K-feldspar from the Republic Mine are quite poorly evolved. Table 35 shows a representative list of analyses.

| K-FELDSPAR – REPUBLIC MINE PEGMATITE | | | | | | | | |
|---|---|---|---|---|---|---|---|---|
| Wt% ox | RM-rr Grain 1-1 | RM-rr Grain 1-2 | RM-rr Grain 2-1 | RM-rr Grain 2-2 | RM-rr Grain 3-1 | RM-rr Grain 3-3 | RM-rr Grain 4-1 | RM-rr Grain 4-2 |
| $P_2O_5$ | *bdl* | *bdl* | *bdl* | *bdl* | *bdl* | *bdl* | *bdl* | *bdl* |
| $SiO_2$ | 68.777 | 64.764 | 64.699 | 68.822 | 64.711 | 68.566 | 64.699 | 64.655 |
| $TiO_2$ | 0.000 | 0.013 | 0.009 | 0.000 | 0.021 | 0.000 | 0.009 | 0.013 |
| $Al_2O_3$ | 19.499 | 18.399 | 18.355 | 19.373 | 18.423 | 19.920 | 18.355 | 18.377 |
| $FeO_t$ | 0.000 | 0.009 | 0.008 | 0.000 | 0.009 | 0.000 | 0.008 | 0.013 |
| CaO | 0.231 | 0.000 | 0.000 | 0.211 | 0.000 | 1.366 | 0.000 | 0.000 |
| $Na_2O$ | 10.892 | 0.411 | 0.383 | 11.009 | 0.404 | 10.223 | 0.388 | 0.420 |
| $K_2O$ | 0.155 | 15.985 | 16.114 | 0.211 | 15.995 | 0.083 | 16.011 | 15.955 |
| $Rb_2O$ | 0.000 | 0.011 | 0.012 | 0.000 | 0.014 | 0.000 | 0.011 | 0.000 |
| **Total** | 99.554 | 99.592 | 99.580 | 99.626 | 99.577 | 100.158 | 99.481 | 99.433 |
| *apfu* | | | | | | | | |
| K | 0.009 | 0.945 | 0.953 | 0.012 | 0.946 | 0.005 | 0.948 | 0.944 |
| Na | 0.924 | 0.037 | 0.034 | 0.934 | 0.036 | 0.863 | 0.035 | 0.038 |
| Ca | 0.011 | 0.000 | 0.000 | 0.010 | 0.000 | 0.064 | 0.000 | 0.000 |
| Rb | 0.000 | 0.000 | 0.000 | 0.000 | 0.000 | 0.000 | 0.000 | 0.000 |
| **Σ X-site** | 0.944 | 0.982 | 0.987 | 0.956 | 0.982 | 0.932 | 0.983 | 0.982 |
| Al | 1.005 | 1.005 | 1.003 | 0.999 | 1.006 | 1.022 | 1.004 | 1.005 |
| Fe | 0.000 | 0.000 | 0.000 | 0.000 | 0.000 | 0.000 | 0.000 | 0.000 |
| **Σ Y-site** | 1.005 | 1.005 | 1.003 | 0.999 | 1.006 | 1.022 | 1.004 | 1.005 |
| Si | 3.008 | 3.000 | 3.000 | 3.010 | 2.999 | 2.985 | 3.001 | 3.000 |
| Ti | 0.000 | 0.000 | 0.000 | 0.000 | 0.001 | 0.000 | 0.000 | 0.000 |
| P | 0.000 | 0.000 | 0.000 | 0.000 | 0.000 | 0.000 | 0.000 | 0.000 |
| Al | 0.000 | 0.000 | 0.000 | 0.000 | 0.000 | 0.000 | 0.000 | 0.000 |
| **Σ Z-site** | 3.008 | 3.001 | 3.000 | 3.010 | 2.999 | 2.985 | 3.001 | 3.000 |

Table 35 Representative EMP analyses of K-feldspar. *Apfu* calculations based on 8 oxygens.

## PLAGIOCLASE FELDSPAR

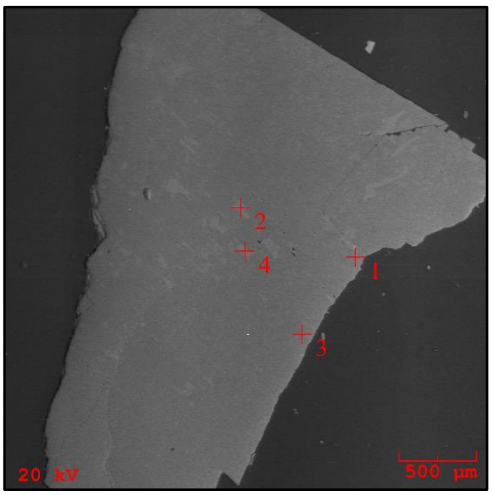


Figure 85 BSE image of polished plagioclase grain (crosshairs 1 & 3). Lighter areas of the grain are K-feldspar (crosshairs 2 & 4).

Plagioclase feldspar appears to be as equally abundant as K-feldspar. Blebs of K-feldspar are present in samples analyzed by SEM. These blebs are irregular in size and shape. As with K-feldspar from the Republic Mine, rubidium, cesium, and barium are below detection limits suggesting poor evolution. Table 36 lists the microprobe analyses.

| PLAGIOCLASE FELDSPAR – REPUBLIC MINE PEGMATITE | | | | | | | | | | |
|---|---|---|---|---|---|---|---|---|---|---|
| Wt% ox | RM-rr grain 5-1 | RM-rr grain 5-2 | RM-rr grain 6-1 | RM-rr grain 6-2 | RM-rr grain 7-1 | RM-rr grain 7-2 | RM-rr grain 8-1 | RM-rr grain 8-2 | RM-rr grain 9-1 | RM-rr grain 9-2 |
| $P_2O_5$ | *bdl* | *bdl* | *bdl* | *bdl* | *bdl* | *bdl* | *bdl* | *bdl* | *bdl* | *bdl* |
| $SiO_2$ | 64.700 | 68.811 | 64.755 | 68.844 | 68.799 | 64.788 | 68.733 | 64.699 | 68.555 | 64.722 |
| $TiO_2$ | 0.008 | 0.000 | 0.011 | 0.000 | 0.000 | 0.009 | 0.000 | 0.009 | 0.000 | 0.012 |
| $Al_2O_3$ | 18.433 | 19.393 | 18.455 | 19.355 | 19.377 | 18.500 | 19.992 | 18.511 | 19.988 | 18.489 |
| $FeO_t$ | 0.027 | 0.000 | 0.011 | 0.000 | 0.000 | 0.011 | 0.000 | 0.009 | 0.000 | 0.012 |
| CaO | 0.000 | 0.178 | 0.000 | 0.156 | 0.201 | 0.000 | 1.411 | 0.000 | 1.411 | 0.000 |
| $Na_2O$ | 0.334 | 10.911 | 0.355 | 11.004 | 10.811 | 0.393 | 10.091 | 0.355 | 10.071 | 0.324 |
| $K_2O$ | 15.975 | 0.211 | 15.885 | 0.195 | 0.155 | 15.755 | 0.071 | 15.710 | 0.089 | 15.686 |
| $Rb_2O$ | 0.000 | 0.000 | 0.012 | 0.000 | 0.000 | 0.013 | 0.000 | 0.012 | 0.000 | 0.010 |
| **Total** | 99.477 | 99.504 | 99.484 | 99.554 | 99.343 | 99.469 | 100.298 | 99.305 | 100.114 | 99.255 |
| *apfu* | | | | | | | | | | |
| K | 0.945 | 0.012 | 0.939 | 0.011 | 0.009 | 0.931 | 0.004 | 0.929 | 0.005 | 0.928 |
| Na | 0.030 | 0.926 | 0.032 | 0.933 | 0.918 | 0.035 | 0.850 | 0.032 | 0.850 | 0.029 |
| Ca | 0.000 | 0.008 | 0.000 | 0.007 | 0.009 | 0.000 | 0.066 | 0.000 | 0.066 | 0.000 |
| Rb | 0.000 | 0.000 | 0.000 | 0.000 | 0.000 | 0.000 | 0.000 | 0.000 | 0.000 | 0.000 |
| **Σ X-site** | 0.975 | 0.946 | 0.971 | 0.952 | 0.936 | 0.967 | 0.920 | 0.962 | 0.921 | 0.958 |
| Al | 1.007 | 1.000 | 1.008 | 0.998 | 1.000 | 1.010 | 1.024 | 1.012 | 1.026 | 1.011 |
| Fe | 0.000 | 0.000 | 0.000 | 0.000 | 0.000 | 0.000 | 0.000 | 0.000 | 0.000 | 0.000 |
| **Σ Y-site** | 1.007 | 1.000 | 1.008 | 0.998 | 1.000 | 1.010 | 1.024 | 1.012 | 1.026 | 1.011 |
| Si | 3.000 | 3.011 | 3.001 | 3.012 | 3.013 | 3.000 | 2.986 | 3.000 | 2.984 | 3.002 |
| Ti | 0.000 | 0.000 | 0.000 | 0.000 | 0.000 | 0.000 | 0.000 | 0.000 | 0.000 | 0.000 |
| P | 0.000 | 0.000 | 0.000 | 0.000 | 0.000 | 0.000 | 0.000 | 0.000 | 0.000 | 0.000 |
| Al | 0.000 | 0.000 | 0.000 | 0.000 | 0.000 | 0.000 | 0.000 | 0.000 | 0.000 | 0.000 |
| **Σ Z-site** | 3.000 | 3.011 | 3.001 | 3.012 | 3.013 | 3.000 | 2.986 | 3.000 | 2.984 | 3.002 |

Table 36 Representative EMP analyses of plagioclase (albite). *Apfu* calculations based on 8 oxygens.

## GARNET

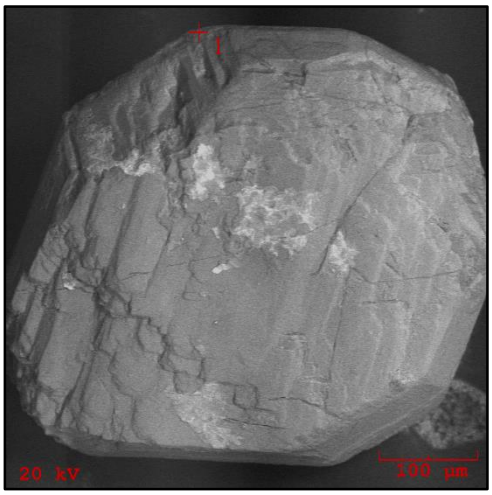


Figure 86 BSE of garnet grain.

Garnet has been identified in heavy mineral separations, investigated by SEM, and confirmed by microprobe analysis. Garnets contain a considerable spessartine component of almost half the total, with almandine comprising most of the remainder. Pyrope and andradite are negligible and the grossular component is below one percent. Grains are euhedral to subhedral and rarely anhedral. Despite having crystal faces, a number of grains appear to have been altered or infilled along fractures. It is suggested that this represents a secondary mineralization that has occurred during infilling or alteration of the original garnet grain. Micas present within some fractures have been qualitatively analyzed by SEM and appear to be muscovite. Other fractures are filled with possible chlorite, as garnet can readily alter to chlorite given appropriate conditions. This supposed chlorite mineralization is depleted in potassium and manganese and relatively more enriched in iron and magnesium. On closer inspection by SEM, fractures also contain inclusions of silicon, yttrium, calcium, and iron as well as possible lutetium. The width of this mineralization prevented microprobe analysis. In a few instances,

garnet seems to have been almost completely altered and only remnant 'islands' remain. Table 37 lists the representative garnet analyses. Components have been normalized.

| **GARNETS – REPUBLIC MINE PEGMATITE** | | | | | | |
|---|---|---|---|---|---|---|
| Wt % Ox | Goi 2 grain 1-1 | Goi 2 grain 1-2 | Goi 2 grain 3-1 | Goi 2 grain 5-1 | Goi 2 grain 6-1 | Goi 2 grain 7-2 |
| $SiO_2$ | 36.807 | 36.722 | 36.556 | 36.587 | 36.565 | 36.433 |
| $TiO_2$ | 0.022 | 0.016 | 0.011 | 0.032 | 0.011 | 0.009 |
| $Al_2O_3$ | 20.091 | 20.100 | 19.977 | 20.088 | 20.232 | 20.400 |
| FeO | 21.871 | 22.012 | 22.223 | 21.981 | 22.143 | 22.092 |
| MnO | 21.113 | 21.211 | 21.004 | 21.334 | 21.144 | 21.223 |
| MgO | 0.191 | 0.200 | 0.189 | 0.211 | 0.156 | 0.109 |
| CaO | 0.123 | 0.181 | 0.234 | 0.212 | 0.232 | 0.300 |
| **Total** | 100.248 | 100.489 | 100.255 | 100.503 | 100.528 | 100.606 |
| *apfu* | | | | | | |
| Ti | 0.001 | 0.001 | 0.001 | 0.002 | 0.001 | 0.001 |
| Fe | 1.506 | 1.514 | 1.534 | 1.514 | 1.524 | 1.520 |
| Mn | 1.472 | 1.478 | 1.469 | 1.488 | 1.474 | 1.479 |
| Mg | 0.023 | 0.025 | 0.023 | 0.026 | 0.019 | 0.013 |
| Ca | 0.011 | 0.016 | 0.021 | 0.019 | 0.020 | 0.026 |
| **Σ X-site** | 3.003 | 3.034 | 3.048 | 3.049 | 3.056 | 3.039 |
| Al | 1.950 | 1.949 | 1.944 | 1.950 | 1.962 | 1.978 |
| **Σ Y-site** | 1.950 | 1.949 | 1.944 | 1.950 | 1.962 | 1.978 |
| Si | 3.030 | 3.021 | 3.018 | 3.013 | 3.009 | 2.997 |
| **Σ Z-site** | 3.030 | 3.021 | 3.018 | 3.013 | 3.009 | 2.997 |
| **Component** | | | | | | |
| Andradite | 00 | 01 | 01 | 01 | 01 | 01 |
| Pyrope | 01 | 01 | 01 | 01 | 01 | 01 |
| Spessartine | 50 | 50 | 50 | 50 | 49 | 49 |
| Almandine | 49 | 48 | 48 | 48 | 49 | 49 |

Table 37 Representative EMP analyses of garnet. *Apfu* calculations based on 12 oxygens.

## ILMENITE

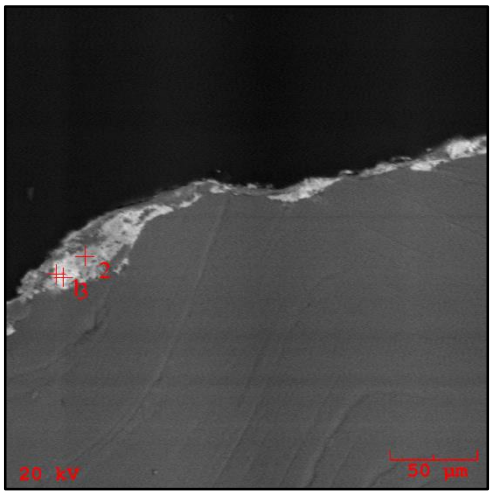


Figure 87 BSE image of ilmenite rim (crosshairs 1 & 3) & rutile (crosshair 2) on mica.

Ilmenite has only been found as a rim on one mica grain. Discrete grains have not been found. Table 38 lists the analysis. Stoichiometry has been calculated based on six oxygens and being that the X-site is less than two and the Y-site is more than two, there is perhaps the possibility that the rim of ilmenite is a product of alteration or represents a solid solution series and does not represent pure ilmenite.

| **ILMENITE – REPUBLIC MINE PEGMATITE** | |
|---|---|
| Wt% Oxide | RM-rr grain 2-4 |
| $TiO_2$ | 60.987 |
| $Al_2O_3$ | 0.121 |
| $SiO_2$ | 0.055 |
| FeO | 34.098 |
| MnO | 0.233 |
| MgO | 0.433 |
| CaO | 0.112 |
| $Nb_2O_5$ | 0.212 |
| $Ta_2O_5$ | *bdl* |
| **Total** | 96.251 |
| *apfu* | |
| FeO | 1.405 |
| MnO | 0.008 |
| MgO | 0.032 |
| CaO | 0.006 |
| Nb | 0.005 |
| Ta | *bdl* |
| **Σ X-site** | 1.456 |
| Ti | 2.261 |
| Al | 0.007 |
| Si | 0.003 |
| **Σ Y-site** | 2.271 |

Table 38 Representative EMP analysis of ilmenite. *Apfu* calculations based on 6 oxygens.

## "MONAZITE"

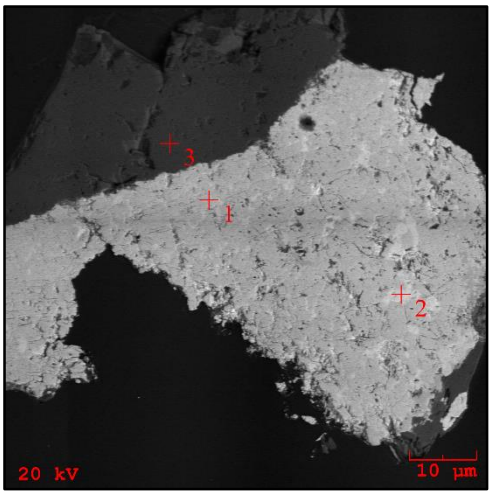


Figure 88 BSE image of polished "monazite" (crosshair 1) and possible Ca-rich monazite (crosshair 2) and quartz (crosshair 3).

"Monazite" has been investigated by SEM and confirmed by microprobe. Only one grain seems to have homogeneous texture and mineralogy. Of the grains analyzed, one "monazite" grain appears to be an overgrowth on a Ca-rich monazite grain as previously discussed. Grain RM-rr 15 appears to be altered in some way and contains thorium- and uranium-rich inclusions. Cerium is the dominant REE in all samples as it represents almost half of the X-site cation occupancy. It follows then that these grains should be classified as monazite-(Ce). Weight percent totals are in excess of 98% with the exception of RM-rr 15, which has a weight percent of ~ 97.5%. Table 39 lists the representative EMP analyses.

| MONAZITE-(CE) – REPUBLIC MINE PEGMATITE | | | |
|---|---|---|---|
| Wt % Ox. | 13-RM-rr-2 | 14-RM-rr-1 | 15-RM-rr-1 |
| $P_2O_5$ | 29.002 | 28.773 | 28.445 |
| $SiO_2$ | 0.344 | 0.121 | 0.084 |
| $TiO_2$ | 0.000 | 0.000 | 0.000 |
| $ThO_2$ | 6.445 | 6.733 | 4.112 |
| $UO_2$ | 0.623 | 0.556 | 0.455 |
| $Al_2O_3$ | 0.033 | 0.078 | 0.112 |
| $La_2O_3$ | 12.223 | 11.091 | 11.760 |
| $Ce_2O_3$ | 27.093 | 28.223 | 28.780 |
| $Pr_2O_3$ | 3.002 | 2.550 | 2.458 |
| $Nd_2O_3$ | 13.893 | 13.112 | 13.433 |
| $Sm_2O_3$ | 1.445 | 1.788 | 1.883 |
| $Eu_2O_3$ | 0.009 | 0.021 | 0.015 |
| $Gd_2O_3$ | 0.522 | 0.677 | 0.700 |
| $Dy_2O_3$ | 0.181 | 0.211 | 0.199 |
| Er2O3 | 0.000 | 0.012 | 0.022 |
| $Yb_2O_3$ | 0.021 | 0.019 | 0.031 |
| $Y_2O_3$ | 0.543 | 0.932 | 0.892 |
| $Sc_2O_3$ | 0.030 | 0.000 | 0.000 |
| CaO | 2.223 | 3.443 | 3.622 |
| MnO | 0.044 | 0.011 | 0.002 |
| FeO | 0.345 | 0.277 | 0.311 |
| PbO | 0.224 | 0.165 | 0.145 |
| **Total** | 98.245 | 98.793 | 97.461 |
| *apfu* | | | |
| Th | 0.058 | 0.061 | 0.037 |
| U | 0.006 | 0.005 | 0.004 |
| Al | 0.002 | 0.004 | 0.005 |
| La | 0.180 | 0.162 | 0.174 |
| Ce | 0.395 | 0.410 | 0.422 |
| Pr | 0.044 | 0.037 | 0.036 |
| Nd | 0.198 | 0.186 | 0.192 |
| Sm | 0.020 | 0.024 | 0.026 |
| Eu | 0.000 | 0.000 | 0.000 |
| Gd | 0.007 | 0.009 | 0.009 |
| Dy | 0.002 | 0.003 | 0.003 |
| Y | 0.012 | 0.020 | 0.019 |
| Sc | 0.001 | 0.000 | 0.000 |
| Ca | 0.095 | 0.146 | 0.155 |
| Mn | 0.001 | 0.000 | 0.000 |
| Fe | 0.011 | 0.009 | 0.010 |
| Pb | 0.002 | 0.002 | 0.002 |
| **Σ X** | 1.034 | 1.079 | 1.096 |
| P | 0.978 | 0.967 | 0.965 |
| Si | 0.014 | 0.005 | 0.003 |
| **Σ Y** | 0.992 | 0.972 | 0.968 |

Table 39 Representative EMP analyses of monazite-(Ce). *Apfu* calculations based on 4 oxygens.

## CA-RICH MONAZITE

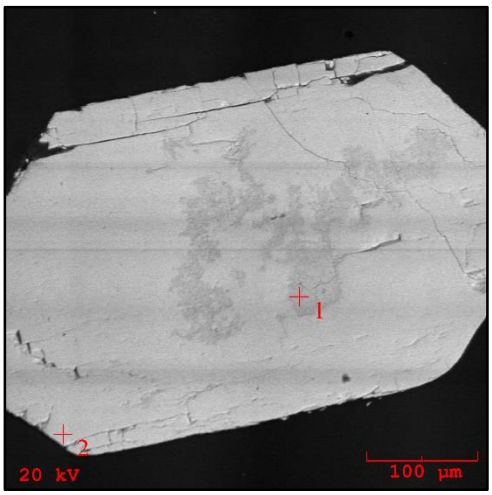


Figure 89 BSE image of polished grain of monazite (crosshair 2) with Ca-rich monazite core (crosshair 1).

What appears to be a core of Ca-rich monazite within a grain of monazite-(Ce) has been identified by SEM and confirmed by microprobe analysis. Table 40 shows the analysis. Weight percent totals are almost 100% which suggests that little or no alteration has occurred.

| **CA-RICH MONAZITE - CROCKLEY** | |
|---|---|
| Wt % Ox. | 13-RM-rr-1 |
| $P_2O_5$ | 26.200 |
| $SiO_2$ | 0.456 |
| $ThO_2$ | 0.000 |
| $UO_2$ | 34.894 |
| $Al_2O_3$ | 2.112 |
| $La_2O_3$ | 0.043 |
| $Ce_2O_3$ | 5.895 |
| $Pr_2O_3$ | 12.655 |
| $Nd_2O_3$ | 1.221 |
| $Sm_2O_3$ | 6.223 |
| $Gd_2O_3$ | 0.655 |
| $Dy_2O_3$ | 0.011 |
| $Yb_2O_3$ | 0.065 |
| $Y_2O_3$ | 0.633 |
| CaO | 7.223 |
| MnO | 0.020 |
| FeO | 0.211 |
| PbO | 0.788 |
| **Total** | 99.580 |
| *apfu* | |
| Th | 0.329 |
| U | 0.019 |
| Al | 0.002 |
| La | 0.090 |
| Ce | 0.192 |
| Pr | 0.018 |
| Nd | 0.092 |
| Sm | 0.009 |
| Y | 0.014 |
| Mn | 0.001 |
| Fe | 0.007 |
| Ca | 0.320 |
| Pb | 0.009 |
| **Σ X - Site** | 1.108 |
| P | 0.918 |
| Si | 0.019 |
| **Σ Y - Site** | 0.937 |

Table 40 Representative EMP analysis of Ca-rich monazite.
*Apfu* calculations based on 4 oxygens.

## MUSCOVITE

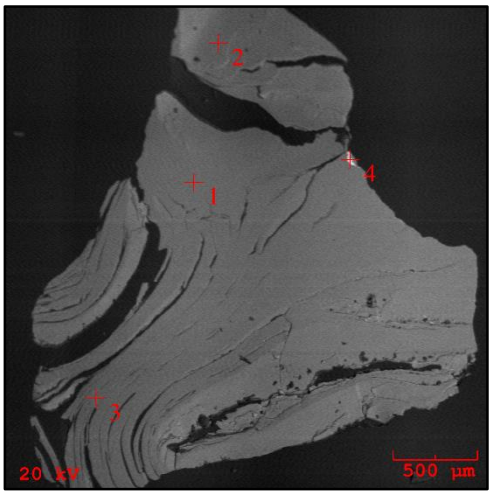


Figure 90 BSE image of polished muscovite grain (crosshairs 1, 2, & 3) and zircon (crosshair 4).

Muscovite mica is much more abundant than biotite mica in samples collected from the Republic Mine pegmatite. It has been identified in heavy mineral separations, qualitatively investigated by SEM, and confirmed by microprobe analysis (Figure 185). Muscovite mica has also been analyzed by DCP and titration for lithium and trivalent iron respectively. The dioctahedral equation specific to fluorine content is used to calculate the weight percent of lithium in muscovite samples owing to the presence of lithium from DCP analyses: 0.3935 * fluorine weight percent$^{1.326}$ (Tischendorf, 1997). Two analyses of muscovite mica reveal lithium content as 0.312 and 0.502 weight percent. The latter value is much closer to calculated values. Titration analysis has yielded a FeO weight percent value of 4.028, greater than results from microprobe analyses. It is assumed then that trivalent iron in muscovite mica is absent or well below detection limits. Cesium is below detection limits and rubidium is just within detection limits suggesting that muscovite mica from Republic Mine pegmatite are poorly evolved. Table 41 lists the representative EMP analyses. Additional analyses listed in appendices (Table 88).

| **MUSCOVITE – REPUBLIC MINE PEGMATITE** | | | | | | |
|---|---|---|---|---|---|---|
| Wt % Ox. | RM-rr grain 1-1 | RM-rr grain 2-1 | RM-rr grain 3-1 | RM-rr set 1 grain 1-1 | RM-rr set 1 grain 2-1 | RM-rr set 2 grain 1-2 |
| $SiO_2$ | 46.576 | 46.484 | 46.444 | 45.977 | 45.799 | 45.782 |
| $TiO_2$ | 0.233 | 0.188 | 0.244 | 0.112 | 0.099 | 0.088 |
| $Al_2O_3$ | 34.644 | 34.631 | 34.686 | 35.321 | 35.623 | 35.770 |
| $Fe_2O_3$ | 0.000 | 0.000 | 0.000 | 0.000 | 0.000 | 0.000 |
| FeO | 2.211 | 2.343 | 2.890 | 2.711 | 2.723 | 2.556 |
| MnO | 0.034 | 0.027 | 0.021 | 0.022 | 0.020 | 0.014 |
| MgO | 0.899 | 0.862 | 0.455 | 0.333 | 0.288 | 0.233 |
| CaO | 0.022 | 0.018 | 0.034 | 0.454 | 0.223 | 0.312 |
| $Li_2O$ (*calc.*) | 0.582 | 0.547 | 0.513 | 0.575 | 0.491 | 0.557 |
| $Na_2O$ | 0.777 | 0.833 | 0.654 | 0.785 | 0.774 | 0.656 |
| $K_2O$ | 10.007 | 9.881 | 9.944 | 10.022 | 10.044 | 10.066 |
| $Rb_2O$ | 0.033 | 0.017 | 0.022 | 0.031 | 0.023 | 0.026 |
| $Cs_2O$ | *bdl* | *bdl* | *bdl* | *bdl* | *bdl* | *bdl* |
| F | 1.344 | 1.282 | 1.221 | 1.332 | 1.181 | 1.300 |
| $H_2O$ | 3.896 | 3.916 | 3.939 | 3.897 | 3.960 | 3.907 |
| F=O | - 0.566 | - 0.540 | - 0.514 | - 0.561 | - 0.497 | - 0.547 |
| **Total** | 100.692 | 100.489 | 100.552 | 101.012 | 100.751 | 100.720 |
| *apfu* | | | | | | |
| Si | 6.161 | 6.161 | 6.165 | 6.087 | 6.076 | 6.069 |
| $^{IV}Al$ | 1.839 | 1.839 | 1.835 | 1.913 | 1.924 | 1.931 |
| **Σ T-site** | 8.000 | 8.000 | 8.000 | 8.000 | 8.000 | 8.000 |
| $^{VI}Al$ | 3.563 | 3.571 | 3.591 | 3.600 | 3.645 | 3.658 |
| Ti | 0.023 | 0.019 | 0.024 | 0.011 | 0.010 | 0.009 |
| $Fe_t$ | 0.245 | 0.260 | 0.321 | 0.300 | 0.302 | 0.283 |
| Mn | 0.004 | 0.003 | 0.002 | 0.002 | 0.002 | 0.002 |
| Mg | 0.177 | 0.170 | 0.090 | 0.066 | 0.057 | 0.046 |
| Li (*calc.*) | 0.310 | 0.292 | 0.274 | 0.307 | 0.262 | 0.297 |
| **Σ Y-site** | 4.322 | 4.315 | 4.302 | 4.286 | 4.278 | 4.295 |

Table 41 Representative EMP analyses of muscovite mica. *Apfu* calculations based on 24 anions.
Table continues on next page.

| | | | | | | |
|---|---|---|---|---|---|---|
| K | 1.689 | 1.671 | 1.684 | 1.693 | 1.700 | 1.702 |
| Ca | 0.003 | 0.003 | 0.005 | 0.064 | 0.032 | 0.044 |
| Na | 0.199 | 0.214 | 0.168 | 0.202 | 0.199 | 0.169 |
| Rb | 0.003 | 0.001 | 0.002 | 0.003 | 0.002 | 0.002 |
| Cs | *bdl* | *bdl* | *bdl* | *bdl* | *bdl* | *bdl* |
| **Σ X-site** | 1.894 | 1.889 | 1.859 | 1.962 | 1.933 | 1.918 |
| F | 0.562 | 0.537 | 0.513 | 0.558 | 0.495 | 0.545 |
| OH (*calc.*) | 3.438 | 3.463 | 3.487 | 3.442 | 3.505 | 3.455 |
| **Σ W-site** | 4.000 | 4.000 | 4.000 | 4.000 | 4.000 | 4.000 |

## RUTILE

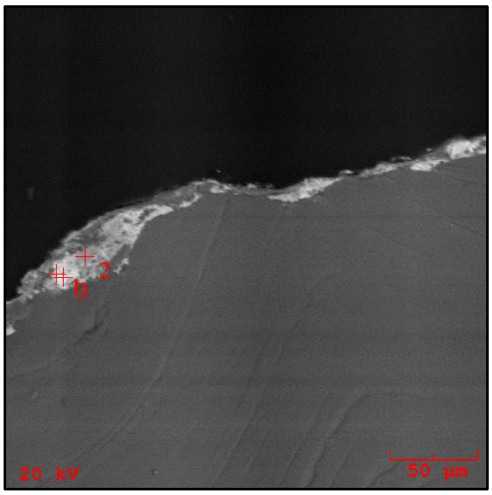


Figure 91 BSE image of rutile rim on mica grain (crosshair 2) and ilmenite (crosshairs 1 & 3).

Rutile has been discovered along with ilmenite on a single grain of mica. No discrete grains have been found. Niobium and tantalum are both below detection limits. Table 42 lists the representative microprobe analyses.

| **RUTILE – REPUBLIC MINE PEGMATITE** | |
|---|---|
| Wt% Oxide | RM-rr grain 2-5 |
| $TiO_2$ | 98.770 |
| $Al_2O3$ | 0.032 |
| FeO | 0.881 |
| MnO | 0.011 |
| MgO | 0.014 |
| CaO | 0.009 |
| $SiO_2$ | 0.012 |
| **Total** | 99.729 |
| *apfu* | |
| Ti | 0.994 |
| Al | 0.001 |
| Fe | 0.010 |
| Mn | 0.000 |
| Mg | 0.000 |
| Ca | 0.000 |
| Si | 0.000 |
| **Σ X-site** | 1.005 |

Table 42 Representative EMP analysis of rutile. *Apfu* calculations based on 2 oxygens.

## THALÉNITE

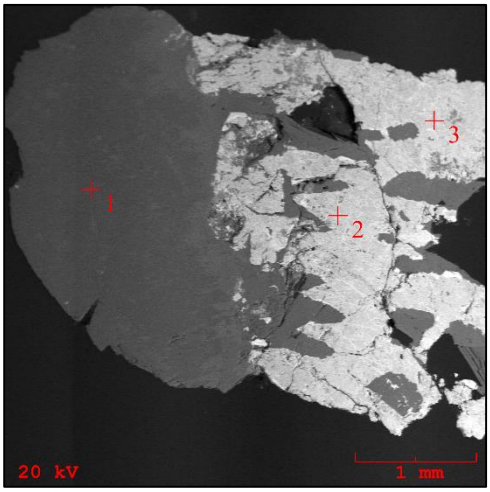


Figure 92 BSE image of thalénite (crosshairs 2 & 3) and feldspar (crosshair 1).

Thalénite is relatively common in Republic Mine heavy mineral separations. Thalénite has been quantitatively confirmed by microprobe. Weight percent totals are almost 100%, which suggests that no alteration of the grain has occurred. Yttrium is the dominant cation in the A-site and therefore classification is thalénite-(Y). This is the first confirmed occurrence of thalénite-(Y) at the Republic Mine pegmatite and the first confirmed occurrence of thalénite-(Y) in the state of Michigan. Table 43 lists the representative analysis.

| **THALÉNITE-(Y) – REPUBLIC MINE PEGMATITE** | |
|---|---|
| Wt % Ox. | Rm-rr GOI |
| $P_2O_5$ | 0.055 |
| $SiO_2$ | 32.115 |
| $TiO_2$ | 0.211 |
| $ThO_2$ | 0.285 |
| $UO_2$ | 0.015 |
| $Al_2O_3$ | 0.893 |
| $La_2O_3$ | 0.022 |
| $Ce_2O_3$ | 0.154 |
| $Nd_2O_3$ | 0.021 |
| $Gd_2O_3$ | 0.484 |
| $Tb_2O_3$ | 0.300 |
| $Dy_2O_3$ | 1.967 |
| $Ho_2O_3$ | 1.145 |
| $Er_2O_3$ | 4.650 |
| $Tm_2O_3$ | 1.810 |
| $Yb_2O_3$ | 7.676 |
| $Lu_2O_3$ | 0.500 |
| $Y_2O_3$ | 42.433 |
| MgO | 0.020 |
| CaO | 2.165 |
| MnO | 0.676 |
| FeO | 0.733 |
| PbO | 0.021 |
| F | 0.000 |
| $H_2O$ | 1.607 |
| **Total** | 99.958 |
| *apfu* | |
| Ti | 0.015 |
| Th | 0.006 |
| U | 0.000 |
| Al | 0.098 |
| La | 0.001 |
| Ce | 0.005 |
| Nd | 0.001 |
| Gd | 0.015 |
| Tb | 0.009 |
| Dy | 0.059 |
| Ho | 0.034 |
| Er | 0.136 |
| Tm | 0.053 |
| Yb | 0.218 |
| Lu | 0.014 |
| Y | 2.107 |
| Mg | 0.003 |
| Ca | 0.216 |
| Mn | 0.053 |
| Fe | 0.057 |
| Pb | 0.001 |
| **Σ A** | 2.989 |
| P | 0.004 |
| Si | 2.996 |
| **Σ B** | 3.000 |
| OH | 1.000 |
| **Σ C** | 1.000 |

Table 43 Representative EMP analysis of thalénite. *Apfu* calculations based on 11 anions.

## TOURMALINE

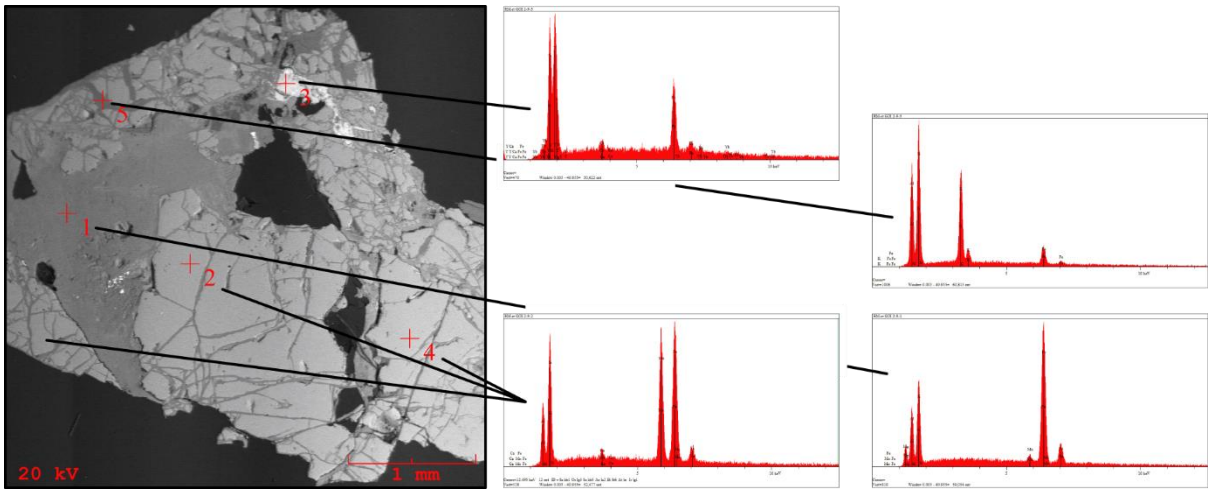


Figure 93 BSE image of polished tourmaline mount and associated EDS spectra.

Tourmaline has been identified in heavy mineral separations by SEM and confirmed by microprobe. Republic Mine tourmalines belong to the alkali group based on X-site dominance (Figure 193). There are apparently two groups of tourmaline found at the Republic Mine pegmatite. The first group owing to there being more sodium, negligible calcium, and fewer vacancies as opposed to the second group of tourmalines having relatively less sodium enrichment and relatively more calcium enrichment and vacancies in the X-site. Y-site dominance determines that both groups of tourmalines are schorl (Figure 194), although there is a trend showing progressive depletion in magnesium and relatively greater enrichment in calculated lithium and iron. Fluorine is dominant over the hydroxyl ion so that all tourmaline analyzed should be classified as fluor-schorl (Figure 195). It should be noted that sodium *apfu* between the two groups ranges by only a couple of tenths. Grains are, for all intents and purposes, geochemically homogeneous. Table 44 lists the representative EMP analyses. Additional analyses are listed in Table 89 of the appendices.

| TOURMALINE – REPUBLIC MINE PEGMATITE | | | | | | |
|---|---|---|---|---|---|---|
| Wt.% Oxide | grain 4-1 | grain 1-1 | grain 3-1 | grain 7-1 | grain 9-1 | grain 10-1 |
| $SiO_2$ | 36.282 | 36.201 | 36.300 | 36.255 | 36.321 | 36.255 |
| $TiO_2$ | 0.092 | 0.144 | 0.0177 | 0.113 | 0.143 | 0.126 |
| $Al_2O_3$ | 30.223 | 29.892 | 29.882 | 30.033 | 29.882 | 29.544 |
| $B_2O_3$ (*calc*.) | 10.330 | 10.330 | 10.350 | 10.310 | 10.350 | 10.330 |
| FeOt | 13.565 | 13.334 | 13.221 | 13.400 | 13.223 | 13.245 |
| MnO | 0.223 | 0.422 | 0.446 | 0.299 | 0.443 | 0.383 |
| MgO | 3.334 | 4.093 | 4.223 | 3.783 | 4.223 | 4.678 |
| CaO | 0.033 | 0.020 | 0.544 | 0.223 | 0.312 | 0.255 |
| $Na_2O$ | 2.334 | 2.334 | 1.871 | 1.912 | 1.871 | 1.981 |
| $K_2O$ | 0.020 | 0.030 | 0.034 | 0.021 | 0.030 | 0.021 |
| $Li_2O$ (*calc*.) | 0.320 | 0.140 | 0.160 | 0.210 | 0.130 | 0.050 |
| $H_2O$ (*calc*.) | 3.040 | 3.030 | 3.040 | 2.990 | 3.030 | 3.090 |
| F | 1.112 | 1.119 | 1.114 | 1.200 | 1.134 | 1.009 |
| F=O | - 0.470 | - 0.470 | - 0.470 | - 0.510 | - 0.480 | - 0.420 |
| **Total** | 100.44 | 100.62 | 100.74 | 100.24 | 100.61 | 100.54 |
| *apfu* | | | | | | |
| Na | 0.762 | 0.761 | 0.609 | 0.625 | 0.609 | 0.646 |
| Ca | 0.006 | 0.004 | 0.098 | 0.040 | 0.056 | 0.046 |
| K | 0.004 | 0.006 | 0.007 | 0.005 | 0.006 | 0.005 |
| Vac (*calc*.) | 0.228 | 0.229 | 0.286 | 0.331 | 0.328 | 0.303 |
| **Σ X-site** | 1.000 | 1.000 | 1.000 | 1.000 | 1.000 | 1.000 |
| Fe | 1.909 | 1.876 | 1.856 | 1.888 | 1.858 | 1.864 |
| Mg | 0.830 | 0.952 | 0.970 | 0.915 | 0.974 | 1.032 |
| Al | 0.000 | 0.000 | 0.000 | 0.000 | 0.000 | 0.000 |
| Mn | 0.032 | 0.060 | 0.063 | 0.043 | 0.063 | 0.055 |
| Li (*calc*.) | 0.217 | 0.094 | 0.108 | 0.140 | 0.087 | 0.034 |
| Ti | 0.012 | 0.018 | 0.002 | 0.014 | 0.018 | 0.016 |
| **Σ Y-site** | 3.000 | 3.000 | 3.000 | 3.000 | 3.000 | 3.000 |
| Al | 5.994 | 5.926 | 5.913 | 5.965 | 5.916 | 5.859 |
| Mg | 0.006 | 0.074 | 0.087 | 0.035 | 0.084 | 0.141 |
| **Σ Z-site** | 6.000 | 6.000 | 6.000 | 6.000 | 6.000 | 6.000 |
| Si | 6.106 | 6.089 | 6.095 | 6.109 | 6.102 | 6.100 |
| Al | 0.000 | 0.000 | 0.000 | 0.000 | 0.000 | 0.000 |
| **Σ T-site** | 6.106 | 6.089 | 6.095 | 6.109 | 6.102 | 6.100 |
| B (*calc*.) | 3.000 | 3.000 | 3.000 | 3.000 | 3.000 | 3.000 |
| H (*calc*.) | 3.408 | 3.405 | 3.408 | 3.360 | 3.398 | 3.463 |
| F | 0.592 | 0.595 | 0.592 | 0.640 | 0.602 | 0.537 |
| **Σ W+V sites** | 4.000 | 4.000 | 4.000 | 4.000 | 4.000 | 4.000 |
| | | | | | | |
| **Species** | *fluor-schorl* | *fluor-schorl* | *fluor-schorl* | *fluor-schorl* | *fluor-schorl* | *fluor-schorl* |

Table 44 Representative EMP analyses of fluorschorl. *Apfu* calculations based on 31 anions.

## ZIRCON

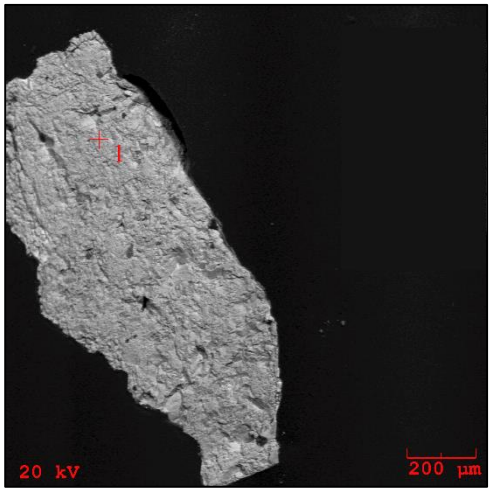


Figure 94 BSE image of polished zircon grain.

Zircon has been qualitatively investigated and confirmed by microprobe. Of the grains analyzed, only two are assumed to be unaltered. The range in total weight percent for altered grains ranges from approximately 93% to 95%. Hafnium content is less than one weight percent for altered grains and ranges from 1.4 to 1.7 weight percent for unaltered grains. Zircon from the Republic Mine pegmatite are considered to be relatively poorly evolved. Table 45 lists the representative analyses for both altered and unaltered grains. Additional analyses are listed in Table 90 of the appendices.

| ZIRCON – REPUBLIC MINE PEGMATITE | | | | | | |
|---|---|---|---|---|---|---|
| Wt % Oxide | grain 1-3 Mica Incl | | grain 8-RM-rr-1 | | grain 9-RM-rr-1 | |
| $SiO_2$ | 34.132 | 33.993 | 30.110 | 29.882 | 28.800 | 29.131 |
| $TiO_2$ | 0.011 | 0.009 | 0.020 | 0.013 | 0.009 | 0.014 |
| $Al_2O_3$ | 0.322 | 0.282 | 0.121 | 0.081 | 0.100 | 0.089 |
| $ZrO_2$ | 62.500 | 62.750 | 58.760 | 57.986 | 58.000 | 57.923 |
| $HfO_2$ | 1.455 | 1.476 | 0.892 | 0.800 | 0.910 | 0.961 |
| FeOt | 0.444 | 0.383 | 3.560 | 3.780 | 3.450 | 3.600 |
| MnO | 0.011 | 0.013 | 0.200 | 0.112 | 0.088 | 0.070 |
| MgO | 0.000 | 0.000 | 0.000 | 0.011 | 0.000 | 0.000 |
| CaO | 0.788 | 0.800 | 0.343 | 0.282 | 2.221 | 2.091 |
| $UO_2$ | 0.071 | 0.081 | 0.010 | 0.019 | 0.011 | 0.014 |
| $ThO_2$ | 0.221 | 0.215 | 0.011 | 0.015 | 0.020 | 0.026 |
| **Total** | 99.955 | 100.002 | 94.027 | 92.981 | 93.609 | 93.919 |
| *apfu* | | | | | | |
| Zr | 0.922 | 0.926 | 0.940 | 0.937 | 0.940 | 0.934 |
| Hf | 0.017 | 0.017 | 0.011 | 0.010 | 0.012 | 0.012 |
| U | 0.000 | 0.001 | 0.000 | 0.000 | 0.000 | 0.000 |
| Th | 0.002 | 0.001 | 0.000 | 0.000 | 0.000 | 0.000 |
| Fe | 0.011 | 0.010 | 0.098 | 0.105 | 0.096 | 0.100 |
| Mn | 0.000 | 0.000 | 0.006 | 0.003 | 0.002 | 0.002 |
| Mg | 0.000 | 0.000 | 0.000 | 0.001 | 0.000 | 0.000 |
| Ca | 0.026 | 0.026 | 0.012 | 0.010 | 0.079 | 0.074 |
| **Σ X-site** | 0.978 | 0.981 | 1.066 | 1.066 | 1.129 | 1.122 |
| Si | 1.032 | 1.029 | 0.987 | 0.990 | 0.957 | 0.963 |
| Ti | 0.000 | 0.000 | 0.000 | 0.000 | 0.000 | 0.000 |
| Al | 0.011 | 0.010 | 0.005 | 0.003 | 0.004 | 0.003 |
| **Σ Y-site** | 1.044 | 1.044 | 0.961 | 0.967 | 0.961 | 0.967 |

Table 45 Representative EMP analyses of zircon. *Apfu* calculations based on 4 oxygens.

## BLACK RIVER PEGMATITE

Figure 95 Black River pegmatite.

The Black River pegmatite is located west of Hwy M-95 and a few miles north of the village of Republic. An old railroad bed provides access to the pegmatite. As this pegmatite is frequently visited by rock hounds and the curious, it was some work to remove material from the pegmatite. The Black River pegmatite is in sharp contact with country rock. It is medium to coarse grained and the overall hue of feldspars ranges from a light pink to orange. Visual inspection of the pegmatite revealed that there is abundant mica, feldspar, quartz, and fluorite. Apatite, columbite, feldspar, fluorite, iron oxides, "monazite", muscovite, scheelite, quartz, zircon, and "xenotime" were identified qualitatively by SEM. Ferrocolumbite, ferrotantalite, plagioclase (albite), monazite-(Ce), and muscovite were quantitatively confirmed by electron microprobe.

## APATITE

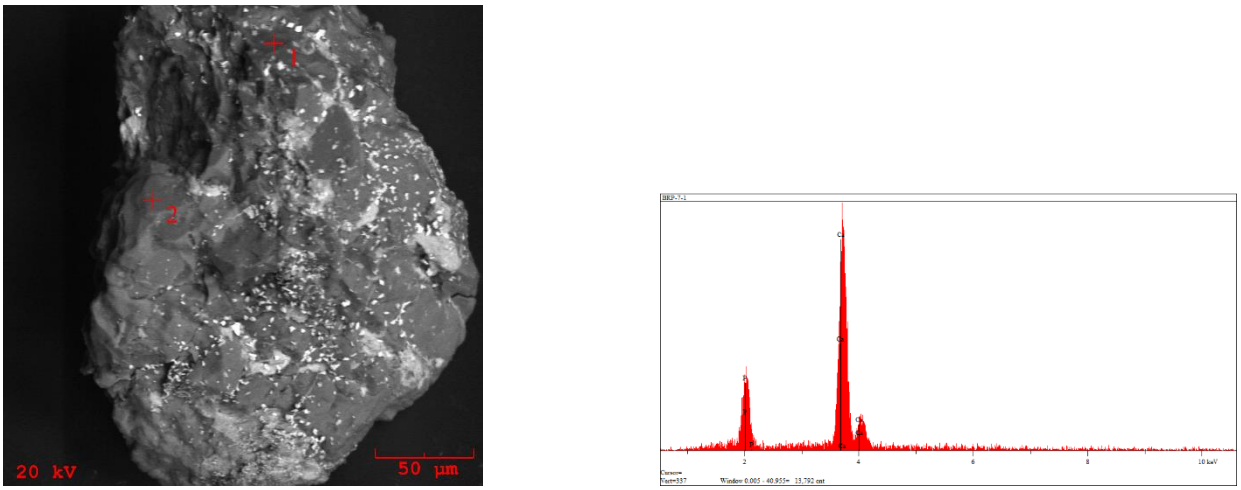


Figure 96 BSE of apatite grain with corresponding EDS spectrum (crosshairs 1 & 2).

Apatite is exceedingly rare in heavy mineral separations as only two grains have been identified by SEM. Efforts to discover more by UV light has been unsuccessful. This represents the first reported occurrence of apatite at the Black River pegmatite.

Unfortunately, neither grain survived sample preparation for further investigation by microprobe.

## COLUMBITE/TANTALITE

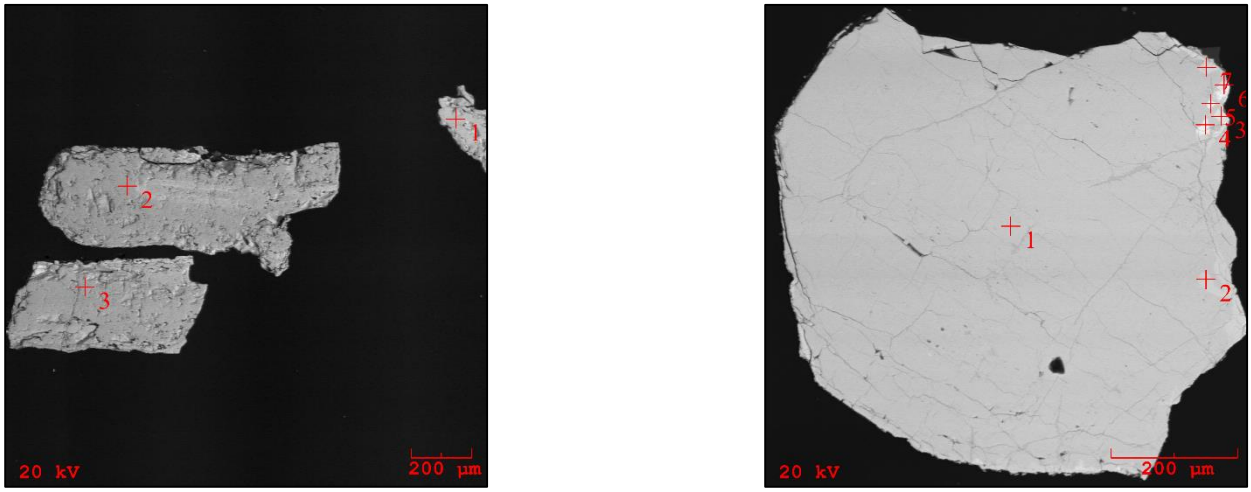


Figure 97 BSE image of polished columbite grains (left) & ferrocolumbite grain (right) with regions of ferrotantalite (lighter areas of the grains). Visible zoning (left middle grain) is present and corresponds to higher Ta content.

Abundant columbite/tantalite grains have been found in heavy mineral separations collected from the Black River pegmatite. Discrete grains of ferrocolumbite have identified by SEM and confirmed by microprobe. One grain in particular has visible zonation due to relatively elevated levels of tantalum. The analyses associated with the grain (grain 3 BRP Goi-1; Table 46) show that tantalum content is sufficient to classify this area of enrichment as ferrotantalite (Figure 170). Buchholz *et al*. (2014) have confirmed the occurrence of ferrocolumbite at Black River pegmatite, but their analyses did not detect sufficient Ta enrichment for classification as ferrotantalite. Table 46 lists the representative microprobe analyses.

| FERROCOLUMBITE – BLACK RIVER | | | | | | | |
|---|---|---|---|---|---|---|---|
| Wt% Ox | BRP grain 1-1 | | BRP grain 3-1 | | grain 3 BRP Goi-1 | | |
| $Nb_2O_5$ | 66.898 | 66.643 | 69.644 | 69.223 | 67.344 | 32.092 | 30.334 |
| $Ta_2O_5$ | 11.788 | 11.987 | 10.004 | 10.532 | 11.244 | 51.225 | 52.892 |
| $SiO_2$ | 0.022 | 0.034 | 0.043 | 0.023 | 0.055 | 0.044 | 0.023 |
| $TiO_2$ | 0.997 | 1.054 | 0.055 | 0.211 | 1.091 | 0.445 | 0.000 |
| $Al_2O_3$ | 0.000 | 0.000 | 0.022 | 0.000 | 0.041 | 0.059 | 0.038 |
| FeO | 17.004 | 17.100 | 17.265 | 17.433 | 16.554 | 11.912 | 10.012 |
| MnO | 2.877 | 2.783 | 3.093 | 2.872 | 3.244 | 4.221 | 6.677 |
| MgO | *bdl* | *bdl* | *bdl* | *bdl* | *bdl* | *bdl* | *bdl* |
| Total | 99.586 | 99.601 | 100.126 | 100.294 | 99.573 | 99.998 | 99.976 |
| *apfu* | | | | | | | |
| Fe | 0.838 | 0.843 | 0.843 | 0.851 | 0.813 | 0.699 | 0.595 |
| Mn | 0.144 | 0.139 | 0.153 | 0.142 | 0.161 | 0.251 | 0.402 |
| Si | 0.001 | 0.002 | 0.003 | 0.001 | 0.003 | 0.003 | 0.002 |
| Al | 0.000 | 0.000 | 0.002 | 0.000 | 0.003 | 0.005 | 0.003 |
| Mg | *bdl* | *bdl* | *bdl* | *bdl* | *bdl* | *bdl* | *bdl* |
| **Σ X-site** | 0.982 | 0.982 | 0.997 | 0.993 | 0.977 | 0.955 | 1.001 |
| Nb | 1.782 | 1.776 | 1.838 | 1.827 | 1.788 | 1.018 | 0.975 |
| Ta | 0.189 | 0.192 | 0.159 | 0.167 | 0.180 | 0.978 | 1.023 |
| Ti | 0.044 | 0.047 | 0.002 | 0.009 | 0.048 | 0.023 | 0.000 |
| **Σ Y-site** | 2.015 | 2.015 | 1.999 | 2.004 | 2.016 | 2.019 | 1.998 |

Table 46 Representative EMP analyses of ferrocolumbite. *Apfu* calculations based on 6 oxygens.

## PLAGIOCLASE FELDSPAR

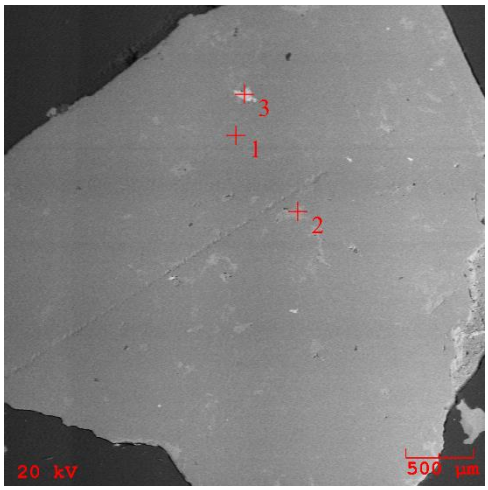


Figure 98 BSE image of polished plagioclase grain (crosshair 1), K-feldspar bleb (crosshair 2), & fluorite inclusion (crosshair 3).

Grains of plagioclase feldspar have been analyzed by SEM and quantitatively investigated by microprobe. Feldspar grains are revealed to be $albite_{92}$. Blebs of K-feldspar are present; these blebs are irregular in shape and orientation. Strontium, barium, cesium, and rubidium are all either at or below detection limits. This suggests that feldspars from the Black River pegmatite are poorly evolved. Table 47 lists the plagioclase feldspar analyses. A sample of feldspar has been analyzed by XRD (Figure 173). Even though no discrete grains of K-feldspar have been found or analyzed by SEM or microprobe, the analysis plots near the maximum microcline field suggesting a high degree of structural ordering (Wright & Stewart, 1968).

| PLAGIOCLASE FELDSPAR – BLACK RIVER PEGMATITE | | | | | | |
|---|---|---|---|---|---|---|
| Wt% ox | BRP grain1-3 | BRP grain1-4 | BRP grain2-1 | BRP grain2-2 | BRP grain3-1 | BRP grain3-2 |
| $P_2O_5$ | *bdl* | *bdl* | *bdl* | *bdl* | *bdl* | 0.011 |
| $SiO_2$ | 64.875 | 68.822 | 68.804 | 64.867 | 68.796 | 64.844 |
| $TiO_2$ | 0.017 | 0.000 | 0.000 | 0.014 | 0.000 | 0.012 |
| $Al_2O_3$ | 18.316 | 19.734 | 19.761 | 18.400 | 19.733 | 18.373 |
| $FeO_t$ | 0.011 | 0.000 | 0.000 | 0.009 | 0.000 | 0.009 |
| CaO | 0.000 | 0.366 | 0.378 | 0.009 | 0.364 | 0.011 |
| $Na_2O$ | 0.499 | 10.871 | 10.855 | 0.512 | 10.900 | 0.484 |
| $K_2O$ | 16.282 | 0.134 | 0.165 | 16.188 | 0.181 | 16.111 |
| $Rb_2O$ | 0.017 | 0.000 | 0.000 | 0.000 | 0.000 | 0.000 |
| **Total** | 100.017 | 99.936 | 99.963 | 99.999 | 99.974 | 99.855 |
| *apfu* | | | | | | |
| K | 0.960 | 0.007 | 0.009 | 0.954 | 0.010 | 0.951 |
| Na | 0.045 | 0.919 | 0.917 | 0.046 | 0.921 | 0.043 |
| Ca | 0.000 | 0.017 | 0.018 | 0.000 | 0.017 | 0.001 |
| Rb | 0.001 | 0.000 | 0.000 | 0.000 | 0.000 | 0.000 |
| **Σ X-site** | 1.006 | 0.943 | 0.944 | 1.001 | 0.948 | 0.995 |
| Al | 0.998 | 1.014 | 1.015 | 1.002 | 1.014 | 1.002 |
| Fe | 0.000 | 0.000 | 0.000 | 0.000 | 0.000 | 0.000 |
| **Σ Y-site** | 0.998 | 1.014 | 1.015 | 1.002 | 1.014 | 1.002 |
| Si | 2.999 | 2.999 | 2.998 | 2.997 | 2.998 | 2.999 |
| Ti | 0.001 | 0.000 | 0.000 | 0.000 | 0.000 | 0.000 |
| P | 0.000 | 0.000 | 0.000 | 0.000 | 0.000 | 0.000 |
| Al | 0.000 | 0.000 | 0.000 | 0.000 | 0.000 | 0.000 |
| **Σ Z-site** | 3.000 | 2.999 | 2.998 | 2.998 | 2.998 | 3.000 |

Table 47 Representative EMP analyses of plagioclase (albite). *Apfu* calculations based on 8 oxygens.

## FLUORITE

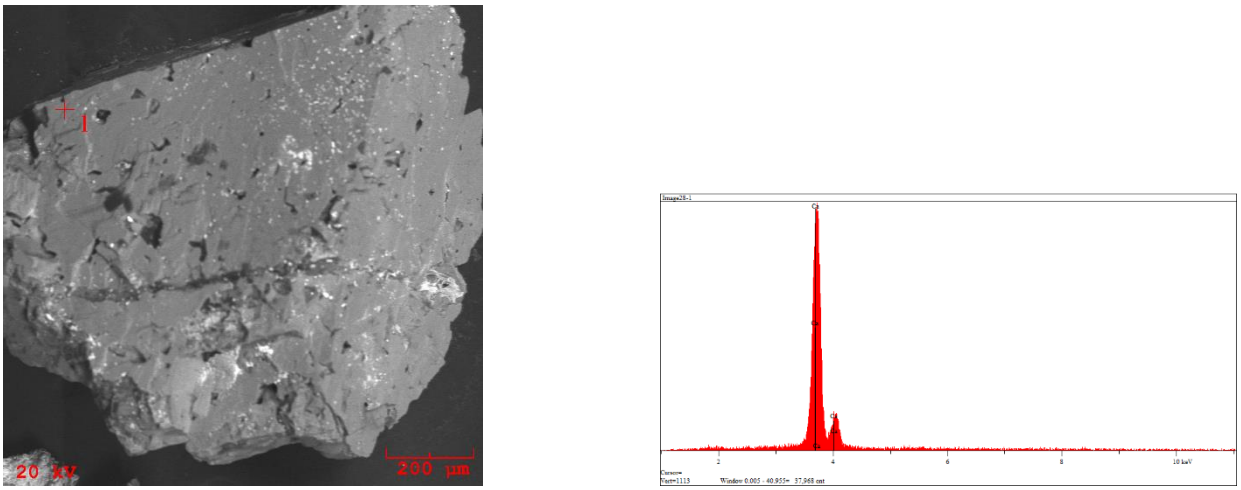


Figure 99 BSE image of fluorite grain and corresponding EDS spectrum.

Fluorite has been identified in heavy mineral samples and qualitatively confirmed by SEM. Flourite has been identified at the Black River pegmatite previously.

## IRON OXIDE

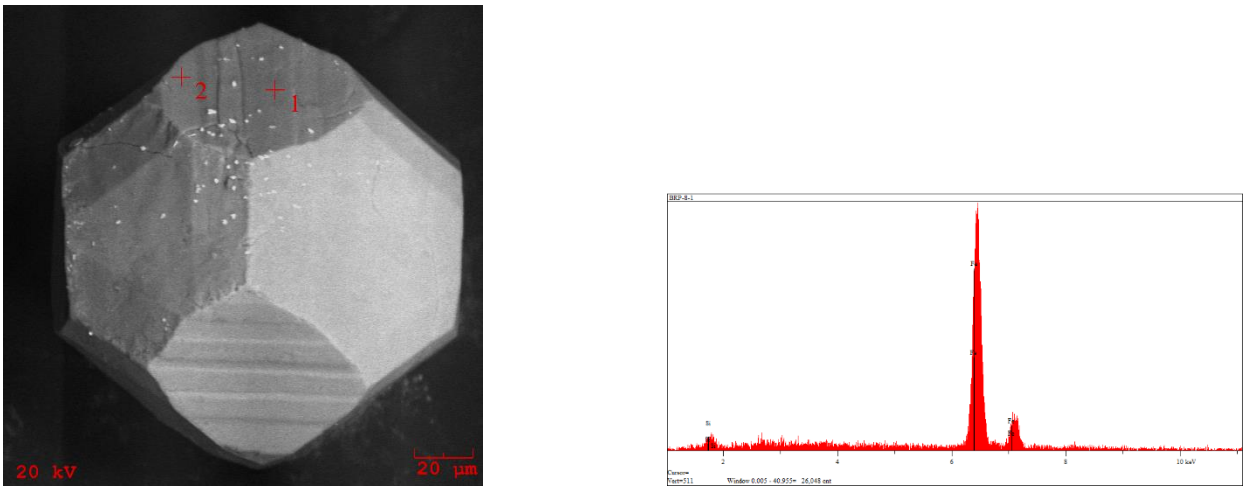


Figure 100 BSE image and EDS spectrum of magnetite grain.

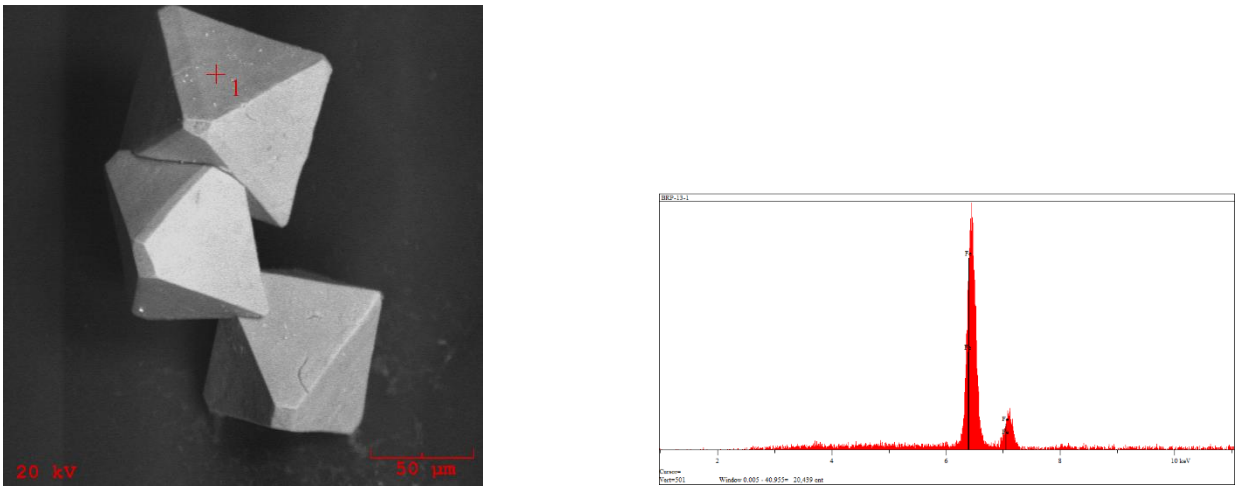


Figure 101 BSE image and EDS spectrum of hematite grains.

Excellent crystal specimens of iron oxide have been found in heavy mineral separations and further investigated by SEM. Magnetite is present as well as hematite. Both of these minerals represent the first reported case of either one of these two iron oxides at the Black River pegmatite.

## "MONAZITE"

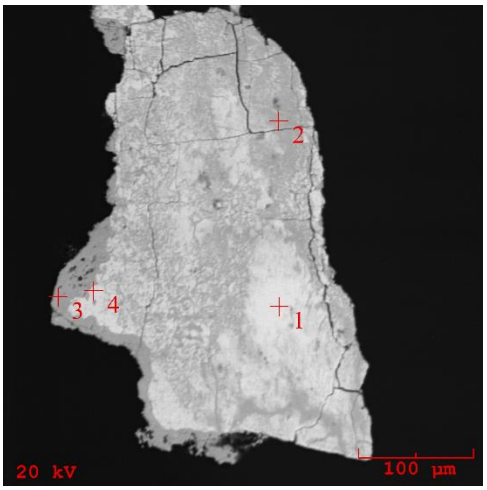


Figure 102 BSE image of polished "monazite" grain.

"Monazite" has been qualitatively identified by SEM and confirmed by microprobe. Based on the dominance of cerium in the X-site, classification should be monazite-(Ce). Both grains analyzed by SEM lack homogeneity; however, microprobe investigation did yield a weight percent total close to 100%, suggesting that there are some areas of the grain that are intact. The above grain has a rim that is relatively depleted in the LREE's and relatively more enriched in yttrium and ytterbium, suggesting that there is an overgrowth of unconfirmed "xenotime". Table 48 lists the analysis.

| **MONAZITE-(CE) – BLACK RIVER** | |
|---|---|
| Wt % Ox. | GOI-23 BRP grain 2 |
| $P_2O_5$ | 28.776 |
| $SiO_2$ | 0.122 |
| $ThO_2$ | 0.000 |
| $UO_2$ | 7.554 |
| $Al_2O_3$ | 0.870 |
| $La_2O_3$ | 0.060 |
| $Ce_2O_3$ | 12.012 |
| $Pr_2O_3$ | 27.555 |
| $Nd_2O_3$ | 2.431 |
| $Sm_2O_3$ | 14.999 |
| $Gd_2O_3$ | 0.462 |
| $Dy_2O_3$ | 0.188 |
| $Yb_2O_3$ | 0.100 |
| $Y_2O_3$ | 0.678 |
| $Sc_2O_3$ | 0.025 |
| MgO | 0.000 |
| CaO | 2.113 |
| MnO | 0.045 |
| FeO | 0.042 |
| PbO | 0.225 |
| **Total** | 99.357 |
| *apfu* | |
| Th | 0.029 |
| U | 0.003 |
| Al | 0.001 |
| La | 0.074 |
| Ce | 0.168 |
| Pr | 0.015 |
| Nd | 0.089 |
| Sm | 0.006 |
| Dy | 0.001 |
| Y | 0.006 |
| Mn | 0.000 |
| Fe | 0.015 |
| Ca | 0.038 |
| Mn | 0.001 |
| Fe | 0.001 |
| Pb | 0.001 |
| **Σ X** | 1.033 |
| P | 0.962 |
| Si | 0.009 |
| **Σ Y** | 0.971 |

Table 48 Representative EMP analysis of monazite-(Ce).
*Apfu* calculations based on 4 oxygens.

## MUSCOVITE

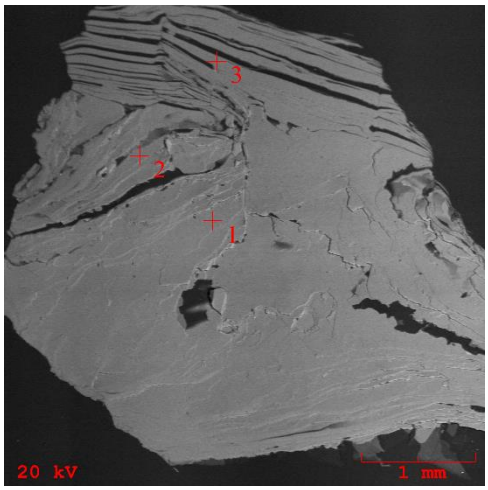


Figure 103 BSE image of polished muscovite grain (1-3).

Muscovite mica is the dominant mica species found in Black River pegmatite (Figure 185) heavy mineral separations. Biotite is not present in heavy mineral separations and is not currently listed as being found at the Black River pegmatite. Analyses by DCP reveal lithium weight percent totals of 0.209 and 0.517 and is accounted for stoichiometrically by the equation $0.3935*\text{Fluorine wt\%}^{1.326}$ (Tischendorf, 1997). The latter value is much closer to calculated weight percent. Rubidium weight percent values are just within detectable limits and cesium is below detection limits, suggesting that muscovite mica at the Black River pegmatite is poorly evolved. Table 49 lists representative analyses via microprobe.

| MUSCOVITE – BLACK RIVER PEGMATITE | | | | | | | | | | |
|---|---|---|---|---|---|---|---|---|---|---|
| Wt % Ox. | BRP grain 1-1 | BRP grain 1-2 | BRP grain 2-1 | BRP grain 2-2 | BRP grain 3-1 | BRP grain 3-2 | BRP grain 4-1 | BRP grain 4-2 | BRP grain 5-1 | BRP grain 5-2 |
| $SiO_2$ | 46.599 | 46.622 | 46.578 | 46.655 | 46.644 | 46.711 | 46.598 | 46.644 | 46.619 | 46.723 |
| $TiO_2$ | 0.277 | 0.311 | 0.332 | 0.316 | 0.343 | 0.381 | 0.341 | 0.400 | 0.382 | 0.377 |
| $Al_2O_3$ | 34.444 | 34.478 | 34.376 | 34.312 | 34.476 | 34.500 | 34.448 | 34.387 | 34.665 | 35.600 |
| $Fe_2O_3$ | 0.000 | 0.000 | 0.000 | 0.000 | 0.000 | 0.000 | 0.000 | 0.000 | 0.000 | 0.000 |
| FeO | 2.876 | 3.092 | 3.213 | 3.267 | 3.222 | 3.195 | 3.099 | 3.367 | 3.287 | 3.311 |
| MnO | 0.092 | 0.097 | 0.100 | 0.088 | 0.083 | 0.090 | 0.083 | 0.095 | 0.111 | 0.109 |
| MgO | 1.011 | 1.111 | 1.157 | 1.220 | 1.191 | 1.200 | 0.999 | 1.091 | 1.045 | 1.154 |
| CaO | 0.012 | 0.017 | 0.020 | 0.018 | 0.020 | 0.018 | 0.023 | 0.019 | 0.016 | 0.021 |
| $Li_2O$ (*calc.*) | 0.459 | 0.509 | 0.514 | 0.564 | 0.455 | 0.442 | 0.459 | 0.501 | 0.596 | 0.767 |
| $Na_2O$ | 0.477 | 0.412 | 0.378 | 0.393 | 0.282 | 0.272 | 0.299 | 0.302 | 0.234 | 0.250 |
| $K_2O$ | 9.700 | 9.671 | 9.788 | 9.800 | 9.778 | 9.766 | 9.823 | 9.669 | 9.723 | 9.723 |
| $Rb_2O$ | 0.010 | 0.013 | 0.010 | 0.009 | 0.011 | 0.013 | 0.011 | 0.016 | 0.013 | 0.011 |
| $Cs_2O$ | *bdl* | *bdl* | *bdl* | *bdl* | *bdl* | *bdl* | *bdl* | *bdl* | *bdl* | *bdl* |
| F | 1.123 | 1.215 | 1.223 | 1.312 | 1.115 | 1.091 | 1.123 | 1.200 | 1.367 | 1.654 |
| $H_2O$ | 3.995 | 3.965 | 3.961 | 3.926 | 4.016 | 4.033 | 3.999 | 3.975 | 3.908 | 3.837 |
| F=O | 0.473 | 0.512 | 0.515 | 0.552 | 0.469 | 0.459 | 0.473 | 0.505 | 0.576 | 0.696 |
| **Total** | 100.602 | 101.002 | 101.135 | 101.328 | 101.166 | 101.252 | 100.833 | 101.161 | 101.390 | 102.840 |
| *apfu* | | | | | | | | | | |
| Si | 6.172 | 6.156 | 6.151 | 6.151 | 6.154 | 6.156 | 6.166 | 6.156 | 6.136 | 6.063 |
| $^{IV}Al$ | 1.828 | 1.844 | 1.849 | 1.849 | 1.846 | 1.844 | 1.834 | 1.844 | 1.864 | 1.937 |
| **Σ T-site** | 8.000 | 8.000 | 8.000 | 8.000 | 8.000 | 8.000 | 8.000 | 8.000 | 8.000 | 8.000 |
| $^{VI}Al$ | 3.550 | 3.522 | 3.501 | 3.483 | 3.515 | 3.515 | 3.538 | 3.505 | 3.514 | 3.507 |
| Ti | 0.028 | 0.031 | 0.033 | 0.031 | 0.034 | 0.038 | 0.034 | 0.040 | 0.038 | 0.037 |
| $Fe_t$ | 0.319 | 0.341 | 0.355 | 0.360 | 0.356 | 0.352 | 0.343 | 0.372 | 0.362 | 0.359 |
| Mn | 0.010 | 0.011 | 0.011 | 0.010 | 0.009 | 0.010 | 0.009 | 0.011 | 0.012 | 0.012 |
| Mg | 0.200 | 0.219 | 0.228 | 0.240 | 0.234 | 0.236 | 0.197 | 0.215 | 0.205 | 0.223 |
| Li (*calc.*) | 0.244 | 0.271 | 0.273 | 0.299 | 0.241 | 0.234 | 0.244 | 0.266 | 0.315 | 0.400 |
| **Σ Y-site** | 4.351 | 4.395 | 4.401 | 4.423 | 4.389 | 4.385 | 4.365 | 4.409 | 4.446 | 4.538 |

Table 49 Representative EMP analyses of muscovite mica. *Apfu* calculations based on 24 anions. Table continues on next page.

| | | | | | | | | | | |
|---|---|---|---|---|---|---|---|---|---|---|
| K | 1.639 | 1.629 | 1.649 | 1.648 | 1.646 | 1.642 | 1.658 | 1.628 | 1.633 | 1.610 |
| Ca | 0.002 | 0.002 | 0.003 | 0.003 | 0.003 | 0.003 | 0.003 | 0.003 | 0.002 | 0.003 |
| Na | 0.123 | 0.105 | 0.097 | 0.100 | 0.072 | 0.070 | 0.077 | 0.077 | 0.060 | 0.063 |
| Rb | 0.001 | 0.001 | 0.001 | 0.001 | 0.001 | 0.001 | 0.001 | 0.001 | 0.001 | 0.001 |
| Cs | *bdl* | *bdl* | *bdl* | *bdl* | *bdl* | *bdl* | *bdl* | *bdl* | *bdl* | *bdl* |
| **Σ X-site** | 1.765 | 1.737 | 1.750 | 1.752 | 1.722 | 1.716 | 1.739 | 1.709 | 1.696 | 1.677 |
| F | 0.470 | 0.507 | 0.511 | 0.547 | 0.465 | 0.455 | 0.470 | 0.501 | 0.569 | 0.679 |
| OH (*calc.*) | 3.530 | 3.493 | 3.489 | 3.453 | 3.535 | 3.545 | 3.530 | 3.499 | 3.431 | 3.321 |
| **Σ W-site** | 4.000 | 4.000 | 4.000 | 4.000 | 4.000 | 4.000 | 4.000 | 4.000 | 4.000 | 4.000 |

SCHEELITE

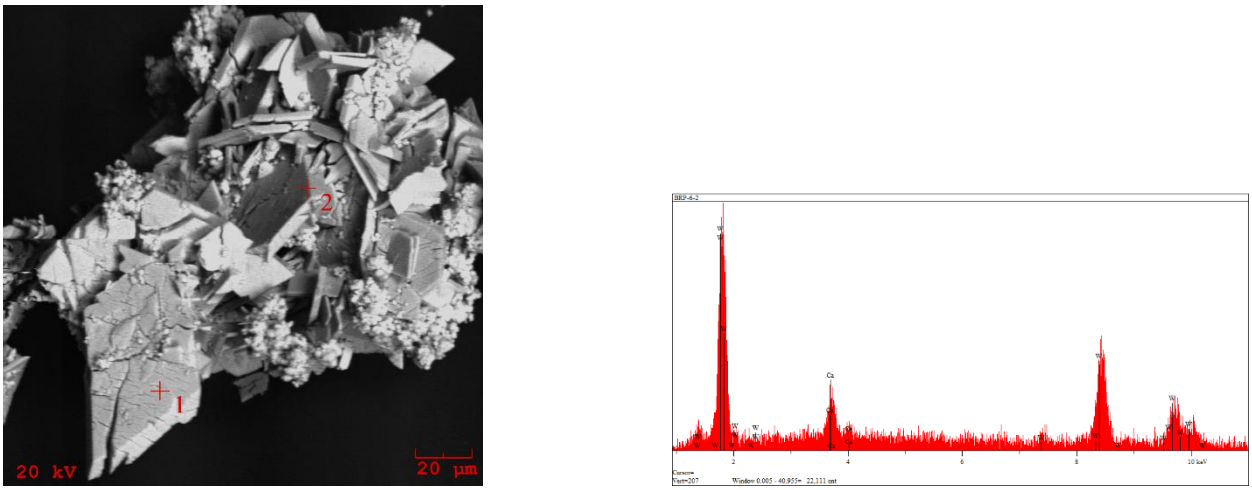


Figure 104 BSE image of possible scheelite with corresponding EDS spectrum.

What is possibly scheelite has been qualitatively identified by SEM. Only a few of these grains have been found in heavy mineral separations. If indeed scheelite, this will represent the first reported occurrence at the Black River pegmatite.

## "XENOTIME"

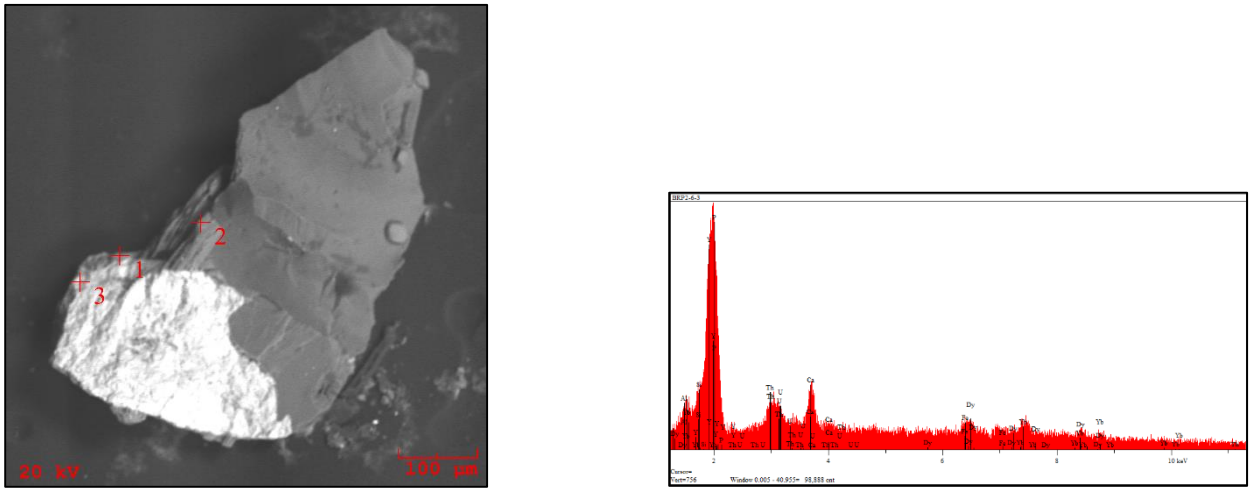


Figure 105 BSE image of "xenotime" grain (crosshair 3) & associated EDS spectrum on feldspar grain (crosshairs 1 & 2).

A single grain of what is possibly "xenotime" has been identified by SEM. The grain appears to be relatively enriched in yttrium, ytterbium, and dysprosium. Efforts to quantitatively investigate the mineral further by electron microprobe have been unsuccessful.

## ZIRCON

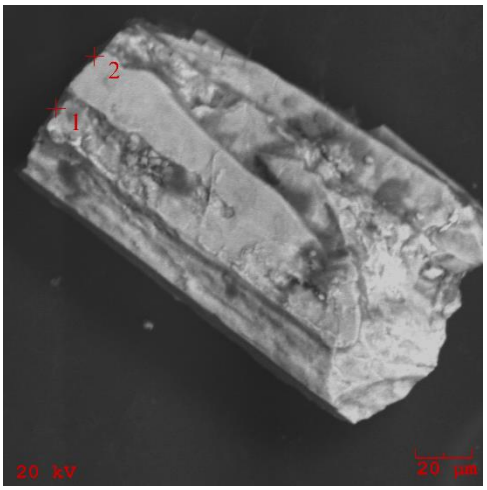


Figure 106 BSE image of zircon grain.

Zircon is not overly abundant in samples from the Black River pegmatite. Only a few grains have been discovered in heavy mineral separations and qualitatively analyzed by SEM. None have survived sample preparation, owing perhaps to the size of the grains. Hafnium appears to be below detectable limits of SEM analyses and thus it is suggested that zircon is relatively poorly evolved.

## HWY69 PEGMATITE


Figure 107 Hwy 69 Pegmatite exposure.

The Hwy69 pegmatite is, as its name implies, located on Hwy69 in Dickinson County, Michigan. Visually, the Hwy69 pegmatite has pink to reddish-orange feldspar, mica, and quartz. Within the larger pegmatitic body, there are numerous fractures filled with presumably biotite mica. In addition, there are areas that have been preferentially weathered away, which look like pock-marks of variable size. None of these pock marks are very large and are only perhaps an inch or so in diameter and approximately a half inch deep. The Hwy69 pegmatite is poorly exposed as can be seen from the above photograph. The following minerals were qualitatively and quantitatively analyzed: apatite, biotite, chalcopyrite, columbite group minerals, euxenite group minerals, feldspar, garnet, ilmenite, “monazite”, muscovite, pyrite, quartz, and zircon have been analyzed by SEM; ferrocolumbite, fersmite from the euxenite group minerals, K-feldspar

and plagioclase feldspar, garnet, monazite-(Ce), and muscovite mica have been analyzed by electron microprobe.

## APATITE

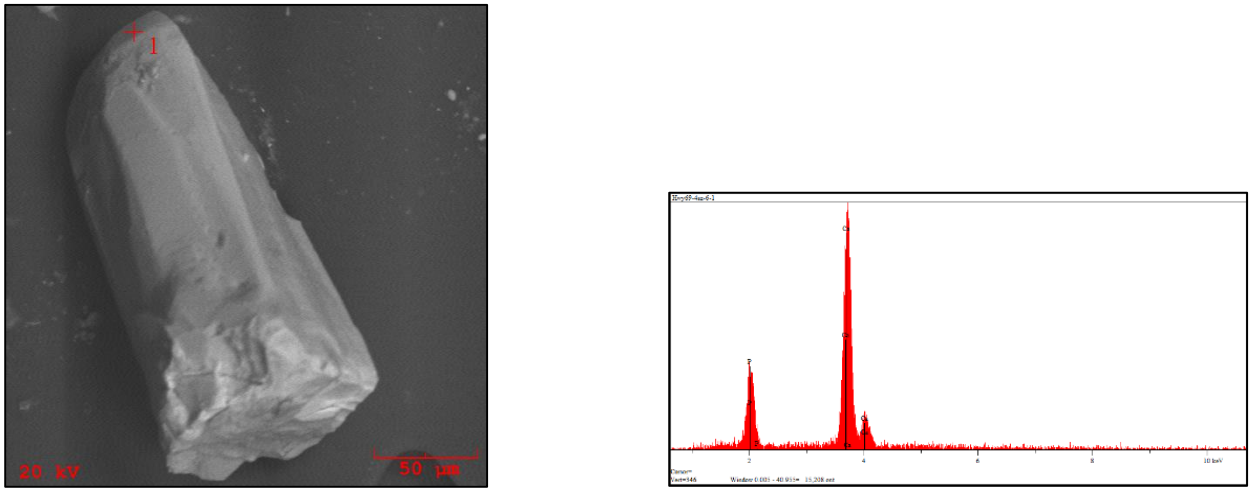


Figure 108 BSE image of apatite grain along with associated EDS spectrum.

Only five discrete grains of apatite have been found at the Hwy69 pegmatite. Aside from "monazite", apatite was the only phosphorus-bearing accessory mineral. Apatite was qualitatively analyzed by SEM.

BIOTITE

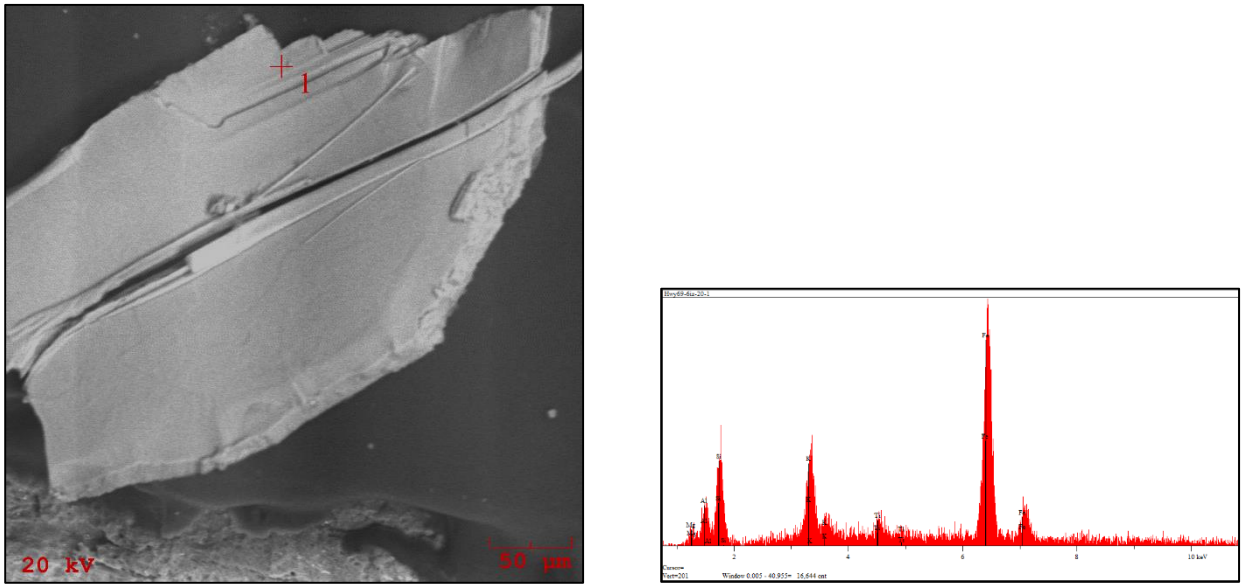


Figure 109 BSE image of biotite mica grain along with corresponding EDS spectrum.

Biotite is exceedingly rare in heavy mineral separations and only found in fractures at the Hwy69 pegmatite. It has been identified in heavy mineral separations and qualitatively investigated by SEM and later confirmed by microprobe. Table 50 lists the representative analyses. There was not enough homogeneous material with which to titrate for trivalent iron content. Lithium was detected in DCP analysis of muscovite mica. Lithium has been calculated based on magnesium weight percent: 155 * Mg wt%$^{-3.1}$, based on Tischendorf's equations (1997).

| **Fe-Biotite – Hwy69 Pegmatite** | | | | |
|---|---|---|---|---|
| Wt % Ox. | 4sz-2-1 | 4sz-1-2 | 4sz-1-3 | 4sz-3-1 |
| $SiO_2$ | 34.887 | 34.786 | 34.877 | 34.533 |
| $TiO_2$ | 3.099 | 2.967 | 3.234 | 3.095 |
| $Al_2O_3$ | 17.988 | 18.099 | 18.103 | 18.200 |
| $Fe_2O_3$ | 0.000 | 0.000 | 0.000 | 0.000 |
| FeO | 22.233 | 22.178 | 22.112 | 21.899 |
| MnO | 0.433 | 0.377 | 0.544 | 0.630 |
| MgO | 8.004 | 7.788 | 8.044 | 8.233 |
| CaO | 0.044 | 0.067 | 0.040 | 0.035 |
| $Li_2O$ (*calc.*) | 0.246 | 0.267 | 0.242 | 0.225 |
| $Na_2O$ | 0.233 | 0.191 | 0.234 | 0.155 |
| $K_2O$ | 9.650 | 9.788 | 9.698 | 9.433 |
| $Rb_2O$ | 0.010 | 0.009 | 0.000 | 0.000 |
| $Cs_2O$ | *bdl* | *bdl* | *bdl* | *bdl* |
| F | 1.099 | 1.104 | 0.973 | 0.977 |
| $H_2O$ | 3.405 | 3.389 | 3.478 | 3.453 |
| F=O | - 0.463 | - 0.465 | - 0.410 | - 0.411 |
| **Total** | 100.868 | 100.546 | 101.169 | 100.457 |
| *apfu* | | | | |
| Si | 5.328 | 5.331 | 5.309 | 5.288 |
| $^{IV}Al$ | 2.672 | 2.669 | 2.691 | 2.712 |
| **Σ T-site** | 8.000 | 8.000 | 8.000 | 8.000 |
| $^{VI}Al$ | 0.566 | 0.600 | 0.558 | 0.572 |
| Ti | 0.356 | 0.342 | 0.371 | 0.357 |
| $Fe_t$ | 2.840 | 2.843 | 2.815 | 2.804 |
| Mn | 0.056 | 0.049 | 0.070 | 0.082 |
| Mg | 1.822 | 1.779 | 1.826 | 1.879 |
| Li (*calc.*) | 0.151 | 0.165 | 0.148 | 0.139 |
| **Σ Y-site** | 5.790 | 5.778 | 5.787 | 5.833 |

Table 50 Representative EMP analyses of Fe-biotite mica. *Apfu* calculations based on 24 anions.
Table continues on next page.

| | | | | |
|---|---|---|---|---|
| K | 1.880 | 1.914 | 1.884 | 1.843 |
| Ca | 0.007 | 0.011 | 0.007 | 0.006 |
| Na | 0.069 | 0.057 | 0.069 | 0.046 |
| Rb | 0.001 | 0.001 | 0.000 | 0.000 |
| Cs | *bdl* | *bdl* | *bdl* | *bdl* |
| **Σ X-site** | 1.957 | 1.983 | 1.960 | 1.895 |
| F | 0.531 | 0.535 | 0.468 | 0.473 |
| OH (*calc.*) | 3.469 | 3.465 | 3.532 | 3.527 |
| **Σ W-site** | 4.000 | 4.000 | 4.000 | 4.000 |

## CHALCOPYRITE

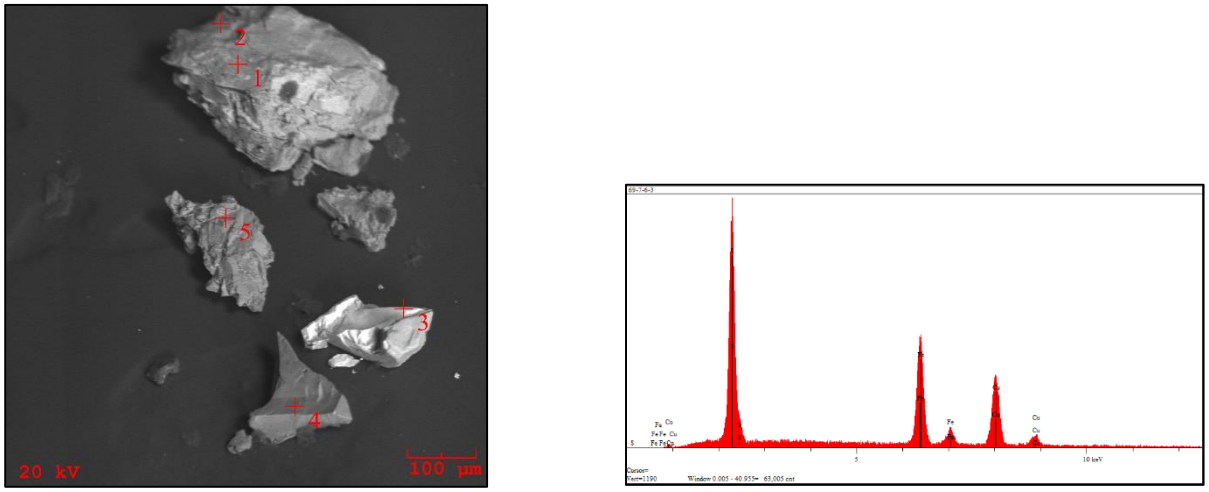


Figure 110 BSE image of chalcopyrite grain (crosshair 3) with corresponding EDS spectrum. Mica (crosshairs 1 & 2), quartz (crosshair 4), & K-feldspar (crosshair 5).

Two grains of chalcopyrite have been identified in heavy mineral separations and qualitatively confirmed via SEM. These grains lack crystal faces and are approximately 100 microns in width.

## COLUMBITE/TANTALITE

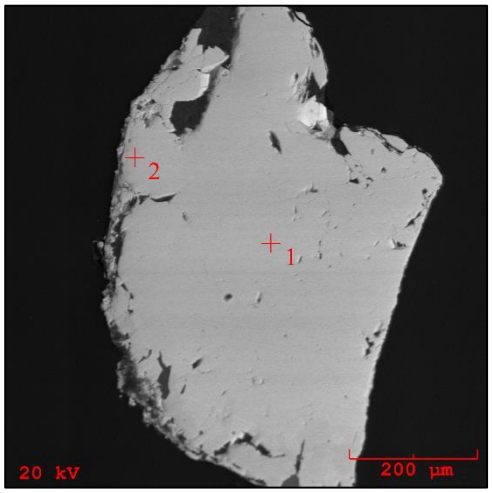


Figure 111 BSE image of polished ferrocolumbite grain (1 & 2).

Columbite/tantalite is relatively ubiquitous in heavy mineral separations. Grains have been qualitatively identified by SEM and confirmed by microprobe. Analyses suggest that grains be identified as ferrocolumbite due to iron and niobium dominance over manganese and tantalum. Stoichiometric manganese ranges between 20 and approximately 40 percent; tantalum *apfu* ranges are between 20 and approximately 23 percent. Grains are texturally and geochemically homogeneous and are sub-, an-, as well as euhedral in appearance. Table 51 lists microprobe analyses.

| **FERROCOLUMBITE – HWY69 PEGMATITE** | | | | | | | | |
|---|---|---|---|---|---|---|---|---|
| Wt% Ox | hwy 69 grain 12-1 | | hwy 69 grain 13-1 | | hwy 69 grain 14-1 | | hwy 69 grain 15-1 | |
| $Nb_2O_5$ | 67.112 | 67.051 | 66.093 | 66.112 | 65.900 | 65.899 | 66.900 | 67.112 |
| $Ta_2O_5$ | 12.566 | 12.766 | 13.650 | 13.988 | 14.222 | 14.430 | 13.009 | 12.877 |
| $SiO_2$ | 0.022 | 0.040 | 0.022 | 0.015 | 0.011 | 0.056 | 0.021 | 0.054 |
| $TiO_2$ | 0.021 | 0.018 | 0.021 | 0.050 | 0.022 | 0.025 | 0.012 | 0.020 |
| $Al_2O_3$ | 0.000 | 0.000 | 0.000 | 0.000 | 0.000 | 0.000 | 0.000 | 0.000 |
| FeO | 12.566 | 12.433 | 16.005 | 15.988 | 15.443 | 13.450 | 13.112 | 14.655 |
| MnO | 7.645 | 7.711 | 3.938 | 3.983 | 4.554 | 6.112 | 7.300 | 4.877 |
| MgO | *bdl* | *bdl* | *bdl* | *bdl* | *bdl* | *bdl* | *bdl* | *bdl* |
| Total | 99.932 | 100.019 | 99.729 | 100.136 | 100.152 | 99.972 | 100.354 | 99.595 |
| *apfu* | | | | | | | | |
| Fe | 0.621 | 0.615 | 0.797 | 0.794 | 0.767 | 0.669 | 0.647 | 0.727 |
| Mn | 0.383 | 0.386 | 0.199 | 0.200 | 0.229 | 0.308 | 0.365 | 0.245 |
| Si | 0.001 | 0.002 | 0.001 | 0.001 | 0.001 | 0.003 | 0.001 | 0.003 |
| Al | 0.000 | 0.000 | 0.000 | 0.000 | 0.000 | 0.000 | 0.000 | 0.000 |
| Mg | *bdl* | *bdl* | *bdl* | *bdl* | *bdl* | *bdl* | *bdl* | *bdl* |
| **Σ X-site** | 1.005 | 1.003 | 0.997 | 0.995 | 0.997 | 0.980 | 1.013 | 0.975 |
| Nb | 1.794 | 1.792 | 1.779 | 1.774 | 1.770 | 1.772 | 1.785 | 1.800 |
| Ta | 0.202 | 0.205 | 0.221 | 0.226 | 0.230 | 0.233 | 0.209 | 0.208 |
| Ti | 0.001 | 0.001 | 0.001 | 0.002 | 0.001 | 0.001 | 0.001 | 0.001 |
| **Σ Y-site** | 1.997 | 1.998 | 2.001 | 2.002 | 2.001 | 2.006 | 1.995 | 2.009 |

Table 51 Representative EMP analyses of ferrocolumbite. *Apfu* calculations based on 6 oxygens.

## EUXENITE GROUP

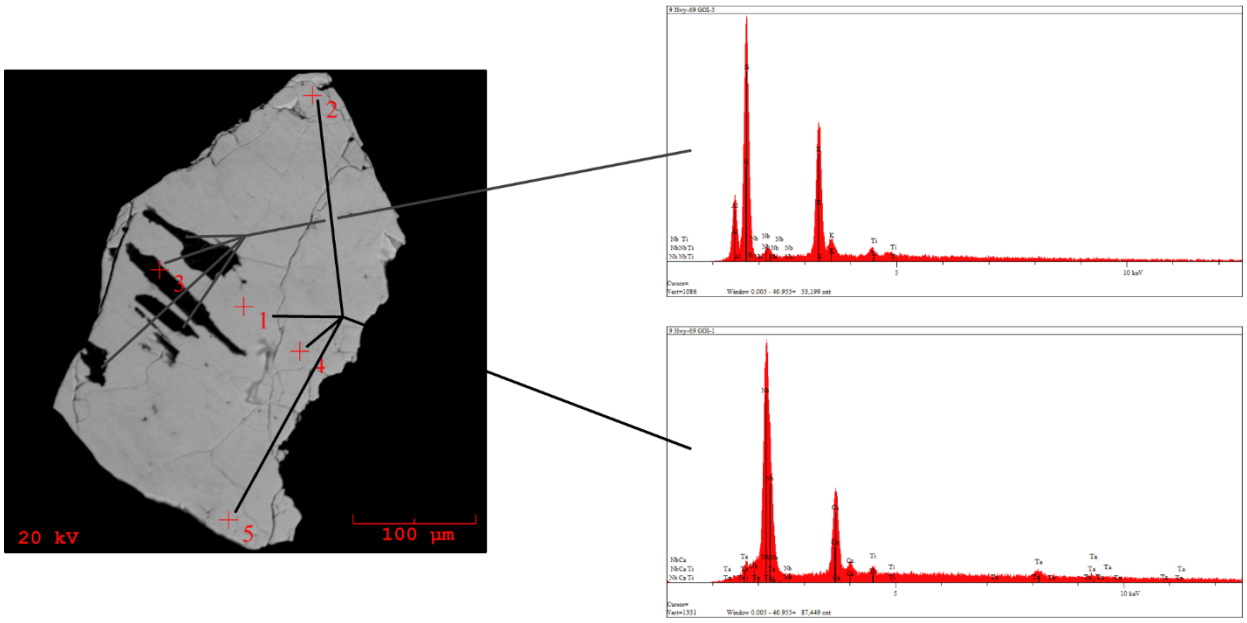


Figure 112 BSE image of polished fersmite grain (crosshairs 1, 2, 4, & 5) and K-feldspar inclusions (crosshair 3).

A grain quantitatively analyzed by microprobe revealed that it belongs to the euxenite group of minerals. The analyses show niobium dominance over tantalum and calcium dominance over divalent iron, manganese, and magnesium. The sample was not analyzed for cerium, neodymium, and yttrium; however, weight percent totals are very close to 100 percent suggesting that these three elements are at or below detection limits. Due to calcium dominance in the A-site and niobium dominance in the M-site, these should be classified as fersmite. Table 52 lists the representative analysis.

| EUXENITE GROUP – FERSMITE<br>HWY69 PEGMATITE | | |
|---|---|---|
| Wt% Ox | grain 9 Hwy 69 Goi-1 | |
| $Nb_2O_5$ | 78.612 | 78.555 |
| $Ta_2O_5$ | 3.003 | 3.336 |
| $SiO_2$ | 0.114 | 0.112 |
| $TiO_2$ | 0.088 | 0.188 |
| $Al_2O_3$ | 0.121 | 0.144 |
| CaO | 17.698 | 17.711 |
| FeO | 0.112 | 0.091 |
| MnO | 0.033 | 0.024 |
| MgO | 0.011 | 0.014 |
| Total | 99.792 | 100.175 |
| *apfu* | | |
| Ca | 1.029 | 1.027 |
| Fe | 0.005 | 0.004 |
| Mn | 0.002 | 0.001 |
| Si | 0.006 | 0.006 |
| Al | 0.008 | 0.009 |
| Mg | 0.001 | 0.001 |
| **Σ A-site** | 1.051 | 1.048 |
| Nb | 1.929 | 1.921 |
| Ta | 0.044 | 0.049 |
| Ti | 0.004 | 0.008 |
| **Σ M-site** | 1.978 | 1.977 |

Table 52 Representative euxenite group mineral EMP analyses. *Apfu* calculations based on 6 oxygens.

## FELDSPARS

### K-FELDSPAR

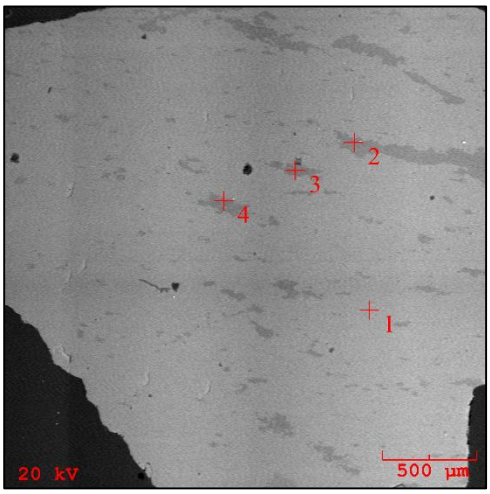


Figure 113 BSE image of polished K-feldspar grain (crosshair 1) with plagioclase blebs (crosshairs 2, 3, & 4).

K-feldspar has been qualitatively investigated by SEM and confirmed by microprobe. Blebs of plagioclase feldspar are present. These are elongated, irregular in shape, and roughly parallel. K-feldspar is pink to reddish-orange in hue. Rubidium weight percentages are just within detectable limits. Cesium is below detectable limits. Only one grain analyzed has detectable barium and strontium, but these values are just within limits of detectability. This suggests that K-feldspar is relatively poorly evolved. An XRD analysis reveal that there is a high degree of structural ordering in K-feldspars, as the analysis plots near the maximum microcline field (Wright & Stewart, 1968). Table 53 has a list of analyses.

| K-FELDSPAR – HWY69 PEGMATITE | | | | |
|---|---|---|---|---|
| Wt% ox | hwy69 vz grain 1-1 | | hwy69 vz grain 2-1 | |
| $P_2O_5$ | *bdl* | *bdl* | *bdl* | *bdl* |
| $SiO_2$ | 64.811 | 68.984 | 64.851 | 68.966 |
| $TiO_2$ | 0.012 | 0.000 | 0.009 | 0.000 |
| $Al_2O_3$ | 18.444 | 19.544 | 18.411 | 19.488 |
| $FeO_t$ | 0.013 | 0.000 | 0.015 | 0.000 |
| CaO | 0.009 | 0.454 | 0.011 | 0.446 |
| $Na_2O$ | 0.393 | 10.565 | 0.399 | 10.522 |
| $K_2O$ | 16.005 | 0.211 | 15.899 | 0.191 |
| $Rb_2O$ | 0.012 | 0.000 | 0.010 | 0.000 |
| **Total** | 99.699 | 99.758 | 99.627 | 99.626 |
| *apfu* | | | | |
| K | 0.945 | 0.012 | 0.939 | 0.011 |
| Na | 0.035 | 0.894 | 0.036 | 0.891 |
| Ca | 0.000 | 0.021 | 0.001 | 0.021 |
| Rb | 0.000 | 0.000 | 0.000 | 0.000 |
| **Σ X-site** | 0.980 | 0.927 | 0.976 | 0.923 |
| Al | 1.006 | 1.005 | 1.005 | 1.003 |
| Fe | 0.000 | 0.000 | 0.000 | 0.000 |
| **Σ Y-site** | 1.006 | 1.005 | 1.005 | 1.003 |
| Si | 2.999 | 3.009 | 3.002 | 3.012 |
| Ti | 0.000 | 0.000 | 0.000 | 0.000 |
| P | 0.000 | 0.000 | 0.000 | 0.000 |
| Al | 0.000 | 0.000 | 0.000 | 0.000 |
| **Σ Z-site** | 2.999 | 3.009 | 3.002 | 3.012 |

Table 53 Representative EMP analyses of K-feldspar. *Apfu* calculations based on 8 oxygens.

PLAGIOCLASE FELDSPAR

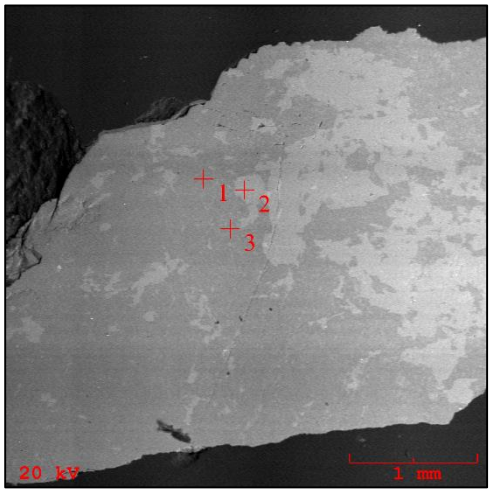


Figure 114 BSE image of polished plagioclase grain (crosshair 1 & 3) with K-feldspar exsolution blebs (crosshair 2).

Plagioclase has been qualitatively investigated by SEM and confirmed by microprobe analysis. Grains not only have blebs of K-feldspar, but also excellent examples of thin, parallel, approximately one micron thick, exsolution lamellae of K-feldspar. Of the plagioclase grains that have been analyzed by microprobe, barium, strontium, cesium, and rubidium are just at or below detection limits. Table 54 shows a list of the plagioclase analyses.

| PLAGIOCLASE FELDSPAR – HWY69 PEGMATITE | | | | | | | | |
|---|---|---|---|---|---|---|---|---|
| Wt% ox | hwy69 6iz grain 1-1 | | hwy69 6iz grain 2-1 | | hwy69 7 grain 1-1 | | hwy69 7 grain 2-1 | |
| $P_2O_5$ | *bdl* | *bdl* | *bdl* | *bdl* | *bdl* | 0.011 | | |
| $SiO_2$ | 64.788 | 64.699 | 64.803 | 64.566 | 64.606 | 64.799 | 64.588 | 64.805 |
| $TiO_2$ | 0.021 | 0.000 | 0.014 | 0.000 | 0.000 | 0.011 | 0.000 | 0.009 |
| $Al_2O_3$ | 18.422 | 22.089 | 18.433 | 22.113 | 22.091 | 18.438 | 22.143 | 18.455 |
| $FeO_t$ | 0.009 | 0.000 | 0.011 | 0.000 | 0.000 | 0.009 | 0.000 | 0.011 |
| CaO | 0.009 | 3.122 | 0.012 | 3.433 | 3.322 | 0.010 | 3.522 | 0.000 |
| $Na_2O$ | 0.376 | 9.904 | 0.365 | 9.455 | 9.600 | 0.344 | 9.455 | 0.355 |
| $K_2O$ | 16.100 | 0.143 | 16.094 | 0.134 | 0.155 | 16.101 | 0.213 | 16.045 |
| $Rb_2O$ | 0.010 | 0.000 | 0.010 | 0.000 | 0.000 | 0.011 | 0.000 | 0.012 |
| **Total** | 99.735 | 99.957 | 99.742 | 99.701 | 99.774 | 99.723 | 99.921 | 99.692 |
| *apfu* | | | | | | | | |
| K | 0.951 | 0.008 | 0.950 | 0.008 | 0.009 | 0.951 | 0.012 | 0.947 |
| Na | 0.034 | 0.847 | 0.033 | 0.810 | 0.822 | 0.031 | 0.809 | 0.032 |
| Ca | 0.000 | 0.147 | 0.001 | 0.162 | 0.157 | 0.000 | 0.166 | 0.000 |
| Rb | 0.000 | 0.000 | 0.000 | 0.000 | 0.000 | 0.000 | 0.000 | 0.000 |
| **Σ X-site** | 0.985 | 1.002 | 0.984 | 0.980 | 0.988 | 0.982 | 0.987 | 0.980 |
| Al | 1.005 | 1.000 | 1.006 | 1.000 | 1.000 | 1.006 | 1.000 | 1.007 |
| Fe | 0.000 | 0.000 | 0.000 | 0.000 | 0.000 | 0.000 | | |
| **Σ Y-site** | 1.005 | 1.000 | 1.006 | 1.000 | 1.000 | 1.006 | 1.000 | 1.007 |
| Si | 2.999 | 2.852 | 2.999 | 2.851 | 2.852 | 2.999 | 2.848 | 2.999 |
| Ti | 0.001 | 0.000 | 0.000 | 0.000 | 0.000 | 0.000 | 0.000 | 0.000 |
| P | 0.000 | 0.000 | 0.000 | 0.000 | 0.000 | 0.000 | 0.000 | 0.000 |
| Al | 0.000 | 0.148 | 0.000 | 0.151 | 0.149 | 0.000 | 0.151 | 0.000 |
| **Σ Z-site** | 2.999 | 3.000 | 2.999 | 3.002 | 3.001 | 2.999 | 2.999 | 2.999 |

Table 54 Representative EMP analyses of plagioclase (albite). *Apfu* calculations based on 8 oxygens.

GARNET

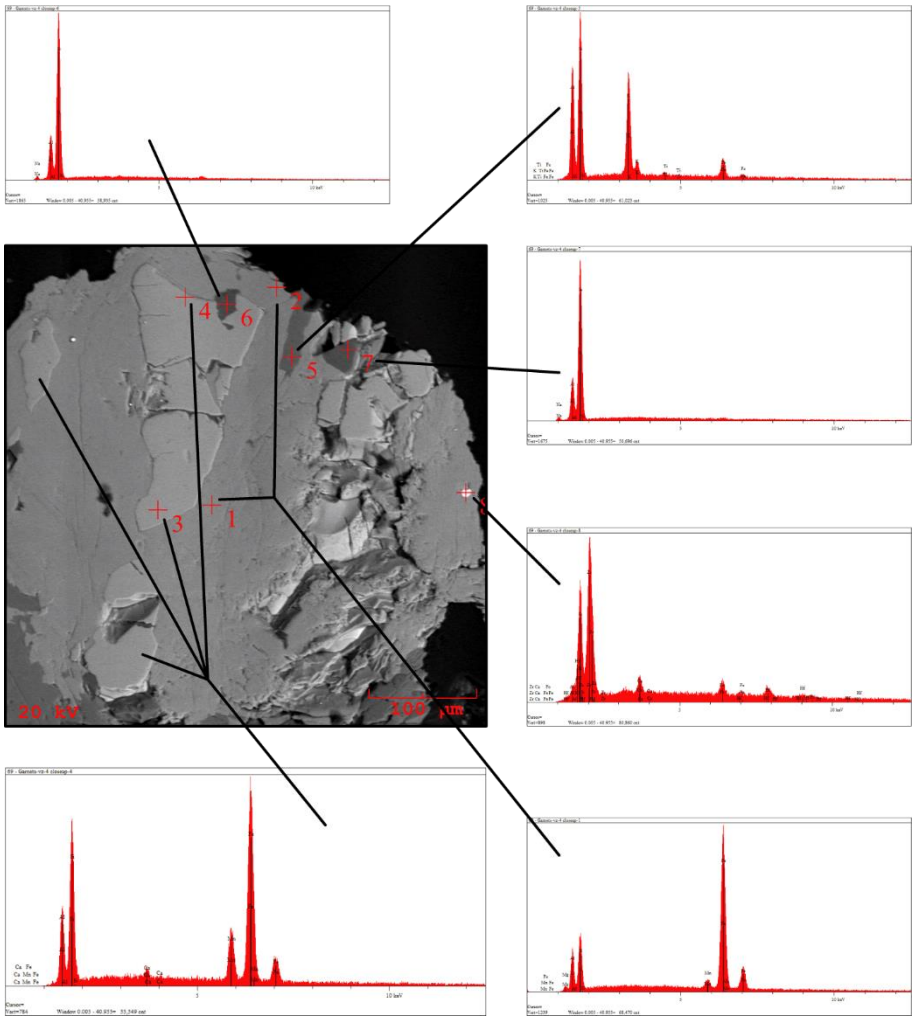


Figure 115 BSE image of Type 1 garnet with fractures and inclusions along withassociated spectra.

Garnets from Hwy69 are of two types. The first are typified by being sub- to anhedral in appearance. These garnets contain fractures and have inclusions. Most of the garnets of the Type 1 (Figure 116) have weight percent totals equaling less than 100 percent suggesting that there has been some alteration that has occurred. The second type are eu- to subhedral. This second type appears to have been fractured and the original garnet replaced or altered. This alteration/replacement region has a lower spessartine component and higher almandine

component than the original/primary garnet. The grossular and pyrope components fluctuate as well, although not to the same degree as the range in spessartine and almandine. The portions of the grains supposed to be the original garnet have weight percent totals very close to 100 percent; alteration/replacement areas have weight percent totals near 96-97 percent, supporting the notion of some type of alteration/replacement. In addition to the geochemical characteristics, the original area of the grains appear to be more resistant to polishing and have some amount of beveled relief to the replaced/altered portions giving grains of the second type an "island" texture. These islands that represent remnant garnets, range in size, shape, and number. Additionally, what is curious about this second type, is that both altered/replaced and original garnet chemistry are homogeneous in texture and geochemistry. Meaning that there appears to be very little to no zonation in composition of the original garnet chemistry within a single grain, regardless of which remnant "island" is investigated and a similar trend is seen as well in the replaced/altered portion within a single grain. Tables 55 and 56 list the representative garnet analyses. Additional analyses are listed in Tables 91 and 92 of the appendices.

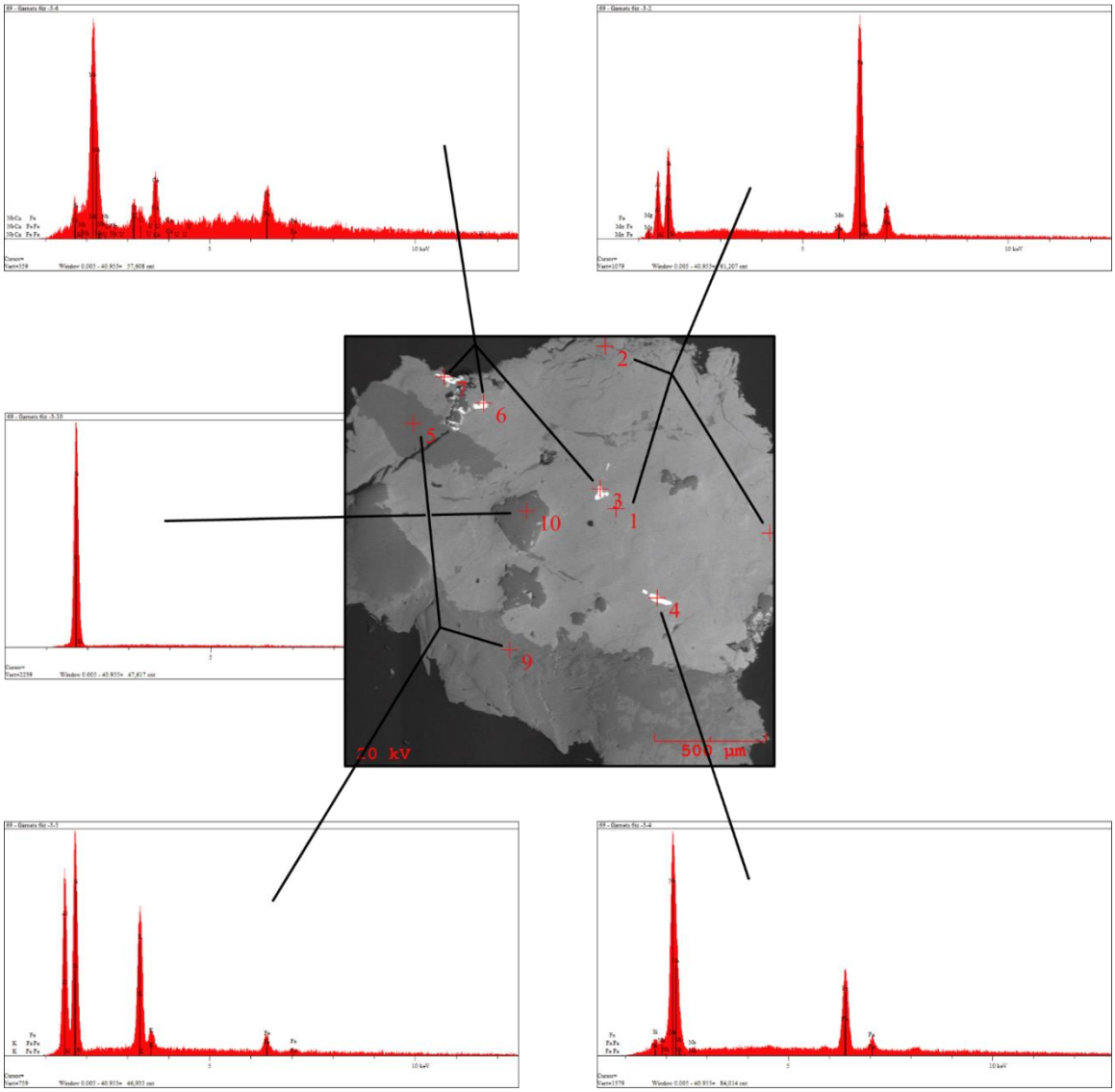


Figure 116  BSE image of Type 1 garnet with inclusions along with corresponding EDS spectra.

| GARNETS TYPE 1 – HWY69 | | | | | | | | | |
|---|---|---|---|---|---|---|---|---|---|
| Wt % Ox | Grain 1-1 | Grain 2-1 | Grain 3-1 | Grain 4-1 | Grain 5-1 | grain6-1 | | grain7-1 | |
| $SiO_2$ | 36.565 | 36.455 | 36.344 | 36.400 | 36.512 | 36.534 | 36.445 | 36.433 | 36.377 |
| $TiO_2$ | 0.032 | 0.019 | 0.011 | 0.020 | 0.018 | 0.015 | 0.009 | 0.024 | 0.009 |
| $Al_2O_3$ | 20.077 | 20.005 | 19.956 | 20.109 | 20.200 | 20.066 | 20.100 | 20.111 | 20.089 |
| FeO | 38.049 | 37.800 | 37.878 | 37.654 | 37.723 | 37.344 | 33.421 | 37.565 | 33.112 |
| MnO | 0.899 | 0.983 | 0.923 | 1.023 | 0.892 | 1.433 | 8.676 | 0.984 | 9.022 |
| MgO | 0.788 | 0.844 | 0.755 | 0.723 | 0.752 | 0.712 | 0.554 | 0.743 | 0.455 |
| CaO | 0.676 | 0.888 | 0.845 | 0.834 | 0.840 | 0.766 | 0.751 | 0.785 | 0.855 |
| **Total** | 97.086 | 96.994 | 96.712 | 96.763 | 96.937 | 96.870 | 100.013 | 96.645 | 99.978 |
| *apfu* | | | | | | | | | |
| Ti | 0.004 | 0.002 | 0.001 | 0.003 | 0.002 | 0.002 | 0.001 | 0.003 | 0.001 |
| Fe | 2.718 | 2.694 | 2.711 | 2.703 | 2.706 | 2.678 | 2.272 | 2.703 | 2.252 |
| Mn | 0.064 | 0.070 | 0.066 | 0.073 | 0.063 | 0.102 | 0.607 | 0.070 | 0.632 |
| Mg | 0.098 | 0.106 | 0.095 | 0.091 | 0.094 | 0.089 | 0.068 | 0.093 | 0.056 |
| Ca | 0.061 | 0.080 | 0.076 | 0.075 | 0.075 | 0.069 | 0.066 | 0.071 | 0.076 |
| **Σ X-site** | 2.945 | 2.942 | 2.949 | 2.945 | 2.940 | 2.940 | 3.014 | 2.940 | 3.017 |
| Al | 1.984 | 1.979 | 1.981 | 1.993 | 1.997 | 1.986 | 1.956 | 1.994 | 1.957 |
| **Σ Y-site** | 1.984 | 1.979 | 1.981 | 1.993 | 1.997 | 1.986 | 1.956 | 1.994 | 1.957 |
| Si | 3.065 | 3.060 | 3.061 | 3.061 | 3.062 | 3.068 | 3.008 | 3.065 | 3.006 |
| **Σ Z-site** | 3.065 | 3.060 | 3.061 | 3.061 | 3.062 | 3.068 | 3.008 | 3.065 | 3.006 |
| **Component** | | | | | | | | | |
| Andradite | 00 | 00 | 00 | 00 | 00 | 00 | 02 | 00 | 02 |
| Pyrope | 03 | 04 | 03 | 03 | 03 | 03 | 02 | 03 | 02 |
| Spessartine | 02 | 02 | 02 | 02 | 02 | 04 | 20 | 03 | 21 |
| Grossular | 02 | 03 | 03 | 03 | 03 | 02 | 01 | 02 | 01 |
| Almandine | 93 | 91 | 92 | 92 | 92 | 91 | 75 | 92 | 74 |

Table 55 Representative EMP analyses of Type 1 garnet. *Apfu* calculations based on 12 oxygens. Components are normalized to 100.

| GARNETS TYPE 2 – HWY69 | | | | | | | | |
|---|---|---|---|---|---|---|---|---|
| Wt % Ox | Grain 4-1 | | grain 5-1 | | grain 6-1 | | grain 7-1 | |
| $SiO_2$ | 36.333 | 36.265 | 36.554 | 36.523 | 36.588 | 36.620 | 36.555 | 36.612 |
| $TiO_2$ | 0.014 | 0.025 | 0.020 | 0.013 | 0.014 | 0.031 | 0.025 | 0.015 |
| $Al_2O_3$ | 20.110 | 19.981 | 20.140 | 20.112 | 20.144 | 20.092 | 20.000 | 20.044 |
| FeO | 34.544 | 37.640 | 37.555 | 34.430 | 34.510 | 37.554 | 34.551 | 37.476 |
| MnO | 6.895 | 0.944 | 1.101 | 6.445 | 6.500 | 1.211 | 6.488 | 1.311 |
| MgO | 0.676 | 0.766 | 0.800 | 0.644 | 0.595 | 0.822 | 0.544 | 0.809 |
| CaO | 0.740 | 0.899 | 0.844 | 0.894 | 0.900 | 0.855 | 0.783 | 0.822 |
| **Total** | 99.349 | 96.520 | 97.014 | 99.073 | 99.263 | 97.185 | 98.957 | 97.089 |
| *apfu* | | | | | | | | |
| Ti | 0.001 | 0.002 | 0.001 | 0.001 | 0.001 | 0.002 | 0.002 | 0.001 |
| Fe | 2.395 | 2.655 | 2.632 | 2.386 | 2.388 | 2.629 | 2.399 | 2.626 |
| Mn | 0.484 | 0.067 | 0.078 | 0.452 | 0.456 | 0.086 | 0.456 | 0.093 |
| Mg | 0.084 | 0.096 | 0.100 | 0.080 | 0.073 | 0.103 | 0.067 | 0.101 |
| Ca | 0.066 | 0.081 | 0.076 | 0.079 | 0.080 | 0.077 | 0.070 | 0.074 |
| **Σ X-site** | 3.030 | 2.901 | 2.887 | 2.998 | 2.998 | 2.897 | 2.994 | 2.895 |
| Al | 1.965 | 1.986 | 1.990 | 1.965 | 1.965 | 1.982 | 1.957 | 1.979 |
| **Σ Y-site** | 1.965 | 1.986 | 1.990 | 1.965 | 1.965 | 1.982 | 1.957 | 1.979 |
| Si | 3.012 | 3.059 | 3.064 | 3.027 | 3.027 | 3.065 | 3.035 | 3.068 |
| **Σ Z-site** | 3.012 | 3.059 | 3.064 | 3.027 | 3.027 | 3.065 | 3.035 | 3.068 |
| **Component** | | | | | | | | |
| Andradite | 01 | 00 | 00 | 01 | 01 | 00 | 01 | 00 |
| Pyrope | 03 | 03 | 03 | 03 | 03 | 03 | 02 | 03 |
| Spessartine | 16 | 02 | 03 | 15 | 15 | 03 | 15 | 03 |
| Grossular | 01 | 03 | 03 | 02 | 02 | 03 | 02 | 03 |
| Almandine | 79 | 92 | 91 | 79 | 79 | 91 | 80 | 91 |

Table 56 Representative EMP analyses of Type 2 garnets. *Apfu* calculations based on 12 oxygens.

## ILMENITE

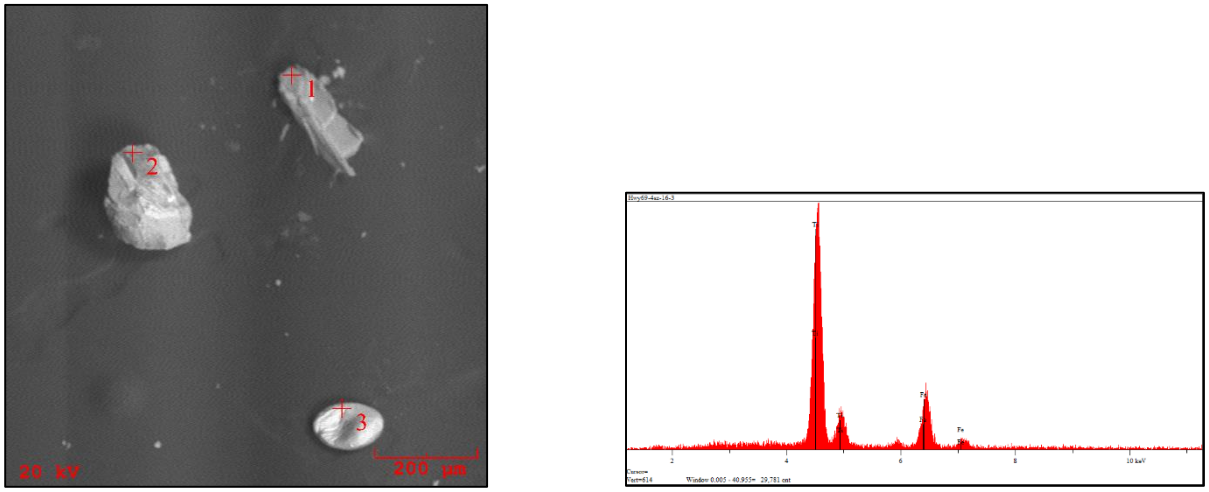


Figure 117 BSE image of ilmenite grain (crosshair 3) with EDS spectrum. Mica (crosshair 1) & garnet (crosshair 2).

Ilmenite has been discovered in heavy mineral separations while qualitatively investigating grains by SEM. The EDS spectrum (Figure 117) corresponds to the grain on the lower right in the BSE image (left; crosshair 3).

## "MONAZITE"

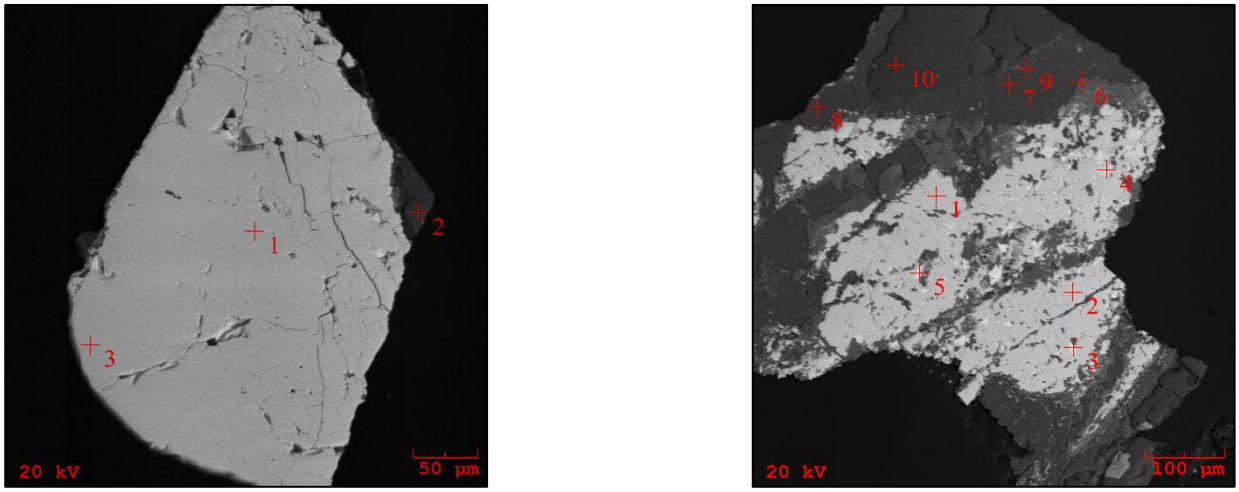


Figure 118 BSE images of unaltered (left) and altered (right) "monazite" grains. Left grain: "monazite" (crosshairs 1 & 3) and mica (crosshair 2). See Figure 119 for associated spectra for right grain.

"Monazite" has been identified by SEM and confirmed by microprobe. The BSE images in Figure 118 show the range of grain textures and crystal faces present in two of the grains analyzed. The first BSE image (left) is sub- to euhedral and the BSE image of the grain on the right is anhedral. The grain on the right has numerous inclusions of a thorium-rich phosphate. The grain on the left is free of inclusions and it appears to lack zonation. Based on X-site cation dominance, all of the grains analyzed should be classified as monazite-(Ce). Although, to note, that the inclusions within the grain (right) have a thorium weight percent of close to 20% as opposed to the other analyses that yielded thorium weight percentages ranging between three and seven percent. There is also an elevation of calcium weight percent in the areas of the grain that have elevated amounts of thorium, as these two elements often form a coupled substitution to satisfy charge balances in "monazites". Table 57 lists the representative monazite-(Ce) analyses.

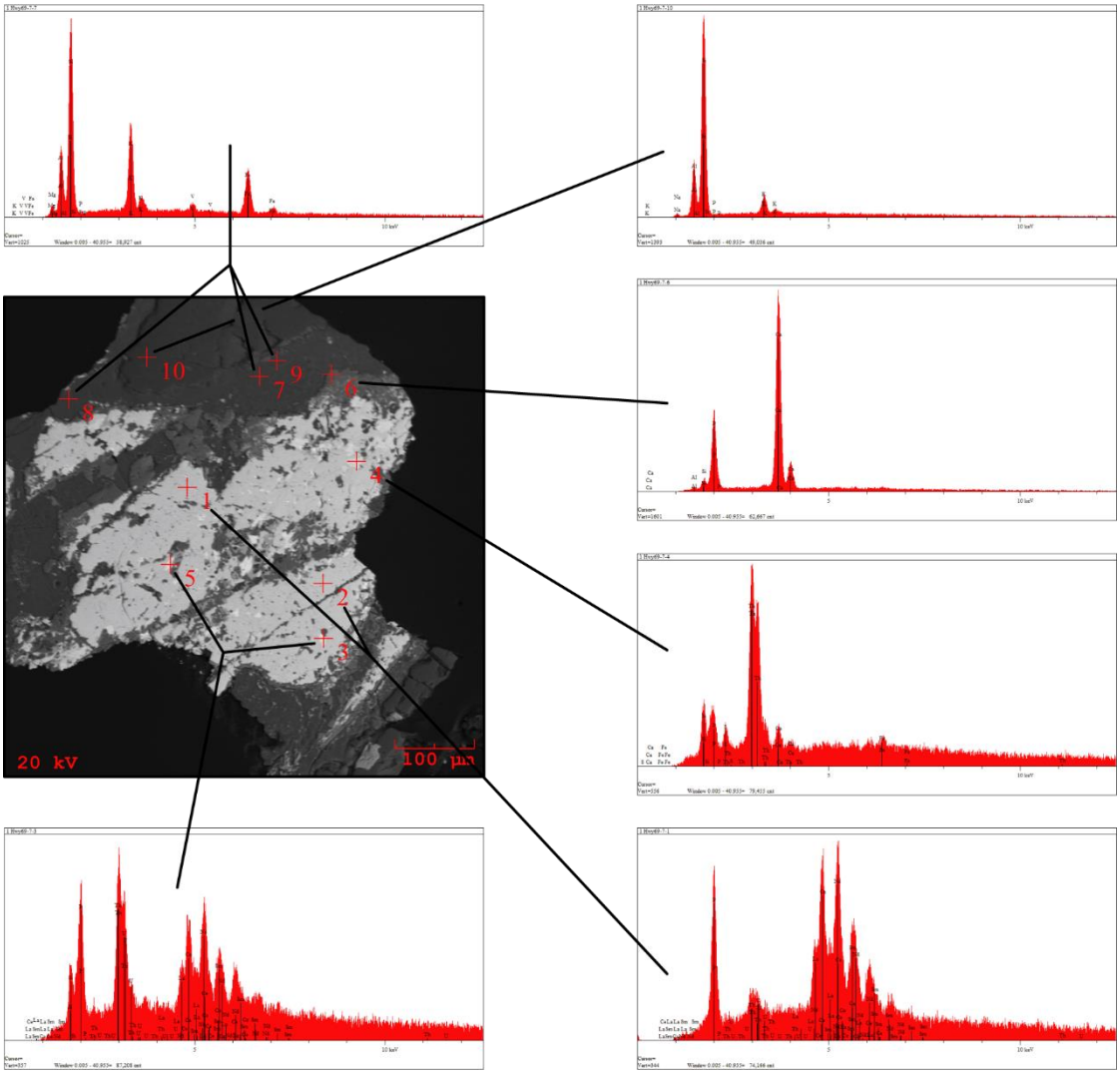


Figure 119  BSE image of right grain in Figure 118 along with associated spectra.

| MONAZITE-(CE) – HWY69 PEGMATITE | | | |
|---|---|---|---|
| Wt % Ox. | 1 hwy69-7-1 | | 2 hwy69-7-1 |
| $P_2O_5$ | 29.765 | 28.219 | 29.454 |
| $SiO_2$ | 0.211 | 0.187 | 0.244 |
| $TiO_2$ | 0.000 | 0.000 | 0.000 |
| $ThO_2$ | 3.775 | 19.221 | 6.554 |
| $UO_2$ | 0.445 | 0.389 | 1.223 |
| $Al_2O_3$ | 0.076 | 0.055 | 0.060 |
| $La_2O_3$ | 13.433 | 6.543 | 12.344 |
| $Ce_2O_3$ | 28.554 | 20.544 | 27.115 |
| $Pr_2O_3$ | 2.452 | 2.009 | 2.654 |
| $Nd_2O_3$ | 14.765 | 12.633 | 14.551 |
| $Sm_2O_3$ | 1.556 | 1.765 | 1.091 |
| $Eu_2O_3$ | 0.009 | 0.008 | 0.010 |
| $Gd_2O_3$ | 0.676 | 0.854 | 0.566 |
| $Dy_2O_3$ | 0.334 | 0.393 | 0.255 |
| Er2O3 | *bdl* | *bdl* | *bdl* |
| $Yb_2O_3$ | 0.023 | 0.000 | 0.020 |
| $Y_2O_3$ | 0.677 | 0.788 | 0.744 |
| $Sc_2O_3$ | 0.030 | 0.224 | 0.053 |
| MgO | 0.045 | 0.043 | 0.020 |
| CaO | 2.654 | 3.788 | 2.090 |
| MnO | 0.066 | 0.054 | 0.033 |
| FeO | 0.221 | 0.422 | 0.245 |
| PbO | 0.122 | 0.876 | 0.233 |
| **Total** | 99.889 | 99.015 | 99.559 |
| *apfu* | | | |
| Th | 0.033 | 0.177 | 0.059 |
| U | 0.004 | 0.003 | 0.011 |
| Al | 0.003 | 0.003 | 0.003 |
| La | 0.193 | 0.097 | 0.179 |
| Ce | 0.406 | 0.304 | 0.391 |
| Pr | 0.035 | 0.030 | 0.038 |
| Nd | 0.205 | 0.182 | 0.205 |
| Sm | 0.021 | 0.025 | 0.015 |
| Eu | 0.000 | 0.000 | 0.000 |
| Gd | 0.009 | 0.011 | 0.007 |
| Dy | 0.004 | 0.005 | 0.003 |
| Y | 0.014 | 0.017 | 0.016 |
| Sc | 0.001 | 0.008 | 0.002 |
| Mg | 0.003 | 0.003 | 0.001 |
| Ca | 0.111 | 0.164 | 0.088 |
| Mn | 0.002 | 0.002 | 0.001 |
| Fe | 0.007 | 0.014 | 0.008 |
| Pb | 0.001 | 0.010 | 0.002 |
| **Σ X** | 1.052 | 1.053 | 1.029 |
| P | 0.979 | 0.964 | 0.981 |
| Si | 0.008 | 0.008 | 0.010 |
| **Σ Y** | 0.987 | 0.972 | 0.991 |

Table 57 Representative EMP analyses of monazite-(Ce). *Apfu* calculations based on 4 oxygens.

## MUSCOVITE

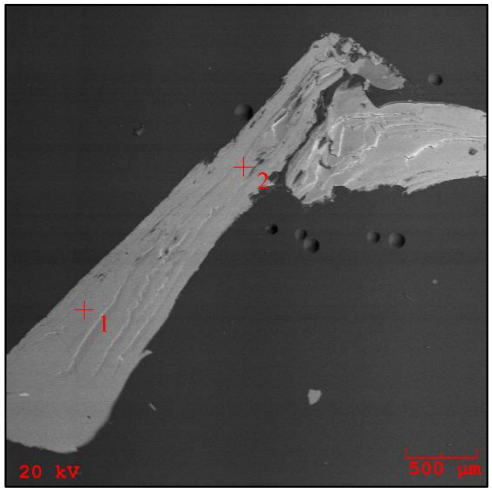


Figure 120 BSE image of polished muscovite mica grain.

Muscovite has been identified in heavy mineral separations, qualitatively investigated by SEM, and later confirmed by microprobe. Analyses reveal that grains are indeed muscovite, as defined by Tischendorf's (1997) mica classification scheme (Figure 185). Muscovite mica is far more common than biotite in Hwy69 samples. Muscovite has been analyzed by DCP for lithium content and is accounted for stoichiometrically by the equation 0.3935* fluorine weight percent$^{1.326}$ (Tischendorf, 1997). Calculated lithium content is higher than DCP results of 0.273 weight percent. Rubidium weight percent is either just within or below detection limits. Cesium is below detection limits. This suggests that muscovite micas from the Hwy69 pegmatite are rather poorly evolved. Table 58 lists the representative analyses.

| **MUSCOVITE – HWY69 PEGMATITE** | | | | | | |
|---|---|---|---|---|---|---|
| Wt % Ox. | 4sz-3-2 | .7.2-1 | .7.2-2 | .7.3-1 | iz-1-1 | iz-2-1 |
| $SiO_2$ | 46.165 | 45.998 | 45.896 | 45.799 | 46.009 | 45.985 |
| $TiO_2$ | 0.022 | 0.017 | 0.009 | 0.014 | 0.010 | 0.014 |
| $Al_2O_3$ | 32.127 | 33.977 | 34.009 | 34.223 | 34.277 | 34.533 |
| $Fe_2O_3$ | 0.000 | 0.000 | 0.000 | 0.000 | 0.000 | 0.000 |
| FeO | 2.544 | 2.009 | 2.332 | 2.111 | 2.002 | 2.033 |
| MnO | 0.211 | 0.132 | 0.113 | 0.092 | 0.098 | 0.093 |
| MgO | 1.322 | 1.225 | 1.344 | 1.540 | 1.233 | 1.091 |
| CaO | 0.033 | 0.055 | 0.065 | 0.070 | 0.056 | 0.042 |
| $Li_2O$ (*calc.*) | 0.513 | 0.470 | 0.384 | 0.470 | 0.431 | 0.447 |
| $Na_2O$ | 0.677 | 0.599 | 0.733 | 0.855 | 0.778 | 0.833 |
| $K_2O$ | 9.844 | 9.754 | 9.566 | 9.733 | 9.566 | 9.455 |
| $Rb_2O$ | 0.015 | 0.016 | 0.013 | 0.011 | 0.009 | 0.013 |
| $Cs_2O$ | *bdl* | *bdl* | *bdl* | *bdl* | *bdl* | *bdl* |
| F | 1.221 | 1.143 | 0.982 | 1.144 | 1.071 | 1.100 |
| $H_2O$ | 3.822 | 3.915 | 3.995 | 3.937 | 3.963 | 3.955 |
| F=O | - 0.514 | - 0.481 | - 0.413 | - 0.482 | - 0.451 | - 0.463 |
| **Total** | 98.001 | 98.829 | 99.027 | 99.517 | 99.052 | 99.130 |
| *apfu* | | | | | | |
| Si | 6.291 | 6.189 | 6.170 | 6.132 | 6.171 | 6.160 |
| $^{IV}Al$ | 1.709 | 1.811 | 1.830 | 1.868 | 1.829 | 1.840 |
| **Σ T-site** | 8.000 | 8.000 | 8.000 | 8.000 | 8.000 | 8.000 |
| $^{VI}Al$ | 3.451 | 3.576 | 3.559 | 3.532 | 3.590 | 3.612 |
| Ti | 0.002 | 0.002 | 0.001 | 0.001 | 0.001 | 0.001 |
| $Fe_t$ | 0.290 | 0.226 | 0.262 | 0.236 | 0.225 | 0.228 |
| Mn | 0.024 | 0.015 | 0.013 | 0.010 | 0.011 | 0.011 |
| Mg | 0.269 | 0.246 | 0.269 | 0.307 | 0.247 | 0.218 |
| Li (*calc.*) | 0.281 | 0.254 | 0.208 | 0.253 | 0.233 | 0.241 |
| **Σ Y-site** | 4.317 | 4.319 | 4.312 | 4.339 | 4.307 | 4.311 |

Table 58 Representative EMP analyses of muscovite mica. *Apfu* calculations based on 24 anions. Table continues on next page.

| | | | | | | |
|---|---|---|---|---|---|---|
| K | 1.711 | 1.674 | 1.641 | 1.662 | 1.637 | 1.616 |
| Ca | 0.005 | 0.008 | 0.009 | 0.010 | 0.008 | 0.006 |
| Na | 0.179 | 0.156 | 0.191 | 0.222 | 0.202 | 0.216 |
| Rb | 0.001 | 0.001 | 0.001 | 0.001 | 0.001 | 0.001 |
| Cs | *bdl* | *bdl* | *bdl* | *bdl* | *bdl* | *bdl* |
| **Σ X-site** | 1.896 | 1.839 | 1.842 | 1.895 | 1.848 | 1.839 |
| F | 0.526 | 0.486 | 0.418 | 0.484 | 0.454 | 0.466 |
| OH (*calc.*) | 3.474 | 3.514 | 3.582 | 3.516 | 3.546 | 3.534 |
| **Σ W-site** | 4.000 | 4.000 | 4.000 | 4.000 | 4.000 | 4.000 |

PYRITE

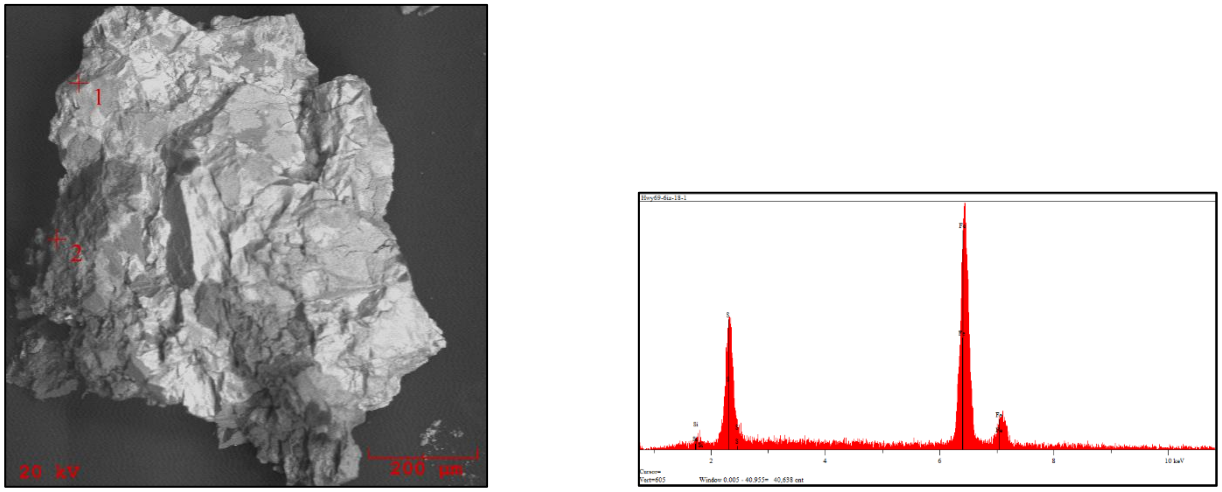


Figure 121  BSE image of pyrite grain with corresponding EDS spectrum.

Pyrite has been identified in heavy mineral separations and qualitatively analyzed by SEM.

## PYROCHLORE SUPERGROUP

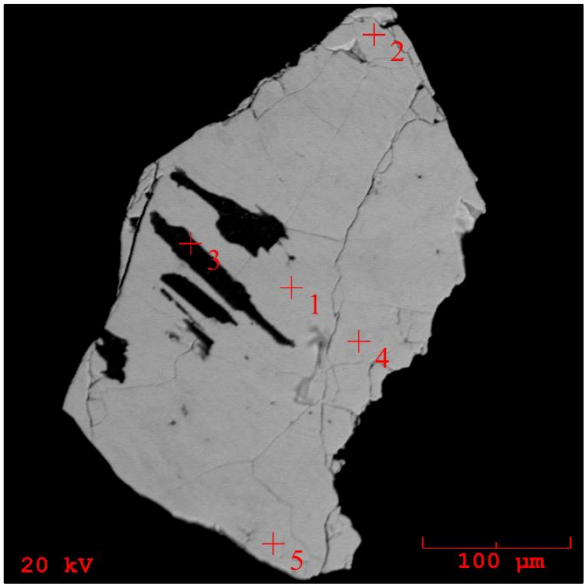


Figure 122 BSE image of pyrochlore (crosshairs 1, 2, 4, & 5) and K-feldspar (crosshair 3) inclusions from Hwy69.

A member of the pyrochlore supergroup has been quantitatively confirmed from Hwy69 samples. The grain has K-feldspar inclusions, but is otherwise geochemically homogeneous. Weight percent totals are very near 100%. The grain is subhedral. This sample is niobium dominant and based on oxygen and calcium dominance, classification should be oxycalciopyrochlore.

ZIRCON

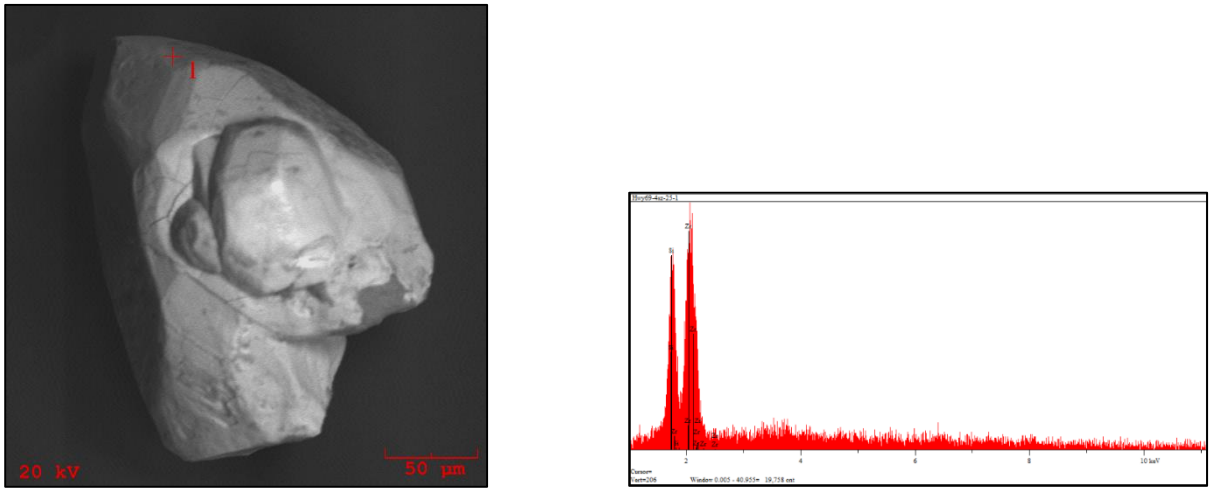


Figure 123 BSE image of zircon grain along with corresponding EDS spectrum.

Zircon has been identified in heavy mineral separations and qualitatively investigated by SEM. Zircon is uncommon in heavy mineral separations. Grains are small, being over just a couple of hundred microns. None have survived sample preparation for further microprobe analysis. SEM analyses have been unable to detect a hafnium, so the assumption is that zircon from the Hwy69 pegmatite is poorly evolved.

## STURGEON RIVER PEGMATITE

Figure 124 Field pictures of Sturgeon River pegmatite.

The Sturgeon River pegmatite has by far the largest exposure of any of the pegmatites visited. It is located in Dickinson County, Michigan. It is about six miles west of the Hwy69 pegmatite and just west of the North branch of the Sturgeon River. Visually, the Sturgeon River contains pink to orange colored feldspar, mica, black tourmaline, and quartz. The following minerals have been qualitatively and quantitatively identified by SEM and EMP: apatite, "bastnäsite", biotite, feldspar, fluorite, garnet, ilmenite, iron oxides, "monazite", muscovite mica, pyrite, rutile, tourmaline, uraninite, "xenotime", quartz, and zircon have been analyzed by SEM; fluorapatite, bastnäsite-(Ce), Fe-biotite, K-feldspar and plagioclase feldspar, garnet, ilmenite, monazite-(Ce), muscovite, rutile, and fluorschorl tourmaline have been quantitatively confirmed by microprobe.

## APATITE

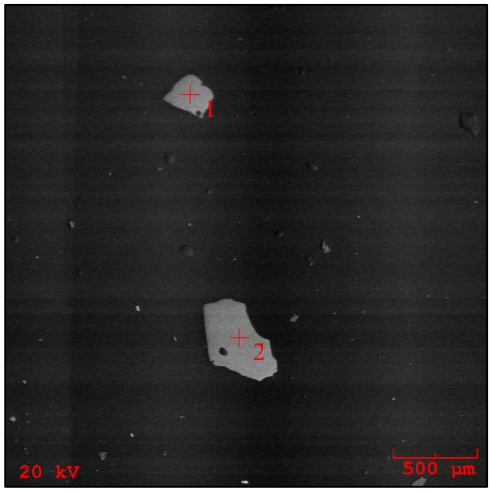


Figure 125 BSE image of polished apatite grains (1 & 2).

Apatite is relatively common at the Sturgeon River pegmatite. Grains are sub- to euhedral and lack visible zonation. Apatites are fluorine dominant and therefore classified as fluorapatite. Apatite has been discovered at Sturgeon River before; however, it is only qualitatively listed as the generic 'apatite'. This is the first set of analyses quantitatively identifying the mineral by its end-member nomenclature. Aside from "xenotime" and "monazite", apatite is the only accessory phosphate mineral at the Sturgeon River. Table 59 lists the representative analyses.

| **APATITE – GROVELAND MINE PEGMATITE** | | |
|---|---|---|
| Wt % Oxide | 2SR-1 | 2SR-2 |
| $P_2O_5$ | 42.210 | 42.156 |
| $SiO_2$ | 0.023 | 0.044 |
| $Al_2O_3$ | 0.000 | 0.021 |
| FeO | 0.000 | 0.008 |
| MnO | 0.000 | 0.009 |
| CaO | 55.610 | 55.675 |
| $H_20$ (*calc.*) | 0.402 | 0.353 |
| F | 2.892 | 3.001 |
| F=O | - 1.218 | - 1.264 |
| Total | 99.920 | 99.986 |
| *apfu* | | |
| Ca | 5.001 | 5.006 |
| Fe | 0.000 | 0.000 |
| **Σ X** | 5.001 | 5.006 |
| P | 2.999 | 2.995 |
| Si | 0.002 | 0.004 |
| Al | 0.000 | 0.002 |
| **Σ Y** | 3.001 | 3.001 |
| F | 0.768 | 0.796 |
| H (*calc.*) | 0.232 | 0.204 |
| **Σ W** | 1.000 | 1.000 |

Table 59 Representative EMP analyses of apatite.
*Apfu* calculations based on 13 anions.

## BASTNÄSITE

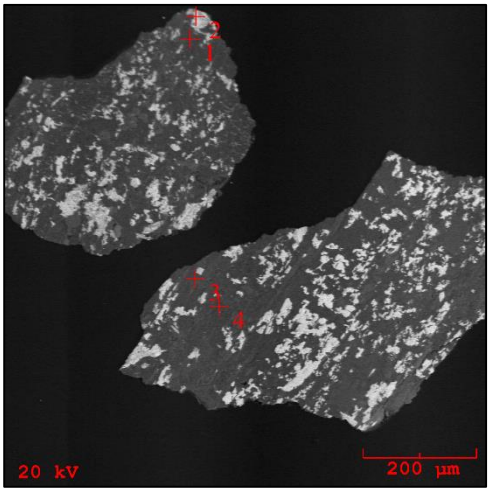


Figure 126 BSE image of polished grain with "bastnäsite".

"Bastnäsite" has been qualitatively investigated by SEM and confirmed via microprobe. "Bastnäsite" is a rare earth fluorocarbonate classified based on the dominance of yttrium, lanthanum, and cerium. Microprobe analyses reveal that cerium is the dominant cation, thus classification is bastnäsite-(Ce). No discrete grains of bastnäsite-(Ce) have been found, only inclusions in other grains. The above sample has a mottled appearance with mica and feldspar. This represents the first reported occurrence of bastnäsite-(Ce) at the Sturgeon River pegmatite. Bastnäsite-(Ce) is a rare earth element accessory mineral that has been found at the Sturgeon River in addition to "monazite" and "xenotime". Table 60 lists the representative analysis.

| **BASTNÄSITE – STURGEON RIVER PEGMATITE** | |
|---|---|
| Wt. % oxide | SR-1 |
| $P_2O_5$ | 0.232 |
| $SiO_2$ | 0.092 |
| $UO_2$ | 0.055 |
| $ThO_2$ | 5.565 |
| $Y_2O_3$ | 0.809 |
| $Al_2O_3$ | 0.088 |
| $La_2O_3$ | 15.223 |
| $Ce_2O_3$ | 29.766 |
| $Pr_2O_3$ | 2.530 |
| $Nd_2O_3$ | 15.445 |
| $Sc_2O_3$ | 0.044 |
| $Sm_2O_3$ | 1.122 |
| $Eu_2O_3$ | 0.000 |
| $Gd_2O_3$ | 0.500 |
| $Dy_2O_3$ | 0.176 |
| $Yb_2O_3$ | 0.029 |
| FeO | 0.332 |
| MnO | 0.033 |
| CaO | 2.665 |
| PbO | 0.022 |
| F | 6.850 |
| $CO_2$(calc) | 20.082 |
| $H_2O$ | 1.223 |
| **Sub-Total** | 102.883 |
| Ox. cor for F | 2.883 |
| **Total** | 100.000 |

Table 60 Representative EMP analyses for bastnäsite.
*Apfu* calculations based on 4 anions. Table continues on next page.

| *apfu* | |
|---|---|
| P | 0.007 |
| Si | 0.003 |
| U | 0.000 |
| Th | 0.046 |
| Y | 0.016 |
| Al | 0.004 |
| Fe | 0.000 |
| La | 0.205 |
| Ce | 0.397 |
| Pr | 0.034 |
| Nd | 0.201 |
| Sc | 0.001 |
| Sm | 0.014 |
| Eu | 0.000 |
| Gd | 0.006 |
| Dy | 0.002 |
| Yb | 0.000 |
| Fe | 0.010 |
| Mn | 0.001 |
| Ca | 0.104 |
| Pb | 0.000 |
| F | 0.790 |
| C | 1.000 |
| OH | 0.297 |
| **Σ REE** | 0.861 |
| **REE + Ca** | 0.965 |
| **Σ A Site** | 1.043 |

BIOTITE

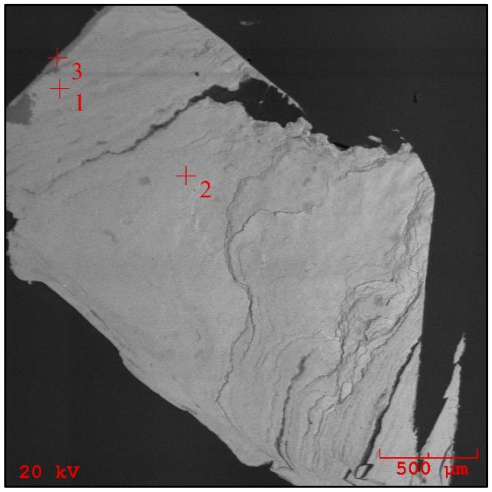


Figure 127 BSE image of polished biotite mica grain (1, 2, & 3).

Fe-biotite mica has been identified in heavy mineral separations, qualitatively analyzed by SEM, and confirmed by electron microprobe analysis as Fe-biotite based on Tischendorf's (1997) mica classification scheme (Figure 186). It has been further tested by DCP in order to determine lithium content. DCP analysis has revealed muscovite micas from the Sturgeon River pegmatite contain lithium and has been stoichiometrically accounted for in biotites based on the equation of Tischendorf (1997): 155 * magnesium weight percent$^{-3.1}$. Rubidium and cesium are both below detectable limits. Muscovite mica is currently listed as a mica species found at the Sturgeon River, but this is the first reported occurrence of biotite mica that has been quantitatively confirmed. The Sturgeon River pegmatite is in direct contact with a vein of biotite schist. Although this biotite has not been quantitatively confirmed by microprobe, SEM EDS spectral analyses reveal that this mica appears to be relatively more enriched in magnesium and depleted in iron, than the biotite from the pegmatite itself. Titration of biotite from schist reveal a FeO weight percent of 15.697, which is lower than biotite from pegmatite samples. Results from titration of pegmatite biotite yield 27.045 weight percent, a value in excess of microprobe

analysis. The difference in FeO content might be due to relatively higher magnesium content in SEM analyses. Table 61 lists the representative analysis. Only one analysis is listed due to equipment error when analyzing the other biotite mica grains.

| **BIOTITE – STURGEON RIVER PEGMATITE** | |
|---|---|
| Wt % Ox. | SR grain 2-1 |
| $SiO_2$ | 35.388 |
| $TiO_2$ | 2.776 |
| $Al_2O_3$ | 17.722 |
| $Fe_2O_3$ | 0.000 |
| FeO | 21.334 |
| MnO | 0.566 |
| MgO | 8.766 |
| CaO | 0.031 |
| $Li_2O$ (*calc.*) | 0.185 |
| $Na_2O$ | 0.221 |
| $K_2O$ | 9.457 |
| $Rb_2O$ | 0.000 |
| $Cs_2O$ | *bdl* |
| F | 0.966 |
| $H_2O$ | 3.476 |
| F=O | - 0.407 |
| **Total** | 100.481 |
| *apfu* | |
| Si | 5.394 |
| $^{IV}Al$ | 2.606 |
| **Σ T-site** | 8.000 |
| $^{VI}Al$ | 0.578 |
| Ti | 0.318 |
| $Fe_t$ | 2.720 |
| Mn | 0.073 |
| Mg | 1.992 |
| Li (*calc.*) | 0.114 |
| **Σ Y-site** | 5.795 |

Table 61 Representative EMP analyses of biotite mica. *Apfu* calculations based on 24 anions. Table continues on next page.

| | |
|---|---|
| K | 1.839 |
| Ca | 0.005 |
| Na | 0.065 |
| Rb | 0.000 |
| Cs | *bdl* |
| **Σ X-site** | 1.909 |
| F | 0.466 |
| OH* | 3.534 |
| **Σ W-site** | 4.000 |

## FELDSPARS

### K-FELDSPAR

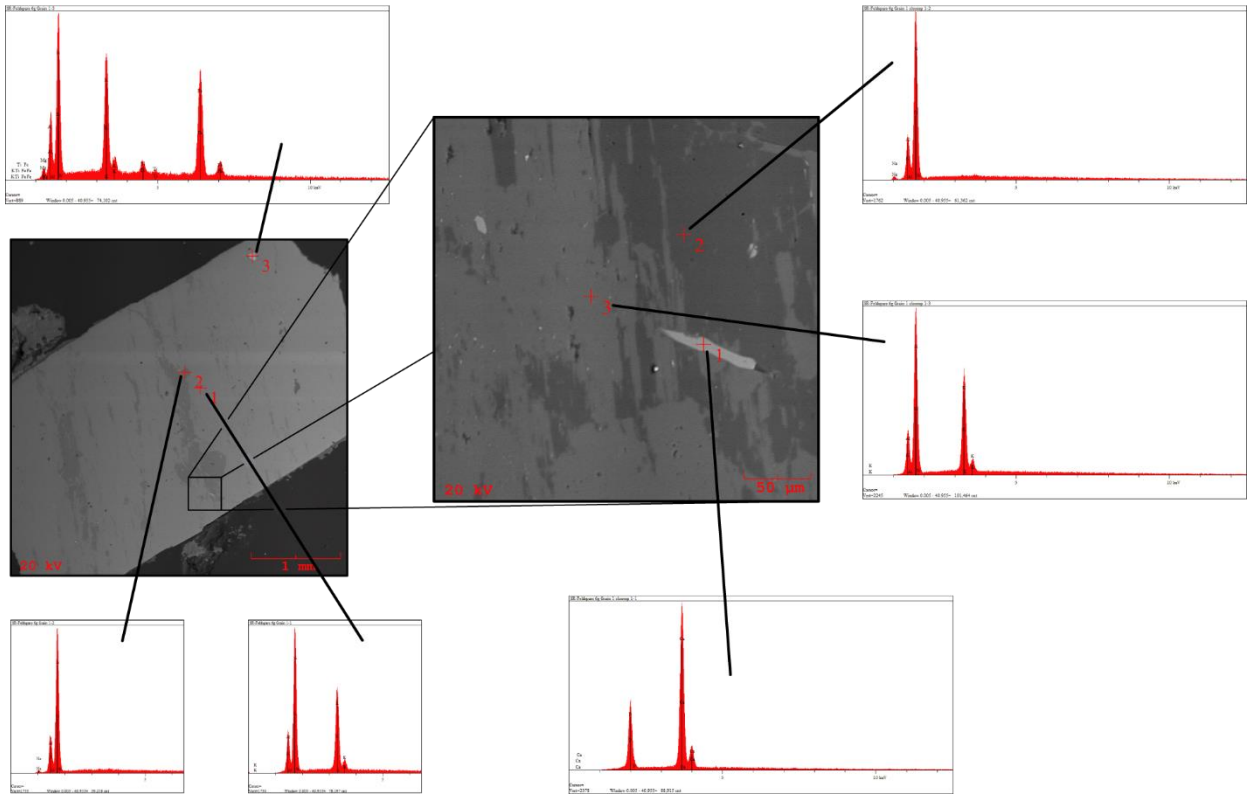


Figure 128 BSE image of polished K-feldspar grain with close-up. Associated EDS spectra are included.

K-Feldspar is present at the Sturgeon River pegmatite. The rubidium content in K-feldspar analyzed by microprobe is just within detection limits suggesting that K-feldspar at the Sturgeon River pegmatite is poorly evolved. Cesium, barium, and strontium are all below detectable limits. Grains have irregular blebs of plagioclase as well as occasional inclusions of apatite and biotite mica (Figure 128; BSE image left; crosshair 1). K-feldspar grains have been further analyzed by XRD and it has been determined that there is a large degree of structural ordering, therefore K-feldspar should be classified as microcline (Figure 173) (Wright & Stewart, 1968). Table 62 lists the representative microprobe analyses.

| K-FELDSPAR – STURGEON RIVER PEGMATITE | | | | | | | | |
|---|---|---|---|---|---|---|---|---|
| Wt% ox | 6c grain 1-1 | 6c grain 1-2 | 6c grain 2-1 | 6c grain 3-1 | 6g grain 1-1 | 6g grain 1-2 | 6g grain 2-1 | 6g grain 2-2 |
| $P_2O_5$ | *bdl* | *bdl* | *bdl* | *bdl* | *bdl* | *bdl* | *bdl* | *bdl* |
| $SiO_2$ | 64.672 | 64.711 | 64.699 | 64.700 | 64.833 | 69.055 | 64.799 | 68.889 |
| $TiO_2$ | 0.012 | 0.008 | 0.009 | 0.015 | 0.010 | 0.000 | 0.012 | 0.000 |
| $Al_2O_3$ | 18.383 | 18.391 | 18.373 | 18.341 | 18.341 | 19.566 | 18.355 | 19.499 |
| $FeO_t$ | 0.011 | 0.009 | 0.008 | 0.009 | 0.009 | 0.000 | 0.011 | 0.000 |
| CaO | 0.000 | 0.000 | 0.000 | 0.008 | 0.009 | 0.312 | 0.012 | 0.245 |
| $Na_2O$ | 0.454 | 0.393 | 0.434 | 0.393 | 0.595 | 10.871 | 0.494 | 10.982 |
| $K_2O$ | 16.222 | 16.181 | 16.181 | 16.282 | 15.985 | 0.233 | 16.112 | 0.233 |
| $Rb_2O$ | 0.014 | 0.015 | 0.016 | 0.020 | 0.011 | 0.000 | 0.013 | 0.000 |
| **Total** | 99.768 | 99.708 | 99.720 | 99.768 | 99.793 | 100.037 | 99.808 | 99.848 |
| *apfu* | | | | | | | | |
| K | 0.959 | 0.956 | 0.957 | 0.963 | 0.944 | 0.013 | 0.951 | 0.013 |
| Na | 0.041 | 0.035 | 0.039 | 0.035 | 0.053 | 0.918 | 0.044 | 0.929 |
| Ca | 0.000 | 0.000 | 0.000 | 0.000 | 0.000 | 0.015 | 0.001 | 0.011 |
| Rb | 0.000 | 0.000 | 0.000 | 0.001 | 0.000 | 0.000 | 0.000 | 0.000 |
| **Σ X-site** | 1.000 | 0.991 | 0.996 | 0.999 | 0.997 | 0.946 | 0.996 | 0.953 |
| Al | 1.004 | 1.004 | 1.003 | 1.002 | 1.000 | 1.004 | 1.001 | 1.003 |
| Fe | 0.000 | 0.000 | 0.000 | 0.000 | 0.000 | 0.000 | 0.000 | 0.000 |
| **Σ Y-site** | 1.004 | 1.004 | 1.003 | 1.002 | 1.000 | 1.004 | 1.001 | 1.003 |
| Si | 2.996 | 2.998 | 2.998 | 2.998 | 3.000 | 3.007 | 2.999 | 3.006 |
| Ti | 0.000 | 0.000 | 0.000 | 0.001 | 0.000 | 0.000 | 0.000 | 0.000 |
| P | 0.000 | 0.000 | 0.000 | 0.000 | 0.000 | 0.000 | 0.000 | 0.000 |
| Al | 0.000 | 0.000 | 0.000 | 0.000 | 0.000 | 0.000 | 0.000 | 0.000 |
| **Σ Z-site** | 2.996 | 2.998 | 2.998 | 2.999 | 3.000 | 3.007 | 2.999 | 3.006 |

Table 62 Representative EMP analyses of K-feldspar. *Apfu* calculated based on 8 oxygens.

PLAGIOCLASE FELDSPAR

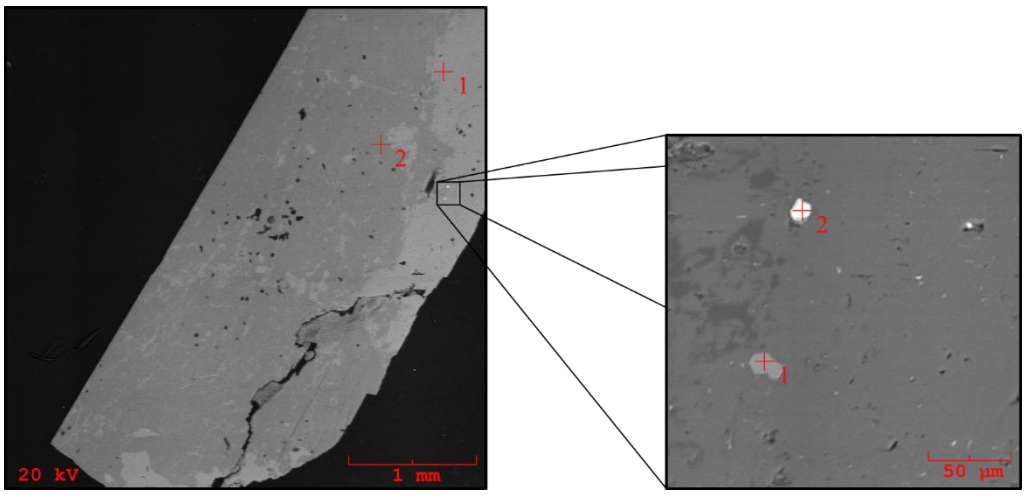


Figure 129 BSE images of plagioclase feldspar grain (left) with close-up (right). Plagioclase grain (left; crosshair 2), K-feldspar blebs (crosshair 1). Close-up (right): apatite (crosshair 1) & pyrite (crosshair 2).

Plagioclase feldspar is present in heavy mineral separations and has been further investigated by SEM as well as by electron microprobe. Plagioclase feldspar grains contain inclusions of Fe-rich mica, apatite, and pyrite. Plagioclase also have blebs as well as thin, irregularly shaped ribbons of K-feldspar. Rubidium, barium, and cesium are all below detectable limits. Table 63 lists the representative analyses.

| PLAGIOCLASE FELDSPAR – STURGEON RIVER PEGMATITE | | | | | | | | |
|---|---|---|---|---|---|---|---|---|
| Wt% ox | feldspar uncl-2-1 | feldspar uncl-2-2 | 1a grain 1-1 | 1a grain 1-2 | 1a grain 2-1 | 1a grain 2-2 | 6h grain 1-1 | 6h grain 1-2 |
| $P_2O_5$ | 0.013 | *bdl* | *bdl* | *bdl* | *bdl* | *bdl* | *bdl* | *bdl* |
| $SiO_2$ | 64.903 | 64.922 | 64.885 | 64.784 | 64.756 | 68.674 | 68.677 | 64.800 |
| $TiO_2$ | 0.017 | 0.013 | 0.008 | 0.011 | 0.014 | 0.000 | 0.000 | 0.008 |
| $Al_2O_3$ | 18.392 | 18.410 | 18.388 | 18.393 | 18.412 | 19.988 | 19.733 | 18.411 |
| $FeO_t$ | 0.011 | 0.014 | 0.011 | 0.014 | 0.009 | 0.000 | 0.000 | 0.009 |
| CaO | 0.009 | 0.000 | 0.000 | 0.000 | 0.000 | 0.971 | 0.487 | 0.000 |
| $Na_2O$ | 0.455 | 0.464 | 0.512 | 0.544 | 0.467 | 10.512 | 10.588 | 0.383 |
| $K_2O$ | 16.093 | 16.008 | 16.100 | 16.093 | 16.006 | 0.167 | 0.178 | 16.004 |
| $Rb_2O$ | 0.013 | 0.012 | 0.014 | 0.016 | 0.015 | 0.000 | 0.000 | 0.012 |
| **Total** | 99.906 | 99.843 | 99.931 | 99.869 | 99.679 | 100.312 | 99.663 | 99.627 |
| *apfu* | | | | | | | | |
| K | 0.949 | 0.944 | 0.949 | 0.950 | 0.946 | 0.009 | 0.010 | 0.946 |
| Na | 0.041 | 0.042 | 0.046 | 0.049 | 0.042 | 0.886 | 0.897 | 0.034 |
| Ca | 0.000 | 0.000 | 0.000 | 0.000 | 0.000 | 0.045 | 0.023 | 0.000 |
| Rb | 0.000 | 0.000 | 0.000 | 0.000 | 0.000 | 0.000 | 0.000 | 0.000 |
| **Σ X-site** | 0.990 | 0.986 | 0.995 | 0.999 | 0.988 | 0.940 | 0.930 | 0.980 |
| Al | 1.002 | 1.003 | 1.002 | 1.003 | 1.005 | 1.024 | 1.016 | 1.005 |
| Fe | 0.000 | 0.000 | 0.000 | 0.000 | 0.000 | 0.000 | 0.000 | 0.000 |
| **Σ Y-site** | 1.002 | 1.003 | 1.002 | 1.003 | 1.005 | 1.024 | 1.016 | 1.005 |
| Si | 2.999 | 3.001 | 2.999 | 2.997 | 2.999 | 2.985 | 3.000 | 3.001 |
| Ti | 0.001 | 0.000 | 0.000 | 0.000 | 0.000 | 0.000 | 0.000 | 0.000 |
| P | 0.001 | 0.000 | 0.000 | 0.000 | 0.000 | 0.000 | 0.000 | 0.000 |
| Al | 0.000 | 0.000 | 0.000 | 0.000 | 0.000 | 0.000 | 0.000 | 0.000 |
| **Σ Z-site** | 3.001 | 3.001 | 2.999 | 2.997 | 2.999 | 2.985 | 3.000 | 3.001 |

Table 63 Representative EMP analyses of plagioclase (albite). *Apfu* calculations based on 8 oxygens.

## FLUORITE

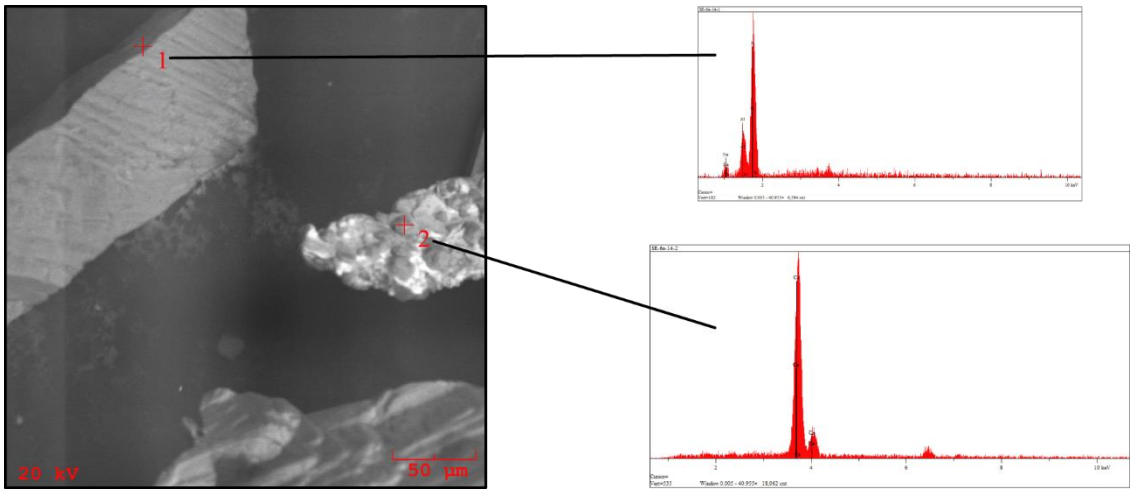


Figure 130 BSE image of fluorite grain. Lighter colored matrix is of undetermined chemistry. Bottom grain (right) is garnet.

Fluorite (crosshair 2) has been discovered in heavy mineral separations and qualitatively confirmed by SEM. Fluorite in heavy mineral separations is relatively rare at the Sturgeon River. This represents the first reported occurrence of fluorite at the Sturgeon River.

## GARNET

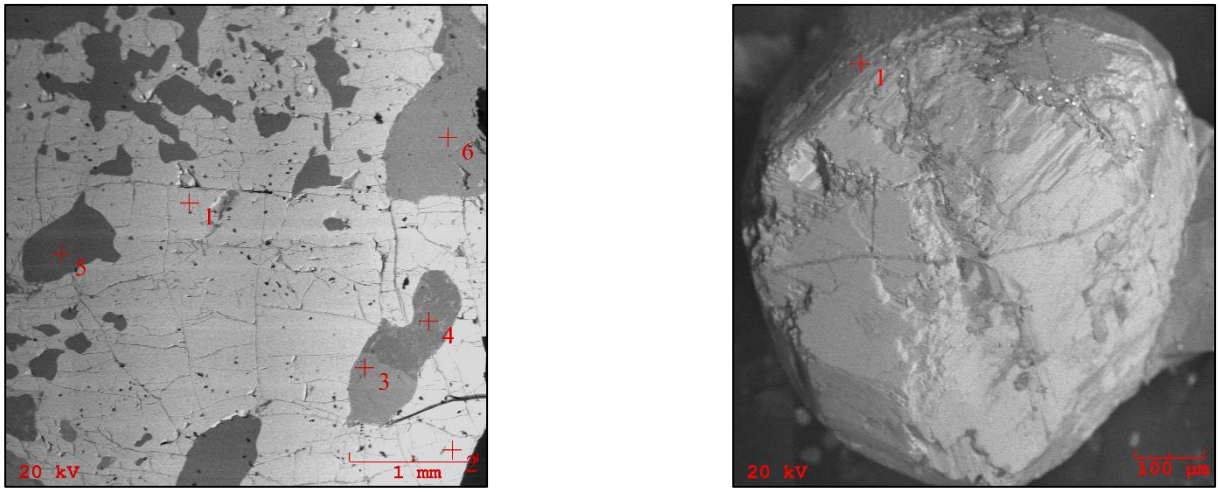


Figure 131 BSE image of polished garnet grain (left) with inclusions: Garnet (crosshairs 1 & 2), K-feldspar (crosshairs 3 & 6), plagioclase (crosshair 4), and quartz (crosshair 5). Unpolished garnet grain (right; crosshair 1).

Abundant garnet is found in heavy mineral separations. Garnets have been qualitatively analyzed by SEM and quantitatively confirmed by electron microprobe. Despite the lack of textural homogeneity, garnet from the Sturgeon River is surprisingly geochemically homogeneous from core to rim. All grains investigated have fractures, which have been subsequently filled, as well as numerous inclusions of quartz, muscovite mica, feldspar, zircon, and rare "monazite" and "xenotime". The fracture infills appear to be a member of the mica species. The almandine component in garnets ranges from 83-86% and the spessartine component 14-16%. The pyrope, andradite, and grossular components are either not present or below 01%. Table 64 lists the representative analyses. An X-ray map of elemental composition for a grain of garnet with an inclusion of "monazite" and quartz is shown (Figure 132) to illustrate the presence of fractures and associated inclusions. Additional analyses are listed in Tables 93, 94, and 95 of the appendices.

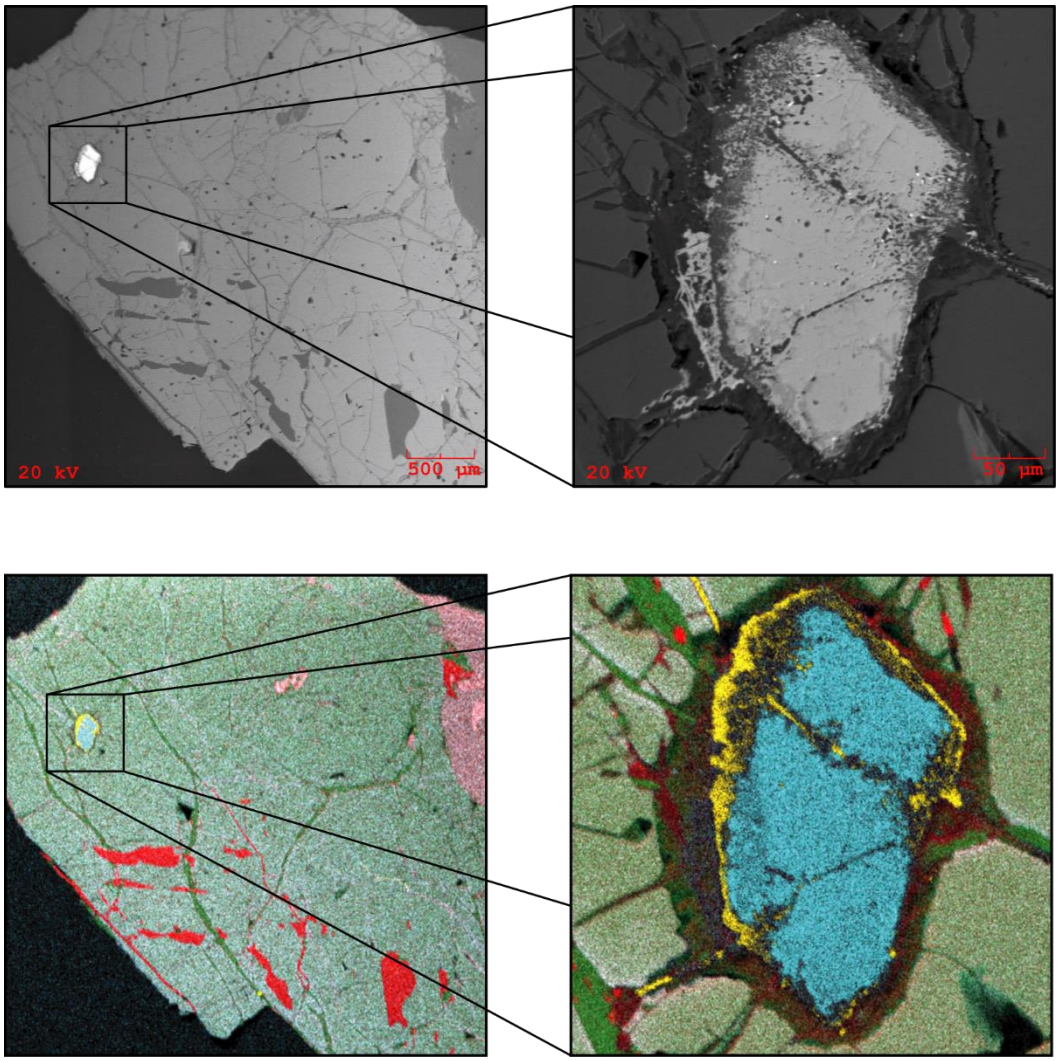


Figure 132 BSE image of garnet with "monazite" inclusion (above). X-ray map with elemental color overlay (below). Quartz (red), garnet (mottled light green), mica fracture infill (dark green), feldspar (mottled pink; upper right), apatite (yellow), & "monazite" (bright blue).

An X-ray map has been conducted to investigate homogeneity of a garnet grain. The above set of images in Figure 132 includes BSE images of a garnet grain with a close-up of a "monazite" inclusion. Quartz inclusions can be clearly seen (red) as well as the fracture infills of an Fe-rich mica species (darker green). The "monazite" in the close-up BSE image (bright blue) is suggested to be cerium dominant. The yellow rim surrounding most of the grain is apatite.

The uniform coloration illustrates the geochemical homogeneity of garnets found at the Sturgeon River.

| **GARNETS – STURGEON RIVER PEGMATITE** | | | | | | | |
|---|---|---|---|---|---|---|---|
| Wt % Ox | grain 1-2 | grain 2-1 | grain 3-1 | grain 4-1 | grain 5-1 | grain 6-1 | grain 7-1 |
| $SiO_2$ | 36.522 | 36.498 | 36.488 | 36.466 | 36.488 | 36.522 | 36.505 |
| $TiO_2$ | 0.009 | 0.011 | 0.008 | 0.009 | 0.009 | 0.013 | 0.021 |
| $Al_2O_3$ | 20.600 | 20.577 | 20.489 | 20.568 | 20.466 | 20.540 | 20.544 |
| FeO | 36.198 | 36.088 | 36.333 | 36.522 | 36.600 | 36.766 | 36.544 |
| MnO | 7.009 | 7.099 | 6.785 | 6.400 | 6.555 | 6.330 | 6.766 |
| MgO | 0.054 | 0.033 | 0.028 | 0.041 | 0.040 | 0.029 | 0.028 |
| CaO | 0.077 | 0.054 | 0.044 | 0.027 | 0.029 | 0.040 | 0.029 |
| **Total** | 100.469 | 100.360 | 100.175 | 100.033 | 100.187 | 100.240 | 100.437 |
| *apfu* | | | | | | | |
| Ti | 0.001 | 0.001 | 0.000 | 0.001 | 0.001 | 0.001 | 0.001 |
| Fe | 2.493 | 2.489 | 2.510 | 2.531 | 2.527 | 2.540 | 2.518 |
| Mn | 0.488 | 0.495 | 0.474 | 0.447 | 0.458 | 0.442 | 0.472 |
| Mg | 0.007 | 0.004 | 0.003 | 0.005 | 0.005 | 0.004 | 0.003 |
| Ca | 0.007 | 0.005 | 0.004 | 0.002 | 0.003 | 0.004 | 0.003 |
| **Σ X-site** | 2.996 | 2.994 | 2.991 | 2.986 | 2.994 | 2.991 | 2.997 |
| Al | 1.997 | 1.997 | 1.992 | 1.999 | 1.990 | 1.995 | 1.994 |
| **Σ Y-site** | 1.997 | 1.997 | 1.992 | 1.999 | 1.990 | 1.995 | 1.994 |
| Si | 3.004 | 3.005 | 3.010 | 3.007 | 3.010 | 3.009 | 3.006 |
| **Σ Z-site** | 3.004 | 3.005 | 3.010 | 3.007 | 3.010 | 3.009 | 3.006 |
| **Component** | | | | | | | |
| Pyrope | 00 | 00 | 00 | 00 | 00 | 00 | 00 |
| Spessartine | 16 | 17 | 16 | 15 | 15 | 15 | 16 |
| Grossular | 00 | 00 | 00 | 00 | 00 | 00 | 00 |
| Almandine | 84 | 83 | 84 | 85 | 85 | 85 | 84 |

Table 64 Representative EMP analyses of garnet. *Apfu* calculations based on 12 oxygens.

ILMENITE

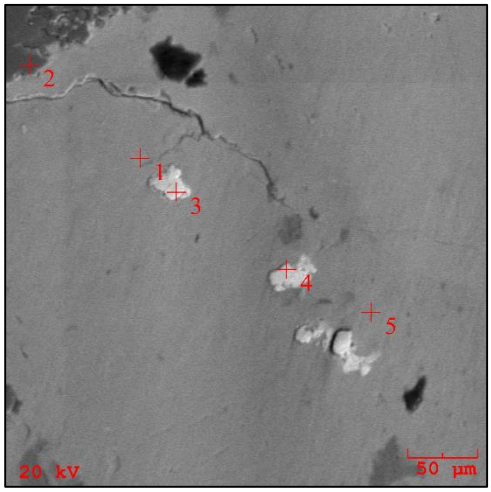


Figure 133 BSE image of ilmenite grain. Mica (crosshairs 1 & 5), quartz (crosshair 2), & ilmenite (crosshairs 3 & 4).

Ilmenite has been identified via SEM and confirmed by microprobe. Only a single discrete grain of ilmenite has been found in heavy mineral separations collected from the Sturgeon River pegmatite. Inclusions of ilmenite are found in mica grains (Figure 133). Table 65 lists the representative analysis. Weight percent totals are approximately 96% suggesting that there may be some alteration of the grain.

| **ILMENITE – STURGEON RIVER PEGMATITE** | |
|---|---|
| Wt% Oxide | SR grain 2-3 |
| $TiO_2$ | 50.099 |
| $Al_2O_3$ | 0.091 |
| $SiO_2$ | 0.055 |
| FeO | 42.433 |
| MnO | 2.988 |
| MgO | *bdl* |
| CaO | *bdl* |
| $Nb_2O_5$ | *bdl* |
| $Ta_2O_5$ | *bdl* |
| **Total** | 95.543 |
| *apfu* | |
| FeO | 1.021 |
| MnO | 0.160 |
| MgO | *bdl* |
| CaO | *bdl* |
| Nb | *bdl* |
| Ta | *bdl* |
| **Σ X-site** | 1.181 |
| Ti | 2.409 |
| Al | 0.002 |
| Si | 0.000 |
| **Σ Y-site** | 2.411 |

Table 65 Representative EMP analysis of ilmenite.
*Apfu* calculations based on 6 oxygens.

## IRON OXIDE

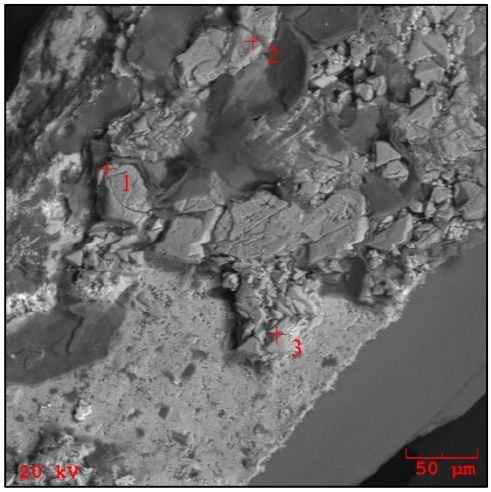


Figure 134 BSE image of iron oxide (crosshair 3) and feldspar (crosshairs 1 & 2).

Iron oxide (either hematite or magnetite) was present in heavy mineral separations and investigated by SEM.

## "MONAZITE"

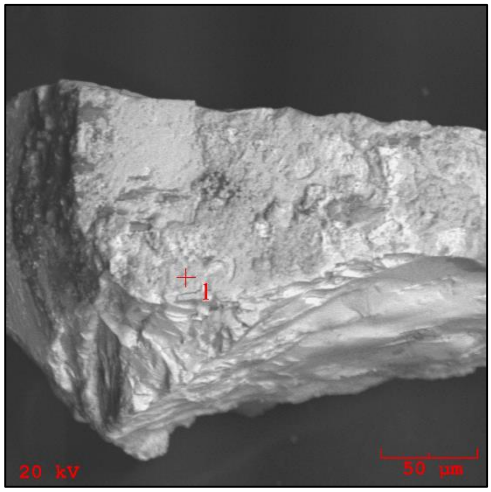


Figure 135 BSE image of "monazite" grain.

"Monazite" has been found as inclusions as well as discrete grains at the Sturgeon River pegmatite. "Monazite" has been qualitatively analyzed by SEM and confirmed by electron microprobe. Cerium is the dominant X-site cation, therefore classification is monazite-(Ce). Weight percent is near 99%, suggesting that only slight (if any) alteration has occurred with the analyzed grain. Other than apatite and "xenotime", monazite-(Ce) is the only accessory phosphate mineral. "Monazite" is relatively more common REE-bearing mineral than either "xenotime" or "bastnäsite" in samples. Both of the latter occur as rare inclusions. Table 66 lists the representative analysis.

| **MONAZITE-(CE) – STURGEON RIVER PEGMATITE** | |
|---|---|
| Wt % Ox. | 8 SR-2 |
| $P_2O_5$ | 29.166 |
| $SiO_2$ | 0.154 |
| $ThO_2$ | 0.000 |
| $UO_2$ | 5.895 |
| $Al_2O_3$ | 0.893 |
| $La_2O_3$ | 0.052 |
| $Ce_2O_3$ | 12.544 |
| $Pr_2O_3$ | 27.860 |
| $Nd_2O_3$ | 2.443 |
| $Sm_2O_3$ | 14.215 |
| $Gd_2O_3$ | 0.512 |
| $Dy_2O_3$ | 0.236 |
| $Yb_2O_3$ | 0.031 |
| $Y_2O_3$ | 0.677 |
| $Sc_2O_3$ | 0.022 |
| MgO | 0.032 |
| CaO | 2.245 |
| MnO | 0.031 |
| FeO | 0.322 |
| PbO | 0.182 |
| **Total** | 98.626 |
| *apfu* | |
| Th | 0.053 |
| U | 0.008 |
| Al | 0.002 |
| La | 0.184 |
| Ce | 0.405 |
| Pr | 0.035 |
| Nd | 0.202 |
| Sm | 0.015 |
| Y | 0.014 |
| Sc | 0.001 |
| Mg | 0.000 |
| Ca | 0.096 |
| Mn | 0.001 |
| Fe | 0.011 |
| **Σ X** | 1.041 |
| P | 0.981 |
| Si | 0.006 |
| **Σ Y** | 0.987 |

Table 66 Representative EMP analyses of monazite-(Ce).
*Apfu* calculations based on 4 oxygens.

MUSCOVITE

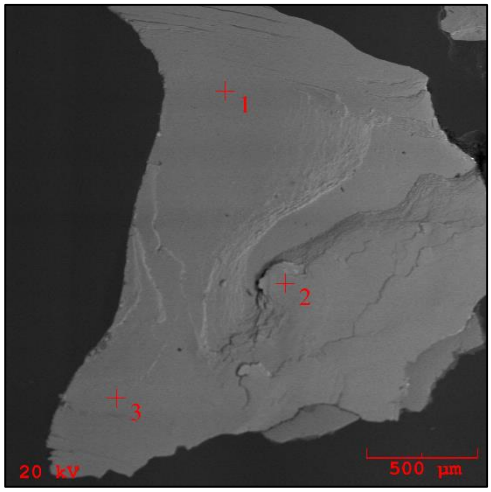


Figure 136 BSE image of polished muscovite mica grain (1, 2 & 3).

Muscovite mica has been identified in heavy mineral separations, qualitatively investigated, and confirmed as muscovite (Figure 185) by microprobe using Tischendorf's classification scheme of micas (1997). Muscovite mica has rubidium contents just within detectable limits. Cesium is below detection limits. DCP analyses reveal a lithium weight percent of 0.338 and 0.627 and as such, is stoichiometrically calculated for by the equation: 0.3935 * fluorine weight percent$^{1.326}$. Calculated lithium weight percent falls in between these two values. Table 67 lists the representative muscovite mica analyses.

| **MUSCOVITE – STURGEON RIVER PEGMATITE** | | | | | | | | | | |
|---|---|---|---|---|---|---|---|---|---|---|
| Wt % Ox. | SR mu 6g-1 | SR mu 6g-2 | SR mu 1a-1 | SR mu 1a-2 | grain 2-2 | grain 3-1 | grain 4-1 | grain 5-2 | grain 6-1 | grain 7-1 |
| $SiO_2$ | 44.974 | 44.906 | 44.877 | 44.9 | 45.784 | 45.788 | 45.644 | 46.077 | 45.778 | 45.800 |
| $TiO_2$ | 0.015 | 0.013 | 0.012 | 0.023 | 0.009 | 0.021 | 0.014 | 0.009 | 0.011 | 0.014 |
| $Al_2O_3$ | 31.945 | 31.677 | 32.001 | 31.891 | 34.099 | 34.533 | 34.668 | 34.336 | 34.655 | 34.745 |
| $Fe_2O_3$ | 0.000 | 0.000 | 0.000 | 0.000 | 0.000 | 0.000 | 0.000 | 0.000 | 0.000 | 0.000 |
| FeO | 3.224 | 3.399 | 3.114 | 3.500 | 2.899 | 1.999 | 1.891 | 2.112 | 2.009 | 1.651 |
| MnO | 0.655 | 0.587 | 0.544 | 0.443 | 0.077 | 0.093 | 0.100 | 0.092 | 0.143 | 0.114 |
| MgO | 1.332 | 1.544 | 1.5 | 1.734 | 1.122 | 0.761 | 0.671 | 0.722 | 0.687 | 0.633 |
| CaO | 0.177 | 0.212 | 0.225 | 0.167 | 0.055 | 0.071 | 0.121 | 0.088 | 0.072 | 0.078 |
| $Li_2O$ (*calc.*) | 0.442 | 0.455 | 0.514 | 0.455 | 0.384 | 0.454 | 0.382 | 0.411 | 0.446 | 0.457 |
| $Na_2O$ | 0.673 | 0.543 | 0.566 | 0.512 | 0.766 | 0.687 | 0.855 | 0.723 | 0.677 | 0.595 |
| $K_2O$ | 9.512 | 9.121 | 9.023 | 8.923 | 9.444 | 9.335 | 9.451 | 9.500 | 9.444 | 9.655 |
| $Rb_2O$ | 0.015 | 0.014 | 0.011 | 0.013 | 0.013 | 0.022 | 0.015 | 0.012 | 0.012 | 0.014 |
| $Cs_2O$ | *bdl* | *bdl* | *bdl* | *bdl* | *bdl* | *bdl* | *bdl* | *bdl* | *bdl* | *bdl* |
| F | 1.092 | 1.116 | 1.223 | 1.115 | 0.981 | 1.113 | 0.978 | 1.033 | 1.099 | 1.119 |
| $H_2O$ | 3.829 | 3.803 | 3.760 | 3.815 | 3.995 | 3.919 | 3.980 | 3.966 | 3.931 | 3.918 |
| F=O | - 0.460 | - 0.470 | - 0.515 | - 0.469 | - 0.413 | - 0.469 | - 0.412 | - 0.435 | - 0.463 | - 0.471 |
| **Total** | 97.425 | 96.921 | 96.855 | 97.021 | 99.214 | 98.327 | 98.358 | 98.646 | 98.501 | 98.322 |
| *apfu* | | | | | | | | | | |
| Si | 6.204 | 6.215 | 6.200 | 6.197 | 6.156 | 6.174 | 6.159 | 6.201 | 6.166 | 6.174 |
| $^{IV}Al$ | 1.796 | 1.785 | 1.800 | 1.803 | 1.844 | 1.826 | 1.841 | 1.799 | 1.834 | 1.826 |
| **Σ T-site** | 8.000 | 8.000 | 8.000 | 8.000 | 8.000 | 8.000 | 8.000 | 8.000 | 8.000 | 8.000 |
| $^{VI}Al$ | 3.398 | 3.382 | 3.412 | 3.386 | 3.559 | 3.662 | 3.674 | 3.647 | 3.668 | 3.694 |
| Ti | 0.002 | 0.001 | 0.001 | 0.002 | 0.001 | 0.002 | 0.001 | 0.001 | 0.001 | 0.001 |
| $Fe_t$ | 0.372 | 0.393 | 0.360 | 0.404 | 0.326 | 0.226 | 0.213 | 0.238 | 0.226 | 0.186 |
| Mn | 0.077 | 0.069 | 0.064 | 0.052 | 0.009 | 0.011 | 0.011 | 0.010 | 0.016 | 0.013 |
| Mg | 0.274 | 0.319 | 0.309 | 0.357 | 0.225 | 0.153 | 0.135 | 0.145 | 0.138 | 0.127 |
| Li (*calc.*) | 0.245 | 0.253 | 0.286 | 0.252 | 0.207 | 0.246 | 0.207 | 0.222 | 0.242 | 0.248 |
| **Σ Y-site** | 4.370 | 4.417 | 4.432 | 4.453 | 4.327 | 4.300 | 4.241 | 4.263 | 4.291 | 4.269 |

Table 67 Representative EMP analyses of muscovite mica. *Apfu* calculations based on 24 anions. Table continues on next page.

| | | | | | | | | | | |
|---|---|---|---|---|---|---|---|---|---|---|
| K | 1.674 | 1.610 | 1.590 | 1.571 | 1.620 | 1.606 | 1.627 | 1.631 | 1.623 | 1.660 |
| Ca | 0.026 | 0.031 | 0.033 | 0.025 | 0.008 | 0.010 | 0.017 | 0.013 | 0.010 | 0.011 |
| Na | 0.180 | 0.146 | 0.152 | 0.137 | 0.200 | 0.180 | 0.224 | 0.189 | 0.177 | 0.156 |
| Rb | 0.001 | 0.001 | 0.001 | 0.001 | 0.001 | 0.002 | 0.001 | 0.001 | 0.001 | 0.001 |
| Cs | *bdl* | *bdl* | *bdl* | *bdl* | *bdl* | *bdl* | *bdl* | *bdl* | *bdl* | *bdl* |
| **Σ X-site** | 1.881 | 1.788 | 1.776 | 1.734 | 1.829 | 1.798 | 1.869 | 1.834 | 1.811 | 1.828 |
| F | 0.476 | 0.488 | 0.534 | 0.487 | 0.417 | 0.475 | 0.417 | 0.440 | 0.468 | 0.477 |
| OH (*calc.*) | 3.524 | 3.512 | 3.465 | 3.513 | 3.583 | 3.525 | 3.583 | 3.560 | 3.532 | 3.523 |
| **Σ W-site** | 4.000 | 4.000 | 4.000 | 4.000 | 4.000 | 4.000 | 4.000 | 4.000 | 4.000 | 4.000 |

## PYRITE

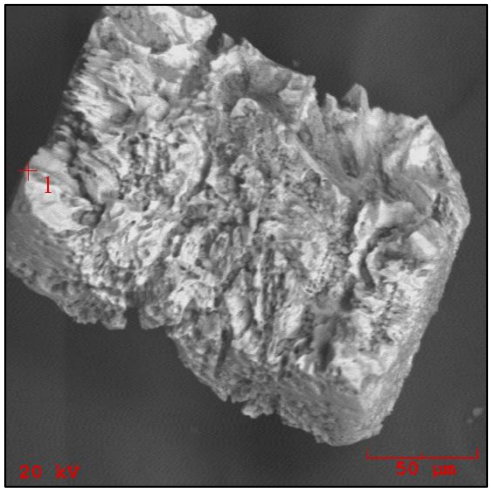


Figure 137 BSE image of pyrite grain (crosshair 1).

In addition to inclusions of pyrite in feldspar grains, discrete grains of pyrite have been found in heavy mineral separations. Grains have been qualitatively analyzed by SEM. Pyrite was relatively abundant at the Sturgeon River pegmatite.

## RUTILE

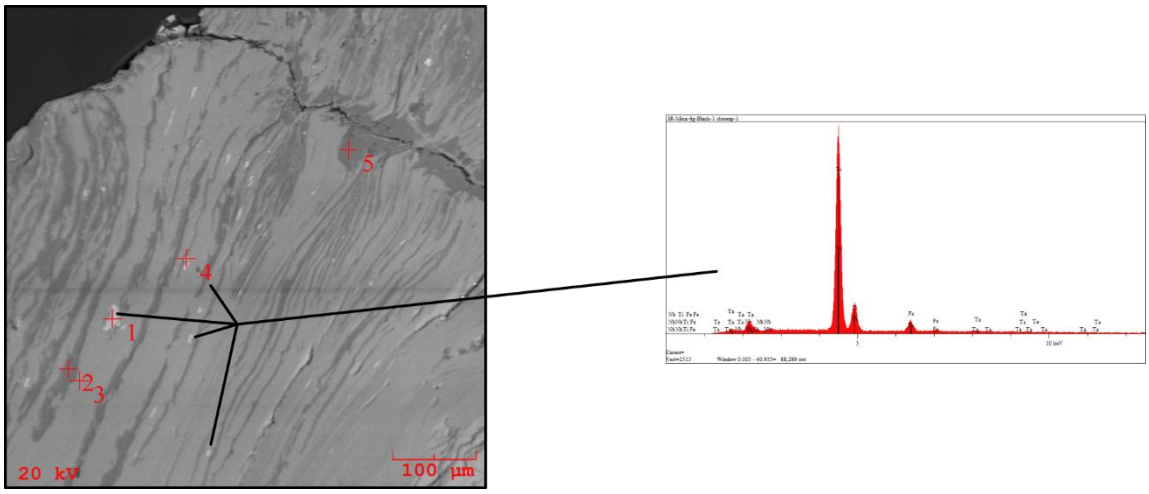


Figure 138 BSE image of mica grain with rutile inclusions along with associated spectrum. Muscovite mica (crosshairs 2 & 5) & biotite mica (crosshair 3).

Rutile at the Sturgeon River pegmatite consists of rare inclusions in mica and even rarer discrete grains. SEM analyses reveal a detectable amount of niobium in the sample. The single microprobe analysis however, lacks detectable amounts of niobium. Due to the stoichiometric quantity of iron, there is some doubt as to whether the microprobe analysis represents rutile at all and may in actuality be ilmenorutile instead. Table 68 lists this analysis.

| **RUTILE – REPUBLIC MINE PEGMATITE** | |
|---|---|
| Wt% Oxide | SR grain 2-4 |
| $TiO_2$ | 73.994 |
| $Al_2O3$ | 0.121 |
| FeO | 23.983 |
| MnO | 1.445 |
| MgO | 0.055 |
| CaO | 0.100 |
| $SiO_2$ | 0.000 |
| **Total** | 99.698 |
| *apfu* | |
| Ti | 0.839 |
| Al | 0.002 |
| Fe | 0.302 |
| Mn | 0.014 |
| Mg | 0.001 |
| Ca | 0.002 |
| Si | 0.000 |
| **Σ X-site** | 1.160 |

Table 68 Representative EMP analysis of rutile. *Apfu* calculations based on 2 oxygens.

## TOURMALINE

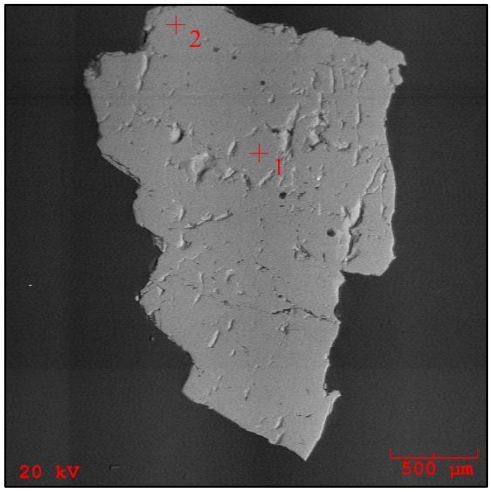


Figure 139 BSE image of polished tourmaline grain (1 & 2).

Tourmaline is rather ubiquitous at the Sturgeon River pegmatite. Tourmaline has been identified in heavy mineral separations and investigated by SEM. Tourmaline has been confirmed via microprobe as fluorschorl. Sturgeon River tourmalines are part of the alkali group based on X-site dominance. Tourmalines are relatively depleted in calcium as well as potassium. Sodium is the dominant alkali element. Sturgeon River pegmatites are somewhat enriched in magnesium, with a small amount of calculated lithium. Fluorine is dominant versus hydroxyl ions. Inclusions of quartz, intergrowths of quartz, K-feldspar, and mica are present in grains. Many grains are texturally and geochemically homogeneous. Table 69 has a list of representative analyses. Additional analyses listed in Tables 96 and 97 of the appendices.

| TOURMALINE – STURGEON RIVER PEGMATITE | | | | | | | | | | |
|---|---|---|---|---|---|---|---|---|---|---|
| Wt.% Oxide | grain 1-1 | grain 1-2 | grain 2-1 | grain 2-2 | grain 3-1 | grain 3-2 | grain 4-1 | grain 4-2 | grain 5-1 | grain 5-2 |
| $SiO_2$ | 36.311 | 36.331 | 36.400 | 36.238 | 36.351 | 36.333 | 36.400 | 36.412 | 36.550 | 36.417 |
| $TiO_2$ | 0.044 | 0.052 | 0.043 | 0.115 | 0.110 | 0.091 | 0.103 | 0.114 | 0.106 | 0.145 |
| $Al_2O_3$ | 29.772 | 29.800 | 29.922 | 30.293 | 29.956 | 30.093 | 30.110 | 30.096 | 30.100 | 30.085 |
| $B_2O_3$ (*calc.*) | 10.323 | 10.320 | 10.345 | 10.339 | 10.317 | 10.334 | 10.346 | 10.346 | 10.371 | 10.346 |
| FeOt | 13.893 | 13.734 | 13.655 | 13.588 | 13.600 | 13.595 | 13.499 | 13.562 | 13.600 | 13.593 |
| MnO | 0.161 | 0.143 | 0.121 | 0.234 | 0.113 | 0.131 | 0.129 | 0.173 | 0.188 | 0.167 |
| MgO | 3.788 | 3.800 | 3.755 | 3.344 | 3.412 | 3.415 | 3.600 | 3.484 | 3.356 | 3.365 |
| CaO | 0.022 | 0.031 | 0.024 | 0.024 | 0.030 | 0.035 | 0.029 | 0.033 | 0.028 | 0.040 |
| $Na_2O$ | 2.355 | 2.292 | 2.400 | 2.412 | 2.334 | 2.412 | 2.292 | 2.312 | 2.400 | 2.343 |
| $K_2O$ | 0.033 | 0.044 | 0.021 | 0.040 | 0.033 | 0.034 | 0.032 | 0.026 | 0.045 | 0.031 |
| $Li_2O$ (*calc.*) | 0.232 | 0.251 | 0.286 | 0.299 | 0.369 | 0.350 | 0.310 | 0.333 | 0.402 | 0.368 |
| $H_2O$ (*calc.*) | 3.077 | 3.039 | 3.064 | 3.002 | 2.991 | 2.999 | 3.042 | 3.052 | 3.083 | 3.526 |
| F | 1.022 | 1.100 | 1.066 | 1.191 | 1.200 | 1.194 | 1.113 | 1.091 | 1.044 | 0.091 |
| F=O | - 0.430 | - 0.463 | - 0.449 | - 0.501 | - 0.505 | - 0.503 | - 0.469 | - 0.459 | - 0.440 | - 0.038 |
| **Total** | 100.602 | 100.475 | 100.653 | 100.617 | 100.310 | 100.514 | 100.537 | 100.575 | 100.834 | 100.479 |
| *apfu* | | | | | | | | | | |
| Na | 0.769 | 0.748 | 0.782 | 0.786 | 0.763 | 0.787 | 0.747 | 0.753 | 0.780 | 0.763 |
| Ca | 0.004 | 0.006 | 0.004 | 0.004 | 0.005 | 0.006 | 0.005 | 0.006 | 0.005 | 0.007 |
| K | 0.007 | 0.009 | 0.005 | 0.009 | 0.007 | 0.007 | 0.007 | 0.006 | 0.010 | 0.007 |
| Vac (*calc.*) | 0.220 | 0.237 | 0.209 | 0.201 | 0.225 | 0.200 | 0.241 | 0.235 | 0.205 | 0.223 |
| **Σ X-site** | 1.000 | 1.000 | 1.000 | 1.000 | 1.000 | 1.000 | 1.000 | 1.000 | 1.000 | 1.000 |
| Fe | 1.956 | 1.934 | 1.919 | 1.910 | 1.916 | 1.912 | 1.896 | 1.905 | 1.906 | 1.910 |
| Mg | 0.858 | 0.869 | 0.865 | 0.838 | 0.804 | 0.821 | 0.863 | 0.831 | 0.783 | 0.799 |
| Al | 0.000 | 0.000 | 0.000 | 0.002 | 0.000 | 0.000 | 0.000 | 0.000 | 0.000 | 0.000 |
| Mn | 0.023 | 0.020 | 0.017 | 0.033 | 0.016 | 0.019 | 0.018 | 0.025 | 0.027 | 0.024 |
| Li (*calc.*) | 0.157 | 0.170 | 0.193 | 0.202 | 0.250 | 0.237 | 0.210 | 0.225 | 0.271 | 0.249 |
| Ti | 0.006 | 0.007 | 0.005 | 0.015 | 0.014 | 0.012 | 0.013 | 0.014 | 0.013 | 0.018 |
| **Σ Y-site** | 3.000 | 3.000 | 3.000 | 3.000 | 3.000 | 3.000 | 3.000 | 3.000 | 3.000 | 3.000 |
| Al | 5.908 | 5.915 | 5.925 | 6.000 | 5.947 | 5.965 | 5.961 | 5.959 | 5.945 | 5.957 |
| Mg | 0.092 | 0.085 | 0.075 | 0.000 | 0.053 | 0.035 | 0.039 | 0.041 | 0.055 | 0.043 |
| **Σ Z-site** | 6.000 | 6.000 | 6.000 | 6.000 | 6.000 | 6.000 | 6.000 | 6.000 | 6.000 | 6.000 |
| Si | 6.114 | 6.118 | 6.116 | 6.092 | 6.124 | 6.111 | 6.115 | 6.117 | 6.125 | 6.118 |
| Al | 0.000 | 0.000 | 0.000 | 0.000 | 0.000 | 0.000 | 0.000 | 0.000 | 0.000 | 0.000 |
| **Σ T-site** | 6.114 | 6.118 | 6.116 | 6.092 | 6.124 | 6.111 | 6.115 | 6.117 | 6.125 | 6.118 |
| B (*calc.*) | 3.000 | 3.000 | 3.000 | 3.000 | 3.000 | 3.000 | 3.000 | 3.000 | 3.000 | 3.000 |
| H (*calc.*) | 0.456 | 0.414 | 0.434 | 0.367 | 0.361 | 0.365 | 0.409 | 0.420 | 0.447 | 0.952 |
| F | 0.544 | 0.586 | 0.566 | 0.633 | 0.639 | 0.635 | 0.591 | 0.580 | 0.553 | 0.048 |
| **Σ W+V sites** | 4.000 | 4.000 | 4.000 | 4.000 | 4.000 | 4.000 | 4.000 | 4.000 | 4.000 | 4.000 |
| | | | | | | | | | | |
| **Species** | *fluor-schorl* | *fluor-schorl* | *fluor-schorl* | *fluor-schorl* | *fluor-schorl* | *fluor-schorl* | *fluor-schorl* | *fluor-schorl* | *fluor-schorl* | *fluor-schorl* |

Table 69 Representative EMP analyses of tourmaline. *Apfu* calculations based on 31 anions.

## URANINITE

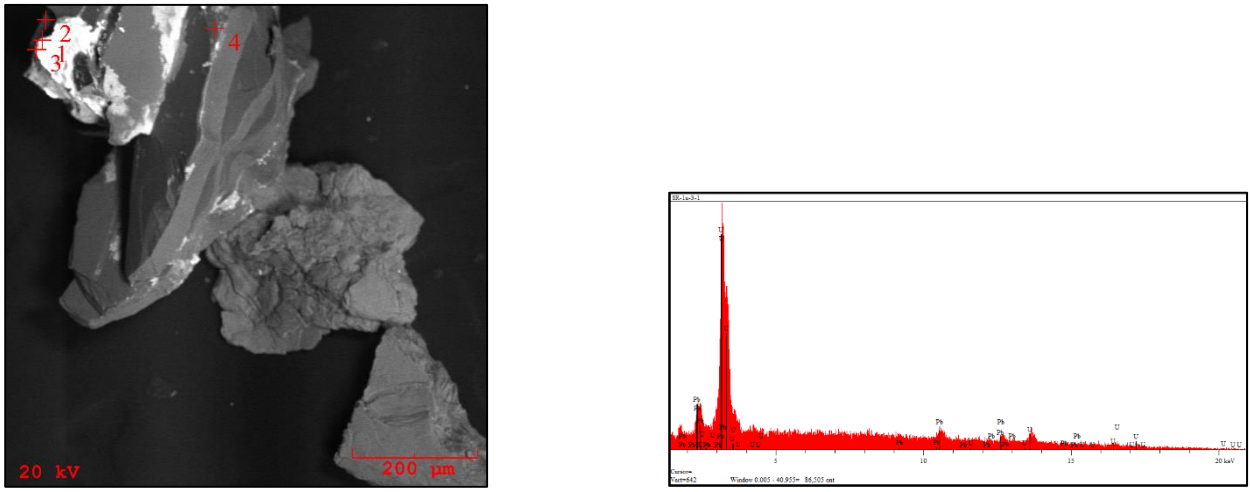


Figure 140 BSE image of uraninite (crosshairs 1 & 2) on mica (crosshairs 2 & 4) along with corresponding EDS spectrum.

Uraninite with possible radiogenic lead has been discovered qualitatively in grains from heavy mineral separations by SEM. The associated EDS spectrum shows the uranium and lead peaks.

## "XENOTIME"

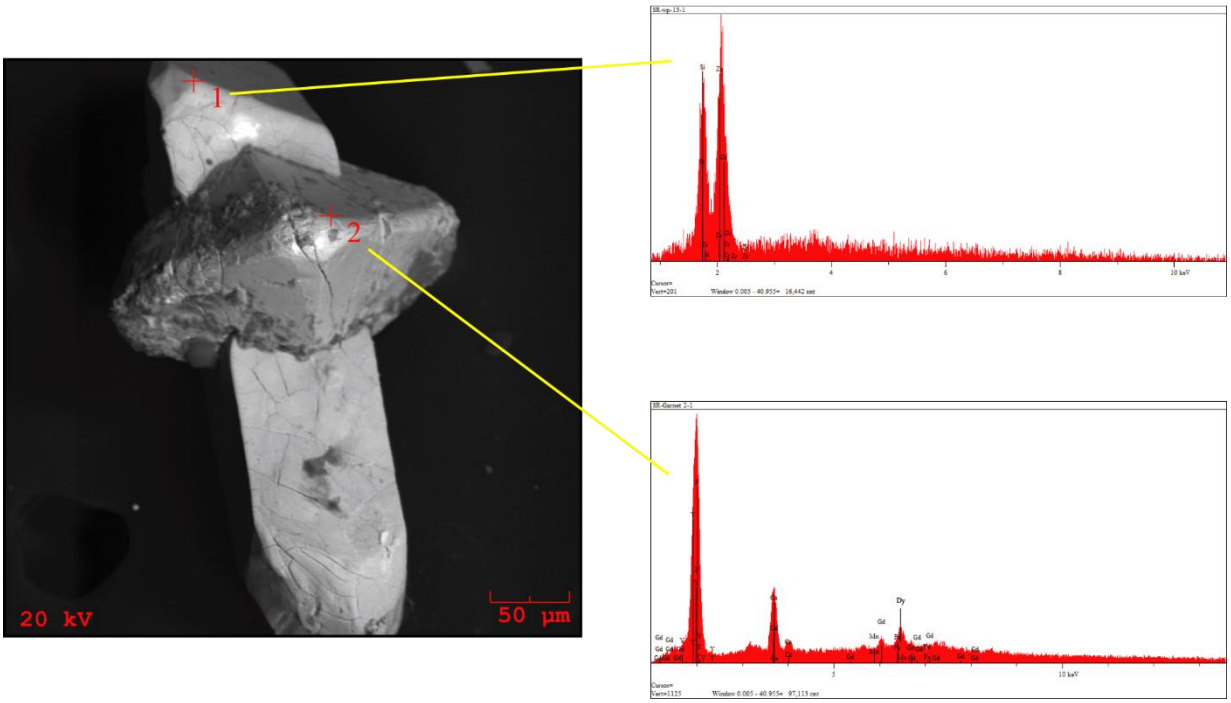


Figure 141 BSE image of epitaxial overgrowth of "xenotime" and zircon along with associated EDS spectra.

Even though "xenotime" is exceedingly rare in heavy mineral separations, a spectacular example of epitaxial intergrowth of single crystals of zircon and "xenotime" has been discovered. Efforts to further explore the sample by microprobe have failed due to the fragility of the grain. It is suggested that this particular grain be classified as xenotime-Y; however, without quantitative confirmation, this classification is uncertain.

ZIRCON

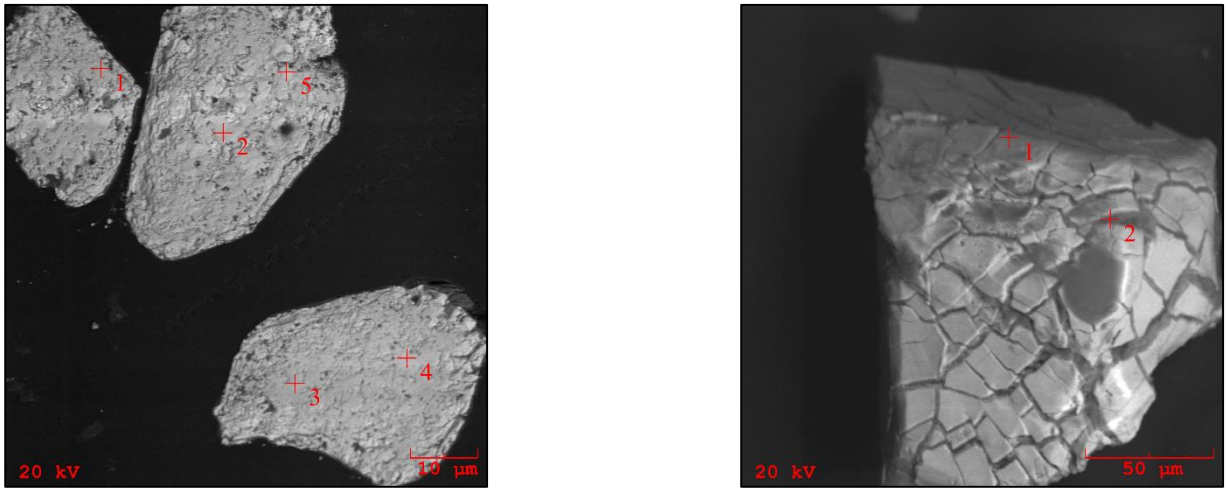


Figure 142 BSE images of polished (left) and unpolished (right) zircon grains.

Zircon is relatively common in heavy mineral separations and has been investigated by SEM. Efforts to gain meaningful microprobe data has not been possible due to the heavily altered nature of the grains. It is important to note that SEM analyses of a few of the grains did reveal a detectable amount of hafnium.

## GROVELAND PEGMATITE

Figure 143 Field picture of Groveland Mine pegmatite exposure.

The Groveland Mine pegmatite is located in Dickinson County, Michigan just off of Hwy69 on Groveland Mine Rd. It is on the property included with the Groveland Iron Ore Mine from where it gets its name. Production stopped in the 1980's and the mine is currently owned by the Yelsky sisters who permitted access to the pegmatite. The pegmatite is poorly exposed. Visual inspection reveals abundant feldspar, quartz, and mica as well as beryl. Feldspar at the Groveland Mine is a brick red hue; the darkest shade of any of the samples collected. Of interest is that there are muscovite mica books that are kinked (Figure 144). Previous work on the Groveland Mine has been conducted and 24 minerals have been identified. Qualitative identification of heavy minerals by SEM reveal: apatite, beryl, biotite, columbite, K-feldspar and plagioclase feldspar, fluorite, gahnite, garnet, iron oxides, magnetite, "monazite", muscovite,

pyrite, pyrophanite, quartz, rutile, tantalite, tourmaline, “xenotime”, and zircon. The following minerals were quantitatively confirmed by electron microprobe: fluorapatite, beryl, Fe-biotite, ferrocolumbite, K-feldspar and plagioclase feldspar, gahnite, garnet, magnetite, monazite-(Ce), muscovite mica, pyrophanite, ferrotantalite, fluorschorl, xenotime-(Y), and zircon.


Figure 144 Close-up of kinked mica book from the Groveland Mine pegmatite.

## APATITE

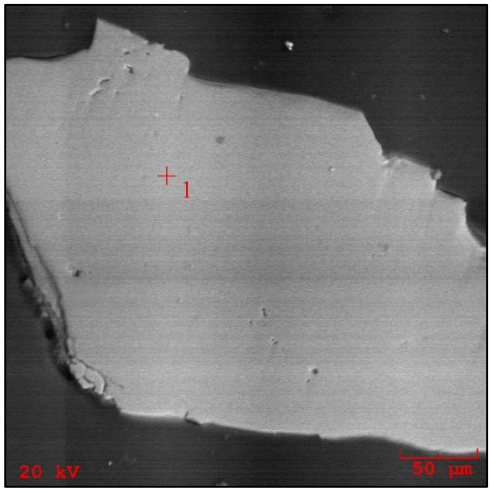


Figure 145 BSE image of polished apatite grain (1).

Apatite is extremely rare in heavy mineral separations and has been identified by using UV light. Only a single discrete grain has been found. Apatite is clear and colorless. Fluorine is dominant over both hydroxyl ions and chlorine, therefore apatite should be classified as fluorapatite. Table 70 lists the representative analyses. Along with "monazite" and "xenotime", apatite is an accessory phosphate mineral found at the Groveland Mine pegmatite.

| **APATITE – GROVELAND MINE PEGMATITE** | | |
|---|---|---|
| Wt % Oxide | GMP-1 | GMP-2 |
| $P_2O_5$ | 42.344 | 42.178 |
| $SiO_2$ | 0.033 | 0.055 |
| $Al_2O_3$ | 0.000 | 0.009 |
| FeO | 0.000 | 0.008 |
| MnO | 0.000 | 0.009 |
| CaO | 55.622 | 55.700 |
| $H_20$ (*calc.*) | 0.392 | 0.354 |
| F | 2.922 | 3.001 |
| F=O | - 1.230 | - 1.264 |
| Total | 100.083 | 100.050 |
| *apfu* | | |
| Ca | 4.991 | 5.005 |
| Fe | 0.000 | 0.001 |
| **Σ X** | 4.991 | 5.006 |
| P | 3.003 | 2.995 |
| Si | 0.003 | 0.005 |
| Al | 0.000 | 0.001 |
| **Σ Y** | 3.006 | 3.001 |
| F | 0.774 | 0.796 |
| H (*calc.*) | 0.226 | 0.204 |
| **Σ W** | 1.000 | 1.000 |

Table 70 Representative EMP analyses of apatite.
*Apfu* calculations based on 13 anions.

## BERYL

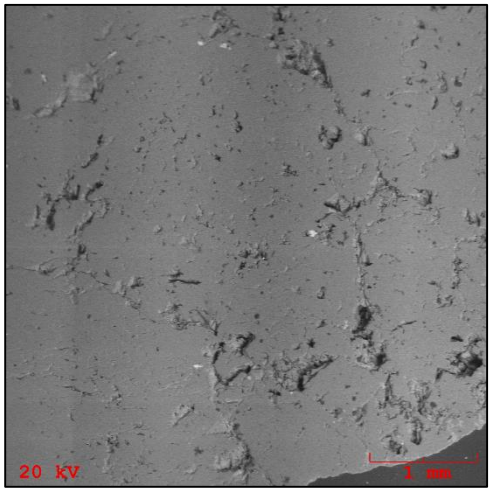


Figure 146 BSE image of polished beryl grain.

Beryl is relatively quite common at the Groveland Mine pegmatite. All samples have a light yellow-green hue. None are of gem quality. Beryl has been investigated by SEM and further analyzed by microprobe. DCP analysis of beryl reveals a lithium weight percent content of 0.329. SEM investigation has revealed an inhomogeneous texture. One grain in particular has a four millimeter long, few micron thick fracture which has been subsequently infilled by an aluminum-rich mica. A few beryl grains have inclusions approximately 50 microns in diameter. These inclusions are iron-rich, as well as calcium, aluminum, silicon, and phosphorus poor. One inclusion appears to be a thorium-rich phosphate. Only the beryl grains themselves have been analyzed by microprobe, owing to the size and rarity of the inclusions. Beryl grains are geochemically homogeneous from core to rim. Table 71 lists the representative analyses.

| BERYL – GROVELAND MINE PEGMATITE | | | | | | | |
|---|---|---|---|---|---|---|---|
| Wt% ox | Beryl 1-1 | Beryl 1-2 | Beryl 2-1 | Beryl 3-1 | Beryl 3-2 | Beryl 4-1 | Beryl 5-1 |
| $SiO_2$ | 66.996 | 67.044 | 66.974 | 66.962 | 66.950 | 66.972 | 66.956 |
| $TiO_2$ | 0.000 | 0.000 | 0.009 | 0.011 | 0.000 | 0.000 | 0.000 |
| $Al_2O_3$ | 18.967 | 18.944 | 19.004 | 18.956 | 18.897 | 18.900 | 18.988 |
| BeO (calc.) | 14.001 | 14.019 | 14.021 | 13.998 | 13.982 | 13.990 | 14.003 |
| FeO | 0.221 | 0.388 | 0.341 | 0.211 | 0.144 | 0.215 | 0.154 |
| MnO | 0.000 | 0.009 | 0.009 | 0.011 | 0.000 | 0.000 | 0.000 |
| MgO | 0.044 | 0.033 | 0.031 | 0.021 | 0.009 | 0.000 | 0.000 |
| CaO | 0.022 | 0.030 | 0.055 | 0.055 | 0.021 | 0.022 | 0.000 |
| $Rb_2O$ | 0.000 | 0.000 | 0.000 | 0.000 | 0.011 | 0.000 | 0.000 |
| $Cs_2O$ | 0.000 | 0.000 | 0.000 | 0.000 | 0.000 | 0.000 | 0.000 |
| $Na_2O$ | 0.322 | 0.345 | 0.411 | 0.365 | 0.433 | 0.437 | 0.533 |
| $K_2O$ | 0.065 | 0.052 | 0.062 | 0.042 | 0.055 | 0.044 | 0.065 |
| **Total** | 100.638 | 100.864 | 100.917 | 100.632 | 100.502 | 100.580 | 100.699 |
| *apfu* | | | | | | | |
| Be (calc.) | 3.000 | 3.000 | 3.000 | 3.000 | 3.000 | 3.000 | 3.000 |
| **Σ Be** | 3.000 | 3.000 | 3.000 | 3.000 | 3.000 | 3.000 | 3.000 |
| Al | 1.971 | 1.963 | 1.961 | 1.969 | 1.970 | 1.968 | 1.969 |
| Fe | 0.016 | 0.029 | 0.025 | 0.016 | 0.011 | 0.016 | 0.011 |
| Mn | 0.000 | 0.001 | 0.001 | 0.001 | 0.000 | 0.000 | 0.000 |
| Mg | 0.006 | 0.004 | 0.004 | 0.003 | 0.001 | 0.000 | 0.000 |
| Ca | 0.002 | 0.003 | 0.005 | 0.005 | 0.002 | 0.002 | 0.000 |
| **Σ Octahedral** | 1.995 | 1.980 | 1.996 | 1.994 | 1.984 | 1.986 | 1.980 |
| Si | 5.976 | 5.973 | 5.966 | 5.975 | 5.981 | 5.979 | 5.972 |
| Al | 0.024 | 0.027 | 0.034 | 0.025 | 0.019 | 0.021 | 0.028 |
| Ti | 0.000 | 0.000 | 0.001 | 0.001 | 0.000 | 0.000 | 0.000 |
| **Σ Tetrahedral** | 6.000 | 6.000 | 6.001 | 6.001 | 6.000 | 6.000 | 6.000 |
| Na | 0.056 | 0.060 | 0.071 | 0.063 | 0.075 | 0.076 | 0.092 |
| K | 0.007 | 0.006 | 0.007 | 0.005 | 0.006 | 0.005 | 0.007 |
| **Σ Channel** | 0.063 | 0.066 | 0.078 | 0.068 | 0.081 | 0.081 | 0.099 |

Table 71 Representative EMP analyses of beryl. *Apfu* calculations based on 18 oxygens.

BIOTITE

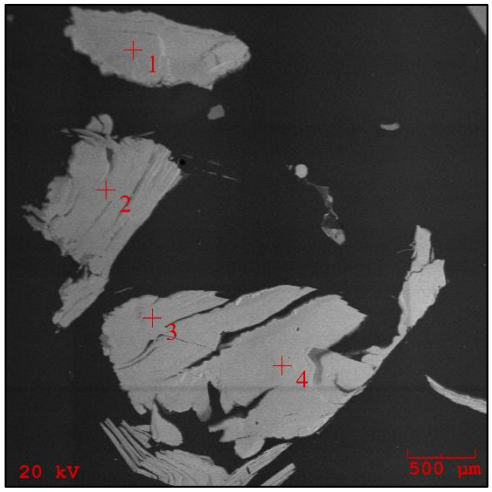


Figure 147 BSE image of polished biotite mica grains (1-4).

Biotite mica is relatively common at the Groveland Mine pegmatite. Fe-biotite present in hand samples and heavy mineral separations has been qualitatively investigated by SEM and later confirmed (Figure 186) as such by microprobe using Tischendorf's classification scheme (1997). Rubidium is just within detectable limits and cesium, below detection limits. DCP analyses detected lithium in muscovite mica samples and the equation (2.7 / (0.35 + magnesium weight percent)) - 0.13 has been used to stoichiometrically account for lithium (Tischendorf, 1997). Titration of biotite mica has yielded divalent iron contents of 27.959 weight percent, in excess of total iron in microprobe analyses, suggesting that biotite micas may contain divalent iron only. Weight percent totals are approximately 96% suggesting that biotites from the Groveland may have been altered.

One very notable example of alteration is a biotite grain that has numerous parallel alteration patterns. The overall grain chemistry suggests either biotite or possible chlorite (owing to the lack of potassium in SEM analyses). The outer most borders of the line of alteration is quartz, just inside of the quartz border is a mica species (possibly muscovite or biotite), and all

along the inner most zone are grains which appear to be a niobium-tantalum (possibly columbite/tantalite) species that is tantalum dominant. In some cases the length of the alteration line is in excess of a millimeter; the width of the line is about 40 microns.

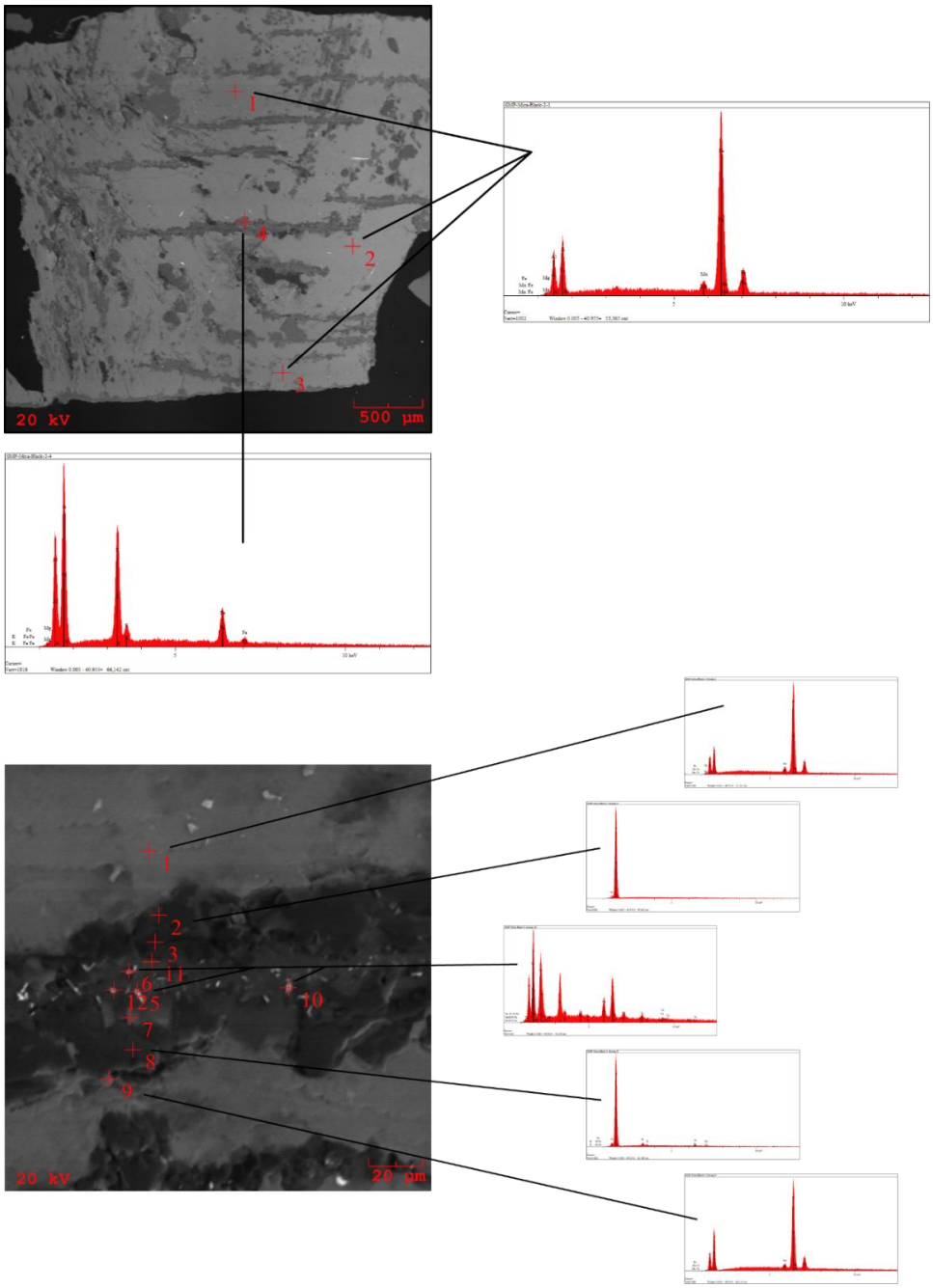


Figure 148 BSE image (top) of mica grain and EDS spectra. BSE image (bottom) of alteration with corresponding EDS spectra.

## COLUMBITE

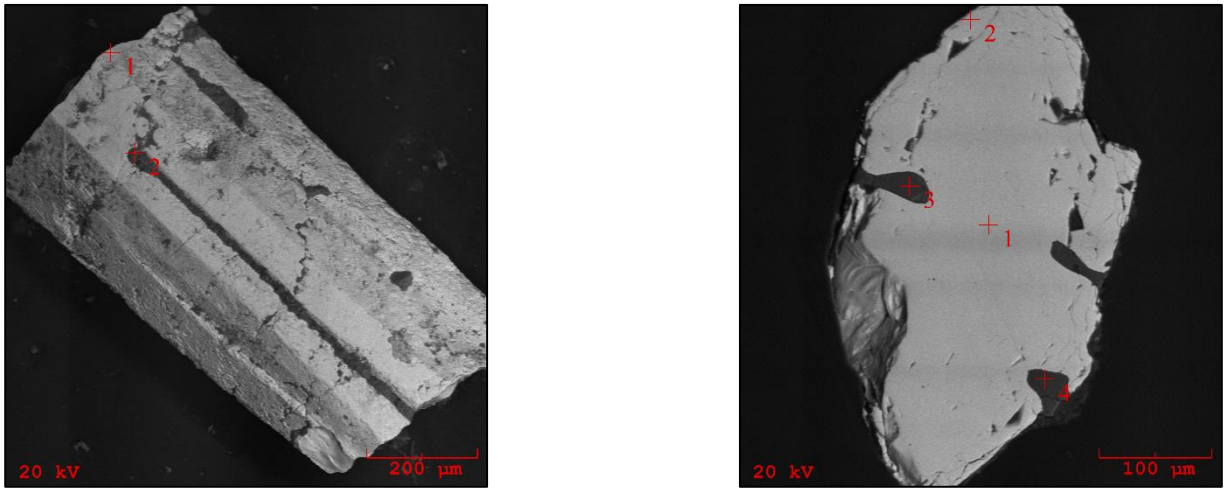


Figure 149 BSE images of columbite/tantalite grain (left; crosshair 1) and polished grain (right; crosshairs 1 & 2) with inclusions of plagioclase (left; crosshair 2 & right; crosshairs 3 & 4).

Columbite is relatively very common at the Groveland Mine pegmatite. Some excellent (albeit small) crystals have been identified in heavy mineral separations. Grains are, for the most part, texturally and geochemically homogeneous. Microprobe analyses reveal that columbite grains are iron dominant and should be classified as ferrocolumbite. Table 72 lists representative analyses. Additional analyses listed in Table 98 of the appendices.

| FERROCOLUMBITE – GROVELAND MINE PEGMATITE | | | | | | | | | | |
|---|---|---|---|---|---|---|---|---|---|---|
| Wt% Ox | GMP grain 5-1 | | GMP grain 6-1 | | GMP grain 7-1 | | GMP grain 8-1 | | GMP grain 9-1 | |
| $Nb_2O_5$ | 69.666 | 69.643 | 69.333 | 69.400 | 69.786 | 69.722 | 66.778 | 66.734 | 65.578 | 65.600 |
| $Ta_2O_5$ | 9.877 | 9.909 | 10.232 | 10.377 | 9.678 | 9.700 | 13.122 | 13.217 | 14.446 | 14.541 |
| $SiO_2$ | 0.033 | 0.042 | 0.034 | 0.033 | 0.044 | 0.045 | 0.022 | 0.030 | 0.000 | 0.020 |
| $TiO_2$ | 0.034 | 0.031 | 0.012 | 0.014 | 0.026 | 0.030 | 0.021 | 0.022 | 0.121 | 0.091 |
| $Al_2O_3$ | 0.000 | 0.000 | 0.000 | 0.000 | 0.000 | 0.000 | 0.022 | 0.000 | 0.000 | 0.000 |
| FeO | 16.778 | 16.562 | 14.876 | 14.700 | 16.800 | 16.712 | 15.311 | 15.265 | 15.899 | 15.766 |
| MnO | 3.588 | 3.700 | 5.612 | 5.589 | 3.447 | 3.512 | 4.800 | 4.779 | 4.212 | 4.311 |
| MgO | *bdl* | *bdl* | *bdl* | *bdl* | *bdl* | *bdl* | *bdl* | *bdl* | *bdl* | *bdl* |
| Total | 99.976 | 99.887 | 100.099 | 100.113 | 99.781 | 99.721 | 100.076 | 100.047 | 100.256 | 100.329 |
| *apfu* | | | | | | | | | | |
| Fe | 0.820 | 0.810 | 0.728 | 0.719 | 0.822 | 0.818 | 0.758 | 0.756 | 0.790 | 0.783 |
| Mn | 0.178 | 0.183 | 0.278 | 0.277 | 0.171 | 0.174 | 0.241 | 0.240 | 0.212 | 0.217 |
| Si | 0.002 | 0.002 | 0.002 | 0.002 | 0.003 | 0.003 | 0.001 | 0.002 | 0.000 | 0.001 |
| Al | 0.000 | 0.000 | 0.000 | 0.000 | 0.000 | 0.000 | 0.002 | 0.000 | 0.000 | 0.000 |
| Mg | *bdl* | *bdl* | *bdl* | *bdl* | *bdl* | *bdl* | *bdl* | *bdl* | *bdl* | *bdl* |
| **Σ X-site** | 0.998 | 0.994 | 1.006 | 0.996 | 0.993 | 0.992 | 1.000 | 0.996 | 1.002 | 1.000 |
| Nb | 1.841 | 1.842 | 1.833 | 1.835 | 1.846 | 1.845 | 1.787 | 1.787 | 1.761 | 1.761 |
| Ta | 0.157 | 0.158 | 0.163 | 0.165 | 0.154 | 0.154 | 0.211 | 0.213 | 0.233 | 0.235 |
| Ti | 0.001 | 0.001 | 0.001 | 0.001 | 0.001 | 0.001 | 0.001 | 0.001 | 0.005 | 0.004 |
| **Σ Y-site** | 2.000 | 2.001 | 1.996 | 2.000 | 2.001 | 2.001 | 1.999 | 2.000 | 2.000 | 2.000 |

Table 72 Representative EMP analyses of ferrocolumbite. *Apfu* calculations based on 6 oxygens.

## FELDSPARS

### K-FELDSPAR

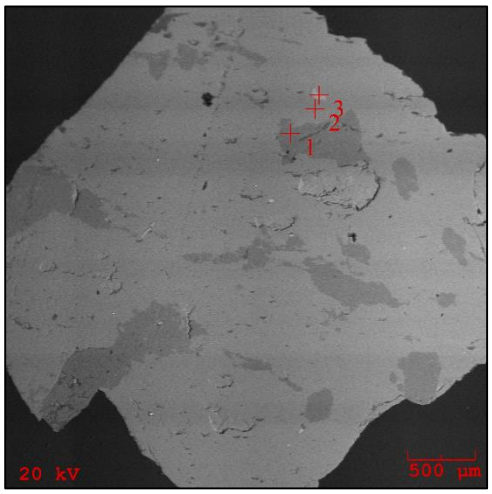


Figure 150 BSE image of polished K-feldspar grain (crosshair 2), plagioclase blebs (crosshair 2), and mica inclusion (crosshair 3).

K-feldspar has been qualitatively investigated and confirmed by microprobe analysis. K-feldspar grains are a dark red hue. Blebs of plagioclase, when present, are irregular in shape and orientation. Barium, strontium, and cesium are all below detection limits. Rubidium, when present, is just within detectable limits. This suggests that feldspar from the Groveland Mine is poorly evolved. XRD analyses reveal that K-feldspar from the Groveland Mine may have a certain degree of disorder as the analysis did not plot quite within the maximum microcline field (Figure 173). Table 73 lists the representative analyses.

| K-FELDSPAR – GROVELAND MINE PEGMATITE | | | | | | |
|---|---|---|---|---|---|---|
| Wt% ox | GMP grain 3-1 | | GMP grain 5-1 | | GMP grain 7-1 | |
| $P_2O_5$ | *bdl* | *bdl* | *bdl* | *bdl* | *bdl* | *bdl* |
| $SiO_2$ | 64.833 | 68.745 | 68.764 | 64.788 | 68.698 | 64.800 |
| $TiO_2$ | 0.011 | 0.000 | 0.000 | 0.014 | 0.000 | 0.017 |
| $Al_2O_3$ | 18.383 | 19.811 | 19.733 | 18.413 | 19.655 | 18.511 |
| $FeO_t$ | 0.015 | 0.000 | 0.000 | 0.011 | 0.000 | 0.012 |
| CaO | 0.009 | 0.211 | 0.112 | 0.000 | 0.000 | 0.000 |
| $Na_2O$ | 0.700 | 11.511 | 11.654 | 0.674 | 11.500 | 0.733 |
| $K_2O$ | 15.755 | 0.100 | 0.120 | 15.899 | 0.188 | 15.512 |
| $Rb_2O$ | 0.025 | 0.000 | 0.000 | 0.020 | 0.000 | 0.025 |
| **Total** | 99.731 | 100.378 | 100.383 | 99.819 | 100.041 | 99.610 |
| *apfu* | | | | | | |
| K | 0.930 | 0.006 | 0.007 | 0.938 | 0.010 | 0.915 |
| Na | 0.063 | 0.971 | 0.983 | 0.060 | 0.973 | 0.066 |
| Ca | 0.000 | 0.000 | 0.000 | 0.000 | 0.000 | 0.000 |
| Rb | 0.001 | 0.000 | 0.000 | 0.001 | 0.000 | 0.001 |
| **Σ X-site** | 0.994 | 0.976 | 0.995 | 0.999 | 0.983 | 0.982 |
| Al | 1.002 | 1.015 | 1.012 | 1.004 | 1.011 | 1.009 |
| Fe | 0.000 | 0.000 | 0.000 | 0.000 | 0.000 | 0.000 |
| **Σ Y-site** | 1.002 | 1.015 | 1.012 | 1.004 | 1.011 | 1.009 |
| Si | 2.999 | 2.989 | 2.991 | 2.997 | 2.996 | 2.997 |
| Ti | 0.000 | 0.000 | 0.000 | 0.000 | 0.000 | 0.001 |
| P | 0.000 | 0.000 | 0.000 | 0.000 | 0.000 | 0.000 |
| Al | 0.000 | 0.000 | 0.000 | 0.000 | 0.000 | 0.000 |
| **Σ Z-site** | 2.999 | 2.989 | 2.991 | 2.997 | 2.996 | 2.998 |

Table 73 Representative EMP analyses of K-feldspar. *Apfu* calculations based on 8 oxygens.

PLAGIOCLASE FELDSPAR

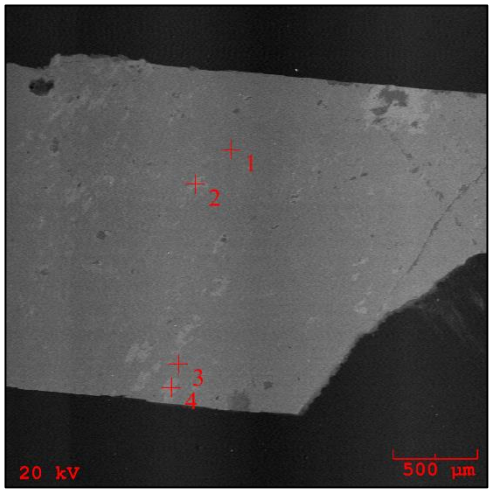


Figure 151 BSE image of polished plagioclase grain (crosshairs 1 & 3) and K-feldspar blebs (crosshairs 2 & 4).

Plagioclase feldspar has been qualitatively identified by SEM and confirmed by microprobe. As with K-feldspar grains, plagioclase is also a dark red hue. Barium, strontium, and cesium are all below detectable limits. A detectable amount of rubidium is present in the blebs of K-feldspar that have exsolved. Blebs of K-feldspar are irregular in shape and size. A list of representative analyses is listed in Table 74. Additional analyses listed in Table 100 of the appendices.

| PLAGIOCLASE FELDSPAR – GROVELAND MINE PEGMATITE | | | | | | | | |
|---|---|---|---|---|---|---|---|---|
| Wt% ox | GMP grain 1-1 | | GMP grain 2-1 | | GMP grain 4-1 | | GMP grain 5b-1 | |
| $P_2O_5$ | 0.011 | 0.000 | 0.000 | 0.009 | 0.000 | 0.000 | 0.012 | 0.000 |
| $SiO_2$ | 64.894 | 68.800 | 68.782 | 64.833 | 64.833 | 68.823 | 64.698 | 68.743 |
| $TiO_2$ | 0.009 | 0.000 | 0.000 | 0.011 | 0.011 | 0.000 | 0.011 | 0.000 |
| $Al_2O_3$ | 18.411 | 19.484 | 19.600 | 18.383 | 18.383 | 19.745 | 18.455 | 19.745 |
| $FeO_t$ | 0.015 | 0.000 | 0.000 | 0.015 | 0.015 | 0.000 | 0.016 | 0.000 |
| CaO | 0.008 | 0.032 | 0.051 | 0.009 | 0.009 | 0.091 | 0.000 | 0.000 |
| $Na_2O$ | 0.655 | 11.781 | 11.688 | 0.700 | 0.700 | 11.611 | 0.678 | 11.455 |
| $K_2O$ | 15.766 | 0.160 | 0.091 | 15.755 | 15.755 | 0.092 | 15.682 | 0.212 |
| $Rb_2O$ | 0.032 | 0.000 | 0.000 | 0.025 | 0.025 | 0.000 | 0.023 | 0.000 |
| **Total** | 99.801 | 100.257 | 100.212 | 99.740 | 99.731 | 100.362 | 99.575 | 100.155 |
| *apfu* | | | | | | | | |
| K | 0.930 | 0.009 | 0.005 | 0.930 | 0.930 | 0.005 | 0.927 | 0.012 |
| Na | 0.059 | 0.995 | 0.987 | 0.063 | 0.063 | 0.979 | 0.061 | 0.968 |
| Ca | 0.000 | 0.001 | 0.002 | 0.000 | 0.000 | 0.004 | 0.000 | 0.000 |
| Rb | 0.001 | 0.000 | 0.000 | 0.001 | 0.001 | 0.000 | 0.001 | 0.000 |
| **Σ X-site** | 0.990 | 1.005 | 0.994 | 0.994 | 0.994 | 0.988 | 0.989 | 0.980 |
| Al | 1.003 | 1.001 | 1.006 | 1.002 | 1.002 | 1.012 | 1.007 | 1.014 |
| Fe | 0.000 | 0.000 | 0.000 | 0.000 | 0.000 | 0.000 | 0.000 | 0.000 |
| **Σ Y-site** | 1.003 | 1.001 | 1.006 | 1.002 | 1.002 | 1.012 | 1.007 | 1.014 |
| Si | 2.999 | 2.998 | 2.996 | 2.999 | 2.999 | 2.993 | 2.996 | 2.995 |
| Ti | 0.000 | 0.000 | 0.000 | 0.000 | 0.000 | 0.000 | 0.000 | 0.000 |
| P | 0.001 | 0.000 | 0.000 | 0.000 | 0.000 | 0.000 | 0.000 | 0.000 |
| Al | 0.000 | 0.000 | 0.000 | 0.000 | 0.000 | 0.000 | 0.000 | 0.000 |
| **Σ Z-site** | 2.999 | 2.998 | 2.996 | 2.999 | 2.999 | 2.993 | 2.996 | 2.995 |

Table 74 Representative EMP analyses of plagioclase (albite). *Apfu* calculations based on 8 oxygens.

## FLUORITE

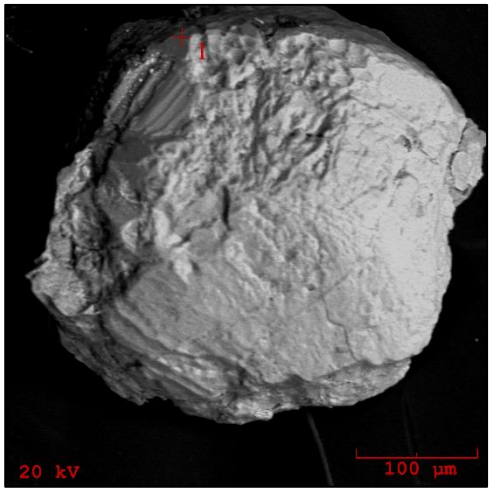


Figure 152 BSE image of fluorite grain (1).

Fluorite is not very abundant in heavy mineral separations. Fluorite has been qualitatively investigated by SEM. Grains contain purple splotches and have visible inclusions when viewed under binocular microscope.

## GAHNITE

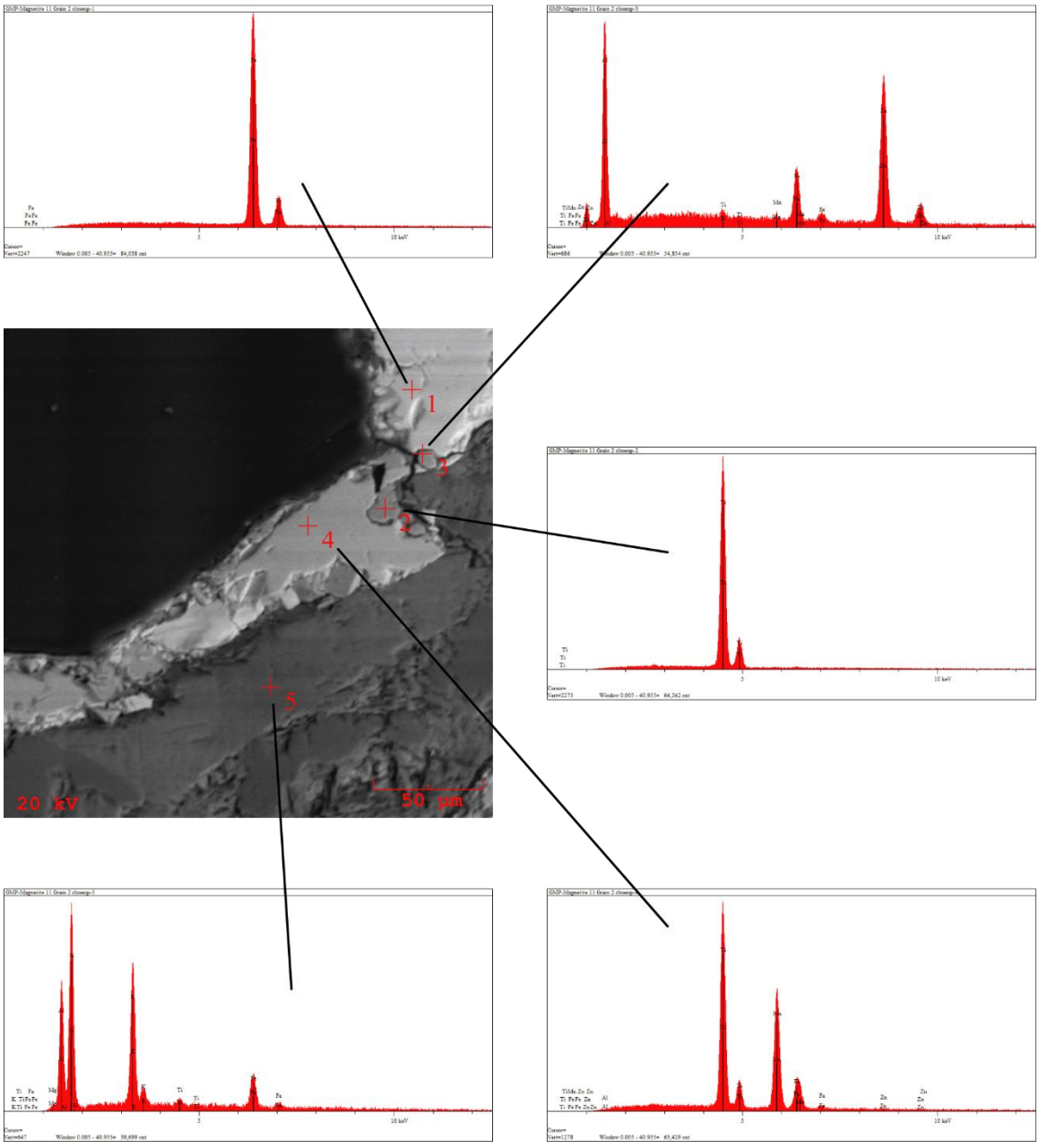


Figure 153 BSE close-up image of gahnite as well as other inclusions with associated EDS spectra.

Gahnite, a zinc spinel, has been identified qualitatively by SEM and confirmed by microprobe. Grains are approximately 20 microns in diameter and incredibly rare. Gahnite is associated with mica, magnetite, rutile, and pyrophanite. Table 75 lists the analyses.

| GAHNITE – GROVELAND MINE PEGMATITE | | |
|---|---|---|
| Wt % Oxide | grain 2-1 | grain 2-2 |
| TiO2 | 0.133 | 0.099 |
| Al2O3 | 55.998 | 56.023 |
| Cr2O3 | 0.140 | 0.130 |
| FeOt | 8.980 | 9.344 |
| MnO | 1.221 | 1.116 |
| NiO | 0.000 | 0.000 |
| MgO | 0.230 | 0.100 |
| ZnO | 33.678 | 33.672 |
| **Total** | 100.38 | 100.48 |
| *apfu* | | |
| $Fe^{2+}$ | 0.212 | 0.221 |
| Mn | 0.031 | 0.028 |
| Ni | 0.000 | 0.000 |
| Mg | 0.010 | 0.004 |
| Zn | 0.746 | 0.746 |
| **Σ A-site** | 0.999 | 0.999 |
| Ti | 0.002 | 0.001 |
| $Fe^{2+}$ | 0.002 | 0.001 |
| $Fe^{3+}$ | 0.005 | 0.006 |
| Cr | 0.002 | 0.002 |
| Al | 0.990 | 0.991 |
| **Σ B-site** | 1.001 | 1.001 |
| **End Members** | | |
| Spinel | 0.010 | 0.004 |
| Hercynite | 0.203 | 0.212 |
| Galaxite | 0.031 | 0.028 |
| **Gahnite** | **0.746** | **0.746** |
| Trevorite | 0.000 | 0.000 |
| Magnetite | 0.005 | 0.006 |
| Chromite | 0.002 | 0.002 |
| Ulvöspinel | 0.003 | 0.002 |

Table 75 Representative EMP analyses of gahnite.
*Apfu* calculations based on 4 oxygens.

## GARNET

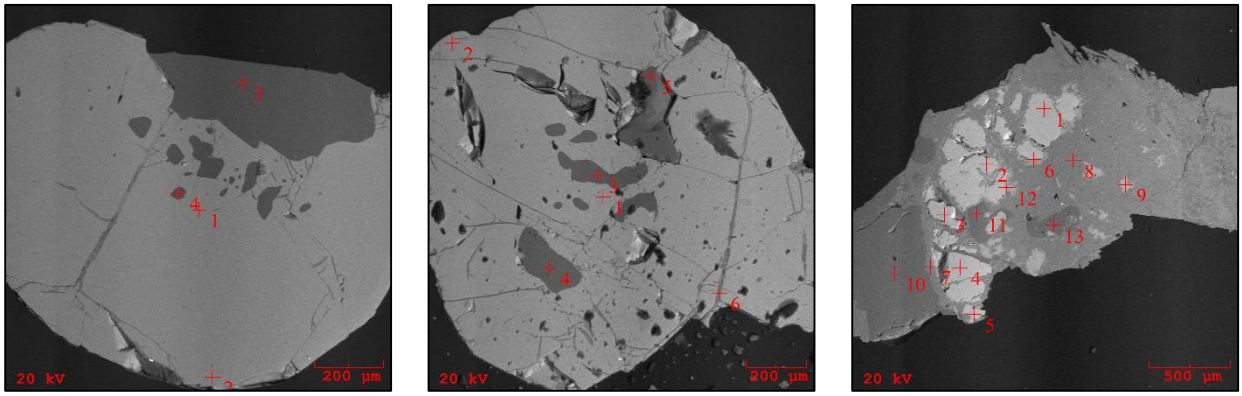


Figure 154 BSE images of polished garnet grains.

Garnet is relatively common at the Groveland Mine pegmatite. There are a number of textural characteristics present in analyzed grains. A few grains are subhedral with little to very few inclusions and fractures (above left). There are anhedral grains that appear to be almost completely altered with only a few remnants of the original grain present (above right). "Intermediate" grains have wider fractures and relatively more inclusions, yet still preserve a subhedral appearance (above center). Inclusions are typically either quartz or mica. All of the original areas of the grains that have been analyzed have very similar components. Almandine components range from 80-85% and spessartine components range from 13% to just over 16% in some cases. The grossular and pyrope components are >01% and in rare instances grains contain an andraditic component of less than >01%. One grain has a very high almandine component of 95%; however, the original grain appears almost completely obliterated and very few areas of the original grain are present. Of importance is that fractures that have been infilled and/or altered appear to be manganese poor. Table 76 lists the representative analyses. Additional analyses listed in Table 101 of the appendices.

| GARNETS – GROVELAND MINE PEGMATITE | | | | | | | | |
|---|---|---|---|---|---|---|---|---|
| Wt % Ox | grain 1-1 | | grain 2-1 | | grain 3-1 | | grain 5-1 | |
| $SiO_2$ | 36.500 | 36.477 | 36.388 | 36.555 | 36.459 | 36.466 | 36.500 | 36.499 |
| $TiO_2$ | 0.015 | 0.020 | 0.009 | 0.011 | 0.009 | 0.012 | 0.008 | 0.010 |
| $Al_2O_3$ | 20.544 | 20.577 | 20.533 | 20.588 | 20.544 | 20.455 | 20.488 | 20.533 |
| FeO | 36.544 | 36.600 | 36.722 | 36.800 | 36.773 | 36.435 | 36.700 | 36.555 |
| MnO | 6.330 | 6.211 | 6.112 | 6.077 | 6.112 | 6.131 | 5.605 | 6.255 |
| MgO | 0.044 | 0.033 | 0.031 | 0.034 | 0.027 | 0.030 | 0.030 | 0.027 |
| CaO | 0.233 | 0.244 | 0.228 | 0.217 | 0.231 | 0.218 | 0.211 | 0.243 |
| **Total** | 100.210 | 100.162 | 100.023 | 100.282 | 100.155 | 99.747 | 99.542 | 100.122 |
| *apfu* | | | | | | | | |
| Ti | 0.001 | 0.001 | 0.001 | 0.001 | 0.001 | 0.001 | 0.000 | 0.001 |
| Fe | 2.519 | 2.524 | 2.537 | 2.534 | 2.537 | 2.521 | 2.541 | 2.522 |
| Mn | 0.442 | 0.434 | 0.428 | 0.424 | 0.427 | 0.430 | 0.393 | 0.437 |
| Mg | 0.005 | 0.004 | 0.004 | 0.004 | 0.003 | 0.004 | 0.004 | 0.003 |
| Ca | 0.021 | 0.022 | 0.020 | 0.019 | 0.020 | 0.019 | 0.019 | 0.021 |
| **Σ X-site** | 2.988 | 2.985 | 2.990 | 2.982 | 2.988 | 2.975 | 2.957 | 2.984 |
| Al | 1.996 | 2.000 | 1.999 | 1.998 | 1.997 | 1.995 | 1.999 | 1.996 |
| **Σ Y-site** | 1.996 | 2.000 | 1.999 | 1.998 | 1.997 | 1.995 | 1.999 | 1.996 |
| Si | 3.009 | 3.007 | 3.006 | 3.010 | 3.007 | 3.017 | 3.022 | 3.010 |
| **Σ Z-site** | 3.009 | 3.007 | 3.006 | 3.010 | 3.007 | 3.017 | 3.022 | 3.010 |
| **Component** | | | | | | | | |
| Pyrope | 00 | 00 | 00 | 00 | 00 | 00 | 00 | 00 |
| Spessartine | 15 | 14 | 14 | 14 | 14 | 14 | 13 | 15 |
| Grossular | 01 | 01 | 01 | 01 | 01 | 01 | 01 | 01 |
| Almandine | 84 | 85 | 85 | 85 | 85 | 86 | 86 | 84 |

Table 76 Representative EMP analyses of garnet. *Apfu* calculations based on 12 oxygens. Components are normalized to 100.

## IRON OXIDE

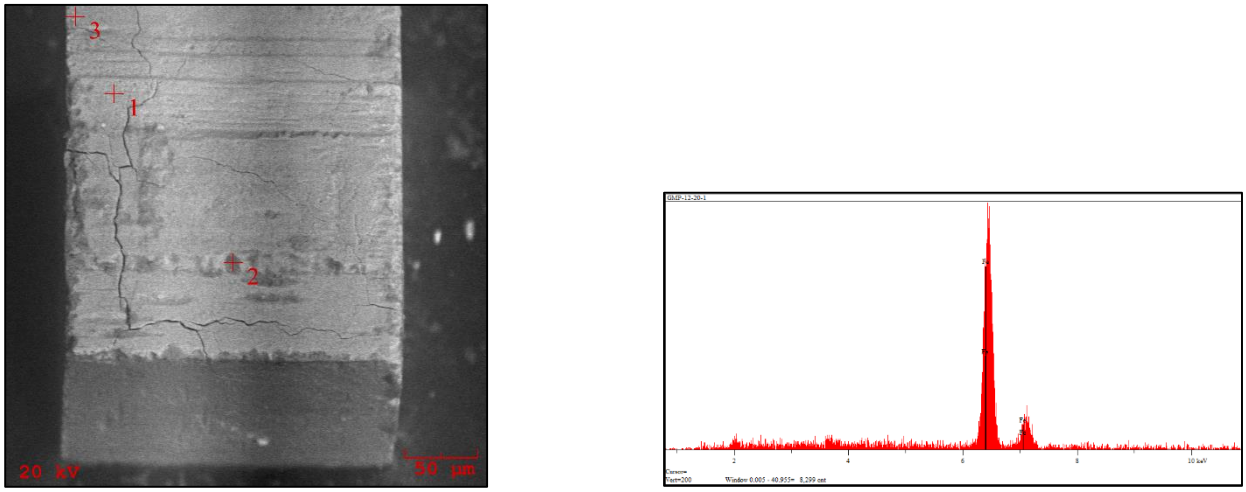


Figure 155 BSE image of iron oxide grain with corresponding EDS spectra (crosshairs 1-3).

Iron oxide is present in heavy mineral separations and qualitatively investigated by SEM.

## MAGNETITE

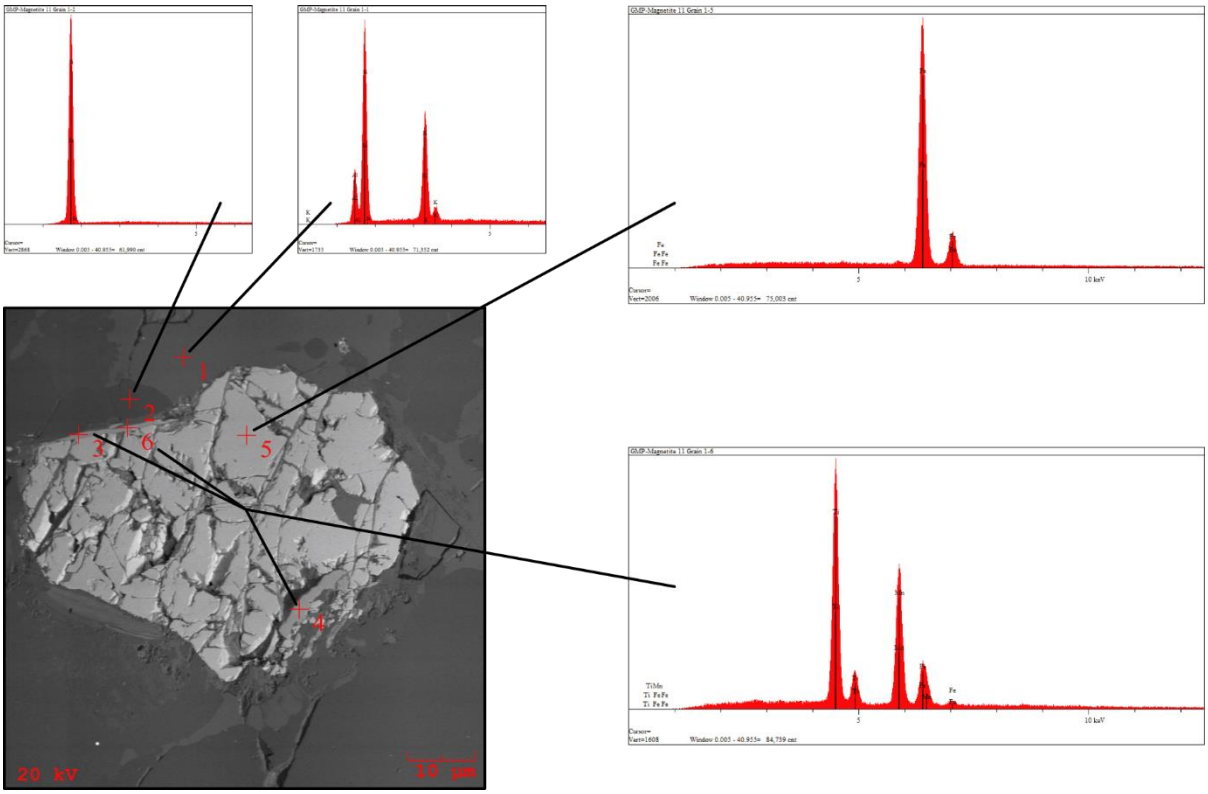


Figure 156 BSE image of magnetite grain (crosshair 5) with K-feldspar (crosshair 1), quartz (crosshair 2), and pyrophanite (crosshairs 3, 4, & 6).

Magnetite is relatively very common in heavy mineral separations. In one set of heavy mineral separations, magnetite comprises approximately 90% of the sample! A magnet has been placed against the plastic test tube and then moved around, in order to determine the amount of magnetite present in each set of heavy mineral separations.

MICROLITE

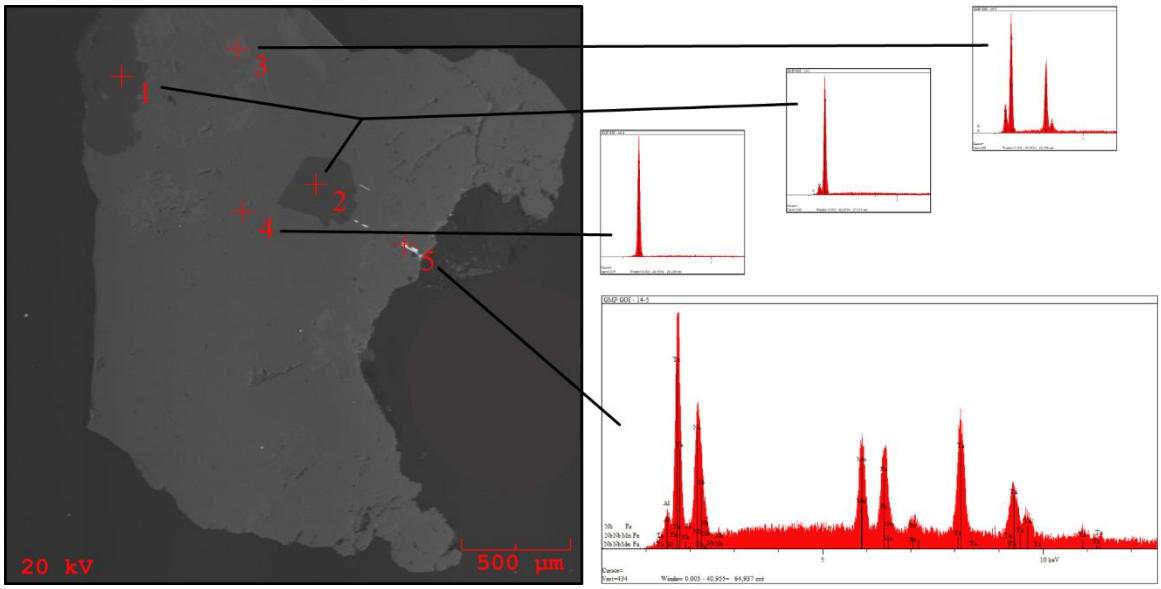


Figure 157 BSE image and associated spectra of quartz grain with plagioclase, K-feldspar, and columbite group mineral from Groveland Mine samples.

An overgrowth of microlite on a columbite group mineral inclusion in a quartz grain with associated plagioclase and K-feldspar was discovered via microprobe analysis. Tantalum is dominant as is calcium and oxygen. Classification should therefore be oxycalciomicrolite.

## "MONAZITE"

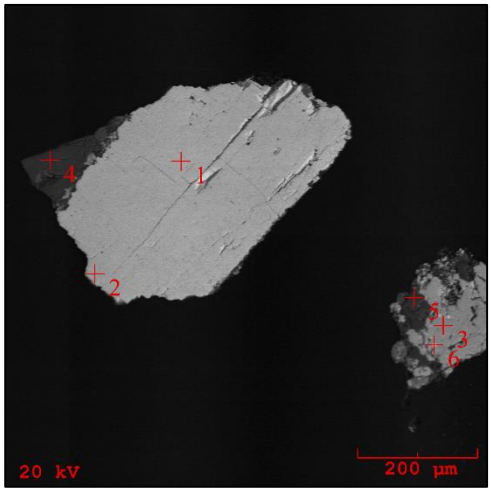


Figure 158 BSE image of polished "monazite" grain.

"Monazite" is present in heavy mineral separations, has been qualitatively investigated by SEM, and has been confirmed as monazite-(Ce) by microprobe. Cerium is the dominant X-site cation, although one of the grains analyzed has relatively elevated levels of thorium. This grain also has greater amounts of calcium due to preferential incorporation of calcium in the X-site whenever thorium is present. Calcium and thorium frequently form a coupled substitution in "monazites" to satisfy charge balances. Along with apatite and "xenotime", monazite-(Ce) is an accessory phosphate mineral present in heavy mineral separations and is the only REE-bearing mineral other than "xenotime" discovered in samples. Table 77 lists the representative EMP analyses.

| **MONAZITE-(CE) – GROVELAND MINE PEGMATITE** | | |
|---|---|---|
| Wt % Ox. | 9 GMP-1 | 10 GMP-1 |
| $P_2O_5$ | 27.892 | 29.437 |
| $SiO_2$ | 0.135 | 0.088 |
| $ThO_2$ | 0.000 | 0.000 |
| $UO_2$ | 22.133 | 5.776 |
| $Al_2O_3$ | 0.544 | 0.923 |
| $La_2O_3$ | 0.022 | 0.033 |
| $Ce_2O_3$ | 6.344 | 12.982 |
| $Pr_2O_3$ | 18.833 | 27.671 |
| $Nd_2O_3$ | 1.981 | 2.822 |
| $Sm_2O_3$ | 12.334 | 14.235 |
| $Gd_2O_3$ | 0.773 | 0.393 |
| $Dy_2O_3$ | 0.400 | 0.211 |
| $Yb_2O_3$ | 0.044 | 0.009 |
| $Y_2O_3$ | 0.898 | 0.565 |
| $Sc_2O_3$ | 0.011 | 0.021 |
| MgO | 0.024 | 0.000 |
| CaO | 2.920 | 2.004 |
| MnO | 0.032 | 0.020 |
| FeO | 0.334 | 0.232 |
| PbO | 0.983 | 0.176 |
| **Total** | 98.437 | 99.160 |
| *apfu* | | |
| Th | 0.207 | 0.052 |
| U | 0.005 | 0.008 |
| Al | 0.001 | 0.002 |
| La | 0.096 | 0.189 |
| Ce | 0.284 | 0.401 |
| Pr | 0.030 | 0.041 |
| Nd | 0.181 | 0.201 |
| Sm | 0.026 | 0.021 |
| Gd | 0.011 | 0.005 |
| Dy | 0.005 | 0.003 |
| Yb | 0.001 | 0.000 |
| Y | 0.020 | 0.012 |
| Sc | 0.000 | 0.001 |
| Mg | 0.001 | 0.000 |
| Ca | 0.129 | 0.085 |
| Mn | 0.001 | 0.001 |
| Fe | 0.011 | 0.008 |
| Pb | 0.011 | 0.002 |
| **Σ X** | 1.020 | 1.031 |
| P | 0.972 | 0.986 |
| Si | 0.006 | 0.003 |
| **Σ Y** | 0.978 | 0.989 |

Table 77 Representative EMP analyses of monazite-(Ce). *Apfu* calculations based on 4 oxygens.

## MUSCOVITE

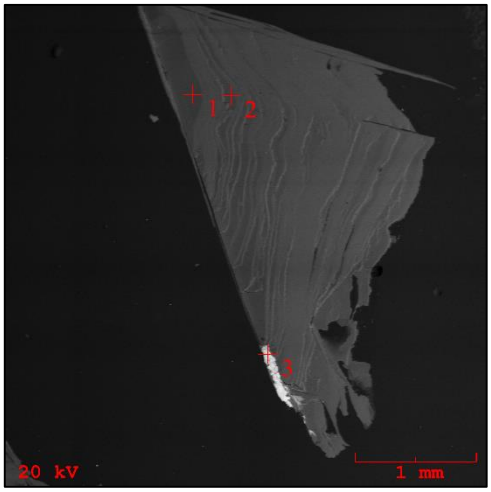


Figure 159 BSE image of polished muscovite mica (crosshairs 1 & 2) and a columbite/tantalite species (crosshair 3).

Muscovite mica has been identified in heavy mineral separations, qualitatively investigated by SEM, and confirmed as muscovite mica (Figure 185) by microprobe using Tischendorf's classification scheme (1997). Rubidium is just within detection limits and cesium is below detection limits. DCP analyses have detected lithium weight percent ranging from 0.200 to 0.628 in mica samples and has been stoichiometrically accounted for by using the equation 0.3935 * fluorine weight percent$^{1.326}$ (Tischendorf, 1997). Calculated weight percent of lithium ranges from 0.384 to just over one weight percent. Table 78 lists representative analyses.

| **MUSCOVITE – GROVELAND MINE PEGMATITE** | | | | | | | | |
|---|---|---|---|---|---|---|---|---|
| Wt % Ox. | GMP mica 1-1 | GMP mica 4-1 | GMP mica 4-2 | GMP mica 11-1 | GMP mica 2-1 | GMP mica 5-1 | GMP mica loose | GMP mica iz-1 |
| $SiO_2$ | 46.678 | 46.585 | 46.595 | 46.523 | 46.566 | 46.623 | 46.587 | 46.634 |
| $TiO_2$ | 0.312 | 0.265 | 0.277 | 0.244 | 0.044 | 0.144 | 0.160 | 0.100 |
| $Al_2O_3$ | 34.982 | 35.334 | 35.565 | 34.223 | 36.233 | 34.655 | 34.500 | 34.563 |
| $Fe_2O_3$ | 0.000 | 0.000 | 0.000 | 0.000 | 0.000 | 0.000 | 0.000 | 0.000 |
| FeO | 2.872 | 2.233 | 2.114 | 3.632 | 1.700 | 3.093 | 3.154 | 2.892 |
| MnO | 0.077 | 0.123 | 0.154 | 0.092 | 0.114 | 0.121 | 0.112 | 0.088 |
| MgO | 0.872 | 0.721 | 0.674 | 1.123 | 0.322 | 0.981 | 1.387 | 1.430 |
| CaO | 0.053 | 0.044 | 0.065 | 0.038 | 0.054 | 0.055 | 0.034 | 0.042 |
| $Li_2O$ (*calc.*) | 0.974 | 1.047 | 1.035 | 0.464 | 0.903 | 0.507 | 0.458 | 0.384 |
| $Na_2O$ | 0.455 | 0.487 | 0.555 | 0.332 | 0.675 | 0.422 | 0.466 | 0.465 |
| $K_2O$ | 9.556 | 9.600 | 9.367 | 9.677 | 9.500 | 9.454 | 9.022 | 9.343 |
| $Rb_2O$ | 0.021 | 0.019 | 0.020 | 0.016 | 0.020 | 0.014 | 0.013 | 0.015 |
| $Cs_2O$ | *bdl* | *bdl* | *bdl* | *bdl* | *bdl* | *bdl* | *bdl* | *bdl* |
| F | 1.981 | 2.092 | 2.074 | 1.133 | 1.871 | 1.211 | 1.122 | 0.982 |
| $H_2O$ | 3.640 | 3.583 | 3.597 | 3.992 | 3.688 | 3.961 | 4.003 | 4.069 |
| F=O | - 0.834 | - 0.881 | - 0.873 | - 0.477 | - 0.788 | - 0.510 | - 0.472 | - 0.413 |
| **Total** | 101.639 | 101.252 | 101.219 | 101.013 | 100.902 | 100.732 | 100.546 | 100.594 |
| *apfu* | | | | | | | | |
| Si | 6.113 | 6.106 | 6.100 | 6.159 | 6.103 | 6.164 | 6.160 | 6.166 |
| $^{IV}Al$ | 1.887 | 1.894 | 1.900 | 1.841 | 1.897 | 1.836 | 1.840 | 1.834 |
| **Σ T-site** | 8.000 | 8.000 | 8.000 | 8.000 | 8.000 | 8.000 | 8.000 | 8.000 |
| $^{VI}Al$ | 3.512 | 3.565 | 3.587 | 3.499 | 3.701 | 3.564 | 3.537 | 3.553 |
| Ti | 0.031 | 0.026 | 0.027 | 0.024 | 0.004 | 0.014 | 0.016 | 0.010 |
| $Fe_t$ | 0.315 | 0.245 | 0.232 | 0.402 | 0.187 | 0.342 | 0.349 | 0.320 |
| Mn | 0.009 | 0.014 | 0.017 | 0.010 | 0.013 | 0.014 | 0.013 | 0.010 |
| Mg | 0.170 | 0.141 | 0.132 | 0.222 | 0.063 | 0.193 | 0.274 | 0.282 |
| Li (*calc.*) | 0.513 | 0.552 | 0.545 | 0.247 | 0.476 | 0.270 | 0.244 | 0.204 |
| **Σ Y-site** | 4.550 | 4.543 | 4.540 | 4.404 | 4.444 | 4.397 | 4.433 | 4.379 |

Table 78 Representative EMP analyses of muscovite mica. *Apfu* calculations based on 24 anions. Table continues on next page.

| | | | | | | | | |
|---|---|---|---|---|---|---|---|---|
| K | 1.597 | 1.605 | 1.564 | 1.634 | 1.589 | 1.595 | 1.522 | 1.576 |
| Ca | 0.007 | 0.006 | 0.009 | 0.005 | 0.008 | 0.008 | 0.005 | 0.006 |
| Na | 0.116 | 0.124 | 0.141 | 0.085 | 0.172 | 0.108 | 0.120 | 0.119 |
| Rb | 0.002 | 0.002 | 0.002 | 0.001 | 0.002 | 0.001 | 0.001 | 0.001 |
| Cs | *bdl* | *bdl* | *bdl* | *bdl* | *bdl* | *bdl* | *bdl* | *bdl* |
| **Σ X-site** | 1.722 | 1.737 | 1.716 | 1.725 | 1.771 | 1.712 | 1.648 | 1.702 |
| F | 0.820 | 0.867 | 0.859 | 0.474 | 0.776 | 0.506 | 0.469 | 0.411 |
| OH (*calc.*) | 3.180 | 3.133 | 3.141 | 3.526 | 3.224 | 3.494 | 3.531 | 3.589 |
| **Σ W-site** | 4.000 | 4.000 | 4.000 | 4.000 | 4.000 | 4.000 | 4.000 | 4.000 |

PYRITE

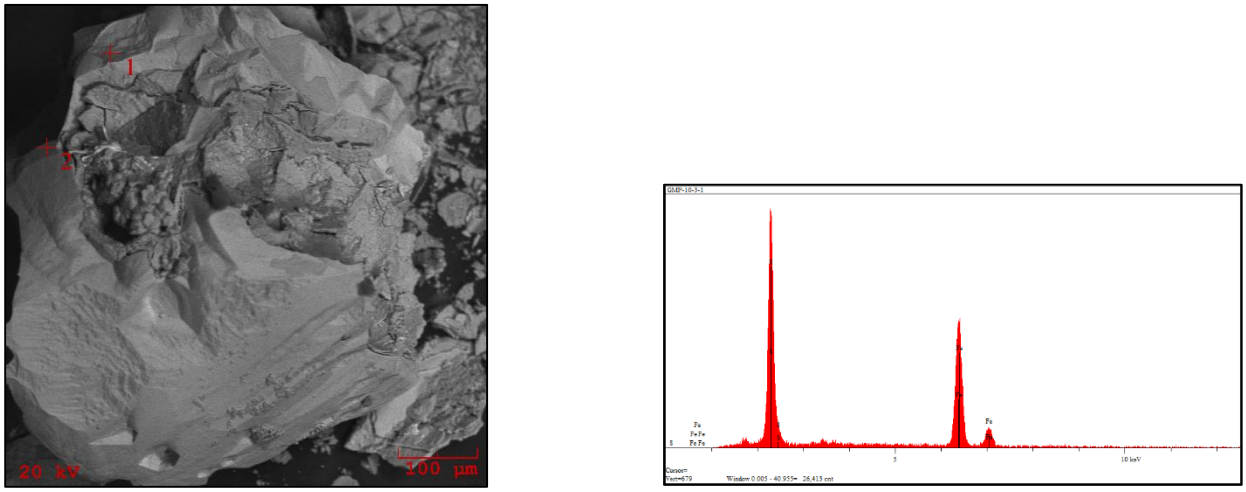


Figure 160 BSE image of pyrite grain with corresponding EDS spectrum (1 & 2).

Pyrite is present and relatively abundant in heavy mineral separations. Pyrite has been qualitatively analyzed by SEM.

PYROPHANITE

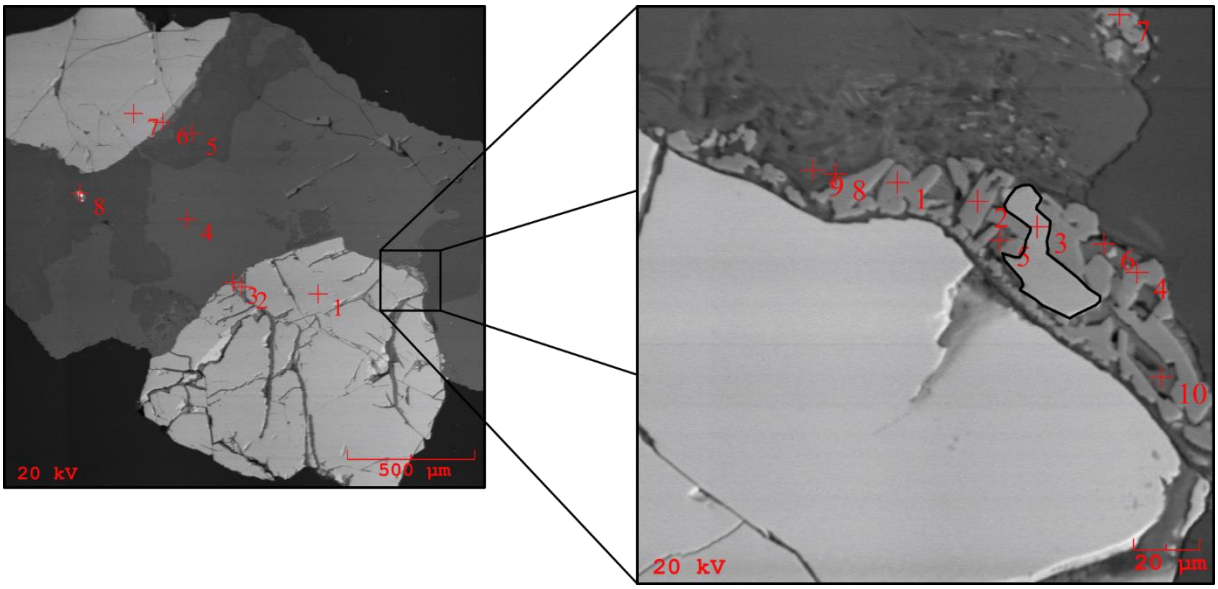


Figure 161 BSE close-up image of pyrophanite (right; outlined in black; crosshair 3). BSE image - left: magnetite (crosshairs 1 & 7), ilmenite/rutile (crosshairs 2 & 3), K-feldspar (crosshair 4), plagioclase (crosshair 5), pyrophanite (crosshair 6), and zircon (crosshair 8). BSE image close-up - right: Rutile (crosshairs 1, 2, 4, & 7), pyrophanite (outlined; crosshair 3), titanium species (crosshair 5), fluorite (crosshair 6 & 10), quartz (crosshair 8), & mica (crosshair 9).

Pyrophanite is very rare and is closely associated with magnetite and gahnite. Pyrophanite is present as overgrowths on magnetite and is also associated with rutile, gahnite, and mica. This is the first reported and quantitatively confirmed occurrence of pyrophanite (outlined are, right BSE image; Figure 161) at the Groveland Mine pegmatite. Table 79 lists the representative analyses.

| **PYROPHANITE – GROVELAND MINE PEGMATITE** | | |
|---|---|---|
| Wt% Oxide | GMP Magnetite 11 | |
| $TiO_2$ | 52.777 | 52.699 |
| $Al_2O_3$ | 0.112 | 0.134 |
| $SiO_2$ | 0.034 | 0.062 |
| FeO | 7.433 | 7.845 |
| MnO | 39.677 | 39.623 |
| MgO | 0.017 | 0.02 |
| CaO | 0.065 | 0.055 |
| $Nb_2O_5$ | *bdl* | *bdl* |
| $Ta_2O_5$ | *bdl* | *bdl* |
| **Total** | 100.115 | 100.438 |
| *apfu* | | |
| FeO | 0.145 | 0.153 |
| MnO | 1.722 | 1.719 |
| MgO | 0.001 | 0.001 |
| CaO | 0.005 | 0.004 |
| Nb | *bdl* | *bdl* |
| Ta | *bdl* | *bdl* |
| **Σ X-site** | 1.873 | 1.877 |
| Ti | 2.060 | 2.057 |
| Al | 0.002 | 0.002 |
| Si | 0.002 | 0.003 |
| **Σ Y-site** | 2.064 | 2.062 |

Table 79 Representative EMP analyses of pyrophanite. *Apfu* calculations based on 6 oxygens.

## RUTILE

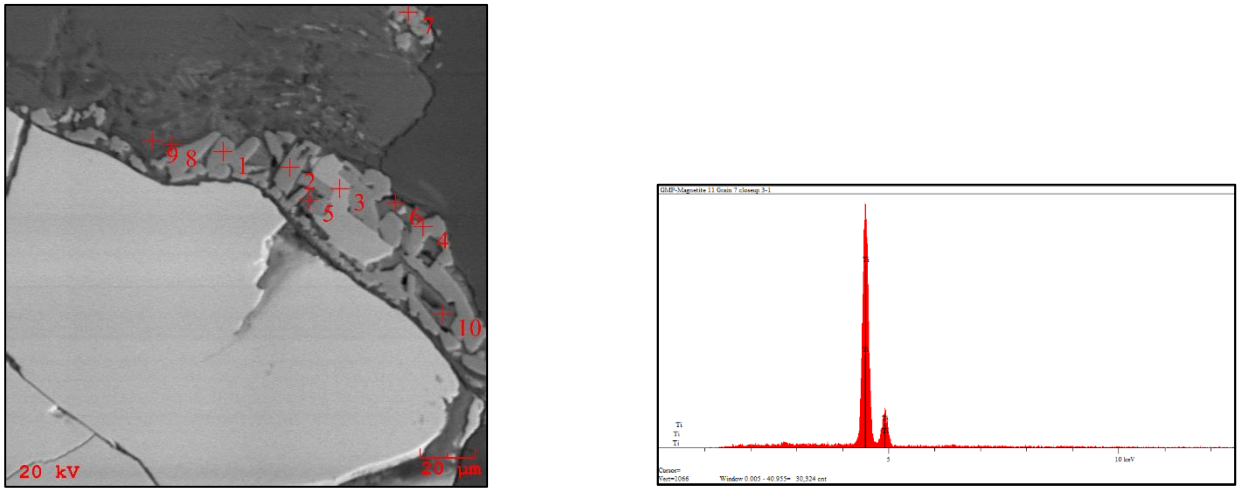


Figure 162 BSE close-up image of rutile overgrowth on magnetite (crosshairs 1, 2, & 4).

Rutile is closely associated with magnetite, pyrophanite, mica, and gahnite at the Groveland Mine pegmatite and has been qualitatively investigated by SEM. Rutile is often found as an overgrowth on magnetite grains. Discrete grains have also been found. Figure 161 shows a complete list of associated spectra and mineralogy.

## TANTALITE

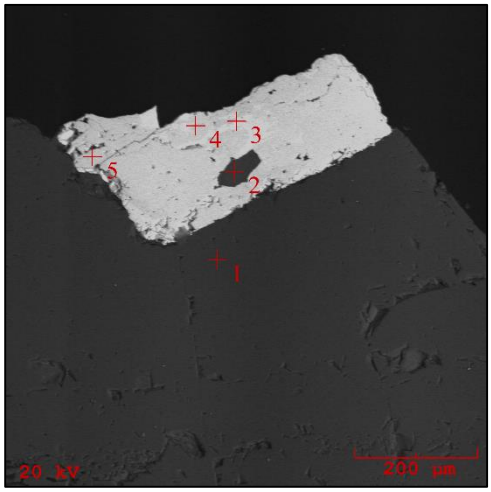


Figure 163 BSE image of polished tantalite grain.

Tantalite appears to be just as ubiquitous as columbite in heavy mineral separations. Tantalite has been qualitatively investigated by SEM and further analysis by microprobe has confirmed tantalum dominance over niobium as well as iron dominance over manganese. Ferrotantalite, and for that matter, ferrotapiolite have both been reported as being found at Groveland Mine pegmatite. Without XRD analysis of grains, it remains uncertain as to whether or not these are ferrotantalite or ferrotapiolite. Buchholz *et al*. (2014) have reported the occurrence of compositions ranging from tantalite-(Fe) to tapiolite-(Fe), although their analyses are relatively more iron-rich. It should be noted that a few analyses plot very close to the manganotantalite field, having a Mn/(Mn+Fe) ratio of 0.496. Table 80 lists the representative analyses. Additional analyses listed in Table 99 of the appendices.

| FERROTANTALITE – GROVELAND MINE PEGMATITE | | | | | | | | | | |
|---|---|---|---|---|---|---|---|---|---|---|
| Wt% Ox | GOI grain 10-1 | | GOI grain 11-1 | | GOI grain 12-1 | | GOI grain 13-1 | | GOI grain 15-1 | |
| $Nb_2O_5$ | 28.565 | 30.444 | 29.788 | 29.544 | 2.877 | 2.834 | 29.544 | 29.655 | 28.665 | 8.766 |
| $Ta_2O_5$ | 54.555 | 52.788 | 53.211 | 53.677 | 82.887 | 82.766 | 53.500 | 53.568 | 54.337 | 75.699 |
| $SiO_2$ | 0.028 | 0.018 | 0.019 | 0.440 | 0.033 | 0.045 | 0.044 | 0.040 | 0.065 | 0.022 |
| $TiO_2$ | 0.000 | 0.000 | 0.000 | 0.000 | 0.000 | 0.000 | 0.000 | 0.000 | 0.000 | 0.000 |
| $Al_2O_3$ | 0.000 | 0.000 | 0.000 | 0.000 | 0.000 | 0.000 | 0.000 | 0.000 | 0.000 | 0.000 |
| FeO | 9.450 | 9.111 | 8.776 | 8.900 | 8.433 | 8.450 | 9.004 | 8.676 | 8.555 | 8.766 |
| MnO | 7.530 | 7.788 | 8.006 | 7.883 | 5.778 | 6.800 | 7.743 | 8.330 | 8.312 | 6.834 |
| MgO | *bdl* | *bdl* | *bdl* | *bdl* | *bdl* | *bdl* | *bdl* | *bdl* | *bdl* | *bdl* |
| Total | 100.128 | 100.149 | 99.800 | 100.444 | 100.008 | 100.895 | 99.835 | 100.269 | 99.934 | 100.087 |
| *apfu* | | | | | | | | | | |
| Fe | 0.566 | 0.541 | 0.524 | 0.526 | 0.591 | 0.586 | 0.538 | 0.516 | 0.513 | 0.566 |
| Mn | 0.457 | 0.468 | 0.484 | 0.472 | 0.410 | 0.477 | 0.469 | 0.502 | 0.505 | 0.457 |
| Si | 0.002 | 0.001 | 0.001 | 0.031 | 0.003 | 0.004 | 0.003 | 0.003 | 0.005 | 0.002 |
| Al | 0.000 | 0.000 | 0.000 | 0.000 | 0.000 | 0.000 | 0.002 | 0.000 | 0.000 | 0.000 |
| Mg | *bdl* | *bdl* | *bdl* | *bdl* | *bdl* | *bdl* | *bdl* | *bdl* | *bdl* | *bdl* |
| **Σ X-site** | 1.025 | 1.010 | 1.009 | 1.029 | 1.004 | 1.067 | 1.012 | 1.021 | 1.013 | 1.025 |
| Nb | 0.926 | 0.977 | 0.962 | 0.944 | 0.109 | 0.106 | 0.955 | 0.954 | 0.929 | 0.926 |
| Ta | 1.063 | 1.019 | 1.034 | 1.032 | 1.888 | 1.866 | 1.040 | 1.037 | 1.060 | 1.063 |
| Ti | 0.000 | 0.000 | 0.000 | 0.000 | 0.000 | 0.000 | 0.000 | 0.000 | 0.000 | 0.000 |
| **Σ Y-site** | 1.989 | 1.996 | 1.996 | 1.976 | 1.997 | 1.972 | 1.995 | 1.991 | 1.989 | 1.989 |

Table 80 Representative EMP analyses of ferrotantalite. *Apfu* calculations based on 6 oxygens.

## TOURMALINE

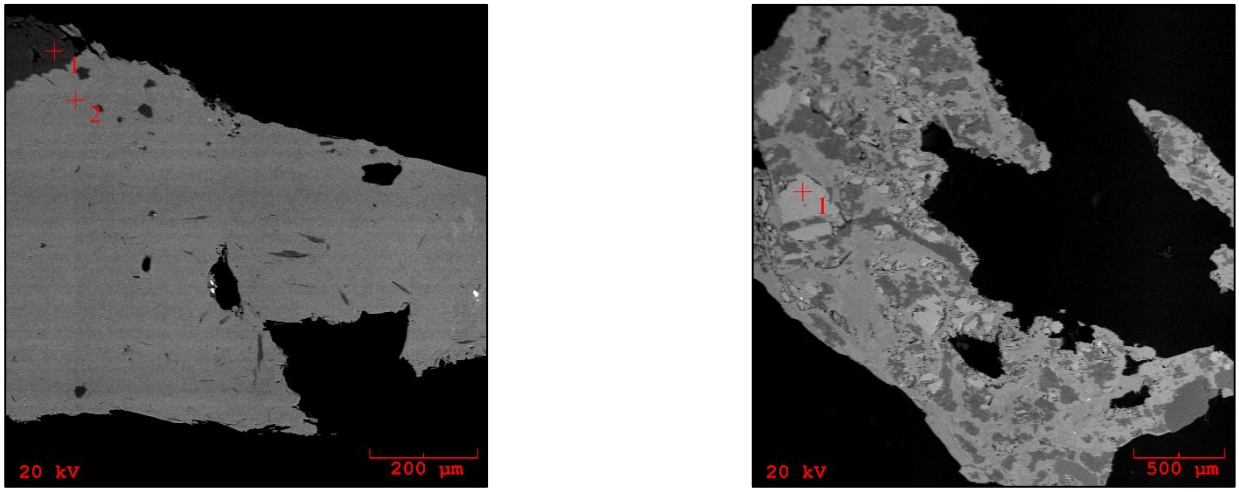


Figure 164 BSE images of polished tourmaline grains. BSE image left: quartz (crosshair 1) & tourmaline (crosshair 2). BSE image right: tourmaline (crosshair 1). Note the degree of alteration in tourmaline grain to the right.

Tourmaline is rather abundant in heavy mineral separations, although it is rare to find unaltered tourmaline (above left) and much more likely to have grains that are to some degree altered in appearance (above right). Tourmaline has been investigated qualitatively by SEM and has been further analyzed by microprobe. Tourmalines are all but depleted in calcium and potassium and much more sodium-rich. Based on X-site dominance, tourmalines from the Groveland Mine are part of the alkali group. There is approximately 25% vacancy in the X-site. Y-site is iron dominant. There is some amount of magnesium (>1 weight percent) and calculated lithium content ranges from 0.6 and 0.8 weight percent. Fluorine is dominant over hydroxyl ions. Tourmaline from the Groveland Mine pegmatite should therefore be classified as fluorschorl. Table 81 lists the representative analyses.

| TOURMALINE – GROVELAND MINE PEGMATITE | | | | | | | | | | |
|---|---|---|---|---|---|---|---|---|---|---|
| Wt.% Oxide | grain 1-1 | | grain 2-1 | | grain 3-1 | | grain 4-1 | | grain 6-1 | |
| $SiO_2$ | 36.500 | 36.522 | 36.544 | 36.499 | 36.499 | 36.511 | 36.488 | 36.500 | 36.455 | 36.500 |
| $TiO_2$ | 0.133 | 0.125 | 0.112 | 0.132 | 0.133 | 0.122 | 0.133 | 0.122 | 0.111 | 0.101 |
| $Al_2O_3$ | 31.819 | 31.834 | 31.412 | 31.755 | 31.533 | 31.566 | 31.002 | 31.121 | 31.511 | 31.488 |
| $B_2O_3$ (*calc.*) | 10.404 | 10.394 | 10.381 | 10.376 | 10.381 | 10.358 | 10.325 | 10.339 | 10.370 | 10.349 |
| FeOt | 11.565 | 14.122 | 11.655 | 14.011 | 11.455 | 14.200 | 14.543 | 14.444 | 11.487 | 11.505 |
| MnO | 3.223 | 0.544 | 3.655 | 0.512 | 3.830 | 0.526 | 0.211 | 0.181 | 3.899 | 2.766 |
| MgO | 0.766 | 0.643 | 0.675 | 0.595 | 0.633 | 0.544 | 0.899 | 0.912 | 0.577 | 0.700 |
| CaO | 0.012 | 0.022 | 0.020 | 0.024 | 0.043 | 0.030 | 0.043 | 0.045 | 0.030 | 0.018 |
| $Na_2O$ | 2.344 | 2.311 | 2.333 | 2.336 | 2.282 | 2.289 | 2.300 | 2.353 | 2.292 | 2.400 |
| $K_2O$ | 0.030 | 0.042 | 0.023 | 0.023 | 0.012 | 0.022 | 0.045 | 0.055 | 0.040 | 0.019 |
| $Li_2O$ (*calc.*) | 0.680 | 0.742 | 0.697 | 0.787 | 0.678 | 0.798 | 0.782 | 0.790 | 0.674 | 0.844 |
| $H_2O$ (*calc.*) | 3.053 | 3.038 | 3.008 | 3.017 | 3.023 | 3.005 | 3.045 | 3.040 | 2.993 | 3.050 |
| F | 1.132 | 1.156 | 1.211 | 1.188 | 1.178 | 1.200 | 1.091 | 1.112 | 1.234 | 1.099 |
| F=O | - 0.477 | - 0.487 | - 0.510 | - 0.500 | 0.496 | - 0.505 | - 0.459 | - 0.468 | - 0.520 | - 0.463 |
| **Total** | 101.18 | 101.01 | 101.22 | 100.75 | 101.18 | 100.67 | 100.45 | 100.55 | 101.15 | 100.38 |
| *apfu* | | | | | | | | | | |
| Na | 0.759 | 0.749 | 0.757 | 0.759 | 0.741 | 0.745 | 0.751 | 0.767 | 0.745 | 0.781 |
| Ca | 0.002 | 0.004 | 0.004 | 0.004 | 0.008 | 0.005 | 0.008 | 0.008 | 0.005 | 0.003 |
| K | 0.006 | 0.009 | 0.005 | 0.005 | 0.003 | 0.005 | 0.010 | 0.012 | 0.009 | 0.004 |
| Vac (*calc.*) | 0.232 | 0.238 | 0.234 | 0.232 | 0.249 | 0.245 | 0.232 | 0.213 | 0.241 | 0.211 |
| **Σ X-site** | 1.000 | 1.000 | 1.000 | 1.000 | 1.000 | 1.000 | 1.000 | 1.000 | 1.000 | 1.000 |
| Fe | 1.616 | 1.975 | 1.632 | 1.963 | 1.604 | 1.993 | 2.047 | 2.031 | 1.610 | 1.616 |
| Mg | 0.191 | 0.160 | 0.168 | 0.149 | 0.158 | 0.136 | 0.226 | 0.229 | 0.144 | 0.175 |
| Al | 0.264 | 0.274 | 0.198 | 0.269 | 0.222 | 0.242 | 0.151 | 0.166 | 0.224 | 0.233 |
| Mn | 0.456 | 0.077 | 0.518 | 0.073 | 0.543 | 0.075 | 0.030 | 0.026 | 0.553 | 0.393 |
| Li (*calc.*) | 0.456 | 0.499 | 0.469 | 0.530 | 0.456 | 0.539 | 0.529 | 0.534 | 0.454 | 0.570 |
| Ti | 0.017 | 0.016 | 0.014 | 0.017 | 0.017 | 0.015 | 0.017 | 0.015 | 0.014 | 0.013 |
| **Σ Y-site** | 3.000 | 3.000 | 3.000 | 3.000 | 3.000 | 3.000 | 3.000 | 3.000 | 3.000 | 3.000 |
| Al | 6.000 | 6.000 | 6.000 | 6.000 | 6.000 | 6.000 | 6.000 | 6.000 | 6.000 | 6.000 |
| Mg | 0.000 | 0.000 | 0.000 | 0.000 | 0.000 | 0.000 | 0.000 | 0.000 | 0.000 | 0.000 |
| **Σ Z-site** | 6.000 | 6.000 | 6.000 | 6.000 | 6.000 | 6.000 | 6.000 | 6.000 | 6.000 | 6.000 |
| Si | 6.097 | 6.107 | 6.118 | 6.114 | 6.111 | 6.126 | 6.142 | 6.136 | 6.110 | 6.130 |
| Al | 0.000 | 0.000 | 0.000 | 0.000 | 0.000 | 0.000 | 0.000 | 0.000 | 0.000 | 0.000 |
| **Σ T-site** | 6.097 | 6.107 | 6.118 | 6.114 | 6.111 | 6.126 | 6.142 | 6.136 | 6.110 | 6.130 |
| B (*calc.*) | 3.000 | 3.000 | 3.000 | 3.000 | 3.000 | 3.000 | 3.000 | 3.000 | 3.000 | 3.000 |
| H (*calc.*) | 3.402 | 3.389 | 3.359 | 3.371 | 3.376 | 3.363 | 3.419 | 3.409 | 3.346 | 3.416 |
| F | 0.598 | 0.611 | 0.641 | 0.629 | 0.624 | 0.637 | 0.581 | 0.591 | 0.654 | 0.584 |
| **Σ W+V sites** | 4.000 | 4.000 | 4.000 | 4.000 | 4.000 | 4.000 | 4.000 | 4.000 | 4.000 | 4.000 |
| | | | | | | | | | | |
| **Species** | *fluor-schorl* | *fluor-schorl* | *fluor-schorl* | *fluor-schorl* | *fluor-schorl* | *fluor-schorl* | *fluor-schorl* | *fluor-schorl* | *fluor-schorl* | *fluor-schorl* |

Table 81 Representative EMP analyses of tourmaline. *Apfu* calculations based on 31 anions.

## "XENOTIME"

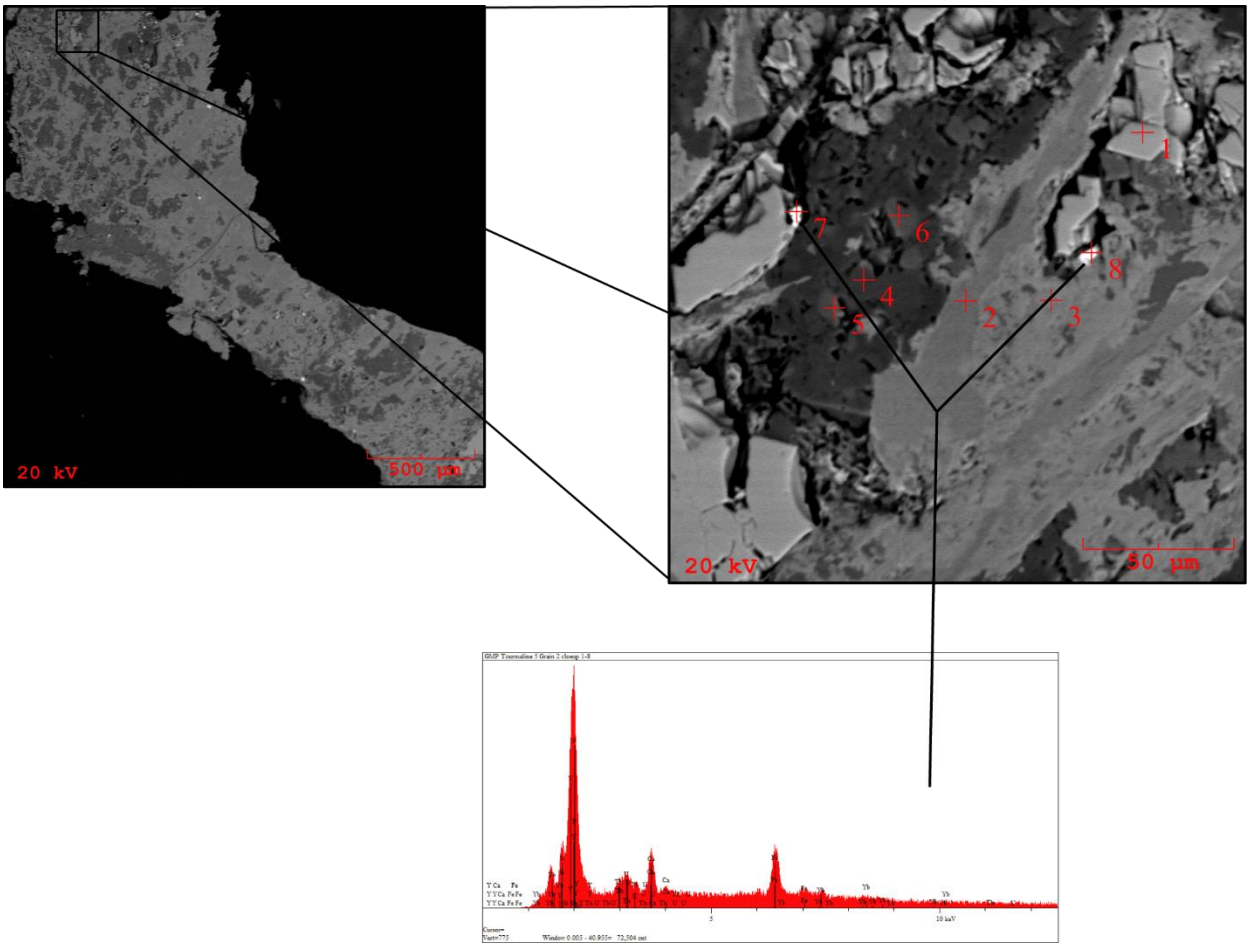


Figure 165 BSE image of tourmaline grain with close-up of "xenotime" inclusion; associated EDS spectrum included.

"Xenotime" occurs as small inclusion in tourmaline grains as well as discrete grains. "Xenotime" has been quantitatively confirmed by microprobe and should be classified as xenotime-(Y) due to yttrium dominance in the X-site. Yttrium comprises approximately 70% of the cations in the X-site. Not one of the HREE's that are present account for greater than 10% of cations in the X-site. Other than Xenotime-(Y) being found as inclusions, only two discrete grains have been discovered. These grains are associated with zircon. Table 82 lists the representative analyses of the inclusions.

| **XENOTIME-(Y) – GROVELAND MINE PEGMATITE** | | |
|---|---|---|
| Wt % Ox. | 9 GMP-1 | 10 GMP-1 |
| $P_2O_5$ | 33.765 | 33.877 |
| $SiO_2$ | 0.244 | 0.211 |
| $ThO_2$ | 0.000 | 0.000 |
| $UO_2$ | 2.654 | 3.655 |
| $Al_2O_3$ | 0.221 | 0.232 |
| $Nd_2O_3$ | 0.011 | 0.013 |
| $Sm_2O_3$ | 0.022 | 0.020 |
| $Gd_2O_3$ | 3.650 | 3.766 |
| $Tb_2O_3$ | 0.889 | 0.922 |
| $Dy_2O_3$ | 7.090 | 7.320 |
| $Ho_2O_3$ | 1.009 | 1.100 |
| $Er_2O_3$ | 4.033 | 3.899 |
| $Tm_2O_3$ | 0.776 | 0.832 |
| $Yb_2O_3$ | 6.099 | 6.455 |
| $Lu_2O_3$ | 0.232 | 0.233 |
| $Y_2O_3$ | 38.443 | 37.231 |
| $Sc_2O_3$ | 0.020 | 0.016 |
| MgO | 0.000 | 0.000 |
| CaO | 0.044 | 0.041 |
| MnO | 0.009 | 0.000 |
| FeO | 0.013 | 0.020 |
| PbO | 0.009 | 0.011 |
| **Total** | 99.310 | 99.898 |
| *apfu* | | |
| Th | 0.021 | 0.029 |
| U | 0.002 | 0.002 |
| Al | 0.003 | 0.002 |
| Nd | 0.000 | 0.000 |
| Sm | 0.000 | 0.000 |
| Gd | 0.042 | 0.043 |
| Tb | 0.010 | 0.010 |
| Dy | 0.079 | 0.082 |
| Ho | 0.011 | 0.012 |
| Er | 0.044 | 0.042 |
| Tm | 0.008 | 0.009 |
| Yb | 0.064 | 0.068 |
| Lu | 0.002 | 0.002 |
| Y | 0.708 | 0.686 |
| Sc | 0.001 | 0.000 |
| Mg | 0.000 | 0.000 |
| Ca | 0.002 | 0.002 |
| Mn | 0.000 | 0.000 |
| Fe | 0.000 | 0.001 |
| Pb | 0.000 | 0.000 |
| **Σ X** | 0.999 | 0.991 |
| P | 0.990 | 0.994 |
| Si | 0.008 | 0.007 |
| **Σ Y** | 0.998 | 1.001 |

Table 82 Representative EMP analyses of xenotime-(Y). *Apfu* calculations based on 4 oxygens.

ZIRCON

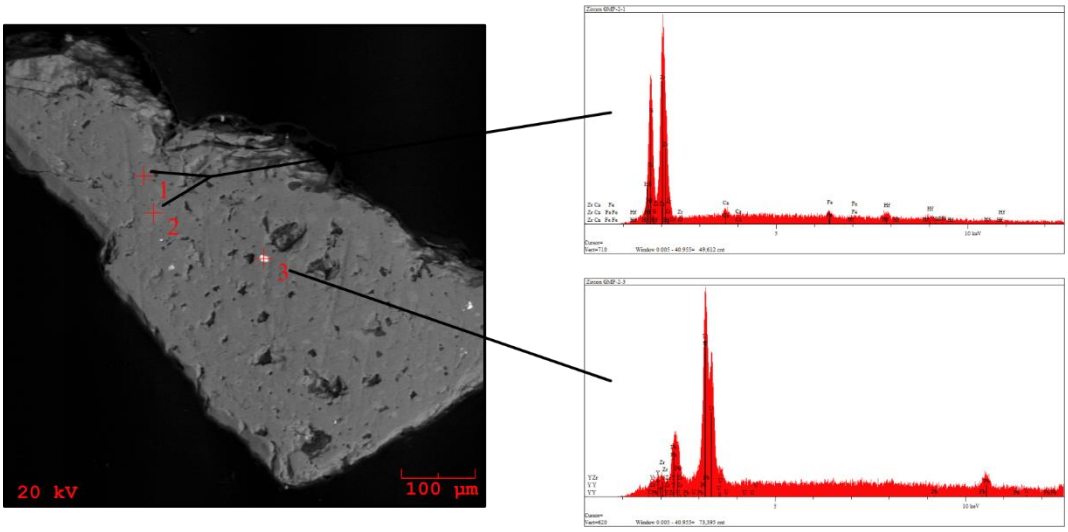


Figure 166 BSE image of polished zircon grain and uraninite inclusion with possible radiogenic lead.

Zircon has been found in heavy mineral separations and has been further analyzed by SEM and microprobe. Little to no detectable zonation is present in the zircons that have been analyzed. Hafnium weight percent ranges from 1.60-2.30% in zircons. As such, zircon samples are relatively primitive. Some grains appear to be altered as weight percent totals are below 98%. Table 83 lists the representative analyses.

| ZIRCON – GROVELAND MINE PEGMATITE | | | | | | | | | | |
|---|---|---|---|---|---|---|---|---|---|---|
| Wt % Oxide | grain 1-GMP-1 | | grain 2-GMP-1 | | grain 3-GMP-1 | | grain 4-GMP-1 | | grain 5-GMP-1 | |
| $SiO_2$ | 30.541 | 30.494 | 31.344 | 31.600 | 31.870 | 32.002 | 32.211 | 32.300 | 32.043 | 31.981 |
| $TiO_2$ | 0.000 | 0.013 | 0.010 | 0.012 | 0.011 | 0.014 | 0.020 | 0.023 | 0.014 | 0.018 |
| $Al_2O_3$ | 0.044 | 0.048 | 0.055 | 0.063 | 0.040 | 0.010 | 0.050 | 0.062 | 0.032 | 0.028 |
| $ZrO_2$ | 63.770 | 64.112 | 64.667 | 64.700 | 64.780 | 64.662 | 64.440 | 64.213 | 64.044 | 63.873 |
| $HfO_2$ | 1.988 | 1.934 | 1.599 | 1.711 | 1.677 | 1.599 | 1.981 | 1.955 | 1.761 | 2.334 |
| FeOt | 0.454 | 0.494 | 0.332 | 0.292 | 0.388 | 0.400 | 0.311 | 0.256 | 0.432 | 0.393 |
| MnO | 0.022 | 0.025 | 0.012 | 0.020 | 0.011 | 0.015 | 0.000 | 0.011 | 0.022 | 0.025 |
| MgO | 0.000 | 0.000 | 0.000 | 0.000 | 0.000 | 0.000 | 0.000 | 0.000 | 0.000 | 0.000 |
| CaO | 0.566 | 0.623 | 0.334 | 0.343 | 0.299 | 0.282 | 0.300 | 0.285 | 0.338 | 0.356 |
| $UO_2$ | 0.033 | 0.040 | 0.021 | 0.018 | 0.033 | 0.029 | 0.016 | 0.020 | 0.019 | 0.023 |
| $ThO_2$ | 0.112 | 0.091 | 0.100 | 0.077 | 0.100 | 0.091 | 0.067 | 0.094 | 0.055 | 0.043 |
| **Total** | 97.530 | 97.874 | 98.474 | 98.836 | 99.209 | 99.104 | 99.396 | 99.219 | 98.760 | 99.074 |
| *apfu* | | | | | | | | | | |
| Zr | 0.988 | 0.990 | 0.987 | 0.983 | 0.979 | 0.977 | 0.970 | 0.967 | 0.970 | 0.967 |
| Hf | 0.024 | 0.024 | 0.019 | 0.021 | 0.020 | 0.019 | 0.024 | 0.023 | 0.021 | 0.028 |
| U | 0.000 | 0.000 | 0.000 | 0.000 | 0.000 | 0.000 | 0.000 | 0.000 | 0.000 | 0.000 |
| Th | 0.001 | 0.001 | 0.001 | 0.001 | 0.001 | 0.001 | 0.000 | 0.001 | 0.000 | 0.000 |
| Fe | 0.012 | 0.013 | 0.009 | 0.008 | 0.010 | 0.010 | 0.008 | 0.007 | 0.011 | 0.010 |
| Mn | 0.001 | 0.001 | 0.000 | 0.001 | 0.000 | 0.000 | 0.000 | 0.000 | 0.001 | 0.001 |
| Mg | 0.000 | 0.000 | 0.000 | 0.000 | 0.000 | 0.000 | 0.000 | 0.000 | 0.000 | 0.000 |
| Ca | 0.019 | 0.021 | 0.011 | 0.011 | 0.010 | 0.009 | 0.010 | 0.009 | 0.011 | 0.012 |
| **Σ X-site** | 1.045 | 1.050 | 1.027 | 1.025 | 1.020 | 1.016 | 1.012 | 1.007 | 1.014 | 1.018 |
| Si | 0.970 | 0.966 | 0.981 | 0.984 | 0.988 | 0.992 | 0.995 | 0.998 | 0.995 | 0.992 |
| Ti | 0.000 | 0.000 | 0.000 | 0.000 | 0.000 | 0.000 | 0.000 | 0.001 | 0.000 | 0.000 |
| Al | 0.002 | 0.002 | 0.002 | 0.002 | 0.001 | 0.000 | 0.002 | 0.002 | 0.001 | 0.001 |
| **Σ Y-site** | 0.972 | 0.968 | 0.983 | 0.986 | 0.989 | 0.992 | 0.997 | 1.001 | 0.996 | 0.993 |

Table 83 Representative EMP analyses of zircon. *Apfu* calculations based on 4 oxygens.

# Results & Discussion

## Mineral Chemistry

### Apatite Group

Apatite is the most abundant of the phosphorus-bearing minerals and found in almost all igneous rocks. Apatite is typically rare in NYF-type pegmatites (Simmons *et al*., 2003) owing to their phosphorus-depleted nature (London *et al*., 2008). Apatite group minerals are classified by the dominant anion fluorine and chlorine as well as the hydroxyl ion; generally, the fluorine dominant end-member, fluorapatite, is the most abundant. Apatite is extremely rare in samples from all locations. Discrete apatite grains from the Sturgeon River, Groveland Mine, Crockley, and Grizzly pegmatites were analyzed by EMP and determined that the apatites were fluorapatite (Figure 167). Other locations did yield apatite, but these are inclusions associated with other minerals.

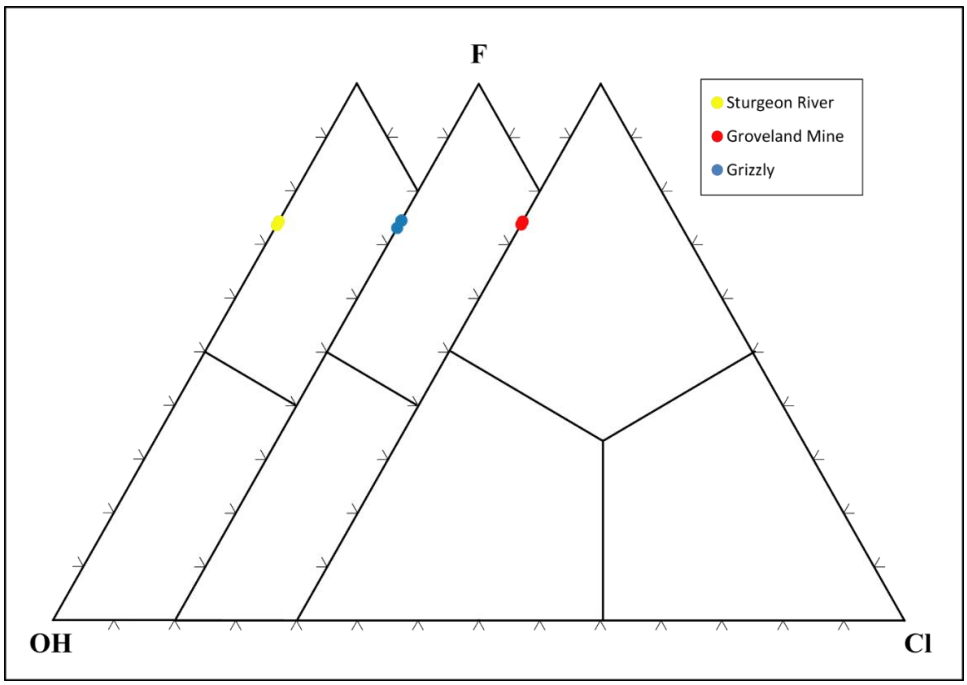


Figure 167 Anion dominance ternary for apatites.

## BASTNÄSITE

Although extremely rare in samples collected, "bastnäsite" happens to be one of the more abundant rare earth element-bearing minerals. "Bastnäsite" consists of a family of three fluorocarbonate minerals: bastnäsite-(Ce), bastnäsite-(La), and bastnäsite-(Y). "Bastnäsite" has only been found in samples from the Sturgeon River and Crockley pegmatites. Both sets of samples are cerium dominant (Figure 168) and therefore are classified as bastnäsite-(Ce). One analysis from Crockley pegmatite samples is relatively more enriched in calcium than other analyses from Sturgeon River or Crockley pegmatites.

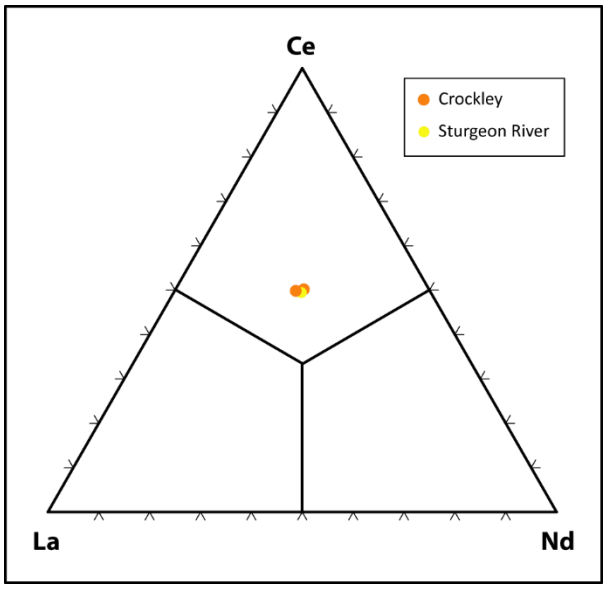


Figure 168 Cerium, Lanthanum, Neodymium in bastnäsite group minerals. Yttrium is >0.02 *apfu*.

## BERYL GROUP

Beryl is typically more abundant in the more peraluminous LCT-type pegmatites; however, it can occur in NYF-type pegmatites as well. Trace element content of beryl often reflects the geochemical evolution of a pegmatite and beryl varieties are often used to determine

the degree of evolution the pegmatite has attained (Simmons *et al*., 2003); however, analyses for trace element content were not conducted. Beryl was only found at the Groveland Mine pegmatite. Samples are pale green with a slight yellow hue and range in size from about ½ cm to 1 cm in length with a diameter roughly ½ cm. All samples have excellent crystal faces, but no discernable terminations. SEM analyses show a slight Fe peak with no detectable zonation from core to rim. Some samples have fracture infillings of Mg-rich biotite composition. One sample has inclusions of a Th-rich silicate/phosphate (see beryl in Groveland Mine pegmatite section). None of the analyzed samples appear to be texturally homogeneous. Figure 169 reveals that although the Groveland is peraluminous and enriched in boron, beryl from the Groveland Mine is relatively primitive and typical of NYF-type pegmatites (Černý, 1992).

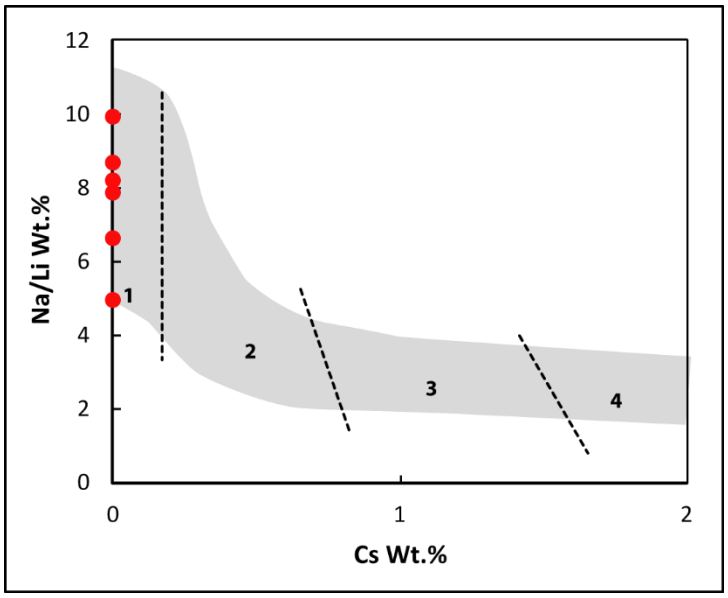


Figure 169 Beryl from Groveland Mine pegmatite. Na/Li versus Cs Wt.%. Region 1 – typical of NYF-type pegmatites; Region 2 – beryl-type pegmatites; Region 3 – complex pegmatites; Region 4 – highly fractionated, pollucite-bearing pegmatites. Modified from Černý, 1992.

## BISMUTH (NATIVE)

Native bismuth has only been found as inclusions in fluorite samples from the Grizzly pegmatite. No other pegmatite contains elemental bismuth or any other bismuth mineralogy

## CHALCOPYRITE

Chalcopyrite is brass-yellow, has a metallic luster and is often tarnished or iridescent. Chalcopyrite is an important ore for copper, the most widely occurring copper-bearing mineral, and has a variety of paragenetic origins. Chalcopyrite has been found in samples collected from the Crockley and Hwy69 pegmatites.

## CHLORITE

Chlorites are a group of minerals very similar to micas in that they are layered and have perfect basal cleavage. Garnets (especially almandine) can become "chloritized" meaning that alteration of the garnet grain can give rise to chlorite. Given that garnets analyzed had some degree of alteration and/or fracture infilling, it is suggested here that some of these garnets have been chloritized although this has not been quantitatively confirmed by microprobe analysis. One grain from the Bell Creek granite (Figure 12) was qualitatively analyzed by SEM and assumed to be chlorite based on EDS spectral analysis and the platy texture of the grain.

## COLUMBITE/TANTALITE GROUP

The columbite-tantalite group (CTG) consists of four end-members (Černý & Ercit, 1986) based on the relative enrichment of Fe vs. Mn and Ta vs. Nb. Columbite-tantalite group members are excellent indicators of the geochemical evolution of pegmatites. The ratios Mn/(Mn+Fe) and Ta/(Ta+Nb) tends to increase with increasing degree of evolution of the pegmatite (Černý, 1992). Discrete grains of the columbite-tantalite group minerals have been identified from the Crockley, Black River, Groveland Mine, and Hwy69 pegmatites. Other CTG occur as inclusions in mica. The CTG quadrilateral (Figure 170) reveals that samples are mostly ferrocolumbite, with the exception of ferrotantalites from Groveland Mine and Black River samples.

CTG is relatively more abundant at the Groveland Mine pegmatite than any other sampled location. The Groveland Mine samples are unique in that some analyses show enrichment of tantalum over niobium, which is unusual for NYF-type pegmatites. These analyses plot within the ferrotantalite-tapiolite, two phase field. Without further analysis by XRD, it is uncertain how to classify these grains. Also, these same analyses are relatively more enriched in manganese than Hwy69, Crockley, and other Groveland samples plotting in the ferrocolumbite field. One analysis in particular has a Mn/(Mn+Fe) ratio of 0.496, which is on the cusp for classification as a manganotantalite. Manganotantalites are typically only found in LCT-type pegmatites. A Black River CTG analysis has progressive enrichment of tantalum from core to rim. The rim analysis is plotting in the ferrotantalite field and the core plots within the ferrocolumbite field.

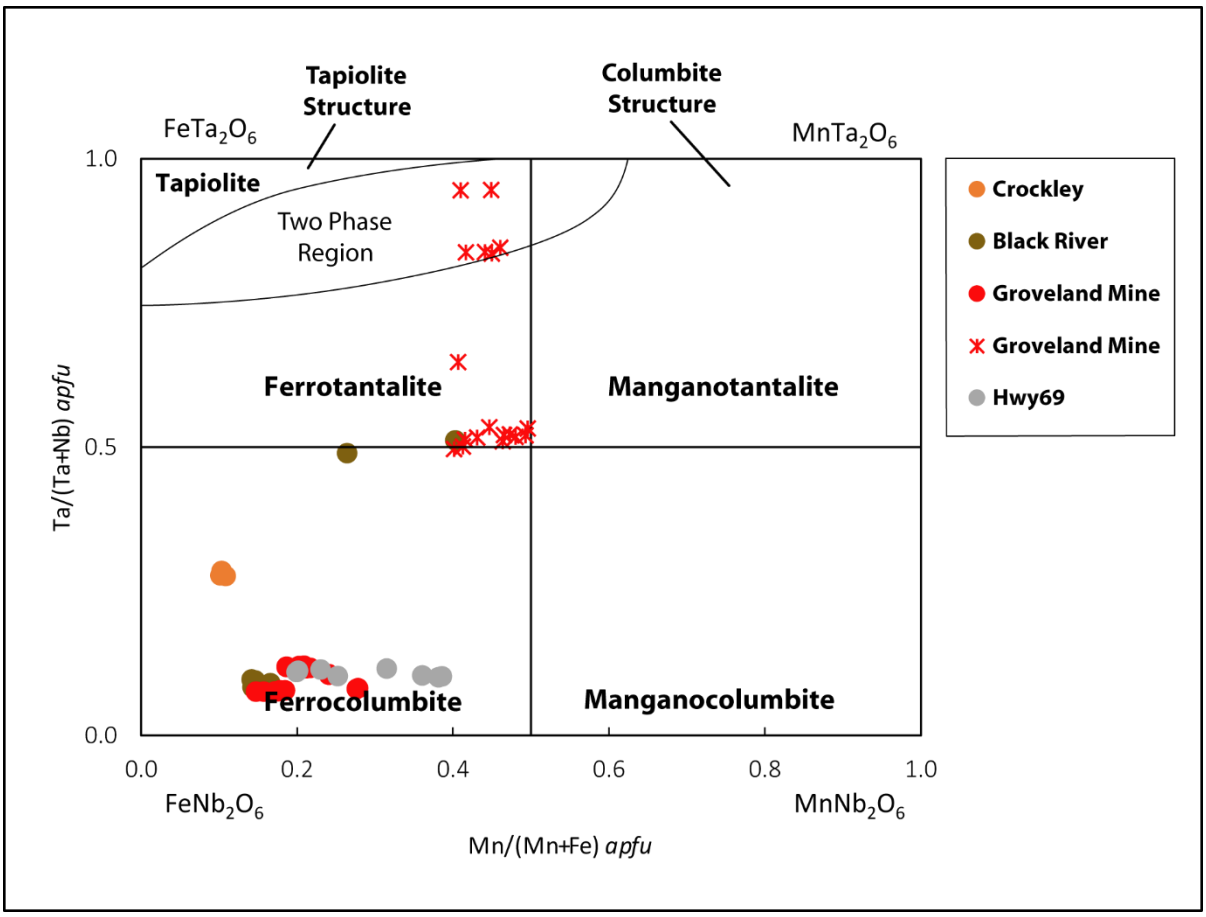


Figure 170 Columbite/Tantalite quadrilateral.

## EUXENITE GROUP

Fersmite is a member of the euxenite group of minerals. It has only been found in samples from the Hwy69 pegmatite. The ternaries in Figure 171 show the analysis being calcium and niobium dominant.

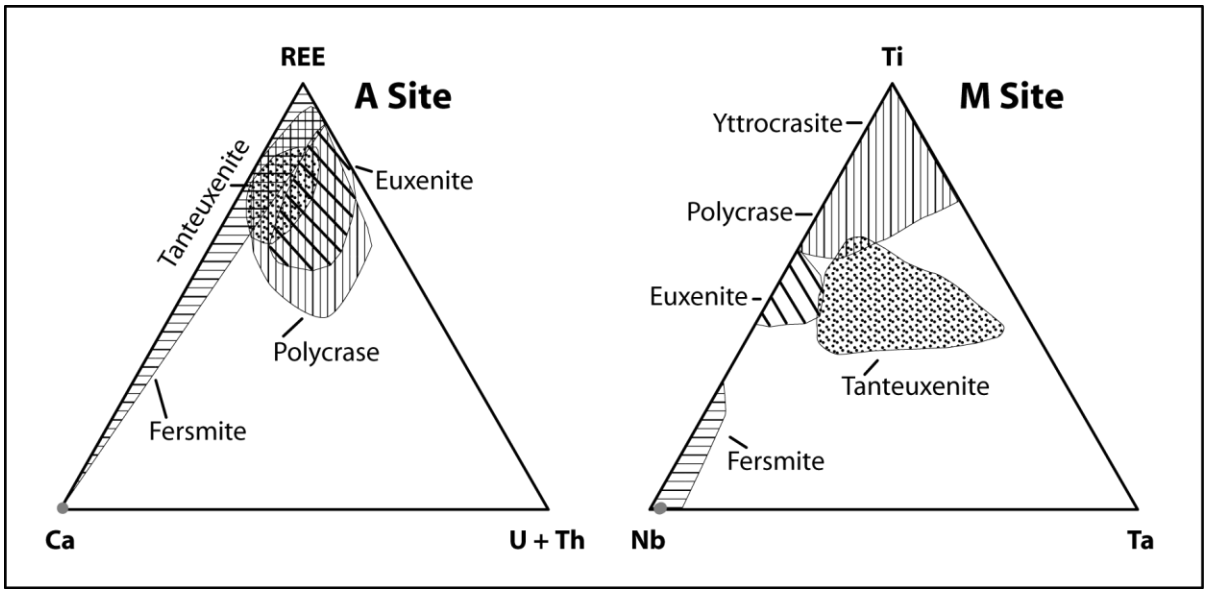


Figure 171 Euxenite Group ternary classification. Modified from Černý & Ercit, 1989.

## FELDSPARS

Feldspar is one of three most abundant minerals found in granites and granitic pegmatites. Plagioclase members form a solid solution series and are classified based on percentages of sodium and calcium content. Typically only the more sodium-rich end members (Albite – $Ab_{00}$-$Ab_{10}$) are found in granitic pegmatites. Potassium-rich feldspars ($KAlSi_3O_8$) are typically classified based on the degree of structural ordering of their polymorphs: high temperature, disordered sanidine, intermediate orthoclase, and low temperature, ordered microcline. NYF-type pegmatites usually have highly ordered microcline, as alkalic fluids and water content present in the pegmatitic melt promote ordering. Rubidium and cesium can substitute for K and K/Rb and K/Cs ratios are used as a measure of degree of evolution of the pegmatite. Analyses have been plotted on the feldspar ternary (Figure 172). Plagioclase feldspar analyses from the Crockley, Grizzly, and Hwy69 pegmatites plot in the albite field and

oligoclase fields. K-feldspars have been analyzed by X-ray Diffraction and structural states have been plotted on the Wright (1968) diagram (Figure 173). All are maximum microcline with the exception of samples analyzed from the Dolfin and Grizzly pegmatites and Humboldt and Bell Creek granite samples. Even with the margin of error, samples still fall within or near the maximum microcline field indicating that there is a high degree of structural ordering in K-feldspar samples. Rubidium and cesium are either below or at detection limits for all K-feldspars analyzed.

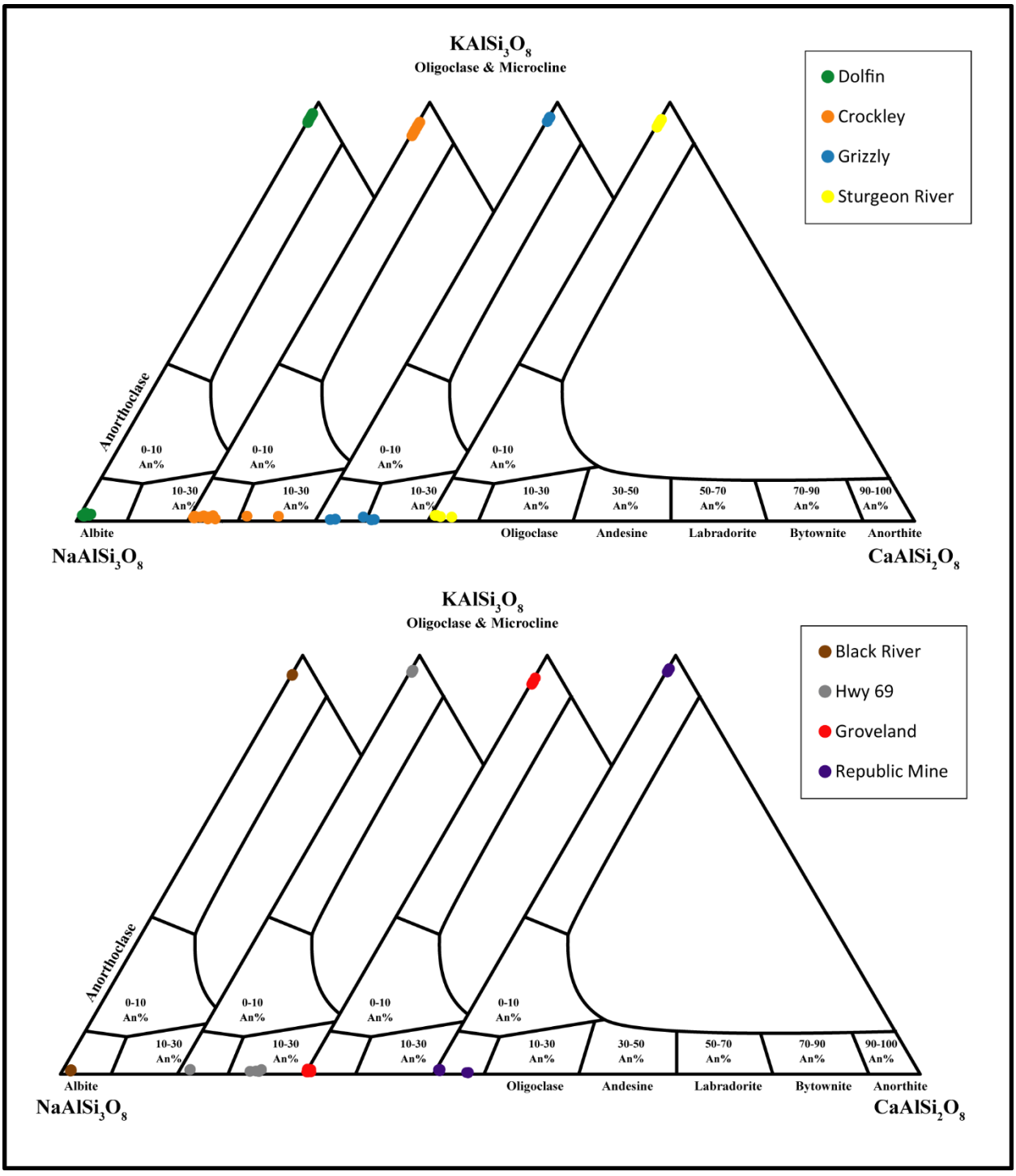


Figure 172 Feldspar classification ternaries for all pegmatites.

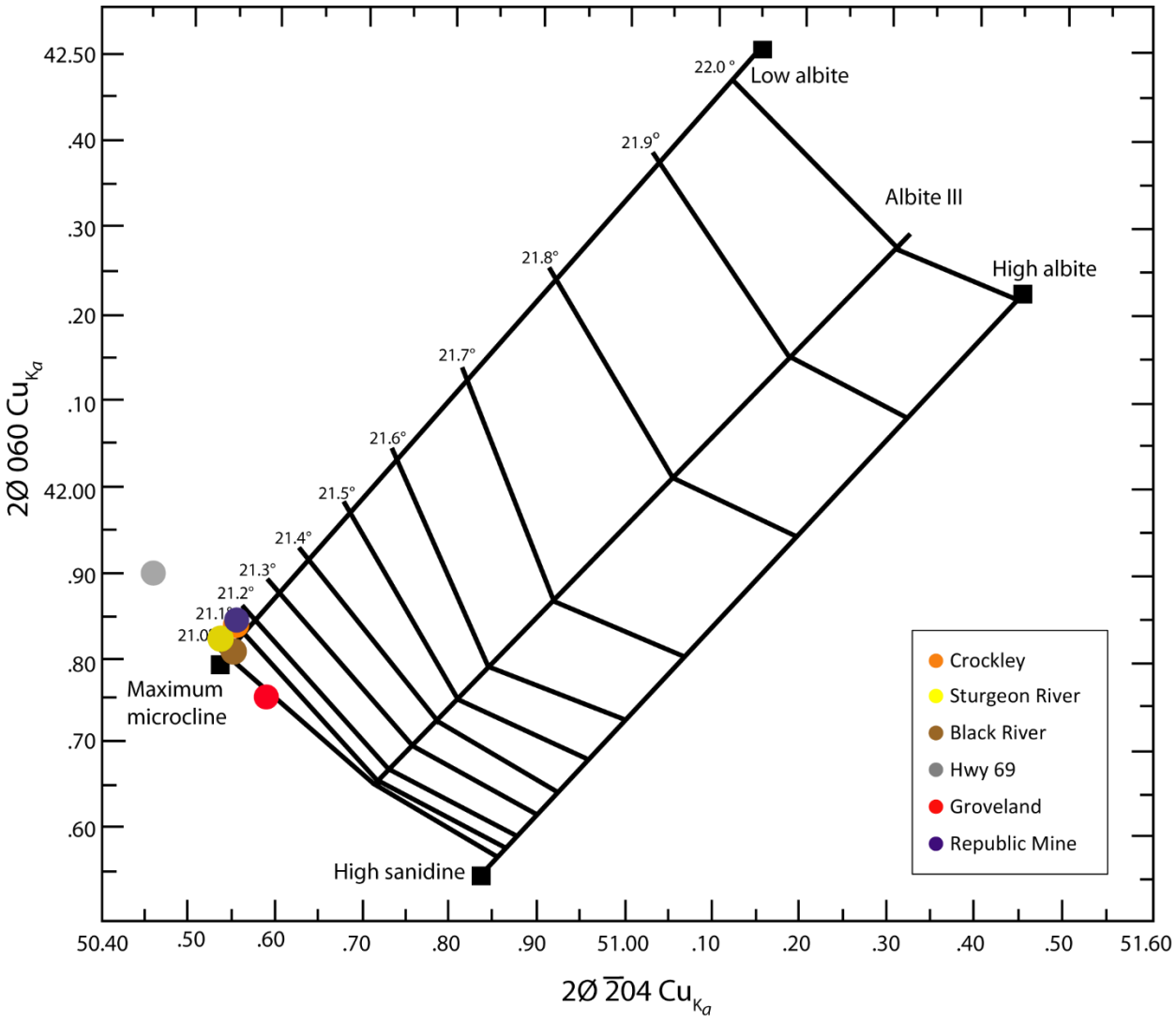


Figure 173 Modified alkali feldspar structural state diagram (Wright, 1968).

## FLUORITE

Fluorite is a relatively abundant accessory mineral in granitic pegmatites. It is easily recognized by its vitreous luster, cubic habit, and its perfect octahedral cleavage. The color of fluorite can range from shades of purple, green, red, and yellow, in addition to colorless. The samples collected are either colorless with purple splotches, to a shade of purple so dark as to be black in appearance. These darkest grains are associated with the greisen material collected near

the Grizzly pegmatite. The dark purple fluorite grains are closely associated with uraninite grains. When heat treated, these samples turn colorless revealing abundant inclusions. Most polished mounts investigated by SEM have inclusions. Other fluorite grains have visible inclusions readily seen under binocular microscope.

The chemistry of most fluorite is at least 99% pure, but substitutions can and do occur. Substitutions for calcium include strontium, yttrium, and cerium. Yttrofluorite, a variety of fluorite, can contain an $YF_3$ component between 10-20% in some cases. Yttrium is present in some microprobe analyses (as well as peaks in EDS spectra from SEM analyses), EMP analysis of fluorites are not sufficiently enriched in yttrium for classification as yttrofluorite. Samples from the Crockley (assumed to be apatite due to fluorescence) were analyzed by SEM and microprobe. These fluorescent grains were determined by SEM to be in fact, fluorite grains. No other samples from any other pegmatite or granite contains fluorescent fluorite.

## GAHNITE

Gahnite is part of the spinel group of minerals. It can be green, blue, yellow, grey, or brown. Gahnite has only been found in Groveland Mine samples where it is closely associated with rutile, magnetite, and pyrophanite. Composition of gahnite is expressed in terms of divalent iron (hercynite), magnesium (spinel), and zinc (gahnite) content. Compositional trends can be used to determine the petrogenesis (Figure 174) of gahnite (Batchelor & Kinnaird, 1984). Ratios of zinc and manganese over aluminum versus iron and magnesium over aluminum (Figure 175) can also be used to determine petrogenesis of gahnite as well as the degree of evolution of gahnite, as can Zn/Fe ratios (Batchelor & Kinnaird, 1984). Lower Zn/Fe ratios are associated

with Li-poor, NYF-type pegmatites and conversely, higher Zn/Fe ratios are typically associated with Li-rich, LCT-type pegmatites (Batchelor & Kinnaird, 1984; Heimann, 2010). Zn/Fe ratios of gahnite from Groveland are ~3.49 and ~3.36, suggesting that they are poorly evolved and that gahnite is more closely associated with NYF-type pegmatites. Higher Mg content is typically associated with a metamorphic origin (Batchelor & Kinnaird, 1984). Based on compositional relationships of Fe, Zn, and Mg, and molecular ratios of gahnite from Groveland Mine has an igneous petrogenetic origin (Figures 174 & 175).

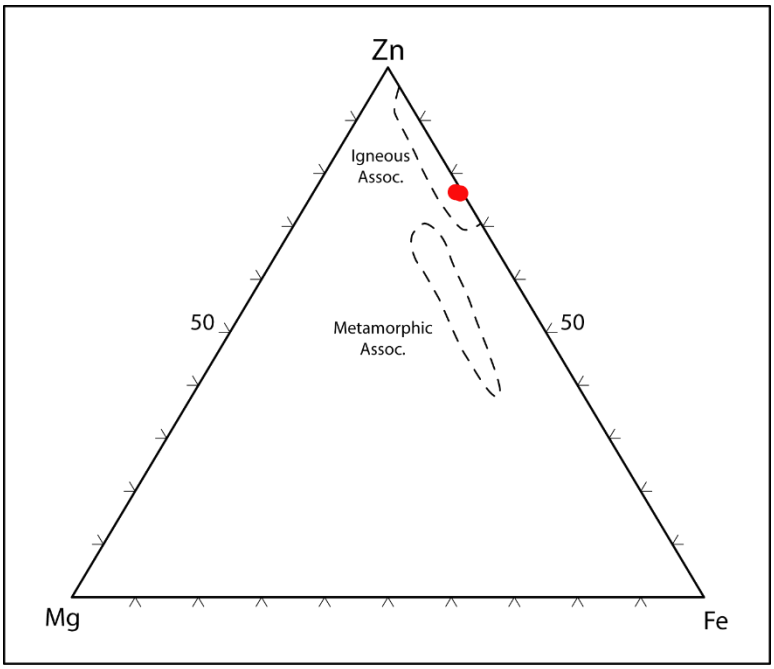


Figure 174 Magnesium (spinel), zinc (gahnite), and $Fe^{2+}$ (hercynite) petrogenesis ternary based on molecular ratios. Modified from Batchelor & Kinnaird, 1984.

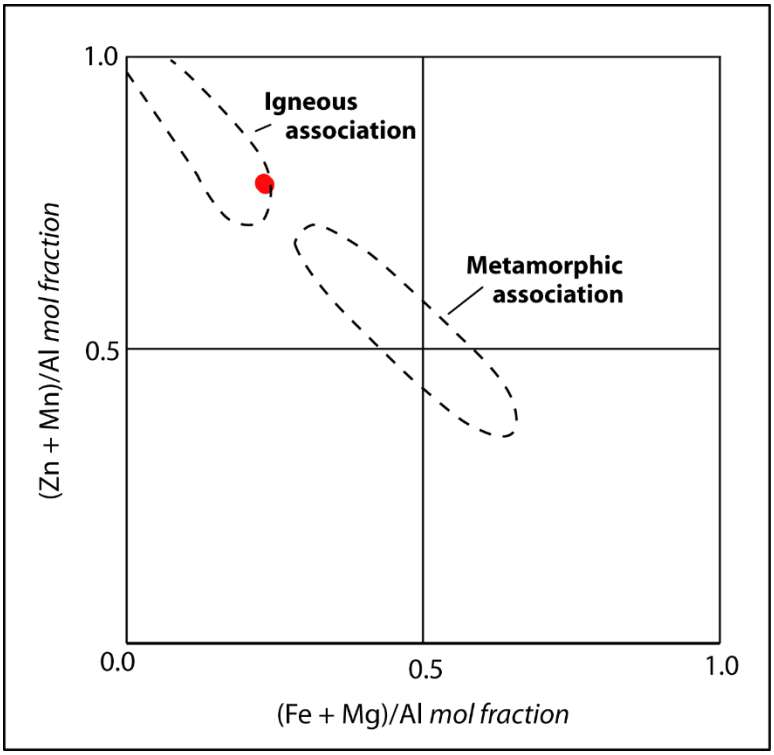


Figure 175 Petrogenetic association based on molecular ratios of (Zn+Mn)/Al versus (Fe+Mg)/Al. Modified from Batchelor & Kinnaird, 1984.

## GARNET GROUP

The garnet group has quite a bit of compositional variation; however, the generalized formula of a garnet unit cell consists of $X_3Y_2Z_3O_{12}$. The structure consists of alternating $YO_6$ octahedra and $ZO_4$ tetrahedra that share corners to form a three-dimensional network. The oxygen anions shared between the $YO_6$ and $ZO_4$ create distorted cubes of eight oxygens, which contain the X-site cations. Fe and Mn, as well as Ca, Mg, Ti, Cr, and V can occupy the X-site. Garnets are a typical accessory mineral in pegmatites from an aluminous source and are often associated with other peraluminous minerals, such as muscovite and members of the tourmaline group (London, 2008). Garnets are relatively more abundant in LCT-type pegmatites due to the more peraluminous signature, but garnets are present in NYF-type pegmatites as well. Garnet

composition is often explained in terms of the dominant component at the X-site. Garnets from inner zones of LCT-type pegmatites often contain a significant spessartine ($Mn^{2+}$ in X-site) component or can be dominantly spessartine due to other phases in the pegmatite competing for iron (Simmons *et al*., 2003). The relationship between iron and manganese can also be used to determine the degree of evolution within a pegmatite or be used to compare spatially related pegmatites within a field or group.

Distinct garnet grains have been identified in hand sample and heavy mineral separations at the Dolfin pegmatite, Groveland Mine, Sturgeon River, and Hwy69 pegmatites. Grains from all locations are either euhedral to subhedral and occasionally anhedral. Garnets that have been analyzed from the Dolfin pegmatite appear to be texturally and compositionally homogeneous from core to rim. Garnets from Groveland Mine, Sturgeon River, and Hwy69, however, contain textural and compositional characteristics not seen in Dolfin samples. Garnet from these three locations are fractured to various degrees with what appears to be secondary garnet within the fractures. Others contain inclusions. What is interesting about the mineralization of inferred primary garnet chemistry present in the Groveland Mine, Sturgeon River, and Hwy69 garnets is that it is very similar to the chemistry of garnets analyzed from the Dolfin pegmatite (Figure 176).

But there are distinct dissimilarities both compositionally and texturally between the primary and inferred secondary garnet. The garnet in the fractures shows negative polishing relief. The chemical compositions are also different. The chemical compositions are also different. Primary garnet is lower in almandine and spessartine components ($Alm_{76}Sp_{17}Py_2Gro_2And_2$). The fracture filling garnet composition is richer in almandine component ($Alm_{90}Py_3Sp_2Gro_2$) and the spessartitic component is reduced, the andraditic

component is below detection limits, and the pyrope component remains essentially the same. The Fe-Mg-Mn and Fe-Ca-Mn ternaries (Figures 178 & 179) illustrate the compositional differences of garnet from all pegmatites. Another interesting aspect in regards to composition is that from core to rim, both initial and secondary chemistry seem to be homogeneous, or at the very least, contain little or no detectable zonation.

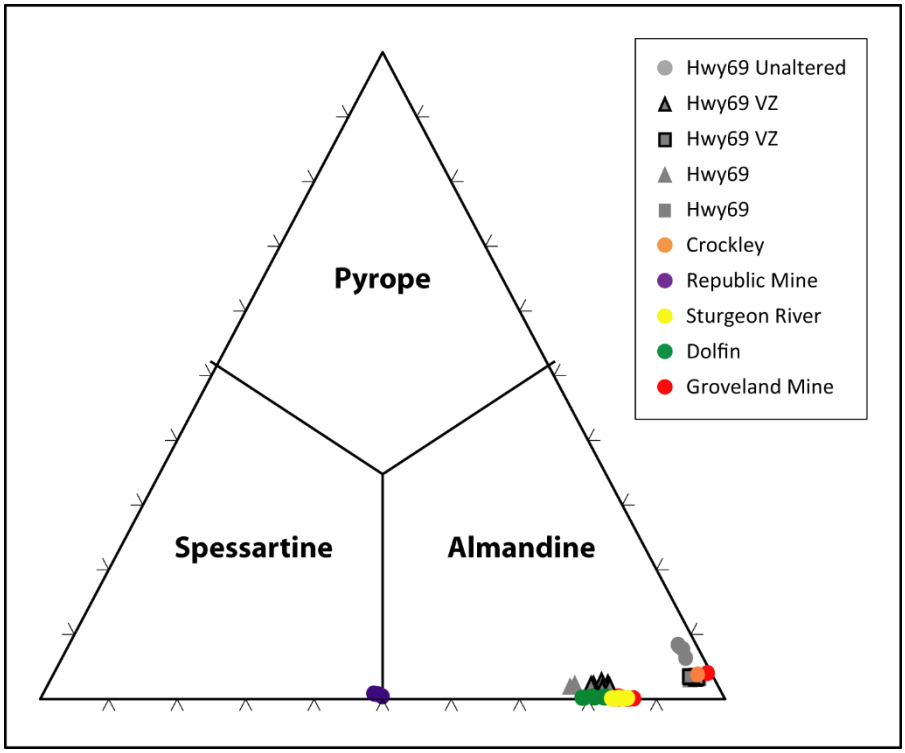


Figure 176 Garnet compositional ternary. Circles represent garnets with no alteration. Triangles represent areas of garnet assumed to be primary. Squares are secondary garnet.

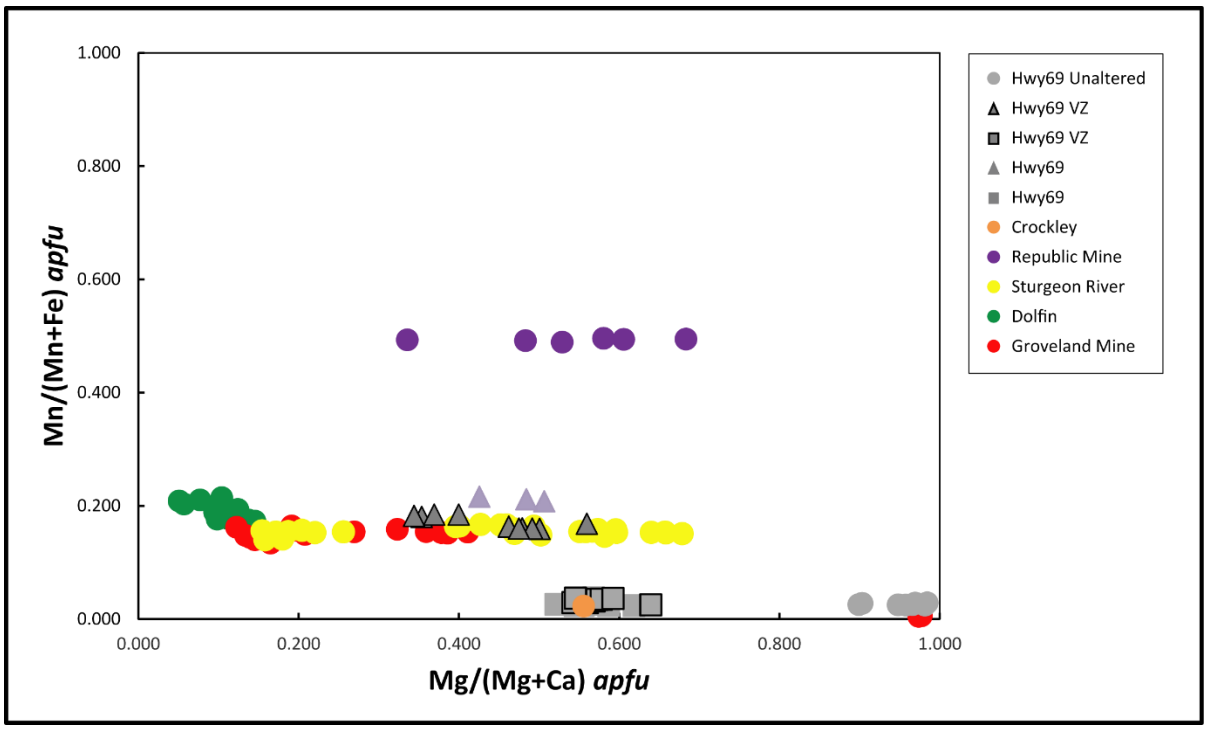


Figure 177 Garnet chemistry ratios. Circles represent garnets with no alteration. Triangles represent areas of garnet assumed to be primary. Squares are secondary garnet.

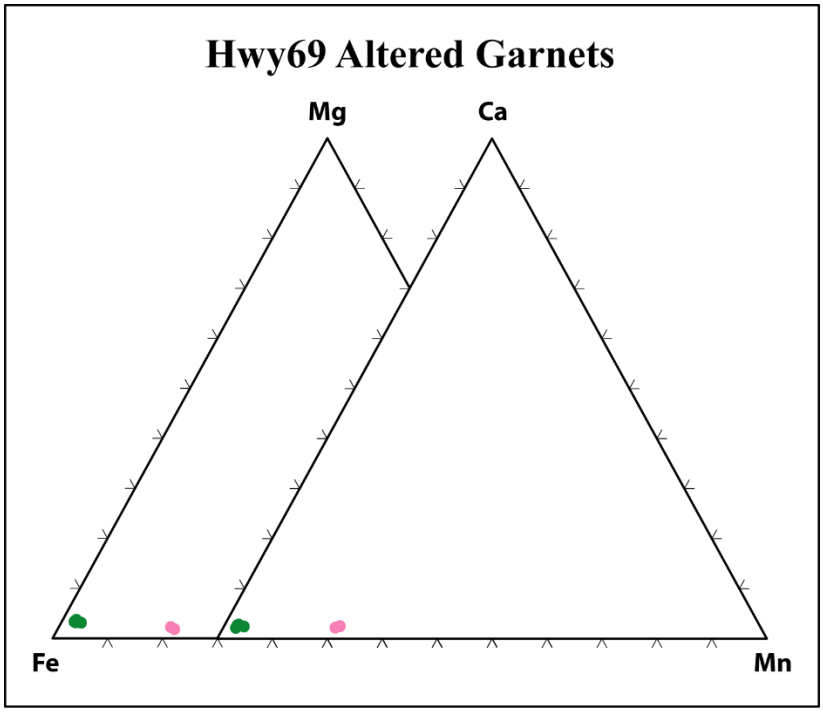


Figure 178 X-site dominance for altered garnets. Pink dots represent initial garnet chemistry. Green dots represent secondary garnet chemistry.

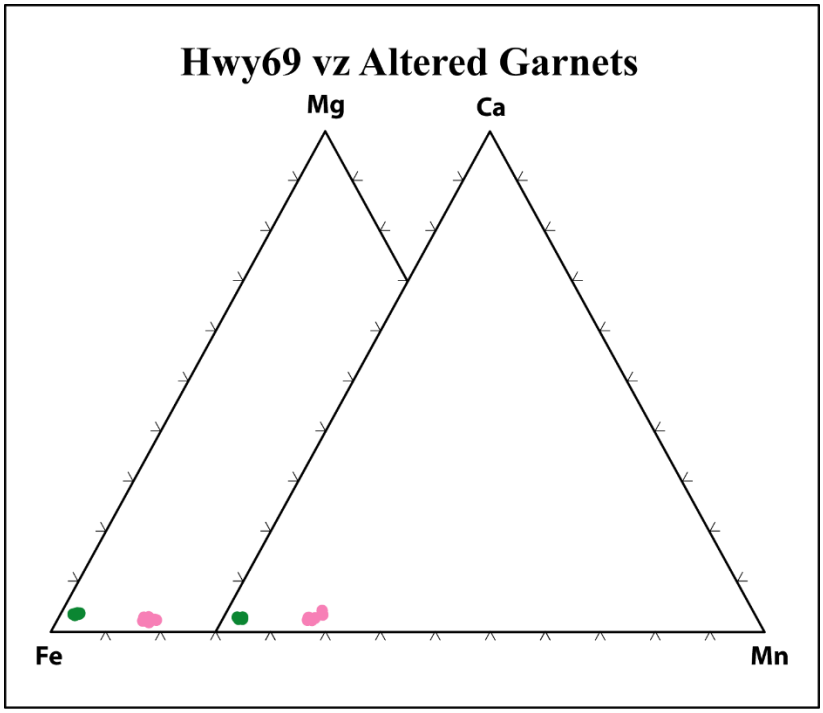


Figure 179 X-site dominance for altered garnets. Pink dots represent initial garnet chemistry. Green dots represent secondary garnet chemistry.

ILMENITE/PYROPHANITE

Ilmenite is an iron titanium oxide whose molecular formula can be more fully defined as $(Fe,Mg,Mn)TiO_3$. There is the ilmenite (Fe-dominant) - pyrophanite (Mn-dominant) series as well as an ilmenite - geikielite (Mg-dominant) series. Ilmenite has been identified in heavy mineral separations by SEM for Humboldt granite, Crockley pegmatite, Grizzly, Republic Mine, Hwy69, Sturgeon River, and Groveland Mine pegmatites. Only samples from Republic Mine, Crockley, Grizzly, and Sturgeon River have been quantitatively confirmed by microprobe analysis.

The Groveland Mine pegmatite does have ilmenite that has been identified in heavy mineral separations by SEM; however, only pyrophanite was quantitatively confirmed by microprobe analysis.

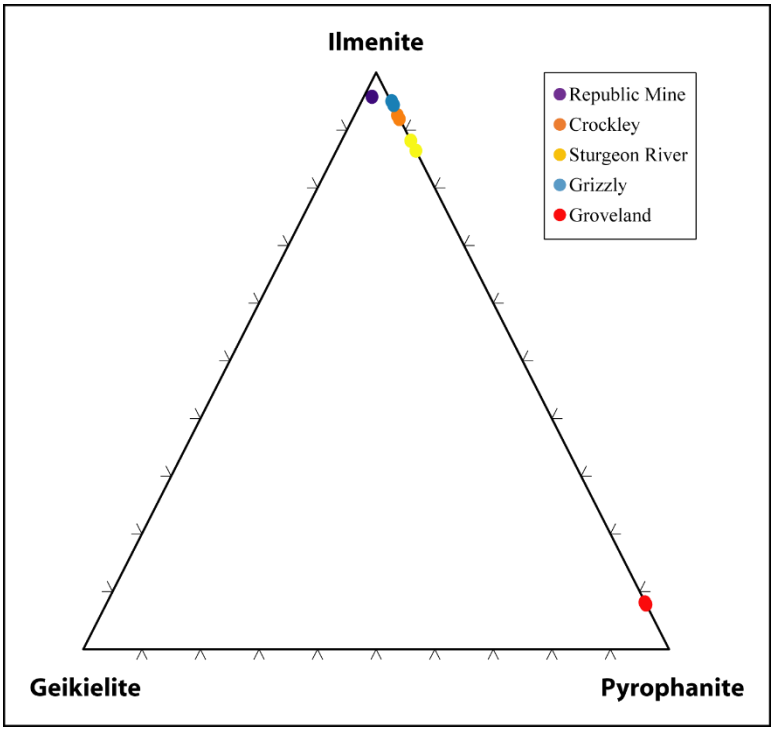


Figure 180 Ternary of Mg (geikielite) versus Fe (ilmenite) versus Mn (pyrophanite).

## MAGNETITE

Magnetite is a member of the spinel group of minerals and the pure end-member can best be expressed as $(Fe^{2+}, Fe^{3+})_3O_4$. Magnetite is one of the most abundant oxide minerals and it is a typical accessory mineral in many igneous rock assemblages. Magnetite is found in all heavy mineral separations including the Humboldt granite samples, Republic Mine, Dolfin, Crockley, Hwy69, Black River, Groveland Mine, and Sturgeon River. The Bell Creek granite and Grizzly pegmatite have very little or no magnetite. Samples collected from the Groveland Mine exhibited a high degree of abundance of magnetite in heavy mineral separations. One set of heavy mineral separations was almost completely composed of magnetite (near 90%!).

MONAZITE GROUP

"Monazite" group minerals are an REE-bearing phosphate found as accessory phases in both LCT- and NYF-type pegmatites, but they prefer NYF-type and alkalic pegmatites (Simmons *et al*., 2003). The most abundant is monazite-(Ce). Thorium and calcium can form a coupled substitution in lieu of light and heavy rare earth elements and Figure 182 shows the negative correlation of Th and Ca in "monazites" analyses. The $Th^{4+}$ ion is closer in size to $Ce^{3+}$ and therefore $Ca^{2+}$ can enter the monazite structure in order to complete charge balances (Rapp & Watson, 1986).

"Monazites" were found in all but the Humboldt granite. Hoffman (1987) lists "monazite" analyses for the Bell Creek and Clotted granite in his dissertation; however, it appears he was unable to recover any samples for the Humboldt. Microprobe analyses reveal that all samples are monazite-(Ce) (Figure 181) with a few notable exceptions. "Monazite" plots reveal the relative greater enrichment of Ca in samples from Hwy69, Groveland Mine, Crockley, and especially one sample from the Republic Mine (Figure 181). The ternary modified from Linthout (2007) reveals that the Hwy69, Groveland Mine, and Crockley samples are relatively more enriched in Ca relative to other monazites except for the Republic Mine sample, which is relatively more enriched in Ca with regard to monazites from the other pegmatites and the Bell Creek granite (Figure 183).

Chondrite normalized plots of REE contents in monazite (Figure 184) show that the Republic Mine Ca-rich sample is relatively less enriched in REE's relative to other monazites. Monazites from the Crockley, Hwy69, and Groveland Mine that are relatively less enriched in La, Ce, and Pr correspond to Ca-rich samples. All other normalized plots from the Bell Creek granite, and Hwy69, Grizzly, Sturgeon River, Groveland Mine, Dolfin, Black River and

Republic Mine pegmatites show a very similar trend. There are exceptions: the Republic Mine is relatively erbium poor with regard to the other analyses; the Groveland Mine is relatively ytterbium poor; Bell Creek granite and Black River pegmatite analyses have some the most relatively enriched in ytterbium.

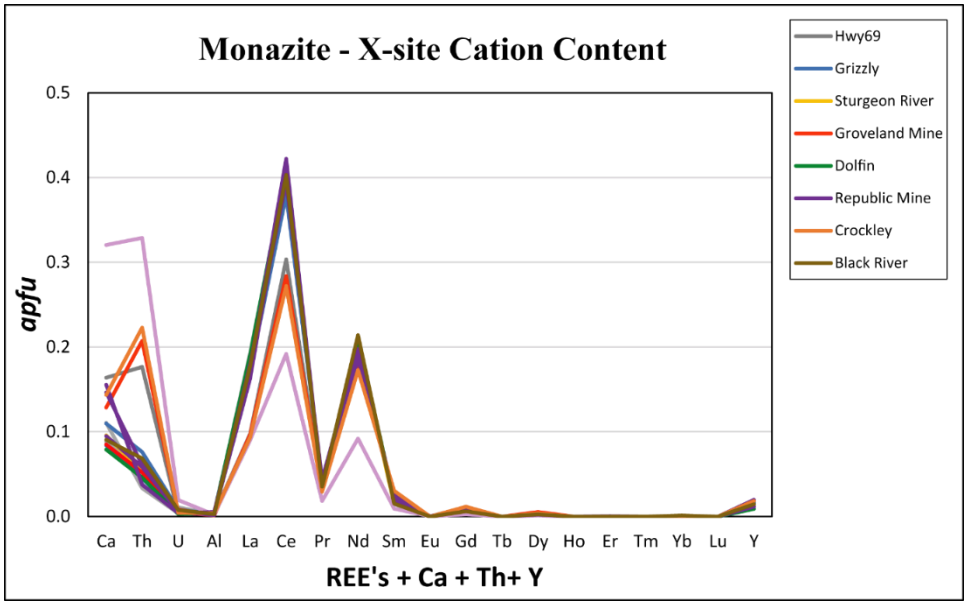


Figure 181 Line plot for "monazite" X-site cation *apfu* content for all analyzed samples. Lighter purple line represents the Republic Mine sample that is relatively more enriched in Th and Ca.

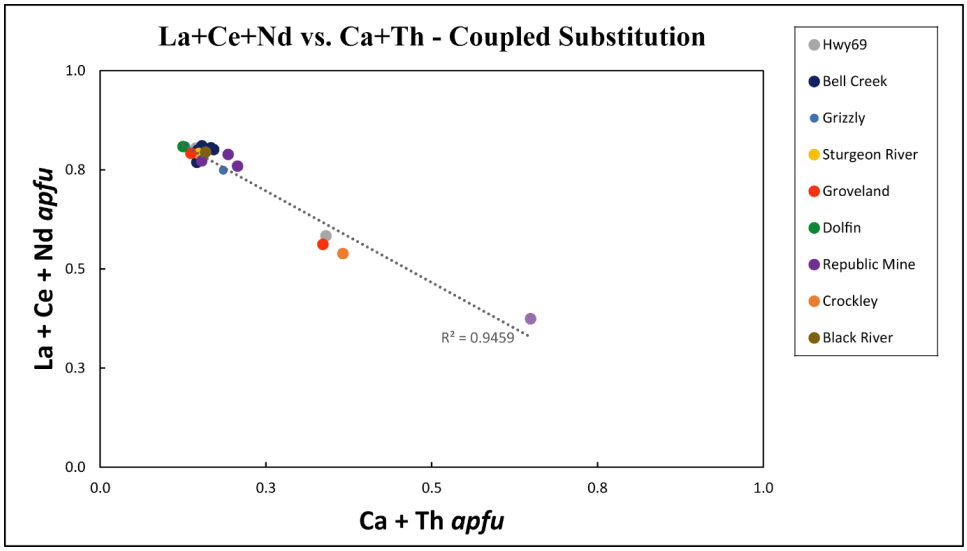


Figure 182 Coupled substitution plot of negative correlation between Ca + Th *apfu* and La + Ce + Nd *apfu*. Lighter purple marker corresponds to a Republic Mine sample relatively more enriched in Th.

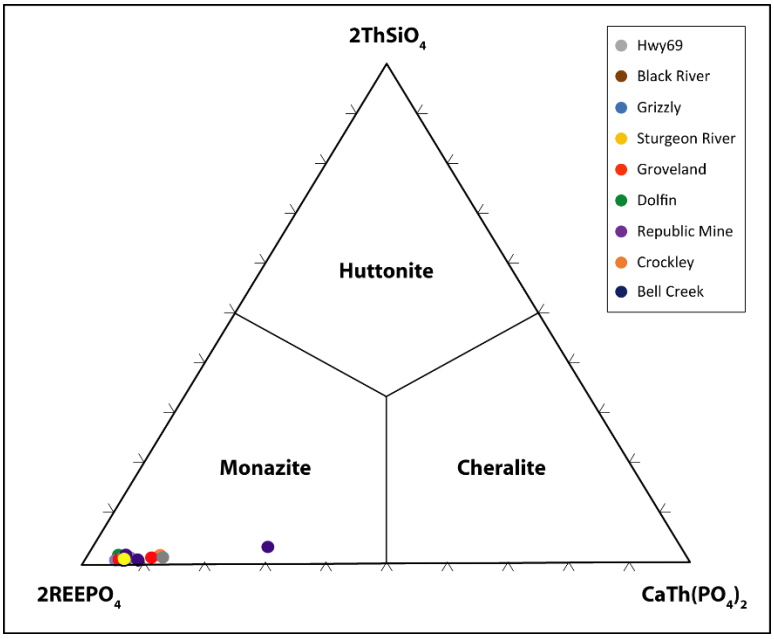


Figure 183 Classification scheme modified from Linthout, 2007. Samples from Groveland Mine, Hwy69, and Crockley are slightly more enriched in Ca & Th relative to other monazites except a sample from the Republic Mine pegmatite.

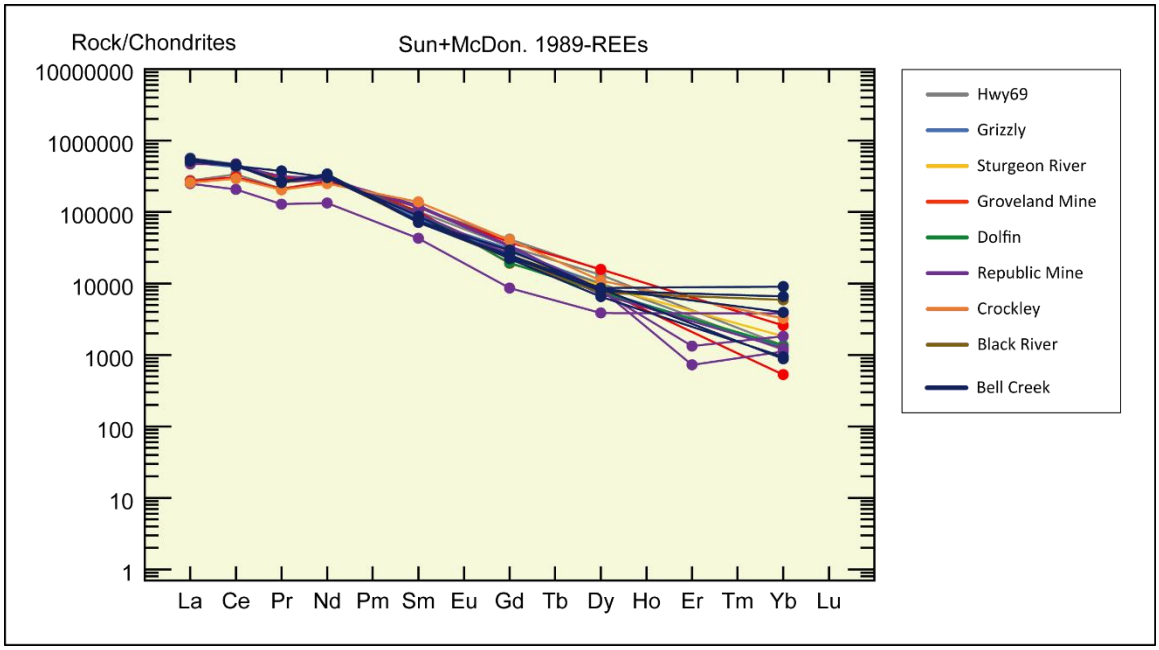


Figure 184 Chondrite normalized plot for REE's in "monazites".

## MICA GROUP

Mica group minerals have a generalized formula of $X_2Y_{4\text{-}6}Z_8O_{20}(OH,F)_4$ (based on 24 anions) and belong to the larger phyllosilicate mineral group. The mica group displays considerable variation in terms of physical and compositional properties. Mica minerals have a composite sheet in which two layers of $(Si,Al)O_4$ tetrahedra sandwich an octahedrally coordinated layer of cations. The two composite sheets are linked by a plane of cations. Biotite is relatively abundant in many pegmatites and includes annite-phlogopite to siderophyllite-eastonite. Biotite is a trioctohedral mica meaning that three divalent cations are present in the Y-site as opposed to muscovite, which is dioctahedral. Dioctahedrally coordinated micas have two trivalent cations in the Y-site. Muscovite micas are typically more abundant in peraluminous pegmatites, but can occur in both LCT- and NYF-pegmatites. Muscovite grains plot within the

muscovite field (Tichendorf, 1997) with the exception of samples from the Grizzly, which hover between phengite and muscovite composition (Figure 185).

Analyzed biotite grains plot within the Fe-biotite field (Tichendorf, 1997). There is a distinction in that samples from the Sturgeon River, Hwy69, and Republic Mine biotite is relatively more enriched in magnesium (Figure 185). This suggests that biotite mica from these two locations is somewhat more primitive. Biotite composition can be used to determine the tectonic conditions under which the pegmatitic melt was generated (Webber, 2000). All biotites plot within the orogenic field (Webber, 2000). Samples from Sturgeon River, Hwy69, and Republic Mine pegmatites plot closer to the anorogenic field than the Crockley and Grizzly pegmatites. Humboldt granite samples from Hoffman (1987) plot in the anorogenic field. The biotite discrimination diagram of Abdel-Rahman (1996) show that samples plot within the P-field, suggesting a more peraluminous nature. Figure 190 shows that all biotites are hydroxyl dominant. Figure 190 shows that biotite samples from the Groveland Mine and Grizzly pegmatites and one analysis from the Humboldt granite is relatively more enriched in iron. There is some overlap in that Crockley and Dolfin pegmatite samples plot near the lower range of iron enrichment of the Grizzly pegmatite. Biotite samples from the Dolfin pegmatite and Bell Creek and Humboldt granites are all relatively more enriched in fluorine, although it should be pointed out that F/(F+OH) ratios only range from approximately 0.100 to 0.170. The Sturgeon River biotite samples are relatively more enriched in magnesium.

For muscovite mica analyses, all samples are hydroxyl dominant, although the Groveland Mine samples are slightly more enriched in fluorine than samples from other pegmatites and granites. Muscovite samples from the Humboldt granite and Crockley pegmatite are relatively more enriched in iron. The Grizzly pegmatite muscovite analysis shows relatively greater

enrichment in magnesium. With respect to octahedrally coordinated Al ratios, all muscovite samples are within approximately 5% of one another. Sturgeon River muscovite samples being at the lower threshold of octahedrally coordinated Al enrichment and Grizzly pegmatite samples being at the upper threshold of octahedral Al enrichment.

DCP analyses have been conducted in order to determine the weight percent content of lithium. Suitable quantities of homogeneous micas are only available from the Grizzly, Groveland Mine, Black River, Republic Mine, Sturgeon River, and Hwy69 pegmatites. Lithium content is highest in micas from the Groveland Mine and Sturgeon River pegmatites, although each had an analysis that has the lowest weight percent content of lithium. Titration results yielded $Fe^{3+}/(Fe^{3+} + Fe^{2+})$ ratios of >1%, indicating that biotites analyzed contained very little to no trivalent iron.

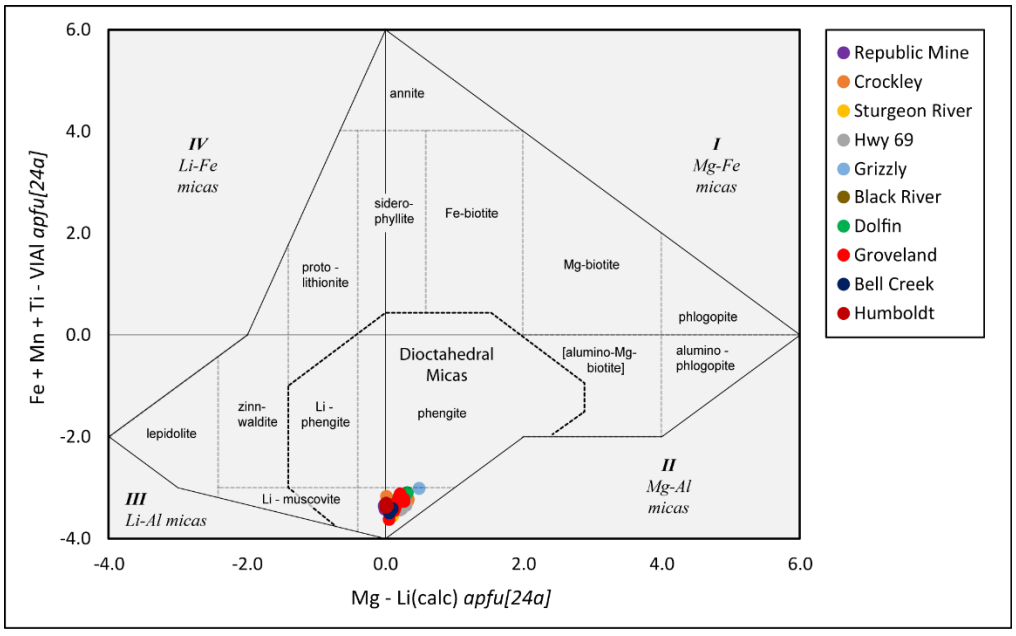


Figure 185 Modified from Tischendorf classification scheme of micas. All dioctahedral micas are muscovite mica.

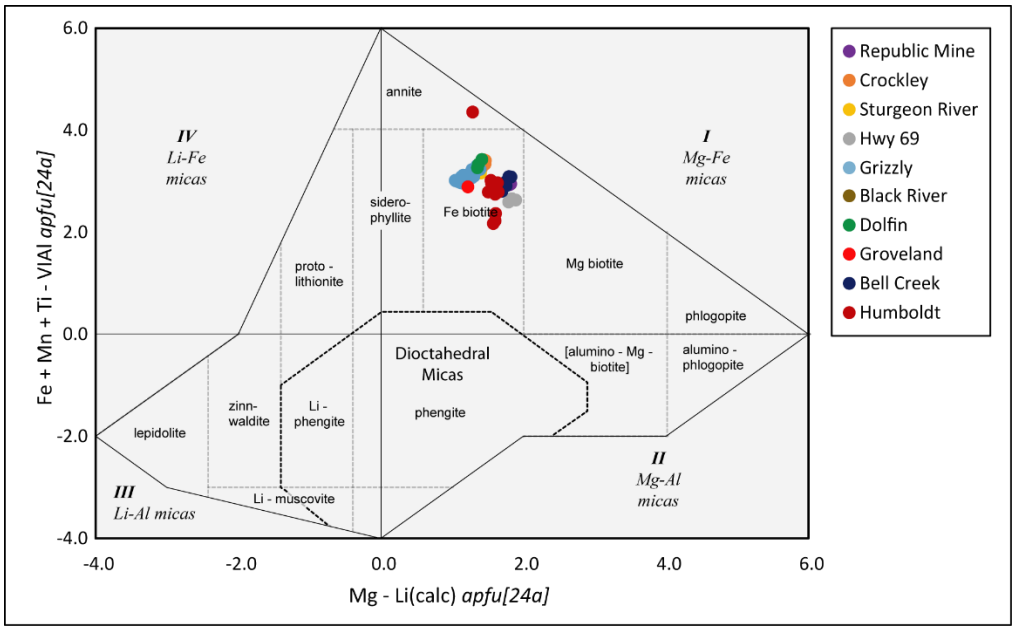


Figure 186 Modified from Tischendorf's classification scheme of micas.
All trioctahedral micas are Fe-biotites with the exception annite from Humboldt.

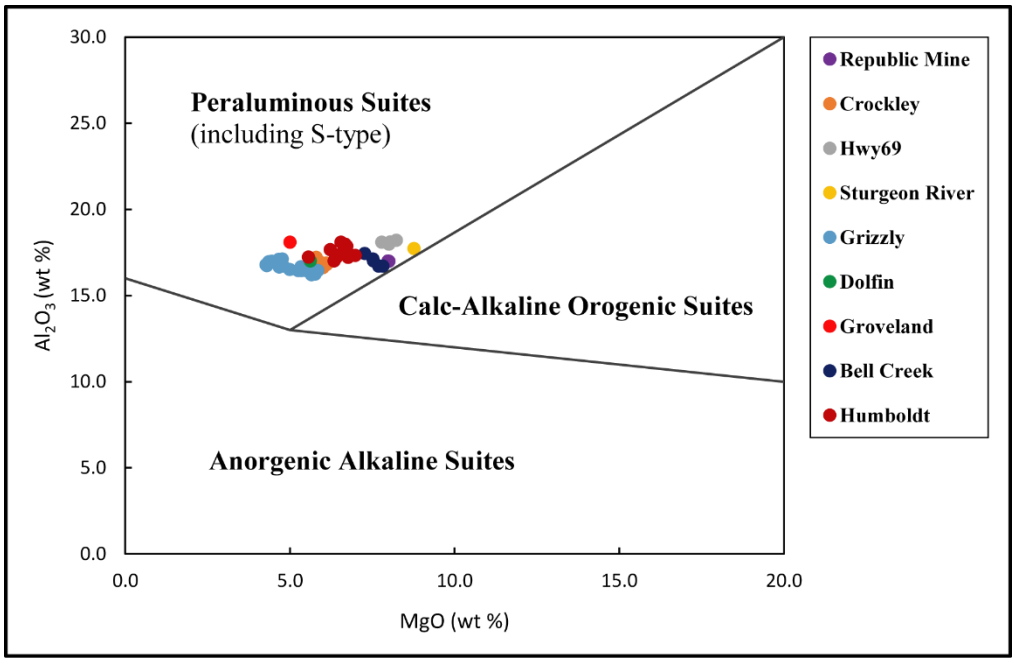


Figure 187 Modified from Abdel-Rahman (1996) Biotite Discrimination Diagram.

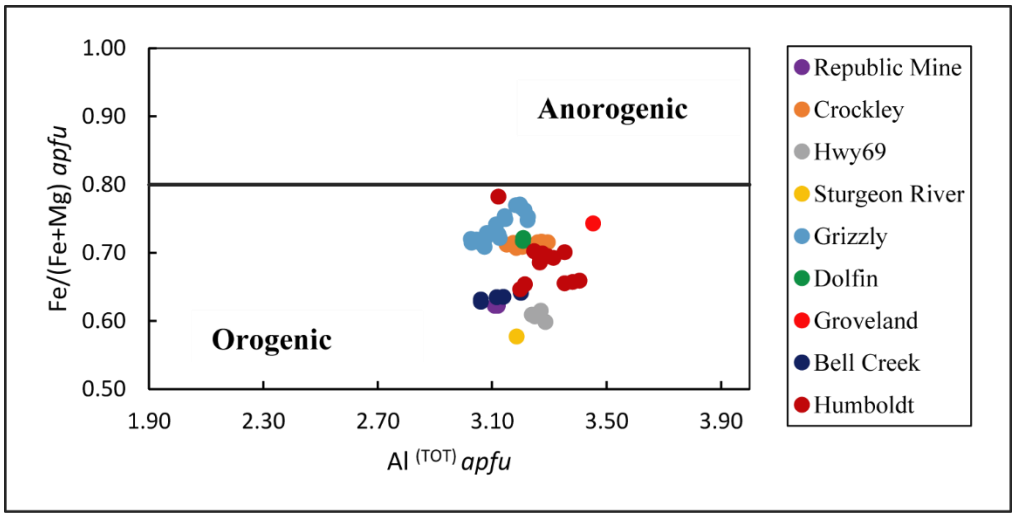


Figure 188 Biotite discrimination diagram based on Fe/(Fe+Mg) versus total aluminum (Webber *et al*., 2000).

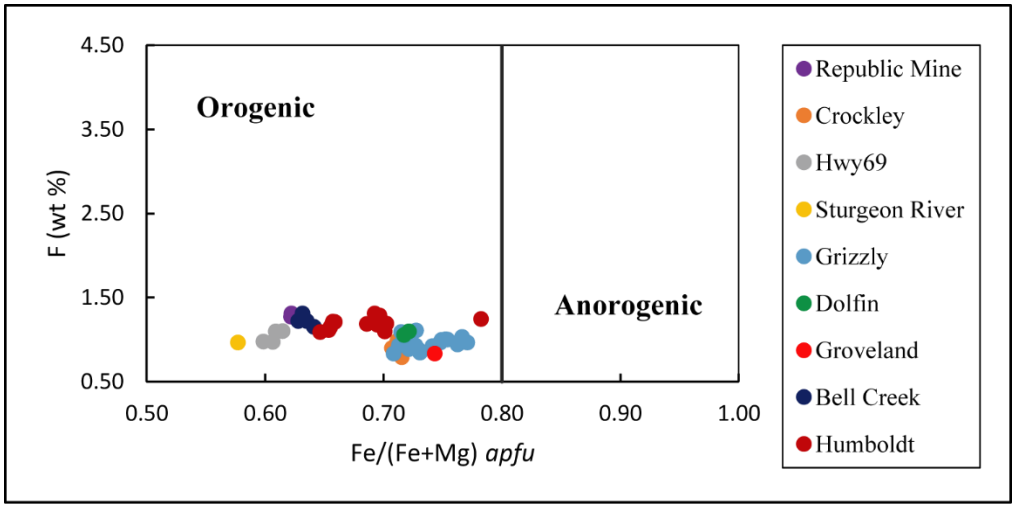


Figure 189 Biotite discrimination diagram based on F Wt.% versus Fe/(Fe+Mg) (Webber *et al*., 2000).

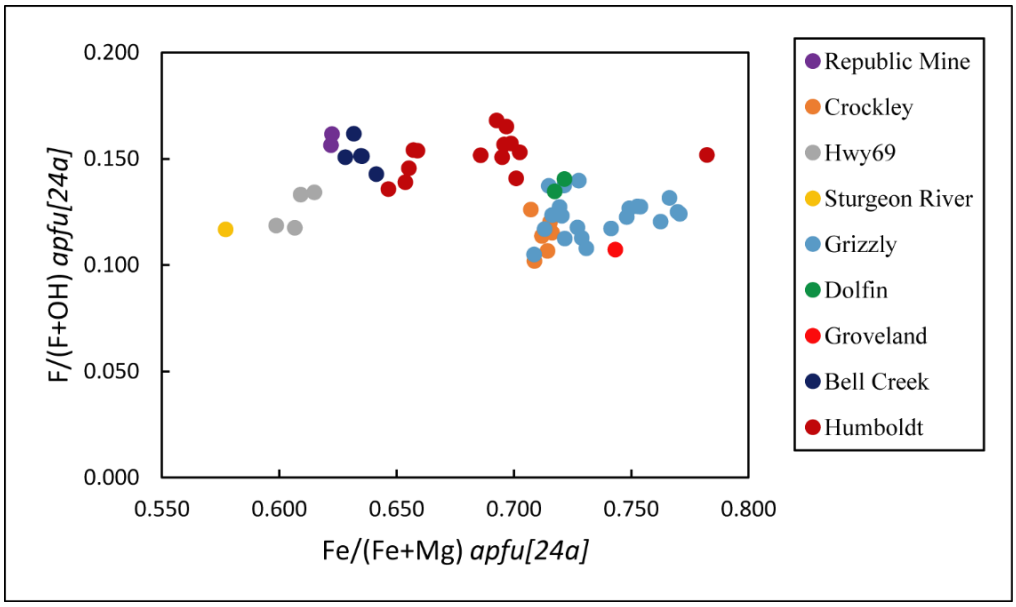


Figure 190 F/(F+OH) *apfu*[24a] ratio versus $^{VI}Al/(^{VI}Al+Fe_{tot}+Mg)$ *apfu*[24a] ratio for biotite.

## PYRITE

Pyrite is the most abundant sulfide mineral and can be found in a variety petrogenetic environments. Pyrite has been identified in heavy mineral separations from the Humboldt granite, the Dolfin, Crockley, Hwy69, Sturgeon River, and Groveland Mine pegmatites.

## PYROCHLORE

Pyrochlore belongs to the larger pyrochlore supergroup of minerals which also include microlite, betafite, elsmoreite, and roméite. These five group members are categorized based on B-site dominance (Figure 191) of either niobium, as is the case with pyrochlore, tantalum (microlite), titanium (betafite), tungsten (elsmoreite) or antimony (roméite). These minerals are further classified by the dominance of sodium, calcium, and other cations in the A-site (Figure

191) as well as anion dominance in the Y-site. Pyrochlore was only found in Crockley pegmatite samples. W and $Sb^{5+}$ were below detection limits.

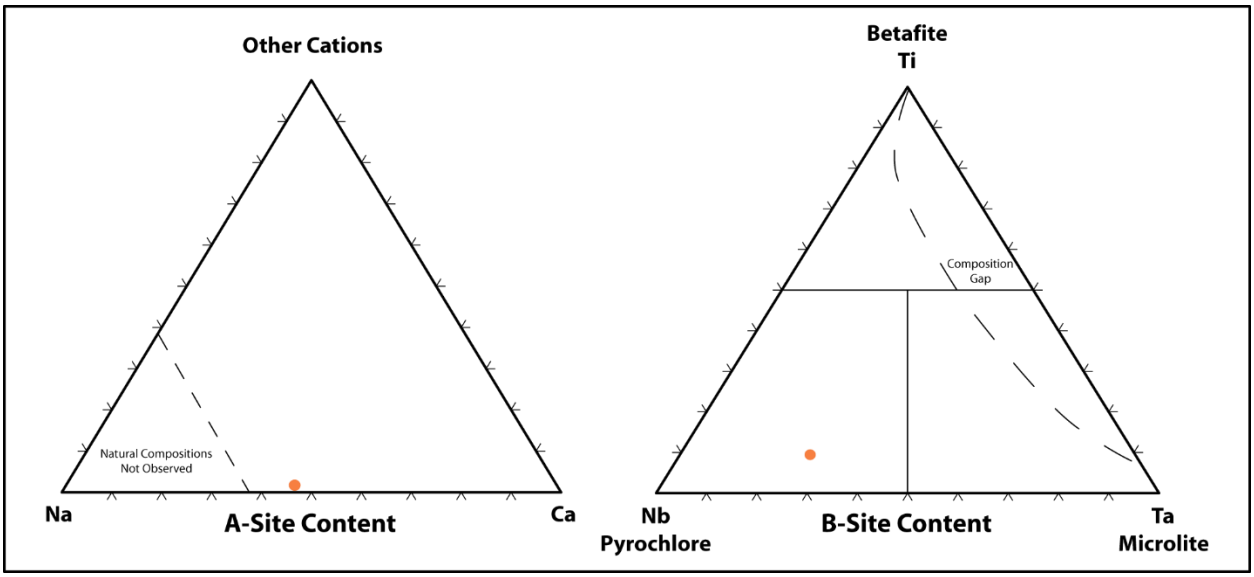


Figure 191 A-site and B-site content modified from Atencio *et al*., 2010

## RUTILE

Essentially $TiO_2$, Rutile can incorporate niobium and tantalum owing to the similarity of their ionic radii to titanium. Larger crystals are not typically abundant in granitic pegmatites. Generally only a minor accessory mineral, but especially so in NYF-type pegmatites (Simmons *et al*., 2003). Rutile has been identified in heavy mineral separations by SEM. Rutile was rather rare and in most cases, was found only as inclusions or overgrowths on other minerals such as ilmenite and mica. Only samples from the Republic Mine and Crockley pegmatites were quantitatively analyzed by microprobe. The Grizzly, Sturgeon River, and Groveland Mine pegmatites all had rutile as well. One analysis from the Crockley pegmatite contained just over 2 weight percent of niobium as well as a detectable amount of tantalum (0.221 wt %).

## SCHEELITE

Scheelite, a calcium tungstate, is unusual in granitic pegmatites. However, one sample has been identified from the Black River pegmatite. It was only qualitatively identified by SEM. No other samples have been found in either the Black River pegmatite or any other location.

## THALÉNITE

Thalénite is a rare yttrium silicate; however, it is relatively common in Republic Mine pegmatite samples. Chondrite normalized plots (Figure 192) reveal that thalénite from the Republic Mine has LREE enrichment in Ce that ranges from one to two orders of magnitude below HREE enrichment. This is the first confirmed and reported occurrence of thalénite in the state of Michigan.

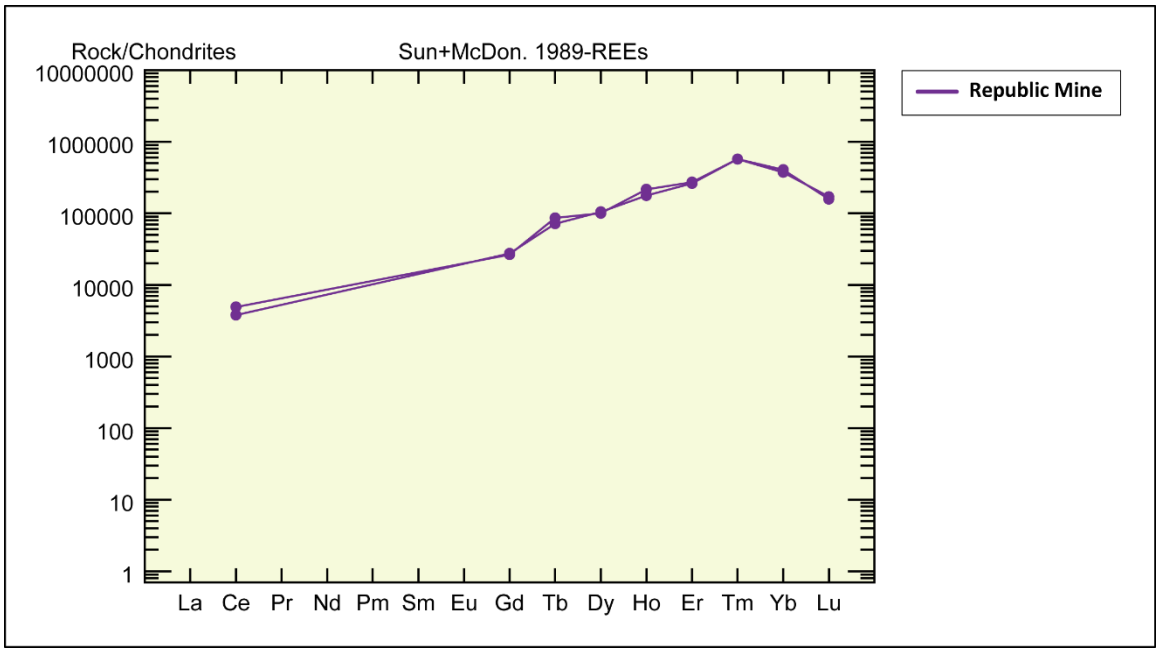


Figure 192 Chondrite normalized plot of REE's in thalénite from Republic Mine pegmatite.

## TITANITE

Titanite (or sphene) can occur as an accessory mineral in felsic igneous rocks as well as granitic pegmatites. Titanite has been identified in heavy mineral separations from the Bell Creek granite by SEM only.

## TOURMALINE GROUP

The borosilicate tourmaline mineral group has a general structural formula of $XY_3Z_6[T_6O_{18}][BO_3]_3V_3W$. Each site has specific accommodation and charge limitations that determine occupation of each site by particular ions. Tourmaline is a very useful indicator for the degree of evolution of a pegmatite as there are generally specific geochemical trends taking place as a pegmatite crystalizes. Tourmaline-group minerals are found in granites, granitic pegmatites, and aplites and are typically found in LCT-type pegmatites. NYF-type pegmatites are generally depleted in boron and tend to be more alkaline (aluminum poor) than LCT-type pegmatites and thus have insufficient amounts of either boron or aluminum to produce tourmaline. However, tourmaline has been identified in hand samples and heavy mineral separations from the Groveland Mine, Sturgeon River, and Republic Mine pegmatites. Confirmation by SEM and analysis by EMP has determined that tourmaline from these three pegmatites be classified as fluorshorl due to alkali dominance and fluorine and iron enrichment.

Tourmaline-group minerals are divided into three groups, based on principal composition of X-site chemistry (Figure 193). Tourmalines from the Groveland and Sturgeon River plot along the baseline of the Alkali Group X-site ternary due to very little calcium enrichment. Tourmalines from the Republic Mine pegmatite have two distinct clusters. The first group has a

similar chemistry as the Groveland and Sturgeon River. The second cluster is relatively more calcium enriched (although only marginally) as well as having more X-site vacancy. The Alkali Group is further divided into Dravite, Elbaite, and Schorl (Figure 194). Tourmalines from all three locations plot within the Schorl field. Groveland tourmalines, however, are relatively more enriched in calculated lithium than either the Sturgeon River or Republic Mine suggesting that these are slightly more evolved. The Republic Mine tourmalines are relatively more enriched in magnesium than those from the Groveland or Sturgeon pegmatites suggesting that these tourmalines are more primitive; however, there appears to be a trend of evolving toward the Elbaite field. All tourmalines are F-dominant (Figure 195). Republic Mine tourmalines plot in two clusters owing to the relatively depleted sodium content.

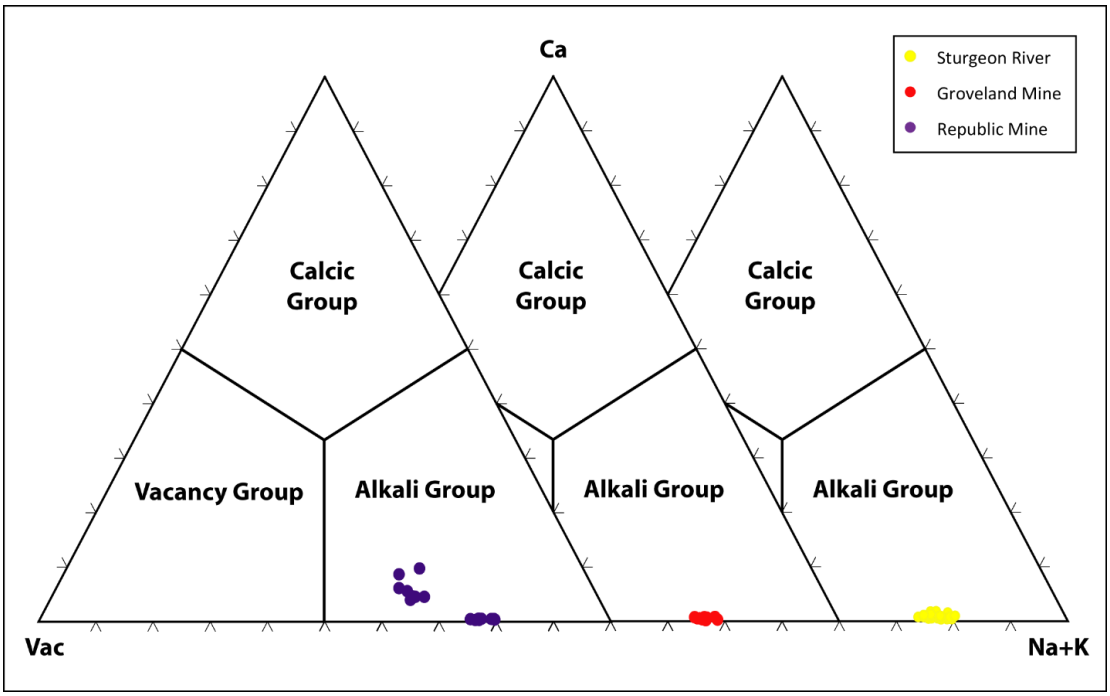


Figure 193: Primary tourmaline group based on X-site dominance (Henry *et al*., 2001).

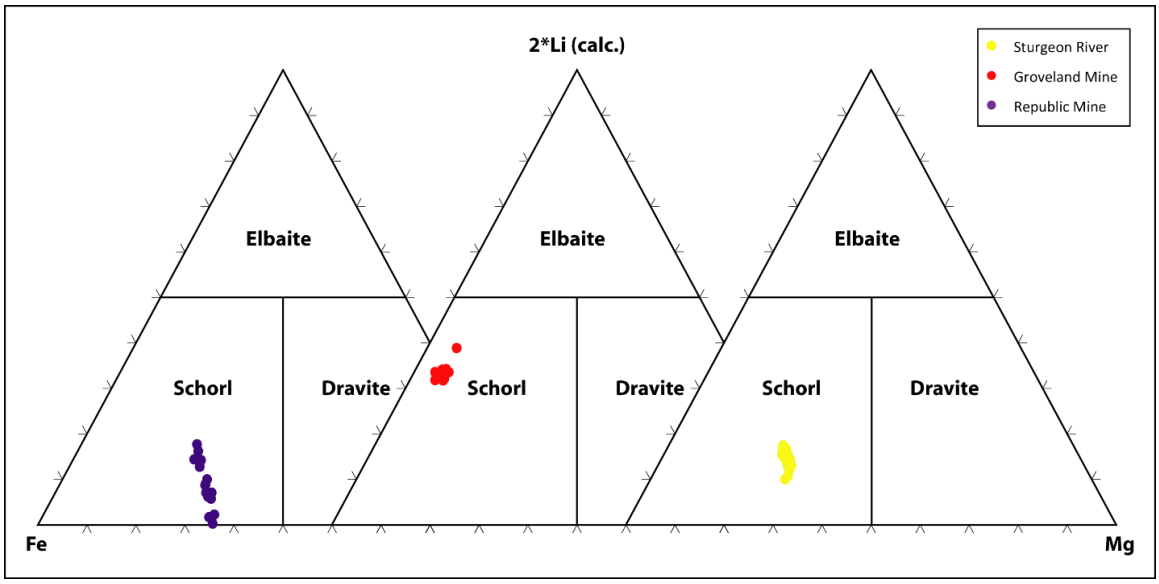


Figure 194: Alkali subgroup based on Schorl-Elbaite-Dravite ternary (Henry at al., 2011).

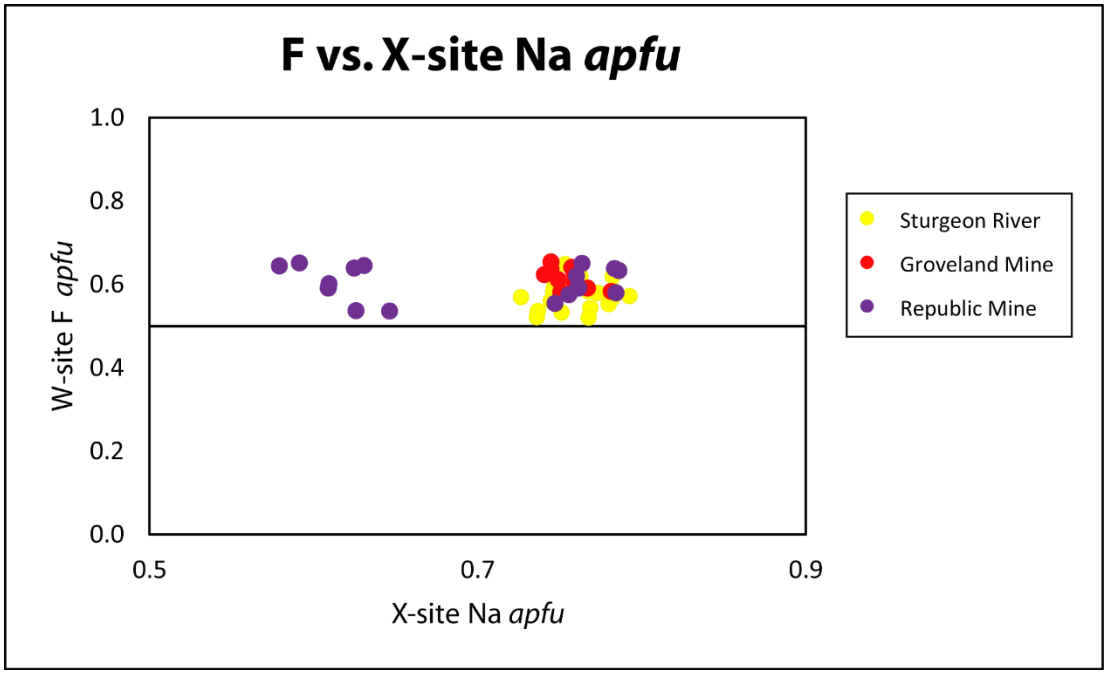


Figure 195: F vs X-site Na apfu. All tourmalines are fluorine dominant.

### URANINITE

Uraninite has been identified in greisen material that is spatially associated with the Grizzly and Bell Creek, but it is uncertain if the greisen material is genetically related. Zircons from the Dolfin pegmatite contain inclusions of uraninite, but no discrete grains have been found. The Sturgeon River has uraninite that contains possible radiogenic lead.

### VANADINITE

One grain was identified; however, it inferred to be from sample contamination.

### XENOTIME GROUP

As with monazite, xenotime-(Y) is also a rare accessory phosphate mineral typically found in NYF-type pegmatites (Simmons, *et al*., 2003). Xenotime is relatively more enriched in the smaller HREE's than the larger LREE's due to the large ionic radius of $Y^{3+}$ (Rapp & Watson, 1986). There is also generally too little room for accommodation of the larger $SiO_4$ tetrahedral group, the result being very little silicon enrichment (Demartin *et al*., 1991). "Xenotime" has been qualitatively identified in heavy mineral separations from the Grizzly, Dolfin, Black River, Sturgeon River, and Groveland Mine pegmatites. Xenotime-(Y) has been quantitatively confirmed (Figure 196) via microprobe for samples from the Dolfin and Groveland Mine pegmatites. Chondrite normalized analyses show that both the Dolfin and Groveland Mine samples have very similar trends (Figure 197). EDS spectral analysis of "xenotimes" reveals that samples are relatively depleted in HREE's relative to yttrium.

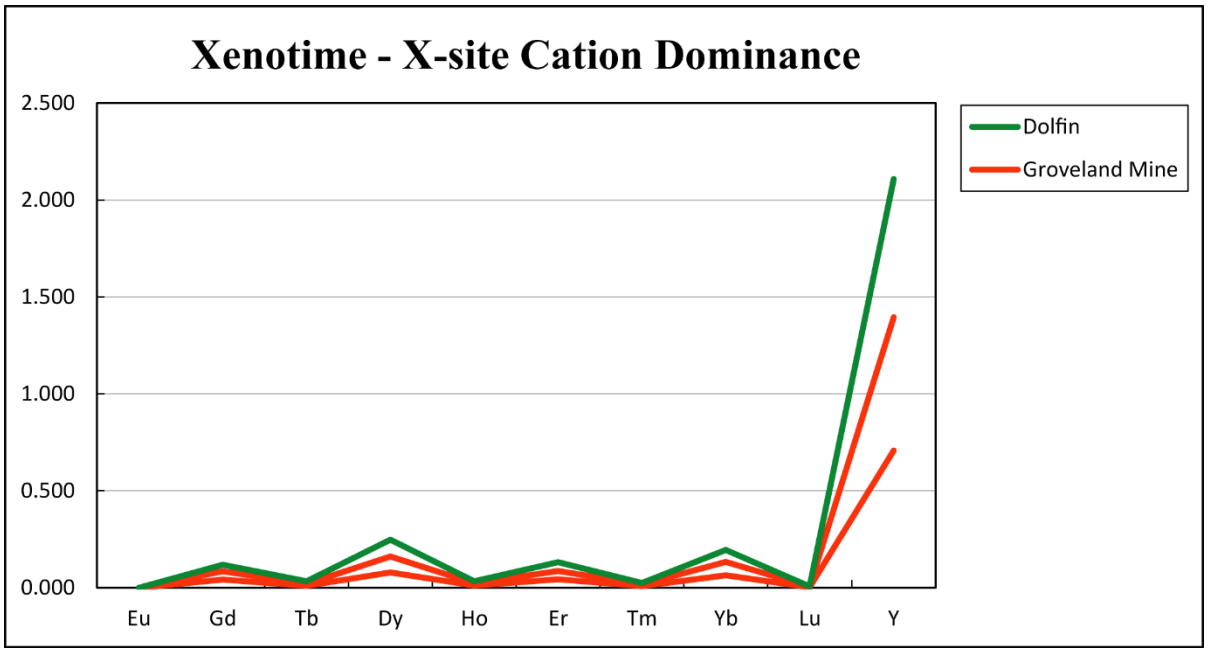


Figure 196 Line plot for "xenotime" X-site cation *apfu* content for all analyzed samples.

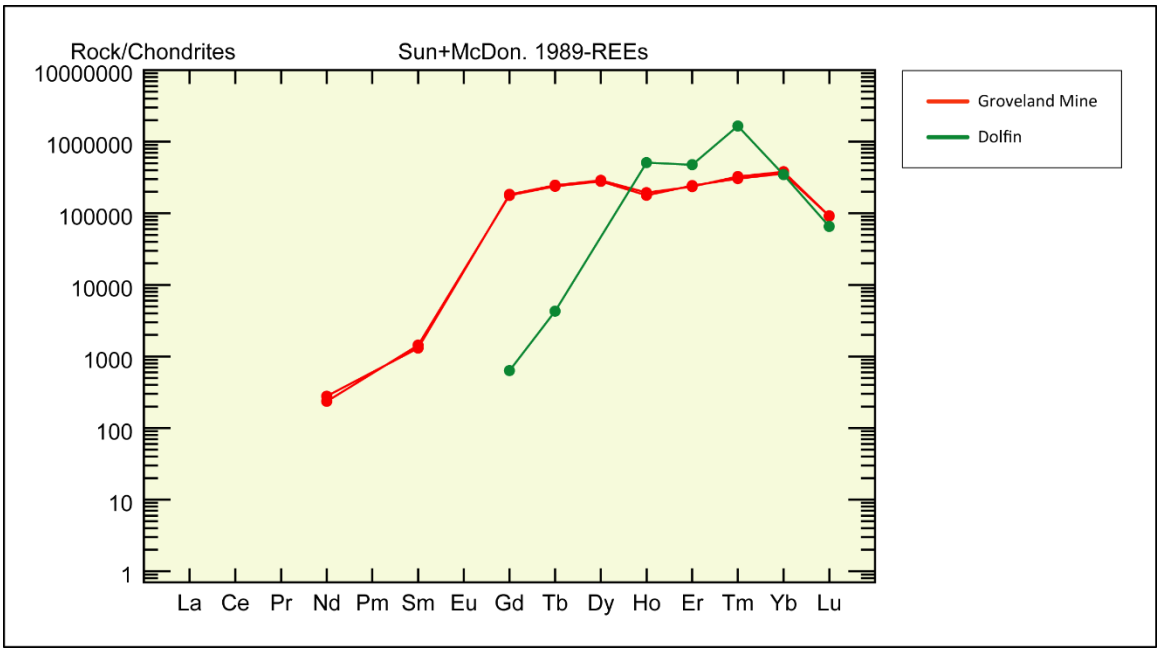


Figure 197 Chondrite normalized plot of REEs in "xenotimes" from the Groveland and Dolfin pegmatites.

## ZIRCON GROUP

Pegmatites often contain trace quantities of zircon; however, its abundance can increase as compositions become more alkaline (London, 2008). Zircon typically contains some amount of hafnium, but NYF-type pegmatites typically have low-hafnium zircon (Simmons, *et al*., 2003). Hafnium and zircon ratios are a good indicator for the degree of evolution of a pegmatite. Weight percent totals of hafnium from microprobe analyses range from slightly less than 0.8% to as much as 2.3%. Zircons from the Humboldt and Bell Creek granites and Republic Mine, Crockley, and Groveland Mine pegmatites have been analyzed by electron microprobe and have been plotted using Zr/Hf apfu vs $HfO_2$ wt% totals (Figure 198). Bell Creek are only slightly less evolved than the Humboldt samples. The relatively least evolved samples are from the Republic Mine and the relatively most evolved samples are from the Dolfin pegmatite. There is one analysis from the Republic Mine which plots nearer to Groveland Mine samples, but for the most part, there is a clear gap between samples analyzed from the Republic Mine and other locations. The Crockley samples are curious in that thorium contents are higher than samples from other locations. The Th-Hf-U ternary (Figure 199) illustrates the relative enrichment of Hf over Th and U in all samples with the exception of the Crockley.

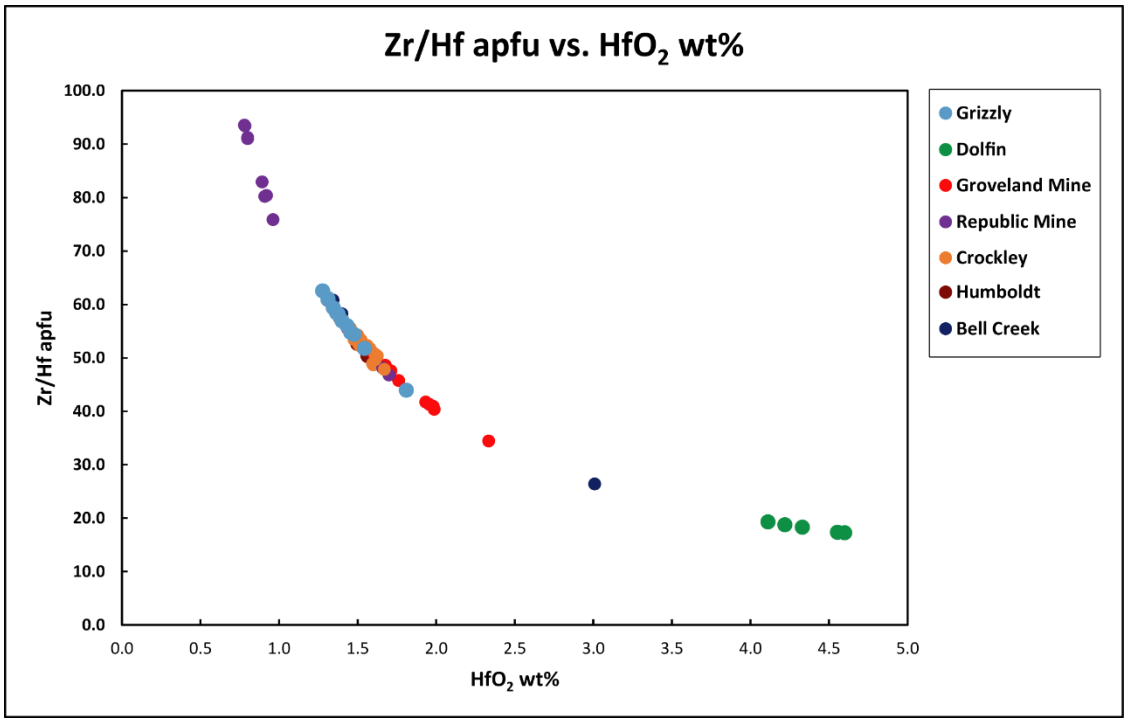


Figure 198 Zr/Hf *apfu* versus $HfO_2$ Wt% plot for zircons.

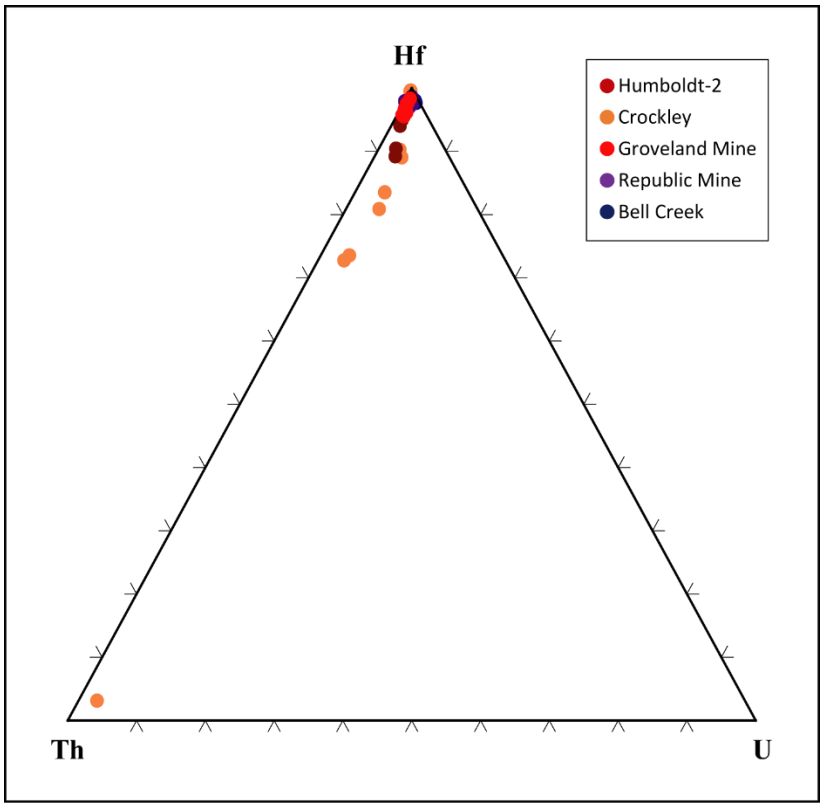


Figure 199 Hafnium – Thorium – Uranium ternary for zircons based on normalized *apfu's*.

## WHOLE-ROCK GEOCHEMISTRY

Five whole-rock samples, one from Humboldt granite, three from Bell Creek granite, and one sample of granitic material collected from the Crockley pegmatite location were analyzed by Fusion ICP-OES and ICP-MS methods. Geochemical data includes 10 major elements (shown by weight percent) and 45 trace elements (parts per million-ppm). The geochemical data have been used to create the following plots in this section. Unfortunately, owing to analytical methods, few of the Hoffman (1987) analyses are appropriate for plotting with current samples from the Bell Creek, Humboldt, and Crockley as trace element geochemistry necessary for these plots is unavailable.

### MAJOR ELEMENTS

Igneous rock types can be geochemically distinguished using $Na_2O + K_2O$ versus $SiO_2$ diagram of Bateman *et al*. (1989). Samples from Humboldt, Crockley, and Bell Creek plot in the granite field, but some of the Hoffman (1987) samples included plot in the Quartz Monzonite field as well as the Diorite, Quartz Diorite, Tonalite and Gabbro, Diabase fields (Figure 200). Granites are also further classified into peralkaline, metaluminous, and peraluminous groups via the Shand's Index plot of Maniar and Piccoli (1989), which graphically illustrates relative dominance of either alkali/alkaline earth elements K, Na, and Ca or aluminum (Figure 201). Two Bell Creek samples are relatively more peralumnious than all other samples including the Hoffman analyses. Hoffman, Bell Creek, and Clotted Granite samples, as well as the more recent Bell Creek samples are relatively slightly more peraluminous than Hoffman Albite granite and the more recent Crockley and Humboldt granite samples. The Humboldt sample plots on the line dividing the metaluminous and peraluminous fields. It is important to note that muscovite

mica is found in both the more recent Humboldt, Bell Creek, and Crockley samples, which coincides with s more peraluminous nature and biotite micas plot in the peraluminous field of Abdel-Rahman's discrimination diagram (Figure 187).

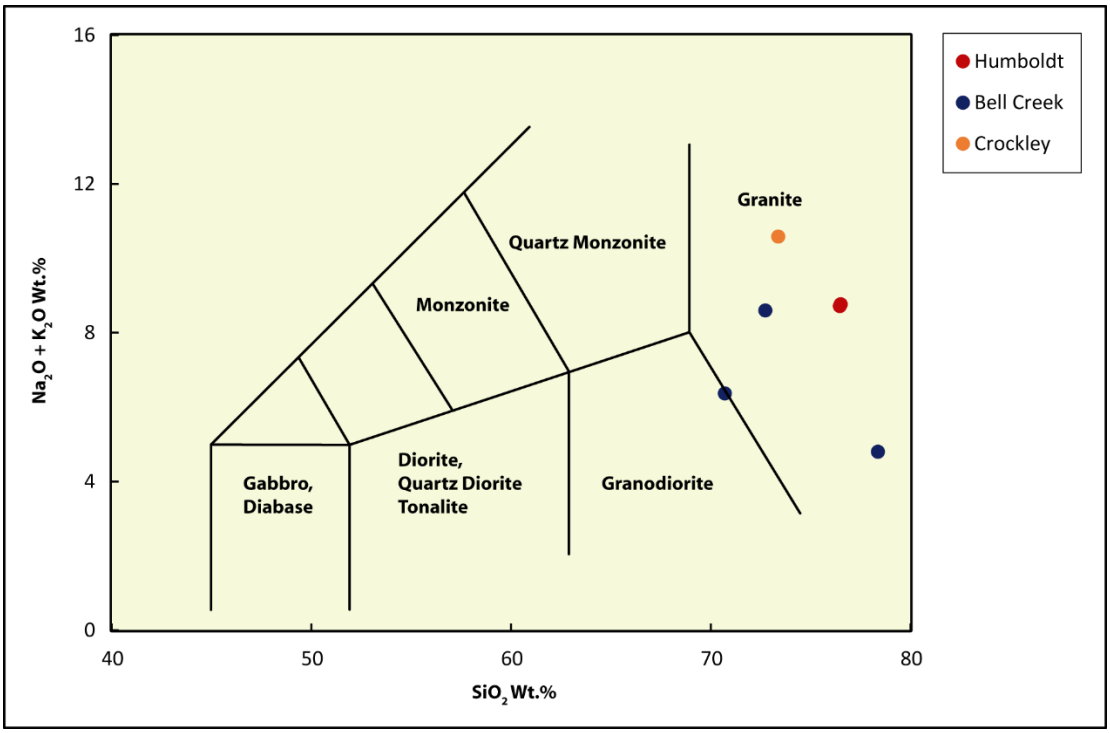


Figure 200 Bateman *et al*. (1989) alkalis versus silica diagram.

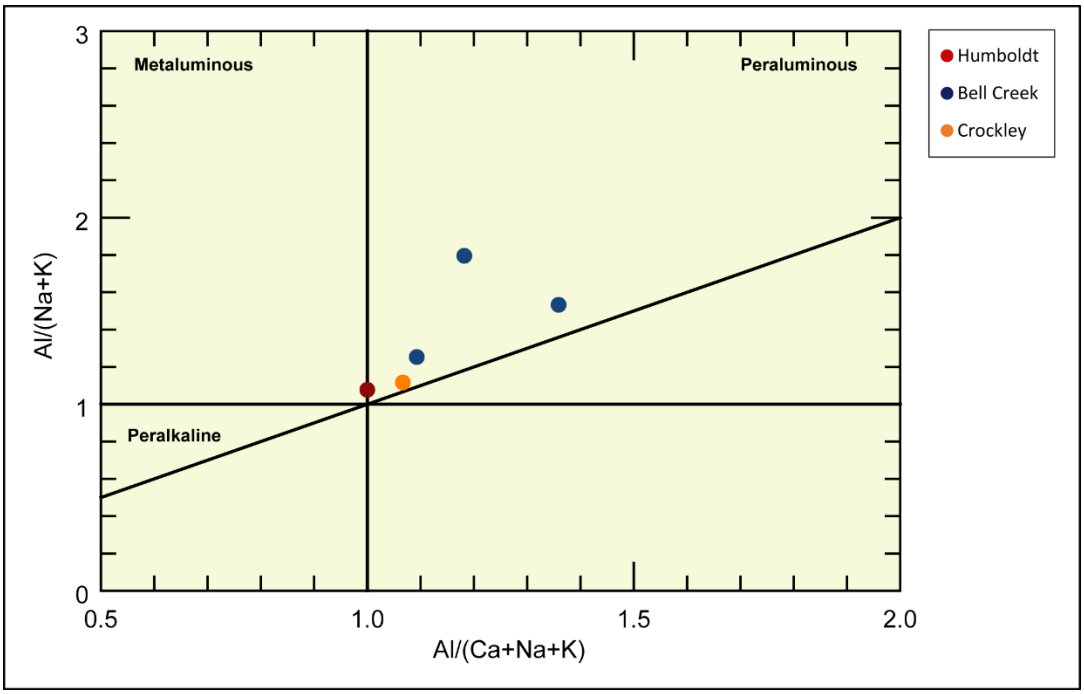


Figure 201 Shand's Index diagram of Maniar & Piccoli (1989).

Igneous rock classification can also be divided into the mutually exclusive alkaline and subalkaline magma series. The $R_1R_2$ discrimination diagram of De La Roche *et al*. (1980) plot whole-rock data and show that Bell Creek samples (both Hoffman and most recent), Humboldt, Crockley, Albite Granite, and Clotted Granite samples all plot within the subalkaline field meaning these all have abundant silica (Figure 202). The subalkaline group can be further subdivided into a calc-alkaline (Fe-poor) and tholeiitic (Fe-rich) magma series (Figure 203). Based on the discrimation diagram of Miyashiro (1975), the more recent Bell Creek samples plot within the calc-alkaline field and the Hoffman Bell Creek samples are plotting within both the tholeiitic and calc-alkaline fields. More recent biotite mica samples from the Bell Creek granite show relative enrichment in magnesium than Humboldt and Crockley pegmatite samples, which corresponds nicely with the calc-alkaline affinity of Bell Creek granite whole rock geochemistry. Clotted Granite samples of Hoffman plot within the calc-alkaline field. Humboldt granite and

Crockley samples plot within the tholeiitic field, with the Humboldt sample having a relatively extreme tholeiitic signature owing to the relative enrichment of iron over magnesium in this sample. Hoffman's Albite Granite sample is not shown due to magnesium being below detectable limits in the analysis.

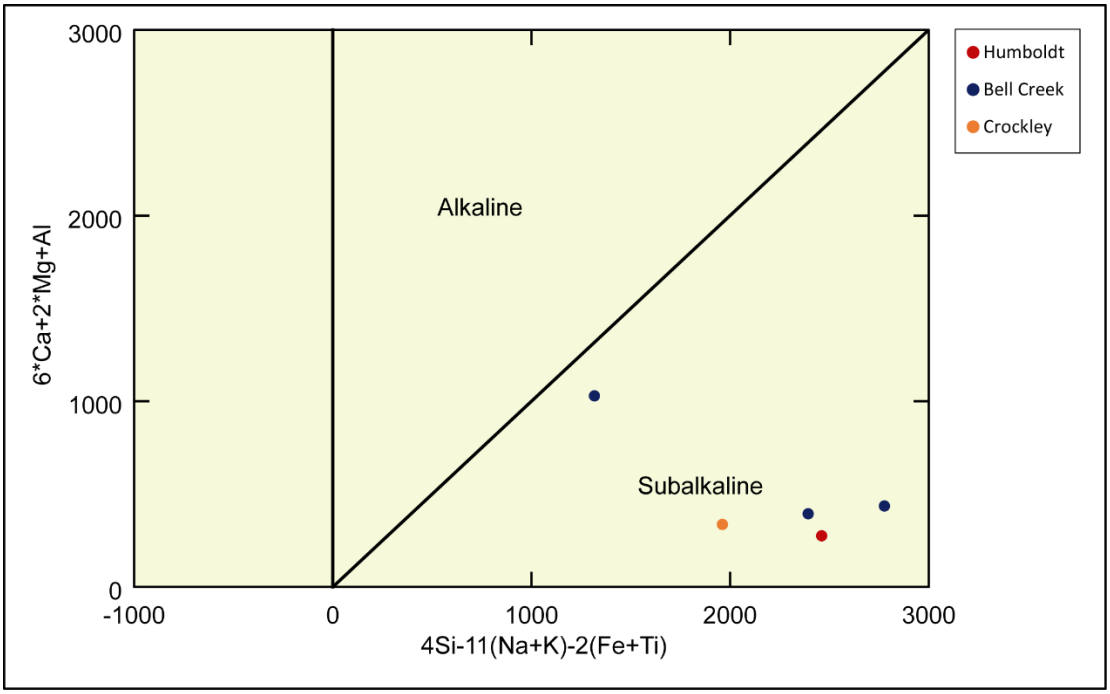


Figure 202 $R_1R_2$ discrimination diagram of De La Roche *et al*. (1980).

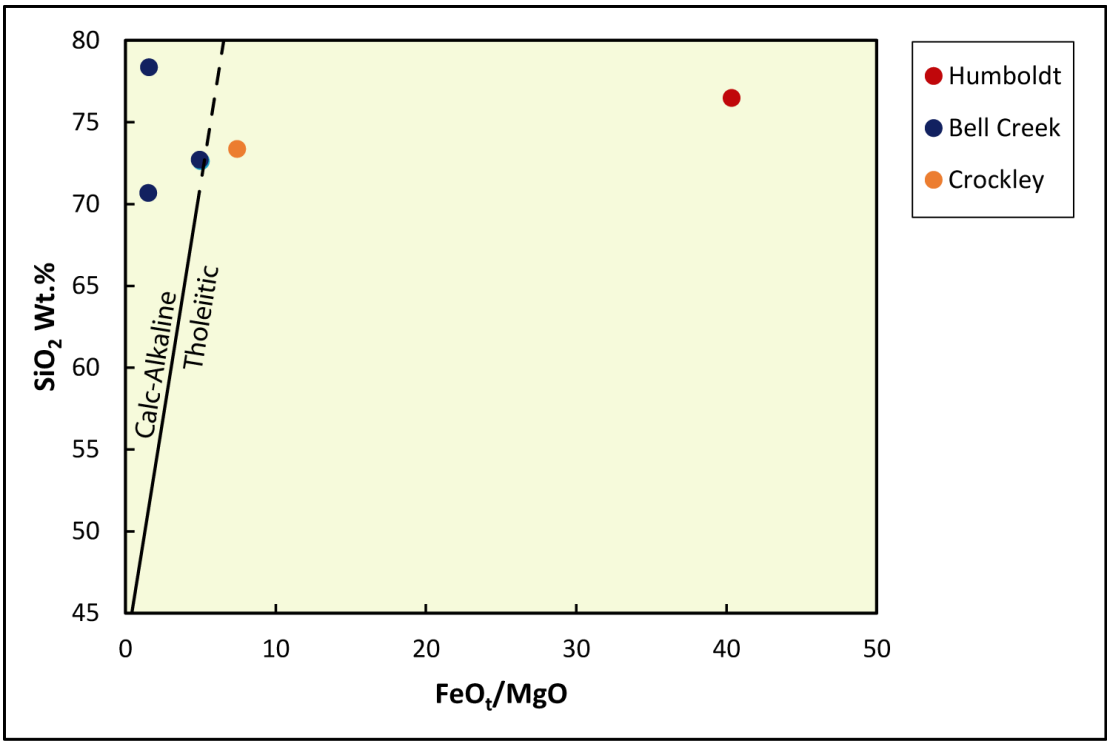


Figure 203 Calc-alkaline versus tholeiitic magma series affiliation of Miyashiro (1975).

## TRACE ELEMENTS

The ratios and content of trace elements in granites and pegmatites are often used to determine the degree of evolution as well as to explore potential genetic relationships. Rubidium, for example, is a relatively incompatible substitution for potassium in K-feldspars, therefore the K/Rb ratio is a useful indicator for the degree of evolution when plotted against Rb ppm content as the K/Rb ratio generally decreases with progressive crystallization of a granitic melt (Černý *et al*., 1985). Figure 204 shows that Bell Creek granite samples have a higher K/Rb ratio and relatively lower enrichement in rubidium. The Crockley sample has a similar K/Rb ratio as the Bell Creek samples, but it is relatively more enriched in rubidium than Bell Creek samples. The Humboldt granite sample has a relatively lower K/Rb ratios than either Crockley or Bell Creek, meaning that Humboldt granite samples are relatively more evolved than Bell Creek and Crockley. The Crockley sample is intermediately evolved when compared with Bell Creek and Humboldt samples. Hoffman Clotted Granite samples are relatively depleted in Rb and have some the highest K/Rb ratios of all other samples. Hoffman Bell Creek samples are also relatively depleted in Rb; however, one of his samples has a relatively low K/Rb ratio, six of his samples have a relatively high K/Rb ratio, and two of his Bell Creek samples have intermediate ratios between these two extremes.

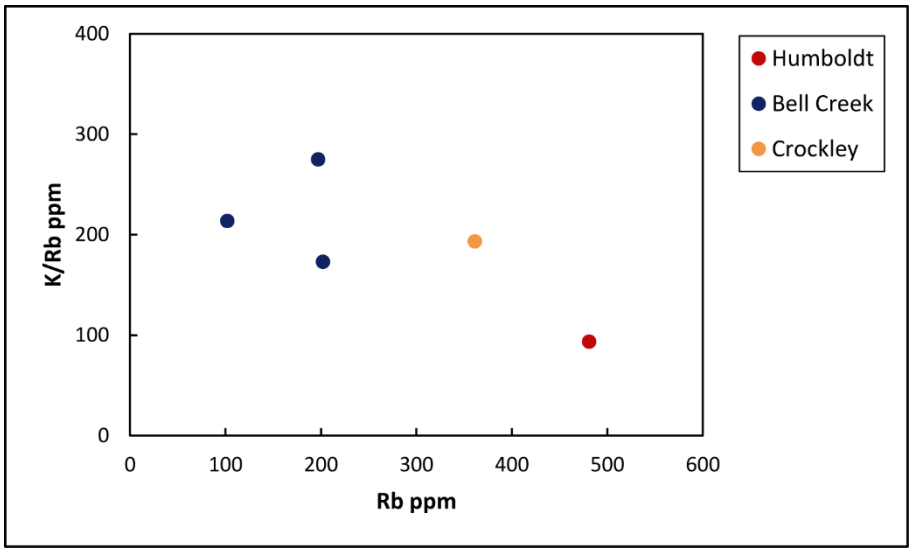


Figure 204 K/Rb ratios versus Rb ppm enrichment.

The ternary diagrams in Figures 205, 206, and 207 compare the normalized percentages of Ce, La, and Nd; Ce, La, and Y; and Ti, Nb, and Ta enrichment/depletion respectively. Bell Creek, Humboldt, and Crockley samples cluster within cerium dominant field, which coincides with cerium dominant monazite-(Ce) samples from the Bell Creek and Humboldt granites as well as cerium dominant "monazites" and "bastnäsites" from the Crockley pegmatite. In the Ce, La, Y ternary (Figure 206), samples from the Bell Creek all cluster in the cerium dominant field. The Crockley and Humboldt samples are both yttrium dominant as well as relatively less enriched in lanthanum than the Bell Creek samples.

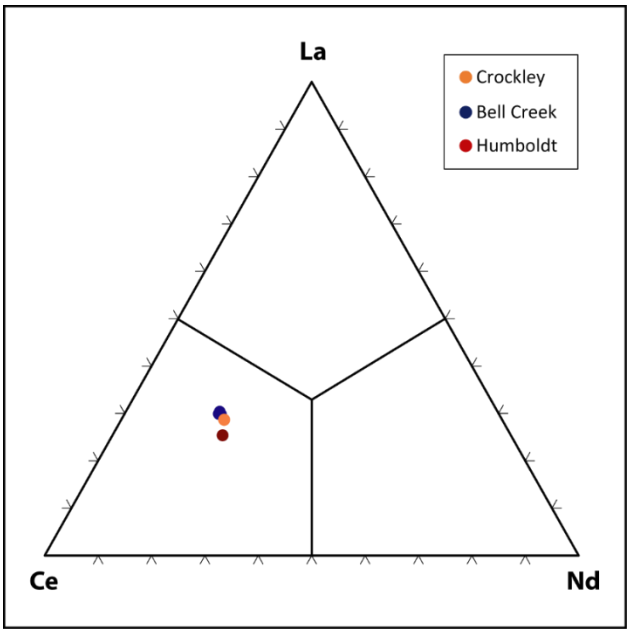


Figure 205  Ce-La-Nd ternary diagram.

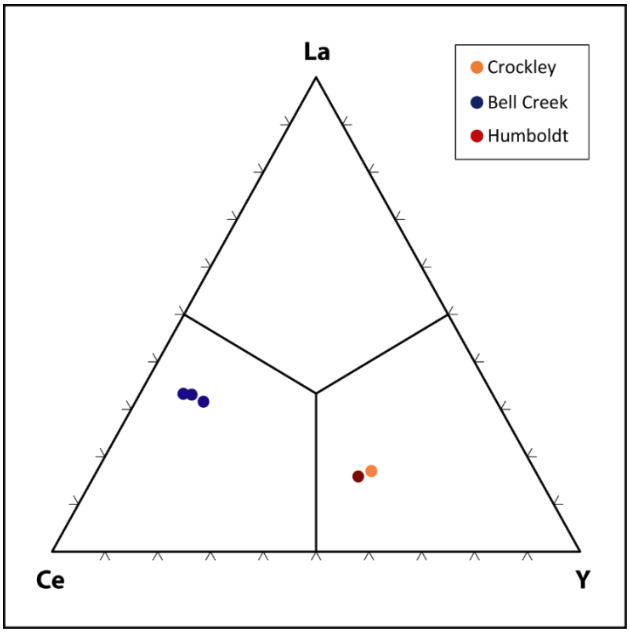


Figure 206  Ce-La-Y ternary diagram.

In the Ti, Nb, Ta ternary, Bell Creek samples are extremely relatively dominant in titanium than either Humboldt or Crockley samples.  This dominance nicely with the fact that

biotite micas from the Bell Creek are relatively more titanium rich than biotites from any other sampled location (Figure 186). The Crockley sample does show a trend of being relatively more enriched in titanium than either niobium or tantalum, although the Crockley sample is relatively more enriched in niobium than tantalum. Columbite samples and biotite micas from the Crockley pegmatite are niobium dominant and relatively more enriched in titanium respectively than the sample from Humboldt granite. The Humboldt granite sample also shows a trend of being relatively more enriched in Nb over Ta, although this sample is relatively depleted in Ti with regards to Bell Creek and Crockley samples. In addition, Crockley and Humboldt samples are niobium dominant and even though relative titanium enrichment in Bell Creek samples eclipse both niobium and tantalum enrichment combined, samples are relatively more enriched in niobium than tantalum as one would expect from NYF-type systems.

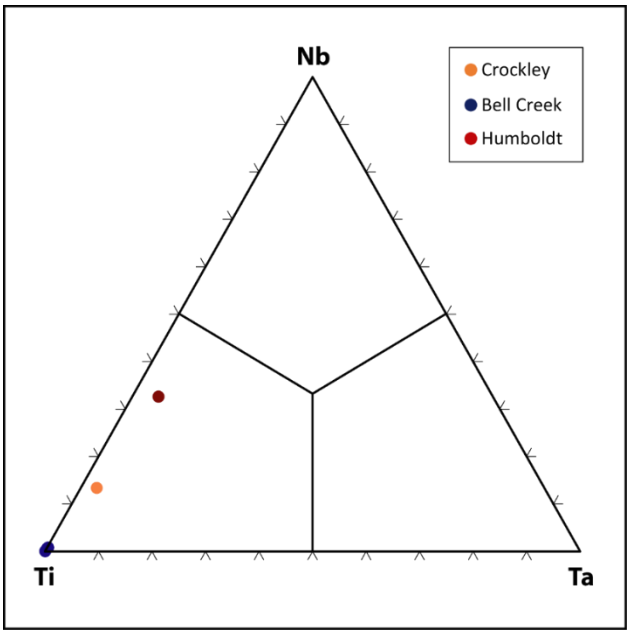


Figure 207 Ti-Nb-Ta ternary diagram.

The chondrite-normalized REE diagram of Sun and McDonough (1989) is an effective means to evaluate lanthanide-series REE enrichment or depletion in a rock relative to a primitive, homogeneous crust (Figure 208). Europium is the only REE than has a divalent charge and therefore can be depleted when the common rock-forming minerals (plagioclase specifically) crystallize from a melt. This leads to what is commonly referred to as a negative europium anomaly. This anomaly is used to determine the degree of evolution of a rock.

All Bell Creek samples have a similar trend of being relatively more enriched in LREE's than HREE's. Bell Creek samples also have a relatively modest negative europium anomaly compared to samples from the Crockley and Humboldt. The Humboldt granite sample has LREE enrichment that is similar in both trend and magnitude with regard to Bell Creek; however, this sample has an HREE enrichment that is more similar to that seen in anorogenic, NYF pegmatites. The Crockley sample has a similar trend as the Humboldt sample, but is an order of magnitude lower. The Humboldt and Crockley samples both have a very similar negative europium anomaly, suggesting that both are relatively more evolved than Bell Creek samples.

Another useful spider diagram is the primitive mantle-normalized plot (Figure 209) of Sun and McDonough (1989). As with the chondrite-normalized plot, all Bell Creek samples exhibit a very similar geochemical signature. Bell Creek samples are relatively more enriched in Ba, Th, and U as well as Sr and P. This plot also reveals the geochemical similarities that both the Humboldt and Crockley samples share with Bell Creek samples. The Humboldt sample has similar enrichment in Th and U, Nd, Zr, and Sm as Bell Creek, but is relatively more enriched in Rb than Bell Creek. The Humboldt sample is also roughly an order of magnitude more enriched in Nb and Ta as well as Y, Yb, and Lu with regard to Bell Creek samples. Sr, P, and Ti are each

approximately an order of magnitude depleted in the Humboldt granite sample with regard to Bell Creek granite samples.

The Crockley sample exhibits a roughly intermediate geochemical signature between Bell Creek and Humboldt samples. The Crockley sample is relatively more enriched in Rb than Bell Creek, but not as enriched as the Humboldt. The Crockley sample is relatively depleted in Ba with regard to Bell Creek, but not nearly as depleted with regard to the Humboldt granite. The Crockley sample has a similar enrichment in Nb and Ta as Humboldt, but not to the same degree as the Humboldt, yet is still relatively more enriched in both than Bell Creek samples. The Crockley sample is, however, relatively more depleted in La, Ce, Nd, Zr, and Sm than either Bell Creek or Humboldt samples, but still follows a similar trend at a magnitude below Bell Creek and Humboldt samples. The Crockley is relatively more enriched in Sr than Humboldt, although P is below detection limits. The Crockley has a similar depletion in Eu and Ti as the Humboldt as well as a similar enrichment in Y, Yb, and Lu as Bell Creek sample, although the enrichment is not an order of magnitude lower as seen in Bell Creek samples with regard to the Humboldt. All samples cluster at both potassium and lead.

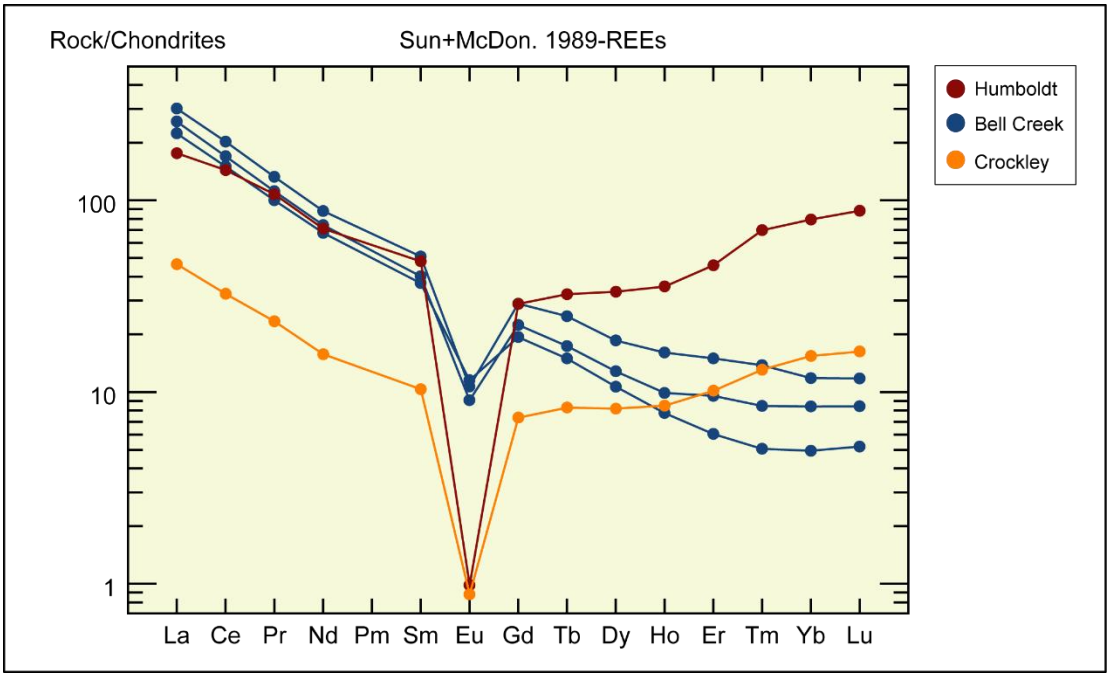


Figure 208 Chondrite-normalized REE diagram of Sun & McDonough (1989).

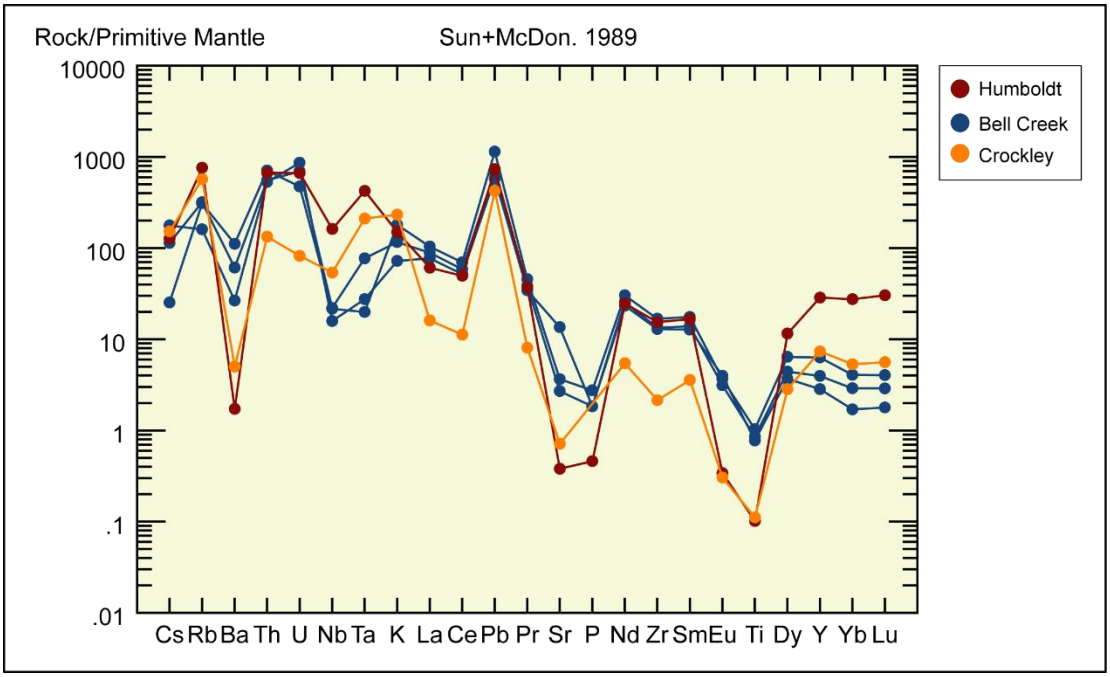


Figure 209 Sun and McDonough primitive mantle-normalized spider diagram.

## TECTONIC DISCRIMINATION DIAGRAMS

Another utility of trace element geochemistry is that certain ratios and concentrations are associated with potential tectonic settings of granitic development. Classification of tectonic settings is typically one of three types: A-type (anorogenic) are typically tholeiitic, relatively potassic and anhydrous, not associated with orogenic events and hence, rarely deformed; S-type (sedimentary) are highly peraluminous, relatively potassic, and high in silica due to the partial melting of metasedimentary packages; I-type (igneous) vary in silica content, are relatively sodium-rich, metaluminous to peraluminous and derived from the fractional crystallization of more mafic magmas (Frost *et al*., 2001).

The discrimination diagram developed by Whalen *et al.* (1987) uses zirconium, gallium, and aluminum to geochemically differentiate between A-type, S-type, and I-type granites (Figure 210). The Bell Creek samples span the I- & S-type field and A-type field. Hoffman (1987) originally interpretted the Bell Creek granite as syntectonic, therefore this result provides support for his hypothesis. The Humboldt and Crockley samples are all plotting within the A-type field. The Humboldt granite has been interpretted to be associated with post orogenic collapse, which can give an anorogenic signature (Hoffman, 1987; Martin *et al*., 2005).

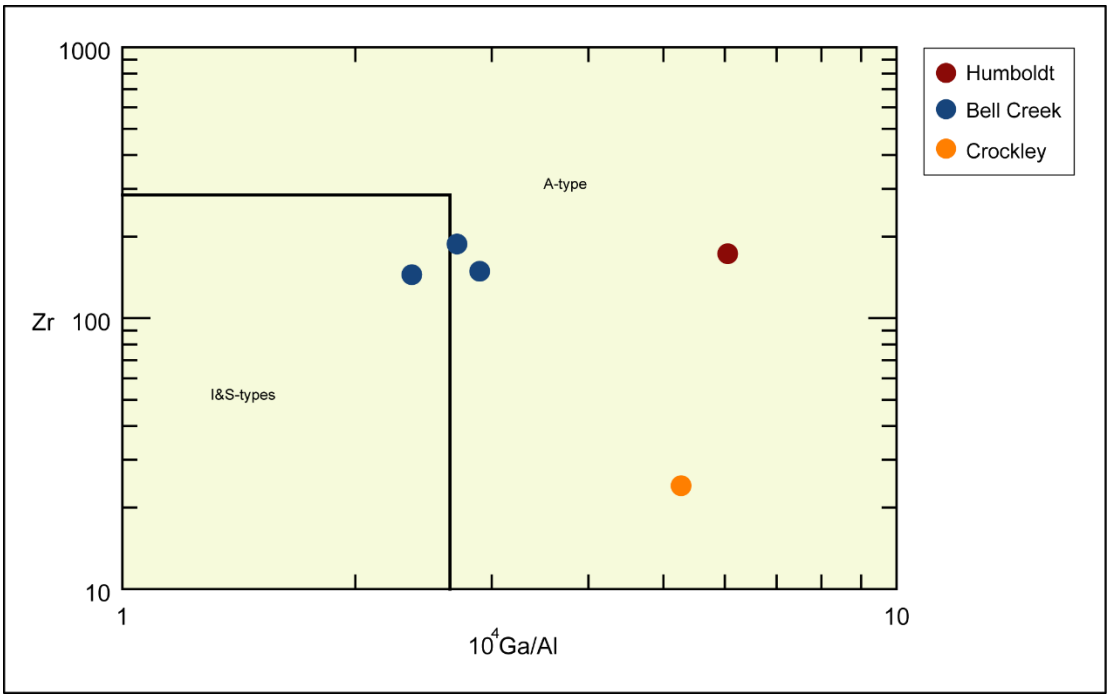


Figure 210 Whalen *et al*. (1987) tectonic discrimination diagram.

The A-type classification of Whalen *et al*. (1987) is further divided into A1 and A2 subtypes (Figure 211) (Eby, 1992). A1 group subtypes have geochemical characteristics that are similar to ocean island basalts. The implication being that these granites are derived from differentiation of magma related to intraplate magmatism and continental rifting. A2 group subtypes have geochemical characteristics that are more similar to island-arc basalts and continental crust, which suggests that this subtype is derived from an underplated crust or continental source rock. The Humboldt sample plots within the A1 field, which is in agreement with Hoffman's interpretation (1987) that the Humboldt granite was emplaced during Penokean post orogenic collapse; however, the sample hovers just near the boundary between the A1 and A2 fields. This suggests that the Humboldt sample has geochemical characteristics that are similar to both an ocean island- and island arc-basalts and continental source rocks. This could suggest possible contamination of the melt that produced the HG2 sample during formation. The

Crockley sample plots near the HG2 sample for both the Y, Nb, Zr and Y, Nb, Ce ternaries yet does not plot quite as near to the A2 field as HG2; however, the Crockley sample plots closer to the Bell Creek samples in the Y, Nb, Ga*3 ternary. It appears that the Crockley sample has similar enrichment in yttrium as Bell Creek, but is less enriched in niobium. It is the gallium*3 value that is greatest influence on the Crockley sample and its proximity to Bell Creek samples.

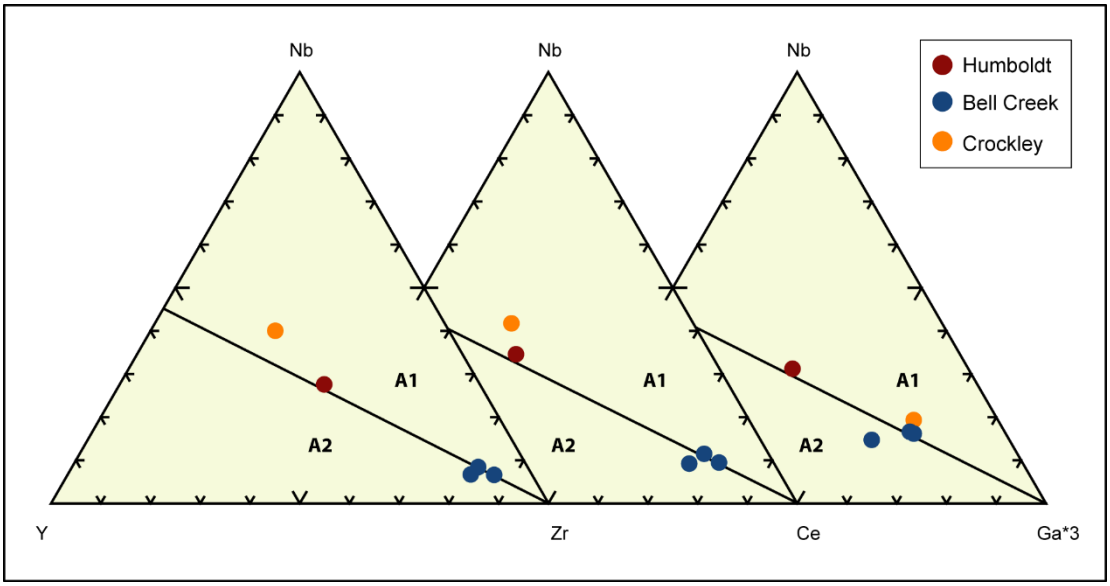


Figure 211 Eby A1- & A2-subtype discrimination diagrams (1992, 2006).

Pearce *et al*. (1984) developed another important set of tectonic discrimination diagrams (Figure 212) that separate granites into ocean ridge granites (ORG), volcanic arc granites (VAG), within plate granites (WPG), syn-collisional granites (syn-COLG), and post collisional granites. Post collisional granite field is shown in the Rb versus Y + Nb diagram. The WPG class of Pearce *et al*. (1984) is similar to the A1 anorogenic subtype of Eby (1992). The post-collisional granite class consists of the I- and S-types, but is also somewhat like the A2 subtype of Whalen *et al*. (1984). The Bell Creek samples are all plotting in either both the VAG and syn-COLG

fields or as is the case in Rb versus Y + Nb, plots in the post-COLG field. The Crockley sample also plots in the post-COLG field, but in the larger WPG field like the Humboldt sample. The Humboldt sample plots in the WPG field. This is in agreement with the A1 subtype classification of Eby (1992) as the Humboldt granite is associated with Penokean post orogenic collapse.

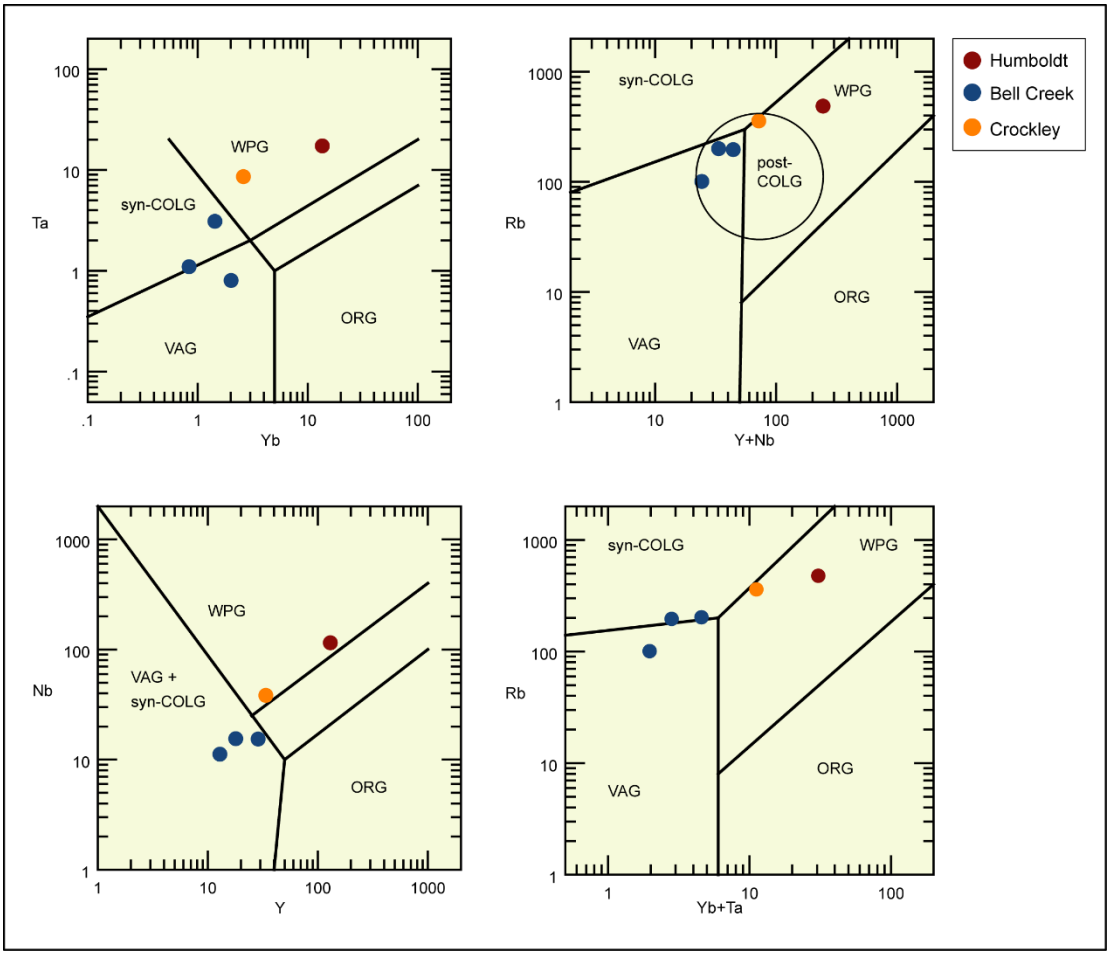


Figure 212 Pearce *et al*. (1984) tectonic discrimination diagrams.

## DISCUSSION

Černý and Ercit (2005) use depth of emplacement and petrogenetic parameters to classify pegmatites. Pegmatites are categorized into broader types as being Abyssal, Muscovite, Muscovite-Rare Element, Rare Element, and Miarolitic (Černý & Ercit, 2005; Černý, 2012). The Rare-Element class of pegmatite is further classified into families of pegmatites, based on elemental enrichment, as either being NYF-type (niobium, yttrium, and fluorine), LCT-type (lithium, cesium, and tantalum), or a mixture of these two types (Černý & Ercit, 2005; Černý, 2012). Martin and DeVito (2005) suggest using tectonic regime as a mechanism to predict geochemical characteristics of pegmatites: melts generated by orogenesis typically produce LCT-type pegmatites, NYF-type develop as a result of melts produced during anorogenesis, and Mixed-type are a product of contamination of the parental melt. Neither of these methods are fully suitable in the classification of these particular pegmatites; however, Martin and DeVito (2005) do acknowledge that some pegmatites are produced by the partial melting of either mantle or crustal rocks.

There are a number of factors to consider that complicate classification of these pegmatites: 1) there has been two phases of anatexis involving gneiss domes, Archean and Paleoproterozoic, driven by two orogenic events; 2) melts produced from Bell Creek gneiss in the Archean by anatexis of Bell Creek gneiss could have likely involved either primitive sedimentary packages and/or felsic components of the Twin Lake Assemblage in a reducing environment; 3) anatectic melts produced during the Paleoproterozoic likely involved granitic basement established during the Archean phase of gneiss dome formation, granitic plutons associated with gneiss domes and their subsequent remobilization, or remnant felsic components of the Bell Creek gneiss/granite; 4) contamination of Paleoproterozoic melts would have

involved metasedimentary and metavolcanics produced in an oxidizing environment; 5) anorogenic (Humboldt) or igneous gabbroic (Peavy Pond Complex) melts produced during the Penokean orogeny or during Penokean post-orogenic collapse could have likely been contaminated by any and all of these packages; 6) location of the melt in either domes or troughs would have likely influenced the amount and type of contamination; and 7) anatectic melts would have likely been not only a product of, but also have been influenced by, the metamorphic isograd in which they are located, as well as the overall influence of the isograd on the capacity of the melt to assimilate metasedimentary and metavolcanic packages.

| Class | Subclass | Type | Subtype | Family |
|---|---|---|---|---|
| **Abyssal** | **HREE<br>LREE<br>U** | | | **NYF** |
| | **B, Be** | | | **LCT** |
| **Muscovite** | | | | |
| **Muscovite-<br>Rare Element** | **REE** | | | **NYF** |
| | **Li** | | | **LCT** |
| **Rare Element** | **REE** | **allanite-monazite<br>euxenite<br>gadolinite** | | **NYF** |
| | **Li** | **beryl** | beryl-columbite<br>beryl-columbite-phosphate | **LCT** |
| | | **complex** | spodumene<br>petalite<br>lepidolite<br>elbaite<br>amblygonite | |
| | | **albite-spodume<br>albite** | | |
| **Miarolitic** | **REE** | **topaz-beryl<br>gadolinite-<br>fergusonite** | | **NYF** |
| | **Li** | **topaz-beryl<br>lepidolite** | | **LCT** |

Figure 213 Černý (2012) classification of pegmatites.

The Bell Creek granite is believed to have formed during the Archean phase of gneiss dome formation (Hoffman, 1987; Tinkham & Marshak, 2004) by the partial melting of the more felsic components of the Bell Creek gneiss. Based on spatial proximity, as well as geochemical and mineralogical similarities it is suggested that the Grizzly pegmatite fractionated from the Bell Creek granite. Hoffman (1987) suggests that the Bell Creek granite is syntectonic and is associated with the collision of the Southern and Northern Complexes ~ 2.69 Ga along the Great Lakes Tectonic Zone. Tinkham and Marshak (2004) hypothesize that the Bell Creek gneiss penetratively deformed and metamorphosed the Twin Lake Assemblage, which consists of felsic and mafic gneisses. It seems possible then that the Bell Creek granite is not only a product of the partial melting of the felsic components of the Bell Creek gneiss, but also contamination of the anatectic melt with the primitive felsic components of the Twin Lake Assemblage as well. This might explain why the Bell Creek granite has geochemical characteristics similar to an underplated crust or continental source rock as well as to intraplate magmatism and continental rifting. This might also explain why the Bell Creek has I- & S-, and a slight A-type signature as well as a VAG/syn-COLG signature. There is also the matter of Bell Creek samples that plot in the post-collisional field in tectonic discrimination diagrams (Pearce *et al*., 1984).

Černý (1991a) suggests that I-type granites produced from mafic to intermediate igneous rocks, including immature sedimentary rocks of igneous provenance, could evolve toward more peraluminous compositions. He also suggests that I-types be included with the LCT-type family, even if they should lack characteristic enrichment associated with LCT-type pegmatites (London, 2008). The suggestion is that the Archean Bell Creek granite has been produced under a combination of these circumstances. The Grizzly pegmatite is peraluminous (Abdel-Rahman, 1996) and having fractionated from the Bell Creek granite, should be classified as an LCT-type

pegmatite based on Černý's classification scheme (1991a), even though the residual melt from the Bell Creek granite was relatively too primitive and insufficiently enriched to produce a highly evolved LCT-type pegmatite. In fact the Grizzly pegmatite lacks any enrichment in Li, Ce, and T, making classification of the Grizzly as LCT-type problematic.

The Humboldt granite has an A-type signature and is associated with Penokean post-orogenic collapse. Based on subtype classification of Eby (1992; 2006), the Humboldt is more related to differentiation of magma associated with intraplate magmatism and continental rifting. Further, trace geochemistry shows the Humboldt is a within-plate granite. However, biotites analyzed from the Humboldt show an orogenic signature, rather than anorogenic. Meaning, that when the granitic melt intruded into the Northern Penokean terrane, there may have been limited input from the MRSG or that the anorogenic melt that produced the Humboldt may have been contaminated with Bell Creek gneiss/granite. This would explain why the Humboldt, and for that matter the Crockley, have a similar LREE geochemical signature as the Bell Creek, even though the Crockley is an order of magnitude below Humboldt and Bell Creek LREE enrichment. This would also explain the post-collisional signature the Crockley shares with Bell Creek samples.

One of the original goals of this study was to use monazite age dating techniques in order to determine if any of the pegmatites could be associated with the formation of the Humboldt granite. No suitable monazites were found for reliable age dates. However, one granitic sample from the Crockley pegmatite was collected for bulk compositional analysis. Heinrich (1962) suggested that the Crockley pegmatite is related to the 'Republic Granite'. Other than his mention of the Republic Granite, no further literature is present. It is suggested that the Crockley pegmatite is geochemically related the Humboldt granite as bulk compositional analyses reveal

the Crockley granitic sample is very similar to Humboldt granite samples. Hoffman (1987) collected many granitic samples from the Bell Creek, Clotted, and Albite granites. Even though his analyses do not include many of the trace elements in modern techniques, geochemistry available for comparison with current analyses shows that the Crockley pegmatite granitic sample is more similar to both the Humboldt and Albite granites than either the Clotted or Bell Creek granites (Figure 214, Figure 215,Figure 216). Therefore it is suggested that the Crockley pegmatite is genetically related to the Humboldt granite and trace geochemistry supports this claim.

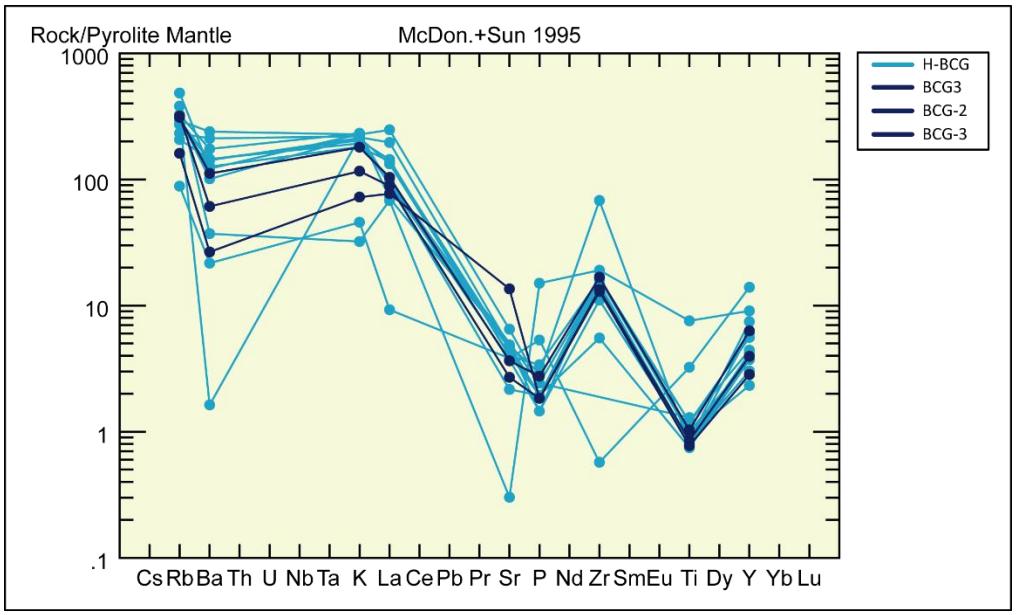


Figure 214 Trace geochemistry of Hoffman (1987; light blue) & current (dark blue) Bell Creek granite samples.

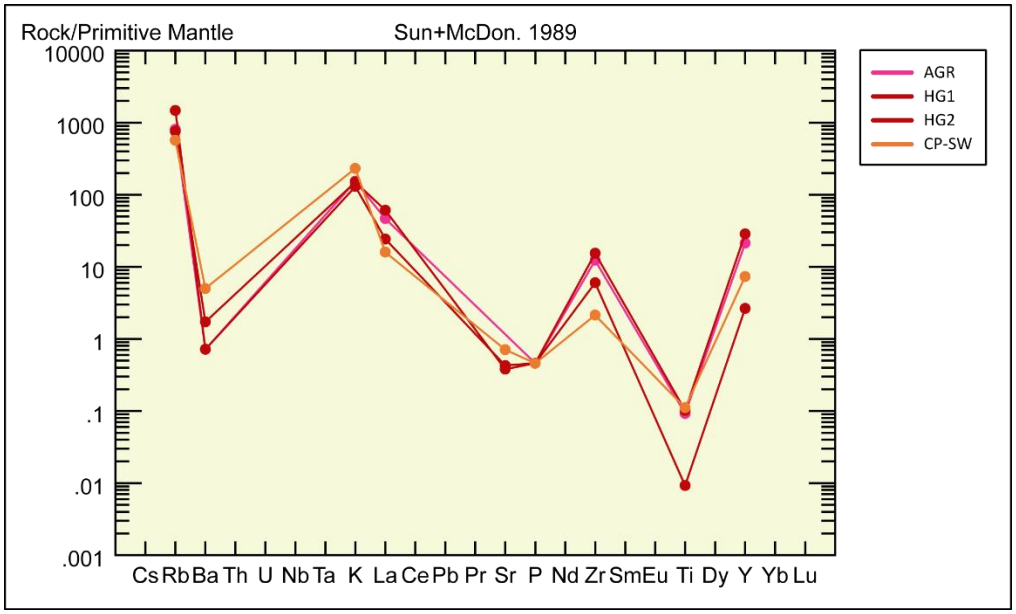


Figure 215 Trace geochemistry of Albite Granite (AGR) from Hoffman (1987) dissertation. Humboldt (HG1 & HG2) and Crockley samples (CP-SW) are analyses conducted for this study. Note the change in scale to accommodate stronger relative enrichment of Rb & stronger relative depletion of Ti compared to Bell Creek and Clotted Granites.

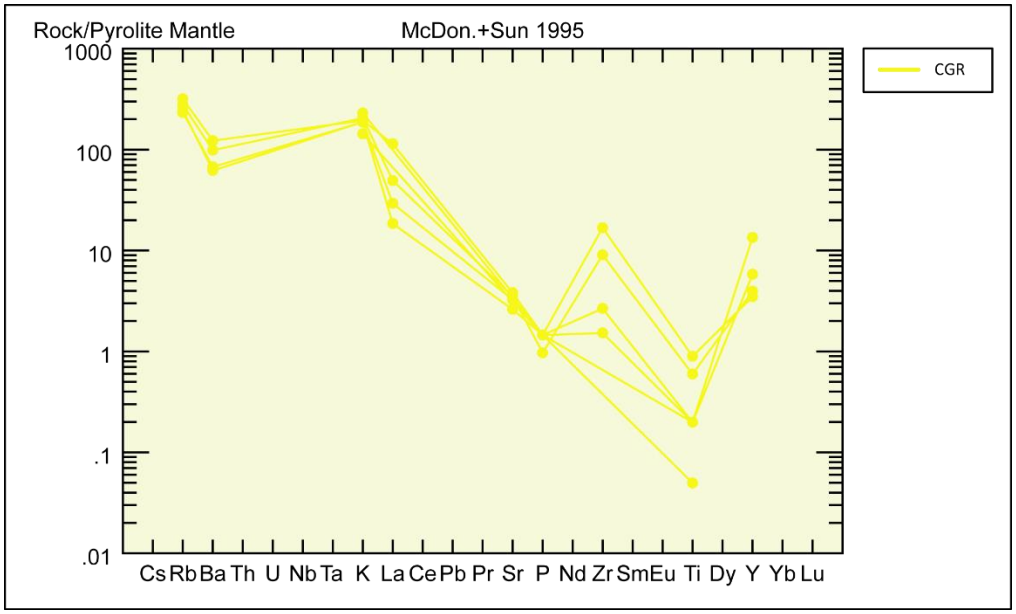


Figure 216 Trace geochemistry of Hoffman (1987) Clotted Granite samples.

The second phase of gneiss dome formation involved original domal architecture present (Marshak *et al*., 1997; Tinkham & Marshak, 2004). Reactivation of the Southern Complex during the Paleoproterozoic involved displacement along shear zones and deposition of MRSG into grabens and keels (Marshak, 1997; Tinkham & Marshak, 2004). If anatexis is intimately linked with gneiss dome formation as Eskola (1949) and Yin (2004) believe, then it seems possible that a second anatectic melt could have been produced from remnant felsic components of Archean gneiss domes during the Penokean Orogeny. Also just as likely is that these melts could have become subsequently contaminated with MRSG, assisted in part by the regional metamorphism related to the gneiss domes.

This scenario seems especially likely for the Republic Mine pegmatite. The Republic Mine is considered to be peraluminous due to the presence of relatively abundant muscovite mica and garnet as well as biotites that plot within the peraluminous field (Abdel-Rahman, 1996). Tourmaline is also present, which is indicative of a more peraluminous nature, but also that the melt which produced the Republic Mine pegmatite had become enriched in boron, presumably from contamination of the melt with MRSG. Even though tourmaline is present, they are rather primitive due to their relative enrichment in magnesium and calcium. Biotites are also rather primitive, despite being peraluminous, as they are relatively enriched in magnesium, much like Bell Creek biotites. Magnesium is typically not abundant in granites, and especially pegmatites, as it is preferentially taken up in the early rock-forming minerals (Batchelor & Kinnaird, 1984). Zircons from the Republic Mine have the most primitive Zr/Hf ratios out of all the pegmatites in this study and also have some of the highest calcium contents as well.

The Republic Mine pegmatite is suggested to be a product of partial melting of Bell Creek gneiss as well as contamination of that melt with MRSG. The Archean Bell Creek

granites have calcium-rich plagioclase inclusions (Hoffman, 1987) as does the Grizzly pegmatite. If the Bell Creek granite has been produced from the Bell Creek gneiss during an Archean phase of anatexis and gneiss dome formation, then the Paleoproterozoic phase of partial melting involving the Bell Creek gneiss and domes would likely produce a melt with similar geochemical characteristics. If the second anatectic melt became contaminated with MRSG sediments and metavolcanics, this would explain why biotite micas are plotting within the orogenic field (Webber *et al*., 2000) and peraluminous field (Abdel-Rahman, 1996), something the Republic Mine shares with both the Bell Creek and Grizzly. This would explain the presence of tourmaline, but also how the overall nature of the Republic Mine itself, is primitive. It should be noted that biotites from Grizzly pegmatite are less enriched in magnesium than either the Bell Creek or the Republic Mine. However, this is believed to be through the process of fractionation that preferentially depleted magnesium before the Grizzly pegmatite was formed. Tourmaline is absent from both Bell Creek granite and Grizzly pegmatite suggesting that boron was not present in sufficient quantities in the melt that produced either of these igneous bodies. Therefore, if the formation of the Republic Mine pegmatite represents a second anatectic melt produced during the Paleoproterozoic from the Bell Creek gneiss, then boron enrichment would have had to have been introduced by contamination.

It follows then that perhaps all of the pegmatites in this study, with the exception of the Grizzly pegmatite, may have become contaminated by metasediments and metavolcanics of the MRSG or primitive sedimentary packages. The quantity and type of assimilated packages would then affect the overall geochemistry to such a degree so as to produce a hybrid pegmatite that has characteristics of both the original geochemistry and the assimilated packages. The Sturgeon and Hwy69 pegmatites could have been generated under similar circumstances as the Republic Mine,

owing to the more peraluminous and primitive nature. The Sturgeon River pegmatite has abundant tourmaline and garnet as well as muscovite mica. Hwy69 has both garnet and muscovite mica, which suggests that contamination of the Hwy69 pegmatite did not include packages sufficiently enriched in boron to produce tourmaline. Although, considering the spatial relationship it has with the Sturgeon River and Groveland Mine pegmatites, it seems promising that the Hwy69 does contain tourmaline, but perhaps of limited quantity. Biotite micas from both cluster near Bell Creek and Republic Mine samples in the calc-alkaline field (Figure 187). However, the near calc-alkaline affinity of biotite from these two pegmatites could have come from contamination of the melt with Chocolay group, which contain algal dolomite (Ueng & Larue, 1988).

The Groveland Mine pegmatite is especially interesting in that it is spatially associated with the Peavy Pond Complex (PPC): a syntectonic igneous gabbroic body that assimilated parts of the Michigamme Formation (MF) during the Penokean Orogeny (Bayley, 1959). There is abundant garnet, muscovite mica, tourmaline, and also beryl. Biotite micas are peraluminous (Figure 187) and plot with the orogenic field (Figures 188 & 189). In addition, there are a number of minerals present, which are typically associated with LCT-type pegmatites, such as pyrophanite, tantalite, microlite, and gahnite. Not to suggest that these minerals never occur in NYF-type pegmatites, but that the elemental constituents necessary for their formation are typically insufficient to produce them in NYF pegmatite systems. As an example, NYF-type pegmatites are typically enriched in niobium relative to tantalum. Tantalum is generally not sufficient to become the dominant phase, especially in columbite group minerals. LCT-type pegmatites are generally relatively more enriched in Ta and have mangano- and ferrotantalites, whereas NYF-types have mangano- and ferrocolumbites. LCT-type pegmatites also tend to be

more manganese rich and NYF-type pegmatites, more iron rich. The fact that the Groveland has ferrotantalites as well as samples that plot on the cusp of being classified as manganotantalite, is unusual.

Bayley (1959) offers a suitable explanation for the more peraluminous nature of the Groveland Mine. The PPC, located very near the Groveland Mine pegmatite, intruded and assimilated siliceous greywacke and slate of the Michigamme Formation (MF) (Bayley, 1959). The contamination of a more gabbroic melt with greywacke and slate of the MF, would have given rise to various felsic and intermediate magma types (Bayley, 1959). Bayley (1959) further concludes that there was a gradual transition to a more felsic composition depending, of course, on the amount of MF metasedimentary material incorporated into the melt. Cooling of the melt was undoubtedly slow, as the area was experiencing regional metamorphism related to gneissic dome remobilization during the Penokean Orogeny (Bayley, 1959). The Groveland Mine pegmatite is located in the staurolite facies metamorphic isograd and the PPC is located to the west in the metamorphic high sillimanite facies isograd of the Peavy node.

Bayley (1959) concluded that the reaction of greywacke and slate of the MF would have produced granodiorites, granites, and pegmatitic melts. Bayley (1959) listed the following components available for reaction within the rocks as $H_2O$, $CO_2$, $K_2O$, $Na_2O$, $SiO_2$, $Al_2O_3$, B, and F. These components would explain the presence of minerals more closely associated with LCT-type and peraluminous pegmatites. It is further suggested that due to the close proximity to Groveland Mine itself (which has been mined for iron ore in the past) as well as to banded-iron formation deposits, that assimilation of the surrounding formations included these iron deposits. This would explain the relative greater abundance of magnetite and hematite at the Groveland Mine pegmatite itself given that these deposits were produced during more oxidizing conditions.

The Bell Creek granite and Grizzly pegmatite contain little to no magnetite, and the implication is that trivalent iron contents were insufficient to produce hematite. Hematite frequently affects the color of feldspars by occurring as microscopic inclusions. The Bell Creek granite and Grizzly pegmatite were produced when the environment was more reducing and even if a melt had assimilated metasediments, trivalent iron would not have been available. Other than the Grizzly, feldspar from the other pegmatites in this study are, to some degree, a hue of red. The Groveland Mine is the most extreme, as feldspar from the Groveland is not only brick red, heavy mineral separations frequently contain quite a bit of magnetite. The broader implication being that there is a relative abundance of trivalent iron present in the Groveland Mine that likely came from assimilation of banded-iron formations.

Garnets from the Groveland can be used to further add to Bayley's hypothesis of contamination of the Peavy Pond Complex with Michigamme Formation. Garnets are frequently fractured and these fractures appear to have been subsequently infilled or recrystallization has occurred. Recrystallization is favored as the 'infilling' does not extend outside of garnet grain boundaries. Analyses show an original garnet chemistry with a higher spessartine component than secondary chemistry, which has a lower spessartine component and higher almandine component. This is unusual in that garnets preferentially incorporate Mn over Fe (London, 2008). If these garnets are in fact relic grains from the MRSG and exposed to an acidic melt such as one produced when the PPC assimilated MF, then perhaps these grains have been chemically attacked. Given the abundance of Fe available from assimilation of sedimentary packages, recrystallization of garnet in fractures could have involved more Fe. Especially if Mn had been sequestered into other mineral phases.

With coexisting ilmenite and magnetite present in metamorphic and igneous rocks for example, Mn is preferentially incorporated into ilmenite (Deer *et al*., 1962; 1992). Magnetite is locally abundant at the Groveland Mine pegmatite and only pyrophanite, not ilmenite, has been found in heavy mineral separations from this study and others (Buchholz *et al*., 2014). Also, tantalites are relatively enriched in Mn. If Mn was liberated from relict garnets in MRSG packages, there could have been a combination of competition for Mn as well as the relative enrichment of Fe over Mn when the PPC incorporated MRSG and banded-iron formations. Hwy69 and Sturgeon River also display a similar trend with garnets; however, these two pegmatites lack the Mn enrichment present at the Groveland.

A very tenuous suggestion about the presence of gahnite specifically, is that sulfide deposits in the area might be related to zinc enrichment in the melt (suitable enough to produce at least trace quantities of gahnite). If sphalerite were present in the MF and was subsequently assimilated, the likelihood of sulfur being lost to a gaseous phase (Martin & DeVito, 2005), could have possibly provided the zinc necessary to form gahnite. Another explanation is that trace quantities of zinc can be sequestered in biotites and with assimilation of MF, zinc could have been liberated into the melt. It is prudent though, after all this speculation, to mention even with the additional mineralogy of the Groveland Mine, that beryl from the Groveland Mine is poorly evolved (Figure 169), typical of NYF-type pegmatites. Gahnite, though rare, likewise is poorly evolved and well within range of NYF-type pegmatites (Heimann, 2010). It has more to do with the beryl-phosphate-columbite assemblage that complicates the categorization of the Groveland Mine as either LCT- or NYF-type. It should also be mentioned that associated lithium and cesium enrichment and mineralogy, typical of peraluminous LCT-type pegmatites, is absent.

A final word about the Groveland. Based on previous studies, intrusion of the PPC preceded peak regional metamorphism (Bayley, 1959). James (1955) had determined that peak deformation preceded peak metamorphism during the Penokean Orogeny as the PPC lacks signs of deformation, as opposed to the surrounding country rock. Muscovite mica books present at the Groveland Mine pegmatite are kinked (Figure 144). Buchholz *et al*., (2014) has also commented on the presence of "kinked" muscovite mica. This suggests that deformation of the pegmatite occurred after its formation and that there has been some overlap of peak deformation and peak metamorphism as originally hypothesized by Bayley (1959).

Given the mineralogical and geochemical signatures of the Bell Creek, it is possible to suggest that the Grizzly pegmatite has been produced during the Archean phase of anatexis and that the Grizzly has fractionated from a parental melt with a post-collisional, VAG/syn-COLG signature. Given the similarities the Republic Mine shares with the Bell Creek and Grizzly, it is suggested that the Republic Mine pegmatite has been produced during the Paleoproterozoic phase of anatexis and is a result of partial melting of remnant felsic components and/or granitic basement initially established in the Archean during gneiss dome formation. It is further suggested that the Republic Mine has been influenced by contamination, which accounts for the additional mineralogy not seen in either the Bell Creek granite or Grizzly pegmatite.

Given the geochemistry that the Crockley granitic sample shares with the Humboldt and Bell Creek samples, it is suggested that the Crockley is a hybrid pegmatite and is a result of contamination of an anorogenic melt with Bell Creek gneiss/granite during Penokean post-orogenic collapse. It should be pointed out that the Humboldt granite sample also appears to be a hybrid, although it is quite possible that there are Humboldt granitic bodies that do not exhibit this hybrid signature. Buchholz *et al*. (2014) has suggested that the Black River pegmatite is also

genetically related to the Humboldt granite; however, future study should include bulk compositional analysis of wall zone material from this pegmatite to determine any geochemical similarity it might have with Bell Creek and/or Humboldt as seen in the Crockley.

There is a similar quandary in classification of the other pegmatites. Biotite micas plot in the peraluminous field of Abdel-Rahman's discrimination diagram and orogenic fields in the tectonic discrimination diagrams of Webber *et al*. (2000) yet each have mineralogy and geochemistry closely associated with NYF-type pegmatites, or at the very least, these pegmatites lack mineralogy and characteristic enrichment typically associated with LCT-type pegmatites. Orogenic and peraluminous signatures could very well have been imparted from an anatectic melt produced from Bell Creek gneiss/granite during the Paleoproterozoic and seeing as the Bell Creel granite and Grizzly pegmatite lack characteristic enrichment in Li, Ce, and Ta, any pegmatite that has been contaminated with anorogenic melts or MRSG, would likely readily exhibit the geochemical characteristics from the contamination source. It should also be pointed out that biotite mica from the Grizzly pegmatite appears to be evolving toward an anorogenic signature, which might explain why these pegmatites are exhibiting a more NYF-type character. The Groveland Mine pegmatite especially deserves further study as it is the most geochemically and mineralogically diverse pegmatite with regards to the other pegmatites in this study.

Granitic material or wall rock samples should be analyzed to determine if any hybrid geochemical signatures exist as those seen in Crockley and Humboldt samples. Also, more work should be conducted in order to determine to what degree (if any) metamorphic isograds influence the evolution of the pegmatites as the Dolfin is located in the sillimanite isograd of the Republic node. Zircons from the Dolfin pegmatite are relatively more evolved than any other sampled location. Xenotimes from the Dolfin also have a chondrite-normalized enrichment

trend that is quite different than those from the Groveland. Dolfin xenotimes are also relatively more enriched in Y than GMP xenotimes. However, Dolfin pegmatites are similarly enriched in Mn as garnets from other sampled locations, with the exception of the Republic Mine, which are relatively more enriched in Mn.

The Dolfin, Hwy69, and Sturgeon River pegmatites should be classified as Rare Element, REE, NYF-type. There is an overall lack of geochemical and mineralogical association with LCT-type, with the exception of the Black River pegmatite, which has some slight tantalum enrichment expressed in the rare presence of ferrotantalites.

## STANDARDS

## APATITE

Standards for EMP analyses of garnet

| | |
|---|---|
| Acceleration potential: | 15 kV |
| Beam current: | 15 nA |
| Beam width: | 2 microns |
| Count time: | 45 seconds per spot |

| | | |
|---|---|---|
| Clinopyroxene | "Cpx-26" | (Si,Al,Mg,Fe) |
| Fluorapatite | Cerro de Mercado | (F,Ca,P) |
| Lithiophilite | Emmons, ME | (Mn) |

Other MAN standards used in addition to main standards when applicable

| | |
|---|---|
| $Al_2O_3$ | synthetic |
| Hematite | Elba |
| MgO | synthetic |
| PbO | synthetic |
| $V_2O_5$ | synthetic |
| ZnO | synthetic |
| $ZrO_2$ | synthetic |

## COLUMBITE/TANTALITE

Standards for EMP analyses of garnet

| | |
|---|---|
| Acceleration potential: | 20 kV |
| Beam current: | 22 nA |
| Beam width: | 2 microns |
| Count time: | 45 seconds per spot |

| | | |
|---|---|---|
| Bismuto-tantalite | | (Bi) |
| Cassiterite | | (Sn) |
| $CaWO_4$ | synthetic | (W) |
| Clinopyroxene | "Cpx-26" | (Mg,Si,Ca) |
| Corundum | synthetic | (Al) |
| Hematite | Elba | (Fe) |
| Manganotantalite | Himalaya Pegmatite, CA | (Mn,Ta) |
| Microlite | Harding Pegmatite, NM | (Na,Ca,Ta) |
| Samarskite | Afghan | (U) |
| $TiO_2$ | synthetic | (Ti) |
| $YNbO_4$ | synthetic | (Nb) |

Other MAN standards used in addition to main standards when applicable

| | |
|---|---|
| $Al_2O_3$ | synthetic |
| Hematite | Elba |
| MgO | synthetic |
| PbO | synthetic |
| $V_2O_5$ | synthetic |
| ZnO | synthetic |
| $ZrO_2$ | synthetic |

## GARNET

Standards for EMP analyses of garnet

| | |
|---|---|
| Acceleration potential: | 15 kV |
| Beam current: | 15 nA |
| Beam width: | 2 microns |
| Count time: | 45 seconds per spot |

| | | |
|---|---|---|
| Andalusite | Minas Gerais | (Al,Si) |
| Clinopyroxene | "Cpx-26" | (Mg,Si,Ca) |
| Fayalite | | (Fe) |
| Spessartine | | (Mn) |

Other MAN standards used in addition to main standards when applicable

| | |
|---|---|
| $Al_2O_3$ | synthetic |
| Hematite | Elba |
| MgO | synthetic |
| PbO | synthetic |
| $V_2O_5$ | synthetic |
| ZnO | synthetic |
| $ZrO_2$ | synthetic |

## ILMENITE/PYROPHANITE

Standards for EMP analyses of ilmenite-pyrophanite

| | |
|---|---|
| Acceleration potential: | 20 kV |
| Beam current: | 20 nA |
| Beam width: | 2 microns |
| Count time: | 45 seconds per spot |

| | | |
|---|---|---|
| Clinopyroxene | "Cpx-26" | (Mg,Si,Al,Ca) |
| Hematite | Elba | (Fe) |
| Manganotantalite | RGN Brazil | (Mn,Ta) |
| $TiO_2$ | synthetic | (Ti) |
| $YNbO_4$ | synthetic | (Nb) |

Other MAN standards used in addition to main standards when applicable

| | |
|---|---|
| $Al_2O_3$ | synthetic |
| MgO | synthetic |
| PbO | synthetic |
| $V_2O_5$ | synthetic |
| ZnO | synthetic |
| $ZrO_2$ | synthetic |

## K-FELDSPAR

Standards for EMP analyses of K-feldspar

| | |
|---|---|
| Acceleration potential: | 15 kV |
| Beam current: | 15 nA |
| Beam width: | 2 microns |
| Count time: | 45 seconds per spot |

| | | |
|---|---|---|
| Adularia | Fibbia | (K,Si) |
| Albite | Tiburon | (Si,Al,Na) |
| $An_{50}$ | Nine, Canada | (Ca,Al) |
| $BaSO_4$ | synthetic | (Ba) |
| Clinopyroxene | "Cpx-26" | (Fe,Mg) |
| Fluorapatite | Cerro de Mercado | (P) |
| Pollucite | Tanco | (Cs) |
| Rhodonite | Broken Hill | (Mn) |
| $RbAlSi_2O_6$ | synthetic | (Rb) |
| $SrSO_4$ | synthetic | (Sr) |
| $TiO_2$ | synthetic | (Ti) |

Other MAN standards used in addition to main standards when applicable

| | |
|---|---|
| $Al_2O_3$ | synthetic |
| Hematite | Elba |
| MgO | synthetic |
| PbO | synthetic |
| $V_2O_5$ | synthetic |
| ZnO | synthetic |
| $ZrO_2$ | synthetic |

## MICA

Standards for EMP analyses of K-feldspar

| | |
|---|---|
| Acceleration potential: | 15 kV |
| Beam current: | 15 nA |
| Beam width: | 2 microns |
| Count time: | 45 seconds per spot |

| | | |
|---|---|---|
| Adularia | Fibbia | (K,Si) |
| Albite | Tiburon | (Si,Al,Na) |
| $An_{50}$ | Nine, Canada | (Ca,Al) |
| $BaSO_4$ | synthetic | (Ba) |
| Clinopyroxene | "Cpx-26" | (Fe,Mg) |
| Fluorapatite | Cerro de Mercado | (P) |
| Fluorphlogopite | synthetic | (F) |
| Pollucite | Tanco | (Cs) |
| $RbAlSi_2O_6$ | synthetic | (Rb) |
| Rhodonite | Broken Hill | (Mn) |
| $TiO_2$ | synthetic | (Ti) |

Other MAN standards used in addition to main standards when applicable

| | |
|---|---|
| $Al_2O_3$ | synthetic |
| Hematite | Elba |
| MgO | synthetic |
| PbO | synthetic |
| $V_2O_5$ | synthetic |
| ZnO | synthetic |
| $ZrO_2$ | synthetic |

## TITANITE

Standards for EMP analyses of titanite

| | |
|---|---|
| Acceleration potential: | 15 kV |
| Beam current: | 15 nA |
| Beam width: | 2 microns |
| Count time: | 45 seconds per spot |

| | | |
|---|---|---|
| Clinopyroxene | "Cpx-26" | (Fe,Mg,Si,Al,Ca) |
| Manganotantalite | RGN Brazil | (Mn,Ta) |
| $TiO_2$ | synthetic | (Ti) |
| Fluorphlogopite | synthetic | (F) |
| $YNbO_4$ | synthetic | (Nb) |

Other MAN standards used in addition to main standards when applicable

| | |
|---|---|
| $Al_2O_3$ | synthetic |
| Hematite | Elba |
| MgO | synthetic |
| PbO | synthetic |
| $V_2O_5$ | synthetic |
| ZnO | synthetic |
| $ZrO_2$ | synthetic |

## TOURMALINE

Standards for EMP analyses of tourmaline

| | |
|---|---|
| Acceleration potential: | 15 kV |
| Beam current: | 15 nA |
| Beam width: | 2 microns |
| Count time: | 45 seconds per spot |

| | | |
|---|---|---|
| Adularia | Fibbia | (K) |
| Albite | Tiburon | (Na) |
| Andalusite | Minas Gerais | (Al,Si) |
| $Bi_4Ge_30_{12}$ | synthetic | (Bi) |
| Chromite | Stillwater MT | (Cr) |
| Clinopyroxene | "Cpx-26" | (Fe,Mg,Ca,Ti) |
| Fluortopaz | Thomas Range, UT | (F) |
| PbO | synthetic | (Pb) |
| Rhodonite | Broken Hill | (Mn) |
| $TiO_2$ | synthetic | (Ti) |
| $V_2O_5$ | synthetic | (V) |
| ZnO | synthetic | (Zn) |

Other MAN standards used in addition to main standards when applicable

| | |
|---|---|
| $Al_2O_3$ | synthetic |
| Fayalite | |
| Hematite | Elba |
| MgO | synthetic |
| $SrSO_4$ | synthetic |
| $TiO_2$ | synthetic |
| $ZrO_2$ | synthetic |

# ZIRCON

Standards for EMP analyses of zircon

| | |
|---|---|
| Acceleration potential: | 20 kV |
| Beam current: | 20 nA |
| Beam width: | 2 microns |
| Count time: | 45 seconds per spot |

| | | |
|---|---|---|
| Andaluria | Fibbia | (K) |
| $CaWO_4$ | synthetic | (W) |
| Clinopyroxene | "Cpx-26" | (Fe,Mg,Si,Al,Ca) |
| Fluorapatite | Cerro de Mercado | (P) |
| $HfO_2$ | synthetic | (Hf) |
| Manganotantalite | RGN Brazil | (Mn,Ta) |
| $ThO_2$ | synthetic | (Th) |
| $TiO_2$ | synthetic | (Ti) |
| $UO_2$ | synthetic | (U) |
| $YNbO_4$ | synthetic | (Nb) |
| $ZrO_2$ | synthetic | (Zr) |

Other MAN standards used in addition to main standards when applicable

| | |
|---|---|
| $Al_2O_3$ | synthetic |
| Hematite | Elba |
| MgO | synthetic |
| PbO | synthetic |
| $V_2O_5$ | synthetic |
| ZnO | synthetic |
| $ZrO_2$ | synthetic |

## WHOLE ROCK

Standards for DCP analyses

DCP analyses were performed by Maine Mineral & Gem Museum

Li 0.1 ppm standard = 0.096 ppm
$\lambda$ = 670.784 nm
calibration range = 0.02 to 10 mg/l
count time = 20 seconds

## REFERENCES


AMATO, J.M., WRIGHT, J.E., GANS, P.B., & MILLER, E.L. (1994): Magmatically induced metamorphism and deformation in the Kigluaik gneiss dome, Seward Peninsula, Alaska. Tectonics, **13**, 515-527.

ATENCIO, D., ANDRADE M.B., CHRISTY, A.G., GIERÉ, R, & KARTASHOV, P.M. (2010): The Pyrochlore Supergroup of Minerals: Nomenclature. The Canadian Mineralogist, **48**, 673-698.

ATTOH, K. (2000): Contrasting metamorphic record of heat production anomalies in the Penokean Orogen of northern Michigan. Journal of Geology, **108**, 353-361.

ATTOH, K. & KLASNER, J.S. (1989): Tectonic implications of metamorphism and gravity field in the Penokean orogen of northern Michigan. American Geophysical Union. Tectonics, **8**, no. 4, 911-933.

BAYLEY, R.W. (1959): Geology of the Lake Mary quadrangle, Iron County, Michigan. U.S. Geological Survey Bulletin, **1077**, 112 p.

BAROVICH, K.M., PATCHETT, P.J., PETERMAN, Z.E., & SIMS, P.K. (1989): Nd isotopes and the origin of 1.9-1.7 Ga Penokean continental crust of the Lake Superior region. Geological Society of America Bulletin, **101**, 333-338.

BECK, J.W. & MURTHY, V.R. (1982): Rb-Sr and Sm-Nd studies of Proterozoic mafic dikes in northeastern Minnesota [abs]: 28th Annual Institute on Lake Superior Geology, International Falls, Minnesota. Proceedings, 5 p.

BECK, J.W. & MURTHY, V.R. (1991): Evidence for continental crustal assimilation in the Hemlock Formation flood basalts of the Early Proterozoic Penokean orogen, Lake Superior region. U.S. Geological Survey Bulletin, **1904-I**, 25 p.

BROWN, C. (1999): Mineralogy of NYF granitic pegmatites. Canadian Mineralogist, **37**, 848-849 (abstract).

BUCHHOLZ, T.W., FALSTER, A.U., & SIMMONS, W.B. (2014): Accessory mineralogy of an evolved Dickinson County, Michigan pegmatite. 41st Rochester Mineralogical Symposium: Contributed Papers in Specimen Mineralogy, 11-12.

BUCHHOLZ, T.W., FALSTER, A.U., & SIMMONS, W.B. (2014): Accessory mineralogy of the Black River pegmatite and Humboldt granite, Marquette County, Michigan. Fortieth Rochester Mineralogical Symposium: Contributed Papers in Specimen Mineralogy – Part 1, Rocks & Minerals **89:4**, 371-372.

CAMBRAY, F.W. (1984): Proterozoic geology, Lake Superior, south shore. Geological Association of Canada Annual Meeting Field Trip Guidebook, 55 p.

CANNON, W.F. (1973): The Penokean orogeny in northern Michigan, in Young, G.M., ed., Huronian stratigraphy and sedimentation. Geological Association of Canada Special Paper, **12**, 251-271.

CANNON, W.F. (1986): Bedrock geologic map of the Iron River 1ºX2º quadrangle, Michigan and Wisconsin. U.S. Geological Survey Miscellaneous Investigations Series Map I-1360-b, scale 1:250,000.

ČERNÝ, P. (1991a): Rare-element granite pegmatites. I. Anatomy and internal evolution of pegmatite deposits. Geoscience Canada, **18**, 49-67.

ČERNÝ, P. (1992): Geochemical and petrogenetic features of mineralization in rare-element granitic pegmatites in the light of current research. Applied Geochemistry, **7**, 393-416.

ČERNÝ, P. & ERCIT, T.S. (1986): Mineralogy of niobium and tantalum: Crystal chemical relationships, paragenetic aspects and their economic implications, 27-79. In P. Moller *et al*., Eds. Lanthanides, Tantalum, and Niobium. Special Publication of the Society for Geology Applied to Mineral Deposits. Springer Verlag, New York, 380 p.

ČERNÝ, P. & ERCIT, T.S. (2005): The classification of granitic pegmatites revisited. The Canadian Mineralogist **43**, 2005-2026.

DEER, W., HOWIE. R., & ZUSSMAN, J. (1962, 1992): An introduction to the rock-forming minerals. Longmans, Green, & Co. Ltd., London, 2nd ed.

DEMARTIN, F., PILATI, T., DIELLA, V., DONZELLI, S., GENTILE, P., & GRAMACCIOLI, C.M. (1991): The chemical composition of xenotime from fissure and pegmatites in the Alps. Canadian Mineralogist, **29**, 69-75.

EDWARDS, M.A., KIDD, W.S.F., & SCHNEIDER, D.A. (2002): A guide to dome improvement, Lesson 1: Is your dome built on granite or gneiss?. Geological Society of America Abstracts with Programs, **34**, no.6, 109.

ESKOLA, P.E. (1949): The problem of mantled gneiss domes: Quarterly Journal of the Geological Society of London, **104**, 461-476.

FOX, T.P. (1983): Geochemistry of the Hemlock Metabasalt and Kiernan sills, Iron County, Michigan [Unpublished M.S. thesis]. East Lansing, Michigan, Michigan State University, 81 p.

GREGG, W.J. (1993): Structural geology of parautochthonous and allocthonous terranes of the Penokean Orogeny of Upper Michigan–Comparisons with Northern Appalachians tectonics. U.S. Geological Survey Bulletin, **1904-Q**, Q1-Q28.

GREGG, W.J. & SAJA, D.B. (1998): Field evidence for orogenic collapse, examples from the Penokean orogeny in Upper Michigan [abs]: Geological Society of America Abstracts with Programs, **30**, A-95.

HOFFMAN, M.A. (1987): The Southern Complex: Geology, geochemistry, mineralogy, and mineral chemistry of selected uranium- and thorium-rich granites. Michigan Technological University.

HOLDAWAY, M.J. (1971): Stability of andalucite and the alumino-silicate phase diagram. American Journal of Science, **271**, 97-131.

HOLM, D.K. & LUX, D.R. (1996): Core complex model proposed for gneiss dome development during collapse of the Paleoproterozoic Penokean orogen, Minnesota. Geology, **35**, 1143-1151.

HOLM, D.K., DARRAH, K.S. & LUX, D.R. (1998): Evidence for widespread ~1760 Ma metamorphism and rapid crustal stabilization of the Early Proterozoic (1870-1820 Ma) Penokean Orogen, Minnesota. American Journal of Science, **298**, 60-81.

HOLM, D.K., SCHNEIDER, D.A., & COATH, C. (1998b): Age and deformation of Early Proterozoic quartzites in the southern Lake Superior region: Implications for extent of foreland deformation during final assembly of Laurentia. Geology, **26**, 907-910.

HOLM, D.K., VAN SCHMUS, W.R., & MACNEILL, L.C. (2001): Age of the Humboldt Granite, northern Michigan; implications for the origin of the Republic metamorphic node, in Mudrey, M.G., Jr., ed., 47th Annual Meeting, Institute on Lake Superior Geology, Proceedings, Program, and Abstracts: Institute on Lake Superior Geology, **47**, 31-32.

HOLM, D.K., VAN SCHMUS, W.R., MACNEILL, L.C., BOERHOOM, T.J., SCHWEITZER, D., SCHNEIDER, D. (2005): U-Pb zircon geochronology of Paleoproterozoic plutons from the northern midcontinent, USA: Evidence for subduction flip and continued convergence after geon 18 Penokean orogenesis. GSA Bulletin, **117**, no. 3/4, 259-275.

JAMES, H.L. (1955): Zones of regional metamorphism in the Precambrian of northern Michigan. Geological Society of America Bulletin, **66**, 1455-1487.

LARUE, D.K. (1983): Early Proterozoic tectonics of the Lake Superior region: Tectonostratigraphic terranes near the purported collision zone. Geological Society of America, Memoir **160**, 33-47.

LARUE, D.K. & SLOSS, L.L. (1980): Early Proterozoic sedimentary basins of the Lake Superior region–Summary. Geological Society of America Bulletin, **91**, 450-452.

LINTHOUT, K. (2007): Tripartite division of the system $2REEPO_4 – CaTh(PO_4)_2 – 2ThSiO_4$, discreditation of brabantite, and recognition of cheralite as the name for members dominated by $CaTh(PO_4)_2$. The Canadian Mineralogist, **45**, 503-508.

MAASS, R.S., MEDARIS, L.G., JR., & VAN SCHMUS, W.R. (1980): Penokean deformation in central Wisconsin. Geological Society of America Special Paper, **182**, 147-157.

MARSHAK, S. (1999): Deformation style way back when: Thoughts on the contrasts between Archean/Paleoproterozoic and contemporary orogens. Journal of Structural Geology, **21**, 1175-1182.

MARSHAK, S., ALKMIM, F.F., JORDT-EVANGELISTA, H. (1992): Proterozoic crustal extension and the generation of dome-and-keel structure in an Archaean granite-greenstone terrane. Nature, **357**, 491-493.

MARSHAK, S., TINKHAM, D.K., ALKMIM, F.F., BRUECKNER, H., & BORNHORST, T. (1997): Dome and keel provinces formed during the Paleoproterozoic orogenic collapse – core complexes, diapirs, or neither?: Examples from the Quadrilateral Ferrifero and the Penokean orogen. Geology, **25**, 415-418.

MARTIN, R.F. & DE VITO, C. (2005): The Patterns of Enrichment in Felsic Pegmatites Ultimately Depend on Tectonic Setting. The Canadian Mineralogist, **43**, 2027-2048.

MASAU, M. (2003): Mineralogy and geochemistry of the searchlight granite-pegmatite-aplite district, Clark County, Nevada. University of New Orleans.

MCKENZIE, D.P. (1978): Some remarks on the development of sedimentary basins. Earth and Planetary Science Letters, **40**, 25-32.

MOREY, G.B. (1993): Continental margin assemblage. Archean and Proterozoic geology, Lake Superior region, 1993. U.S. Geological Society Professional Paper, **1556**, 30-44.

RAPP, R.P & WATSON, B. (1986): Monazite solubility and dissolution kinetics: implications for the thorium and light rare earth chemistry of felsic magmas. Contributions to Mineralogy and Petrology, **94**, 304-316.

RILLER, U., SCHWERDTNER, W.M., HALLS, H.C., & CARD, K.D. (1999): Transpressive tectonism in the eastern Penokean orogen, Canada Consequences for Proterozoic crustal kinematics and continental fragmentation. Precambrian Research, **93**, 51-71.

ROSE, S., SCHNEIDER, D.A., LOOFBORO, J., & HOLM, D.K. (2003): Results and implications of monazite geochronology from the central Penokean orogen, WI & MI [abs]: Geological Society of America Abstracts with Programs, **35**, no.6, 206-208.

SCHNEIDER, D.A., HOLM, D.K., & LUX, D.R. (1996): On the origin of Early Proterozoic gneiss domes and metamorphic nodes, northern Michigan. Canadian Journal of Earth Sciences, **33**, 1053-1063.

SCHNEIDER, D.A., BICKFORD, M.E., CANNON, W.F., SCHULZ, K.J., & HAMILTON, M.A. (2002): Timing of Marquette Range Supergroup deposition and Penokean collision-related basin formation, southern Lake Superior region: implications for Paleoproterozoic tectonic reconstruction. Canadian Journal of Earth Science, **39**, 999-1012.

SCHNEIDER, D.A, HOLM, D.K., O'BOYLE, C., HAMILTON, M., JERCINOVIC, M. (2004): Paleo Proterozoic development of gneiss dome corridor in the southern Lake Superior region, USA. In: Whitney, D.L., Teyssier, C., Siddoway, C.S. eds., Gneiss Domes in Orogeny. Geological Society of America, Special Paper, **380**, 339-357.

SCHMITZ, M.D., BOWRING, S.A., SOUTHWICK, D.L., BOERBOOM, T.J., WIRTH, K.R. (2006): High-precision U-Pb geochronology in the Minnesota River Valley sub-province and its bearing on the Neoarchean to Paleoproterozoic evolution of the southern Superior Province. Geological Society of America Bulletin, **118**, 82-93.

SCHULZ, K.J. (1984): Early Proterozoic Penokean igneous rocks of the Lake Superior region– Geochemistry and tectonic implications. 30th Annual Institute on Lake Superior Geology, Wausau, Wisconsin, Abstracts, 65-66.

SIMS, P.K. (1980): Boundary between Archean greenstone and gneiss terranes in northern Wisconsin and Michigan. Geological Society of America Special Paper, **182**, 113-124.

SIMS, P.K. (1992): Geologic map of Precambrian rocks, southern Lake Superior region, Wisconsin and northern Michigan. U.S. Geological Survey Miscellaneous Investigations Series Map MI-2185, scale 1:500,000, 1 sheet.

SIMS, P.K. (1993): Great Lakes Tectonic Zone. Archean and Proterozoic geology, Lake Superior region, 1993. U.S. Geological Society Professional Paper, **1556**, 24-28.

SIMS, P.K. (1993): Minnesota River Valley Subprovince (Archean Gneiss Terrane). Archean and Proterozoic geology, Lake Superior region, 1993. U.S. Geological Society Professional Paper, **1556**, 14-23.

SIMS, P.K. (1993): Structure of continental margin. Archean and Proterozoic geology, Lake Superior region, 1993. U.S. Geological Society Professional Paper, **1556**, 44-51.
SIMS, P.K. (1996): Regional tectonic elements, in Sims, P.K. & Carter, L.M.H., eds., Archean and Proterozoic geology of the Lake Superior region, U.S.A., 1993. U.S. Geological Survey Professional Paper, Reston, Virginia, U.S. Geological Survey, 95-99.
SIMS, P.K. & DAY, W.C. (1993): The Great Lakes Tectonic Zone–Revisited. US Geological Society Bulletin. **91**, 11.
SIMS, P.K. & MOREY, G.B. (1993): Penokean orogen and related epicrationic rocks. In: Reed Jr., J.C., Bickford, M.E., Houston, R.S., Link, P.K., Rankin, D.W., Sims, P.K., Van Schmus, W.R. (Eds.), Precambrian : Conterminous U.S., Boulder Colorado, Geological Society of America, The Geology of North America, **C-2**, 45-56.
SIMS, P.K. & PETERMAN, Z.E. (1983) Evolution of Penokean foldbelt, Lake Superior region, and its tectonic environment. Geological Society of America Memoir **160**, 3-14.
SIMS, P.K. & PETERMAN, Z.E. (1984): A partisan view of the Early Proterozoic geology of Wisconsin and adjacent Michigan. 30th Annual Institute on Lake Superior Geology, Wausau, Wisconsin. Abstracts. 73-76.
SNELGROVE, A. K., SEAMAN, W. A., & AYRES,V. L. (1943): Strategic Minerals Investigations in Marquette and Baraga Counties.
TEYSSIER, C. & WHITNEY, D.L. (2002): Gneiss domes and orogeny: Geology, **21**, no.4, 1028.
TINKHAM, D.K. & MARSHAK, S. (2004): Precambrian dome-and-keel structure in the Penokean orogenic belt of northern Michigan, USA. Geological Society of America, Special Paper **380**, 321-338.
TOHVER, E., HOLM, D.K., VAN DER PLUIJM, B.A., ESSENE, E.J., & CAMBRAY, F.W. (2007): Late Paleozoic (geon 18 and 17) reactivation of the Neoarchean Great Lakes Tectonic Zone, northern Michigan, USA: Evidence from kinematic analysis, thermobarometry and $^{40}Ar/^{39}Ar$ geochronology. Precambrian Research **157**, 144-168.
UENG, W.C. & LARUE, D.K. (1998): The early Proterozoic structural and tectonic history of the South Central Lake Superior Region. Tectonics, **7**, no. 3, 369-388.
UENG, W.C., FOX, T.P., LARUE, D.K., & WILBAND, J.T. (1988): Geochemistry and petrogenesis of the Early Proterozoic Hemlock volcanic rocks and the Kiernan sills, southern Lake Superior region. Canadian Journal of Earth Sciences, **25**, 528-546.
WHITNEY, D.L., TEYSSIER, C., & VANDERHAEGHE, O. (2004): Gneiss domes and crustal flow: Gneiss Dome in Orogeny. Geological Society of America, Special Paper, **380**, 15-26.
WRIGHT, T.L. (1968): X-ray and optical study of alkali feldspar: II. An X-ray method for determining the composition and structural state from measurement of 2θ values for three reflections. The American Mineralogist, **53**, 88-104.
VAN SCHMUS, W.R. (1976): Early and Middle Proterozoic history of the Great Lakes area, North America. Royal Society of London Philosophical Transactions, **280**, Series A, 605-628.
VAN SCHMUS W.R. (1980): Chronology of igneous rocks associated with the Penokean Orogeny in Wisconsin. Geological Society of America, Special Paper **182**, 159-168.
YIN, A. (2004): Gneiss domes and gneiss dome systems. Gneiss Domes in Orogeny: Geological Society of America, Special Paper, **380**, 1-14.
YOUNG, G.M. (1983): Tectono-sedimentary history of early Proterozoic rocks of the northern Great Lakes region. Geological Society of America Memoir, **160**, 15-31.

# APPENDICES

## TITRATION RESULTS

| Redox AMV & Fe Titration | | | | | |
|---|---|---|---|---|---|
| Location | W: Biotite (mg) | AMV (mg) | y': FAmSO4 (mL) | x | z |
| Blank 1 | | 101.600 | 23.200 | 22.835 | 2.656 |
| Blank 2 | | 109.700 | 25.100 | 22.881 | |
| | | | Average | 22.858 | |
| | | | | | |
| | | | | x' | wt% FeO |
| Sr-uncl | 110.500 | 102.600 | 12.200 | 23.452 | 27.045 |
| Sr-BS | 111.200 | 112.400 | 19.120 | 25.692 | 15.697 |
| GrP-3 | 111.700 | 102.600 | 13.100 | 23.452 | 24.615 |
| GMP loose | 117.300 | 109.800 | 12.750 | 25.098 | 27.959 |
| DP | 113.400 | 108.000 | 14.200 | 24.686 | 24.560 |
| RM-rr | 115.700 | 105.500 | 22.360 | 24.115 | 4.028 |
| BRP | 110.400 | 113.800 | 24.210 | 26.012 | 4.335 |
| | | | | | |
| | | wt % FeO = [100(x'-y')z]/w | | | |
| | | | | | |

Table 84 Fe Titration results for all mica samples. Sturgeon River, Grizzly, Groveland Mine, and Dolfin results are from biotite micas. Muscovite mica from Republic Mine and Black River was used, which explains the lower FeO wt%.

## ADDITIONAL ANALYSES

### DOLFIN PEGMATITE

| **K-FELDSPAR - DOLFIN PEGMATITE** | | | | | |
|---|---|---|---|---|---|
| Wt% ox | DP8 grain 1-1 | DP8 loose grain 1-1 | DP8 loose grain 1-2 | DP8 loose grain 3-1 | DP 8 loose grain 3-2 |
| $P_2O_5$ | 0.000 | 0.000 | 0.000 | 0.000 | 0.000 |
| $SiO_2$ | 68.622 | 64.809 | 64.688 | 64.800 | 68.811 |
| $TiO_2$ | 0.000 | 0.014 | 0.009 | 0.011 | 0.000 |
| $Al_2O_3$ | 19.722 | 18.455 | 18.400 | 18.454 | 19.393 |
| $FeO_t$ | 0.000 | 0.010 | 0.011 | 0.013 | 0.000 |
| CaO | 0.453 | 0.000 | 0.000 | 0.000 | 0.178 |
| $Na_2O$ | 10.643 | 0.455 | 0.411 | 0.255 | 10.911 |
| $K_2O$ | 0.211 | 15.823 | 15.877 | 15.900 | 0.211 |
| Rb2O | 0.000 | 0.013 | 0.013 | 0.009 | 0.000 |
| **Total** | 99.662 | 99.579 | 99.409 | 99.442 | 99.504 |
| *apfu* | | | | | |
| K | 0.012 | 0.934 | 0.940 | 0.940 | 0.012 |
| Na | 0.902 | 0.041 | 0.037 | 0.023 | 0.926 |
| Ca | 0.021 | 0.000 | 0.000 | 0.000 | 0.008 |
| Rb | 0.000 | 0.000 | 0.000 | 0.000 | 0.000 |
| **Σ X-site** | 0.935 | 0.976 | 0.977 | 0.963 | 0.946 |
| Al | 1.016 | 1.007 | 1.006 | 1.008 | 1.000 |
| Fe | 0.000 | 0.000 | 0.000 | 0.000 | 0.000 |
| **Σ Y-site** | 1.016 | 1.007 | 1.006 | 1.008 | 1.000 |
| Si | 2.999 | 3.000 | 3.001 | 3.003 | 3.011 |
| Ti | 0.001 | 0.000 | 0.000 | 0.000 | 0.000 |
| P | 0.000 | 0.000 | 0.000 | 0.000 | 0.000 |
| Al | 0.000 | 0.000 | 0.000 | 0.000 | 0.000 |
| **Σ Z-site** | 2.999 | 3.001 | 3.001 | 3.003 | 3.011 |

Table 85 Additional feldspar analyses from Dolfin pegmatite samples. *Apfu* calculations based on 8 oxygens.

| GARNETS – DOLFIN PEGMATITE | | | | | | | | | | |
|---|---|---|---|---|---|---|---|---|---|---|
| Wt % Ox | garnets-10-1 | garnets-10-2 | garnets-12-1 | garnets-12-2 | garnets-13-1 | garnets-13-2 | garnets-16-1 | garnets-16-2 | garnets-18-1 | garnets-18-2 |
| $SiO_2$ | 36.500 | 36.441 | 36.504 | 36.459 | 36.388 | 36.466 | 36.488 | 36.508 | 36.449 | 36.487 |
| $TiO_2$ | 0.015 | 0.009 | 0.022 | 0.017 | 0.013 | 0.012 | 0.010 | 0.009 | 0.011 | 0.012 |
| $Al_2O_3$ | 20.512 | 20.452 | 20.511 | 20.566 | 20.533 | 20.600 | 20.566 | 20.622 | 20.522 | 20.478 |
| FeO | 34.003 | 34.223 | 34.300 | 34.287 | 34.500 | 34.398 | 34.555 | 34.600 | 34.700 | 34.844 |
| MnO | 7.322 | 7.143 | 7.322 | 7.687 | 7.299 | 7.400 | 7.177 | 7.211 | 7.155 | 7.088 |
| MgO | 0.082 | 0.093 | 0.086 | 0.077 | 0.067 | 0.060 | 0.073 | 0.080 | 0.098 | 0.093 |
| CaO | 0.872 | 0.871 | 0.955 | 0.876 | 0.855 | 0.766 | 0.677 | 0.722 | 0.800 | 0.793 |
| **Total** | 99.306 | 99.232 | 99.700 | 99.969 | 99.655 | 99.702 | 99.546 | 99.752 | 99.735 | 99.795 |
| *apfu* | | | | | | | | | | |
| Ti | 0.001 | 0.001 | 0.001 | 0.001 | 0.001 | 0.001 | 0.001 | 0.001 | 0.001 | 0.001 |
| Fe | 2.354 | 2.372 | 2.368 | 2.364 | 2.385 | 2.376 | 2.389 | 2.388 | 2.397 | 2.406 |
| Mn | 0.513 | 0.501 | 0.512 | 0.537 | 0.511 | 0.518 | 0.503 | 0.504 | 0.501 | 0.496 |
| Mg | 0.010 | 0.011 | 0.011 | 0.009 | 0.008 | 0.007 | 0.009 | 0.010 | 0.012 | 0.011 |
| Ca | 0.077 | 0.077 | 0.084 | 0.077 | 0.076 | 0.068 | 0.060 | 0.064 | 0.071 | 0.070 |
| **Σ X-site** | 2.973 | 2.977 | 2.985 | 2.993 | 2.989 | 2.982 | 2.977 | 2.980 | 2.988 | 2.989 |
| Al | 1.997 | 1.995 | 1.994 | 1.998 | 1.999 | 2.002 | 2.000 | 2.003 | 1.996 | 1.992 |
| **Σ Y-site** | 1.997 | 1.995 | 1.994 | 1.998 | 1.999 | 2.002 | 2.000 | 2.003 | 1.996 | 1.992 |
| Si | 3.015 | 3.015 | 3.011 | 3.005 | 3.006 | 3.007 | 3.011 | 3.008 | 3.008 | 3.011 |
| **Σ Z-site** | 3.015 | 3.015 | 3.011 | 3.005 | 3.006 | 3.007 | 3.011 | 3.008 | 3.008 | 3.011 |
| **Component** | | | | | | | | | | |
| Spessartine | 17 | 17 | 17 | 18 | 17 | 17 | 17 | 17 | 17 | 17 |
| Grossular | 03 | 03 | 03 | 03 | 03 | 03 | 02 | 02 | 03 | 03 |
| Almandine | 80 | 80 | 80 | 79 | 80 | 81 | 81 | 81 | 80 | 81 |

Table 86 additional garnet analyses from Dolfin pegmatite samples. *Apfu* calculations based on 12 oxygens.

| FELDSPAR - CROCKLEY PEGMATITE | | | | | | | | |
|---|---|---|---|---|---|---|---|---|
| Wt% ox | CP 6 grain 3-1 | CP 6 grain 3-2 | CP 6 grain 1-1 | CP 6 grain 1-2 | CP 6 grain 2-1 | CP 6 grain 2-2 | CP 6 grain 3-1 | CP 6 grain 3-2 |
| $P_2O_5$ | *bdl* | *bdl* | *bdl* | *bdl* | *bdl* | *bdl* | *bdl* | *bdl* |
| $SiO_2$ | 64.822 | 68.887 | 64.800 | 64.823 | 64.388 | 68.911 | 64.822 | 68.887 |
| $TiO_2$ | 0.011 | 0.000 | 0.015 | 0.009 | 0.008 | 0.000 | 0.011 | 0.000 |
| $Al_2O_3$ | 18.433 | 19.101 | 18.409 | 18.422 | 18.433 | 19.004 | 18.433 | 19.101 |
| $FeO_t$ | 0.009 | 0.000 | 0.013 | 0.009 | 0.009 | 0.000 | 0.009 | 0.000 |
| CaO | 0.000 | 0.199 | 0.000 | 0.000 | 0.000 | 0.188 | 0.000 | 0.199 |
| $Na_2O$ | 0.544 | 11.045 | 0.575 | 0.499 | 0.605 | 11.066 | 0.544 | 11.045 |
| $K_2O$ | 16.300 | 0.211 | 16.202 | 16.411 | 16.226 | 0.155 | 16.300 | 0.211 |
| Rb2O | 0.013 | 0.000 | 0.012 | 0.014 | 0.010 | 0.000 | 0.013 | 0.000 |
| **Total** | 100.132 | 99.452 | 100.026 | 100.187 | 99.679 | 99.334 | 100.132 | 99.452 |
| *apfu* | | | | | | | | |
| K | 0.961 | 0.012 | 0.955 | 0.967 | 0.961 | 0.009 | 0.961 | 0.012 |
| Na | 0.049 | 0.938 | 0.052 | 0.045 | 0.054 | 0.941 | 0.049 | 0.938 |
| Ca | 0.000 | 0.009 | 0.000 | 0.000 | 0.000 | 0.009 | 0.000 | 0.009 |
| Rb | 0.000 | 0.000 | 0.000 | 0.000 | 0.000 | 0.000 | 0.000 | 0.000 |
| **Σ X-site** | 1.010 | 0.960 | 1.007 | 1.012 | 1.015 | 0.959 | 1.010 | 0.960 |
| Al | 1.004 | 0.986 | 1.003 | 1.003 | 1.009 | 0.982 | 1.004 | 0.986 |
| Fe | 0.000 | 0.000 | 0.000 | 0.000 | 0.000 | 0.000 | 0.000 | 0.000 |
| **Σ Y-site** | 1.004 | 0.986 | 1.003 | 1.003 | 1.009 | 0.982 | 1.004 | 0.986 |
| Si | 2.994 | 3.018 | 2.995 | 2.994 | 2.989 | 3.021 | 2.994 | 3.018 |
| Ti | 0.000 | 0.000 | 0.001 | 0.000 | 0.000 | 0.000 | 0.000 | 0.000 |
| P | 0.000 | 0.000 | 0.000 | 0.000 | 0.000 | 0.000 | 0.000 | 0.000 |
| Al | 0.000 | 0.000 | 0.000 | 0.000 | 0.000 | 0.000 | 0.000 | 0.000 |
| **Σ Z-site** | 2.994 | 3.018 | 2.996 | 2.994 | 2.989 | 3.021 | 2.994 | 3.018 |

Table 87 Additional feldspar analyses from Crockley pegmatite samples. *Apfu* calculations based on 8 oxygens.

| **MUSCOVITE – REPUBLIC MINE PEGMATITE** | | | | | | | | | | |
|---|---|---|---|---|---|---|---|---|---|---|
| Wt % Ox. | RM-rr grain 1-2 | RM-rr grain 2-1 | RM-rr grain 3-1 | RM-rr set 1 grain 1-1 | RM-rr set 1 grain 2-1 | RM-rr set 2 grain 1-2 | RM-rr set 2 grain 3-1 | RM-rr set 2 grain 3-2 | RM-rr set 3 grain 2-1 | RM-rr set 3 grain 2-2 |
| $SiO_2$ | 46.505 | 46.484 | 46.444 | 45.977 | 45.799 | 45.782 | 45.634 | 45.665 | 45.545 | 45.600 |
| $TiO_2$ | 0.254 | 0.188 | 0.244 | 0.112 | 0.099 | 0.088 | 0.045 | 0.056 | 0.177 | 0.143 |
| $Al_2O_3$ | 35.673 | 34.631 | 34.686 | 35.321 | 35.623 | 35.770 | 35.223 | 35.312 | 35.772 | 35.679 |
| $Fe_2O_3$ | 0.000 | 0.000 | 0.000 | 0.000 | 0.000 | 0.000 | 0.000 | 0.000 | 0.000 | 0.000 |
| FeO | 2.334 | 2.343 | 2.890 | 2.711 | 2.723 | 2.556 | 2.892 | 2.966 | 2.872 | 2.800 |
| MnO | 0.028 | 0.027 | 0.021 | 0.022 | 0.020 | 0.014 | 0.012 | 0.011 | 0.022 | 0.023 |
| MgO | 0.872 | 0.862 | 0.455 | 0.333 | 0.288 | 0.233 | 0.244 | 0.256 | 0.300 | 0.292 |
| CaO | 0.031 | 0.018 | 0.034 | 0.454 | 0.223 | 0.312 | 0.211 | 0.234 | 0.191 | 0.181 |
| $Li_2O$ (*calc.*) | 0.578 | 0.547 | 0.513 | 0.575 | 0.491 | 0.557 | 0.515 | 0.532 | 0.582 | 0.622 |
| $Na_2O$ | 0.802 | 0.833 | 0.654 | 0.785 | 0.774 | 0.656 | 0.488 | 0.523 | 0.555 | 0.562 |
| $K_2O$ | 9.988 | 9.881 | 9.944 | 10.022 | 10.044 | 10.066 | 10.211 | 10.181 | 10.132 | 10.091 |
| $Rb_2O$ | 0.029 | 0.017 | 0.022 | 0.031 | 0.023 | 0.026 | 0.021 | 0.027 | 0.023 | 0.021 |
| $Cs_2O$ | *bdl* | *bdl* | *bdl* | *bdl* | *bdl* | *bdl* | *bdl* | *bdl* | *bdl* | *bdl* |
| F | 1.337 | 1.282 | 1.221 | 1.332 | 1.181 | 1.300 | 1.225 | 1.256 | 1.344 | 1.412 |
| $H_2O$ | 3.948 | 3.916 | 3.939 | 3.897 | 3.960 | 3.907 | 3.907 | 3.903 | 3.883 | 3.848 |
| F=O | - 0.563 | 0.540 | 0.514 | 0.561 | 0.497 | 0.547 | 0.516 | 0.529 | 0.566 | 0.595 |
| **Total** | 101.816 | 100.489 | 100.552 | 101.012 | 100.751 | 100.720 | 100.112 | 100.394 | 100.833 | 100.679 |
| *apfu* | | | | | | | | | | |
| Si | 6.087 | 6.161 | 6.165 | 6.087 | 6.076 | 6.069 | 6.097 | 6.087 | 6.041 | 6.053 |
| $^{IV}Al$ | 1.913 | 1.839 | 1.835 | 1.913 | 1.924 | 1.931 | 1.903 | 1.913 | 1.959 | 1.947 |
| **Σ T-site** | 8.000 | 8.000 | 8.000 | 8.000 | 8.000 | 8.000 | 8.000 | 8.000 | 8.000 | 8.000 |
| $^{VI}Al$ | 3.590 | 3.571 | 3.591 | 3.600 | 3.645 | 3.658 | 3.644 | 3.635 | 3.634 | 3.636 |
| Ti | 0.025 | 0.019 | 0.024 | 0.011 | 0.010 | 0.009 | 0.005 | 0.006 | 0.018 | 0.014 |
| $Fe_t$ | 0.255 | 0.260 | 0.321 | 0.300 | 0.302 | 0.283 | 0.323 | 0.331 | 0.319 | 0.311 |
| Mn | 0.003 | 0.003 | 0.002 | 0.002 | 0.002 | 0.002 | 0.001 | 0.001 | 0.002 | 0.003 |
| Mg | 0.170 | 0.170 | 0.090 | 0.066 | 0.057 | 0.046 | 0.049 | 0.051 | 0.059 | 0.058 |
| Li (*calc.*) | 0.304 | 0.292 | 0.274 | 0.306 | 0.262 | 0.297 | 0.277 | 0.285 | 0.311 | 0.332 |
| **Σ Y-site** | 4.347 | 4.315 | 4.302 | 4.285 | 4.278 | 4.295 | 4.299 | 4.309 | 4.343 | 4.354 |

Table 88 Additional muscovite mica samples from Republic Mine pegmatite. *Apfu* calculations based on 24 anions.
Table continues on next page.

| | | | | | | | | | | |
|---|---|---|---|---|---|---|---|---|---|---|
| K | 1.668 | 1.671 | 1.684 | 1.693 | 1.700 | 1.702 | 1.741 | 1.731 | 1.715 | 1.709 |
| Ca | 0.004 | 0.003 | 0.005 | 0.064 | 0.032 | 0.044 | 0.030 | 0.033 | 0.027 | 0.026 |
| Na | 0.204 | 0.214 | 0.168 | 0.202 | 0.199 | 0.169 | 0.126 | 0.135 | 0.143 | 0.145 |
| Rb | 0.002 | 0.001 | 0.002 | 0.003 | 0.002 | 0.002 | 0.002 | 0.002 | 0.002 | 0.002 |
| Cs | *bdl* | *bdl* | *bdl* | *bdl* | *bdl* | *bdl* | *bdl* | *bdl* | *bdl* | *bdl* |
| **Σ X-site** | 1.878 | 1.889 | 1.859 | 1.962 | 1.933 | 1.918 | 1.899 | 1.902 | 1.887 | 1.881 |
| F | 0.553 | 0.537 | 0.513 | 0.558 | 0.495 | 0.545 | 0.518 | 0.529 | 0.564 | 0.593 |
| OH (*calc.*) | 3.447 | 3.463 | 3.487 | 3.442 | 3.505 | 3.455 | 3.482 | 3.471 | 3.436 | 3.407 |
| **Σ W-site** | 4.000 | 4.000 | 4.000 | 4.000 | 4.000 | 4.000 | 4.000 | 4.000 | 4.000 | 4.000 |

| TOURMALINE – REPUBLIC MINE PEGMATITE | | | | | | | | | | | |
|---|---|---|---|---|---|---|---|---|---|---|---|
| Wt.% Oxide | grain 4-2 | grain 4-3 | grain 4-4 | grain 4-5 | grain 4-6 | grain 1-2 | grain 1-3 | grain 3-2 | grain 7-2 | grain 9-2 | grain 10-2 |
| $SiO_2$ | 36.311 | 36.266 | 36.238 | 36.292 | 36.223 | 36.198 | 36.322 | 36.328 | 36.300 | 36.411 | 36.300 |
| $TiO_2$ | 0.119 | 0.106 | 0.115 | 0.920 | 0.133 | 0.134 | 0.113 | 0.143 | 0.105 | 0.145 | 0.130 |
| $Al_2O_3$ | 30.093 | 30.110 | 30.293 | 30.116 | 30.200 | 29.900 | 29.945 | 29.845 | 30.022 | 29.900 | 29.622 |
| $B_2O_3$ (*calc*.) | 10.312 | 10.304 | 10.339 | 10.390 | 10.322 | 10.325 | 10.336 | 10.350 | 10.330 | 10.387 | 10.349 |
| FeOt | 13.499 | 13.505 | 13.588 | 13.400 | 13.451 | 13.400 | 13.262 | 13.217 | 13.456 | 13.500 | 13.400 |
| MnO | 0.213 | 0.211 | 0.234 | 0.209 | 0.225 | 0.398 | 0.410 | 0.454 | 0.312 | 0.465 | 0.400 |
| MgO | 3.129 | 3.200 | 3.344 | 3.292 | 3.334 | 3.983 | 3.883 | 4.199 | 3.832 | 4.430 | 4.700 |
| CaO | 0.029 | 0.031 | 0.024 | 0.022 | 0.028 | 0.019 | 0.027 | 0.485 | 0.254 | 0.345 | 0.258 |
| $Na_2O$ | 2.400 | 2.335 | 2.412 | 2.344 | 2.400 | 2.315 | 2.292 | 1.779 | 1.934 | 1.823 | 1.922 |
| $K_2O$ | 0.019 | 0.032 | 0.040 | 0.015 | 0.043 | 0.026 | 0.022 | 0.031 | 0.019 | 0.034 | 0.023 |
| $Li_2O$ (*calc*.) | 0.424 | 0.385 | 0.299 | 0.330 | 0.335 | 0.160 | 0.229 | 0.154 | 0.199 | 0.038 | 0.007 |
| $H_2O$ (*calc*.) | 3.041 | 2.976 | 3.002 | 3.028 | 2.992 | 3.050 | 3.071 | 2.995 | 2.989 | 3.000 | 3.091 |
| F | 1.089 | 1.221 | 1.191 | 1.174 | 1.200 | 1.081 | 1.044 | 1.215 | 1.213 | 1.232 | 1.012 |
| F=O | - 0.459 | - 0.514 | - 0.501 | - 0.494 | - 0.505 | - 0.455 | - 0.440 | - 0.512 | - 0.511 | - 0.519 | - 0.426 |
| **Total** | 100.220 | 100.169 | 100.617 | 101.039 | 100.381 | 100.533 | 100.517 | 100.683 | 100.455 | 101.191 | 100.788 |
| *apfu* | | | | | | | | | | | |
| Na | 0.784 | 0.764 | 0.786 | 0.760 | 0.784 | 0.756 | 0.747 | 0.579 | 0.631 | 0.591 | 0.626 |
| Ca | 0.005 | 0.006 | 0.004 | 0.004 | 0.005 | 0.003 | 0.005 | 0.087 | 0.046 | 0.062 | 0.046 |
| K | 0.004 | 0.007 | 0.009 | 0.003 | 0.009 | 0.006 | 0.005 | 0.007 | 0.004 | 0.007 | 0.005 |
| Vac (*calc*.) | 0.206 | 0.224 | 0.201 | 0.233 | 0.202 | 0.235 | 0.243 | 0.327 | 0.319 | 0.339 | 0.323 |
| **Σ X-site** | 1.000 | 1.000 | 1.000 | 1.000 | 1.000 | 1.000 | 1.000 | 1.000 | 1.000 | 1.000 | 1.000 |
| Fe | 1.903 | 1.905 | 1.910 | 1.874 | 1.894 | 1.886 | 1.865 | 1.856 | 1.893 | 1.889 | 1.882 |
| Mg | 0.764 | 0.790 | 0.838 | 0.758 | 0.830 | 0.932 | 0.908 | 0.958 | 0.914 | 1.001 | 1.040 |
| Al | 0.000 | 0.000 | 0.002 | 0.000 | 0.000 | 0.000 | 0.000 | 0.000 | 0.000 | 0.000 | 0.000 |
| Mn | 0.030 | 0.030 | 0.033 | 0.030 | 0.032 | 0.057 | 0.058 | 0.065 | 0.044 | 0.066 | 0.057 |
| Li (*calc*.) | 0.288 | 0.261 | 0.202 | 0.222 | 0.227 | 0.108 | 0.155 | 0.104 | 0.135 | 0.025 | 0.005 |
| Ti | 0.015 | 0.013 | 0.015 | 0.116 | 0.017 | 0.017 | 0.014 | 0.018 | 0.013 | 0.018 | 0.016 |
| **Σ Y-site** | 3.000 | 3.000 | 3.000 | 3.000 | 3.000 | 3.000 | 3.000 | 3.000 | 3.000 | 3.000 | 3.000 |
| Al | 5.978 | 5.985 | 6.000 | 5.937 | 5.993 | 5.932 | 5.934 | 5.906 | 5.953 | 5.896 | 5.863 |
| Mg | 0.022 | 0.015 | 0.000 | 0.063 | 0.007 | 0.068 | 0.066 | 0.094 | 0.047 | 0.104 | 0.137 |
| **Σ Z-site** | 6.000 | 6.000 | 6.000 | 6.000 | 6.000 | 6.000 | 6.000 | 6.000 | 6.000 | 6.000 | 6.000 |
| Si | 6.120 | 6.117 | 6.092 | 6.071 | 6.099 | 6.094 | 6.108 | 6.100 | 6.107 | 6.092 | 6.096 |
| Al | 0.000 | 0.000 | 0.000 | 0.000 | 0.000 | 0.000 | 0.000 | 0.000 | 0.000 | 0.000 | 0.000 |
| **Σ T-site** | 6.120 | 6.117 | 6.092 | 6.071 | 6.099 | 6.094 | 6.108 | 6.100 | 6.107 | 6.092 | 6.096 |
| B (*calc*.) | 3.000 | 3.000 | 3.000 | 3.000 | 3.000 | 3.000 | 3.000 | 3.000 | 3.000 | 3.000 | 3.000 |
| H (*calc*.) | 3.420 | 3.349 | 3.367 | 3.379 | 3.361 | 3.424 | 3.445 | 3.355 | 3.355 | 3.348 | 3.462 |
| F | 0.580 | 0.651 | 0.633 | 0.621 | 0.639 | 0.576 | 0.555 | 0.645 | 0.645 | 0.652 | 0.538 |
| **Σ W+V sites** | 4.000 | 4.000 | 4.000 | 4.000 | 4.000 | 4.000 | 4.000 | 4.000 | 4.000 | 4.000 | 4.000 |
| | | | | | | | | | | | |
| **Species** | *fluor-schorl* | *fluor-schorl* | *fluor-schorl* | *fluor-schorl* | *fluor-schorl* | *fluor-schorl* | *fluor-schorl* | *fluor-schorl* | *fluor-schorl* | *fluor-schorl* | *fluor-schorl* |

Table 89 Additional tourmaline analyses from Republic Mine samples. *Apfu calculations based on 31 anions.*

| ZIRCON – REPUBLIC MINE PEGMATITE | | | | | | |
|---|---|---|---|---|---|---|
| Wt % Oxide | grain 6-RM-rr=1 | | grain 7-RM-rr-1 | | grain 10-RM-rr-1 | |
| $SiO_2$ | 31.760 | 31.799 | 29.720 | 29.542 | 27.787 | 28.799 |
| $TiO_2$ | 0.031 | 0.022 | 0.023 | 0.014 | 0.020 | 0.023 |
| $Al_2O_3$ | 0.056 | 0.070 | 0.454 | 0.421 | 0.034 | 0.086 |
| $ZrO_2$ | 63.445 | 63.200 | 58.760 | 57.970 | 57.854 | 58.112 |
| $HfO_2$ | 1.660 | 1.700 | 0.920 | 0.780 | 0.800 | 0.783 |
| FeOt | 1.110 | 0.812 | 4.340 | 4.950 | 4.330 | 4.094 |
| MnO | 0.100 | 0.088 | 0.212 | 0.245 | 0.022 | 0.050 |
| MgO | 0.000 | 0.000 | 0.012 | 0.015 | 0.000 | 0.000 |
| CaO | 0.678 | 0.760 | 0.668 | 0.652 | 4.334 | 3.983 |
| $UO_2$ | 0.030 | 0.035 | 0.000 | 0.012 | 0.012 | 0.015 |
| $ThO_2$ | 0.066 | 0.054 | 0.033 | 0.034 | 0.030 | 0.037 |
| **Total** | 98.936 | 98.540 | 95.142 | 94.635 | 95.223 | 95.982 |
| *apfu* | | | | | | |
| Zr | 0.962 | 0.961 | 0.933 | 0.926 | 0.933 | 0.923 |
| Hf | 0.020 | 0.021 | 0.012 | 0.010 | 0.010 | 0.010 |
| U | 0.000 | 0.000 | 0.000 | 0.000 | 0.000 | 0.000 |
| Th | 0.000 | 0.000 | 0.000 | 0.000 | 0.000 | 0.000 |
| Fe | 0.029 | 0.021 | 0.118 | 0.136 | 0.120 | 0.112 |
| Mn | 0.003 | 0.002 | 0.006 | 0.007 | 0.001 | 0.001 |
| Mg | 0.000 | 0.000 | 0.001 | 0.001 | 0.000 | 0.000 |
| Ca | 0.023 | 0.025 | 0.023 | 0.023 | 0.154 | 0.139 |
| **Σ X-site** | 1.037 | 1.030 | 1.093 | 1.103 | 1.218 | 1.185 |
| Si | 0.988 | 0.991 | 0.968 | 0.968 | 0.918 | 0.938 |
| Ti | 0.001 | 0.001 | 0.001 | 0.000 | 0.000 | 0.001 |
| Al | 0.002 | 0.003 | 0.017 | 0.016 | 0.001 | 0.003 |
| **Σ Y-site** | 0.991 | 0.995 | 0.986 | 0.984 | 0.919 | 0.942 |
| **Zr/Hf Ratios** | 48.128 | 46.814 | 80.427 | 93.587 | 91.064 | 93.457 |

Table 90 Additional zircon analyses from Republic Mine pegmatite. *Apfu* calculations based on 4 oxygens.

HWY69 PEGMATITE

| GARNETS – HWY69VZ | | | | | | | | | | |
|---|---|---|---|---|---|---|---|---|---|---|
| Wt % Ox | grain 1-1 | grain 1-2 | grain 2-1 | grain 2-2 | grain 3-1 | grain 3-2 | grain 4-1 | grain 4-2 | grain 5-1 | grain 5-2 |
| $SiO_2$ | 36.455 | 36.500 | 36.512 | 36.483 | 36.366 | 36.400 | 36.333 | 36.265 | 36.554 | 36.523 |
| $TiO_2$ | 0.012 | 0.013 | 0.015 | 0.018 | 0.023 | 0.021 | 0.014 | 0.025 | 0.020 | 0.013 |
| $Al_2O_3$ | 20.101 | 20.077 | 20.110 | 20.106 | 20.066 | 20.006 | 20.110 | 19.981 | 20.140 | 20.112 |
| FeO | 34.009 | 34.100 | 33.993 | 34.056 | 37.750 | 37.554 | 34.544 | 37.640 | 37.555 | 34.430 |
| MnO | 7.400 | 7.512 | 7.600 | 7.599 | 1.113 | 0.983 | 6.895 | 0.944 | 1.101 | 6.445 |
| MgO | 0.550 | 0.503 | 0.533 | 0.505 | 0.722 | 0.722 | 0.676 | 0.766 | 0.800 | 0.644 |
| CaO | 1.400 | 1.334 | 1.113 | 1.200 | 0.787 | 0.566 | 0.740 | 0.899 | 0.844 | 0.894 |
| **Total** | 99.989 | 100.103 | 99.927 | 100.024 | 96.827 | 96.252 | 99.349 | 96.520 | 97.014 | 99.073 |
| *apfu* | | | | | | | | | | |
| Ti | 0.001 | 0.001 | 0.001 | 0.001 | 0.001 | 0.001 | 0.001 | 0.002 | 0.001 | 0.001 |
| Fe | 2.346 | 2.351 | 2.345 | 2.349 | 2.655 | 2.652 | 2.395 | 2.655 | 2.632 | 2.386 |
| Mn | 0.517 | 0.525 | 0.531 | 0.531 | 0.079 | 0.070 | 0.484 | 0.067 | 0.078 | 0.452 |
| Mg | 0.068 | 0.062 | 0.066 | 0.062 | 0.091 | 0.091 | 0.084 | 0.096 | 0.100 | 0.080 |
| Ca | 0.124 | 0.118 | 0.098 | 0.106 | 0.071 | 0.051 | 0.066 | 0.081 | 0.076 | 0.079 |
| **Σ X-site** | 3.056 | 3.057 | 3.001 | 3.009 | 2.937 | 2.915 | 3.020 | 2.931 | 2.927 | 2.998 |
| Al | 1.954 | 1.951 | 1.956 | 1.955 | 1.989 | 1.991 | 1.965 | 1.986 | 1.990 | 1.965 |
| **Σ Y-site** | 1.954 | 1.951 | 1.956 | 1.955 | 1.989 | 1.991 | 1.965 | 1.986 | 1.990 | 1.965 |
| Si | 3.007 | 3.009 | 3.012 | 3.009 | 3.059 | 3.073 | 3.012 | 3.059 | 3.064 | 3.027 |
| **Σ Z-site** | 3.007 | 3.009 | 3.012 | 3.009 | 3.059 | 3.073 | 3.012 | 3.059 | 3.064 | 3.027 |
| **Component** | | | | | | | | | | |
| Andradite | 02 | 02 | 02 | 02 | 00 | 00 | 01 | 00 | 00 | 00 |
| Pyrope | 03 | 02 | 02 | 02 | 03 | 03 | 03 | 03 | 03 | 03 |
| Spessartine | 17 | 18 | 18 | 18 | 03 | 02 | 16 | 02 | 03 | 15 |
| Grossular | 02 | 02 | 02 | 02 | 02 | 02 | 01 | 03 | 03 | 02 |
| Almandine | 76 | 76 | 76 | 76 | 92 | 93 | 79 | 92 | 91 | 80 |

Table 91 Additional garnet analyses from Hwy69 pegmatite. *Apfu* calculations based on 12 oxygens.

| GARNETS – HWY69VZ | | | | | | | | | | |
|---|---|---|---|---|---|---|---|---|---|---|
| Wt % Ox | grain 6-1 | grain 6-2 | grain 7-1 | grain 7-2 | grain 8-1 | grain 8-2 | grain 9-1 | grain 9-2 | grain 10-1 | grain 10-2 |
| $SiO_2$ | 36.588 | 36.620 | 36.555 | 36.612 | 36.523 | 36.499 | 36.500 | 36.566 | 36.455 | 36.512 |
| $TiO_2$ | 0.014 | 0.031 | 0.025 | 0.015 | 0.011 | 0.019 | 0.022 | 0.015 | 0.026 | 0.015 |
| $Al_2O_3$ | 20.144 | 20.092 | 20.000 | 20.044 | 20.005 | 20.055 | 20.044 | 20.014 | 20.112 | 20.066 |
| FeO | 34.510 | 37.554 | 34.551 | 37.476 | 34.333 | 37.400 | 37.500 | 34.444 | 37.600 | 33.900 |
| MnO | 6.500 | 1.211 | 6.488 | 1.311 | 6.623 | 1.338 | 1.400 | 6.455 | 1.393 | 6.966 |
| MgO | 0.595 | 0.822 | 0.544 | 0.809 | 0.484 | 0.777 | 0.822 | 0.477 | 0.800 | 0.403 |
| CaO | 0.900 | 0.855 | 0.783 | 0.822 | 0.784 | 0.900 | 0.787 | 0.734 | 0.833 | 0.866 |
| **Total** | 99.263 | 97.185 | 98.957 | 97.089 | 98.766 | 96.988 | 97.075 | 98.705 | 97.219 | 98.728 |
| *apfu* | | | | | | | | | | |
| Ti | 0.001 | 0.002 | 0.002 | 0.001 | 0.001 | 0.001 | 0.001 | 0.001 | 0.002 | 0.001 |
| Fe | 2.388 | 2.629 | 2.399 | 2.626 | 2.388 | 2.624 | 2.630 | 2.395 | 2.635 | 2.358 |
| Mn | 0.456 | 0.086 | 0.456 | 0.093 | 0.466 | 0.095 | 0.099 | 0.455 | 0.099 | 0.491 |
| Mg | 0.073 | 0.103 | 0.067 | 0.101 | 0.060 | 0.097 | 0.103 | 0.059 | 0.100 | 0.050 |
| Ca | 0.080 | 0.077 | 0.070 | 0.074 | 0.070 | 0.081 | 0.071 | 0.065 | 0.075 | 0.077 |
| **Σ X-site** | 2.989 | 2.932 | 2.986 | 2.931 | 2.983 | 2.934 | 2.938 | 2.978 | 2.942 | 2.979 |
| Al | 1.965 | 1.982 | 1.957 | 1.979 | 1.961 | 1.983 | 1.981 | 1.962 | 1.986 | 1.967 |
| **Σ Y-site** | 1.965 | 1.982 | 1.957 | 1.979 | 1.961 | 1.983 | 1.981 | 1.962 | 1.986 | 1.967 |
| Si | 3.027 | 3.065 | 3.035 | 3.068 | 3.037 | 3.062 | 3.061 | 3.041 | 3.054 | 3.036 |
| **Σ Z-site** | 3.027 | 3.065 | 3.035 | 3.068 | 3.037 | 3.062 | 3.061 | 3.041 | 3.054 | 3.036 |
| **Component** | | | | | | | | | | |
| Andradite | 01 | 00 | 00 | 00 | 00 | 00 | 00 | 00 | 00 | 00 |
| Pyrope | 03 | 03 | 02 | 03 | 02 | 03 | 04 | 02 | 03 | 02 |
| Spessartine | 15 | 03 | 16 | 03 | 16 | 03 | 03 | 16 | 03 | 16 |
| Grossular | 02 | 03 | 02 | 03 | 02 | 03 | 02 | 02 | 03 | 03 |
| Almandine | 79 | 91 | 80 | 91 | 80 | 91 | 91 | 80 | 91 | 79 |

Table 92 Additional garnet analyses from Hwy69 pegmatite. *Apfu* calculations based on 12 oxygens.

| GARNETS – STURGEON RIVER PEGMATITE | | | | | | | |
|---|---|---|---|---|---|---|---|
| Wt % Ox | grain 1-1 | grain 2-1 | grain 3-2 | grain 4-2 | grain 5-2 | grain 6-2 | grain 7-2 |
| $SiO_2$ | 36.507 | 36.498 | 36.522 | 36.500 | 36.509 | 36.499 | 36.543 |
| $TiO_2$ | 0.012 | 0.011 | 0.012 | 0.012 | 0.009 | 0.012 | 0.017 |
| $Al_2O_3$ | 20.566 | 20.577 | 20.541 | 20.600 | 20.470 | 20.566 | 20.600 |
| FeO | 36.233 | 36.088 | 36.409 | 36.466 | 36.588 | 36.800 | 36.499 |
| MnO | 6.988 | 7.099 | 6.554 | 6.733 | 6.534 | 6.233 | 6.622 |
| MgO | 0.041 | 0.033 | 0.030 | 0.035 | 0.033 | 0.032 | 0.031 |
| CaO | 0.087 | 0.054 | 0.034 | 0.033 | 0.031 | 0.032 | 0.033 |
| **Total** | 100.434 | 100.360 | 100.102 | 100.379 | 100.174 | 100.174 | 100.345 |
| *apfu* | | | | | | | |
| Ti | 0.001 | 0.001 | 0.001 | 0.001 | 0.001 | 0.001 | 0.001 |
| Fe | 2.495 | 2.486 | 2.512 | 2.511 | 2.525 | 2.538 | 2.513 |
| Mn | 0.487 | 0.495 | 0.458 | 0.470 | 0.457 | 0.435 | 0.462 |
| Mg | 0.005 | 0.004 | 0.004 | 0.004 | 0.004 | 0.004 | 0.004 |
| Ca | 0.008 | 0.005 | 0.003 | 0.003 | 0.003 | 0.003 | 0.003 |
| **Σ X-site** | 2.996 | 2.991 | 2.978 | 2.989 | 2.990 | 2.981 | 2.983 |
| Al | 1.996 | 1.998 | 1.997 | 1.999 | 1.991 | 1.999 | 1.999 |
| **Σ Y-site** | 1.996 | 1.998 | 1.997 | 1.999 | 1.991 | 1.999 | 1.999 |
| Si | 3.005 | 3.006 | 3.013 | 3.006 | 3.012 | 3.010 | 3.009 |
| **Σ Z-site** | 3.005 | 3.006 | 3.013 | 3.006 | 3.012 | 3.010 | 3.009 |
| **Component** | | | | | | | |
| Pyrope | 00 | 00 | 00 | 00 | 00 | 00 | 00 |
| Spessartine | 16 | 17 | 15 | 16 | 15 | 15 | 16 |
| Grossular | 01 | 00 | 00 | 00 | 00 | 00 | 00 |
| Almandine | 83 | 83 | 85 | 84 | 85 | 85 | 84 |

Table 93 Additional garnet analyses from Sturgeon River pegmatite. *Apfu* calculations based on 12 oxygens.

| GARNETS – STURGEON RIVER PEGMATITE | | | | | | | | |
|---|---|---|---|---|---|---|---|---|
| Wt % Ox | grain 1-1 | grain 1-2 | grain 2-1 | grain 2-2 | grain 3-1 | grain 3-2 | grain 4-1 | grain 4-2 |
| $SiO_2$ | 36.433 | 36.461 | 36.477 | 36.477 | 36.543 | 36.512 | 36.633 | 36.552 |
| $TiO_2$ | 0.012 | 0.015 | 0.010 | 0.014 | 0.009 | 0.016 | 0.012 | 0.011 |
| $Al_2O_3$ | 20.554 | 20.602 | 20.544 | 20.484 | 20.499 | 20.465 | 20.500 | 20.484 |
| FeO | 36.211 | 36.114 | 36.420 | 36.450 | 36.488 | 36.511 | 36.788 | 36.765 |
| MnO | 7.032 | 7.143 | 6.565 | 6.500 | 6.421 | 6.456 | 5.985 | 5.900 |
| MgO | 0.026 | 0.030 | 0.040 | 0.055 | 0.035 | 0.054 | 0.051 | 0.044 |
| CaO | 0.054 | 0.056 | 0.044 | 0.043 | 0.055 | 0.039 | 0.323 | 0.326 |
| **Total** | 100.322 | 100.421 | 100.100 | 100.023 | 100.050 | 100.053 | 100.292 | 100.082 |
| *apfu* | | | | | | | | |
| Ti | 0.001 | 0.001 | 0.001 | 0.001 | 0.001 | 0.001 | 0.001 | 0.001 |
| Fe | 2.497 | 2.487 | 2.513 | 2.517 | 2.518 | 2.521 | 2.532 | 2.536 |
| Mn | 0.491 | 0.498 | 0.459 | 0.455 | 0.449 | 0.451 | 0.417 | 0.412 |
| Mg | 0.003 | 0.004 | 0.005 | 0.007 | 0.004 | 0.007 | 0.006 | 0.005 |
| Ca | 0.005 | 0.005 | 0.004 | 0.004 | 0.005 | 0.003 | 0.028 | 0.029 |
| **Σ X-site** | 2.997 | 2.995 | 2.982 | 2.984 | 2.987 | 2.983 | 2.984 | 2.983 |
| Al | 1.997 | 2.000 | 1.998 | 1.994 | 1.994 | 1.991 | 1.989 | 1.991 |
| **Σ Y-site** | 1.997 | 2.000 | 1.998 | 1.994 | 1.994 | 1.991 | 1.989 | 1.991 |
| Si | 3.004 | 3.002 | 3.010 | 3.012 | 3.016 | 3.014 | 3.015 | 3.015 |
| **Σ Z-site** | 3.004 | 3.002 | 3.010 | 3.012 | 3.016 | 3.014 | 3.015 | 3.015 |
| **Component** | | | | | | | | |
| Pyrope | 00 | 00 | 00 | 00 | 00 | 00 | 00 | 00 |
| Spessartine | 17 | 17 | 15 | 15 | 15 | 15 | 15 | 14 |
| Grossular | 00 | 00 | 00 | 00 | 00 | 00 | 01 | 01 |
| Almandine | 83 | 83 | 85 | 85 | 85 | 85 | 84 | 85 |

Table 94 Additional garnet analyses from Sturgeon River pegmatite. *Apfu* calculations based on 12 oxygens.

| GARNETS – STURGEON RIVER PEGMATITE GOI | | | | | | | | |
|---|---|---|---|---|---|---|---|---|
| Wt % Ox | grain 1-1 | grain 1-2 | grain 2-1 | grain 2-2 | grain 3-1 | grain 3-2 | grain 4-1 | grain 4-2 |
| $SiO_2$ | 3 | 36.500 | 36.505 | 36.512 | 36.477 | 36.473 | 36.447 | 36.511 |
| $TiO_2$ | 0.009 | 0.008 | 0.010 | 0.009 | 0.012 | 0.013 | 0.009 | 0.009 |
| $Al_2O_3$ | 20.494 | 20.445 | 20.477 | 20.513 | 20.483 | 20.495 | 20.480 | 20.506 |
| FeO | 36.488 | 36.472 | 36.431 | 36.404 | 36.522 | 36.486 | 36.500 | 36.400 |
| MnO | 6.556 | 6.676 | 6.520 | 6.634 | 6.448 | 6.523 | 6.568 | 6.477 |
| MgO | 0.050 | 0.047 | 0.055 | 0.051 | 0.045 | 0.048 | 0.045 | 0.052 |
| CaO | 0.202 | 0.255 | 0.412 | 0.388 | 0.305 | 0.322 | 0.272 | 0.256 |
| **Total** | 100.235 | 100.415 | 100.420 | 100.521 | 100.296 | 100.367 | 100.329 | 100.211 |
| *apfu* | | | | | | | | |
| Ti | 0.001 | 0.000 | 0.001 | 0.001 | 0.001 | 0.001 | 0.001 | 0.001 |
| Fe | 2.517 | 2.513 | 2.509 | 2.505 | 2.518 | 2.514 | 2.516 | 2.509 |
| Mn | 0.458 | 0.466 | 0.455 | 0.462 | 0.450 | 0.455 | 0.459 | 0.452 |
| Mg | 0.006 | 0.006 | 0.007 | 0.006 | 0.006 | 0.006 | 0.006 | 0.006 |
| Ca | 0.018 | 0.023 | 0.036 | 0.034 | 0.027 | 0.028 | 0.024 | 0.023 |
| **Σ X-site** | 3.002 | 3.008 | 3.003 | 3.008 | 3.002 | 3.004 | 3.006 | 2.992 |
| Al | 1.993 | 1.985 | 1.987 | 1.989 | 1.990 | 1.990 | 1.990 | 1.992 |
| **Σ Y-site** | 1.993 | 1.985 | 1.987 | 1.989 | 1.990 | 1.990 | 1.990 | 1.992 |
| Si | 3.005 | 3.007 | 3.006 | 3.004 | 3.007 | 3.005 | 3.005 | 3.010 |
| **Σ Z-site** | 3.005 | 3.007 | 3.006 | 3.004 | 3.007 | 3.005 | 3.005 | 3.010 |
| **Component** | | | | | | | | |
| Andradite | 00 | 01 | 00 | 00 | 00 | 00 | 00 | 00 |
| Pyrope | 00 | 00 | 00 | 00 | 00 | 00 | 00 | 00 |
| Spessartine | 15 | 15 | 15 | 15 | 15 | 15 | 15 | 15 |
| Grossular | 01 | 01 | 01 | 01 | 01 | 01 | 01 | 01 |
| Almandine | 84 | 83 | 84 | 84 | 84 | 84 | 84 | 84 |

Table 95 Additional garnet analyses from Sturgeon River pegmatite. *Apfu* calculations based on 12 oxygens.

| TOURMALINE – STURGEON RIVER PEGMATITE | | | | | | | | | |
|---|---|---|---|---|---|---|---|---|---|
| Wt.% Oxide | grain 6-1 | grain 6-2 | grain 7-1 | grain 7-2 | grain 8-1 | grain 8-2 | grain 10-1 | grain 10-2 | grain 11-1 |
| $SiO_2$ | 36.393 | 36.366 | 36.289 | 36.336 | 36.411 | 36.373 | 36.412 | 36.337 | 36.310 |
| $TiO_2$ | 0.126 | 0.121 | 0.109 | 0.133 | 0.098 | 0.121 | 0.133 | 0.127 | 0.109 |
| $Al_2O_3$ | 30.100 | 30.122 | 30.088 | 30.100 | 29.966 | 30.132 | 30.100 | 30.092 | 30.144 |
| $B_2O_3$ (*calc.*) | 10.348 | 10.335 | 10.308 | 10.322 | 10.317 | 10.337 | 10.347 | 10.336 | 10.335 |
| FeOt | 13.484 | 13.568 | 13.700 | 13.561 | 13.677 | 13.569 | 13.600 | 13.634 | 13.700 |
| MnO | 0.155 | 0.140 | 0.156 | 0.145 | 0.121 | 0.140 | 0.141 | 0.151 | 0.101 |
| MgO | 3.512 | 3.278 | 3.122 | 3.277 | 3.224 | 3.434 | 3.413 | 3.444 | 3.312 |
| CaO | 0.043 | 0.038 | 0.054 | 0.065 | 0.056 | 0.045 | 0.065 | 0.070 | 0.088 |
| $Na_2O$ | 2.357 | 2.400 | 2.333 | 2.285 | 2.300 | 2.260 | 2.312 | 2.303 | 2.371 |
| $K_2O$ | 0.031 | 0.028 | 0.023 | 0.031 | 0.023 | 0.030 | 0.034 | 0.033 | 0.040 |
| $Li_2O$ (*calc.*) | 0.341 | 0.392 | 0.396 | 0.379 | 0.420 | 0.332 | 0.355 | 0.323 | 0.355 |
| $H_2O$ (*calc.*) | 3.105 | 3.044 | 3.007 | 3.044 | 3.086 | 3.088 | 3.039 | 3.045 | 3.049 |
| F | 0.981 | 1.101 | 1.160 | 1.091 | 1.000 | 1.009 | 1.121 | 1.100 | 1.091 |
| F=O | - 0.413 | - 0.464 | - 0.488 | - 0.459 | - 0.421 | - 0.425 | - 0.472 | - 0.463 | - 0.459 |
| **Total** | 100.563 | 100.469 | 100.256 | 100.310 | 100.278 | 100.445 | 100.600 | 100.532 | 100.545 |
| *apfu* | | | | | | | | | |
| Na | 0.768 | 0.783 | 0.763 | 0.746 | 0.751 | 0.737 | 0.753 | 0.751 | 0.773 |
| Ca | 0.008 | 0.007 | 0.010 | 0.012 | 0.010 | 0.008 | 0.012 | 0.013 | 0.016 |
| K | 0.007 | 0.006 | 0.005 | 0.007 | 0.005 | 0.006 | 0.007 | 0.007 | 0.009 |
| Vac (*calc.*) | 0.218 | 0.205 | 0.223 | 0.236 | 0.234 | 0.249 | 0.228 | 0.230 | 0.202 |
| **Σ X-site** | 1.000 | 1.000 | 1.000 | 1.000 | 1.000 | 1.000 | 1.000 | 1.000 | 1.000 |
| Fe | 1.894 | 1.908 | 1.932 | 1.910 | 1.927 | 1.908 | 1.910 | 1.917 | 1.927 |
| Mg | 0.838 | 0.792 | 0.764 | 0.796 | 0.759 | 0.832 | 0.813 | 0.827 | 0.805 |
| Al | 0.000 | 0.000 | 0.000 | 0.000 | 0.000 | 0.000 | 0.000 | 0.000 | 0.000 |
| Mn | 0.022 | 0.020 | 0.022 | 0.021 | 0.017 | 0.020 | 0.020 | 0.022 | 0.014 |
| Li (*calc.*) | 0.230 | 0.265 | 0.268 | 0.257 | 0.285 | 0.225 | 0.240 | 0.219 | 0.240 |
| Ti | 0.016 | 0.015 | 0.014 | 0.017 | 0.012 | 0.015 | 0.017 | 0.016 | 0.014 |
| **Σ Y-site** | 3.000 | 3.000 | 3.000 | 3.000 | 3.000 | 3.000 | 3.000 | 3.000 | 3.000 |
| Al | 5.908 | 5.915 | 5.925 | 6.000 | 5.947 | 5.965 | 5.961 | 5.959 | 5.945 |
| Mg | 0.092 | 0.085 | 0.075 | 0.000 | 0.053 | 0.035 | 0.039 | 0.041 | 0.055 |
| **Σ Z-site** | 6.000 | 6.000 | 6.000 | 6.000 | 6.000 | 6.000 | 6.000 | 6.000 | 6.000 |
| Si | 6.113 | 6.115 | 6.119 | 6.118 | 6.134 | 6.116 | 6.116 | 6.110 | 6.106 |
| Al | 0.000 | 0.000 | 0.000 | 0.000 | 0.000 | 0.000 | 0.000 | 0.000 | 0.000 |
| **Σ T-site** | 6.113 | 6.115 | 6.119 | 6.118 | 6.134 | 6.116 | 6.116 | 6.110 | 6.106 |
| B (*calc.*) | 3.000 | 3.000 | 3.000 | 3.000 | 3.000 | 3.000 | 3.000 | 3.000 | 3.000 |
| H (*calc.*) | 3.479 | 3.414 | 3.381 | 3.419 | 3.467 | 3.463 | 3.405 | 3.415 | 3.420 |
| F | 0.521 | 0.586 | 0.619 | 0.581 | 0.533 | 0.537 | 0.595 | 0.585 | 0.580 |
| **Σ W+V sites** | 4.000 | 4.000 | 4.000 | 4.000 | 4.000 | 4.000 | 4.000 | 4.000 | 4.000 |
| | | | | | | | | | |
| **Species** | *fluor-schorl* | *fluor-schorl* | *fluor-schorl* | *fluor-schorl* | *fluor-schorl* | *fluor-schorl* | *fluor-schorl* | *fluor-schorl* | *fluor-schorl* |

Table 96 Additional tourmaline analyses from Sturgeon River pegmatite. *Apfu* calculations based on 31 anions.

| TOURMALINE – STURGEON RIVER PEGMATITE | | | | | | | | |
|---|---|---|---|---|---|---|---|---|
| Wt.% Oxide | grain 12-1 | grain 12-2 | grain 13-1 | grain 13-2 | grain 14-1 | grain 15-1 | grain 16-1 | grain 16-2 |
| $SiO_2$ | 36.344 | 36.338 | 36.404 | 36.383 | 36.367 | 36.341 | 36.400 | 36.377 |
| $TiO_2$ | 0.143 | 0.120 | 0.106 | 0.111 | 0.103 | 0.100 | 0.213 | 0.188 |
| $Al_2O_3$ | 30.105 | 30.100 | 30.089 | 30.077 | 30.210 | 30.188 | 30.192 | 30.166 |
| $B_2O_3$ (*calc.*) | 10.338 | 10.331 | 10.337 | 10.339 | 10.344 | 10.343 | 10.347 | 10.347 |
| FeOt | 13.678 | 13.800 | 13.733 | 13.677 | 13.623 | 13.555 | 13.561 | 13.588 |
| MnO | 0.144 | 0.151 | 0.139 | 0.144 | 0.140 | 0.136 | 0.141 | 0.136 |
| MgO | 3.366 | 3.211 | 3.277 | 3.300 | 3.311 | 3.345 | 3.333 | 3.400 |
| CaO | 0.100 | 0.102 | 0.072 | 0.045 | 0.055 | 0.056 | 0.045 | 0.063 |
| $Na_2O$ | 2.284 | 2.310 | 2.288 | 2.400 | 2.355 | 2.433 | 2.231 | 2.260 |
| $K_2O$ | 0.028 | 0.030 | 0.034 | 0.030 | 0.019 | 0.023 | 0.033 | 0.027 |
| $Li_2O$ (*calc.*) | 0.339 | 0.367 | 0.373 | 0.380 | 0.357 | 0.366 | 0.350 | 0.333 |
| $H_2O$ (*calc.*) | 3.067 | 2.986 | 3.003 | 3.014 | 3.047 | 3.058 | 3.062 | 3.104 |
| F | 1.055 | 1.221 | 1.189 | 1.167 | 1.100 | 1.077 | 1.072 | 0.982 |
| F=O | - 0.444 | - 0.514 | - 0.501 | - 0.491 | - 0.463 | - 0.453 | - 0.451 | - 0.413 |
| **Total** | 100.546 | 100.552 | 100.543 | 100.575 | 100.568 | 100.568 | 100.529 | 100.558 |
| *apfu* | | | | | | | | |
| Na | 0.745 | 0.753 | 0.746 | 0.782 | 0.767 | 0.793 | 0.727 | 0.736 |
| Ca | 0.018 | 0.018 | 0.013 | 0.008 | 0.010 | 0.010 | 0.008 | 0.011 |
| K | 0.006 | 0.006 | 0.007 | 0.006 | 0.004 | 0.005 | 0.007 | 0.006 |
| Vac (*calc.*) | 0.231 | 0.222 | 0.234 | 0.203 | 0.219 | 0.192 | 0.258 | 0.247 |
| **Σ X-site** | 1.000 | 1.000 | 1.000 | 1.000 | 1.000 | 1.000 | 1.000 | 1.000 |
| Fe | 1.923 | 1.942 | 1.931 | 1.923 | 1.914 | 1.905 | 1.905 | 1.909 |
| Mg | 0.809 | 0.773 | 0.784 | 0.786 | 0.812 | 0.816 | 0.811 | 0.823 |
| Al | 0.000 | 0.000 | 0.000 | 0.002 | 0.000 | 0.000 | 0.000 | 0.000 |
| Mn | 0.021 | 0.022 | 0.020 | 0.021 | 0.020 | 0.019 | 0.020 | 0.019 |
| Li (*calc.*) | 0.229 | 0.248 | 0.252 | 0.257 | 0.241 | 0.247 | 0.237 | 0.225 |
| Ti | 0.018 | 0.015 | 0.013 | 0.014 | 0.013 | 0.013 | 0.027 | 0.024 |
| **Σ Y-site** | 3.000 | 3.000 | 3.000 | 3.000 | 3.000 | 3.000 | 3.000 | 3.000 |
| Al | 5.965 | 5.968 | 5.962 | 5.959 | 5.982 | 5.978 | 5.977 | 5.972 |
| Mg | 0.035 | 0.032 | 0.038 | 0.041 | 0.018 | 0.022 | 0.023 | 0.028 |
| **Σ Z-site** | 6.000 | 6.000 | 6.000 | 6.000 | 6.000 | 6.000 | 6.000 | 6.000 |
| Si | 6.110 | 6.113 | 6.121 | 6.116 | 6.110 | 6.106 | 6.114 | 6.110 |
| Al | 0.000 | 0.000 | 0.000 | 0.000 | 0.000 | 0.000 | 0.000 | 0.000 |
| **Σ T-site** | 6.110 | 6.113 | 6.121 | 6.116 | 6.110 | 6.106 | 6.114 | 6.110 |
| B (*calc.*) | 3.000 | 3.000 | 3.000 | 3.000 | 3.000 | 3.000 | 3.000 | 3.000 |
| H (*calc.*) | 3.439 | 3.350 | 3.368 | 3.380 | 3.415 | 3.428 | 3.431 | 3.478 |
| F | 0.561 | 0.650 | 0.632 | 0.620 | 0.585 | 0.572 | 0.569 | 0.522 |
| **Σ W+V sites** | 4.000 | 4.000 | 4.000 | 4.000 | 4.000 | 4.000 | 4.000 | 4.000 |
| | | | | | | | | |
| **Species** | *fluor-schorl* | *fluor-schorl* | *fluor-schorl* | *fluor-schorl* | *fluor-schorl* | *fluor-schorl* | *fluor-schorl* | *fluor-schorl* |

Table 97 Additional tourmaline analyses from Sturgeon River pegmatite. *Apfu* calculations based on 31 anions.

GROVELAND MINE PEGMATITE

| FERROCOLUMBITE – GROVELAND MINE PEGMATITE | | | | | | | | | | | |
|---|---|---|---|---|---|---|---|---|---|---|---|
| Wt% Ox | grain 4-1 | grain 4-2 | grain 10-1 | grain 10-2 | grain 11-1 | grain 11-2 | Goi 10-1 | Goi 12-1 | Goi 13-1 | Goi 14-1 | Goi 14-2 |
| $Nb_2O_5$ | 69.898 | 69.870 | 65.110 | 64.984 | 65.110 | 65.094 | 67.988 | 69.666 | 70.322 | 69.011 | 67.233 |
| $Ta_2O_5$ | 9.655 | 9.621 | 14.887 | 14.900 | 14.699 | 14.667 | 11.311 | 9.877 | 8.454 | 9.456 | 11.870 |
| $SiO_2$ | 0.030 | 0.000 | 0.016 | 0.013 | 0.054 | 0.051 | 0.025 | 0.033 | 0.112 | 0.065 | 0.036 |
| $TiO_2$ | 0.165 | 0.251 | 0.113 | 0.105 | 0.055 | 0.060 | 0.023 | 0.034 | 0.065 | 0.088 | 0.254 |
| $Al_2O_3$ | 0.000 | 0.042 | 0.000 | 0.000 | 0.000 | 0.000 | 0.054 | 0.000 | 0.033 | 0.112 | 0.021 |
| $Sc_2O_3$ | 0.009 | 0.011 | 0.009 | 0.000 | 0.000 | 0.000 | 0.000 | 0.000 | 0.000 | 0.000 | 0.000 |
| FeO | 17.322 | 17.112 | 16.005 | 15.933 | 16.322 | 16.400 | 16.344 | 16.778 | 16.333 | 16.445 | 16.033 |
| MnO | 2.955 | 3.156 | 4.009 | 4.155 | 3.699 | 3.712 | 3.400 | 3.588 | 4.321 | 4.178 | 4.611 |
| MgO | *bdl* | *bdl* | *bdl* | *bdl* | *bdl* | *bdl* | *bdl* | *bdl* | *bdl* | *bdl* | *bdl* |
| Total | 100.034 | 100.063 | 100.149 | 100.090 | 99.939 | 99.984 | 99.145 | 99.976 | 99.640 | 99.355 | 100.058 |
| *apfu* | | | | | | | | | | | |
| Fe | 0.845 | 0.834 | 0.797 | 0.795 | 0.814 | 0.818 | 0.810 | 0.820 | 0.796 | 0.808 | 0.790 |
| Mn | 0.146 | 0.156 | 0.202 | 0.210 | 0.187 | 0.188 | 0.171 | 0.178 | 0.213 | 0.208 | 0.230 |
| Si | 0.002 | 0.000 | 0.001 | 0.001 | 0.003 | 0.003 | 0.001 | 0.002 | 0.007 | 0.004 | 0.002 |
| Al | 0.000 | 0.003 | 0.000 | 0.000 | 0.000 | 0.000 | 0.004 | 0.000 | 0.002 | 0.008 | 0.001 |
| Sc | 0.000 | 0.001 | 0.000 | 0.000 | 0.000 | 0.000 | 0.000 | 0.000 | 0.000 | 0.000 | 0.000 |
| Mg | *bdl* | *bdl* | *bdl* | *bdl* | *bdl* | *bdl* | *bdl* | *bdl* | *bdl* | *bdl* | *bdl* |
| **Σ X-site** | 0.993 | 0.994 | 1.000 | 1.006 | 1.004 | 1.009 | 0.986 | 1.000 | 1.018 | 1.028 | 1.023 |
| Nb | 1.843 | 1.841 | 1.754 | 1.752 | 1.756 | 1.755 | 1.821 | 1.841 | 1.853 | 1.832 | 1.790 |
| Ta | 0.153 | 0.152 | 0.241 | 0.242 | 0.239 | 0.238 | 0.182 | 0.157 | 0.134 | 0.151 | 0.190 |
| Ti | 0.007 | 0.011 | 0.005 | 0.005 | 0.002 | 0.003 | 0.001 | 0.001 | 0.003 | 0.004 | 0.011 |
| **Σ Y-site** | 2.003 | 2.004 | 2.000 | 1.999 | 1.997 | 1.996 | 2.004 | 1.999 | 1.990 | 1.987 | 1.991 |

Table 98 Additional ferrocolumbite analyses from Groveland Mine pegmatite. *Apfu* calculations based on 6 oxygens.

| FERROTANTALITE – GROVELAND MINE PEGMATITE | | | | | | | | |
|---|---|---|---|---|---|---|---|---|
| Wt% Ox | GOI grain 1-1 | GOI grain 1-2 | GOI grain 2-1 | GOI grain 2-2 | GOI grain 3-1 | GOI grain 3-2 | GOI grain 7-1 | GOI grain 7-2 |
| $Nb_2O_5$ | 31.445 | 20.778 | 31.092 | 8.776 | 8.900 | 30.222 | 8.322 | 29.888 |
| $Ta_2O_5$ | 51.677 | 63.511 | 52.005 | 75.623 | 75.445 | 52.966 | 76.112 | 53.210 |
| $SiO_2$ | 0.022 | 0.031 | 0.040 | 0.022 | 0.030 | 0.022 | 0.031 | 0.040 |
| $TiO_2$ | 0.033 | 0.000 | 0.031 | 0.000 | 0.000 | 0.000 | 0.000 | 0.000 |
| $Al_2O_3$ | 0.000 | 0.012 | 0.000 | 0.000 | 0.034 | 0.000 | 0.000 | 0.044 |
| FeO | 10.119 | 9.523 | 9.994 | 8.998 | 8.655 | 9.811 | 8.445 | 9.565 |
| MnO | 6.700 | 6.443 | 6.934 | 6.347 | 6.988 | 6.889 | 7.121 | 7.155 |
| MgO | *bdl* | *bdl* | *bdl* | *bdl* | *bdl* | *bdl* | *bdl* | *bdl* |
| Total | 99.996 | 100.309 | 100.096 | 99.766 | 100.052 | 99.910 | 100.051 | 99.902 |
| *apfu* | | | | | | | | |
| Fe | 0.598 | 0.596 | 0.591 | 0.608 | 0.582 | 0.584 | 0.570 | 0.570 |
| Mn | 0.401 | 0.408 | 0.415 | 0.434 | 0.476 | 0.416 | 0.487 | 0.432 |
| Si | 0.002 | 0.002 | 0.003 | 0.002 | 0.002 | 0.002 | 0.003 | 0.003 |
| Al | 0.000 | 0.001 | 0.000 | 0.000 | 0.003 | 0.000 | 0.000 | 0.004 |
| Mg | *bdl* | *bdl* | *bdl* | *bdl* | *bdl* | *bdl* | *bdl* | *bdl* |
| **Σ X-site** | 1.001 | 1.007 | 1.009 | 1.044 | 1.063 | 1.002 | 1.060 | 1.009 |
| Nb | 1.005 | 0.703 | 0.994 | 0.320 | 0.323 | 0.973 | 0.304 | 0.963 |
| Ta | 0.993 | 1.293 | 1.000 | 1.661 | 1.650 | 1.026 | 1.671 | 1.031 |
| Ti | 0.002 | 0.000 | 0.002 | 0.000 | 0.000 | 0.000 | 0.000 | 0.000 |
| **Σ Y-site** | 2.000 | 1.996 | 1.996 | 1.981 | 1.973 | 1.999 | 1.975 | 1.994 |

Table 99 Additional ferrotantalite analyses from Groveland Mine pegmatite. *Apfu* calculations based on 6 oxygens.

| PLAGIOCLASE FELDSPAR – GROVELAND MINE PEGMATITE | | | | |
|---|---|---|---|---|
| Wt% ox | grain 8-1 | grain 8-2 | grain 10-1 | grain 10-2 |
| $P_2O_5$ | 0.000 | 0.000 | 0.000 | 0.009 |
| $SiO_2$ | 68.540 | 64.678 | 68.544 | 64.599 |
| $TiO_2$ | 0.000 | 0.024 | 0.000 | 0.012 |
| $Al_2O_3$ | 19.740 | 18.553 | 19.683 | 18.573 |
| $FeO_t$ | 0.000 | 0.012 | 0.000 | 0.012 |
| CaO | 0.000 | 0.000 | 0.155 | 0.000 |
| $Na_2O$ | 11.344 | 0.565 | 11.677 | 0.672 |
| $K_2O$ | 0.200 | 15.600 | 0.200 | 15.773 |
| $Rb_2O$ | 0.000 | 0.018 | 0.000 | 0.023 |
| **Total** | 99.824 | 99.450 | 100.259 | 99.673 |
| *apfu* | | | | |
| K | 0.011 | 0.922 | 0.011 | 0.932 |
| Na | 0.961 | 0.051 | 0.987 | 0.060 |
| Ca | 0.000 | 0.000 | 0.007 | 0.000 |
| Rb | 0.000 | 0.001 | 0.000 | 0.001 |
| **Σ X-site** | 1.005 | 0.994 | 0.994 | 0.994 |
| Al | 1.017 | 1.013 | 1.011 | 1.014 |
| Fe | 0.000 | 0.000 | 0.000 | 0.000 |
| **Σ Y-site** | 1.017 | 1.013 | 1.011 | 1.014 |
| Si | 2.995 | 2.996 | 2.988 | 2.991 |
| Ti | 0.000 | 0.001 | 0.000 | 0.000 |
| P | 0.000 | 0.000 | 0.000 | 0.000 |
| Al | 0.000 | 0.000 | 0.000 | 0.000 |
| **Σ Z-site** | 2.995 | 2.996 | 2.988 | 2.991 |

Table 100 Additional plagioclase feldspar analyses from Groveland Mine pegmatite. *Apfu* calculations based on 8 oxygens.

| GARNETS – GROVELAND MINE PEGMATITE | | | | | | | | | | | | |
|---|---|---|---|---|---|---|---|---|---|---|---|---|
| Wt % Ox | GMP 5-grain 6-1 | GMP 5-grain 6-2 | GMP 5 grain 7-1 | GMP 5-grain 7-2 | GMP 5-grain 8-1 | GMP 5-grain 8-2 | GMP 5-grain 9-1 | GMP 5-grain 9-2 | GMP 5-grain 10-1 | GMP 5-grain 10-2 | GMP 5-grain 11-1 | GMP 5-grain 11-2 |
| $SiO_2$ | 36.522 | 36.459 | 36.556 | 36.533 | 36.522 | 36.548 | 36.540 | 36.488 | 36.533 | 36.465 | 36.433 | 36.439 |
| $TiO_2$ | 0.031 | 0.027 | 0.030 | 0.025 | 0.011 | 0.014 | 0.031 | 0.023 | 0.009 | 0.012 | 0.010 | 0.014 |
| $Al_2O_3$ | 20.455 | 20.563 | 20.544 | 20.543 | 20.566 | 20.533 | 20.544 | 20.566 | 20.549 | 20.563 | 20.544 | 20.531 |
| FeO | 36.099 | 36.100 | 36.400 | 36.355 | 36.477 | 36.700 | 41.443 | 41.544 | 36.655 | 36.673 | 36.543 | 36.577 |
| MnO | 6.899 | 7.009 | 6.677 | 6.750 | 6.544 | 6.431 | 0.233 | 0.187 | 6.556 | 6.599 | 6.445 | 6.501 |
| MgO | 0.021 | 0.032 | 0.023 | 0.034 | 0.031 | 0.022 | 0.987 | 1.098 | 0.112 | 0.098 | 0.085 | 0.077 |
| CaO | 0.209 | 0.188 | 0.133 | 0.099 | 0.117 | 0.141 | 0.032 | 0.041 | 0.223 | 0.243 | 0.188 | 0.176 |
| **Total** | 100.236 | 100.378 | 100.363 | 100.339 | 100.268 | 100.389 | 99.810 | 99.956 | 100.648 | 100.668 | 100.248 | 100.317 |
| *apfu* | | | | | | | | | | | | |
| Ti | 0.002 | 0.002 | 0.002 | 0.002 | 0.001 | 0.001 | 0.002 | 0.001 | 0.001 | 0.001 | 0.001 | 0.001 |
| Fe | 2.489 | 2.487 | 2.506 | 2.504 | 2.514 | 2.527 | 2.852 | 2.857 | 2.519 | 2.521 | 2.520 | 2.521 |
| Mn | 0.482 | 0.489 | 0.466 | 0.471 | 0.457 | 0.449 | 0.016 | 0.013 | 0.456 | 0.460 | 0.450 | 0.454 |
| Mg | 0.003 | 0.004 | 0.003 | 0.004 | 0.004 | 0.003 | 0.121 | 0.135 | 0.014 | 0.012 | 0.010 | 0.009 |
| Ca | 0.018 | 0.017 | 0.012 | 0.009 | 0.010 | 0.012 | 0.003 | 0.004 | 0.020 | 0.021 | 0.017 | 0.016 |
| **Σ X-site** | 2.995 | 2.999 | 2.992 | 2.993 | 2.990 | 2.994 | 2.996 | 3.003 | 3.002 | 3.005 | 2.998 | 2.999 |
| Al | 1.988 | 1.996 | 1.994 | 1.994 | 1.997 | 1.993 | 1.993 | 1.993 | 1.990 | 1.993 | 1.996 | 1.995 |
| **Σ Y-site** | 1.988 | 1.996 | 1.994 | 1.994 | 1.997 | 1.993 | 1.993 | 1.993 | 1.990 | 1.993 | 1.996 | 1.995 |
| Si | 3.011 | 3.003 | 3.010 | 3.009 | 3.009 | 3.009 | 3.007 | 3.000 | 3.002 | 2.998 | 3.004 | 3.003 |
| **Σ Z-site** | 3.011 | 3.003 | 3.010 | 3.009 | 3.009 | 3.009 | 3.007 | 3.000 | 3.002 | 2.998 | 3.004 | 3.003 |
| **Component** | | | | | | | | | | | | |
| Andradite | 00 | 00 | 00 | 00 | 00 | 00 | 00 | 00 | 00 | 01 | 00 | 00 |
| Pyrope | 00 | 00 | 00 | 00 | 00 | 00 | 04 | 04 | 01 | 01 | 00 | 00 |
| Spessartine | 16 | 16 | 16 | 16 | 16 | 16 | 01 | 01 | 15 | 14 | 15 | 15 |
| Grossular | 01 | 01 | 00 | 00 | 00 | 00 | 00 | 00 | 00 | 00 | 01 | 01 |
| Almandine | 83 | 83 | 84 | 84 | 84 | 84 | 95 | 95 | 84 | 84 | 84 | 84 |

Table 101 Additional garnet analyses from Groveland Mine pegmatite. *Apfu* calculations based on 12 oxygens.

# VITA

The author was born in Monroe, Louisiana and grew up outside the city limits of West Monroe, Louisiana in the tiny town of Brownsville. His passion for rocks and minerals began when he was a child, as he spent many days collecting rocks in his parents' driveway. He began his collegiate career later than anticipated. He enrolled at the University of New Orleans after much encouragement from a dear friend. Following his early interests, he pursued a Bachelor's degree of Science in Geology and completed his undergraduate degree in May of 2013 summa cum laude with departmental and university of honors.

His undergraduate honors thesis topic focused on carbonate pods of the Mt. Mica pegmatite in Maine under the guidance of Dr. William "Skip" Simmons, Mr. Alexander Falster, and Dr. Karen Webber. He was accepted into the Graduate program in the Fall of 2013 and continued working with these three professors. He has had many travel opportunities to see many different rocks while under their tutelage.

The author has had two name changes during the course of his college academic career. Leopold came from Alexander Falster and represents his academic pursuits. He legally married in his final semester of graduate school and will take his husband's last name of Van Daalen soon. He hopes to legally change his name to Leopold as well.

Leopold will complete his M.S. in Geology in December of 2015 and hopes to begin work soon.